



HAL
open science

Synthesis of anisotropic polymer / inorganic composite particles via RAFT-mediated emulsion polymerization

Ana Maria Cenacchi Pereira

► **To cite this version:**

Ana Maria Cenacchi Pereira. Synthesis of anisotropic polymer / inorganic composite particles via RAFT-mediated emulsion polymerization. Inorganic chemistry. Université Claude Bernard - Lyon I, 2014. English. NNT: 2014LYO10081 . tel-01067453

HAL Id: tel-01067453

<https://theses.hal.science/tel-01067453>

Submitted on 23 Sep 2014

HAL is a multi-disciplinary open access archive for the deposit and dissemination of scientific research documents, whether they are published or not. The documents may come from teaching and research institutions in France or abroad, or from public or private research centers.

L'archive ouverte pluridisciplinaire **HAL**, est destinée au dépôt et à la diffusion de documents scientifiques de niveau recherche, publiés ou non, émanant des établissements d'enseignement et de recherche français ou étrangers, des laboratoires publics ou privés.

THESE DE L'UNIVERSITE DE LYON
Délivrée par
L'UNIVERSITE CLAUDE BERNARD LYON 1

ECOLE DOCTORALE DE CHIMIE (ED 206)
Spécialité : Chimie

DIPLOME DE DOCTORAT
(arrêté du 7 août 2006)

**SYNTHESIS OF ANISOTROPIC POLYMER/INORGANIC
COMPOSITE PARTICLES VIA RAFT-MEDIATED EMULSION
POLYMERIZATION**

Thèse soutenu le 5 juin 2014 par :

Ana Maria CENACCHI PEREIRA

Directrice de thèse : Dr. Elodie BOURGEAT-LAMI

Composition du jury :

M. Philippe CASSAGNAU	Professeur, Université Lyon 1	Examineur
M. Philipp VANA	Professeur, University of Göttingen	Rapporteur
M. Jean-Paul CHAPEL	Chargé de recherche, CNRS	Rapporteur
M^{me} Vanessa PREVOT	Chargée de recherche, CNRS	Examineur
M^{me} Elodie BOURGEAT-LAMI	Directeur de recherche, CNRS	Directrice de thèse
M^{me} Muriel LANSALOT	Chargée de recherche, CNRS	Co-encadrante
M. Antoine THILL	Chercheur CEA	Membre invité
M. Franck D'AGOSTO	Chargé de recherche, CNRS	Membre invité

Acknowledgments

These three years of work were performed from April 2011 to May 2014 in the C2P2 laboratory, in the LCPP team. Here I would like to acknowledge the various people who contributed and supported me to complete this work.

I am grateful for the **IUPAC** for enabling the ENCIRCLE project and the **CNRS** for funding our researches. Without the support of these two organisms this work wouldn't have been possible. I also thank the *École Doctorale de Chimie de Lyon* for their assistance during the thesis submission procedures.

It wouldn't be fair to forget the two directors which were in charge of our laboratory during my PhD work, **Bernadette Charleux** and **Timothy McKenna**. I acknowledge them for all the support and the opportunities they provided me.

I am deeply grateful for **Prof. Philipp VANA** and **Dr. Jean-Paul CHAPEL** for dedicating their precious time to review this thesis and for their wise remarks and interesting discussions brought up during the PhD defense. I would also like to thank all the people who composed the defense committee, **Dr. Vanessa PREVOT**, **Dr. Antoine THILL**, **Dr. Elodie BOURGEAT-LAMI**, **Dr. Muriel LANSALOT**, **Dr. Franck D'AGOSTO** and, in special, **Prof. Philippe CASSAGNAU**, who accepted to be the president of the committee.

J'aimerais maintenant remercier de tout mon cœur mes trois encadrants de thèse : **Elodie BOURGEAT-LAMI**, **Muriel LANSALOT** et **Franck D'AGOSTO**, pour l'opportunité de faire ma thèse au LCPP. **Elodie**, je laisse ici ma profonde gratitude pour tout ce que tu as fait pour moi. Pour ton accueil déjà en 2008, pour m'avoir aidé à m'installer et m'intégrer en France et au labo, et pour m'avoir donné un vœu de confiance pour que je revienne faire ma thèse en France. Je te remercie également pour tous les conseils, les discussions (scientifiques ou pas), les réunions, les voyages, les dîners, les opportunités, les idées que tu as partagé avec moi pendant ces années. Tu as su me motiver, me comprendre (dans la plus part de cas), m'écouter et me guider dans la bonne direction, et tu étais toujours là quand j'ai eu besoin. Je considère avoir en toi une amie. Merci! **Muriel** et **Franck**, je vous remercie énormément pour l'engagement et la participation que vous avez dédiée à mon travail et à ma formation. Je vous remercie pour les échanges, les discussions, les réunions, les présentations, les bons conseils... j'ai appris avec vous des valeurs important qui ont contribués à ma formation professionnelle et personnelle. Avec leurs personnalités différentes, mes trois encadrants de thèse ont contribué pour mon développement en tant que chercheur et en tant qu'être humain. Avec leur orientation, leur humour, leurs idées novatrices, leur patience et leur organisation, ils m'ont appris à faire face aux problèmes pendant mon travail et dans la vie en générale. Ils essayaient toujours de

valoriser mes résultats, pour me pousser et m'encourager à aller plus loin. Ça a été un énorme plaisir de travailler avec vous, et vous me manquerez sûrement !

Não poderia deixar de agradecer ao meu primeiro tutor, quem me iniciou na vida científica e me ensinou “os prazeres” da pesquisa: **Prof. Amilton Martins dos Santos**. Meus sinceros agradecimentos pelas oportunidades, pelos conselhos, pelas conversas, pelo voto de confiança, pela paciência, pelo acompanhamento e pela amizade durante todos esses anos. Também agradeço à **Gizelda Maria Alves** e **Raul Paxeco de Moraes**, pela amizade e por todo auxílio em minha formação.

Je suis également reconnaissante pour toute l'aide reçus par **Dr. Antoine THILL**, **Dr. Erwan PAINEAU** et **Dr. Béatrice GUIOSE** concernant la synthèse des Imogolites, toutes les caractérisations par SAXS et WAXS et les discussions scientifiques très riches que nous avons échangés sur le sujet. Je dois aussi remercier **Dr. Vanessa PREVOT** et **Dr. Dessie KOSTADINOVA**, avec qui j'ai eu le plaisir de travailler, pour leur aide avec la synthèse des HDL, pour les discussions scientifiques et pour la collaboration en générale. Sans ces deux équipes, ce travail n'aurait pas été possible.

Ma gratitude aussi à **Jean-Luc PUTEAUX** et **Maria BACIA** pour leur aide avec les analyses Cryo TEM de haute résolution.

Je dois aussi remercier **Laurent CHAZEAU**, **Cyril VECHAMBRE** et **Florent DALMAS**, qui ont participé à ce projet et qui ont garanti le support concernant les analyses mécaniques et microstructurales des films.

Também registro aqui minha gratidão aos amigos **Prof. Ana BARROS**, **Rodrigo** e **Liliana**, pela contribuição e pelas trocas de experiências, que também trouxeram avanço ao trabalho. Quero agradecer em especial à amiga **Thaíssa**, pelo apoio, amizade, paciência em me escutar, boa vontade, pelas conversas, pelos conselhos científicos, pelos momentos passados juntas e pelo companheirismo, dos quais com certeza sentirei falta!

Une fois au LCPP, j'ai eu l'opportunité de connaître l'équipe de chercheurs et techniciens permanents du laboratoire, et j'ai fait des bons amis. Ici, j'aimerais remercier **Nathalie** pour l'accueil, l'aide avec tous les aspects bureaucratiques, et la sympathie. Je remercie **Jean-Pierre** pour l'aide au niveau bricolage et pour son envie de m'apprendre le français et de m'initier à la vraie musique française ! Je laisse ici mon grand merci à **Pierre-Yves**, non seulement pour toute son aide avec les images Cryo TEM, mais également pour les soirées, les restos, les mangas, les films et séries, les discussions variées (politique, histoire, chimie, faits divers...surtout faits divers !) et pour son amitié, que j'espère garder pour encore plusieurs années avec toi et **Kessy**. Je remercie aussi **Olivier**, pour son humour, pour les discussions, pour la compagnie pendant les TPs et surtout pour son aide avec la

caractérisation de films en DSC et FTIR. Je remercie aussi **Vincent, Sébastien, Jean, Fabrice** et **Christophe** pour les moments partagés soit autour d'un « délicieux » repas à la cantine, soit en salle de pause.

Je remercie maintenant mes collègues de bureau, **Isabelle, Xuewei** et **Emilie V.**, avec qui j'ai partagé de moments de stress, de joie et de réflexion. Merci pour la compagnie et l'amitié. Je remercie aussi mes collègues **Wenjing** (pour son humour singulier et ses délicieux repas!), **Cédric, Céline, Emilie G., Benoît, Guilhem, Laura, Thomas, Keran, Amélie, Arthur, Solmaz, Arash, Manele, Qiao, Leila, Thiago, Bárbara, Anthony, Aaron** et **Ana Carolina**, qui ont rendu la vie au labo plus agréable. Merci **Estevan** pour les bals folks, **Francis** pour les sorties et **Etienne** pour les jeux de mots. Je ne pourrais pas oublier de laisser un très grand merci à mes chers voisins **Julien** et **Elena**. À Julien, mon merci pour tout ! Si je fais une liste de tous ce qu'il a fait pour moi, ça ne rentrerait pas dans une page. Merci !! A Elena, grazie per tutti i momenti che abbiamo passato insieme, per la amicizia, per i viaggi e pela cumplicità. Guarderò nel cuore!

Todo este trabalho não teria sido possível sem o apoio de minha **família**. Sou grata aos meus pais, **Genis** e **Patricia**, pela força, pela compreensão, pelo incentivo, pelos conselhos e orientações e pelo amor, que venho recebendo desde que nasci. Grata também à meus irmãos **João, Tiago, Miguel** e **Paulo**. Grata por todos os gestos de atenção, que me permitiram continuar meu trabalho com serenidade.

Grata ao meu marido, **Filipe**, pela paciência, pela perseverança, pela compreensão, pelo apoio, pela amizade, pelos conselhos e pela coragem de seguir comigo neste caminho!

Ana Maria CENACCHI PEREIRA

Villeurbanne, September, 2014

UNIVERSITE CLAUDE BERNARD – LYON 1

Président de l'Université

Vice-président du Conseil d'Administration

Vice-président du Conseil des Etudes et de la Vie Universitaire

Vice-président du Conseil Scientifique

Directeur Général des Services

M. François-Noël GILLY

M. le Professeur Hamda BEN HADID

M. le Professeur Philippe LALLE

M. le Professeur Germain GILLET

M. Alain HELLEU

COMPOSANTES SANTE

Faculté de Médecine Lyon Est – Claude Bernard

Faculté de Médecine et de Maïeutique Lyon Sud – Charles Mérieux

Faculté d'Odontologie

Institut des Sciences Pharmaceutiques et Biologiques

Institut des Sciences et Techniques de la Réadaptation

Département de formation et Centre de Recherche en Biologie Humaine

Directeur : M. le Professeur J. ETIENNE

Directeur : Mme la Professeure C. BURILLON

Directeur : M. le Professeur D. BOURGEOIS

Directeur : Mme la Professeure C. VINCIGUERRA

Directeur : M. le Professeur Y. MATILLON

Directeur : M. le Professeur P. FARGE

COMPOSANTES ET DEPARTEMENTS DE SCIENCES ET TECHNOLOGIE

Faculté des Sciences et Technologies

Département Biologie

Département Chimie Biochimie

Département GEP

Département Informatique

Département Mathématiques

Département Mécanique

Département Physique

Département Sciences de la Terre

UFR Sciences et Techniques des Activités Physiques et Sportives

Observatoire des Sciences de l'Univers de Lyon

Polytech Lyon

Ecole Supérieure de Chimie Physique Electronique

Institut Universitaire de Technologie de Lyon 1

Institut Universitaire de Formation des Maîtres

Institut de Science Financière et d'Assurances

Directeur : M. le Professeur F. DE MARCHI

Directeur : M. le Professeur F. FLEURY

Directeur : Mme le Professeur H. PARROT

Directeur : M. N. SIAUVE

Directeur : M. le Professeur S. AKKOUCHE

Directeur : M. le Professeur A. GOLDMAN

Directeur : M. le Professeur H. BEN HADID

Directeur : Mme S. FLECK

Directeur : Mme la Professeure I. DANIEL

Directeur : M. C. COLLIGNON

Directeur : M. B. GUIDERDONI

Directeur : M. P. FOURNIER

Directeur : M. G. PIGNAULT

Directeur : M. C. VITON

Directeur : M. A. MOUGNIOTTE

Administrateur provisoire : M. N. LEBOISNE

Synthesis of anisotropic polymer/inorganic composite particles via RAFT-mediated emulsion polymerization

This work describes the elaboration of hybrid latexes of polymer/Imogolite nanotubes and polymer/layered double hydroxide (LDH) nanosheets in aqueous dispersed media. The two inorganic materials were chosen as fillers for their thermal and mechanical properties and especially for their shape anisotropy, which could lead to the formation of nanostructured films. The latexes were synthesized through an original polymerization strategy based on the RAFT process in emulsion. The strategy consists in the use of hydrophilic random copolymers, containing acrylic acid units and a thiocarbonylthio end group, as both coupling agents and stabilizers. These copolymers, herein named macroRAFT agents, were tethered to the surface of the inorganic nanoparticles and chain extended by the polymerization of a hydrophobic monomer in a semi-batch process. Polymer-decorated Imogolite nanotubes or encapsulated nanotube bundles were obtained according to the process conditions. The effect of different parameters on the final morphology and latex stability was studied, and the macroRAFT nature was proven to be the key factor to achieve encapsulation. The same strategy was then applied to LDH materials. The different conditions tested all led to the encapsulation of the nanosheets. In both cases, the morphology of the nanocomposite latexes was characterized by TEM and cryo-TEM and correlated with the surface modification and the experimental conditions. The mechanical properties and the microstructure of hybrid films of polymer/Imogolite were studied by DMA and TEM, respectively, and correlated with the latex particles morphology.

Keywords: Imogolite, nanotubes, layered double hydroxides (LDH), encapsulation, emulsion polymerization, RAFT, latexes, nanocomposites, films, mechanical properties.

Synthèse de particules composites anisotropes polymère/inorganique par polymérisation RAFT en émulsion

Ces travaux décrivent l'élaboration de latex hybrides de polymère/nanotubes d'Imogolite et polymère/nanofeuillets d'hydroxydes doubles lamellaires (HDL) en milieu aqueux dispersé. Les deux charges inorganiques ont été choisies pour leurs propriétés thermiques, mécaniques et pour leur anisotropie de forme, ce qui pourrait permettre l'élaboration de films nanostructurés. Les latex ont été synthétisés par une stratégie originale basée sur le procédé de polymérisation RAFT en émulsion. Cette stratégie consiste à utiliser des copolymères hydrophiles (macroRAFT), comportant à la fois des unités d'acide acrylique et un groupe trithiocarbonate terminal, comme agents de couplage et stabilisants. Dans un premier temps ces macroRAFTs ont été adsorbés à la surface des nanoparticules inorganiques, puis l'extension de ces chaînes a été réalisée par la polymérisation d'un monomère hydrophobe selon un procédé semi-batch. Des nanotubes d'Imogolite décorés de particules de latex ou des nanotubes d'Imogolite encapsulés ont été obtenus, selon les conditions de synthèse adoptées. L'effet de différents paramètres sur la morphologie finale des particules hybrides a été étudié. La nature de l'agent macroRAFT s'est avérée être un paramètre clé pour le succès de l'encapsulation. La même stratégie a été utilisée en vue de l'encapsulation des HDL. Quelles que soient les conditions investiguées, des latex stables contenant des particules d'HDL encapsulées par du polymère ont été formés. Dans tous les cas, la morphologie des latex nanocomposites a été caractérisée par MET et cryo-MET et reliée à la méthode de modification de la surface et aux conditions de polymérisation. Enfin, les propriétés mécaniques ainsi que la microstructure des films hybrides de polymère/nanotubes d'Imogolite ont été étudiées par DMA et MET, respectivement, et reliées à la morphologie des particules de latex.

Mots clés : Nanotubes, Imogolite, hydroxydes doubles lamellaires (HDL), encapsulation, polymérisation en émulsion, RAFT, latex, nanocomposites, films, propriétés mécaniques.

Table of contents

Abbreviations	XV
General Introduction	XIX
Chapter I – Bibliographic Review	XXIII
I.1. Introduction	1
I.2. Polymer/Inorganic Composite Materials	2
I.2.1 Alignment of inorganic particles into polymer matrixes.....	5
I.2.1.1 Linear-template method.....	6
I.2.1.2 Template-free self-assembly.....	7
I.2.1.3 External force-induced nanoparticles assembly.....	8
I.2.1.3.1 Shear-induced nanoparticles alignment.....	9
I.2.1.3.2 Magnetic field-induced nanoparticles alignment.....	10
I.2.1.3.3 Electric field-induced nanoparticles alignment.....	13
I.2.2 Anisotropic particles.....	15
I.3 Polymer-encapsulation of anisotropic particles	18
I.3.1 Free-Radical Emulsion Polymerization.....	18
I.3.2 Reversible Deactivation Radical Polymerization (RDRP) in Emulsion.....	23
I.3.2.1 Nitroxide-mediated polymerization (NMP).....	24
I.3.2.2 Atom transfer radical polymerization (ATRP).....	25
I.3.2.3 Reversible addition-fragmentation chain transfer (RAFT).....	25
I.3.2.4 Reversible Addition-Fragmentation chain Transfer (RAFT) and its application to dispersed media.....	27
I.3.2.4.1 Conventional RAFT emulsion polymerization.....	31
I.3.2.4.2 Polymerization-induced self-assembly (PISA) RAFT emulsion polymerization.....	31
I.3.3 Use of RDRP for the modification and encapsulation of inorganic particles.....	33
I.3.3.1 Grafting from.....	34
I.3.3.1.1 Grafting from using RAFT.....	35
I.3.3.2 Grafting to.....	37
I.3.3.3 Block copolymers self-assembly in presence of inorganic particles.....	39
I.3.3.4 MacroRAFT-assisted encapsulating emulsion polymerization.....	44
I.4. Conclusions	52
I.5. References	54
Chapter II – Polymer/Ge-Imogolite nanocomposite latexes	60
II.1. Introduction	62
II.2 Bibliographic study of Imogolite Nanotubes	64
II.2.1 Imogolite discovery.....	64

II.2.2 Imogolite structure.....	64
II.2.3 Imogolite synthesis and characterization.....	66
II.2.4 Applications.....	74
II.3. MacroRAFT agents synthesis.....	89
II.3.1 Experimental section.....	89
II.3.2 Results and Discussion.....	91
II.3.3 Conclusions.....	96
II.4 Imogolite nanotubes.....	98
II.5 Preliminary Imogolite encapsulating experiments.....	102
II.5.1 Experimental section.....	102
II.5.2 Results and Discussion.....	103
II.6 Acrylic acid-based macroRAFT/Imogolite interactions.....	109
II.6.1 Experimental section.....	110
II.6.2 Results and Discussion.....	111
II.6.3 Conclusions.....	118
II.7 MacroRAFT-assisted encapsulating emulsion polymerization.....	120
II.7.1 Experimental section.....	120
II.7.2 Results and discussion.....	121
II.7.3 Conclusions.....	145
II.8 Towards film-forming latexes.....	147
II.8.1 Latexes synthesis.....	147
II.8.1.1 Experimental section.....	147
II.8.1.2 Results and Discussion.....	148
II.8.1.3 Conclusions.....	160
II.8.2 Film formation and properties.....	161
II.8.2.1 Experimental section.....	161
II.8.2.2 Results and Discussion.....	163
II.8.2.3 Conclusions.....	182
II.9 General conclusions of chapter II.....	183
II.10 References.....	186
<i>Chapter III – Polymer/LDH nanocomposite latexes.....</i>	192
III.1. Introduction.....	193
III.2. Bibliographic study on Layered Double Hydroxide (LDH) materials.....	195
III.2.1 LDH structure.....	195
III.2.2 LDH synthesis.....	196
III.2.3 LDH modification and incorporation into polymer matrixes.....	203
II.2.4 Conclusions.....	222

III.3. Synthesis of colloidal suspensions of LDH platelets.....	223
III.3.1 Experimental section.....	223
III.3.2 Results and Discussion.....	227
III.3.3 Conclusions.....	232
III.4. LDH modification with RAFT and macroRAFT agents.....	234
III.4.1 Experimental section.....	234
III.4.2 Results and Discussion.....	237
III.4.3 Conclusions.....	249
III.5 Grafting from strategy.....	251
III.5.1 Experimental section.....	251
III.5.2 Results and Discussion.....	253
III.5.3 Conclusion.....	261
III.6. MacroRAFT-assisted encapsulating emulsion polymerization (REEP) of colloidal LDH.....	262
III.6.1 Experimental section.....	262
III.6.2 Results and Discussion.....	263
III.6.3 Conclusion.....	270
III.7. General conclusions of chapter III.....	272
III.8. References.....	274
General Conclusions.....	278
<i>Annexes.....</i>	282
A.1 SEC results of the polymerizations performed in the absence of Imogolite using acrylic acid- and methacrylic acid-based macroRAFT agents.....	283
A.2 Stability of the RAFT functionality of the acrylic acid-based macroRAFT copolymer with time at 80 °C and pH = 8.0.....	285
A.3 Effect of the interaction time on final hybrid latex morphology.....	286
A.4 SEC results of the polymerization of MA/BA (80/20 wt/wt) using P(AA-co-BA)-CTPPA macroRAFT at pH = 6.0.....	288
<i>Résumé en français.....</i>	290
Introduction générale.....	291
Chapitre I – Revue bibliographique.....	294
Chapitre II – Synthèse de latex hybrides polymère/nanotubes d’Imogolite.....	295
Chapitre III – Synthèse de latex hybrides polymère/nanofeuillets d’HDL.....	302
Conclusions générales et perspectives.....	306
References:.....	311

Abbreviations

[M]	Monomer concentration
[M] ₀ :	Initial monomer concentration (mol L ⁻¹)
[M] _p	Monomer concentration inside the particles
[P•]	Concentration of active propagating species
[R•]	Concentration of propagating radicals
[RAFT] ₀ :	Initial RAFT agent concentration (mol L ⁻¹)
1D	One-dimensional
2D	two-dimensional
3D	three-dimensional
AA	Acrylic acid
AAM	Acrylamide
ACPA	4,4'-azobis(cyanopentanoic acid)
ADIBA	2,2'-Azobis(<i>N,N'</i> -dimethyleisobutyramidine) dihydrochloride
AFM	Atomic force microscopy
AIBA	2,2'-azobisisobutyramidine dihydrochloride
AIBN	2,2'-Azobisisobutyronitrile
APS	(γ -aminopropyl)triethoxysilane
ARGET ATRP	Activators regenerated by electron transfer atom-transfer radical polymerization
ATR-FTIR	Attenuated total reflectance Fourier transform infrared spectroscopy
ATRA	Atom-transfer radical addition
ATRP	Atom-transfer radical polymerization
AuNPs	Gold nanoparticles
BA	<i>n</i> -butyl acrylate
BCP	Block copolymer
BF-TEM	Bright field transmission electron microscopy
BIBA	α -Bromoisobutyric acid
BMA	<i>n</i> -butyl methacrylate
BMPOPO ₄ (NH ₄) ₂	8-(2-bromo-2-methylpropanoyloxy)octyl phosphate
BN	Boron nitride
BPO	Benzoyl peroxide
BrB	α -Bromobutyrate
BSE-SEM	Back-scattered electrons-Scanning electron microscopy
CMC	Critical micelle concentration
CNT	Carbon nanotubes
CRP	Controlled radical polymerization
CT μ	Centre technologique des microstructures
CTA	Chain transfer agent
CTA'	S,S'-bis(α,α' -dimethyl- α'' -acetic acid) trithiocarbonate
CTAB	Cetyl trimethylammonium bromide
CTPPA	4-cyano-4-thiothiopropylsulfanyl pentanoic acid
\mathcal{D}	Dispersity
DCB	Dichloro benzene
DCB	Dithionite-citrate-bicarbonate
DEAEMA	2-(diethylamino)ethyl methacrylate
DEP	Dielectrophoresis
D _h	Hydrodynamic average particle diameter
DHBC	Double hydrophilic block copolymers
DLS	Dynamic light scattering
DMA	Dynamic mechanical analysis
DMAc	Dimethylacetamide
DMAEA	Dimethylamino ethyl acrylate

DMAEMA	Dimethylamino ethyl methacrylate
DMAPS	3-dimethyl (methacryloyloxyethyl) ammonium propane sulfonate
DMC	2-methacryloyloxyethyl trimethyl ammonium chloride
DMF	Dimethyl formamide
DMSO	Dimethylsulfoxide
DP_n :	Number-average degree of polymerization
DSC	Differential scanning calorimetry
DT	Degenerative transfer
DW	Double-walled
EDAC	1-ethyl-3-(3-dimethylaminopropyl) carbodiimide hydrochloride
EDTA	Ethylenediamine tetraacetic acid
EtOH	Ethanol
EVA	Ethylene-vinyl acetate
FTIR	Fourrier transformed infrared spectroscopy
GO	Graphene oxide
HMTETA	1,1,4,7,10,10-hexamethyltriethylenetetramine
HPLC	High performance liquid chromatography
HPMC	Hydroxypropylmethyl cellulose
HRSNMR	High resolution solid-state nuclear magnetic resonance
HT3OP	2-(5''-hexyl-2,2':5',2''-terthiophen-5-yl)ethylphosphonic acid 1,1-dioxide
HT3P	2-(5''-hexyl-2,2':5',2''-terthiophen-5-yl)ethylphosphonic acid
HTT	Hydrothermal treatment
IBS	Institut de Biologie Structurale
ICCF	Institut de Chimie de Clermont-Ferrand
IEP	Isoelectric point
IR	Infrared spectroscopy
IS	Ionic strength
k_d	Decomposition rate constant
k_p	Propagation rate constant
KPS	Potassium persulfate
L	Length
LAM	Less activated monomers
LbL	Layer-by-layer
LC	Liquid crystals
LDH	Layered double hydroxide
LG	<i>N</i> -lauroyl-glutamate
M^{2+}	Divalent metal ion
M^{3+}	Trivalent metal ion
MA	Methyl acrylate
MAA	Methacrylic acid
macroRAFT	Macromolecular RAFT agent
MADIX	Macromolecular design via the interchange of xanthates
MAM	More activated monomers
MBAA	<i>N,N'</i> -methylene bis (acrylamide)
MFM	Magnetic force microscopy
MMA	Methyl methacrylate
$M_{monomer}$:	Monomer molar mass (g mol^{-1})
MMT	Montmorillonite
$M_{n, exp}$	Experimental number-average molar mass (g mol^{-1})
$M_{n, theo}$	Theoretical number-average molar mass (g mol^{-1})
M_n :	Number-average molar mass (g mol^{-1})
M_{RAFT} :	RAFT agent molar mass (g mol^{-1})
MW	Multi-walled
MWCNT	Multi-walled carbon nanotubes
\bar{n}	Average number of radicals per particle

Na	Avogadro's number
NAM	<i>N</i> -acryloylmorpholine
ND	Nanodiamond
NHS	<i>N</i> -hydroxysuccinimide
NMP	Nitroxide-mediated polymerization
NMR	Nuclear magnetic resonance
N _p	Number of particles
NPs	Nanoparticles
NR	Nanorod
NTs	Nanotubes
NWs	Nanowires
OPA	Octadecylphosphonic acid
P(EM- <i>co</i> -MA)	Poly(ethyl methacrylate- <i>co</i> -methyl acrylate)
P(MAA- <i>co</i> -BMA)	Poly(methacrylic acid- <i>co</i> - <i>n</i> -butyl methacrylate)
P(MMA- <i>co</i> -BA)	Poly(methyl methacrylate- <i>co</i> - <i>n</i> -butyl acrylate)
P2VP	Poly(2-vinylpyridine)
P3HT	Poly(3-hexyl thiophene)
P4VP	Poly(4-vinylpyridine)
PAA	Poly(acrylic acid)
PAAm	Polyacrylamide
PAH	Poly(allylamine hydrochloride)
PAM	Polyacrylamide
PBA	Poly(<i>n</i> -butyl acrylate)
PDADMAC	Poly(diallyldimethylammonium chloride)
PDDAC	Poly(diallyldimethylammonium chloride)
PDMAEA	Poly(dimethylamino ethyl acrylate)
PDMAEMA	Poly(dimethylamino ethyl methacrylate)
PDMAPS	Poly(3-dimethyl (methacryloyloxyethyl) ammonium propane sulfonate)
PDMS	Polydimethylsiloxane
PDP	3- <i>n</i> -pentadecylphenol
PE	Polyelectrolytes
PEI	Poly(ethyleneimine)
PEO	Poly(ethylene oxide)
PEOMA	Poly(ethylene oxide) methacrylate
PGMA	Poly(glycidyl methacrylate)
PHAE	Polyhydroxyaminoether
P-HEMA	2-acidophosphoxyethyl methacrylate
PISA	Polymerization-induced self-assembly
PLLA	Poly(L-lactic acid)
PLSN	Polymer/layered silicate nanocomposites
PMAA	Poly(methacrylic acid)
PMMA	Poy(methyl methacrylate)
POMS	Polyoxometalates
POSS	Polyhedral oligomeric silsesquioxanes
PPEI-EI	Poly(propionylethylenimine- <i>co</i> -ethylenimine)
PS	Polystyrene
PtBA	Poly(<i>tert</i> -butyl acrylate)
PTEA	Poly(trimethylammonium ethylacrylate)
PU	Polyurethane
PVA	Poly(vinyl alcohol)
PVC	Poly(vinyl chloride)
PVP	Polyvinylpyrrolidone
QD	Quantum dots
RAFT	Reversible addition-fragmentation chain transfer
RDRP	Reversible deactivation radical polymerization

REEP	MacroRAFT-assisted encapsulating emulsion polymerization
RITP	Reversible iodine transfer polymerization
SANS	Small angle neutron scattering
SAXS	Small angle X-ray scattering
SBC	Sodium 4-(benzodithioyl)-4-cyanopentanoic salt
SDS	Sodium dodecyl sulfate
SEC	Size exclusion chromatography
SEM	Scanning electron microscopy
SET-LRP	Single-electron transfer living radical polymerization
SI	Surface-initiated
STT	Solvothermal treatment
STY	Styrene
SW	Single-walled
TD	Thermal dissociation
TEM	Transmission electron microscopy
TEMPO	2,2,6,6-tetramethyl piperidine- <i>N</i> -oxide
TERP	Organotellurium-mediated radical polymerization
TG-DSC	Thermo gravimetric-differential scanning calorimetry
T_g	Glass transition temperature
$T_{g, FOX}$	T_g calculated by the Fox equation
TGA	Thermogravimetric analysis
THF	Tetrahydrofuran
TMPT	Trimethylolpropane thioglycolic acetate
TOPO	Trioctylphosphine oxide
Trizma	2-amino-2-(hydroxymethyl)-1,3-propanediol
T_α	Main relaxation temperature
UCBL	Université Claude Bernard
UHMW	Ultrahigh molecular weight
US	Ultrasound
UV-vis	Ultraviolet visible spectroscopy
VCM	Vinyl chloride monomer
VOC	Volatile organic compounds
V_p	Polymerization rate
V_p	Propagation rate
V_t	Termination rate
WAXD	Wide angle X-ray diffraction
WAXS	Wide angle X-ray scattering
X :	Monomer conversion (%)
XPS	X-ray photoelectron spectroscopy
XRD	X-ray diffraction
ZP	Zeta potential

General Introduction

The incorporation of inorganic fillers into polymer matrixes can undoubtedly confer interesting properties to the resulting materials. The combination of these two physically distinct matters allows the marriage between the best attributes of the inorganic part, such as stiffness, mechanical strength, chemical inertness, thermal resistance and optical properties (transparency, opacity) with the process and handling advantages of the organic part. Such materials are of great interest for applications in different areas of industry, like food, inks, paints, adhesives, paper coatings, textiles, pharmaceutical and cosmetics¹. Recent developments in the polymer nanocomposite field also drove their applications to new electronic and photonic technologies².

Physical properties of nanocomposites can be further improved with the controlled orientation of the fillers in the matrix². 1-dimensional (1D) assembly of inorganic particles inside polymer matrixes has thus become a recent field of research together with the development of new strategies for synthesizing polymer/inorganic nanocomposites containing anisotropic fillers.

Several strategies have been reported for the synthesis of such colloidal nanocomposites including heterocoagulation, layer-by-layer assembly techniques, and *in situ* polymerization.^{3, 4} Among the various polymerization methods, emulsion polymerization has attracted extensive attention due to its wide industrial application for the manufacture of various products (e.g. paints, adhesives, impact modifiers) and is especially well documented.¹

One of the greatest contributions to the polymer chemistry field by synthetic chemists was the development of living/reversible deactivation radical polymerization (RDRP) techniques more than 20 years ago, which allow the preparation of well-defined highly functional polymeric building blocks.⁵ The application of RDRP into aqueous dispersed media, in particular to emulsion polymerization, opened up renewed possibilities for the application of the technique to the elaboration of functional colloidal materials.⁵⁻⁷

Reversible addition-fragmentation chain transfer (RAFT) polymerization appears as one of the most versatile RDRP methods. Like other RDRP techniques, the RAFT process enables the preparation of polymers of narrow molar mass distributions and advanced architectures. Besides, it allows the polymerization of a vast range of monomers under mild conditions in aqueous dispersed media. Another interesting advantage that is offered by the RAFT technique is the ability to form architectures that can easily be disassembled by the readily removal of the labile thio thio carbonylated functionality.⁷ It is thus a very interesting technique for the production of functional polymer/inorganic colloidal nanocomposites.⁸

Recently, a clever strategy was developed to produce colloidal nanocomposites in emulsion polymerization employing the RAFT technique. The process consists in the use of living hydrophilic random copolymers obtained by RAFT polymerization (herein called macroRAFT agents) as both coupling agents and stabilizers during the emulsion polymerization of hydrophobic monomers in the presence of inorganic particles. The orderly extension of each polymer chain results in an even build-up of polymer in the layer surrounding the particles, leading to their encapsulation. Using this process, colloidal hybrid latexes can be obtained without the addition of conventional low molar mass stabilizers (i.e. surfactants). To date, the successful encapsulation of various organic or inorganic compounds (e.g. pigments^{9, 10}, gibbsite platelets¹¹, cerium oxide¹² and carbon nanotubes^{13, 14}) has been reported.

This thesis was part of an international project called “polymer-**encapsulation** of anisotropic **inorganic nanoparticles** by RAFT-mediated emulsion polymerization (ENCIRCLE)”. This project was enabled by the International Union of Pure and Applied Chemistry (IUPAC), and it relied on the participation of three countries: France, Brazil and Portugal. The present work was developed in the Chemistry, Catalysis, Polymers and Processes (C2P2) laboratory, in Lyon, France.

In this work, we will explore the utilization of this technique, hereafter referred to as macroRAFT-assisted encapsulating emulsion polymerization (REEP), to produce hybrid colloidal nanocomposites of polymer/aluminogermanate (Ge-Imogolite) nanotubes and polymer/layered double hydroxides (LDH). The process utilized in this work relies on the use of water-soluble macroRAFT agents containing acrylic acid (AA) units, designed to interact with the positive charges of Imogolite surface and the positive charges of the surface and the interlayer galleries of LDH materials. Taking advantage of the tunable water-solubility of the macroRAFT agents synthesized, suspensions of macroRAFT/inorganic particles of different morphologies can be obtained. These suspensions then participate in the polymerization of hydrophobic monomers in emulsion, yielding hybrid latexes of controlled anisotropic morphologies.

This manuscript is divided into three chapters.

Chapter I gives a bibliographic review of the strategies used to align inorganic fillers in polymer matrixes and the different strategies used to incorporate anisotropic fillers into polymer nanocomposites. The application of techniques based on reversible deactivation radical polymerization to produce polymer/anisotropic inorganic nanoparticles hybrids is also reviewed.

Chapter II focuses on the synthesis of polymer/Imogolite hybrid latexes and the investigation of the various parameters that influence the final latex morphology and the final film mechanical properties. First, a bibliographic review of the characteristics of Imogolite nanotubes and their application to the production of polymer/Imogolite materials is given. The subsequent sections then present the effect of

various parameters like the nature, the molar mass and the concentration of the macroRAFT agents, the Imogolite concentration and length, the pH of the medium, and the mixing and interaction pathways on the final morphologies of the different latexes obtained. Finally, the effect of the hydrophobic monomer composition was investigated to produce film-forming latexes, whose microstructural and mechanical properties were evaluated in a last part.

Chapter III deals with the synthesis of polymer/LDH hybrids in aqueous media. First, the synthesis of colloidal LDHs was optimized and their modification with RAFT and macroRAFT agents was further investigated through different strategies (namely, anionic exchange and *in situ* hybrid coprecipitation). Tentative experiments of *grafting from* polymerization of a water-soluble monomer (*N*-acryloylmorpholine, NAM) from well-defined RAFT-containing LDH phases to form a polymer corona around LDHs were then carried out. Finally, the well-defined macroRAFT/LDH hybrid phases were employed in the REEP process, yielding well dispersed and individually encapsulated LDH nanosheets.

We finally draw some general conclusions and perspectives for future works in the last part of the manuscript.

References:

1. Bourgeat-Lami, E.; Lansalot, M. *Adv. Polym. Sci.* **2010**, *233*, 53-123.
2. Tang, Z. Y.; Kotov, N. A. *Adv. Mat.* **2005**, *17*, 951-962.
3. Bourgeat-Lami, E. *J. Nanosci. Nanotech.* **2002**, *2*, 1-24.
4. Bourgeat-Lami, E.; Duguet, E., Polymer Encapsulation of Inorganic Particles. In *Functional Coatings*, Ghosh, S. K., Ed. Wiley-VCH Verlag GmbH & Co. KGaA: 2006; pp 85-152.
5. Qiu, J.; Charleux, B.; Matyjaszewski, K. *Progr. Polym. Sci.* **2001**, *26*, 2083-2134.
6. Cunningham, M. F. *Progr. Polym. Sci.* **2008**, *33*, 365-398.
7. McLeary, J. B.; Klumperman, B. *Soft Matter* **2006**, *2*, 45-53.
8. Charleux, B.; D'Agosto, F.; Delaitre, G. *Adv. Polym. Sci.* **2010**, *233*, 125-183.
9. Nguyen, D.; Zondanos, H. S.; Farrugia, J. M.; Serelis, A. K.; Such, C. H.; Hawket, B. S. *Langmuir* **2008**, *24*, 2140-2150.
10. Nguyen, D.; Such, C.; Hawket, B. *J. Polym. Sci. Part A-Polym. Chem.* **2012**, *50*, 346-352.
11. Ali, S. I.; Heuts, J. P. A.; Hawket, B. S.; van Herk, A. M. *Langmuir* **2009**, *25*, 10523-10533.
12. Zgheib, N.; Putaux, J.-L.; Thill, A.; Bourgeat-Lami, E.; D'Agosto, F.; Lansalot, M. *Polym. Chem.* **2013**, *4*, 607-614.
13. Nguyen, D.; Such, C. H.; Hawket, B. S. *J. Polym. Sci. Part A-Polym. Chem.* **2013**, *51*, 250-257.
14. Zhong, W.; Zeuna, J. N.; Claverie, J. P. *J. Polym. Sci. Part A-Polym. Chem.* **2012**, *50*, 4403-4407.

Chapter I - Bibliographic Review

Table of contents

I.1. Introduction.....	1
I.2. Polymer/Inorganic Composite Materials	2
I.2.1 Alignment of inorganic particles into polymer matrixes	5
I.2.1.1 Linear-template method	6
I.2.1.2 Template-free self-assembly	7
I.2.1.3 External force-induced nanoparticles assembly	8
I.2.1.3.1 Shear-induced nanoparticles alignment	9
I.2.1.3.2 Magnetic field-induced nanoparticles alignment	10
I.2.1.3.3 Electric field-induced nanoparticles alignment.....	13
I.2.2 Anisotropic particles	15
I.3 Polymer-encapsulation of anisotropic particles	18
I.3.1 Free-Radical Emulsion Polymerization	18
I.3.2 Reversible Deactivation Radical Polymerization (RDRP) in Emulsion	23
I.3.2.1 Nitroxide-mediated polymerization (NMP).....	24
I.3.2.2 Atom transfer radical polymerization (ATRP).....	25
I.3.2.3 Reversible addition-fragmentation chain transfer (RAFT)	25
I.3.2.4 Reversible Addition-Fragmentation chain Transfer (RAFT) and its application to dispersed media	27
I.3.2.4.1 Conventional RAFT emulsion polymerization	31
I.3.2.4.2 Polymerization-induced self-assembly (PISA) RAFT emulsion polymerization ...	31
I.3.3 Use of RDRP for the modification and encapsulation of inorganic particles	33
I.3.3.1 Grafting from	34
I.3.3.1.1 Grafting from using RAFT.....	35
I.3.3.2 Grafting to	37
I.3.3.3 Block copolymers self-assembly in presence of inorganic particles.....	39
I.3.3.4 MacroRAFT-assisted encapsulating emulsion polymerization.....	44
I.4. Conclusions.....	52
I.5. References.....	54

I.1. Introduction

In the last decades, polymer science has developed into a modern and multi-research field. Initially devoted to structural applications, polymers are indeed increasingly involved in high added-value functional materials from electronic-, optical- and biomedical-related areas¹⁻³. One way to achieve these targeted properties is by the incorporation of inorganic particles to the polymer matrix, thus combining specific properties of the inorganic (e.g. mechanical strength, thermal resistance, chemical resistance) and the organic (e.g. softness, malleability, processability) phases.

The presence of anisotropic domains in polymer/inorganic nanocomposites significantly participates to the enhancement of the material properties. The simple dispersion of inorganic particles into polymer matrixes already contributes to improve the material properties and reduce the costs, but the spatial orientation of the fillers significantly accentuates the gain in properties. Thus, the alignment of inorganic fillers in polymer matrices is gaining increasing attention. Different strategies enabling the 1D assembly of particles have been developed for different fillers, like magnetic particles^{4, 5}, clays^{6, 7}, carbon nanotubes⁸⁻¹¹ and graphene^{12, 13}. The use of template-, template-free-, and external force-induced-assembly of nanoparticles in polymer matrixes has been reported.

The synthesis of composite materials can be performed through various methods. For instance, polymer/layered materials can be synthesized by techniques such as melt intercalation, exfoliation-adsorption, *in situ* intercalative polymerization and template synthesis. In this bibliographic survey we focused on the *in situ* synthesis via radical polymerization performed in aqueous dispersed media. Reversible deactivation radical polymerization techniques, notably nitroxide-mediated polymerization (NMP), atom transfer radical polymerization (ATRP) and reversible addition-fragmentation chain transfer (RAFT) polymerization are also being currently applied to produce polymer/inorganic nanocomposites. Different strategies have been reported, such as *grafting from*,¹⁴⁻¹⁶ *grafting to*,^{17, 18} and block copolymers self-assembly in presence of inorganic particles,¹⁹⁻²¹ systems in which the polymerization is carried out in solution and (mini)emulsion polymerization assisted by controlling agents, in which the polymerization is carried out in water, a non-solvent of the polymers. Both pathways use the same tool, reversible deactivation radical polymerization, but they rely on very different mechanisms. Particular attention will be paid to RAFT systems, which is the process used throughout this work.

I.2. Polymer/Inorganic Composite Materials

Composite materials are materials consisting of more than one constituent with distinct physical or physicochemical properties that, when combined, give rise to new properties different from the ones of the individual components²².

Polymer/Inorganic composite materials are actually very old engineering materials, and their utilization in the field of household materials and tires dates back from around 1900s.^{23, 24} However, this subject did not attract the attention of scientists until the Toyota group reported the amazing properties obtained with a nanometric-scaled MMT reinforced Nylon-6 twenty years ago.^{25,26} Since then, the incorporation of inorganic nanoparticles into polymer matrixes has become an attractive field of research, making nanocomposite materials the object of intense development and study. Many efforts are dedicated in particular to mastering nanoparticles distribution within the polymer matrix and developing a better understanding of the structure-properties relationship²⁷.

Enhanced properties depend strongly on the interface between the polymer matrix and the inorganic fillers. Thus, during the past two decades, the use of nanometric fillers proved to be very worthy in terms of gain in properties and cost. Small amounts (around 10 wt %) of nano-fillers can increase mechanical properties by a factor higher than 5, eliminating light scattering when efficiently dispersed, and presenting a good polymer-particle interfacial adhesion. These features allow the production of mechanically strong yet transparent films, coatings and membranes²⁸. Moreover, similar techniques used to produce conventional composite materials can be applied to fabricate nanocomposites, making this class of advanced materials particularly attractive from a manufacturing point of view²⁹.

To be classified as a nanocomposite, a composite material must have the inorganic filler with one of its dimensions in the nanoscopic scale. Three main types of nano-fillers can be highlighted (**Figure 1**): fibrilous materials, particulate materials and layered materials. The first class refers to fibers and tubes, with diameters in the nanoscale and lengths up to several microns. The second class deals with spherical particles, where the diameter is in the range of ten to a few hundreds of nanometers. The third class is related to layered materials, most often of the silicate family, in which the sheets thickness is near 1 – 5 nm and the sheet plane can be hundreds of nanometers long²⁹.

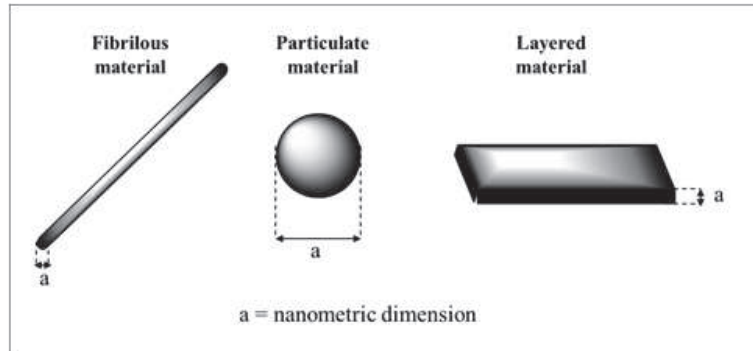


Figure 1. Schematic representation of nanometric filler types.

As far as layered silicates are concerned, the filler distribution in the polymer matrix depends on the initial state of the inorganic material and on the capability of the polymer to migrate into the interlayer spaces and increase the inter-particles distance, intercalating or exfoliating the nanocharges²⁹. For instance, in the case of layered silicates the nanocomposite structures are often called *phase separated*, *intercalated* or *exfoliated* according to their dispersion state (**Figure 2**). Different properties are obtained for each nanocomposite structure. For instance when phase separated nanocomposite materials are formed, properties similar to a micro-scale composite are obtained³⁰. In addition, poorly distribution of the fillers in the matrix may cause degradation of the mechanical properties³¹. In contrast, exfoliated structures contribute to a network formation enabling percolation in the material, which highly enhances mechanical, optical, electrical and thermal properties³⁰.

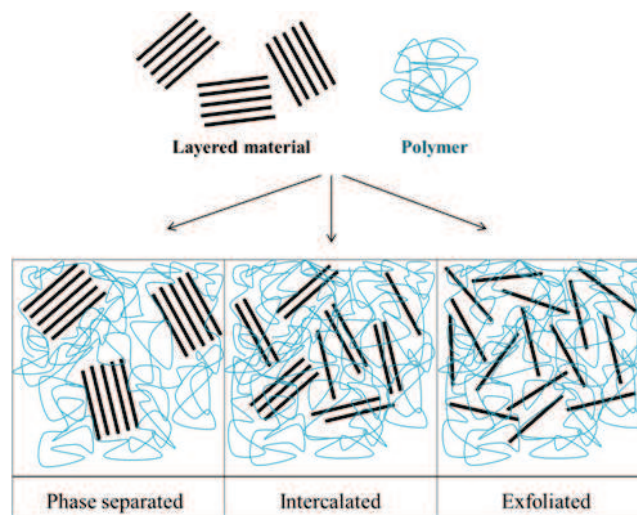


Figure 2. Schematic representation of the dispersion state of layered silicates in a polymer matrix. Adapted from ref²⁹.

According to the properties that one wants to confer to the final nanocomposite, different fillers might be used.³² The nanoparticles most currently used are silica,³³⁻³⁷ layered silicates (clays),^{30, 38} gold nanoparticles³⁹⁻⁴³ and metal oxides.^{5, 44-46} Recently, rod-like particles⁴⁷, carbon nanotubes³¹ and graphene¹⁸ have also gained attention for their interesting properties and applications. Silica nanoparticles are usually employed to obtain specific optical properties and improved mechanical resistance. Layered silicates can provide mechanical reinforcement, thermal resistance and barrier properties to the material. Gold nanoparticles often figure in bio-applicable materials, for instance in bioimaging due to their unique optical properties (e.g. localized surface plasmon resonance, LSPR) and biocompatibility⁴⁸. Metal oxides can be the origin of various properties, like optical, magnetic, electrical, thermal, mechanical, depending on their chemical nature (e.g. ZnO, TiO₂, Al₂O₃, Fe₃O₄, CeO₂). Tubular structures are mainly used to obtain (anisotropic) mechanical reinforcement, thermal resistance and electrical properties (semi-conductivity)^{29, 30}. For alignment and functionalization procedures, nanoparticles with an anisotropic morphology are certainly advantageous. Especially nanotubes possess several different areas of contact (borders, inner and outer surfaces, and structured tube walls) that in principle can be functionalized in several ways. Their basic hollow morphology is almost directly associated with their use as nanoscale host materials⁴⁹. The unique symmetry, electronic, quantum, thermodynamic, mechanical, phonon, superconducting, optical and thermal properties of nanotubes make them a very attractive class of nanofillers. Further details and examples on the use of nanotubes as nanocharges for polymer/inorganic nanocomposites will be given afterwards.

Another class of anisotropic fillers which also attract great interest from researchers, and which we will be interested in as well, is the family of layered silicates. Different techniques can be used to form polymer/layered silicate nanocomposite (PLSN), namely (i) **melt intercalation**, (ii) **exfoliation-adsorption**,(iii) ***in situ* intercalative polymerization** and (iv) **template synthesis**. In the first technique, a thermoplastic polymer is mixed mechanically with the filler at high temperatures using conventional methods like extrusion or injection molding. This technique has the advantage of that it does not need any solvent; however, it usually generates materials with a poor distribution of the filler in the matrix, caused by incompatibility between inorganic and organic phases. The second technique consists in swelling the filler in a solvent and adding a soluble polymer or pre-polymer, which can migrate into the interlayer spaces and adsorb to the inorganic surface. The nanocomposite is then obtained after solvent evaporation. As for the previous technique, the incompatibility of the filler with the polymer may hinder polymer migration into the interlayer space, preventing uniform distribution of the filler in the matrix. *In situ* intercalative polymerization comprehends the swelling of the inorganic filler by the monomer itself followed by heating or radiating the system, where the appropriate initiator was dispersed or attached to the inorganic surface, to start polymerization²⁹. Finally, the template synthesis is a technique where the inorganic filler is synthesized in presence of a

polymer solution, generating intercalated or exfoliated structures. This last method is mainly developed for the production of layered double hydroxide (LDH)-based nanocomposites using water-soluble polymers³⁰, but it was also applied for different inorganic materials (e.g. gold nanoparticles).⁵⁰ For all these techniques, the success of nanocomposite formation lies on the affinity of the inorganic particle with the polymer matrix.

To favor this affinity, the generally hydrophilic fillers are most of the time organically modified³⁰. The modifying agents can be organic molecules such as alkyl ammonium salts or amino acids⁵¹; functional polymers containing hydroxyl groups, maleic anhydrides, alkoxy silanes⁵² or block copolymers containing one block compatible with the filler and the second one compatible with the matrix⁵³.

As pointed out previously, very interesting properties emerge from the incorporation of nano-scaled inorganic particles into soft or semi-crystalline polymer matrices. Such enhancements originate from the physical presence of the nanoparticles, the interaction between the polymer and the fillers and the dispersion state of the inorganic components.²⁸ The presence of the filler contributes to increase stiffness and resistance of the material, provided by the filler itself. The interphase created between the polymer and the filler acts as an extra rigid phase, also contributing to enhance mechanical properties. Finally, the dispersion state of the inorganic particles will define the microstructure formation, enabling or hindering percolation, which is crucial for instance to enhance mechanical and electrical properties⁵⁴.

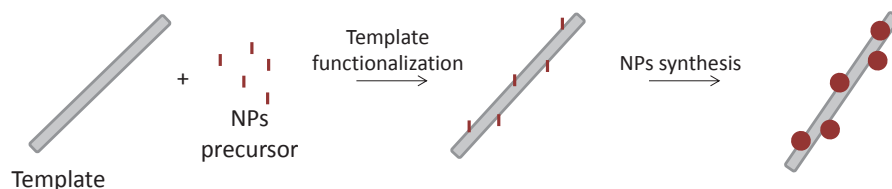
Many efforts have been done to understand the structure-property relationship in these materials, and several groups have shown significant improvement on mechanical, optical, electrical or magnetic properties generated by anisotropic arrangements of the inorganic fillers in polymer matrixes. Thus, our discussion will focus on the alignment of spherical nanoparticles into anisotropic structures and the direct use of anisotropic nanoparticles.

I.2.1 Alignment of inorganic particles into polymer matrixes

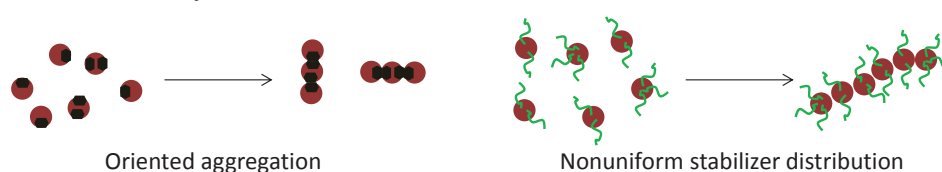
Nanoparticles assemblies are widely performed to produce materials with renewed and specific properties for different applications. Three classes of assemblies can be distinguished, one-dimensional (1D), two-dimensional (2D) and three-dimensional (3D). Anisotropic 1D nanoparticles assemblies are the more challenging class, and it is also the most interesting organization of fillers in terms of structure-property relationship, since they enable inter-nanoparticle electronic, photonic and energy transfer⁵⁵. Different fillers can be the object of alignment, notably: iron oxide⁵⁶, silica and alumina particles³⁷, carbon nanotubes⁵⁷, graphene⁵⁸ and clays⁶.

Different techniques can be used to produce such NPs 1D-assemblies, namely: (i) **linear-template method**, (ii) **template-free self-assembly method** and (iii) **external force-induced nanoparticles assembly**⁵⁵ as illustrated in **Figure 3**.

Linear-template method



Template-free self-assembly



External force-induced self-assembly

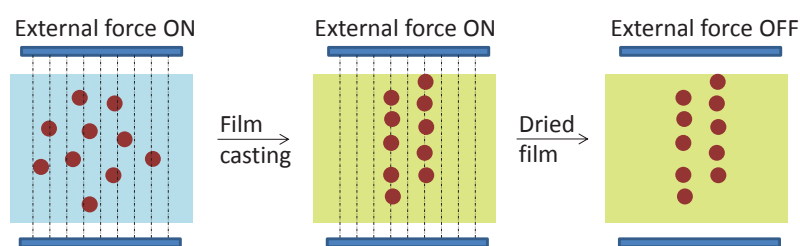


Figure 3. Schematic representation of nanoparticles alignment methods

1.2.1.1 Linear-template method

Linear-template method consists in the use of polyelectrolytes, biomolecules, inorganic nanowires/nanotubes and pores and channels inside polymer, alumina and silica, as templates for the synthesis of nanoparticles. Initially the template is functionalized with the nanoparticles precursor, which after reduction or chemical combination, forms the nanoparticles attached to the template, forming linear chains of NPs. For instance, P2VP was used to form Pd 1D assemblies^{59, 60}; double-hydrophilic block copolymers (DHBC) can be used to form CaCO₃, CdWO₄ and BaCrO₄ assemblies⁶¹⁻⁶³. DNA is often applied to order Ag, Pd, Au, Pt and CdSe nanoparticles^{55, 64, 65} and other linear fibrous biomacromolecules like fibrin, dextran and collagen can also be used as templates for TiO₂, SnO₂, CdS, ZnS and FePt organization⁵⁵. Carbon nanotubes can be used following the same principle to align Au, Ag, Pt, Cu, SnO₂, TiO₂, CdSe, nanoparticles⁶⁶. When inorganic nanowires (NWs) or nanotubes

(NTs) are used, some advantages and disadvantages rise up. They contribute to the stiffness of the material but they have to be removed if the stiffening is undesired⁵⁵.

1.2.1.2 Template-free self-assembly

Specific properties of the NPs can confer them intrinsic anisotropy, enabling their self-assembly due to the inherent anisotropy of NP-NP interactions, excluding the need of templates. When such interactions take place, the method is called **template-free self-assembly**. Tang et al.⁵⁵ classified this method according to the driving force of interaction in four classes: magnetic-dipole moment; electric-dipole moments; oriented aggregation and non-uniform stabilizers distribution. Magnetic-dipole moment covers the “spontaneous” formation of permanent magnetic dipoles that act as a critical orientation system and are, logically, applied for magnetic nanoparticles. Electric-dipole moment can be explored on semiconductor nanoparticles, gold or silver^{67, 68}. Due to either the presence of an anisotropic crystal lattice, or some surface defects^{69, 70}, the inter-nanoparticles interaction is promoted, resulting in particles organization and orientation⁷¹. In this particular case, the interactions may be compensated by steric or electrostatic repulsions caused by the presence of stabilizers on the NPs surface. Removal of such molecules enables the formation of NPs chains mainly by dipole-dipole interactions^{72, 73}. Oriented aggregation occurs via mutual attachment promoting the self-assembly of NPs, resulting from specific crystallographic orientation in primary crystals, as reviewed by Penn in 2004⁷⁴. Ag, TiO₂, ZrO₂, CeO₂, ZnO, Fe₂O₃, core-shell CdS/ZnS, zeolite and many other crystalline materials were shown to have oriented aggregation.

The last route is the non-uniform stabilizers distribution, which consists in differences in the affinity of a stabilizer with the elements present in binary or ternary particles, resulting in an inhomogeneous distribution of such molecules on NPs surface. Even for monocomposite particles, the adsorption strength is varied on different crystal planes. In consequence, the non-uniform distribution of ligands on the surface of nanoparticles provides the possibility to form 1D NP assemblies. These types of assembly were observed for instance for CdSe with trioctylphosphine oxide (TOPO), Ag with PVP, and TiO₂ with Trizma (2-amino-2-(hydroxymethyl)-1,3-propanediol)⁵⁵. The self-assembly of gold nanorods (NRs) non-uniformly functionalized with cetyl trimethyl ammonium bromide (CTAB) also generates 1D gold nanoparticles strings (Figure 4).⁷⁵⁻⁷⁷

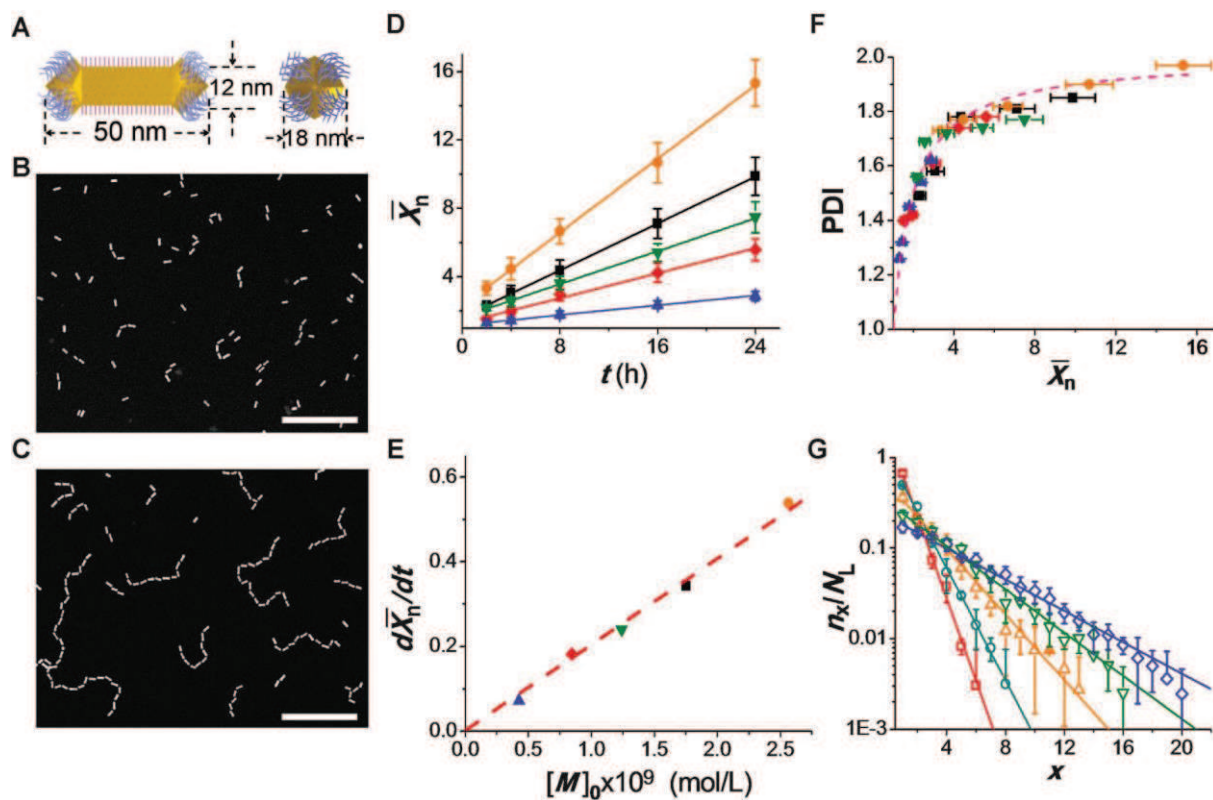


Figure 4. Growth of colloidal polymer chains of gold nanorods. (A) Schematics of the side view of the long face (left) and the edge (right) of the NR carrying CTAB on the long side and thiol-terminated polystyrene (PS-SH) molecules on the ends. (B and C) Dark-field TEM images of the NR chains after 2 (B) and 24 (C) hours assembly. Scale bar, 100 nm (both panels). (D to F) Polymerization of NRs at different initial concentrations of active functional groups of the NRs ($[M]_0$). (D) Variation in the number average degree of polymerization, \bar{X}_n , with time t , h, hours. (E) Dependence of chain growth rate with on $[M]_0$. (F) Variation in the polydispersity index (PDI) of the chain with \bar{X}_n . The dashed line shows the relation $\text{PDI} = (2 - 1/\bar{X}_n)$. For each data point in (D) and (F), the total number of NRs used in the analysis was 5000. (G) The experimental (symbols) and theoretically predicted (lines) fractions of linear x -mer chains, plotted as a function of their degree of polymerization, X_n , for the time of 2 (\square), 4 (\circ), 8 (Δ), 16 (∇) and 24 (\diamond) hours. $[M]_0 = 0.84 \times 10^{-9}$ (mol L $^{-1}$). Error bars indicate standard deviation (SD). Reproduced with permission from ref⁷⁵. © 2010 AAAS.

1.2.1.3 External force-induced nanoparticles assembly

The third and most relevant method for promoting nanoparticles 1D assembly, considering the purpose of our work, consists in applying an external force to promote alignment, and is called **external force-induced nanoparticles assembly**. Such forces may be for instance *mechanical shearing*, *magnetic field* or *electric field*, and can be applied to a suspension of pure nanoparticles, or a mixture of particles plus polymer solution, before or during solvent evaporation (i.e. film casting). Mechanical shearing is almost exclusively applied for anisotropic particles, while magnetic or electric fields application can also work for isotropic particles.

1.2.1.3.1 Shear-induced nanoparticles alignment

The simplest one appears to be shear-induced organization of nanoparticles, but for this method to work properly and provide highly oriented nanoparticles assemblies, the fillers must have anisotropic geometrical dimensions. Nevertheless, shear-induced alignment was also observed for spherical particles like alumina and silica in a polymer coating, as reported by Sapper et al.³⁷. Necklace-like structures were observed on the surface of a polyurethane film after shearing. As shearing increased, the abundance and length of the 1D assembly also increased. The mechanism of formation of such ordered structures was attributed to a combination of shear-induced alignment and oriented aggregation effect.

1D assembly of anisotropic particles under shearing has been studied by several groups. Here we describe the shear-induced alignment of carbon nanotubes and thin layer sheets, specifically boron nitride (BN).

Jin et al.¹⁰ performed the alignment of carbon nanotubes (CNT) in a polyhydroxyaminoether (PHAE) matrix by stretching the films at 100 °C. They observed that even after removal of the external force and cooling the sample to room temperature, the tubes remained aligned and could be characterized by X-ray diffraction and TEM. Cooper et al.⁷⁸ could also align CNT and fibrils in a poly(methyl methacrylate) (PMMA) matrix by extrusion, forming a composite where the tubes were parallel to the extrusion flow direction. Later, Lanticse et al.¹¹ reported the alignment of CNT in a furane resin film using the doctor blade technique, which consists in one blade equipped with a reservoir containing the sample (i.e. composite mixture) to be casted. Two types of doctor blade systems exist: one where the blade slides relatively to the fixed substrate and the other where the blade is fixed and the substrate slides perpendicularly to the blade. The gap between the blade and the substrate defines the film thickness. The authors observed highly aligned CNT parallel to blading direction. Electrical property investigations revealed sample electrical conductivity up to a million times higher in the direction of alignment, compared to the random composite. Zhou et al.⁷⁹ fabricated nanocomposite films of CNTs in a poly(vinyl alcohol) (PVA) matrix and further aligned the tubes by stretching the films. Nanotubes were previously functionalized with poly(propionylethylenimine-*co*-ethylenimine) (PPEI-EI) polymer to result in strong defect-derived luminescence. After aligning the tubes in the stretching direction, luminescence properties were measured, revealing polarized luminescent emissions along the tube axis.

Terao et al.⁸⁰ produced nanocomposite materials of BN nanotubes/PVA for thermal conductivity improvement by electrospinning, so that all BN nanotubes were aligned in the fiber casting direction. Contrary to carbon nanotubes, boron nitride nanotubes have rigid shapes, hindering the formation of entanglements and curved structures and avoiding the presence of air bubbles inside the material, which contributes to enhance properties even more. These fibers were then used to form bulky

polymer films by hot-pressing, which thermal conductivity properties were measured. The highest value of thermal conductivity was found when the measurements followed the direction of the tubes axis, reaffirming the interest in aligning such fillers in a polymer matrix.

Shear-induced one-dimensional alignment has also been employed to orient thin BN inorganic sheets. For instance, Song et al.⁸¹ observed surprisingly enhancement of thermal diffusion properties after the shear-induced alignment of the boron nitride sheets in a PVA matrix. In this case the authors took advantage of PVAs capability of orienting molecular and nanoscale species under shearing to align the BN sheets inside the polymer film.

1.2.1.3.2 Magnetic field-induced nanoparticles alignment

The second method, and probably the more commonly used, to align inorganic nanoparticles in a polymer matrix is the external *magnetic field* application. This method can be applied to align a wide range of magnetic particles, including iso or anisotropic nanoparticles. Iron oxide-based or iron oxide-containing particles are the most frequently reported^{8, 82}. Here we present first the alignment of spherical particles in a polymer matrix, and then one case of carbon nanotubes alignment.

Jestin et al.⁸³ produced anisotropic nanocomposites by mixing a poly(methyl methacrylate-*co*-butyl acrylate)/poly(methacrylic acid) (P(MMA-*co*-BA))/PMAA core/shell latex with silica-coated γ -Fe₂O₃ maghemite particles and casting the film by water evaporation under a magnetic field. Small angle neutron scattering (SANS) analyses showed the formation of chains of magnetic particle aggregates along the polymer matrix, that the authors called “supra-aggregates”. Mechanical properties of the 1D supra-aggregates-containing nanocomposite films were measured, and elongation tests have shown a reinforcement of almost one order of magnitude compared to the pure matrix. Moreover, when the stress was applied parallel to chain orientation, the reinforcement factor was 2 times superior to the perpendicular stretching.

The same group studied the alignment of maghemite particles in a polystyrene (PS) matrix⁸⁴, and reported the successful production of nanocomposites with controlled anisotropic reinforcement triggered by magnetic self-assembly. The effect of NPs size, concentration and magnetic field intensity on final alignment was studied. Nanocomposites were produced by mixing a suspension of maghemite (γ -Fe₂O₃) in dimethylacetamide (DMAc) with a PS solution in the same solvent. Films were casted by gentle solvent evaporation under magnetic field. Different NPs diameters (13 nm, 10.2 nm and 7.4 nm) and concentrations (diluted regime and concentrated regime) were studied for two magnetic field intensities (100G and 600G) and in the absence of magnetic field. The results showed that increased anisotropy was obtained with increasing nanoparticles size or magnetic field intensity in the diluted regime. The same tendency was observed in the concentrated regime, with however a different

mechanism in the assembly process. At low concentration, primary aggregates are formed, which further self-assemble to form the 1D anisotropic structure. Apparently, for high NP loadings, especially when using bigger nanoparticles, primary aggregates are not formed the same way, and chains containing individual nanoparticles interacting mainly through dipolar magnetic interactions induced by the high intensity magnetic field are obtained. Finally, the authors developed a quantitative correlation between the structural local anisotropy and the mechanical reinforcement expressed by the Young modulus in the parallel direction to the alignment. They obtained a proportional relation with a linear increase of the Young modulus with increasing the NP size, the NPs concentration or the magnetic field intensity.

Fragouli et al.^{4, 56} reported the formation of nanocomposite films containing size controlled 1D assemblies of γ -Fe₂O₃ nanoparticles in a poly(ethyl methacrylate-*co*-methyl acrylate) (P(EM-*co*-MA)) matrix, by applying time controlled magnetic field during solvent evaporation. In their work a solution of P(EM-*co*-MA) in chloroform was mixed with an iron oxide nanoparticles suspension in the same solvent. The mixture containing 1% of NPs and 99% of polymer was sonicated for 10 minutes prior to film casting under magnetic field. Topography studies of the surface made by Magnetic Force Microscopy (MFM) revealed the presence of spherical aggregates of nanoparticles, and nanowires (NWs) were rarely found on the surface. After slice cut, NWs were found to be present in the inner parts of the film (**Figure 5**). Magnetic properties of the surface were similar to those of a pure polymer matrix, while the properties of the nanowire (NW)-containing parts were significantly superior to that of the matrix or the aggregates. They also managed to control the structural evolution, the ordering and the spatial localization of arrays of aligned nanowires, by tailoring the time of magnetic field application during solvent evaporation. Thus, they were able to form nanocomposite films with magnetically anisotropic behavior. Highly reproducible morphologies, which depended on NPs concentration and magnetic field time, could be obtained. They have also shown that NPs loadings lower than 0.7% resulted in short NWs with random alignment, yet for 2% and 5% loadings the formation of ordered arrays of long NWs was achieved. Furthermore, it was observed that the formation of such ordered structures starts by the organization of NPs into clusters, which respond better to the magnetic field, facilitating the wires formation. To promote NPs aggregation, the authors treated the γ -Fe₂O₃ nanoparticles with oleic acid, oleylamine or hexadecane-1,2-diol, which interacted via hydrophobic interactions. Magnetic properties measured showed high magnetization for samples where the NWs were parallel to the magnetic field, and these properties were weakly affected by the polymer matrix.

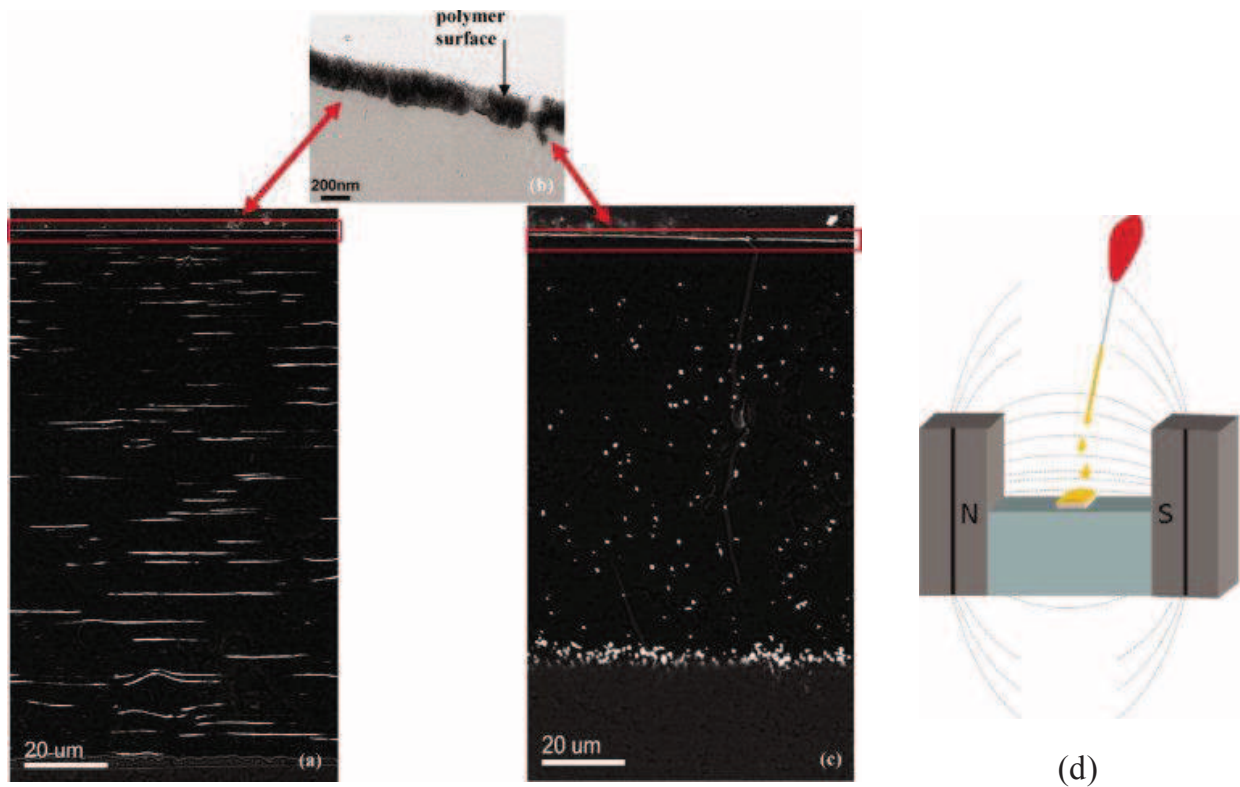


Figure 5. (a) Back-scattered electrons scanning electron microscopy (BSE-SEM) cross sectional image of the whole film. The bright lines represent the NWs while the dark areas is the polymer matrix. The bended NWs, observed at the lower part of the film, are due to the bending of the section. (b) Bright field transmission electron microscopy (BF-TEM) image of the surface of the films, where a continuous layer of nanoparticles is observed. (c) BSE-SEM cross sectional image of the whole film formed after drying of a drop-casted solution without application of external magnetic field. (d) Experimental set up for the preparation of nanocomposites incorporating magnetic NWs formed under the application of a magnetic field. Adapted with permission from ref ⁵⁶. © 2010 Wiley-Liss, Inc.

Pisanello et al.⁵ performed similar experiments as Fragouli, aligning iron oxide particles in a polydimethylsiloxane (PDMS) matrix under magnetic field. They observed that the size and the shape of the macroscopic nanoparticles assemblies depend on the original NPs shape, the polymer matrix nature and the magnetic field intensity. After curing of the iron oxide-containing PDMS matrix under magnetic field, the resulting film presented GHz dielectric permittivity properties.

As evocated before, this technique can also be applied to align anisotropic nanofillers. For instance, Kimura et al.⁸⁵ successfully produced multi-walled carbon nanotubes (MWCNT)/Polyester-PS nanocomposites with highly aligned fillers. Their synthesis pathway consisted in mixing MWCNT (1, 2 and 5 wt%) of diameter of 5 – 50 nm and lengths of thousands of nanometers to a monomer mixture of unsaturated polyester and styrene. Magnetic field was then applied during the polymerization, carried out by adding a radical initiator. The experiment set up was composed of a mold containing the hybrid mixture placed inside a magnet. The use of a mold enables the production of nanocomposites of varied shapes, contrary to the spinning method, which exclusively generates fibers. TEM analyses

confirmed the alignment of the tubes parallel to the magnetic field direction, and magnetic susceptibilities presented higher values at a perpendicular direction compared to parallel one, also indicating a parallel orientation of the tubes in the magnetic field direction. Contrary to other studies, lower magnetic anisotropy was found for higher loadings of nanotubes (2 and 5 wt%), which was explained by the formation of aggregates of MWCNT that compromise the dispersion of the fillers in the matrix. By means of dynamic mechanical analyses (DMA), it was found that the elastic modulus of the nanocomposites was higher for the parallel direction compared to that of the perpendicular direction. It was also observed that the T_g measured parallel to the tubes alignment was slightly higher than the one in the perpendicular direction. From this study, the authors concluded that for the alignment to take place, the magnetic anisotropy of the carbon nanotubes must be higher than the thermal energy of Brownian motion, and also higher than the resistance against rotation in the viscous monomer solution.

Another example of anisotropic objects alignment under magnetic field was given by Xu et al.,⁸⁶ where they produced pH-responsive Fe^{3+} -containing core/shell cylindrical particles. Nanoparticles could be formed at $pH > 7.0$, for which the copolymer, consisting of poly(methacrylic acid)-*b*-poly(oligo(ethylene glycol) methacrylate), was insoluble; and “dissolved” at $pH < 7.0$, for which the polymer would become soluble. Under magnetic field, the hybrid nanoparticles could be aligned forming one-dimensional strings, evidenced by atomic force microscopy (AFM) analyses.

1.2.1.3.3 Electric field-induced nanoparticles alignment

Analogously to the magnetic field utilization, 1D assembly of nanoparticles can be achieved under external *electric field* application. This technique can also be performed with nanoparticles in suspension in a solvent or in a polymer solution. The last one generates polymer/inorganic nanocomposite films after drying. Here we will focus on the production of aligned nanoparticles-containing polymer films. Two strategies can be considered to form 1D ordered structures of nanoparticles in a polymer matrix. The first one consists in using block copolymers, in which one of the blocks responds to electric field. Inorganic nanoparticles being linked to this block are able to orient in a preferential direction under electric field. In consequence, the inorganic nanoparticles will follow the alignment of the polymer, forming one-dimensional structures. This method is based on the reports of Morkved, who elucidated the possibility of block copolymers to orient under electric fields⁸⁷. This strategy was used by Liedel et al.⁸⁸, where they produced nanocomposites containing gold nanoparticles aligned in a polystyrene-*b*-poly(2-vinylpyridine) (PS-*b*-P2VP) matrix, obtained by applying an electric field in the blend.

The second strategy takes advantage of the electrical response of the nanoparticles themselves, following the same principle as for magnetic alignment. In this case, the inorganic particles are incorporated in the polymer matrix and alignment is carried out during solvent evaporation or directly in the melted polymer⁸⁹. Using this second technique, Kumar et al.⁹⁰ reported the alignment of maghemite doped with poly(phenylmethylvinyl siloxane) under electric field before curing the sample. Magneto-optical properties of the final materials were investigated and the alignment proved to be efficient on enhancing such properties.

Gupta et al.⁹¹ also reported interesting findings when performing the alignment of CdSe nanorods in a PMMA matrix. They coated the fillers with alkane, poly(ethylene oxide) (PEO) or PS and mixed it with a PMMA solution in chloroform. Electric field was applied perpendicularly to the film plane during solvent evaporation. Vertical alignment, corresponding to the direction of the electric field, and close packing of nanorods (i.e. corraling) was obtained when the coating was performed with alkanes. This was attributed to the rod-rod distance, which is lower for alkane compared to PEO or PS. The presence of PMMA also contributed to maintaining the orientation even after electric field removal. The authors highlighted the interest of vertically aligned nanorods in photovoltaic applications.

Bao et al.⁹ studied the influence of the surface polarity of carbon nanotubes on their alignment under electric field. Pristine CNT and polar CNT-COOH were dispersed in an Ethylene-Vinyl Acetate (EVA) melt and the mixture was submitted to an electric field to align the NTs. It was observed that the presence of COOH groups (i.e. polar groups) on the surface contributed to a better interaction between NTs and the polymers and reduced the CNTs mobility, preventing consequently any alignment under the electric field.

A similar method used to macroscopically align particles in a polymer matrix or polymer layers is dielectrophoresis (DEP). This method consists in creating an electric field between two electrodes, inducing the particles positioning between the two electrodes perpendicularly to each electrode surface plane⁹². Using an analogous principle, Gennari et al.⁹³ reported in 2013 the successful alignment of carbon-based nanoparticles using a clever electrode-free approach. In their strategy, electric field is spontaneously generated by a pyroelectrical crystal after warming the material. The crystal can trigger dipole-dipole interactions between nanoparticles, which can form 1D chain assemblies in polymer matrixes. The crystals used to generate the electric field, called by the authors “driving crystals”, were lithium niobate (LiNbO₃) or lithium tantalite (LiTaO₃), which both exhibit pyroelectricity. Typically, nanoparticles (CNTs) embedded in a PMMA matrix solution were placed over the “driving crystal” and between two metallic layers. After heating the crystal, the alignment could be observed by the formation of strings perpendicularly to the metal layers surface. Since the alignment is obtained perpendicularly to the metal surface, changing the morphology of the metallic layer would change the string formation direction, and specific patterns could be obtained. For instance, triangular metals

generated strings perpendicularly aligned to each side, and spherical metal plates gave rise to strings oriented radially to the metallic sphere. The formation of carbon-based nanoparticles chains was very reliable and presented a high repeatability, making this method an interesting technique to produce particle patterns on demand.

It can be concluded from the various works described herein that a clear enhancement of various properties results from the anisotropic ordering inside nanocomposites. Thus, many strategies have been developed to form 1D assembly of inorganic fillers inside polymer matrixes, as presented so far. Through the different techniques presented, it is possible to align isotropic particles forming one-dimensional structures that confer anisotropically enhanced specific properties to composite materials. However, a more direct way to obtain such properties is the incorporation of high aspect ratio anisotropic particles to polymer matrixes. These particles are more easily aligned (with or without external force application) and can form continued 1D arrays. The incorporation of anisotropic particles into polymer matrixes will be discussed in the next section.

I.2.2 Anisotropic particles

Due to their non-uniform geometry, anisotropic particles tend to naturally align themselves in a preferential direction, corresponding to their longest axis. This self-aligning property combined with the interesting properties provided by anisotropic particles, make these objects very promising for the production of nanocomposites with targeted applications.

The spontaneous organization of anisotropic particles was first observed for nanoparticles suspensions, forming what is called Liquid Crystals (LC). For instance, the self-alignment and macroscopic ordering of a high aspect ratio $K_4Nb_6O_{17}$ nanosheet in a liquid crystalline sol was demonstrated by Miyamoto et al.⁹⁴. The authors observed a macroscopic organization in the centimeter scale only by gravitational forces. No isotropic phases were observed in the system even at very low concentrations of around 0.004 wt%.

This phenomenon of self-orientation of highly anisotropic particles was further explored to produce polymer composite materials, where the alignment usually takes place during film formation. Different groups have studied the self-alignment of anisotropic particles like carbon nanotubes⁹⁵, clay platelets⁶ and graphene^{13, 58, 96} in suspension and in a polymer matrix. Here we describe the most relevant works related to the field of polymeric materials.

Yousefi et al.^{13, 58} observed the alignment of ultralarge graphene oxide (GO) sheets during the formation of GO/polyurethane (PU) nanocomposite films by simple solvent evaporation after mixing a PU latex with a graphene suspension. The principle applied for their work was an extension of the

liquid crystal formation that was observed for ultralarge GO sheets in suspension⁹⁷. According to the authors, graphene layers tended to self-adjust their basal plane perpendicular to the film, resulting in their alignment. They have also shown that the degree of orientation increased with increasing the GO content, which can be explained by the fact that filling the spaces with anisotropic phases resulted in a reduction of free rotation, causing some “excluded volume”⁹⁸. They also explained that this was an entropic interaction among anisotropic particles resulting in specific arrangements between the sheets, and this interaction was also at the origin of liquid crystals⁹⁹. The authors also observed a significant difference in the critical concentration of GO needed for the alignment to take place when comparing GO suspensions and GO/polymer composites. The concentration needed for polymer nanocomposites was 20 times greater than for GO suspensions. The authors presented two explanations for this difference. The first one was related to the higher viscosity of the PU latex compared to water, which would disfavor the ordered adjustment of the fillers. The second one relied on the smaller aspect ratio of the GO used here compared to their previous study on pure GO suspensions. According to Onsanger’s model⁹⁹ the critical concentration for LC formation is inversely proportional to the aspect ratio. Finally, mechanical and conductivity tests revealed superior properties of the nanocomposites compared to pure polymer or to randomly distributed GO/polymer nanocomposites. Improvement of 1200 % and 300 % in modulus and hardness, respectively, was obtained for the nanocomposite containing 5 wt% of GO. These extraordinary properties were attributed to the highly aligned orientation of graphene sheets in the matrix. Permeability tests have shown a considerable decrease in moisture permeation when increasing the graphene content, arising from the alignment of the high aspect ratio graphene sheets along the horizontal direction. This alignment contributes to the formation of a tortuous path that prevents moisture flow. Inherently high electrical conductivity was obtained. Conductive networks were formed preferentially along the plane direction, which corresponds to the same orientation direction of the graphene sheets.

Herrera Alonso et al.⁶ also obtained very good mechanical and barrier properties of a sulfonated tetrafluoroethylene based copolymer (Nafion)/clay nanocomposites. In their work, aqueous suspensions of Montmorillonite (Na⁺-MMT) were mixed with aqueous or low aliphatic alcohol nafion solutions and submitted to ultrasonic bath for 2h. Films were then formed by solvent casting and their permeability and storage modulus were evaluated. Nafion is known and used for its formation of polymeric aggregates that resemble polymer crystals, which confers capital barrier properties to the materials. The addition of MMT to the Nafion matrix helped Nafion aggregates to orient themselves parallel to the clay platelets. The clay platelets also self-oriented parallel to the membrane plane, thanks to its high aspect ratio and to the gravitational force (**Figure 6**). As expected, increased barrier for methanol was obtained for the nanocomposite film. Elevated storage modulus was obtained over a wide range of temperatures (i.e. from 30 to 240 °C) when measured for the material containing 20

wt% of MMT. At the higher temperature, the storage modulus of pure Nafion was three orders of magnitude lower than that of the nanocomposite with high MMT loading.

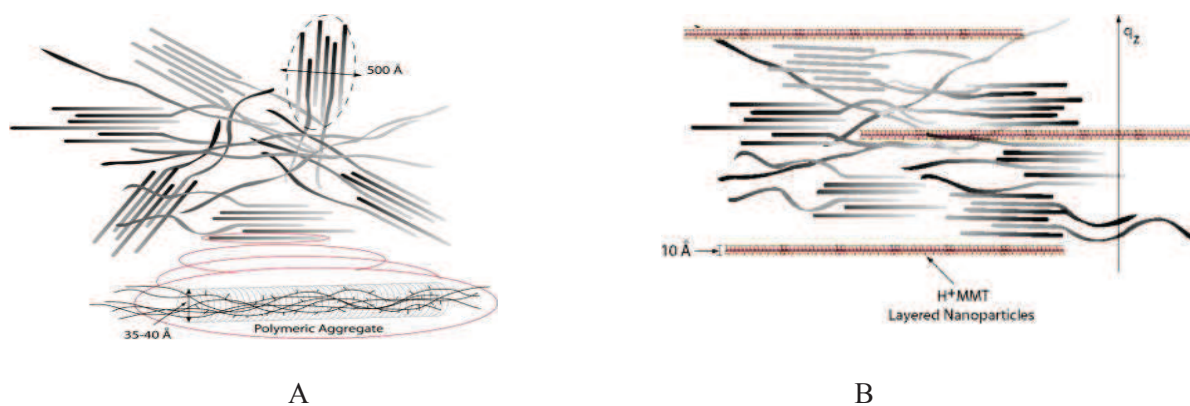


Figure 6. Schematic representation of bundles consisting of locally ordered Nafion elongated aggregates (surrounded by the ionic groups) (A). Schematic representation of nanocomposite Nafion morphology: bundles of polymeric aggregates oriented parallel to the membrane surface (B). Reproduced with permission from ref ⁶. © 2009 Elsevier.

As reported by different groups, to align 2D fillers in a polymer matrix some requirements must be respected, namely: extremely high aspect ratio; high rigidity of the filler; high filler content; low viscosity of dispersing medium; and long film forming time. Each one of these requirements contributes to the self-orientation of anisotropic particles by gravitational force. For instance, high filler contents promote the “excluded volume” effect, and the low viscosity and long film forming time enable the particles mobility and basal plane arrangement. The rigidity of the filler avoids folding and the higher the aspect ratio of the particles, the higher the probability of forming self-oriented phases.

Each method of nanoparticles alignment requires different characteristics of the fillers (e.g. magnetic response, electrical response, anisotropy). Nevertheless, there is a common prerequisite between all the techniques previously described: nanoparticles must be homogeneously distributed in the medium prior to the alignment. Therefore, the pre-treatment of the nanoparticles is necessary in some cases. This treatment may consist of the surface modification with organic molecules, inorganic coating (e.g. silica coating) or polymer coating. Next section will focus on the polymer-coating or polymer-encapsulation of anisotropic particles.

I.3 Polymer-encapsulation of anisotropic particles

Most of the works described so far consisted in mixing a suspension of nanoparticles with a monomer solution, a polymer solution, or introducing directly the nanoparticles into monomers. Films are then casted by solvent evaporation, in the case of polymer solutions, or obtained after polymerization, in the case of monomers. For some cases, the modification of particles surface is necessary to render the particles compatible with the monomers and/or the polymer matrix. One way to better disperse nanoparticles in a matrix, preventing aggregation and sedimentation, is by encapsulating them with a polymer layer and further dispersing them in the preformed polymer matrix or directly drying the solvent to form the desired material.

Different strategies have been employed to surround inorganic particles with polymers, and both spherical (i.e. isotropic) and anisotropic particles have been the object of intensive study. Since the corresponding bibliography is quite extensive, we will concentrate on the techniques used for anisotropic inorganic nanoparticles only.

The formation of a polymer layer around anisotropic particles may be performed either in solution, forming a polymer corona, or in dispersed media, consisting of polymer encapsulation. In solution, the polymer surrounding the particle is soluble, and it is defined as a polymer corona. By encapsulation, one must understand the formation of a polymer shell resulting from the insolubility of the polymer in aqueous media, which causes the polymer to precipitate onto the surface of nanoparticles. This last technique is specifically interesting because it generates hybrid latexes, where the polymer/inorganic particles are stably dispersed in water. These dispersions can be used either in liquid state or to form hybrid films by simple water evaporation. This class of materials has been widely applied in coatings, adhesives, pharmaceuticals, cosmetics and membrane industries.

To produce such hybrid latexes, the (mini)emulsion polymerization technique is the more frequently used, since it consists in an efficient technique to produce waterborne polymer or polymer/inorganic colloids. It is a quite versatile method, in which a wide range of monomers can be polymerized at various temperatures. More recent techniques were developed to control the molar mass of the polymer and the functional group on the extremity of each polymer chain. The principle of these techniques and their use to encapsulate anisotropic nanoparticles will be presently described.

I.3.1 Free-Radical Emulsion Polymerization

Emulsion polymerization is a free-radical polymerization process in dispersed heterogeneous media. This process presents numerous interesting features, such as the production of high molar mass

polymers at high rates, production of latexes at high solids contents (up to 60%) keeping low viscosity, polymerization of a wide range of monomers, specially vinyl monomers, and a very valued feature of being environmental friendly, since the continuous phase is usually water.

Emulsion polymerization is widely used in the pharmaceutical, cosmetic, ink and paint, adhesive and coating industries, representing 15% of the Western World 10^8 tons/year polymer production ¹⁰⁰ in 1995. Nowadays, the demand for emulsion polymers is of 10 million metric tons (dry)/year.¹⁰¹

In an emulsion polymerization system, surfactant, monomer and initiator are initially present in a heterogeneous aqueous medium where the monomers are non-water-soluble. Surfactants are relatively small molecules with a non-polar structure (tail) containing in one extremity a polar group (head). When put in water in a certain concentration, they can assemble in small spherical conformations where the tails are protected by the polar heads that stay on the outer surface, minimizing the surface energy. These formations are called micelles. The minimal concentration in which surfactants can form micelles is called Critical Micelle Concentration (CMC).

In emulsion polymerization, surfactants are usually added in a concentration above the CMC, so micelles are present in the medium. The monomer, which is hydrophobic, is partitioned in big reservoirs (droplets), inside the micelles and a small amount is present in the aqueous phase (**Figure 7 A**). The initiator is water-soluble, and it can be decomposed thermally, photochemically or by the addition of an activator (redox) to form radicals in the aqueous phase. These radicals react with the monomer present in water and form oligoradicals. These oligoradicals continue to grow by adding monomer units, until they reach a critical length for which they are no longer soluble in water, causing their migration to micelles or their precipitation, depending on the nucleation mechanism. Polymerization continues inside micelles, now called particles, swollen by monomer, which is diffused from the droplets to particles core. Along the polymerization, particles grow by the gradual entry and consumption of monomer. Polymerization finishes when all monomer is consumed. The final product consists of polymer particles dispersed in water and stabilized by surfactant molecules (**Figure 7 B**).

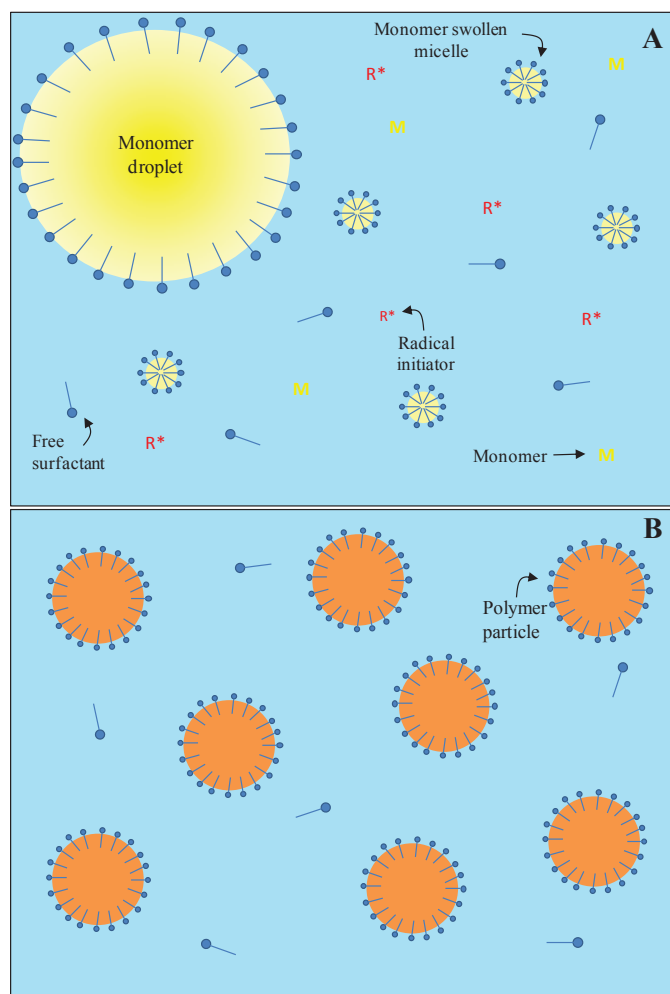


Figure 7. Schematic representation of the (A) initial and (B) final stage of emulsion polymerization.

During the polymerization, two processes occur simultaneously: (i) nucleation, formation and growth of latex particles and (ii) initiation, propagation and termination of the macromolecular polymer chains through a free radical polymerization process.¹⁰² The first process is specific to emulsion polymerization systems, and the second one is general for all radical polymerizations in whichever technique used. The arbitrary division of the former process in three phases was proposed by Smith and Ewart¹⁰³, giving Phase I as the nucleation of particles; Phase II as the growth of particles; and Phase III as the end of polymerization.

- 1- *Phase I* is characterized by the formation of first radicals and oligoradicals in the aqueous phase and their consequent migration to the micelles core, nucleating the first particles. Along this initial phase, polymerization rate is increasing owing to the formation of new particles (i.e. polymerization loci). This phases generally goes from 0 – 15% of conversion. Different types of nucleation can be distinguished according to surfactant concentration, temperature and nature of the monomer, and they can take place simultaneously during polymerization:

- a. Micellar nucleation – occurs when the surfactant concentration is above its CMC and micelles are present. First oligoradicals start to grow until they reach a critical length for which they are no longer soluble in water, causing the migration to the micelles¹⁰⁴.
 - b. Homogeneous nucleation – occurs by the collision of two precipitated oligoradicals, which have also reached a certain length for which they lose solubility in water. This type of nucleation occurs mainly when a large concentration of monomer is found in water or in the absence of micelles¹⁰⁵.
 - c. Coagulative nucleation – can be considered as an extension of homogeneous nucleation. The very small nuclei formed by one of the precedent mechanisms agglomerate to form a new larger particle, due to their poor colloidal stability or difficulty on swelling with monomer^{106, 107}.
- 2- *Phase II* starts after nucleation when the number of particles (N_p) is constant and it consists in the growth of the nucleated particles by consumption of the monomer present inside the swollen particles. Monomer droplets act as reservoirs of monomer, which are constantly feeding the particles by diffusion through the aqueous phase. Polymerization rate is constant during this phase on account of the constant monomer concentration inside each particle and the constant number of particles. Transition from phase II to phase III occurs generally at a monomer conversion between 80 and 90%.

During this phase, the polymerization rate can be generally expressed as:

$$V_p = -\frac{d[M]}{dt} = k_p[M]_p[R\bullet] \quad \text{Equation I.1}$$

Where k_p is the propagation rate constant ($L_p \text{ mol}^{-1} \text{ s}^{-1}$); $[M]_p$ is the monomer concentration inside each particle (mol L_p^{-1}); and $[R\bullet]$ is the radical concentration in the emulsion (mol L_e^{-1}).

The radical concentration can also be expressed as:

$$[R\bullet] = \bar{n} \frac{N_p}{N_A} \quad \text{Equation I.2}$$

Where \bar{n} is the average number of radicals per particle; N_p is the number of particles per unit volume of emulsion and N_A is the Avogadro's number.

Combining equations I.1 and I.2, polymerization rate is given by:

$$V_p = k_p \left(\bar{n} \frac{N_p}{N_A} \right) [M]_p \quad \text{Equation I.3}$$

If $[M]_p$ and N_p are constant and considering \bar{n} also constant and equal to 0.5 (which is true for styrene), the order for the monomer drops to zero, resulting in a linear evolution of conversion with time during this phase (**Figure 8**).

- 3- *Phase III* comprises the consumption of the residual monomer inside latex particles, after all droplets are consumed. During this phase the polymerization rate is decreasing due to the gradual decrease on monomer concentration.

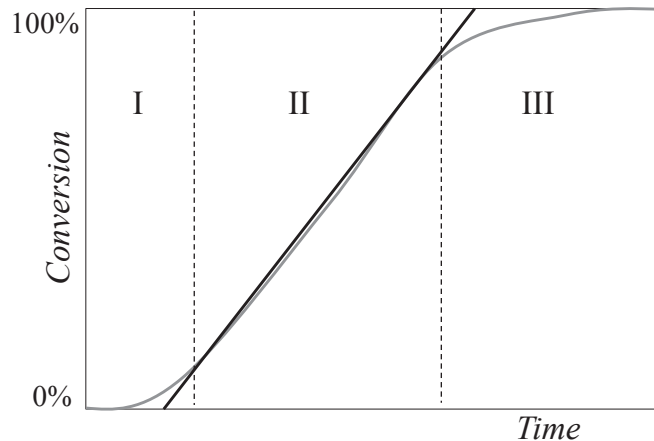


Figure 8. Typical kinetic profile of emulsion polymerization

Emulsion polymerization can be performed under three different processes, namely (i) closed reactor process or batch, (ii) semi-batch or semi-continuous and (iii) continuous.

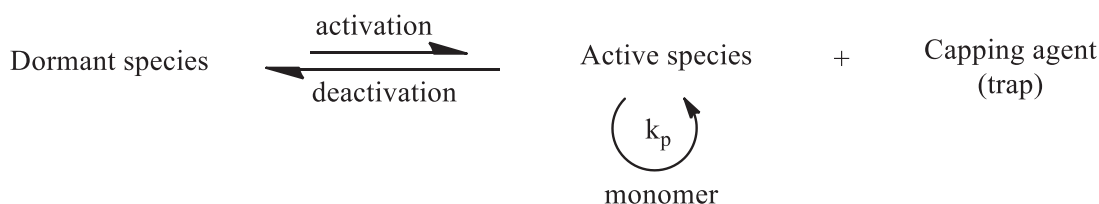
- (i) In closed reactors or batch systems, all reagents are added at the same time before starting polymerization, and time is the only independent variable. This process presents some drawbacks like a low productivity due to charging, discharging and cleaning time, difficulty in controlling thermal exchange and poor reproducibility of the nucleation step. Because of these disadvantages it is rarely used in industrial plants.
- (ii) Semi-batch or semi-continuous process is carried out by initially loading the reactor with part of the reagents, to enable the control over temperature and nucleation and to fix the number of particles in the medium. In a second step, the other reagents are added to continue the process. This technique is nowadays widely used industrially, since it allows the control over polymer composition, by adding different monomers at different specific times of polymerization; the control over particles morphology, by introducing different charges at different polymerization times or by adding surfactant to form new particles. Initiator can also be added to increase polymerization rate or to consume the residual monomer, consisting in a process called cooking phase.

- (iii) Continuous systems are constituted of various reactors connected in series where the reagents are continuously fed and the product is also continuously recovered at the end of the cascade line. This process is used for large scale productions, but it is difficult to finely control the granulometry and the morphology of the particles¹⁰³.

The emulsion polymerization technique was shown to be very interesting for the production of morphology-controlled latex or hybrid latex particles. However, over the years many efforts have been done to develop techniques capable of controlling not only morphology but also composition, molar mass and functionality of the polymer chains formed by this technique. With this aim, reversible deactivation radical polymerization techniques were developed, and will be described in the next section.

I.3.2 Reversible Deactivation Radical Polymerization (RDRP) in Emulsion

In a free-radical polymerization mechanism, the main events responsible for chains heterogeneity in terms of molar mass and functionality are termination and transfer reactions. One way to overcome such reactions is by imposing a dormant state to the propagating species in a way that they stay inert to combination, disproportionation or transfer. Such is the principle of reversible deactivation radical polymerization techniques which are based on a dynamic equilibrium between active propagating radicals and dormant species.



Scheme 9. Dynamic equilibrium involved in reversible deactivation radical polymerization mechanism.

Termination reactions by bimolecular combination are inherent to radical polymerization, and cannot be totally avoided. According to equation I.4, the rate of termination can be minimized by decreasing the number of instantaneous active propagating species. Thus, during reversible deactivation radical polymerization the predominant species are deactivated ones, and the life time of a growing chain is significantly increased.

$$\frac{V_t}{V_p} = \frac{k_t [P\bullet]}{k_p [M]} \quad \text{Equation I.4}$$

Where V_t is the termination rate, V_p is the propagation rate, k_t is the termination rate constant, k_p is the propagation rate constant, $[P\bullet]$ is the concentration of active propagating species, and $[M]$ is the monomer concentration.

Three main techniques are currently reported: Nitroxide-Mediated Polymerization (NMP)¹⁰⁸, Atom-Transfer Radical Polymerization (ATRP)¹⁰⁹ and Reversible Addition-Fragmentation chain Transfer (RAFT)¹¹⁰. The two former methods work under reversible termination reaction, while the RAFT process is based on a reversible chain transfer reaction. These three techniques have opened the access to functional polymers with designed molar masses, narrow molar mass distributions and defined molecular architectures, like block copolymers, graft copolymers and stars, under much less demanding conditions compared to anionic or cationic polymerization techniques.¹¹¹ Although less commonly used, (reverse) iodine transfer polymerization ((R)ITP) and organotellurium-mediated radical polymerization (TERP) also are interesting techniques to produce functional polymers.

1.3.2.1 Nitroxide-mediated polymerization (NMP)

NMP is based on a reversible termination reaction between a growing active (macro)radical and a free nitroxide to form a (macro)alkoxyamine molecule. The (macro)alkoxyamine formed from this reaction, i.e. the dormant species, is the predominant species, and by thermal homolytic cleavage it can regenerate the propagating (macro)radical and the nitroxide¹¹² (**Figure 10**). This technique can be carried out following two pathways, the first one is referred to as bicomponent, and it consists in the addition of a conventional radical initiator plus a free nitroxide to form the (macro)alkoxyamine *in situ*; the second one is characterized by the use of a preformed (macro)alkoxyamine and it is called monocomponent. In the former pathway, the initiation efficiency is difficult to be determined, and thus the number of formed chains is unknown, explaining the necessity of the development of an alternative pathway, i.e. the monocomponent. This technique was the first controlled technique invented, appearing in 1993¹¹³, and it represents one of the most well-established techniques in RDRP.

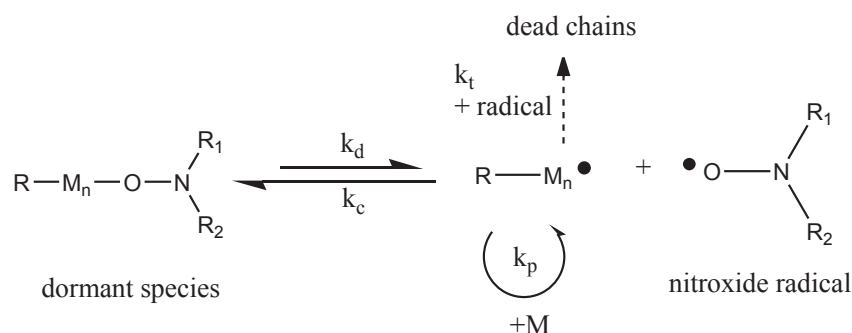


Figure 10. Activation/deactivation characteristic equilibrium in NMP, where k_d is the dissociation rate constant and k_c is the recombination rate constant.

1.3.2.2 Atom transfer radical polymerization (ATRP)

ATRP also relies on a reversible termination process. This technique was developed in 1994 at the same time by Sawamoto¹¹⁴ and Matyjaszewski¹¹⁵ as a derivation of the Atom Transfer Radical Addition (ATRA) from organic chemistry to polymerization. The reversible termination step is induced by a transition metal complex catalyst $[\text{M}_t^n\text{X}_n/\text{L}]$ (L = ligand). An equilibrium between dormant species RM_nX and active propagating radical species $\text{RM}_n\bullet$ is established, where dormant species carry an halogen atom ($\text{X} = \text{Cl}$ or Br) in one extremity and the C-X bond is homolytically cleaved by a reversible redox reaction catalyzed by the transition metal complex (**Figure 11**). Through the transfer of the halogen atom from the dormant species, the catalyst oxidizes to generate an active species and the complex on its superior degree of oxidation $[\text{M}_t^{n+1}\text{X}_{n+1}/\text{L}]$.

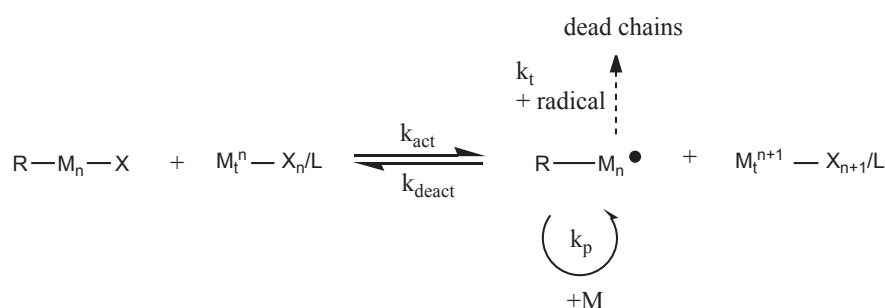


Figure 11. Characteristic activation/deactivation equilibrium of ATRP, with k_{act} = activation rate constant and k_{deact} = deactivation rate constant.

1.3.2.3 Reversible addition-fragmentation chain transfer (RAFT)

The RAFT mechanism operates through a different principle, based on a reversible or degenerative chain transfer. The equilibrium between dormant and active propagating radical species is established by adding a chain transfer agent (CTA), which consists of an organic molecule containing a

thiocarbonylthio functionality ($S=C(Z)-S-R$). When one propagating radical collides with the CTA, it can undergo an addition to the thiocarbonyl group ($S=C-$), forming an intermediate radical, which can fragment liberating the polymeric RAFT agent, named the dormant species, and the new radical growing chain, which is the active species. At the end of the polymerization, the great majority of the chains will have the same end chain functionality, having in one extremity the initiator fragment and on the other the thiocarbonylthio function originated from the RAFT agent. **Figure 12** shows the overall result of the RAFT polymerization process. Among the three techniques, RAFT excels for its capability of well controlling the polymerization of a wide range of monomers, including vinyl esters and vinylamides, and for its workability in varied media, like solution, bulk, aqueous homogeneous or heterogeneous dispersed media¹¹¹. More detailed description of the RAFT mechanism will be given further in this chapter.

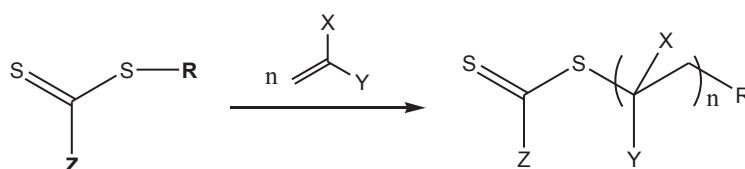


Figure 12. Overall result of the RAFT polymerization process.

All these controlled polymerization techniques were first developed and applied to homogeneous solution or bulk polymerization. However, their implementation to heterogeneous dispersed media, like emulsion, dispersion or miniemulsion, is being increasingly studied.¹¹⁶⁻¹¹⁹ Here we will focus on the application of the RAFT technique to emulsion polymerization.

Radical polymerization in aqueous dispersed media represents one of the most important processes for industrial polymer synthesis. The application of reversible deactivation radical polymerization to such systems is thus very promising. However, some difficulties rapidly appeared when switching from homogeneous to heterogeneous media.

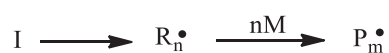
Detailed description of principles and operation of NMP and ATRP techniques can be found in several books and reviews.^{108, 109, 120} Here we focus on the RAFT polymerization technique, that will be the technique employed in this work. Various examples of the application of RDRP techniques to dispersed media can be found in recent reviews and books.^{116-119, 121}

1.3.2.4 Reversible Addition-Fragmentation chain Transfer (RAFT) and its application to dispersed media

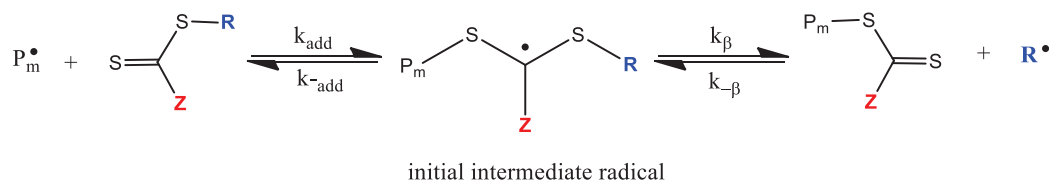
The Reversible Addition-Fragmentation chain Transfer (RAFT) polymerization technique was developed by the group of Rizzardo¹²² and another French group¹²³ almost simultaneously, which named it MADIX (Macromolecular Design via the Interchange of Xanthates). It is based on reversible chain transfer reactions, as briefly introduced before, where the equilibrium between radical propagating active species and dormant species is imposed by the addition of a chain transfer agent, containing a thiocarbonylthio group. The first group employed dithioesters as transfer agents, while the second group worked with dithiocarbonates (also known as xanthates).

Polymerization initiates by the decomposition of the initiator creating the primary radicals. These radicals react with the transfer agent molecule by addition to the thiocarbonylthio group by a weak covalent bond, creating an intermediate radical. This radical will further fragment on the opposite side ideally, liberating temporarily a deactivated species and a new active radical, able to initiate the polymerization. All radicals on their active state, i.e. the active species, can propagate by sequentially adding monomer units, until they encounter a transfer agent and enter the dormant state again. Irreversible termination by combination or disproportionation is also susceptible to occur at any time. To minimize termination, the amount of active radicals, which is also proportional to the initiator concentration, has to be minimized. Thus, high [RAFT]/[initiator] ratios are usually employed. **Figure 13** shows the different steps of the general mechanism of RAFT polymerization.

Initiation



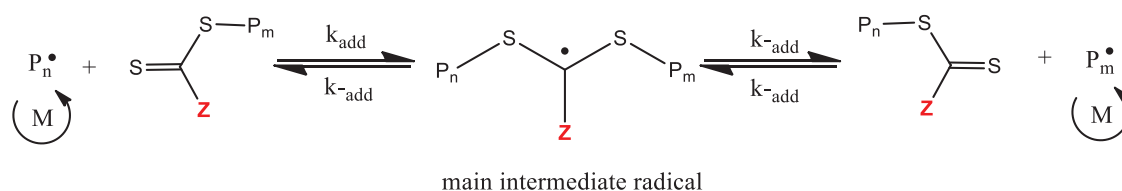
Chain transfer to RAFT agent



Re-initiation



RAFT main equilibrium



Termination

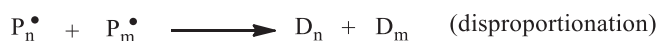


Figure 13. General mechanism of RAFT polymerization, with k_{add} = addition rate constant and k_{-add} = fragmentation rate constant.

The versatility of this technique can be ascribed to the possibility of designing different RAFT agents, according to specific needs. Playing with the nature of the R and Z groups of the thiocarbonylthio-containing molecule, will affect the transfer constant of the RAFT agent, enabling the control of polymerization of different monomers. An efficient RAFT agent has a high transfer constant (C_{tr}), to ensure a rapid rate of exchange between dormant and living chains. The Z group is mainly responsible for the stability of the intermediate radical, also contributing to the transfer constant. To favor a high C_{tr} , Z should activate the C=S group towards radical addition. The R group is generally a good homolytic leaving group, which contributes to the fragmentation of the intermediate radical at the ideal side (opposite side from where the radical was added). Furthermore, it must be able to re-initiate polymerization in its radical form. The addition of RAFT agents should not affect the rate of polymerization, only the molar mass and molar mass distribution of the final product. However, a slow fragmentation may lead to some inevitable consequences, like the consumption of the intermediate species by side reactions, or inefficient reinitiation, and then retardation or inhibition may be observed.

To avoid such effects, one must choose the appropriate RAFT agent according to the monomer(s) to be polymerized¹¹⁰.

Several different transfer agents can be used to control polymerization, including dithioesters, trithiocarbonates, dithiobenzoates, xanthates and dithiocarbamates.^{122, 124, 125} Probably the most widely applied, due to their versatility, are dithioesters and trithiocarbonates (Figure 14).

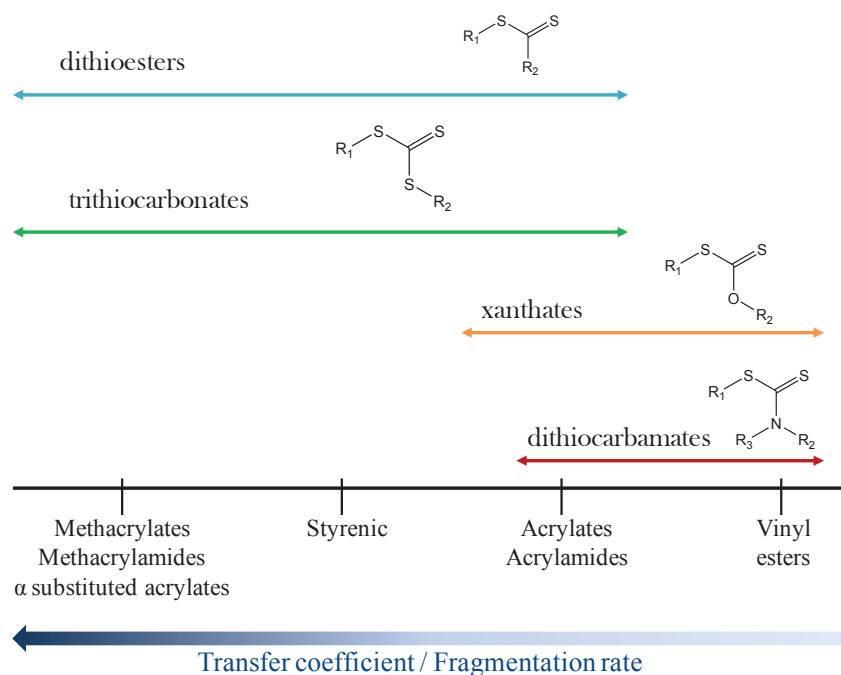


Figure 14. Efficiency of various RAFT agents on controlling the polymerization of different monomers.

The Z group affects both the rate of addition of propagating radicals to the thiocarbonyl in the pre-equilibrium, and in the main equilibrium reactions, and the rate of fragmentation of intermediate radicals for both equilibria as well. It is possible to change by 5 orders of magnitude the addition rate constant k_{add} by changing the Z group¹¹¹. The presence of carbon or sulfur adjacent to the thiocarbonylthio group increases the reactivity of the RAFT agent, which is the case for dithioesters and trithiocarbonates. A lone pair on oxygen or nitrogen adjacent to the thiocarbonyl decreases considerably the reactivity towards radical addition, as it is the case for xanthates and dithiocarbamates¹¹⁰.

More activated monomers (MAM) are classified as those monomers containing the double bond conjugated to an aromatic ring, a carbonyl group, or a nitrile, e.g. styrene, methyl methacrylate, and acrylonitrile, respectively. Less activated monomers (LAM) are those where the double bond is adjacent to saturated carbon, oxygen, nitrogen lone pair, or the heteroatom of a hetero-aromatic ring,

e.g. diallyldimethylammonium chloride, vinyl acetate and *N*-vinylcarbazole, respectively. Propagating radicals carrying a MAM terminal unit show low reactivity towards radical addition, and high rate of radical fragmentation. Thus, a more active RAFT agent, i.e. with a higher transfer coefficient, is required to favor the addition and promote good control. For MAMs, dithioesters and trithiocarbonates are more adapted. In contrast, propagating radicals with LAM terminal unit present high reactivity to radical addition, and a weak fragmentation rate. For these monomers, less active RAFT agents, i.e. with lower transfer coefficient, are required, otherwise fragmentation is slow and inhibition or retardation is likely¹¹⁰.

The R group must be a good homolytic leaving group with respect to P_n^\bullet , so that after addition of P_n^\bullet to the RAFT agent, the intermediate radical fragments liberating the polymeric RAFT agent and R^\bullet , instead of liberating P_n^\bullet again. The expelled radical R^\bullet must also be able to efficiently reinitiate the polymerization. Radical stability, combined with steric factors and polarity, is very important in determining fragmentation rates¹¹⁰. Figure 15 shows the efficiency of different R groups as leaving groups.

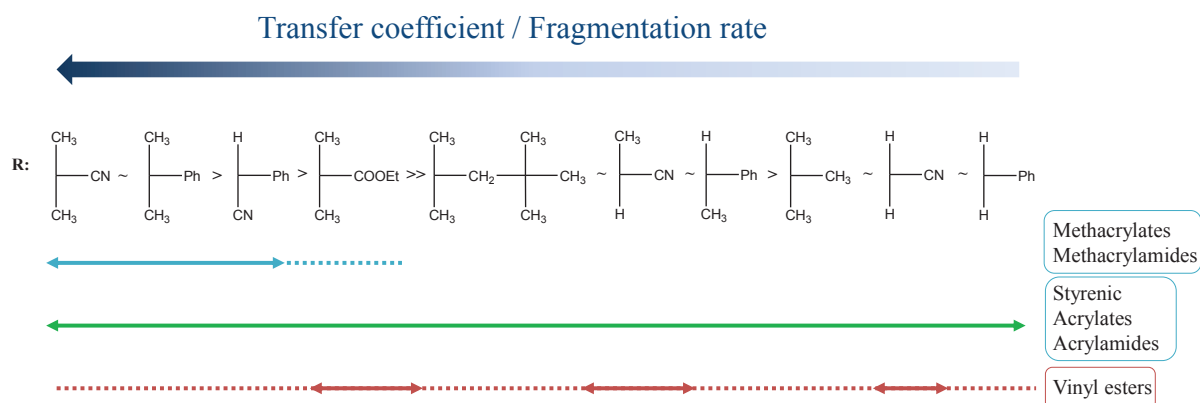


Figure 15. Efficiency of the R group as a leaving group when polymerizing different monomers. Dashed lines mean partial control.

Even though RAFT polymerization could appear easy to apply to aqueous dispersed media, some difficulties arise when going towards polymerization in aqueous heterogeneous systems.

In emulsion, the initiation and the formation of primary radicals occur in water, but polymerization is quickly transferred to micelles/particles core. The generally hydrophobic RAFT agent must be able to transit from water to particles, to correctly establish the equilibrium between active and dormant species, avoiding control and stability problems.

These diffusion issues could partly be avoided using miniemulsion or seeded emulsion polymerization, where the RAFT agent was present from the start in monomer droplets or swelled seed particles (i.e. polymerization loci)¹¹⁷. However, the emulsion technique is considerably simpler to implement and widely applied industrially, which encouraged scientists to explore the application of RAFT polymerization to this technique.

Ab initio RAFT emulsion polymerization could be performed utilizing two general approaches: a conventional approach using RAFT agent, free radical initiator and stabilized by surfactant; and a self-assembly approach where living chains of amphiphilic block copolymers act as both macro-chain transfer agents and stabilizers.

1.3.2.4.1 Conventional RAFT emulsion polymerization

Works performed using the first approach were almost discouraging, showing that the kinetics of such systems is highly complex. The studies¹¹⁷ employed different RAFT agents and different radical initiators, and it provided important conclusions, such as: (i) the diffusion rate of the RAFT agent from the monomer droplets to particles does not depend only on RAFT agent hydrophilicity, but also on the monomer solubility in water; (ii) for the polymerization of styrene, the more hydrophilic the RAFT agent was, the higher the degree of control; (iii) and the RAFT agent may enter particles directly, even before adding some monomer units. Another important conclusion, provided by an additional work, was that under the RAFT mechanism, livingness cannot be achieved if there is a loss in colloidal stability.¹¹⁷

1.3.2.4.2 Polymerization-induced self-assembly (PISA) RAFT emulsion polymerization

The development of the second approach, firstly reported by Ferguson *et al.*^{126, 127}, enabled superior control over *ab initio* RAFT emulsion polymerization. They used an amphiphilic RAFT agent, which was first employed to polymerize a water-soluble monomer (AA) in an aqueous solution polymerization. Secondly, they added butyl acrylate under continuous feed, to avoid droplets formation, in order to form oligomers of AA_x-b-BA_y-RAFT, which formed rigid micelles. These micelles were further swollen with the hydrophobic monomer which was continuously fed, and the reaction occurred under good control yielding a polymer with molar masses in agreement with theoretical values and narrow molar mass distributions. Another advantage of this approach is that no additional stabilizer was needed, since stability was provided by PAA moieties. The final product was composed of core/shell particles of diblock copolymers, with external layer of PAA, and a PBA core.¹²⁶ Triblock copolymers of PAA-b-PBA-b-PS were also formed (macromol 2005).¹²⁷

The application of this technique to batch systems was reported a few years later by Manguian et al.¹²⁸. In this work, they have shown the successful production of stable latexes stabilized by the hydrophilic moieties of the amphiphilic block copolymers formed *in situ* during polymerization. The hydrophilic block, composed of 2-(diethylamino)ethyl methacrylate (DEAEMA), was synthesized in solution in ethanol using a dithiobenzoate RAFT agent. The well-defined and reactive polymer was purified and poured to the aqueous medium reactor to perform the emulsion polymerization of styrene, started by heating after the addition of a cationic free-radical initiator. Stable latexes with relatively small particles diameter were obtained. Two mechanisms of particle nucleation were proposed, in which the first consisted in conventional homogeneous nucleation derived from the precipitation of oligoradicals formed independently of the macroRAFT agent. The second one supposed that oligoradicals formed from the reaction with the macroRAFT agent would form amphiphilic block copolymers, which could self-assemble to form particles. This second mechanism was taken as the main mechanism, and it was supported by the homogeneous and small particles diameter obtained (112 nm). The pH-dependency of latex stability, related to the DEAEMA solubility at different pHs, also confirmed that stabilization was indeed provided by the hydrophilic polymer block. The combination of steric and electrostatic stabilization using PEO and PDMAEMA based polymers was also reported by Santos et al.¹²⁹

Zhang et al.¹³⁰ also reported the use of a hydrophilic macromolecular RAFT (macroRAFT) agent, based on methacrylic acid (MAA) and poly(ethylene oxide) methacrylate (PEOMA) monomers, as stabilizer in the emulsion polymerization of styrene. The macroRAFT was synthesized in solution in 1,4-dioxane and purified and dried in a first step. It was then employed in the RAFT emulsion polymerization of styrene. With the progress of polymerization, the hydrophilic chains of the macroRAFT were chain-extended by the progressive addition of hydrophobic styrene units, forming an amphiphilic block copolymer able to self-assemble forming self-stabilized polymer particles. Beyond the formation of spherical particles, fibers and vesicles were also observed, depending on the hydrophilic/hydrophobic character of each block and its volume fraction. Using the same approach, Boissé et al.¹³¹ reported a study on the influence of the stirring speed on the formation of such non-spherical morphologies, using a macroRAFT based on AA and poly(ethylene oxide) acrylate (PEOA) monomers for the polymerization of styrene in emulsion. The authors showed that at low stirring speed, the formation of fibers was minimized or entirely avoided, due to a reduction in the particle-particle collision probability.

During the following years and inspired by the work of Ferguson et al.¹²⁶, some works were reported in which the synthesis of amphiphilic block copolymers by RAFT emulsion polymerization was performed entirely in water (one-pot process). Chaduc et al.¹³² reported the production of self-stabilized latex particles by this technique. Different hydrophilic and hydrophobic monomers were tested to synthesize the first and the second block, respectively. Poly(methacrylic acid) (PMAA)¹³³, PAA¹³⁴ and poly[methacrylic acid-*co*-poly(ethylene oxide)methacrylate] (P(MAA-*co*-PEOMA))¹³⁵

were reported as components of the hydrophilic block; and PS, PMMA and PBA as the hydrophobic blocks. This process involves two simple steps, starting by the aqueous solution polymerization of the hydrophilic monomer, via RAFT, to produce the first hydrophilic block. After complete consumption of the water-soluble monomer, the second monomer (hydrophobic) is added and a new addition of radical initiator is made. Polymerization proceeds under an emulsion (heterogeneous) system, where primary radicals are formed in water and react with the water-soluble macroRAFT agent. After the addition of a certain number of monomer units, the amphiphilic block formed becomes insoluble and self-assembles forming self-stabilized particles. Polymerization continues inside polymer particles following a similar mechanism as for conventional emulsion polymerization. High rates and good control of polymerization are obtained using this technique, and very stable latexes are formed with solids content up to 40 wt%.¹³⁵

Further works applied this one-pot process to produce non-spherical particles. Varied morphologies can be obtained by playing with the chemical nature, steric hindrance, the DP_n and the hydrophilic/hydrophobic ratio of each block. Spheres transforming into worm-like particles, fibers and vesicles could be statistically obtained (i.e. 100% one-type morphology).¹³⁶ Parallel development of this (PISA) technique was also reported using NMP¹³⁷⁻¹³⁹.

The development of all these processes, enabling the application of reversible reactivation radical polymerization in emulsion, also opened new possibilities to produce morphology-controlled nanocomposite colloids. Since, different strategies have been developed to combine nanocomposite science with controlled polymer synthesis to form waterborne polymer/inorganic nanoparticles.

I.3.3 Use of RDRP for the modification and encapsulation of inorganic particles

Reversible deactivation radical polymerization is being used to generate a large variety of hybrid nanoparticles morphologies. Janus particles^{140, 141}, core/shell particles^{142, 143}, and several types of anisotropic particles (tubular^{17, 144}, nanorods⁴⁷, nanosheets^{145, 146}, etc) can be found. To achieve such structures, different strategies have been developed, such as *grafting from*, *grafting through*, *grafting to*, self-assembly of block copolymers in presence of inorganic particles, layer-by-layer deposition of functional polymers and so on. Here we will focus on *grafting from*, *grafting to*, self-assembly of block copolymers with inorganic particles and macroRAFT-assisted polymer-encapsulation of inorganic particles techniques.

These techniques can be divided in two different classes. One consists in “protecting” the inorganic particles with a polymer brush, either grown from the surface or attached to it, generally produced by

grafting from or grafting to, respectively. *Grafting from* using controlled-radical polymerization is also known as surface-initiated (SI) controlled radical polymerization, even though here we talk about *grafting from* a colloidal particle and not a flat surface. To this approach we will refer to as *modification* of inorganic particles, because it aims at improving compatibility of the filler with a polymer matrix. The second approach is characterized by the formation of a polymer shell around the inorganic particle where the polymer is randomly distributed on the surface, not necessarily covalently bonded or orderly arranged, as it is the case of polymer brushes. This approach can be achieved by the layer-by-layer method, by block copolymers self-assembly in presence of inorganic particles or by a recently developed method herein referred to as macroRAFT-assisted polymer-encapsulating emulsion polymerization (REEP). The polymer-encapsulated particles obtained by this second approach could be added to polymer matrixes or be used as-synthesized to produce materials.

1.3.3.1 Grafting from

The *grafting from* technique consists in treating nanoparticles with organic molecules carrying on one end a functional reactive group (e.g. a monomer or an initiator molecule), which can participate in the polymerization, and on the other extremity a function that can interact with the surface (Figure 16). Through this technique, polymer chains are grown directly from the surface of NPs and are attached covalently or not. High grafting densities and high efficiency of the process can be obtained when using controlled radical polymerization.

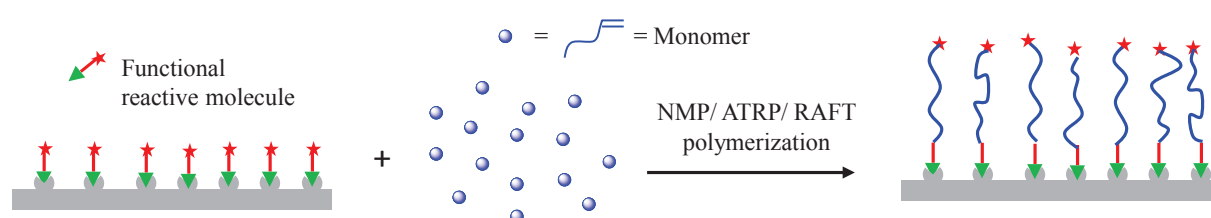


Figure 16. Schematic representation of the *grafting from* approach.

RDRP not only allows the production of polymers with controlled molar masses, molar mass distributions and architectures, but it additionally enables the prediction of polymerization loci (i.e. where polymer chains are effectively being formed), simply by tuning the control agent location. Application of the three main methods of controlled radical polymerization (NMP, ATRP and RAFT) to the *grafting from* technique can be found in the literature^{14-16, 18}.

The polymer-grafted nanoparticles produced present improved compatibility with polymer matrixes, being more easily dispersed. Thus, this technique is widely applied in the polymer/inorganic nanocomposite academic field.

1.3.3.1.1 Grafting from using RAFT

For *grafting from* using NMP and ATRP, the initiator is initially anchored to the surface, while for RAFT the chain transfer agent is immobilized on the surface. This is because in RAFT, the majority of chains contains the transfer agent fragment and propagates through this functional group. The RAFT agent can be linked to the surface either by the R or by the Z groups. Significant differences arise from one or the other approach, since mechanistic aspects of RAFT polymerization become then relevant to establish the main equilibrium between active and dormant species, thus leading to the control of polymerization.

When attached by the Z group, the thiocarbonylthio function of the RAFT agent remains attached to the surface all along the polymerization. The polymer chains grafted to the surface are always dormant, excluding the bimolecular termination of grafted radicals often observed in the R-group approach¹⁸. However, as polymerization progresses, the access to this function may become difficult, damaging the proper establishment of the RAFT equilibrium. When attached by the R group the thiocarbonylthio function remains on chain ends, and is easily accessible all along the polymerization. However, it is periodically detached from the surface, and this may lead to loss of control/livingness of the chains tethered to nanoparticles¹⁸.

As for the NMP *grafting from* polymerization, additional transfer agent is usually employed to improve polymerization control^{147, 148}. Because of that, polymer chains are formed simultaneously on the surface and in solution. Different chain transfer reactions may occur both in solution and on the surface. One propagating radical formed in solution have two possibilities: transfer to a dormant chain in solution or to a dormant chain on the surface. Surface-attached propagating radical has three possibilities: transfer to a dormant chain in solution, transfer to an adjacent dormant chain or transfer to a dormant chain of a second nanoparticle (**Figure 17**)¹⁴⁹. The presence of the additional RAFT agent decreases the probability of termination between adjacent propagating radical species.

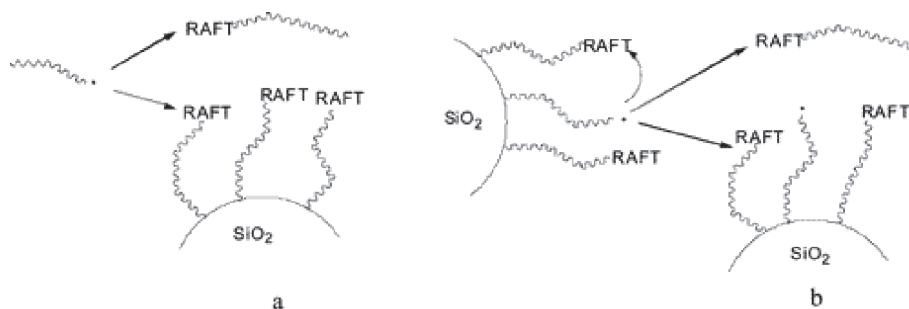


Figure 17. Chain transfer reactions for the radicals in solution (a) and on particles surface (b). Reproduced with permission from ref¹⁴⁹. © 2006 American Chemical Society.

Different nanoparticles have been used to perform *grafting from* polymerization via RAFT. The most commonly reported is silica¹⁴⁸⁻¹⁵³, but TiO₂^{154, 155}, POSS¹⁵⁶, CdSe¹⁵⁷, carbon black¹⁵⁸ and Fe₃O₄@SiO₂¹⁵⁹ can also be found. Gold nanoparticles are also used due to their strong affinity for sulfur compounds present on RAFT agents. However, such strong interactions may hinder the correct participation of the RAFT agent in the polymerization. Because of that, gold is often used to graft preformed polymers containing the RAFT functionality (i.e. *grafting to approach*)⁴³.

A few examples can be found for the application of this technique to anisotropic particles, such as Laponite clay¹⁶⁰ and graphene^{18, 161, 162}.

Chirowodza et al.¹⁶⁰ synthesized PS from the surface of Laponite clay by RAFT polymerization. To achieve that, they designed a cationic RAFT agent capable of intercalating into the clay galleries when quaternised. The RAFT-modified clay was then implicated in the bulk polymerization of styrene. Free RAFT agent was added to help controlling the polymerization. Free and bonded polymers were analyzed by SEC to give some insight into the polymerization process. Similar molar masses were found for both families of polymer chains, showing the successful control of polymerization even on Laponite's surface. However, when increasing the immobilized RAFT agent content, which meant the increase on clay content for a fixed RAFT/clay ratio, the medium became very viscous. The high viscosity minimizes monomer diffusion to the clay surface, resulting in termination occurring by recombination of adjacent propagating chains. The final nanocomposite was tested in terms of thermal stability. As expected, the presence of clay significantly improved thermal properties compared to pure polymer.

Grafting from RAFT polymerization on the surface of graphene was studied by Beckert et al.¹⁶¹ and Cui et al.¹⁶². In the first work the authors polymerized styrene from the surface of graphene previously modified with dithiourethane, dithioester and dithiocarbonate RAFT agents. The graphene modification was preceded by a functionalization step, in which graphene oxide or stearyl-graphene were obtained, and after which the hydroxyl surface groups could react with carbon disulfide, forming

the RAFT agent. All polymerizations yielded satisfactory amount of polymer. However, very poor control over polymerization was obtained, expressed by the broad molar mass distribution measured (2.5 – 5.0). The second report described the *grafting from* polymerization of positively charged poly(dimethyl aminoethyl acrylate), negatively charged poly(acrylic acid), and neutral styrene on the surface of graphene. The transfer agent used was a pyrene functional trithiocarbonate RAFT agent, which was attached to the surface via π - π stacking interactions. Polymerizations were carried out in presence and in absence of free pyrene functionalized RAFT agent. PS-grafted chains cleaved from the surface of graphene were analyzed by SEC. Linear increase of M_n with conversion was obtained, slightly lower than theoretical predictions, and low D (< 1.17) was measured. Differences on polymerization control in presence or absence of free RAFT agent were not discussed, and results concerning the control of polymerization of the other two monomers considered were not indicated. Additional works of RAFT *grafting from* of polymers on the surface of graphene are detailed and can be found in the review of Bradi et al.¹⁸.

The same limitation observed for NMP and ATRP *grafting from* techniques, regarding the grafting density, applies here. For the three techniques, smart strategies have to be developed to increase grafting density without damaging molar mass distribution. Despite this issue, this approach is still considered the most effective for producing highly dense polymer brushes on the surface of nanoparticles.

1.3.3.2 Grafting to

The *grafting to* approach is a postpolymerization process, consisting of grafting a functional group-containing polymer, previously synthesized, to a surface (**Figure 18**). The functionality of the polymer is designed according to the functional groups of the surface. This technique presents a less complex mechanism, and is more versatile in regard to the type of polymer that can be attached to the surface, as one is not restricted by the polymerization mechanism. In addition, it is a better alternative in regard to preservation of intrinsic properties of the targeted material. The major drawback is the limit on the degree of modification that can be imposed by the steric crowding¹⁸.

While RDRP is the most commonly used technique to grow polymers from inorganic surfaces, it is much less popular regarding *grafting to* approach. The later technique can be effectively conducted using polymers synthesized by polymerization techniques other than RDRP. Nevertheless, it is undeniable that RDRP techniques can provide a high degree of control over the functionality, grafting density and thickness of the grafted polymer brush¹⁸ and expand the range of applicable functional polymers to this strategy.

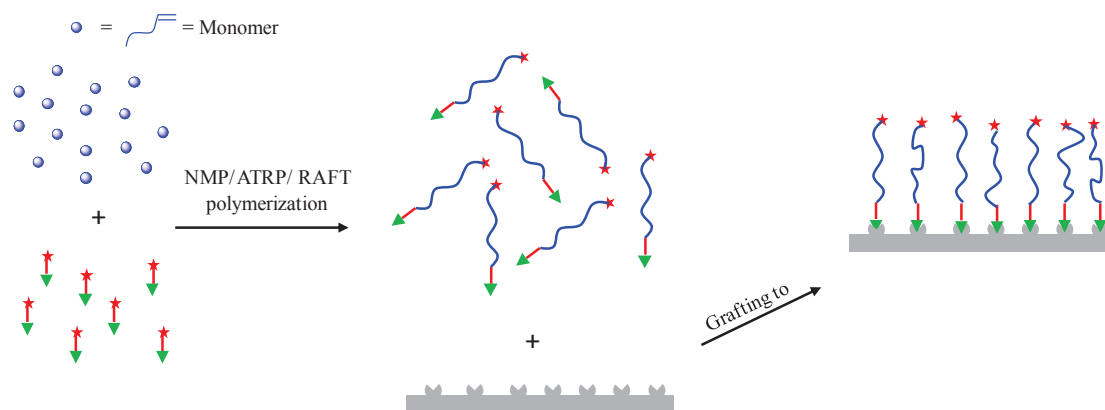


Figure 18. Schematic representation of the *grafting to* approach

Examples of grafting of polymers prepared by NMP and ATRP to the surface of carbon nanotubes can be found in the review of Homenick et al.¹⁷. As described by the authors, the polymers synthesized by NMP could be grafted to the surface by radical coupling reactions between the polymer-centered macroradical and the surface of CNT. Besides radical coupling reactions, CNT also undergo addition reactions. Br-terminated polymers prepared by ATRP could be modified to install a terminal azide group, which suffered a cycloaddition reaction with the tube wall. This reaction is called “Click” reaction, and it is also often used to graft polymers onto carbon nanotubes.¹⁸

Very similar approaches were used to graft polymers onto the surface of graphene or graphene oxide (GO) particles, and are detailed in the review of Badri et al.¹⁸. Polymers prepared by ATRP were grafted by cycloaddition to the GO surface. Atom transfer nitroxide radical coupling reaction was also used to graft polymers prepared by a different controlled polymerization technique (SET-LRP) to the surface of TEMPO-functionalized GO. Grafting of pre-formed polymers onto the surface of graphene/GO has also been performed using “click” chemistry.¹⁸

Grafting to approach performed using RAFT technique has been rarely reported. In the work of Cheng et al.¹⁶³ triblock copolymers of poly(*tert*-butyl acrylate)-*b*-poly(glycol methacrylate)-*b*-PS (*Pt*BA-*b*-PGMA-*b*-PS) synthesized by RAFT polymerization were grafted onto nanodiamond (ND) particles. Attachment was a result of reaction of the epoxy group of PGMA with carboxyl group on the ND surface, forming V-shape block copolymer brushes on the surface.

Few works describe the grafting of polymers prepared by RAFT to reduced GO surface following a noncovalent approach¹⁶⁴. In these works the authors take advantage of the interaction between pyrene and GO surface to draw their strategy. Pyrene-functionalized RAFT agent is synthesized and used to polymerize DMAEA, AA or *N*-isopropylacrylamide (NIPAM) in solution. The well-defined pyrene-functionalized polymers are then grafted to reduced GO surface by π - π stacking (**Figure 19**).

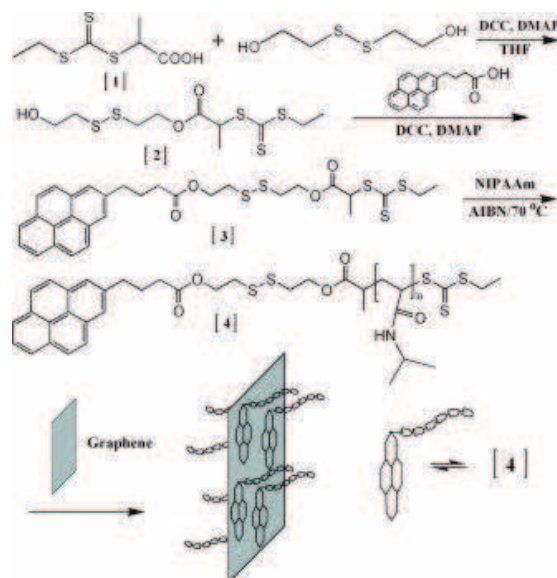


Figure 19. A schematic depicting the synthesis of pyrene-terminated PNIPAM using a pyrene-functional RAFT agent and the subsequent attachment of the polymer to graphene. Reproduced with permission from ref ¹⁶⁴. © 2009 Wiley Periodicals, Inc.

Combination of *grafting from* and *grafting to* strategies is sometimes applied. In this case, for a successful grafting of polymers, the first step must necessarily be the *grafting to*, followed by a *grafting from*. If performed otherwise, the polymer chains formed from the surface may prevent the access to the functional groups still available on the surface, and the grafting is not effective.

1.3.3.3 Block copolymers self-assembly in presence of inorganic particles

It is known that block copolymer melts form specific structured phase separated morphologies, depending on the chemical nature and volume fraction of each block.^{165, 166} For instance, lamellar, cylindrical and spherical morphologies can be obtained when producing a block copolymer melt.¹⁶⁷⁻¹⁶⁹ Self-assembly of amphiphilic block copolymers in liquid media has also been studied intensively in the past few years. Selecting the solvent to tune the solubility of each block allows the generation of different morphologies.^{166, 170} Formation of spheres, worms, fibers (i.e. worms of high aspect ratio), jellyfish, octopi and vesicles has been reported.¹⁷⁰

Inorganic nanoparticles having some affinity for one of the blocks can be added to block copolymer melts, and they will be subjected to the copolymer's self-assembly, decorating the structures formed.¹⁷¹ Some works have been done to incorporate inorganic nanoparticles into copolymer templates. The preferential location of particles in one of the blocks resulted in the formation of 1D array of nanoparticles¹⁷². Here we will focus on the block copolymers self-assembly in presence of inorganic particles performed in (liquid) dispersed media, not in bulk blends.

As briefly discussed before, amphiphilic block copolymers can self-assemble due to solubility differences between each block. Different morphologies appear as a result of three main forces: the degree of stretching of the block constituting the core of the object, the surface tension between the core and the corona/shell, and the repulsive interactions between the chains which form the corona/shell. To control such morphologies, different parameters can be tuned, affecting one of these factors. These parameters can be intrinsic to the copolymer, like the chemical nature, the architecture, the overall molar mass, the composition (i.e. the ratio between the hydrophilic and the hydrophobic block), and the molar mass distribution. Some extrinsic parameters can also impact the final morphology, like the copolymer concentration, the nature of the solvent, the temperature, the presence of additives (e.g. ions, homopolymers), and so on. The process has thus a non negligible influence.¹⁷³ Self-assembly of pure block copolymers could be modeled and generally followed the predictions based on the model. However, the addition of inorganic particles to the mixture may change some parameters, increasing the complexity of the system assembly^{174 171}. Recently, Martin et al.¹⁷⁵ studied the effect of block copolymers nature (i.e. length and composition) in the grafted copolymer sequence at varying monomer-monomer and monomer-particle interactions on size, shape and structure of assembled copolymer grafted nanoparticles, using Monte Carlo simulations. The grafted chain conformations were proven to be closely linked to how the monomer sequence facilitates the chain's ability to form energetically favorable attractive monomer contacts while minimizing unfavorable repulsive monomer contacts. They have also shown that as the sequence block length increased attractive monomer contacts were brought together more easily due to the favorable topological placement of like monomers along the chain. It was also found that the monomer-particle interactions only weakly affected the assembly of copolymer grafted nanoparticles when the particle size is small relative to the graft length, and the strength of particle-monomer interactions are commensurate with the monomer-monomer interactions. The effect of monomer-particle interactions in the cluster size, shape and structure were enhanced with significantly strong particle-monomer interactions and/or with substantially large particle sizes relative to graft lengths. In a previous work comparing alternate copolymers and block copolymers, the same group had shown that depending on the monomer interactions, alternating sequence either favors dispersions, or formation of smaller, isotropic clusters, while the diblock sequence favors assembly producing large anisotropic clusters.¹⁷⁶

Nanoparticles may be linked covalently or non-covalently to the copolymer chains. Thus, the production of such hybrid particles can occur by simple physical mixture (i.e. non-covalent bonding) or by chemical bonding (i.e. covalent bond) through *grafting from* or *grafting to* techniques, for example. After attaching polymer chains to inorganic particles, the self-assembly step is performed, generally by solvent exchange^{177, 178} or annealing.^{21, 179} This method enables the controlled localization of inorganic particles in copolymer micelles, rods, fibers, vesicles and so on.

The selective location of nanoparticles in block copolymer aggregates in solution was reviewed by Mai and Eisenberg¹⁹ (**Figure 20**). They described works carried out with gold, quantum dots (QDs) and iron oxide nanoparticles in presence of various block copolymers. Spherical, cylindrical and vesicle morphologies containing nanoparticles (NPs) in the core, interface or corona, were detailed. The review covered works in which the process was carried out using 1) preformed NPs stabilized with organic chains on the surface, followed by the co-self-assembly of the NPs and block copolymers (BCPs), or 2) the self-assembly involving the NPs alone after being coated with the block copolymers which will form the micelles. Different localizations of the NPs have been achieved by tailoring their surface coating or their size.

For example, using the first strategy, gold nanoparticles were incorporated into spherical micelles of polystyrene-*block*-poly(acrylic acid) (PS-*b*-PAA), which contained only one particle per micelle and were thus called “cherry micelles”.¹⁸⁰ Localization control was accomplished by virtue of a binding competition between a hydrophobic ligand (L_A) and a hydrophilic one (L_B) on the surface of the gold NPs (Au NPs), which leads to selective adsorption of amphiphilic PS-*b*-PAA chains on the L_A attached side of the AuNPs, and consequently the selective localization of the particles in the micelles in positions from the center to the interface. The self-assembly was carried out by a mix-and-heat approach. A mixture of Au NPs, PS-*b*-PAA, and L_A with or without L_B in DMF/H₂O was heated to 110 °C for 2h and slowly cooled to form the micelles. The number of particles per micelle can be varied by changing nanoparticles size.

The second strategy consists in coating NPs directly with block copolymers and mixing them to a solution of unattached block copolymers of the same nature. The formation of micelles is then carried out (e.g. by solvent exchange), and the hydrophobic or hydrophilic block of the diblock chains on the particle surface aggregate together with the corresponding unattached hydrophobic or hydrophilic segments of the micelle-forming diblocks. By changing the copolymer composition or environmental parameters, the spherical structuration transits to cylindrical- or vesicle-like morphologies. Using similar approaches as described for the formation of NPs-loaded micelles, NPs can then be incorporated into the core or the corona of cylindrical micelles and further into the walls, interfaces or corona of vesicles. A recent work from the same group reported the strategy applied to gold nanorods¹⁸¹.

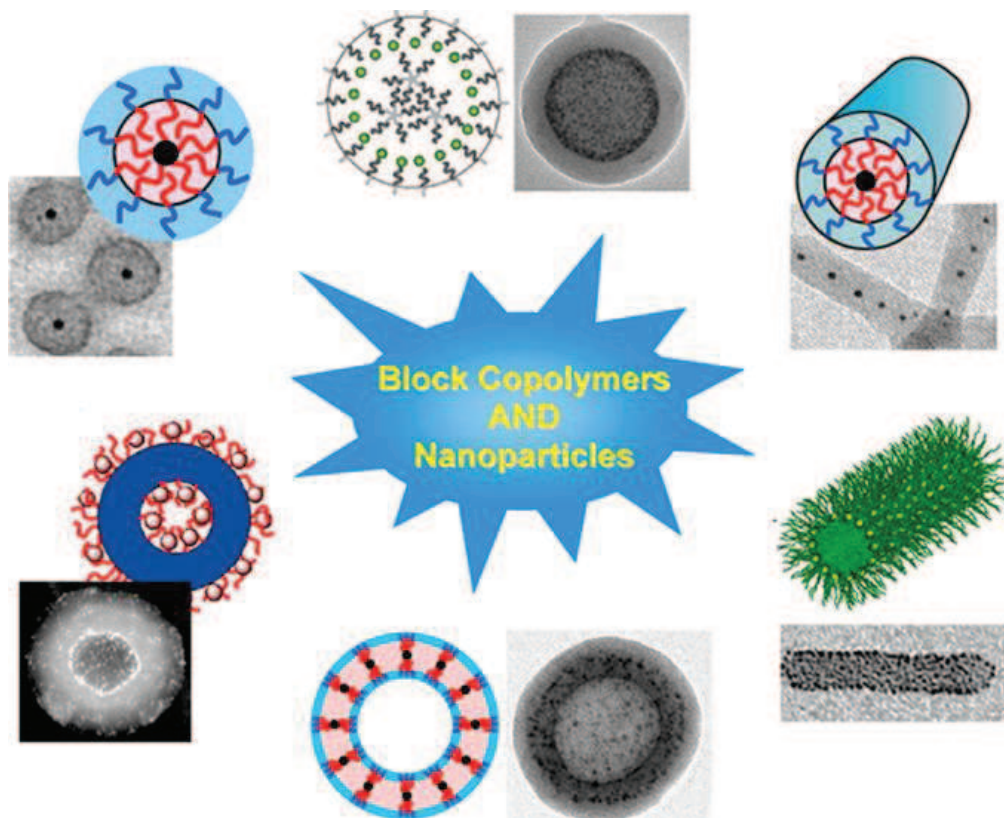


Figure 20. Different hybrid morphologies obtained by block copolymers self-assembly in presence of inorganic nanoparticles. Reproduced with permission from ref¹⁹. © 2012 American Chemical Society.

Nie et al. studied different block copolymers assemblies in the presence of gold spherical particles^{179, 182, 183} and nanorods^{21, 184-186} using the first strategy described above. Gold nanoparticles were usually linked to thiol-functionalized polymer chains (polymer-SH) by the *grafting to* approach. The polymer-Au nanoparticles were then mixed with the block copolymer solution, and the self-assembly process was performed by solvent evaporation followed by annealing. According to the molar mass of each block, different morphologies were formed. For instance, the formation of Au NPs-loaded polymer fibers was reported in the work of Li *et al.*,²¹ (**Figure 21**). Gold nanorods (NRs) were first functionalized with thiol terminated PS (PS-SH) of different molar masses by ligand-exchange approach. The Au NPs/PS-SH were then mixed to PS-*block*-poly(4-vinylpyridine) (3-*n*-pentadecylphenol) (PS-*b*-P4VP(PDP)) solution in chloroform with stoichiometric amount of PDP according to the number of pyridine groups in P4VP. Slow evaporation of chloroform gave rise to the hybrid sample film, followed by solvent annealing under saturated chloroform atmosphere at room temperature over 12h before drying under vacuum for 6h. Finally, the hybrid micelles were dispersed in ethanol and dialyzed against ethanol.

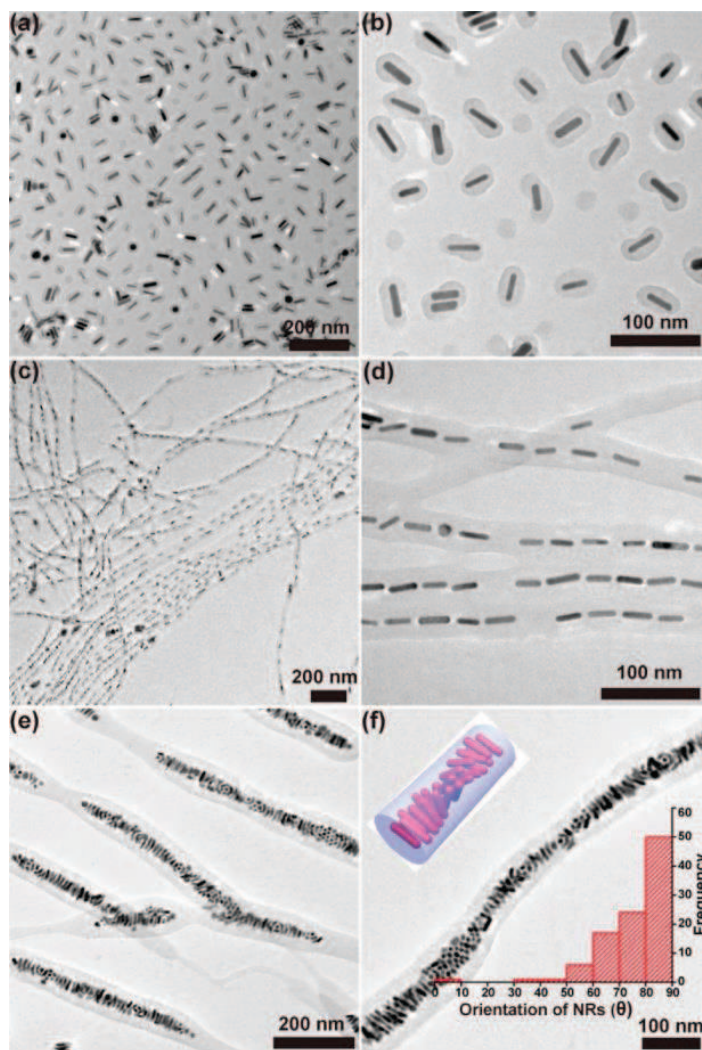


Figure 21. Bright-field TEM images of hybrid micelles formed from: (a, b) PS_{20k}-b-P4VP_{17k}(PDP)₁; (c, d) PS_{51k}-b-P4VP_{17k}(PDP)₂; (e, f) PS_{110k}-b-P4VP_{107k}(PDP)_{1.0} encapsulated NRs (content: ~ 27 vol %) (diameter: 7 nm; length: 29 nm). The NRs were grafted with mixed PS brushes (PS_{2k}:PS_{12k} = 1:1). Upper-left inset in part f is the cartoon showing the arrangement of NRs in the cylinders while the lower-right inset represents the histogram showing the orientation of the NRs. Reproduced with permission from ref ²¹. © 2013 American Chemical Society.

Again, using the first strategy described above, citrated-capped gold nanoparticles were also confined into micelles core or vesicle walls, as described in the works of Kang and Taton¹⁸⁷ and Xu et al.¹⁸⁸, respectively. Kang and Taton concluded that, by tuning the length of the block copolymer, the shell thickness around gold spheres could be controlled, generating defined core/shell nanostructures. Previous reports of Kang and Taton¹⁸⁹ also described the same strategy to encapsulate carbon nanotubes. In the work of Xu *et al.*, gold nanoparticles were functionalized with thiol terminated alkanes prior to the co-self-assembly. It was attested that the entering of AuNP into the vesicles wall depended on the ratio between the NPs diameter and the thickness of the wall. When large AuNPs were employed, micelles with golden core were formed. Hickey et al.^{177, 190} also described the

formation of micelles and vesicles loaded with iron oxide nanoparticles by the application of the same strategy.

Bockstaller *et al.* reported the influence of different inorganic particles (e.g. spherical, disk-like, and tubular particles) on block copolymers self-assembly. Interesting results can be found in a review¹⁷¹.

Using the recently developed technique of polymerization-induced self-assembly (PISA), Deng *et al.*¹⁹¹ reported the encapsulation of polyhedral oligomeric silsesquioxanes (POSS) into micelles or fibers, and in vesicles wall. They first polymerized a methacrylate-containing POSS monomer via RAFT using a dithiobenzoate RAFT agent. This first POSS macromolecular block was then chain extended in a second RAFT polymerization of styrene. The second polymerization was performed in octane, which is a selective solvent for the first block, and the self-assembly followed the PISA mechanism.

Recently, Wang *et al.*¹⁹² published an extensive review on this subject, in which the precise localization of nanoparticles obtained by the encapsulation of inorganic fillers into block copolymer micellar aggregates was discussed. The review covered the preparation of loaded micellar aggregates by the *ex situ* method, which consists in the co-self-assembly of preformed NPs with block copolymers, as presented earlier. In this work, the factors governing the precise localization of NP in micelles was discussed, and it was attested that to avoid NPs aggregation in the polymer micelles, one must reduce the NP-NP attraction and employ strong favorable interactions between NPs and the host polymers to offset the entropic penalty associated with this process. In addition, to control the spatial arrangement of NPs in the micelles, the positional degree of freedom of spherical and anisotropic particles must be minimized, to get ordered structures. To control the above factors, one must tailor different parameters, such as NPs surface chemistry, NPs size, volume fraction of NPs, NPs shape and others.

This technique of block copolymers self-assembly in presence of inorganic fillers enables the production of nanocomposites with well-defined morphologies. Such materials have potential applications in biotechnology, biomedicine and catalysis.¹⁹ When anisotropic arrangements are achieved, further applications can be envisaged, like the utilization of such structures to optoelectronic and microelectronic devices.²¹ However, the self-assembly is not straightforward, and in some cases it requires long dialysis time.

1.3.3.4 MacroRAFT-assisted encapsulating emulsion polymerization

Polymer-encapsulation of inorganic particles using RDRP in aqueous dispersed media has been described using emulsion and miniemulsion polymerization. The miniemulsion process requires a high

shear device (usually an ultrasound probe) to produce nanometric homogeneous monomer droplets, which are stabilized by a surfactant molecule. These droplets are further polymerized and become polymer particles. Ideally, polymer particles result on a one-to-one copy of initial monomer droplets. After organic modification of their surface, the fillers can be incorporated in the hydrophobic phase (i.e. monomer droplets), and be thus encapsulated at the end of the polymerization. This technique was applied using a RAFT process for the encapsulation of MMT clays by Samakande *et al.*¹⁹³. In this work the MMT clay was modified with an anchoring RAFT agent and then incorporated in styrene droplets. The *grafting from* styrene polymerization from MMT surface occurred inside the monomer droplets analogously to a bulk polymerization. However, this technique requires various steps, including the modification of inorganic particles, which must be adapted to the nanoparticle, and the emulsification (i.e. formation of nanometric droplets by an energy-consuming high shear device). In addition, secondary nucleation was described, in which “empty” polymer particles are formed, increasing the overall particles size distribution.

Emulsion polymerization is a much more robust and versatile technique, which is widely employed in diverse industrial processes. The development of reversible deactivation radical polymerization in emulsion systems has recently experienced striking advances, and an exhausting range of monomers can nowadays be polymerized using aqueous RDRP methods, forming controlled and well-defined polymer particles and organic/inorganic hybrid colloids. Taking advantage of these advances, the encapsulation of inorganic particles using RDRP in emulsion polymerization has been developed as an interesting route to encapsulate a variety of inorganic or organic fillers^{142, 144, 145, 194-199}. The RAFT process has almost exclusively been reported for the successful encapsulation of fillers in emulsion. Thus, we will focus on the description of such systems.

The process consists in the use of living amphiphatic random copolymers as both coupling agents and stabilizers during the emulsion polymerization. These copolymers are synthesized via RAFT polymerization, and thus possess the RAFT functionality on one extremity, being able to reinitiate the polymerization. At the same time, their nature allows them to interact with the surface of the inorganic particles, and their relative hydrophilicity provides stability to the objects in water dispersions. These copolymers are called macroRAFT agents. The process is carried out in two steps: first promoting the dispersion of the inorganic particles in aqueous suspensions by the aid of macroRAFT agents; and secondly performing the emulsion polymerization of hydrophobic monomers in batch or starved feed conditions, where the macroRAFT-containing particles act as seeds to nucleation process. The presence of the living copolymers on particles surface facilitates the rapid transfer of hydrophobic polymer growth over the entire particle surface. The orderly extension of each polymer chain results in an even build-up of polymer in the layer surrounding the particles, leading to their encapsulation.

This strategy was reported for the first time almost simultaneously by Nguyen et al.¹⁹⁴ and Daigle et al.¹⁴², applying surfactant-free and surfactant-aided processes, respectively, to encapsulate different pigments and mineral particles (**Figure 22**). The successful encapsulation reported by these two groups encouraged the application of the same technique to different fillers, like uncoated-TiO₂¹⁹⁵, CdS quantum dots¹⁹⁷, cerium oxide¹⁹⁹ and anisotropic particles like Gibbsite,¹⁴⁵ Montmorillonite clays¹⁴⁶ and carbon nanotubes^{144, 196}. The partial engulfment of cerium oxide using this strategy was also reported.²⁰⁰⁻²⁰²

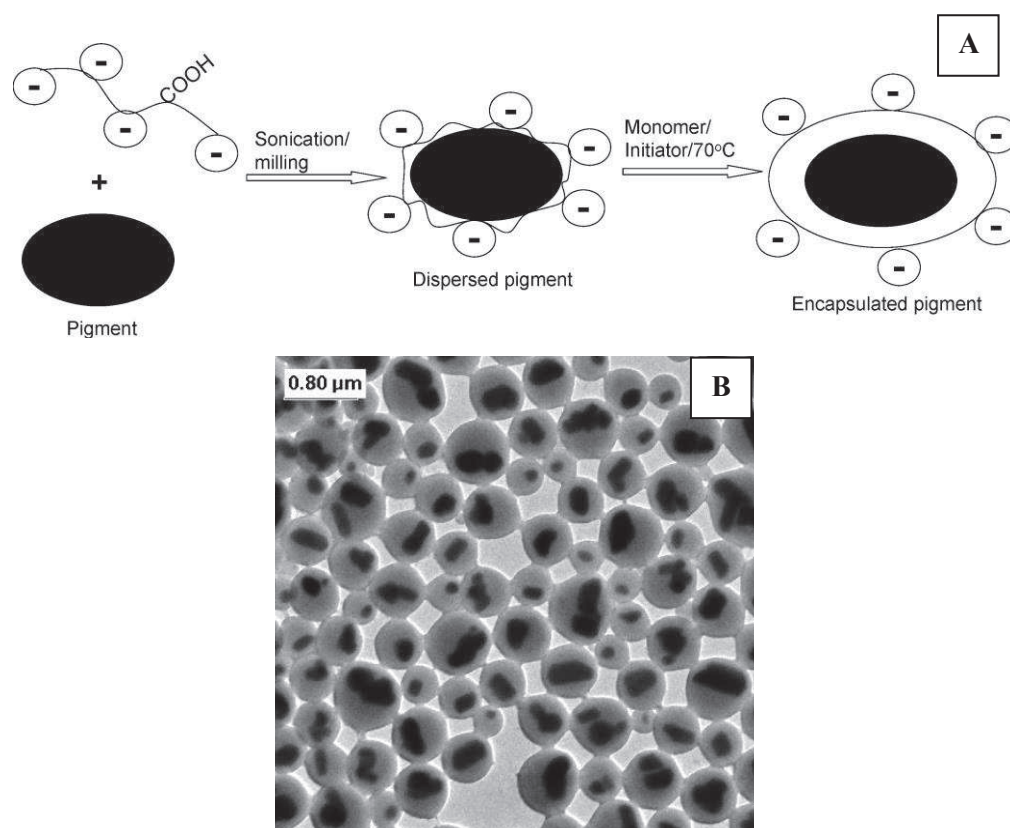


Figure 22. (A) Schematic representation of the dispersion and encapsulation of pigment particles using macroRAFT random copolymers. (B) Encapsulated titanium dioxide pigment particles become spherical after the polymerization of 68% monomer (MMA:BA 10:1) in weight. Reprinted with permission from ref¹⁹⁴. © 2008 American Chemical Society.

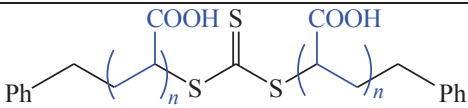
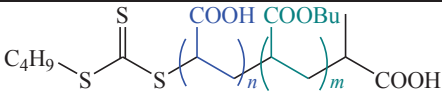

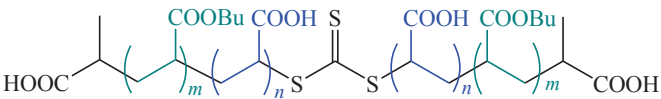
The strategy is often applied using a living random copolymer based on AA and BA monomers. Sulfonated- and phosphonated-based macroRAFT agents were also tested, but no encapsulation was achieved with such copolymers. The failure was attributed to the absence of acrylic acid units^{201, 202}. Generally, the acrylic acid units are responsible at the same time for promoting electrostatic interactions with the inorganic surface and for providing stability to the particles in aqueous dispersions. Butyl acrylate units are added to increase the hydrophobicity of the living copolymer, favoring the chains adsorption onto the surface and increasing the affinity between the particles and the hydrophobic monomers. Random distribution of AA and BA units along the copolymer chains

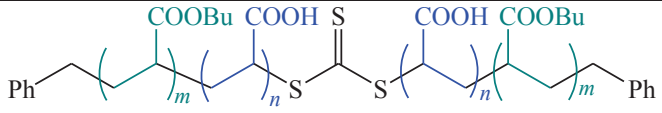
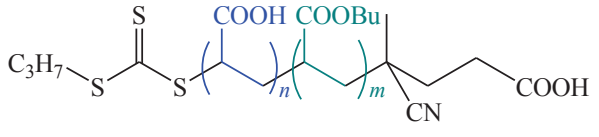
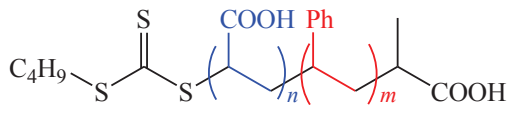
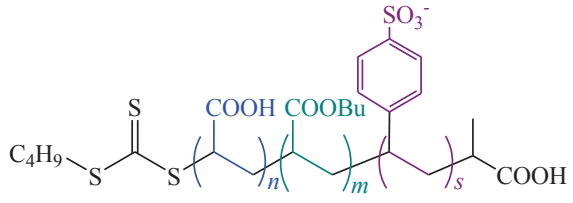
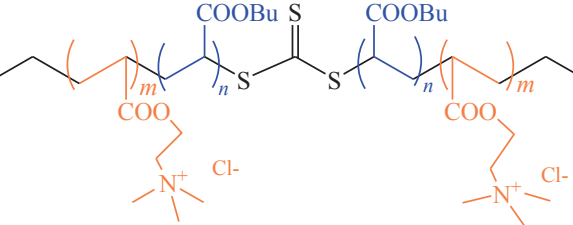
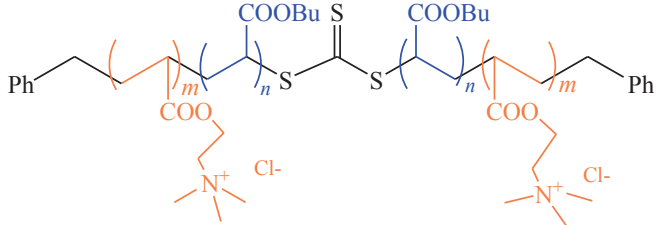
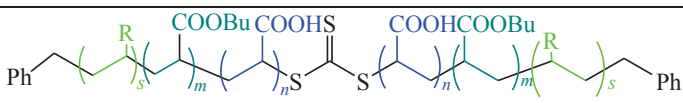
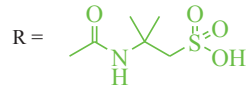
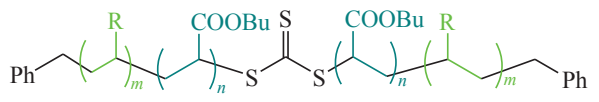
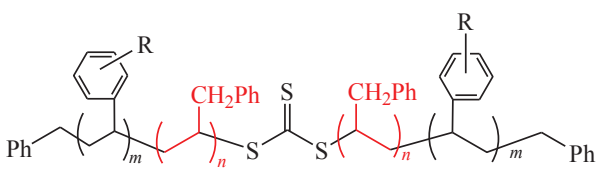
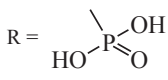
guarantee the non-surfactant-like character of the macromolecules, avoiding micelles formation and decreasing the probability of secondary nucleation. These two requirements have to be fulfilled: enough adsorption of the macroRAFT onto the surface and high affinity of the hydrophobic monomers for the particles environment. Labile copolymer chains (usually AA rich and/or BA poor copolymers) are more likely to remain in the aqueous phase, engendering secondary nucleation. However, too hydrophobic macroRAFTs (BA rich) may form micelle-like aggregates, also resulting in secondary nucleation. Judicious ratio and statistical distribution of the two monomers is crucial to comply with the requirements and achieve encapsulation.

Generally, short macroRAFT chains/oligomers are employed, to provide a high number of RAFT units per particle and to decrease the water sensitivity of the final product (lower content of hydrophilic species). Long macroRAFT copolymers have their solubility in water limited, which could induce their collapse and formation of small particles, favoring secondary nucleation. They also provide smaller number of RAFT per particle, and a lower control over polymerization could be expected. On the other hand, too short macroRAFT agents, possessing few anchoring units, are more labile, and may lead to stability problems. MacroRAFT agents up to $3\ 500\ \text{g mol}^{-1}$ were reported on the successful encapsulation of nanoparticles.

The RAFT agent nature may disturb or contribute to the success of the process. A suitable RAFT agent should provide efficient monomer addition rate to the macroRAFT extremity to avoid monomer accumulation, which could hamper encapsulation, as it will be seen further. In addition, it should not have surfactant-like properties to avoid nucleation of new polymer particles.

Table 1. Chemical structure of macroRAFT agents employed by different groups to encapsulate different inorganic fillers

macroRAFT agent	Reference	Filler	Success
 <p>The structure shows a central disulfide bridge (-S-S-) connecting two polymer chains. Each chain consists of a methylene-interrupted copolymer with carboxylic acid (COOH) and carboxylate (COOBu) groups. The chains are terminated with phenyl (Ph) groups.</p>	Daigle et al., 2008 Das et al., 2011	Minerals CdS QDs	Yes Yes
 <p>The structure shows a disulfide bridge (-S-S-) connecting a butyl-terminated chain (C₄H₉-S-) and a copolymer chain with COOH and COOBu groups.</p>	Das et al., 2012	PbS QDs	Yes
 <p>The structure shows a disulfide bridge (-S-S-) connecting an ethoxy-terminated chain (C₂H₅-O-S-) and a copolymer chain with COOH and COOBu groups.</p>	Nguyen et al., 2008	Pigment NPs	Yes
 <p>The structure shows a disulfide bridge (-S-S-) connecting two copolymer chains, each terminated with a carboxylic acid (COOH) group.</p>			Yes

	Ali et al., 2009	Gibbsite	Yes
	Garnier et al., 2012	CeO ₂	No
	Zgheib et al., 2012	CeO ₂	Yes
	Zhong et al., 2012	Carbon NTs	Yes
	Nguyen et al., 2012	Carbon NTs	Yes
	Mballa et al., 2012	MMT clay	Yes
			
	Garnier et al., 2013	CeO ₂	No
			
			
	Warnant et al., 2013	CeO ₂	No

Another parameter that highly influences morphology during the process is pH. The ionization state of the AA units can be tuned by changing the pH, and it will define the partitioning of the copolymer between the aqueous phase and the surface. Moreover, inorganic particles surface charges are subject to charge inversion above/below a certain pH, defined as the isoelectric point (IEP). Thus, the electrostatic attractive forces between the surface charges and the macroRAFT also depend on pH.

The fate of macroRAFT chains present in the aqueous phase has been described following two scenarios. Some researchers propose that the free copolymer chains in water do not (or insignificantly) chain extend, despite the presence of monomer and free radical species. Instead, they migrate to the surface of particles during the progressive growth of the polymer shell, providing further stability to the former. This mechanism was proposed based on results where no secondary nucleation took place. Plus, the free chains in water could be recovered and reused to repeat the process with new inorganic particles¹⁹⁴. The second mechanism proposed takes into consideration that chain extension occurs simultaneously in water and on the surface of particles. Once polymerization is triggered, the monomer is inserted on the adsorbed and free macroRAFT chains, and this last one becomes more and more hydrophobic. The adsorbed chains form the shell, while the free may form new “empty” particles or adsorb onto the surface offered by nanoparticles. The second option is statistically favored due to the high amount (in weight percent) and high surface of nanoparticles.

The process has been conducted in batch^{142, 197} or starved-feed^{145, 146, 194-196, 198-202} conditions, the second one being preferable for a few reasons. In starved feed conditions, the monomer is instantaneously consumed after its addition, preventing the accumulation of monomer and the formation of monomer droplets. Such hydrophobic droplets could strip the macroRAFT copolymer stabilizers from the surface of particles or cause inorganic particles to adsorb onto the surface of droplets, resulting in nanoparticles agglomeration. The monomer accumulated may also act as plasticizer, decreasing the glass transition temperature (T_g) of the copolymer shell. This decrease in T_g increases the inorganic particles mobility, possibly allowing their migration to the polymer/water interface in a thermodynamic process. In addition, it was observed that phase separation phenomena can occur in batch mode, whereas kinetically trapped morphologies are observed with slow addition rates, leading to an even coating of nanoparticles by the polymer shell. The presence of surfactant molecules did not impede nor contributed to the encapsulation of the fillers, but it was only needed to help stabilization when the batch process was conducted.¹⁴²

The monomer feed composition is another parameter that can affect the final morphology. Depending on the monomer mixture, different hydrophobicity and different T_g are obtained. For instance, a hydrophobic and low T_g monomer mixture (e.g. MMA:BA – 7:3 wt/wt) presents high interfacial tension and high surface energy, which causes the minimization of the surface area and drives the inorganic particles to the polymer/water interface. On the other hand, more hydrophilic monomers presenting higher T_g (e.g. MMA - 100%) generate uneven surface and particles aggregation. The uneven polymer surface is attributed to secondary particles aggregation onto the fillers surface and because of the high T_g , the polymer mobility is not high enough to create smooth surface. Fillers aggregation may result from the increase on surface area (due to the uneven surface) and the low amount of macroRAFT to stabilize the new surface. All the above can be overcome if the adsorption of macroRAFT to the surface is strong enough to provide, at the same time, the affinity required to

transfer the polymerization from the aqueous phase to the surface, and the hydrophobicity needed to impede their migration to the polymer/water interface.

The influence of the polymerization control (i.e. polymers with narrow M_n distributions, \mathcal{D}) on the formation of the polymer shell, on the success of encapsulation and on the control of morphology is not yet completely clear. Both controlled and uncontrolled systems generated polymer-encapsulated fillers^{142, 194}. The key feature of this technique goes beyond the use of reversible deactivation radical polymerization for the sake of controlling molar masses and their distribution, but it takes advantage of the RAFT technique to reinitiate a dormant oligomer which has high chain-end reactivity. Thus, the livingness of macroRAFT copolymers is crucial, even though uncontrolled polymerization sometimes takes place.

Different fillers were encapsulated using this technique, and some tendencies can be highlighted regarding the size and the aspect ratio of the filler. The encapsulation of large fillers often generates morphologies with one filler per particle, reflecting the facility of dispersing and stabilizing such inorganic particles in aqueous media before, during and after polymerization. When very small fillers are used (e.g. CeO_2 ¹⁹⁹ and CdS quantum dots¹⁹⁷), the total surface area is much greater, and stabilization of such a large surface area becomes more challenging. The conditions in which encapsulation is favored (e.g. pH, macroRAFT nature, hydrophilic/lipophilic balance of macroRAFT) are sometimes insufficient to provide the necessary stabilization. In these cases, the fillers tend to aggregate forming finite-size clusters, which are encapsulated at the end of the process (**Figure 23**, A and B). The aspect ratio of the filler does not influence morphology to the same extent. High aspect ratio platelets (e.g. Gibbsite¹⁴⁵ and Montmorillonite¹⁴⁶) and nanotubes^{144, 196} (e.g. SW and MW carbon nanotubes) were successfully encapsulated using the same strategy (**Figure 23**, C and D).

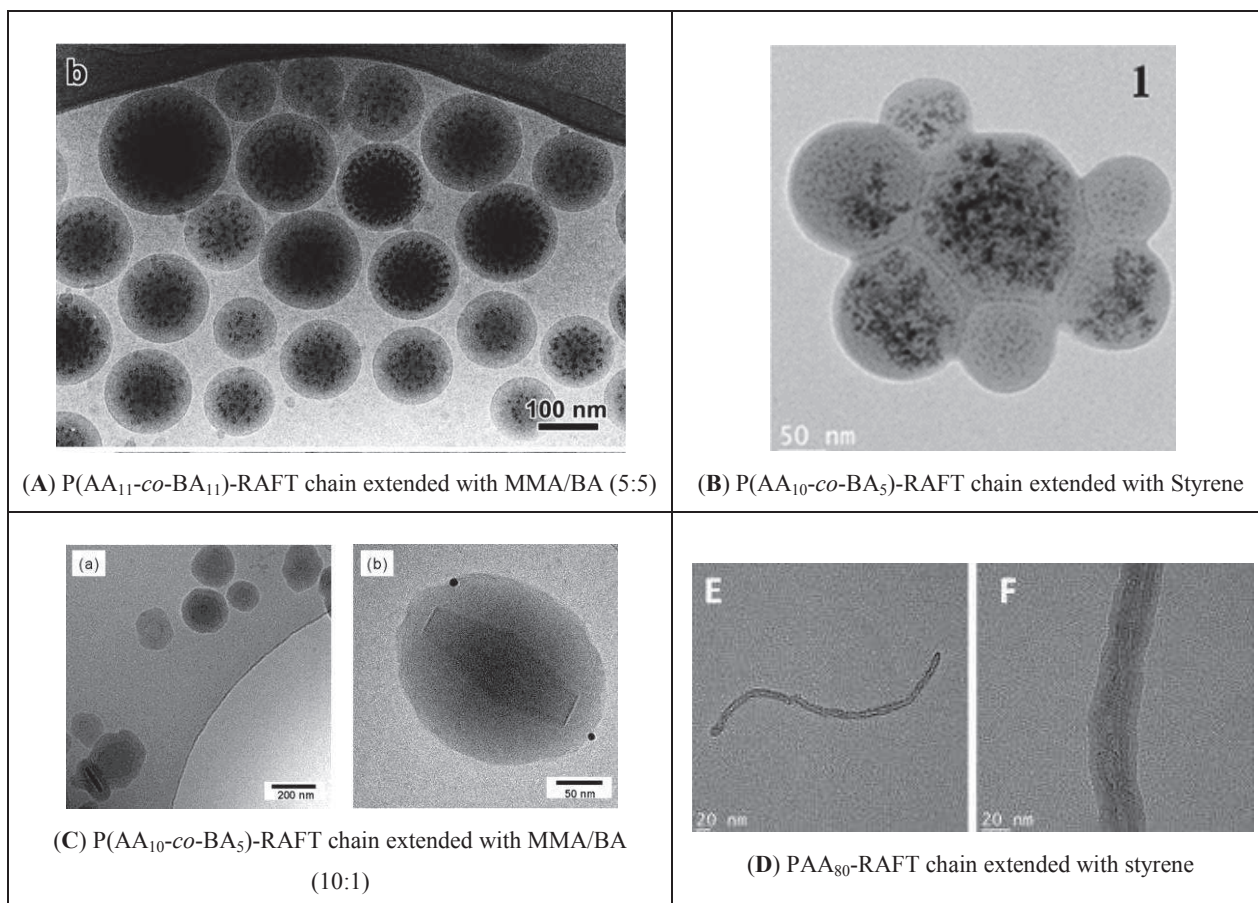


Figure 23. Hybrid latex particles obtained by macroRAFT-assisted polymer-encapsulation of (A) CeO₂ nanoparticles from ref¹⁹⁹; (B) CdS quantum dots from ref¹⁹⁷; (C) Gibbsite platelets from ref¹⁴⁵; and (D) carbon nanotubes from ref¹⁴⁴. All images were reproduced with permission from the publishers. (A) © 2012 RSC. (B) © 2011 Springer-Verlag. (C) © 2009 ACS. (D) © 2012 Wiley Periodicals, Inc.

It can be concluded that this strategy consists in a universal approach to encapsulate inorganic particles in aqueous dispersed media via the RAFT process. By designing the correct macroRAFT agent, which should be able to provide the filler with stability and affinity for the hydrophobic monomers, all kinds of fillers can be potentially encapsulated. It is also very versatile, allowing the polymerization of a vast range of monomers yielding polymers with different glass transition temperatures. Furthermore, such hybrid latexes can be obtained without the use of surfactant, avoiding all the problematic caused by these small molecules on the final product.

I.4. Conclusions

The introduction of anisotropy into polymer/inorganic nanocomposites, by the polymer-encapsulation of nanotubes and layered hydroxides, is the main objective of the present work. As it was seen in this chapter, anisotropy allows the improvement of varied properties, and can be achieved using different approaches. The alignment of isotropic particles incorporated to polymer matrixes^{4, 5}, and the incorporation of anisotropic fillers combined or not with their alignment^{9, 13, 79} have been reported. The second path offers some advantages, due to the high aspect ratio and high surface area provided by these anisotropic fillers. For instance, mechanical and thermal resistance can be improved, due to the huge polymer/filler interface that acts as an additional rigid phase. Moreover, the preferential orientation of the fillers results in enhancement of percolation, increasing mechanical and electrical properties. It also enhances the tortuosity, impeding the diffusion of molecules and increasing barrier properties. Yet, to achieve satisfactory alignment of fillers and effectively enhancement of material properties, the inorganic particles must be initially well dispersed in the medium.

The compatibility between the filler and the matrix is the key factor to achieve a homogeneous distribution of the filler in the matrix. In order to improve this compatibility, different approaches, like the growth of polymer brushes on particles surface, and the encapsulation of inorganic particles with thin polymer layers, have been used. In the past fifteen years, RDRP techniques have been widely applied to graft polymer brushes onto particle surfaces, via *grafting from* or *grafting to* approaches, or to encapsulate the particles with polymers, taking advantage of block copolymers self-assembly or macroRAFT-assisted encapsulating emulsion polymerization. Grafting techniques rely on solvent-borne processes, being less environment-friendly and requiring different modification and purification steps. Encapsulation performed via block copolymers self-assembly generally involves a two-step process, starting by the anchoring of BCP chains on the surface (by grafting techniques), and further solvent exchanging and/or annealing to promote the self-assembly of the polymer. This strategy also relies on solvent-borne processes, and the self-assembly is generally a time-demanding step. The formation of polymer-encapsulated inorganic particles by macroRAFT-assisted emulsion polymerization is a simple two step water-borne process, in which living RAFT copolymers are used as both coupling agents and stabilizers. This strategy allows obtaining well-defined hybrid colloids with tunable polymer layer thicknesses and compositions. It can be applied to almost any kind of filler, and the encapsulation may be performed with a wide range of polymers.

In this work, we will explore the polymer-encapsulation of two inorganic fillers: Imogolite nanotubes and Layered Double Hydroxide (LDH) sheets via the macroRAFT-assisted emulsion polymerization technique. Random living RAFT copolymers based on acrylic acid (AA) and *n*-butyl acrylate (BA) (e.g. P(AA-*co*-BA)), referred to as macroRAFT agents, will be synthesized for that purpose. The carboxylic units of AA moieties are known to interact with inorganic surfaces of opposite charge via

electrostatic interactions, H-bonding or complexation. The introduction of BA units will allow us to further promote the adsorption of macroRAFT agents via inter-chain hydrophobic interactions, which will equally increase the affinity between the monomer and the particles surface. These macroRAFT agents will be further chain extended in aqueous emulsion polymerization with hydrophobic monomers, and we expect to have an efficient transfer of the polymerization from the aqueous phase to the surface, enabling the successful encapsulation of the fillers. The effect of different parameters on the polymerization kinetics, the control over the polymerization, the final particles morphology and the films mechanical properties will be evaluated for both Imogolite and LDH fillers. The parameters that will be investigated are the nature, molar mass and concentration of the macroRAFT agent, the pH, the monomer composition and the size and concentration of the LDH and Imogolite fillers.

I.5. References

1. Gagg, C. R. *Eng. Failure Anal.* **2005**, 12, 1000-1026.
2. Ward, I. M., *Polymers: Chemistry and Physics of Modern Materials*. 3rd edition ed.; Contemporary Physics: 2009; Vol. 50.
3. Mohanty, A. K.; Misra, M.; Hinrichsen, G. *Macromol. Mat. and Eng.* **2000**, 276, 1-24.
4. Fragouli, D.; Buonsanti, R.; Bertoni, G.; Sangregorio, C.; Innocenti, C.; Falqui, A.; Gatteschi, D.; Cozzoli, P. D.; Athanassiou, A.; Cingolani, R. *Acs Nano* **2010**, 4, 1873-1878.
5. Pisanello, F.; De Paolis, R.; Lorenzo, D.; Guardia, P.; Nitti, S.; Monti, G.; Fragouli, D.; Athanassiou, A.; Tarricone, L.; Manna, L.; De Vittorio, M.; Martiradonna, L. *Acs Appl. Mat. & Interf.* **2013**, 5, 2908-2914.
6. Alonso, R. H.; Estevez, L.; Lian, H.; Kellarakis, A.; Giannelis, E. P. *Polymer* **2009**, 50, 2402-2410.
7. Herrera-Alonso, J. M.; Sedlakova, Z.; Marand, E. *J. Membr. Sci.* **2010**, 349, 251-257.
8. Kim, I. T.; Tannenbaum, A.; Tannenbaum, R. *Carbon* **2011**, 49, 54-61.
9. Bao, Y.; Pang, H.; Xu, L.; Cui, C.-H.; Jiang, X.; Yan, D.-X.; Li, Z.-M. *RSC Adv.* **2013**, 3, 24185-24192.
10. Jin, L.; Bower, C.; Zhou, O. *Appl. Phys. Letters* **1998**, 73, 1197-1199.
11. Lanticse, L. J.; Tanabe, Y.; Matsui, K.; Kaburagi, Y.; Suda, K.; Hoteida, M.; Endo, M.; Yasuda, E. *Carbon* **2006**, 44, 3078-3086.
12. Zheng, Q.; Ip, W. H.; Lin, X.; Yousefi, N.; Yeung, K. K.; Li, Z.; Kim, J.-K. *ACS Nano* **2011**, 5, 6039-6051.
13. Yousefi, N.; Gudarzi, M. M.; Zheng, Q.; Lin, X.; Shen, X.; Jia, J.; Sharif, F.; Kim, J.-K. *Comp. Part A-Appl. Sci. and Manuf.* **2013**, 49, 42-50.
14. Charleux, B.; D'Agosto, F.; Delaittre, G. *J. Appl. Polym. Sci.* **2010**, 233, 125-183.
15. Barbey, R.; Lavanant, L.; Paripovic, D.; Schuewer, N.; Sugnaux, C.; Tugulu, S.; Klok, H.-A. *Chem. Rev.* **2009**, 109, 5437-5527.
16. Brinks, M. K.; Studer, A. *Macromol. Rapid Comm.* **2009**, 30, 1043-1057.
17. Homenick, C. M.; Lawson, G.; Adronov, A. *Polym. Rev.* **2007**, 47, 265-290.
18. Badri, A.; Whittaker, M. R.; Zetterlund, P. B. *J. of Polym. Sci. Part A-Polym. Chem.* **2012**, 50, 2981-2992.
19. Mai, Y.; Eisenberg, A. *Acc. of Chem. Res.* **2012**, 45, 1657-1666.
20. Mai, Y.; Eisenberg, A. *Macromol.* **2011**, 44, 3179-3183.
21. Li, W.; Zhang, P.; Dai, M.; He, J.; Babu, T.; Xu, Y.-L.; Deng, R.; Liang, R.; Lu, M.-H.; Nie, Z.; Zhu, J. *Macromol.* **2013**, 46, 2241-2248.
22. *Handbook of Polymer Composites for Engineers*. Woodhead Publishing Ltd.: England, 1994.
23. Baekeland, L. H., Bakelite, a New Composition of matter. *Scientific American* 1909, p 15.
24. Goodyear, C. *Dinglers Polytechnisches Journal* **1856**, 139.
25. Usuki, A.; Kawasumi, M.; Kojima, Y.; Okada, A.; Kurauchi, T.; Kamigaito, O. *J. Mat. Res.* **1993**, 8, 1174-1178.
26. Kojima, Y.; Usuki, A.; Kawasumi, M.; Okada, A.; Fukushima, Y.; Kurauchi, T.; Kamigaito, O. *J. Mat. Res.* **1993**, 8, 1185-1189.
27. Balazs, A. C.; Emrick, T.; Russell, T. P. *Science* **2006**, 314, 1107-1110.
28. Schmidt, G.; Malwitz, M. M. *Curr. Op. Coll. & Interf. Sci.* **2003**, 8, 103-108.
29. Hussain, F.; Hojjati, M.; Okamoto, M.; Gorga, R. E. *J. Comp. Mat.* **2006**, 40, 1511-1575.
30. Alexandre, M.; Dubois, P. *Mat. Sci. & Eng. R-Reports* **2000**, 28, 1-63.
31. Gorga, R. E.; Cohen, R. E. *J. Polym. Sci. Part B-Polym. Phys.* **2004**, 42, 2690-2702.
32. Il Park, C.; Park, O. O.; Lim, J. G.; Kim, H. J. *Polymer* **2001**, 42, 7465-7475.
33. Bartholome, C.; Beyou, E.; Bourgeat-Lami, E.; Chaumont, P.; Zydowicz, N. *Macromol.* **2003**, 36, 7946-7952.
34. Bartholome, C.; Beyou, E.; Bourgeat-Lami, E.; Chaumont, P.; Lefebvre, F.; Zydowicz, N. *Macromol.* **2005**, 38, 1099-1106.

35. Parvole, J.; Laruelle, G.; Guimon, C.; Francois, J.; Billon, L. *Macromol. Rap. Comm.* **2003**, 24, 1074-1078.
36. Parvole, J.; Ahrens, L.; Blas, H.; Vinas, J.; Boissiere, C.; Sanchez, C.; Save, M.; Charleux, B. *J. Polym. Sci. Part A-Polym. Chem.* **2010**, 48, 173-185.
37. Sapper, E. D.; Brickweg, L. J.; Floryancic, B. R.; Fernando, R. H., Shear-Induced One-Dimensional Alignment of Alumina and Silica Nanoparticles in Coatings. In *Nanotechnology Applications in Coatings*, Fernando, R. H.; Sung, L.-P., Eds. American Chemical Society: 2009; Vol. 1008, pp 108-123.
38. Alateyah, A. I.; Dhakal, H. N.; Zhang, Z. Y. *Adv. Polym. Tech.* **2013**, 32.
39. Jewrajka, S. K.; Chatterjee, U. *J. Polym. Sci. Part A-Polym. Chem.* **2006**, 44, 1841-1854.
40. Owens, D. E., III; Eby, J. K.; Jian, Y.; Peppas, N. A. *J. Biomed. Mat. Res. Part A* **2007**, 83A, 692-695.
41. Frischknecht, A. L.; Hore, M. J. A.; Ford, J.; Composto, R. J. *Macromol.* **2013**, 46, 2856-2869.
42. Rossner, C.; Ebeling, B.; Vana, P. *Acs Macro Lett.* **2013**, 2, 1073-1076.
43. Ebeling, B.; Vana, P. *Macromol.* **2013**, 46, 4862-4871.
44. Matsuno, R.; Yamamoto, K.; Otsuka, H.; Takahara, A. *Macromol.* **2004**, 37, 2203-2209.
45. Matsuno, R.; Otsuka, H.; Takahara, A. *Soft Matter* **2006**, 2, 415-421.
46. Chen, F.; Cai, Z.; Huang, Y.; Luo, W.; Chen, J. *Polym. Eng. Sci.* **2013**, 53, 956-962.
47. Hore, M.; Composto, R. *Macromol.* **2013**.
48. Chen, J.; Yang, M.; Zhang, Q.; Cho, E. C.; Cogley, C. M.; Kim, C.; Glaus, C.; Wang, L. V.; Welch, M. J.; Xia, Y. *Adv. Funct. Mat.* **2010**, 20, 3684-3694.
49. Patzke, G. R.; Krumeich, F.; Nesper, R. *Angew. Chem.-Int. Ed.* **2002**, 41, 2446-2461.
50. Rozenberg, B. A.; Tenne, R. *Progress in Polym. Sci.* **2008**, 33, 40-112.
51. Moraes, R. P.; Valera, T. S.; Pereira, A. M. C.; Demarquette, N. R.; Santos, A. M. *J. Appl. Polym. Sci.* **2011**, 119, 3658-3669.
52. Lu, H.; Hu, Y.; Li, M.; Chen, Z.; Fan, W. *Comp. Sci. Tech.* **2006**, 66, 3035-3039.
53. Zhao, B.; Brittain, W. J. *Progr. Polym. Sci.* **2000**, 25, 677-710.
54. Baxter, S. C.; Robinson, C. T. *Comp. Sci. Tech.* **2011**, 71, 1273-1279.
55. Tang, Z. Y.; Kotov, N. A. *Adv. Mat.* **2005**, 17, 951-962.
56. Fragouli, D.; Torre, B.; Bertoni, G.; Buonsanti, R.; Cingolani, R.; Athanassiou, A. *Microsc. Res. Tech.* **2010**, 73, 952-958.
57. Xie, X. L.; Mai, Y. W.; Zhou, X. P. *Mat. Sci. Eng. R-Reports* **2005**, 49, 89-112.
58. Yousefi, N.; Gudarzi, M. M.; Zheng, Q.; Aboutalebi, S. H.; Sharif, F.; Kim, J.-K. *J. Mat. Chem.* **2012**, 22, 12709-12717.
59. Minko, S.; Kiriy, A.; Gorodyska, G.; Stamm, M. *J. Am. Chem. Soc.* **2002**, 124, 10192-10197.
60. Kiriy, A.; Minko, S.; Gorodyska, G.; Stamm, M.; Jaeger, W. *Nano Letters* **2002**, 2, 881-885.
61. Colfen, H.; Qi, L. M. *Chem.-A Europ. J.* **2001**, 7, 106-116.
62. Yu, S. H.; Antonietti, M.; Colfen, H.; Giersig, M. *Angew. Chem.-Int. Ed.* **2002**, 41, 2356-2360.
63. Yu, S. H.; Colfen, H.; Antonietti, M. *Adv. Mat.* **2003**, 15, 133-+.
64. Braun, E.; Eichen, Y.; Sivan, U.; Ben-Yoseph, G. *Nature* **1998**, 391, 775-778.
65. Keren, K.; Krueger, M.; Gilad, R.; Ben-Yoseph, G.; Sivan, U.; Braun, E. *Science* **2002**, 297, 72-75.
66. Moghaddam, M. J.; Taylor, S.; Gao, M.; Huang, S. M.; Dai, L. M.; McCall, M. J. *Nano Letters* **2004**, 4, 89-93.
67. Chang, J. Y.; Chang, J. J.; Lo, B.; Tzing, S. H.; Ling, Y. C. *Chem. Phys. Letters* **2003**, 379, 261-267.
68. Liao, J. H.; Zhang, Y.; Yu, W.; Xu, L. N.; Ge, C. W.; Liu, J. H.; Gu, N. *Coll. Surf. A-Physicochem. Eng. Asp.* **2003**, 223, 177-183.
69. Shim, M.; Guyot-Sionnest, P. *J. Chem. Phys.* **1999**, 111, 6955-6964.
70. Rabani, E. *J. Chem. Phys.* **2001**, 115, 1493-1497.
71. Bu, X.; Zhou, D.; Li, J.; Zhang, X.; Zhang, K.; Zhang, H.; Yang, B. *Langmuir* **2014**.
72. Tang, Z. Y.; Kotov, N. A.; Giersig, M. *Science* **2002**, 297, 237-240.
73. Tang, Z. Y.; Ozturk, B.; Wang, Y.; Kotov, N. A. *J. Phys. Chem. B* **2004**, 108, 6927-6931.
74. Penn, R. L. *J. Phys. Chem. B* **2004**, 108, 12707-12712.

75. Liu, K.; Nie, Z.; Zhao, N.; Li, W.; Rubinstein, M.; Kumacheva, E. *Science* **2010**, 329, 197-200.
76. Liu, K.; Ressetco, C.; Kumacheva, E. *Nanoscale* **2012**, 4, 6574-6580.
77. Lukach, A.; Liu, K.; Therien-Aubin, H.; Kumacheva, E. *J. Am. Chem. Soc.* **2012**, 134, 18853-18859.
78. Cooper, C. A.; Ravich, D.; Lips, D.; Mayer, J.; Wagner, H. D. *Comp. Sci. Tech.* **2002**, 62, 1105-1112.
79. Zhou, B.; Lin, Y.; Veca, L. M.; Fernando, K. A. S.; Harruff, B. A.; Sun, Y. P. *J. Phys. Chem. B* **2006**, 110, 3001-3006.
80. Terao, T.; Zhi, C.; Bando, Y.; Mitome, M.; Tang, C.; Golberg, D. *J. Phys. Chem. C* **2010**, 114, 4340-4344.
81. Song, W.-L.; Wang, P.; Cao, L.; Anderson, A.; Mezziani, M. J.; Farr, A. J.; Sun, Y.-P. *Angew. Chem. -Int. Ed.* **2012**, 51, 6498-6501.
82. Kim, I. T.; Tannenbaum, R., Magnetic Carbon Nanotubes: Synthesis, Characterization and Anisotropic Electrical Properties. In *Electr. Prop. Carb. Nanotubes*, Marulanda, J. M., Ed. 2011.
83. Jestin, J.; Cousin, F.; Dubois, I.; Menager, C.; Schweins, R.; Oberdisse, J.; Boue, F. *Adv. Mat.* **2008**, 20, 2533.
84. Robbes, A.-S.; Cousin, F.; Meneau, F.; Dalmas, F.; Boue, F.; Jestin, J. *Macromol.* **2011**, 44, 8858-8865.
85. Kimura, T.; Ago, H.; Tobita, M.; Ohshima, S.; Kyotani, M.; Yumura, M. *Adv. Mat.* **2002**, 14, 1380-1383.
86. Xu, Y.; Yuan, J.; Fang, B.; Drechsler, M.; Muellner, M.; Bolisetty, S.; Ballauff, M.; Mueller, A. H. E. *Adv. Funct. Mat.* **2010**, 20, 4182-4189.
87. Morkved, T. L.; Lu, M.; Urbas, A. M.; Ehrichs, E. E.; Jaeger, H. M.; Mansky, P.; Russell, T. P. *Science* **1996**, 273, 931-933.
88. Liedel, C.; Schindler, K. A.; Pavan, M. J.; Lewin, C.; Pester, C. W.; Ruppel, M.; Urban, V. S.; Shenhar, R.; Boeker, A. *Small* **2013**, 9, 3276-3281.
89. Xu, Y.; Chen, W.; Yung, K.-L. *Manuf. Eng. Autom. Ii, Pts 1-3* **2012**, 591-593, 1117-1120.
90. Kumar, G.; Mahajan, S. M.; Stretz, H. A.; Apte, S. K. *Opt. Mat. Expr.* **2012**, 2, 864-871.
91. Gupta, S.; Zhang, Q.; Emrick, T.; Russell, T. P. *Nano Letters* **2006**, 6, 2066-2069.
92. Slopek, R. P.; Gilchrist, J. F. *J. Phys. D-Appl. Phys.* **2010**, 43.
93. Gennari, O.; Grilli, S.; Coppola, S.; Pagliarulo, V.; Vespini, V.; Coppola, G.; Bhowmick, S.; Gioffre, M. A.; Gentile, G.; Ambrogi, V.; Cerruti, P.; Carfagna, C.; Ferraro, P. *Langmuir* **2013**, 29, 15503-15510.
94. Miyamoto, N.; Nakato, T. *Adv. Mat.* **2002**, 14, 1267.
95. Yanagi, H.; Sawada, E.; Manivannan, A.; Nagahara, L. A. *Appl. Phys. Lett.* **2001**, 78, 1355-1357.
96. Ansari, S.; Kelarakis, A.; Estevez, L.; Giannelis, E. P. *Small* **2010**, 6, 205-209.
97. Aboutalebi, S. H.; Gudarzi, M. M.; Zheng, Q. B.; Kim, J.-K. *Adv. Funct. Mat.* **2011**, 21, 2978-2988.
98. Park, J. H.; Aluru, N. R. *Surf. Sci.* **2011**, 605, 1616-1620.
99. Guo, F.; Kim, F.; Han, T. H.; Shenoy, V. B.; Huang, J.; Hurt, R. H. *Acs Nano* **2011**, 5, 8019-8025.
100. Gilbert, R. G., Emulsion Polymerization. A mechanistic approach. Academic Press: 1995.
101. Hansen, F. K., Historic Overview. In *Chemistry and Technology of Emulsion Polymerization*, 2nd ed.; van Herk, A. M., Ed. John Wiley & Sons, Ltd.: Oxford, UK, 2013.
102. Moad, G.; Solomon, D. H., *The Chemistry of Radical Polymerization*. 2nd ed.; Elsevier: 2005; p 666.
103. Smith, W. V.; Ewart, R. H. *J. Chem. Phys.* **1948**, 16, 592-599.
104. Harkins, W. D. *J. Am. Chem. Soc.* **1947**, 69, 1428-&.
105. Priest, W. J. *J. Phys. Chem.* **1952**, 56, 1077-1082.
106. Napper, D. H.; Gilbert, R. G. *Makromol. Chem.-Macromol. Symp.* **1987**, 10, 503-520.
107. Feeney, P. J.; Napper, D. H.; Gilbert, R. G. *Macromol.* **1987**, 20, 2922-2930.

108. Nicolas, J.; Guillaneuf, Y.; Lefay, C.; Bertin, D.; Gignes, D.; Charleux, B. *Progr. Polym. Sci.* **2013**, *38*, 63-235.
109. Matyjaszewski, K. *Macromol.* **2012**, *45*, 4015-4039.
110. Keddie, D. J.; Moad, G.; Rizzardo, E.; Thang, S. H. *Macromol.* **2012**, *45*, 5321-5342.
111. Keddie, D. J. *Chem. Soc. Rev* **2013**.
112. Charleux, B.; Nicolas, J. *Polymer* **2007**, *48*, 5813-5833.
113. Georges, M. K.; Veregin, R. P. N.; Kazmaier, P. M.; Hamer, G. K. *Macromol.* **1993**, *26*, 2987-2988.
114. Kato, M.; Kamigaito, M.; Sawamoto, M.; Higashimura, T. *Macromol.* **1995**, *28*, 1721-1723.
115. Wang, J. S.; Matyjaszewski, K. *J. Am. Chem. Soc.* **1995**, *117*, 5614-5615.
116. Charleux, B.; Delaitre, G.; Rieger, J.; D'Agosto, F. *Macromol.* **2012**, *45*, 6753-6765.
117. Cunningham, M. F. *Progr. Polym. Sci.* **2008**, *33*, 365-398.
118. Monteiro, M. J.; Cunningham, M. F. *Macromol.* **2012**, *45*, 4939-4957.
119. Zetterlund, P. B.; Kagawa, Y.; Okubo, M. *Chem. Rev.* **2008**, *108*, 3747-3794.
120. Hawker, C. J.; Bosman, A. W.; Harth, E. *Chem. Rev.* **2001**, *101*, 3661-3688.
121. Barner-Kowollik, C., *Handbook of RAFT Polymerization*. 1st ed.; Wiley-VCH Verlag GmbH & Co.: Darmstadt, Germany, 2008; p 543.
122. Chiefari, J.; Chong, Y. K.; Ercole, F.; Krstina, J.; Jeffery, J.; Le, T. P. T.; Mayadunne, R. T. A.; Meijs, G. F.; Moad, C. L.; Moad, G.; Rizzardo, E.; Thang, S. H. *Macromol.* **1998**, *31*, 5559-5562.
123. Charmot, D.; Corpart, P.; Adam, H.; Zard, S. Z.; Biadatti, T.; Bouhadir, G. *Macromol. Symp.* **2000**, *150*, 23-32.
124. Mayadunne, R. T. A.; Rizzardo, E.; Chiefari, J.; Krstina, J.; Moad, G.; Postma, A.; Thang, S. H. *Macromol.* **2000**, *33*, 243-245.
125. Mayadunne, R. T. A.; Rizzardo, E.; Chiefari, J.; Chong, Y. K.; Moad, G.; Thang, S. H. *Macromol.* **1999**, *32*, 6977-6980.
126. Ferguson, C. J.; Hughes, R. J.; Pham, B. T. T.; Hawket, B. S.; Gilbert, R. G.; Serelis, A. K.; Such, C. H. *Macromol.* **2002**, *35*, 9243-9245.
127. Ferguson, C. J.; Hughes, R. J.; Nguyen, D.; Pham, B. T. T.; Gilbert, R. G.; Serelis, A. K.; Such, C. H.; Hawket, B. S. *Macromol.* **2005**, *38*, 2191-2204.
128. Manguian, M.; Save, M.; Charleux, B. *Macromol. Rap. Comm.* **2006**, *27*, 399-404.
129. dos Santos, A. M.; Pohn, J.; Lansalot, M.; D'Agosto, F. *Macromol. Rap. Comm.* **2007**, *28*, 1325-1332.
130. Zhang, X.; Boisse, S.; Zhang, W.; Beaunier, P.; D'Agosto, F.; Rieger, J.; Charleux, B. *Macromol.* **2011**, *44*, 4149-4158.
131. Boisse, S.; Rieger, J.; Pembouong, G.; Beaunier, P.; Charleux, B. *J. Polym. Sci. Part A-Polym. Chem.* **2011**, *49*, 3346-3354.
132. Chaduc, I.; Zhang, W.; Rieger, J.; Lansalot, M.; D'Agosto, F.; Charleux, B. *Macromol. Rap. Comm.* **2011**, *32*, 1270-1276.
133. Chaduc, I.; Girod, M.; Antoine, R.; Charleux, B.; D'Agosto, F.; Lansalot, M. *Macromol.* **2012**, *45*, 5881-5893.
134. Chaduc, I.; Crepet, A.; Boyron, O.; Charleux, B.; D'Agosto, F.; Lansalot, M. *Macromol.* **2013**, *46*, 6013-6023.
135. Zhang, W.; D'Agosto, F.; Boyron, O.; Rieger, J.; Charleux, B. *Macromol.* **2011**, *44*, 7584-7593.
136. Zhang, W.; D'Agosto, F.; Boyron, O.; Rieger, J.; Charleux, B. *Macromol.* **2012**, *45*, 4075-4084.
137. Qiao, X. G.; Lansalot, M.; Bourgeat-Lami, E.; Charleux, B. *Macromol.* **2013**, *46*, 4285-4295.
138. Groison, E.; Brusseau, S.; D'Agosto, F.; Magnet, S.; Inoubli, R.; Couvreur, L.; Charleux, B. *Acs Macro Letters* **2012**, *1*, 47-51.
139. Brusseau, S.; Groison, E.; Boisse, S.; Zhang, X.; Zhang, W.; Rieger, J.; Lansalot, M.; D'Agosto, F.; Charleux, B.; Magnet, S.; Inoubli, R.; Couvreur, L. *Abs. Pap. Am. Chem. Soc.* **2011**, 242.
140. Liu, J.; Liu, G.; Zhang, M.; Sun, P.; Zhao, H. *Macromol.* **2013**, *46*, 5974-5984.

141. Yang, H.; Liang, F.; Wang, X.; Chen, Y.; Zhang, C.; Wang, Q.; Qu, X.; Li, J.; Wu, D.; Yang, Z. *Macromol.* **2013**, *46*, 2754-2759.
142. Daigle, J.-C.; Claverie, J. P. *J. Nanomat.* **2008**.
143. Beija, M.; Marty, J.-D.; Destarac, M. *Progr. Polym. Sci.* **2011**, *36*, 845-886.
144. Zhong, W.; Zeuna, J. N.; Claverie, J. P. *J. Polym. Sci. Part A-Polym. Chem.* **2012**, *50*, 4403-4407.
145. Ali, S. I.; Heuts, J. P. A.; Hawkett, B. S.; van Herk, A. M. *Langmuir* **2009**, *25*, 10523-10533.
146. Mballa, M. A. M.; Ali, S. I.; Heuts, J. P. A.; van Herk, A. M. *Polym. Int.* **2012**, *61*, 861-865.
147. Pan, G.; Ma, Y.; Zhang, Y.; Guo, X.; Li, C.; Zhang, H. *Soft Matter* **2011**, *7*, 8428-8439.
148. Qu, Z.; Hu, F.; Chen, K.; Duan, Z.; Gu, H.; Xu, H. *J. Coll. Interf. Sci.* **2013**, *398*, 82-87.
149. Li, C.; Han, J.; Ryu, C. Y.; Benicewicz, B. C. *Macromol.* **2006**, *39*, 3175-3183.
150. Li, C. Z.; Benicewicz, B. C. *Macromol.* **2005**, *38*, 5929-5936.
151. Rotzoll, R.; Vana, P. *J. Polym. Sci. Part A-Polym. Chem.* **2008**, *46*, 7656-7666.
152. Yang, Y.; Yang, Z.; Zhao, Q.; Cheng, X.; Tiong, S. C.; Li, R. K. Y.; Wan, X.; Xie, X. *J. Polym. Sci. Part A-Polym. Chem.* **2009**, *47*, 467-484.
153. Ohno, K.; Ma, Y.; Huang, Y.; Mori, C.; Yahata, Y.; Tsujii, Y.; Maschmeyer, T.; Moraes, J.; Perrier, S. *Macromol.* **2011**, *44*, 8944-8953.
154. Hojjati, B.; Sui, R.; Charpentier, P. A. *Polymer* **2007**, *48*, 5850-5858.
155. Hojjati, B.; Charpentier, P. A. *J. Polym. Sci. Part A-Polym. Chem.* **2008**, *46*, 3926-3937.
156. Ye, Y.-S.; Shen, W.-C.; Tseng, C.-Y.; Rick, J.; Huang, Y.-J.; Chang, F.-C.; Hwang, B.-J. *Chem. Comm.* **2011**, *47*, 10656-10658.
157. Skaff, H.; Emrick, T. *Angew. Chem.-Int. Ed.* **2004**, *43*, 5383-5386.
158. Yang, Q.; Wang, L.; Xiang, W.; Zhou, J.; Tan, Q. h. *Polymer* **2007**, *48*, 3444-3451.
159. Li, Q.; Zhang, L.; Bai, L.; Zhang, Z.; Zhu, J.; Zhou, N.; Cheng, Z.; Zhu, X. *Soft Matter* **2011**, *7*, 6958-6966.
160. Chirowodza, H.; Weber, W.; Hartmann, P.; Pasch, H. *Macromol. Symp.* **2012**, *313*-314.
161. Beckert, F.; Friedrich, C.; Thomann, R.; Muelhaupt, R. *Macromol.* **2012**, *45*, 7083-7090.
162. Cui, L.; Liu, J.; Wang, R.; Liu, Z.; Yang, W. *J. Polym. Sci. Part A-Polym. Chem.* **2012**, *50*, 4423-4432.
163. Cheng, J.; He, J.; Li, C.; Yang, Y. *Chem. Mater.* **2008**, *20*, 4224-4230.
164. Liu, J.; Yang, W.; Tao, L.; Li, D.; Boyer, C.; Davis, T. P. *J. Polym. Sci. Part A-Polym. Chem.* **2010**, *48*, 425-433.
165. Bates, F. S.; Fredrickson, G. H. *Physics Today* **1999**, *52*, 32-38.
166. Mai, Y.; Eisenberg, A. *Chem. Soc. Rev.* **2012**, *41*, 5969-5985.
167. Kadota, S.; Aoki, K.; Nagano, S.; Seki, T. *J. Am. Chem. Soc.* **2005**, *127*, 8266-8267.
168. Lohse, D. J.; Hadjichristidis, N. *Curr. Op. Coll. & Interf. Sci.* **1997**, *2*, 171-176.
169. Gurovich, E. *Macromol.* **1994**, *27*, 7339-7362.
170. Blanzas, A.; Armes, S. P.; Ryan, A. J. *Macromol. Rap. Comm.* **2009**, *30*, 267-277.
171. Bockstaller, M. R.; Mickiewicz, R. A.; Thomas, E. L. *Adv. Mat.* **2005**, *17*, 1331-1349.
172. Kim, B. J.; Bang, J.; Hawker, C. J.; Kramer, E. J. *Macromol.* **2006**, *39*, 4108-4114.
173. Zhang, L. F.; Eisenberg, A. *Science* **1995**, *268*, 1728-1731.
174. Larson-Smith, K.; Pozzo, D. C. *Langmuir* **2012**, *28*, 13157-13165.
175. Martin, T. B.; McKinney, C.; Jayaraman, A. *Soft Matter* **2013**, *9*, 155-169.
176. Martin, T. B.; Seifpour, A.; Jayaraman, A. *Soft Matter* **2011**, *7*, 5952-5964.
177. Hickey, R. J.; Haynes, A. S.; Kikkawa, J. M.; Park, S.-J. *J. Am. Chem. Soc.* **2011**, *133*, 1517-1525.
178. Hickey, R. J.; Luo, Q.; Park, S.-J. *ACS Macro Letters* **2013**, *2*, 805-808.
179. He, J.; Liu, Y.; Babu, T.; Wei, Z.; Nie, Z. *J. Am. Chem. Soc.* **2012**, *134*, 11342-11345.
180. Chen, T.; Yang, M.; Wang, X.; Tan, L. H.; Chen, H. *J. Am. Chem. Soc.* **2008**, *130*, 11858-11859.
181. Mai, Y.; Xiao, L.; Eisenberg, A. *Macromol.* **2013**, *46*, 3183-3189.
182. Li, W.; Liu, S.; Deng, R.; Wang, J.; Nie, Z.; Zhu, J. *Macromol.* **2013**, *46*, 2282-2291.
183. He, J.; Huang, X.; Li, Y.-C.; Liu, Y.; Babu, T.; Aronova, M. A.; Wang, S.; Lu, Z.; Chen, X.; Nie, Z. *J. Am. Chem. Soc.* **2013**, *135*, 7974-7984.

184. Nie, Z.; Fava, D.; Kumacheva, E.; Zou, S.; Walker, G. C.; Rubinstein, M. *Nature Mat.* **2007**, *6*, 609-614.
185. Fava, D.; Nie, Z.; Winnik, M. A.; Kumacheva, E. *Adv. Mater.* **2008**, *20*, 4318-4322.
186. He, J.; Wei, Z.; Wang, L.; Tomova, Z.; Babu, T.; Wang, C.; Han, X.; Fourkas, J. T.; Nie, Z. *Angew. Chem.-Int. Ed.* **2013**, *52*, 2463-2468.
187. Kang, Y. J.; Taton, T. A. *Angew. Chem.-Int. Ed.* **2005**, *44*, 409-412.
188. Xu, J.; Han, Y.; Cui, J.; Jiang, W. *Langmuir* **2013**, *29*, 10383-10392.
189. Kang, Y. J.; Taton, T. A. *J. Am. Chem. Soc.* **2003**, *125*, 5650-5651.
190. Kamps, A. C.; Sanchez-Gaytan, B. L.; Hickey, R. J.; Clarke, N.; Fryd, M.; Park, S.-J. *Langmuir* **2010**, *26*, 14345-14350.
191. Deng, Y.; Yang, C.; Yuan, C.; Xu, Y.; Bernard, J.; Dai, L.; Gerard, J.-F. *J. Polym. Sci. Part A-Polym. Chem.* **2013**, *51*, 4558-4564.
192. Wang, J.; Li, W.; Zhu, J. *Polymer* **2014**, *55*, 1079-1096.
193. Samakande, A.; Sanderson, R. D.; Hartmann, P. C. *J. Polym. Sci. Part A-Polym. Chem.* **2008**, *46*, 7114-7126.
194. Nguyen, D.; Zondanos, H. S.; Farrugia, J. M.; Serelis, A. K.; Such, C. H.; Hawckett, B. S. *Langmuir* **2008**, *24*, 2140-2150.
195. Duc, N.; Such, C.; Hawckett, B. *J. Polym. Sci. Part A-Polym. Chem.* **2012**, *50*, 346-352.
196. Duc, N.; Such, C. H.; Hawckett, B. S. *J. Polym. Sci. Part A-Polym. Chem.* **2013**, *51*, 250-257.
197. Das, P.; Zhong, W.; Claverie, J. P. *Coll. Polym. Sci.* **2011**, *289*, 1519-1533.
198. Ali, S. I.; Heuts, J. P. A.; van Herk, A. M. *Langmuir* **2010**, *26*, 7848-7858.
199. Zgheib, N.; Putaux, J.-L.; Thill, A.; Bourgeat-Lami, E.; D'Agosto, F.; Lansalot, M. *Polym. Chem.* **2013**, *4*, 607-614.
200. Garnier, J.; Warnant, J.; Lacroix-Desmazes, P.; Dufils, P.-E.; Vinas, J.; Vanderveken, Y.; van Herk, A. M. *Macromol. Rap. Comm.* **2012**, *33*, 1388-1392.
201. Garnier, J.; Warnant, J.; Lacroix-Desmazes, P.; Dufils, P.-E.; Vinas, J.; van Herk, A. *J. Coll. Int. Sci.* **2013**, *407*, 273-281.
202. Warnant, J.; Garnier, J.; van Herk, A.; Dufils, P.-E.; Vinas, J.; Lacroix-Desmazes, P. *Polym. Chem.* **2013**, *4*, 5656-5663.

Chapter II – Polymer/Ge-Imogolite nanocomposite latexes

Table of contents

II.1. Introduction	62
II.2 Bibliographic study of Imogolite Nanotubes.....	64
II.2.1 Imogolite discovery	64
II.2.2 Imogolite structure.....	64
II.2.3 Imogolite synthesis and characterization.....	66
II.2.4 Applications.....	74
II.3. MacroRAFT agents synthesis.....	89
II.3.1 Experimental section	89
II.3.2 Results and Discussion	91
II.3.3 Conclusions	96
II.4 Imogolite nanotubes	98
II.5 Preliminary Imogolite encapsulating experiments	102
II.5.1 Experimental section	102
II.5.2 Results and Discussion	103
II.6 Acrylic acid-based macroRAFT/Imogolite interactions.....	109
II.6.1 Experimental section	110
II.6.2 Results and Discussion	111
II.6.3 Conclusions	118
II.7 MacroRAFT-assisted encapsulating emulsion polymerization	120
II.7.1 Experimental section	120
II.7.2 Results and discussion	121
II.7.3 Conclusions	145
II.8 Towards film-forming latexes	147
II.8.1 Latexes synthesis	147
II.8.1.1 Experimental section	147

II.8.1.2 Results and Discussion	148
II.8.1.3 Conclusions	160
II.8.2 Film formation and properties	161
II.8.2.1 Experimental section	161
II.8.2.2 Results and Discussion	163
II.8.2.3 Conclusions	182
II.9 General conclusions of chapter II.....	183
II.10 References	186

II.1. Introduction

The addition of anisotropic fillers into polymer matrixes gives rise to interesting properties, such as mechanical reinforcement^{1,2}, optical properties³⁻⁶, and barrier properties⁷⁻¹¹, according to the one-dimensional filler geometry (i.e. aspect ratio) and physico-chemistry. The key point to homogeneously distribute the fillers in the matrix is to promote the affinity between the inorganic and organic parts. Different techniques have been used to favor the interaction between inorganic fillers and polymer matrixes, the most current being the modification of particles with organic molecules or polymers. Such modifications can be performed, for instance, via *grafting from* or *grafting to* approaches. These two approaches usually rely on solvent-borne strategies, and can rarely be performed in aqueous media.

Another clever strategy to improve inorganic/organic affinity is the encapsulation of inorganic particles with a thin polymer layer. The encapsulation of spherical particles has been described through aqueous emulsion¹² or miniemulsion polymerizations¹³⁻¹⁵. However, the encapsulation of high aspect ratio particles seems more challenging. The use of these techniques directly to encapsulate clays, for instance, only generated armored latex particles (platelets being located at the particle surface)¹⁶⁻²¹. Recently, a new strategy built upon the use of reversible deactivation radical polymerization, specifically RAFT polymerization, was developed, and the successful encapsulation of anisotropic particles was reported. This strategy involves the utilization of hydrophilic living copolymers as coupling agents and stabilizers during the emulsion polymerization of hydrophobic monomers in the presence of inorganic particles. The successful application of this strategy to encapsulate pigments^{22, 23}, gibbsite platelets,²⁴ cerium oxide²⁵ and carbon nanotubes^{26, 27} has been reported. This strategy will be called macroRAFT-assisted encapsulating emulsion polymerization (REEP).

The chain extension of preformed hydrosoluble controlling agents with hydrophobic monomers in aqueous media generates amphipathic block copolymers susceptible to self-assemble. Therefore, additionally to conventional spheres, more complex morphologies like vesicles, fibers and worms can be obtained directly in water^{28, 29}. Thus, the self-assembly process also has to be considered when working with REEP which relies on the use of hydrosoluble macroRAFT agents.

Among the existing anisotropic fillers, Imogolite is receiving increasing attention due to its unique one-dimensional structure, high porosity and high surface area. Imogolite is a naturally occurring aluminosilicate tubular mineral of general formula $(\text{OH})_3\text{Al}_2\text{O}_3\text{SiOH}$ ³⁰. Its incorporation into polymer matrixes has been investigated using diverse techniques to produce high performance nanocomposites³¹⁻³⁴. Techniques employed to produce polymer/Imogolite nanocomposites include direct mixing, *grafting from* and *in situ* synthesis of Imogolite in

polymer solutions. Despite the hydrophilic character of Imogolite, most techniques are conducted in bulk or in organic media, and less attention has been paid to waterborne systems.

In this chapter, we aim to perform the macroRAFT-assisted encapsulating emulsion polymerization of Imogolite nanotubes. The envisioned strategy mainly relies on the use of well-defined amphiphilic macroRAFT agents based on poly(acrylic acid-*co*-*n*-butyl acrylate) (P(AA-*co*-BA)) previously adsorbed on the nanotubes surface, and does not require any chemical modification. These macroRAFT agents will be further chain-extended in water to form composite particles following the REEP strategy, which will be detailed in the bibliographic study of this chapter.

In the first part, we separately reviewed the concepts and applications of amphiphilic block copolymers self-assembly and the macroRAFT-assisted polymer-encapsulation of inorganic particles. For the REEP, we focused on the examples applied to anisotropic fillers, since it is directly linked to the objective of this thesis. We also present the state of the art of the production of polymer/Imogolite nanocomposites using different strategies.

In the second part, the different steps towards macroRAFT-assisted polymer-encapsulation of Imogolite are reported. First, well-defined living amphiphilic macroRAFT agents were synthesized via RAFT solution polymerization. In a second step, the effect of different parameters on their adsorption onto Imogolite surface was investigated. After, REEP polymerizations were performed, and the effect of different parameters, like the nature of the macroRAFT, the macroRAFT molar mass, the macroRAFT and Imogolite concentrations, the pH and the monomer composition, on polymerization kinetics and latex morphology was evaluated. Finally, film-forming latexes were synthesized and the mechanical properties of the films casted from these hybrid latexes, investigated. The alignment of the Imogolite nanotubes was also envisaged and preliminary experiments are reported in the last part of this chapter.

II.2 Bibliographic study of Imogolite Nanotubes

II.2.1 Imogolite discovery

Imogolite is a naturally occurring clay mineral. It was first discovered in soils originating from volcanic materials such as pumice and volcanic ash in the region of Hitoyoshi, Japan, by Yoshinaga and Aomine in 1962. The name Imogolite was used for a component present in the clay fraction of the soil (“Imogo”) derived from glassy volcanic ash³⁰. Its structure was elucidated for the first time by Cradwick et al.³⁵ as being an aluminosilicate mineral of tubular shape (**Figure 1**).

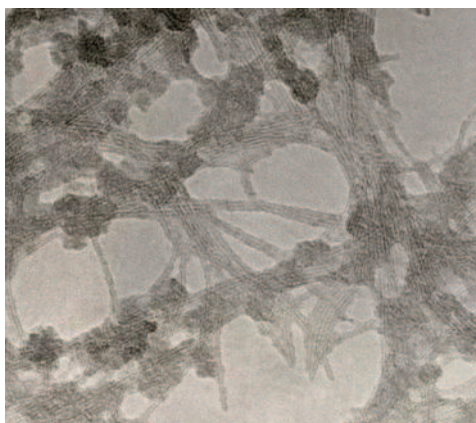


Figure 1. Electron microscopy image of Imogolite nanotubes. Reproduced from ref³⁶.

Allophanes, which are also aluminosilicates but of spherical shape, were discovered first, and at the time Imogolite nanotubes were considered as impurities of allophane soils. The formation and structure of the tubular material were still unknown. Actually, Imogolite was discovered during the search for allophane.

II.2.2 Imogolite structure

After its discovery in 1962, Imogolite became the subject of intensive research, mainly in Japan and in the United States. Researchers like Cradwick, Farmer, Yoshinaga, Aomine, Masson, Russel and Wada, in particular, put a lot of efforts on elucidating Imogolite structure. The chemical composition of Imogolite was soon described by Wada and Yoshinaga in 1969³⁷ as $1.1\text{SiO}_2 \cdot \text{Al}_2\text{O}_3 \cdot 2.3\text{-}2.8\text{H}_2\text{O}$, in which allophane was also taken into account. Imogolite's crystalline structure, however, was unknown.

In the latest 60's, the group of Wada proposed a hypothetical chain structure unit of Imogolite with an ideal composition of $\text{SiO}_2 \cdot \text{Al}_2\text{O}_3 \cdot 2\text{H}_2\text{O}$ ^{38, 39}. In this case, the resulting chain would have

a repeat distance of 2.80 Å along its chain axis. Later, in 1969, new evidences found out by the same group revealed a repeat distance of 8.40 Å, making the previous structure model unvalid³⁷. Bundles of fine tubes, each with 20 Å of diameter, were evidenced by electron microscopy by Wada and Yoshinaga in 1970⁴⁰. However, no acceptable structural model of the crystalline structure of such materials had been reported.

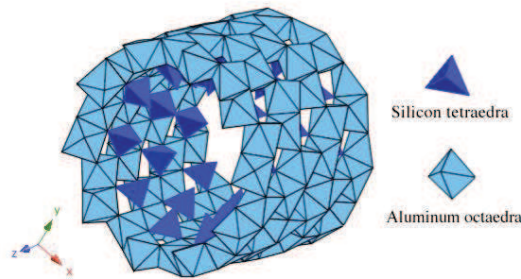


Figure 2. Structure of Imogolite proposed by Cradwick *et al.* in 1972³⁵. Adapted from ref⁴¹.

It was only in 1972, when the researchers who were working on the subject at that time joined their forces that the final model for Imogolite crystalline structure was elucidated³⁵ (**Figure 2**). It was attested that Imogolite nanotubes consist of an outer aluminum hydroxide layer curved by the adsorption of orthosilicate tetrahedra in the inner part of the tubes, as illustrated in **Figure 2**, with a general formula: $(\text{OH})_3\text{Al}_2\text{O}_3\text{SiOH}$.

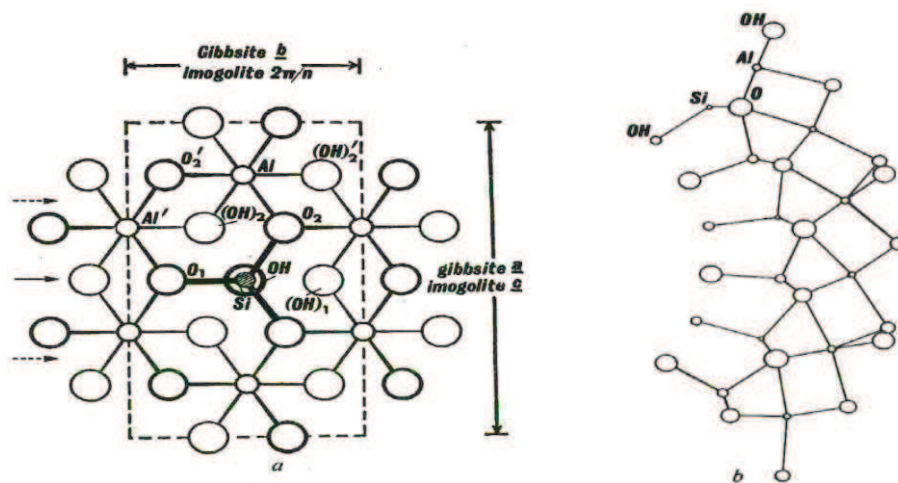


Figure 3. (a) Postulated relationship between the structural unit of Imogolite and that of gibbsite. SiOH groups which would lie on the cell corners in Imogolite were omitted from the diagram. A reflection plane (solid arrow, left) and rotation-reflection planes (broken arrows) are indicated. (b) Curling of the gibbsite sheet induced by contraction of one surface to accommodate SiO_3OH tetrahedral: projection along the axis (Imogolite *c*). Reproduced with permission from ref³⁵.

Imogolite's external layer presents the same chemical composition as gibbsite, a mineral composed of planar sheets of aluminum hydroxide octahedrons. The aluminum octahedral-silicon tetrahedral sheet curvature of Imogolite is attributed to the shortening of the O-O bond distance around the octahedral vacant site, from about 3.2 Å in gibbsite to less than 3 Å in Imogolite³⁵ (**Figure 3**). Recent works on Imogolite structure modeling confirmed these changes on the atom-atom bond distances. It was reported a reduction of the O-O bond distance to near 2.63 Å in the internal sheet and an elongation of the O-O bond distance to 4.1 Å in the external sheet⁴².

II.2.3 Imogolite synthesis and characterization

Imogolite nanotubes can be extracted from soils originating from volcanic ash and glass or weathered pumice beds from all over the world. Their occurrence has been reported in Japan, United States, Canada, Sweden, Germany, King George Island (Antarctic) and many other countries⁴³⁻⁴⁹.

Imogolites are usually combined in tephra (i.e. fragmental material produced by a volcanic eruption) with allophanes (i.e. their spherical analogues), and contain numerous contaminants, such as organic molecules, metal oxides and metal hydroxides³². Therefore, Imogolite is present in nature as a water-swollen gel with a yellow or brown colored aspect. Pure Imogolite gel can be recovered by collecting gel parts from the soil gel containing Imogolite, treating the crude material with hydrogen peroxide and further purifying it from metal contaminants using a chelating agent like ethylenediamine tetraacetic acid (EDTA), for example. The pure gel can be then re-dispersed in water under weak acidic conditions (pH 3.0 or 4.0) by applying ultrasonic waves⁵⁰. Finally, by freeze-drying the sample, a cotton-like solid is obtained (**Figure 4**).

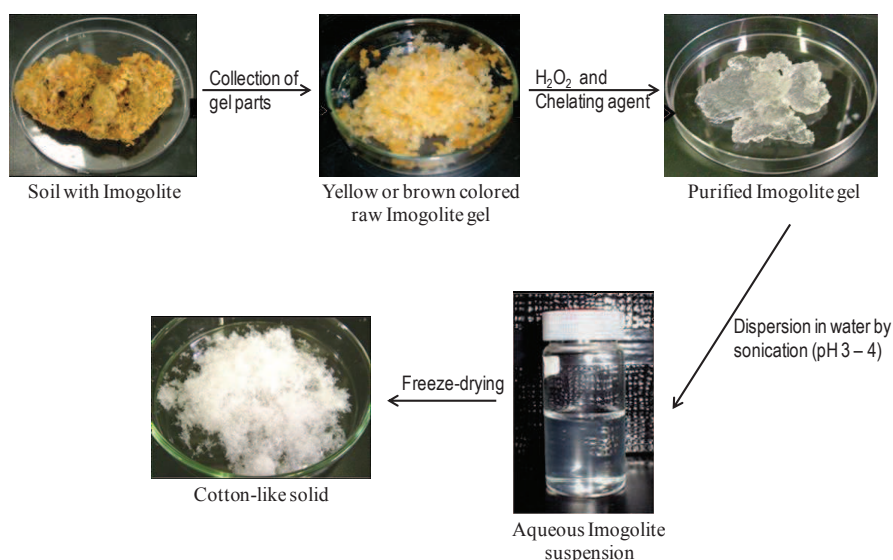


Figure 4. Purification process of natural Imogolite. Adapted from ref³³.

However, it was shown in 1996 by Su and Harsh⁵¹ that the chemical extractants used to obtain Imogolite from natural soils could alter their chemical and structural composition. The study showed a decrease of aluminum and silicon content after treatment with dithionite-citrate-bicarbonate (DCB), used as the chelating agent. The silicon loss was greater than the aluminum, and the Al/Si ratio after extraction was different from the original structure.

In addition to these extraction problems, mining is not an economic way to supply Imogolite. The concentration of natural Imogolite is very low, despite its wide occurrence. This limitation, together with the difficulty of dispersing the tubes in water after extraction, encouraged the development of synthetic routes to produce Imogolite. The first synthesis was performed by Farmer in 1977⁵². $\text{AlCl}_3 \cdot 6\text{H}_2\text{O}$ (2.4 mM in aqueous solution) was precipitated with $\text{Si}(\text{OEt})_4$ (1.4 mM in aqueous solution), the pH was adjusted to 4.5 – 5.0 by NaOH, HCl, CH_3COOH and it was left to grow at 369K for several days. After the heating/growing step, the product was gelled by adding aqueous NaCl and rinsed. The tubes were then dispersed in acidic aqueous solution with the help of sonication and further freeze-dried to obtain a white cotton-like solid, like the natural nanotubes. This route is illustrated in **Figure 5**.

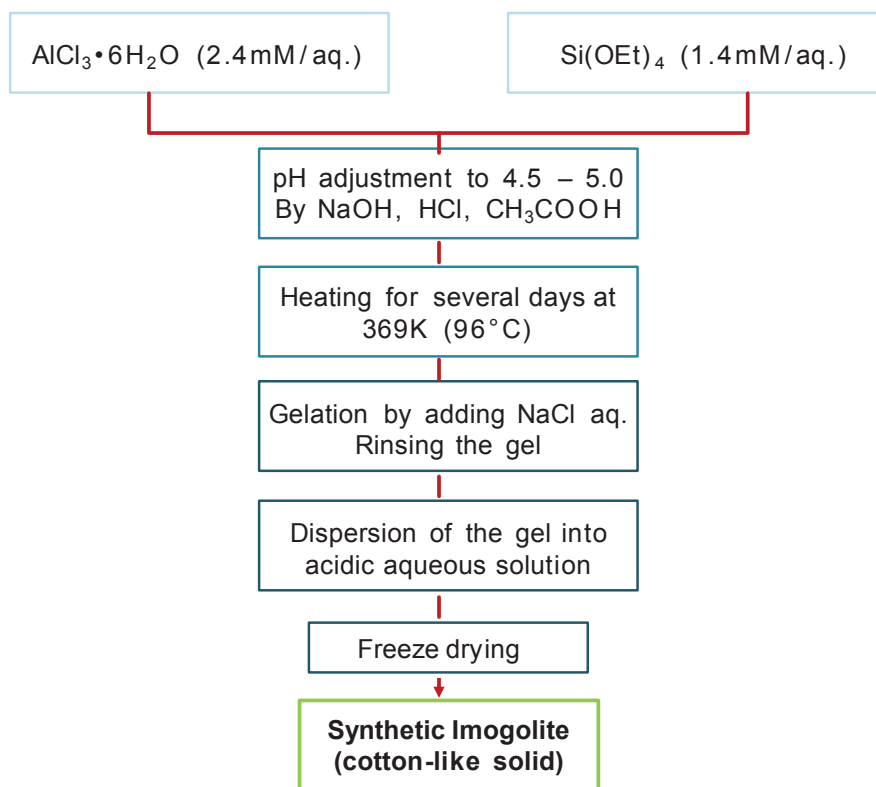


Figure 5. Farmer's method process for synthesizing Imogolite. Adapted from ref⁵³.

This method generates well-defined Imogolite-like aluminum silicate nanotubes with a yield of freeze-dried product of 70%, and can be easily reproduced on a laboratory scale. In addition, synthetic Imogolites are more easily dispersed in water, yielding clear acidic dispersions⁵⁴. Natural Imogolite can be dispersed in water at pH 3.5 – 4.5 by ultrasonic treatment of the wet gels, but such dispersions are opaque and probably contain bundles of tubes. In contrast, the synthetic route allows the formation of transparent aqueous dispersions of individual tubes. However, this synthesis presents some drawbacks, like: the low yield resulting from the limited amount of precursors (aluminum chloride and monomeric orthosilicates) and the time demanding procedure. Attempts to synthesize Imogolite from more concentrated solutions failed as the spherical analogue, Allophane, was mainly obtained in this case^{42,55}. Investigations of alternative synthetic routes have been reported, in which precursors were formed in high concentrated solutions⁵⁶ and the control of nanotubes length was driven by additives.

Despite the advances on producing synthetic Imogolite, some limitations were still encountered. The time-demanding and complicated techniques that allow the formation of such nanotubes in reasonable amounts limit their industrial application, and only a few examples of their use in the industry can be found (e.g. Eastman Kodak Company).

Motivated by these drawbacks of Imogolite synthesis and searching for specific properties of the final products, researchers started to investigate the synthesis of atom-substituted Imogolite-like nanotubes. Attempt was done to replace in part or totally the tetravalent silicon atom by carbon or tin and the trivalent aluminum by iron, gadolinium or indium^{57, 58}. Imogolite analogues of different compositions were shown to be possible in theory⁵⁸. However, no experimental evidence of large quantities of such materials was reported, except in the case of iron substitution, where an iron-doped Imogolite-like structure could be successfully obtained⁵⁷. Despite those efforts, no significant increase of the final amount of product obtained was yet achieved. Finally, in 2008 Levard et al.⁵⁹ reported the successful synthesis of large amounts (ca. 100-fold increase of the concentration) of aluminogermanate Imogolite-like nanotubes by replacing silicon by germanium atoms.

The synthesis described by C. Levard was straightforward and generated well-defined single-walled Ge-Imogolite nanotubes. The material was typically synthesized by coprecipitation of aluminum perchlorate ($\text{Al}(\text{ClO}_4)_3$) and tetraethoxygermanium ($\text{C}_8\text{H}_{24}\text{GeO}_4$), from initial decimolar concentrations, in aqueous solution and partially or totally substituting silicon with germanium. The mixture was then hydrolyzed by addition of sodium hydroxide until the targeted hydrolysis ratio ($[\text{OH}]/[\text{Al}]$) was achieved. A standard synthesis of Ge-Imogolite made at low concentrations ($[\text{Al}]_0 = 0.002 \text{ M}$) generally yields 60 mg from 500 mL of reaction volume. For the same reaction volume, much larger quantities ($\sim 5.0 \text{ g}$) were obtained when the initial concentration was increased to $[\text{Al}]_0 = 0.1 \text{ M}$. Contrary to when silicon was employed, no spherical structures were obtained, but well-defined single-walled nanotubes. This represents an increase of 85 times in the mass of Ge-Imogolite obtained⁵⁹. External diameter of Ge-Imogolite nanotubes formed was determined by TEM ($3.03 \pm 0.11 \text{ nm}$). A schematic representation of the synthesized Ge-Imogolite is given in **Figure 6**.

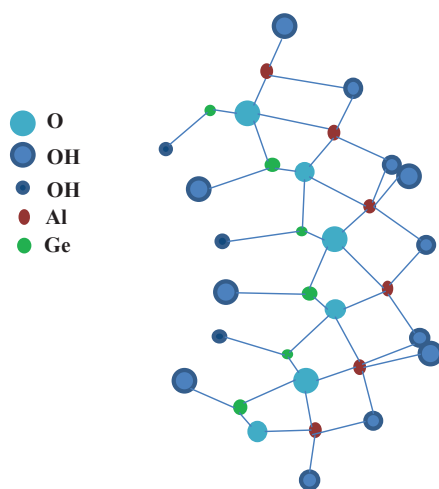


Figure 6. Schematic representation of Ge-Imogolite structure

This work represented a real breakthrough on the development and utilization of these non-carbon nanotubular materials.

In 2009, the same group reported the synthesis of aluminosilicate nanotubes, claiming that Imogolite could be obtained with higher concentrations by simply allowing for slower growth kinetics. Suspensions of proto-Imogolite at relatively high concentrations (i.e. decimolar concentrations) were left aging for 60 days and the formation of well-defined nanotubes was observed. The external tubes diameter determined by transmission electron microscopy (TEM) was approximately 2.6 nm (slightly smaller than for Ge-Imogolite). Kinetic studies showed the first tubular formation after 14 days of aging. No sign of allophane formation was observed, not even for the fresh prepared precursor's suspension⁶⁰.

As mentioned before, Imogolite nanotubes can be single (SW) or double-walled (DW), depending on synthesis conditions such as aluminum and silicon monomers concentrations, hydrolysis ratio ($[\text{OH}]/[\text{Al}]$) and temperature. The single or double-walled character of Ge-Imogolite was evidenced by Maillet *et al.* in 2010⁶¹ through small angle X-ray scattering (SAXS) and cryo-TEM investigations. The authors showed that decreasing the initial aluminum concentration from 0.5 to 0.25 M, different SAXS profiles were observed. At large scattering vectors unexpected modulations revealed an additional structuration in the case of 0.25 M, as seen in **Figure 7**. These modulations could be simulated using double-walled nanotubes model with a low dispersion in tube diameter. Regular oscillations at large angles are characteristic of SW tubes, and irregular oscillations in the same region correspond to DW tubes. DW structures were further confirmed by cryo-TEM imaging. By modeling the SAXS results, the diameters of the external and internal tubes could be determined (4.0 and $2.0 \text{ nm} \pm 0.1 \text{ nm}$, respectively). The distance between the internal and external tubes was also determined by modeling SAXS scatterings (0.27 nm). Nanotubes length cannot be precisely determined by SAXS analyses, and has to be measured by AFM. It was found to vary between 10 nm and 200 nm for SW and between 10 nm and 50 nm for DW tubes, as determined by AFM.

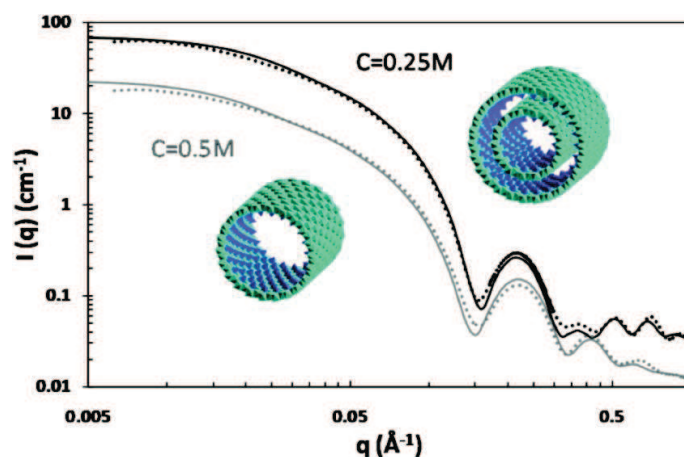


Figure 7. SAXS curves of 0.5 and 0.25 M Al-Ge Imogolite-like nanotubes. Experimental data are plotted using dots, and theoretical scattering curve of the represented structure are plotted using straight lines. The 0.25 M curve is plotted using a x4 offset. Reprinted with permission from ref⁶¹. © 2010 American Chemical Society.

In 2012, Thill *et al.*⁶² proposed a mechanism for the formation of SW and DW Ge-Imogolite nanotubes. They confirmed that the nanotubes originated from the growth of proto-Imogolite, which are slightly curved tile-like species of around 5.0 nm with the same composition and structure than that of Imogolite. The attraction between the inner and the outer surface of these small precursors forms aggregates of proto-Imogolite. These proto-Imogolite aggregates transform progressively in SW or DW nanotubes. According to this mechanism, the preferential final structure is defined by the balance between the attractive energy that tends to maintain the tube in close contact and the curvature energy that is accumulated during this transformation. If the former wins, DW nanotubes are formed. When the curvature energy is greater, SW nanotubes are obtained. As it can be seen in **Figure 8**, when samples were prepared with a hydrolysis ratio of $R = 1.5$, SW nanotubes were formed, while using $R = 2.0$ or 2.5 , DW tubes were obtained.

Imogolite structure has been characterized by diverse means, such as infrared spectroscopy⁶³ (IR), electrophoresis measurements⁶⁴, ²⁹Si and ²⁷Al high resolution solid-state nuclear magnetic resonance spectroscopy⁶⁵ (HRSNMR), X-ray diffraction (XRD)⁶⁶, wide angle X-ray diffraction (WAXD), SAXS⁵⁹, TEM⁴⁰ and rheological behavior of aqueous Imogolite suspensions⁶⁷. The structural purity and quality of Imogolite preparations could only be fully evaluated a few years ago by high resolution TEM. However, strong evidences of the presence of non-tubular structures as well as detailed information on the ordered structure can be now extracted from IR, XRD, WAXD and SAXS analyses thanks to the advances in such techniques in the last few years. For instance, indications of purity can be obtained from an IR spectrum, in which sharp absorptions indicate tubular structures, and broad peaks are related to the presence of

contaminants⁵⁴. Moreover, IR spectra can also indicate if the structure is SW or DW. DW structures present two peaks attributed to Al-O stretching vibrations at 692 and 624 cm^{-1} , while SW tubes present the 624 cm^{-1} peak and another one at 743 cm^{-1} , assigned to shift on peak at 692 cm^{-1} of DW tubes (**Figure 8**). Dried Imogolite can be analyzed by XRD and WAXD, and these analyses provide information about their packing arrangement on solid-state. From XRD and WAXD results, the d -spacing between each plane (e.g. (100), (110), (001) and (211)) can be calculated applying Bragg's Equation⁶⁸. Taking advantage of mathematical modeling equations, SAXS results can be fitted to access the tubular structure and even further determine if SW or DW materials have been formed. The d -spacing can also be calculated from SAXS results. The advantage of this technique is that it can be performed in solid or liquid state.

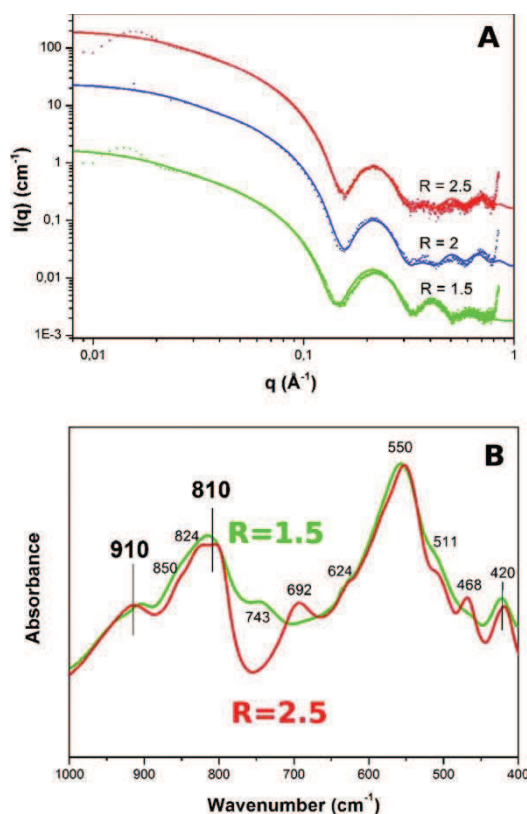


Figure 8. (A) SAXS measurements obtained for samples with an initial aluminium perchlorate concentration of 0.5M and hydrolysis ratios $R = 1.5, 2.0$ and 2.5 . For clarity the signal for $R = 1.5$ was divided by 10 while that for $R = 2.5$ was multiplied by 10. The continuous lines correspond to the scattering form factor of model SW or DW tubes. (B) IR spectra for hydrolysis ratios, R , of 1.5 and 2.5. Reprinted with permission from ref⁶². © 2012 American Chemical Society.

Packing arrangement of Imogolite and Ge-Imogolite nanotubes in the solid state was studied by Mukherjee *et al.*⁶⁶ (**Figure 9**). They used a number of complementary characterization techniques to probe the dimensions, structure and morphology of the nanotubes. It was shown that Imogolite nanotubes pack in a monoclinic arrangement due to hydrogen bonds that are formed between the tubes. Different center-to-center distances were found for each analogue (Si and Ge). Ge-Imogolite nanotubes present a slightly bigger diameter (between 3.0 and 4.0 nm) compared to Si-Imogolites (between 2.0 and 3.0 nm). This difference results from the larger germanium atom radius. Thus, even having the same packing arrangement (i.e. monoclinic), it is logical that the center-to-center distance increases in the case of Ge-Imogolite.

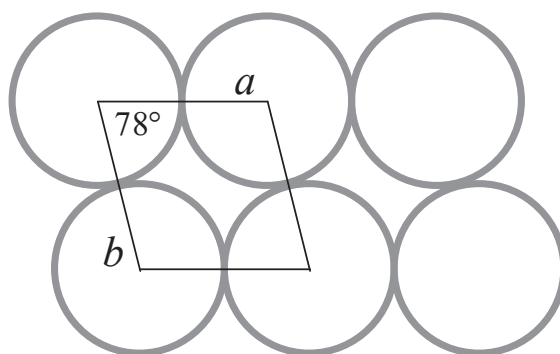


Figure 9. Representation of monoclinic solid-state packing arrangement of Al-Si and Al-Ge Imogolite nanotubes. Adapted with permission from ref⁶⁶. ©2005 American Chemical Society.

The authors calculated the crystalline plane distances (i.e. *d*-spacings) for Si and Ge-Imogolite powders, and the results are shown in **Table 1**.

Table 1. Miller Indices and *d*-spacings of Bragg Reflections obtained from the XRD Spectra of the Al-Si and Al-Ge Nanotubes^{66 a}. Reprinted with permission from ref⁶⁶. ©2005 American Chemical Society.

Al-Si nanotubes ^b				Al-Ge nanotubes ^c			
<i>h</i>	<i>k</i>	<i>l</i>	<i>d</i> -spacing	<i>h</i>	<i>k</i>	<i>l</i>	<i>d</i> -spacing
1	0	0	2.105	1	0	0	3.253
1	1	0	1.672	1	1	0	2.585
0	0	1	0.851	2	2	0	1.292
2	1	1	0.656	0	0	1	0.851
				2	1	1	0.751

^aThe unit cells are monoclinic with dimensions as indicated. ^b Unit cell parameters: $a = b = 2.105$ nm, $c = 0.851$, $\alpha = \beta = 90^\circ$, $\gamma = 78^\circ$. ^c Unit cell parameters: $a = b = 3.235$ nm, $c = 0.851$ nm, $\alpha = \beta = 90^\circ$, $\gamma = 78^\circ$.

Recently, the rheological behavior of Imogolite in an aqueous suspension was investigated by means of viscosity evolution with volume fraction of Imogolite using a concentric cylindrical

viscometer by Tsujimoto *et al.*⁶⁷. Dispersed nanotubes and bundles of Imogolite in suspensions were analyzed and flow curves showed a slight and a significant hysteresis for dispersed Imogolite and bundles, respectively. This hysteresis was higher for nanotubes bundles, being even larger when the volume fraction of Imogolite was increased. In addition, shear thinning, which is the decrease in viscosity with increasing the shear rate, was also observed and followed the same tendency, increasing with Imogolite volume fraction and coagulation. This was attributed to the orientation of the tubes under shear, which contributes to the flow and decreases viscosity. In the case of weakly dispersed Imogolite, aggregates are formed in suspension. These aggregates can be constantly broken by the high shear rate and reformed, in agreement with the higher hysteresis and shear thinning at high Imogolite volume fractions.

II.2.4 Applications

II.2.4.1 Application of Imogolite in clay science

Soils originating from pumice beds and volcanic ash present a great interest as effluent filters and decontaminants. Clays are known since many centuries for their purifying properties, thanks to their high ionic exchange capacity and large surface area. Podzol soils, which are rich in aluminosilicate minerals of different shapes and structures (i.e. allophanes, Imogolite, orthosilicates) were discovered in the early 60's. It was soon realized that these soils were many times more efficient in effluent purifying than layered silicate soils, due to the presence of minerals with even higher exchange capacities and greater surface areas (**Figure 10**).

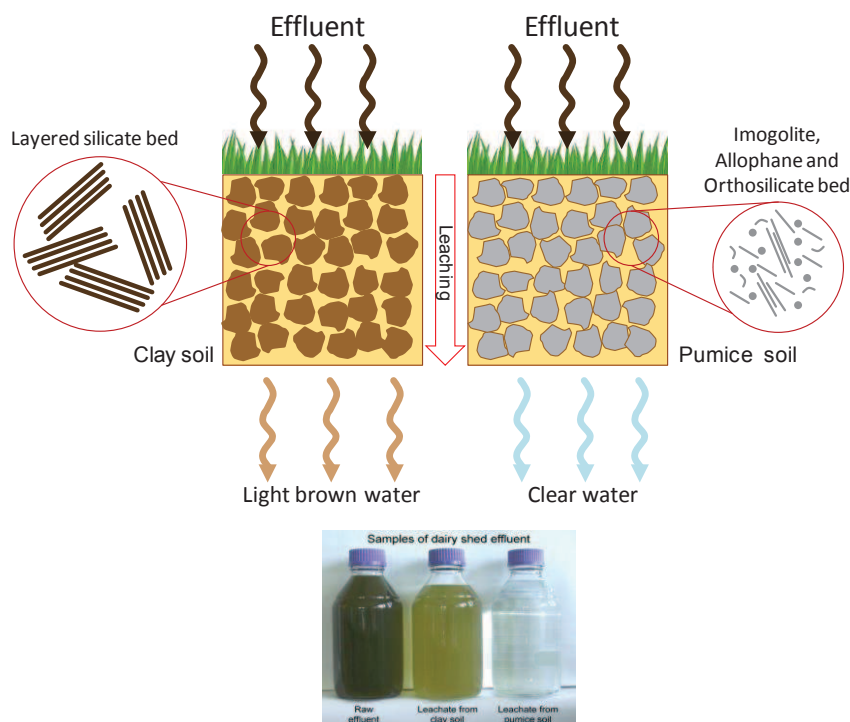


Figure 10. Comparison of effluent leaching with clay soils and pumice soils. Photo from ref³⁶.

Research on Imogolite has focused on the key role it plays in the movement of nutrients and water in the soil, the supply of nutrients and moisture to plants, the accumulation of contaminants etc⁵³. More recently, these materials also found possible applications as high performance engineering materials like fuel storage media for natural gases⁶⁹, catalyst supports, polymer nanocomposites³¹, humidity-controlling materials⁷⁰, and a speed-dry desiccant due to its high adsorption and desorption rates^{53, 71}. Additionally to its nanoscale fibrous microstructure and its enormous surface area, Imogolite nanotubes have powerful water adsorption ability. This feature is due to their high micro, meso and macro porosity as well as its high hydrophilicity, which make them remarkably interesting for anti-dewing applications⁵³. Compared to carbon nanotubes, Imogolite lacks intrinsic semiconductivity, but it can be an interesting condensed phase for heterosupramolecular systems due to its high surface area for molecular components adsorption, abundance of empty surface sites for covalent binding of acidic anchoring groups, and high stability under ambient conditions³³.

Another interesting application of tubular aluminosilicates, evidenced by Lvov and Abdullayev⁷² and widely described for halloysite nanotubes – analogous tubes with innermost alumina and outermost silica – is the controlled release of chemical agents. In the case of halloysite, its external diameter being larger than that of Imogolite (i.e. 10 – 15 nm), it facilitates the entering of a wide range of application-specific chemical inhibitors such as drugs, flame-retardants, anticorrosion, antimicrobial and microcrack self-healing molecules⁷². Even

being smaller, Imogolite contains a silicon-based inner surface, which is compatible with various organic molecules and could accommodate small chemically and biologically active substances.

II.2.4.2 Polymer/Imogolite nanocomposites

In the past few years Imogolite nanotubes have attracted increasing attention due to their unique one dimensional structure, high aspect ratio and large surface area. For instance they can provide orientation to polymers increasing mechanical and optical anisotropy and favoring mechanical, optical and electronic properties, making them promising fillers for organic/inorganic engineering advanced materials. Thermodynamically there is a possibility of homogeneously dispersing unmodified Imogolite in a polymer matrix, if enthalpic interactions between the polymer and the nude Imogolite surface were favored. However, Imogolites being very hydrophilic, their direct incorporation into organic products is compromised and they tend to form nanotube bundles due to their rigidity and high surface energy. These bundles may combine with themselves forming even larger bundles or random aggregates that compromise the final products properties. Thus, some surface modifications are necessary to disperse the tubes in organic solvents or to increase their affinity with polymers.

II.2.4.2.1 Imogolite surface modification with small molecules and oligomers

- Phosphates and phosphonates

Great affinity between Imogolite surface and alkyl phosphonic groups was observed by Yamamoto *et al.*^{73, 74}. The authors obtained modified hydrophobic Imogolite nanotubes by dispersing octadecylphosphonic acid (OPA) and Imogolite powder in a water/ethanol mixture (water: ethanol = 2:3, vol: vol) by the help of sonication. The product was further centrifuged and rinsed with ethanol to extract nonattached OPA. By means of IR, adhesion force of AFM tip to the sample and thermogravimetric analysis (TGA), the authors could confirm and quantify the modification and hydrophobization of the tubes⁷³. The strong interaction between the aluminol (Al-OH) groups of Imogolite and the PO(OH)₂ groups of OPA was ascribed to direct Al-O-P covalent bonds formation or dipole-dipole electrostatic interactions between AlOH₂⁺ and PO(OH)O⁻, as shown in **Figure 11**.

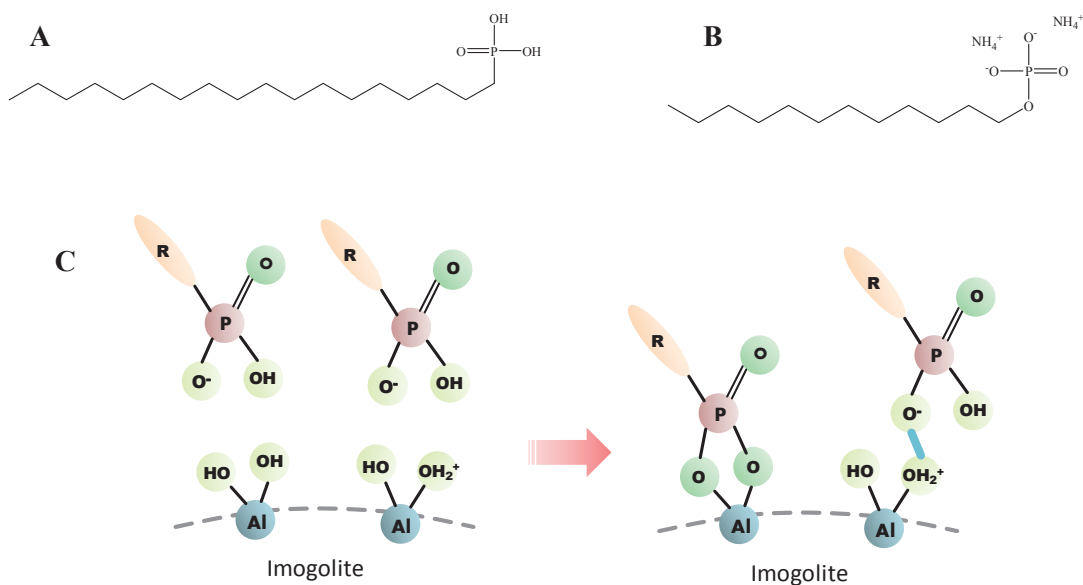


Figure 11. Chemical structure of (A) octadecylphosphonic acid and (B) ammonium salt of dodecylphosphate. (C) Schematic representation of the mode of interaction between Imogolite surface and an alkyl phosphonic acid groups.

The strategies described so far were performed in organic solvent, or in water/ethanol mixtures. However, it is known that Imogolite nanofibers are found individually dispersed only in acidic water. To avoid bundles formation, a new strategy was developed by Ma *et al.*⁷⁵ to modify Imogolite with $\text{PO}(\text{OH})_2$ -containing molecules from aqueous solutions. Thereunto they converted the organo soluble alkyl phosphate molecule to the corresponding water-soluble ammonium salt. The new water-soluble molecule (ammonium salt of dodecylphosphate, $\text{DDPO}_4(\text{NH}_4)_2$, **Figure 11**) was precipitated from 2-propanol solution of dodecylphosphoric acid (DDPO_4H_2) by the addition of ammonia. The grafting was confirmed by IR spectroscopy, high-resolution XPS analyses, WAXD and electron microscopy. IR spectra showed that the $\text{P}=\text{O}$ absorption peak at 1239 cm^{-1} for DDPO_4H_2 and 1201 cm^{-1} for $\text{DDPO}_4(\text{NH}_4)_2$ disappeared from the spectrum of DDPO_4 -Imogolite presumably due to the condensation between the phosphate groups and the aluminol groups. XPS measurements revealed that for pristine Imogolite, the $\text{Al}2\text{p}$ signal was around 74.3 eV with a symmetric peak; while for DDPO_4 -Imogolite, the $\text{Al}2\text{p}$ peak became wide and asymmetric, and could be fitted with two Gaussian curves containing a contribution at 74.3 eV and another one at 76.3 eV . The second component was ascribed to an increase in the positive charge on Al atoms because of the formation of $\text{Al}-\text{O}-\text{P}$ bonds at the surface of Imogolite, while the first indicated the presence of unreacted $\text{Al}-\text{OH}$. Thus, it was concluded that $\text{DDPO}_4(\text{NH}_4)_2$ attaches to the surface through covalent bonds. The modified tubes were analyzed by static-contact-angle, and significant increase of hydrophobicity, with angles varying from 22° for pristine Imogolite to 93° for DDPO_4 -Imogolite, was measured.

WAXD and TEM analyses confirmed the formation of DDPO₄-modified Imogolite. Exfoliated tube bundles were formed after modification of Imogolite with the organic molecule; however individual tubes could not be obtained. The authors explained that the complete exfoliation of Imogolite nanotubes in water starting from cotton-like Imogolite powder is known to be very difficult and is rarely achieved.

The strong affinity between Imogolite surface and phosphate compounds was explored by several groups to graft oligomers and polymers to the surface of the nanotubes for the fabrication of advanced functional materials.

In the attempt of rendering Imogolite nanotubes semiconducting, thiophene oligomers were grafted to the tubes surface by the help of phosphonic acid groups previously attached to the oligomer chain ends⁷⁶. The *grafting to* approach was carried out by adding dropwise the Imogolite solution to a THF solution of 2-(5''-hexyl-2,2':5',2''-terthiophen-5-yl)ethylphosphonic acid (HT3P) and stirring overnight at room temperature in a dark environment. The resulting product was recovered by centrifuging and further rinsing with fresh THF. The product was redispersed in water followed by freeze-drying, and a yellow cotton-like solid was recovered. 2-(5''-hexyl-2,2':5',2''-terthiophen-5-yl)ethylphosphonic acid 1,1-dioxide (HT3OP)/Imogolite hybrids were also prepared by the same method. Control samples were prepared using the equivalent macromolecules containing OH groups instead of P=O(OH)₂ groups, but no precipitate was recovered, confirming poor interaction of these non-phosphorous compounds with the Imogolite surface. FTIR analyses confirmed the chemisorption of both macromolecules to the Imogolite surface. Optical properties of HT3P and HT3OP/Imogolite films were determined by UV-vis spectra. Solid-state optical properties of the hybrids were proven to be highly influenced by the interactions between the oligomers and the Imogolite surface. Further fluorescence spectroscopy suggested the formation of H-type intermolecular interaction of terthiophene on the Imogolite surface.

- Silanes

Organosilanes are widely used to modify inorganic surfaces. However, it has to be performed in dry conditions to prevent side reactions such as homocondensation/polymerization leading to (Si-O-Si) bonds formation. Since Imogolite is very hydrophilic and its interior, i.e. also called lumen, is filled with water molecules, it is very hard to obtain proper organosilane chemistry with Imogolite. Johnson and Pinnavaia⁷⁷ reported in 1990 the fragility of this system showing that surface bonds between organosilanes and the external surface of Imogolite are labile in a humid atmosphere. They hydrolyzed (γ -aminopropyl)triethoxysilane (APS) in acetic acid (pH 3.6), to form only monomer or dimer species and avoid self-condensation to higher molecular weights, and mixed it with freshly synthesized and dialyzed Imogolite suspension in water.

After silylation overnight, the mixture was characterized by FTIR and ^{29}Si magic-angle spinning (MAS) NMR. The authors evidenced that the products are molecular composites, not physical mixtures of separate siloxane and Imogolite. However, they were unable to determine whether the polymer was physisorbed or chemically linked to the surface. After 3 days of dialysis against deionized water at room temperature, it was observed that all of the surface-coupled APS was lost. It was concluded that the organofunctionalization of AlOH curvilinear Imogolite surface using aminosilanes lacked hydrolytic stability. Organophosphorous compounds, on the contrary, are fairly insensitive to nucleophilic substitutions and prefer to heterocondensate forming M-O-P bonds rather than homocondensate forming P-O-P bonds. Consequently, surface modification with organophosphorous compounds can be performed in a wide range of organic solvents and in water³³.

Surface-modified Imogolite nanotubes produced by these diverse strategies were successfully dispersed in organic solvents, and it was generally claimed that the further dispersion of the tubes in polymer matrixes could be equally achieved.

II.2.4.2.3 Imogolite modification/interaction with polymers

- Polymer/Imogolite blends

Choi et al.⁷⁸ reported the first production of polymer/Imogolite nanocomposites by blending Imogolite and poly(vinyl alcohol) (PVA) in dimethylsulfoxide (DMSO) solution. Imogolite dispersion in DMSO was not complete, but water-swollen nanotube bundles were obtained, the water being trapped in the tube pores and originating from Imogolite synthesis. Final mixture had PVA:Imogolite weight fraction of 9:1. Films were then cast by high-temperature zone drawing. It was concluded that Imogolite had a significant influence on the structure and properties of syndiotacticity-rich (63%) ultra-high molecular weight (UHMW, $12,300 \text{ g mol}^{-1}$) PVA films, and the films of PVA/Imogolite blends presented lower tensile modulus but higher tensile strengths. The effects were attributed to PVA chains randomly co-existing with nanotubes, winding around them by hydrogen-bond interactions (**Figure 12**). Imogolite contributes to the orientation of PVA crystalline regions but it disturbs the orientation of amorphous phases. Furthermore, Imogolite tubes embedded in the PVA phase act as physical barrier hindering the extension of PVA chains, so that PVA/Imogolite blends present poor drawability and deformability.

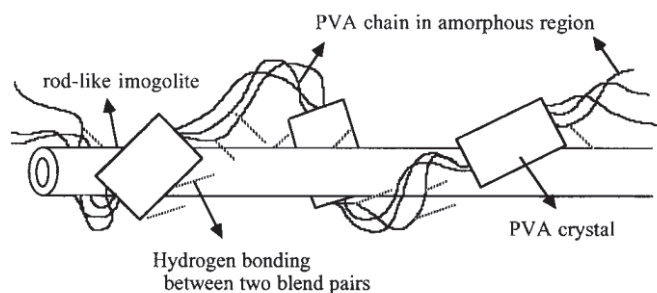


Figure 12. Poly(vinyl alcohol) interaction with Imogolite nanotubes. Reproduced from ref ⁷⁸.

Otsuka and Takahara³² functionalized PVA with phosphonic acid group units at the side chain to increase the affinity of this polymer ($\text{H}_2\text{PO}_3\text{-PVA}$) with Imogolite, allowing the formation of $\text{H}_2\text{PO}_3\text{-PVA/Imogolite}$ nanocomposites with interesting properties. Dynamic mechanical analysis (DMA) showed a shift of the α_a peak of the nanocomposite to higher temperatures compared to pure polymer, resulting from the restriction of thermal molecular motion due to strong interactions of the polymer chains with the surface.

Interactions of Imogolite nanotubes with polymers in aqueous media were also observed by Yang *et al.*⁷⁹ when mixing Imogolite suspensions with polyelectrolyte solutions in water. A poly(acrylic acid) (PAA) solution was added to the Imogolite suspension at room temperature, resulting in the formation of fibrous structures after around 10 days. These structures could be seen by naked eyes. Further investigations by optical and transmission electron microscopy of both dried fibers and suspensions in water showed a bamboo-like structure where fibers wall was mostly composed of PAA structured by Imogolite nanotubes. The formed microfibers were proven to be quite resistant to rough conditions and did not desagglomerate even after sonication for 75 minutes. The strong interaction was attributed to hydrogen bonding between COOH groups from PAA and Al-OH aluminol groups from Imogolite surface. TGA analyses showed that the fibers were composed of only 23% of Imogolite. The relatively low amount of nanotubes in the microfibers suggested that Imogolite acts as a framework in the microfibers formation, and PAA account for most of the mass. This spontaneous assembly of randomly dispersed nanotubes to form micron sized one-dimensional structures was claimed to be an interesting tool to the field of supramolecular assembly.

Hybrid materials of HT3P/Imogolite were used as templates for poly(3-hexyl thiophene) (P3HT) conductive polymer crystallization, by Yah *et al.*⁸⁰. The slow cooling from 80 °C to room temperature of P3HT in anisole was performed in the presence of HT3P/Imogolite

hybrids, and the polymer crystallized on the surface of the nanotubes forming fiber-like semi-crystalline composite structures.

- *In situ synthesis of Imogolite in polymer solution*

Another elegant approach to produce polymer/Imogolite composites avoiding dispersion problems is through the *in situ* synthesis of aluminosilicate tubules in a polymer solution. Using this strategy, Yamamoto et al.^{81, 82} synthesized Imogolite in a PVA solution. Taking advantage of the solubility of PVA in water and relying on the possibility of hydrogen bonding between the polymer and Imogolite as reported earlier by Choi et al.⁷⁸, the authors mixed an aqueous solution of Imogolite precursors with PVA, and allowed tubes growth by heating at 96 °C for 96h. The nanocomposite was recovered by precipitation in ethanol and rinsing with water and ethanol. Imogolite structure could be identified through IR measurements, confirming the successful synthesis. WAXD analyses also evidenced the presence of well-defined aluminosilicate nanotubes individualized in the PVA matrix. Films were prepared by solvent casting and no macroscopic phase separation was observed during water evaporation, confirming the thermodynamic stability of the mixture. Furthermore, the authors observed that the adsorbed PVA chains played an important role on preventing aggregation of the tubes while precipitation in ethanol to recover the product and while casting the film. Interestingly, AFM analyses revealed a significant change of tubes length depending on PVA concentration. The length varied from around 700 nm for the lowest PVA concentration to 180 nm for higher concentrations. Complete inhibition of tubes formation was observed when increasing further the amount of polymer. The influence of the presence of additives on Imogolite formation and growth had been described before by Wada *et al.*⁸³ and Inoue *et al.*⁸⁴. These authors demonstrated that any molecule capable of interacting with aluminum ions could disturb the formation of Imogolite and prevent further fusion of precursors into tubes. Thus, in a similar way, PVA chains can interact with the aluminol groups of the precursor molecule and inhibit tubes growth. In spite of this tube growing issue, this technique is a successful method to produce PVA/Imogolite nanocomposites by carefully tuning the PVA concentration.

- *In situ synthesis of polymers in Imogolite dispersions*

Shikinaka et al.⁸⁵ explored the *in situ* synthesis of polymers in the presence of bare Imogolite nanotubes. In this work, the authors took advantage of the affinity (i.e. non-covalent binding interactions) of acrylamide with the inner surface of Imogolite, as described earlier⁸⁶⁻⁸⁹, to produce polyacrylamide (PAAm)/Imogolite reinforced hydrogels with high mechanical strength. A cross-linker (*N,N'*-methylene bis (acrylamide), MBAA) was also added during polymerization to effectively form the hydrogel. The syntheses were carried out through radical

solution polymerization in phthalate buffer (pH 4.0) at 60°C for 12h using potassium persulfate (KPS) as initiator. After gelation, the products were immersed in water and left standing for a week to reach an equilibrium state. Compressive and tensile measurements of the gels were performed to evaluate their mechanical strength. Imogolite-containing materials presented a turbid aspect that was attributed to the formation of Imogolite bundles, which were not well dispersed in phthalate. The presence of tubes also allowed the formation of a gel even in the absence of cross-linker, suggesting an interaction between acrylamide (AAm) and the inner sites of Imogolite or hydrogen bonding with the surface. Since simple addition of PAAm to an Imogolite suspension does not form a gel, it is expected that AAm monomers interact with silanol groups in the inner cavity of Imogolite. Mechanical tests revealed superior elongation properties for the hybrid gel, resulting from the stress equalization provided by Imogolite tubes. In the presence of high cross-linker concentrations, however, Imogolite mobility was restricted, and the gels could be easily broken.

Later, the same group studied the isotropic-anisotropic structural transition of PAAm/Imogolite hydrogels induced by small tensile strains⁹⁰. The hybrid gels were prepared as described above. Birefringence of about 7×10^{-5} due to the anisotropic diffraction appeared and disappeared upon applying strain or releasing the gel (**Figure 13**).

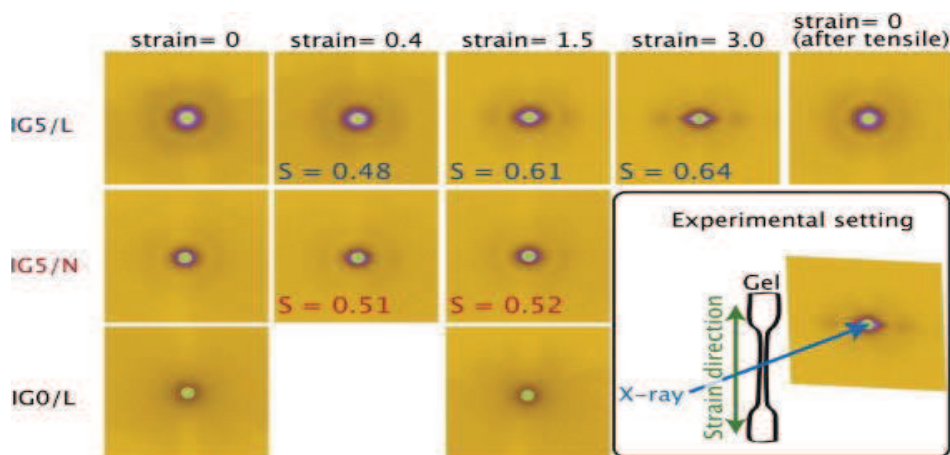


Figure 13. Two-dimensional SAXS patterns and order parameter S of Imogolite gels with (IG5/L; top) or without (IG5/N; middle) crosslinker and ordinary PAAm gel (IG0/L; bottom) under strain. The experiment setup of SAXS measurements is shown at the bottom right of the figure. Reproduced with permission from ref⁹⁰. © 2013 Elsevier.

The *in situ* synthesis of polymers in Imogolite suspensions was also performed using two techniques: “grafting through” and “grafting from”. These techniques provide a strong, and usually chemical, bond between the polymer and the inorganic surface, improving the dispersion of the filler in the polymer matrix.

Yamamoto *et al.*⁹¹ prepared poly(methyl methacrylate) (PMMA)/Imogolite hybrids by radical polymerization of methyl methacrylate (MMA) in the presence of 2-acidophosphoxyethyl methacrylate (P-HEMA)-modified Imogolite nanotubes, by “grafting through”. The tubes modification was carried out by mixing an aqueous Imogolite suspension with P-HEMA dissolved in water at room temperature and stirring for 24h after sonication treatment. Imogolite:P-HEMA weight ratios were varied (1:0.2, 1:0.6 and 1:1). The modified-Imogolite solid was recovered by centrifugation and washed with water followed by freeze-drying to give a white solid. The resulting organotubes were dispersed in MMA and by addition of AIBN and heating at 70 °C polymerization was performed for 3h. PMMA/Imogolite hybrid nanocomposites were analyzed by IR and the presence of PMMA was confirmed by CH₂ and C=O absorption peaks at 2996, 2953 and 1727 cm⁻¹, respectively. The P-O bond vibrations were found at 1080 cm⁻¹. In addition, the C=O band peak at 1727 cm⁻¹ from grafted PMMA was shifted to lower wavenumbers, due to different environments of free PMMA and linked chains. Retention of the Imogolite structure after polymerization was also confirmed by IR, where characteristic bands of the inorganic material were found. TGA results of bare Imogolite and PMMA/Imogolite hybrids confirmed the presence of polymer chains on the surface of the tubes. PMMA/Imogolite films were also analyzed by DMA. The mechanical tests revealed storage modulus 1.5 times higher for the reinforced matrix when compared to pure polymer. Transparency of the nanocomposite films was measured by light transmission, and the presence of Imogolite was proven not to affect the film optical properties.

The growth of polymer chains on the surface of Imogolite through the *grafting from* technique was also reported using activators regeneration by electron transfer atom transfer radical polymerization (ARGET ATRP)^{92, 93} and gamma ray radiation for surface radical production⁹⁴.

The group of Takahara⁹² reported the grafting of PMMA from the surface of Imogolite using an ATRP initiator previously attached to the surface. They used a bifunctional molecule containing the ATRP initiator on one extremity and the anchoring phosphate group on the other. Mixing a solution of this ammonium salt of 8-(2-bromo-2-methylpropanoyloxy)octyl phosphate [BMPOPO₄(NH₄)₂] (**Figure 14**) and Imogolite aqueous suspension at room temperature for 48h, followed by filtration and centrifugation, they recovered a white product of BMPOPO₄-modified Imogolite. Successful modification of the surface by the molecule was attested by FTIR and XPS measurements. IR spectra presented the characteristic vibration peaks for both Imogolite and BMPOPO₄ species. For the organic molecule, the absence of N-H vibration band confirmed the non-adsorption of the ammonium counter cations to the surface. X-ray photoelectron spectroscopy (XPS) results evidenced a shift on Al_{2p} peak position, indicating a decrease on Al positive charge. This decrease was attributed to electrostatic adsorption of the initiator to the surface, since Al-O-P covalent bond formation is usually reported to cause an

increase of positive charges of Al atoms. By TGA analyses, the amount of BMPOPO₄ on the modified-Imogolite was estimated to be 49 wt%. BMPOPO₄-Imogolite could be dispersed in a wide range of monomers, however a poor homogeneity and limited stability were observed. This probably indicates the formation of small Imogolite bundles. The polymerization of MMA by surface-initiated ARGET ATRP was then carried out in anisole at 40 °C in the presence of CuBr₂ and using ascorbic acid as the reducing agent. Polymeric products were recovered by precipitation from methanol and PMMA was cleaved off from the surface using a strong acid solution of HF/HCl. SEC analyses showed that the number-average molar mass of the polymer formed (M_n) at 50 and 90 minutes of reaction was 26,600 and 32,700 g mol⁻¹ with dispersity of weight-average molar mass $M_w/M_n = 1.22$ and 1.33, respectively, confirming the controlled character of the polymerization. WAXD and scanning force microscopy (SFM) analyses of the PMMA-g-Imogolite revealed a core/shell structure where bundles of BMPOPO₄-Imogolite formed the core and grafted PMMA chains formed the external brush/shell. In addition, after MMA polymerization, these Imogolite bundles could be better dispersed in THF, chloroform and toluene and were stable for more than two months.

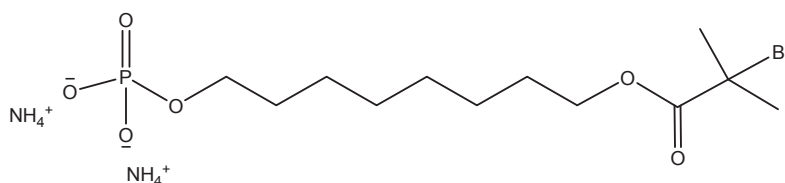


Figure 14. Chemical structure of the 8-(2-bromo-2-methylpropanoyloxy) octyl phosphate [BMPOPO₄(NH₄)₂] ATRP initiator used to polymerize MMA from the surface of Imogolite⁹².

Later, Ma *et al.* proposed the incorporation of the PMMA-g-Imogolite into a poly(vinyl chloride) (PVC) matrix⁹³. The incorporation was performed in THF starting from separate solutions of both components in THF and in the presence of an organic tin thermal stabilizer. The mixtures were left at room temperature for 18h, followed by precipitation in water and vacuum drying at 40 °C and 60 °C for 1 day and 3 days, respectively. The films were prepared by compression molding at 190 °C for 6 min, and their exact composition was assessed by TGA. DSC showed a T_g of 76.4 °C for PVC, 127.6 °C for PVC/PMMA blend and 84.6 °C for the hybrid blend. The presence of a third T_g , different from that of pure PVC and from the PVC/PMMA blend, suggested a good dispersion of the PMMA-g-Imogolite in the PVC matrix. SEM images of the product after being fractured at different temperatures showed that at liquid nitrogen and at room temperatures the interfacial adhesion between PMMA-g-Imogolite and PVC was weaker than at 90 °C, proving the influence of the environment on the adhesion performance of the nanofiller in the matrix. This work represents a practical demonstration of

the interest of growing a polymer directly from the surface of Imogolite, to achieve effective and homogeneous dispersion of nanotubes in a polymer matrix.

Another strategy used to grow a polymer from the surface of Imogolite nanotubes was the use of gamma-ray radiation to transform the Al-OH surface hydroxide groups into peroxide functions (Al-OOH). This strategy has already been used before for silica particles^{95, 96}. Lee *et al.*⁹⁴ used this process to polymerize acrylic acid (AA) using γ -ray-irradiated Imogolite (Imogolite-OOH) as initiator *and* cross-linker to form hybrid hydrogels with exceptional elongation properties. 1 wt% Imogolite suspension in water was irradiated with ⁶⁰Co γ -ray under ambient conditions for 2h. The Imogolite suspension was first freeze-thawed in the presence of acrylic acid to remove all the oxygen and the polymerization was carried out by further increasing the temperature to 40 °C, temperature in which the peroxide groups are changed to radicals. The authors claimed that Imogolite nanotubes acted as cross-linker for the formation of the PAA gel. Mechanical tests revealed excellent properties of the hydrogels, especially in elongation. The axial tensile strength increased with increasing Imogolite content. In terms of elongation at break, lower elongations were obtained at high Imogolite contents. This behavior was attributed, among other causes, to the formation of shorter polymer chains, which present lower contour lengths and relaxed end-to-end distance, parameters that strongly affect the degree of chain extension before breakage. Nevertheless, with PAA/Imogolite weight ratios of 1:2, 1:1 and 2:1, the elongation of the hydrogel at break point was found to be greater than 1800%, 1000% and 600% of the original length, respectively. The alignment of the tubes in the hydrogel under tensile stress was evaluated using SAXS analyses. It was shown that the tubes tend to align parallel to tensile direction, contributing to elongation resistance. Anisotropic patterns, revealed for the Imogolite-containing hydrogel, contribute to the elongation performance of the hydrogel, and 0.2 MPa is enough to achieve elongation. In comparison, silica particles give isotropic patterns, and 1 MPa is needed to elongation. In conclusion, this strategy seems to be a direct mode to grow polymers from the surface of Imogolite and successfully obtain reinforced organic/inorganic hybrid hydrogels with excellent mechanical properties. However, the extrapolation of this γ -ray radiation process to large scale production is not possible.

- *Biomolecule/Imogolite hybrid hydrogels*

High performance Imogolite-containing hydrogels were also targeted for biological applications. The first system reported was a hydrogel of Imogolite immobilizing enzymes. The enzyme used was pepsin, which is negatively charged and possesses a phosphoric acid group. Thus, it can interact by both electrostatic interactions and specific affinity between phosphoric groups and aluminol functions of Imogolite. The gelation process is easily achieved with

Imogolite, given the fact that it gels itself under certain conditions such as high concentrations or alkaline pH. Taking advantage of these features, Inoue et al.⁹⁷ produced pepsin/Imogolite hybrid hydrogels by putting in contact Imogolite and pepsin solutions in water under shaking. The amount of immobilized enzyme could reach values as high as 1.8 mg per mg of Imogolite, thanks to the high specific surface area of the nanotubes. Homogeneous distribution of the enzyme in the gel was observed by fluorescence microscopy. In addition, the immobilized pepsin, contrary to the free one, could be easily recovered and reused.

The success on immobilizing pepsin on Imogolite surface opened the possibilities to apply this strategy to other interesting biomolecules. DNA was chosen for its high interest in medical applications. Unbound DNA is known to degrade under certain conditions, while surface-bound DNA presents a higher resistance against degradation by nucleases preserving their biological activity such as gene delivery. Furthermore, DNA contains phosphate groups on its outer double helix, which are expected to strongly interact with Imogolite surface. Jiravanichanun *et al.*⁹⁸ produced hybrid hydrogels of DNA/Imogolite using a method similar to that reported above for pepsin/Imogolite (**Figure 15**). Aqueous solutions of Imogolite and DNA were mixed and shaken overnight at 37 °C, followed by centrifugation to recover the gel. The DNA amount in the hybrid hydrogel reached even higher values than pepsin, and hydrogels with 3 mg of DNA per 1 mg of Imogolite could be obtained. This high DNA loading was attributed to the strong affinity between the phosphate groups of the biological polymer and the aluminol surface of the nanotubes. Imogolite/DNA hydrogel has the potential to act as a DNA reservoir for DNA storage and also to control its release. Thus, the group studied the release of DNA under different pH and NaCl concentrations, registering a very slow release even at severe conditions such as high pH and high ionic strength. This observation suggested an effective protection of DNA by the immobilization and hybridization with Imogolite.

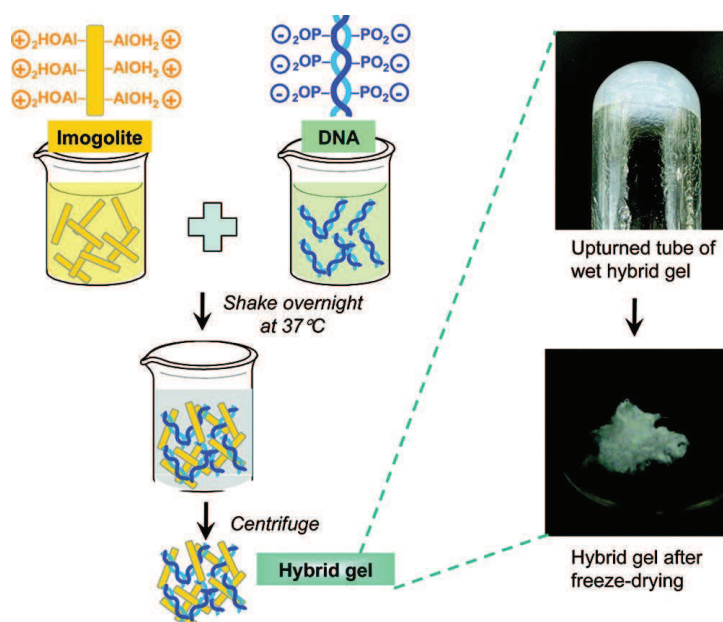


Figure 15. Schematic representation for the preparation of hybrid gels from Imogolite and DNA. Reprinted with permission from ref⁹⁸. © 2012 American Chemical Society.

Studies on the cellular response of human and mouse osteoblast-like cells (Saos-2 and MC3T3-E1, respectively) to Imogolite scaffolds revealed a good proliferation of osteoblasts on the aluminosilicate scaffolds. Fair biocompatibility and greater mineralization of the cells were observed in the Imogolite substrate compared to the control (i.e. in the absence of Imogolite)⁹⁹. This work reinforced the interest of researchers in the use of Imogolite for biological applications, especially in the field of bone-growing implants. Coating of poly(L-lactic acid) (PLLA)-based composite microfibers containing siloxane-doped calcium carbonate particles with Imogolite by electrophoretic deposition was studied by Yamazaki *et al.*¹⁰⁰. An improvement of cell attachment and extension was observed after Imogolite coating. Applying the same approach, Maeda *et al.*¹⁰¹ coated a zirconia substrate with PLLA-vaterite composites to introduce bioactivity to the material and further coated it with Imogolite to improve biocompatibility. These reports brought out the use of Imogolite coating as one of the best approaches to enhance hydrophilicity and cellular compatibility of biomaterials for bone regeneration.

- Imogolite as coagulation agent

An additional feature of Imogolite was also investigated by Kobayashi *et al.*¹⁰²: Imogolite-induced latex coagulation and charging. In this work, the authors took advantage of the interaction of Imogolite with latex particles (commercial sulfate and amidine latexes) to coagulate the latex under different Imogolite concentrations and at three pH values i.e. 4.0, 6.5

and 10.0 (i.e. different surface charge density). Mainly two mechanisms of coagulation could be distinguished: charge neutralization and sweep coagulation, depending on Imogolite loading, initial dispersion state and charge densities of both Imogolite and latex particles. When Imogolite and the latex particles were oppositely charged and Imogolite was well dispersed, coagulation only occurred around the isoelectric point, due to charge neutralization. If latex particles and Imogolite are oppositely charged but Imogolite is weakly dispersed, coagulation occurs through charge neutralization and sweep coagulation, where Imogolite aggregates engender latex particles coagulation. Finally, if they are similarly charged, coagulation only occurs at high ratios of Imogolite concentration to latex, by sweep coagulation mechanism. This work has shown the successfulness of using Imogolite as coagulant in the field of additive-induced coagulation to facilitate the separation of organic and inorganic impurities from water, for instance.

The overview of this bibliographic study revealed that besides PVA and PMMA, very few polymers were explored for the production of Imogolite-based nanocomposites.

Based on all these works and advances in polymer/Imogolite nanocomposites, we decided to focus our strategy on the *in situ* synthesis of polymers in the presence of Imogolite nanotubes, with the objective of encapsulating individual tubes that could be dispersed in a stable way in an aqueous medium, forming hybrid latexes. In order to do that, we have chosen to work in aqueous media for the surface modification of Imogolite *and* for polymerization. Thus, we employed reversible deactivation radical polymerization in emulsion. Moreover, instead of working with natural or synthetic aluminosilicate Imogolite, we used synthetic aluminogermanate Imogolite (Ge-Imogolite). From this brief bibliographic study, it can be seen that Ge-Imogolite nanotubes have been poorly explored for the preparation of polymer/fiber hybrid materials, despite their advantages in comparison to Si-Imogolite, such as the possibility of large quantity synthesis, the facility of dispersion in water in a wider range of pH (i.e. higher Al-OH pKa compared to Si-Imogolite) and the slight increase on tube diameter, enabling the introduction of molecular species on Imogolite lumen. In addition, the synthesis of such Ge-containing nanotubes is nowadays mastered by the group of Antoine Thill (CEA, Saclay), who provided us with well-defined SW or DW Ge-Imogolite nanotubes with controlled tube lengths.

In the next sections, we will report the synthesis of polymer/Ge-Imogolite hybrid latexes using the macroRAFT-assisted encapsulating emulsion polymerization (REEP) technique. We first describe the synthesis of the macroRAFT agents, which were designed to display a good interaction with the surface of Imogolite as well as to stabilize the resulting particles in an aqueous medium. Some physicochemical characteristics of the Ge-Imogolite nanotubes used in this work will be then presented. Finally, we will describe the polymerizations conducted to encapsulate the Ge-Imogolite nanotubes.

II.3. MacroRAFT agents synthesis

II.3.1 Experimental section

II.3.1.1 Materials

The 4-cyano-4-thiothiopropylsulfanyl pentanoic acid (CTPPA) RAFT agent was synthesized following the methodology described elsewhere^{103, 104}. It was purified in a silica gel Gerduran[®] Si 60 (40 – 63 μm pore size, Merck) column after synthesis and stored at 4 °C under argon atmosphere. The monomers, *n*-butyl acrylate (BA) (99%, stabilized, Acros Organics), acrylic acid (AA) (anhydrous, 99%, Sigma-Aldrich), *n*-butyl methacrylate (BMA) (99%, Sigma-Aldrich) and methacrylic acid (MAA) (99.5%, stabilized, Acros Organics) were used as received. The initiator 4,4'-azobis(cyanopentanoic acid) (ACPA, 99%), 1,3,5-trioxane (> 99%), 1,4-dioxane (puriss. p.a., > 99.5%), dimethyl sulfoxide- d_6 (DMSO- d_6 , 99%), diethyl ether (> 99.5%) and petroleum ether were all purchased from Sigma-Aldrich and used with no further purification. Tetrahydrofuran (THF) (HPLC, stabilized/BHT, Sigma-Aldrich) for SEC analysis and THF (VWR Rectapur, stabilized) for methylation were used as received.

II.3.1.2 Methods

Four different hydrophilic living polymers (hereafter referred to as macroRAFTs) were synthesized, poly(acrylic acid) (PAA), poly(acrylic acid-*co*-*n*-butyl acrylate) (P(AA-*co*-BA)), poly(methacrylic acid) (PMAA) and poly(methacrylic acid-*co*-*n*-butyl methacrylate) (P(MAA-*co*-BMA)), all of them containing a trithiocarbonate chain end. In a typical run, 1 mmol of RAFT agent (CTPPA) was introduced in a round-bottom glass flask and 1.97 mmol of trioxane, 23.6 mmol of AA, 23.6 mmol of BA and 0.1 mmol of ACPA were added. The mixture was dissolved in 8 mL of 1,4-dioxane and the flask was purged with nitrogen for 30 minutes and sealed. The glass flask was then heated to 80 °C to start the polymerization. The reaction was conducted for 5h. Samples were taken during polymerization to determine conversion as a function of time and molar mass evolution with conversion. **Table 2** summarizes the polymerization conditions used for macroRAFT agents syntheses.

Table 2. Polymerization recipes for the synthesis of the macroRAFT agents used in this thesis.

Entry	[CTPPA] ₀ (mmol L ⁻¹)	[AA] ₀ (mol L ⁻¹)	[MAA] ₀ (mol L ⁻¹)	[BA] ₀ (mol L ⁻¹)	[BMA] ₀ (mol L ⁻¹)	[ACPA] ₀ (mmol L ⁻¹)
AC19	67	3.00	-	-	-	6.7
AC110	80	-	3.00	-	-	8.0
AC11	127.2	3.00	-	3.00	-	12.7
AC13	145	-	3.00	-	3.00	14.5

1,3,5-trioxane was added as internal reference for NMR analyses.

Before synthesizing each macroRAFT agent, for all four syntheses the kinetics was first followed to determine conversion profiles. Then in a second step, syntheses were performed with no sampling and stopped at the desired conversion (< 100%) to obtain the macroRAFT agent that will be used further in the emulsion polymerization. Polymerization was stopped at c.a. 60% conversion to guarantee high chain end fidelity. All macroRAFT agents were precipitated in a large volume of petroleum ether, solubilized in diethyl ether, and transferred to a smaller flask, where they were dried and stored at 2 – 4 °C.

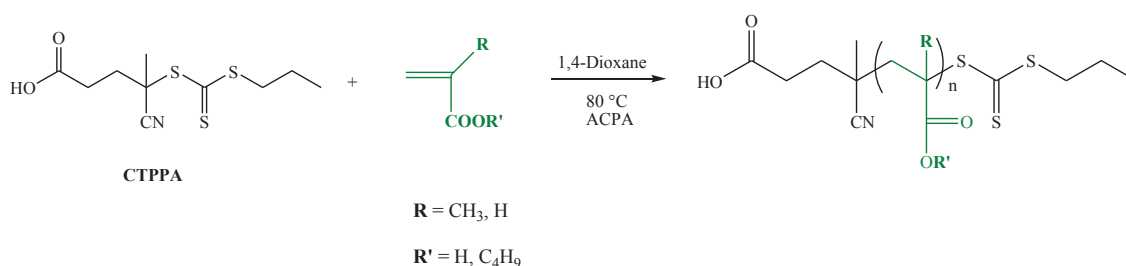


Figure 16. Synthetic route towards poly(acrylic acid), poly(methacrylic acid), poly(acrylic acid-*co-n*-butyl acrylate) and poly(methacrylic acid-*co-n*-butyl methacrylate) macroRAFT agents.

II.3.1.3 Characterizations

All samples taken during polymerizations were characterized by ¹H liquid NMR spectroscopy by diluting the crude reaction medium in DMSO-*d*₆. Monomer conversion was determined by the relative integration of the protons of 1,3,5-trioxane and the vinylic protons of the monomers. To do so, 1,3,5-trioxane was added in a molar ratio of 1/12 related to monomer(s).

Molar masses were determined by Size Exclusion Chromatography in THF (THF-SEC). SEC measurements were carried out at 40 °C with a flow rate of 1 mL min⁻¹ using toluene as a flow rate marker. Before analyses, carboxylic acid groups of the polymers were methylated in a THF/H₂O (90/10 v/v%) mixture using tri(methylsilyl)diazomethane methylation agent¹⁰⁵ to

prevent interactions between acid groups and the stationary phase. Samples were filtered on a 0.45 μm pore size membrane and analyzed at 3 mg mL⁻¹. Separation was carried out on three columns from Malvern Instruments [T6000 M General Mixed Org (300 \times 8 mm)]. The device (Viscotek TDA305) was equipped with a refractive index (RI) detector ($\lambda = 670$ nm). The number-average molar mass (M_n) and dispersity ($D = M_w/M_n$, with M_w : weight-average molar mass) were derived from the RI signal using a calibration curve based on polystyrene or poly(methyl methacrylate) standards (PS and PMMA from Polymer Laboratories). In this work the [RAFT] / [initiator] molar ratio was fixed at 10. Under these conditions, most of the polymer chains carried the R group from the RAFT agent, and the number of chains originating from the initiator could be thus neglected. Hence, the theoretical number-average molar mass and number-average degree of polymerization ($M_{n,th}$ and $DP_{n,th}$, respectively) were determined using the following equations:

$$DP_{n,th} = \frac{X}{100} \times \frac{[M]_0}{[RAFT]_0} \quad \text{Equation II.1}$$

$$M_{n,th} = \frac{X}{100} \times \frac{[M]_0}{[RAFT]_0} \times M_{monomer} + M_{RAFT} \quad \text{Equation II.2}$$

With,

X : Monomer conversion (%)

$[M]_0$: Initial monomer(s) concentration (mol L⁻¹)

$[RAFT]_0$: Initial RAFT agent concentration (mol L⁻¹)

$M_{monomer}$: Monomer molar mass (g mol⁻¹)

M_{RAFT} : RAFT agent molar mass (g mol⁻¹)

For certain experiments, two monomers were copolymerized, and for these cases the $[M]_0$ and $M_{monomer}$ corresponded to the concentration and molar mass of the monomer mixture, respectively.

II.3.2 Results and Discussion

Two families of macroRAFT agents were synthesized: acrylic acid- and methacrylic acid-based (co)polymers. **Table 3** summarizes the results for the four syntheses in terms of final theoretical and experimental number-average molar masses ($M_{n,th}$ and $M_{n,exp}$, respectively), dispersity (D) and final individual conversion of each monomer (X (%)). All four macroRAFT syntheses were followed in terms of kinetics. Especially in the case of copolymers, the individual conversion of each monomer was determined to verify if any composition drift was observed during polymerization. When it comes to the controlled radical copolymerization of a hydrophobic

monomer and a hydrophilic monomer (either BA with AA or BMA with MAA), this parameter is of great importance because it is directly linked to the ability of the resulting copolymer to form micelles. In the present work, the macroRAFT agent adsorbed to the inorganic surface will be chain extended with a hydrophobic monomer to encapsulate the inorganic particles. The presence of micelles could contribute to secondary nucleation, damaging the encapsulation strategy. To avoid micelles, a statistical copolymer must be obtained.

Table 3. Theoretical and experimental molar mass, dispersity and individual monomer conversion for the final (co)polymer macroRAFT agents synthesized in this thesis.

Entry	macroRAFT	$M_{n,theo}$ (g mol ⁻¹)	$M_{n,exp}$ (g mol ⁻¹) ^a	\mathcal{D}	X_{AA}/X_{BA} (%)	X_{MAA}/X_{BMA} (%)
AC19	PAA-CTPPA	3400	3900	1.19	95/-	-
AC110	PMAA-CTPPA	3200	3900	1.19	-	90/-
AC11	P(AA-co-BA)-CTPPA	4900	5300	1.10	97/97	-
AC13	P(MAA-co-BMA)-CTPPA	4400	4800	1.11	-	86/89

^a M_n values have been recalculated to designate the non-methylated mass of the polymer

Figure 17A shows the complete consumption of AA after approximately 5h of reaction. It also shows a linear increase of number-average molar masses with conversion (**Figure 17B**) and the complete shift of the SEC chromatograms towards high molar masses (**Figure 17C**), indicating a good control of the AA homopolymerization. The experimental molar masses obtained were in good agreement with the theoretical molar masses predicted. Narrowly distributed molar masses ($\mathcal{D} \sim 1.2$) were also obtained.

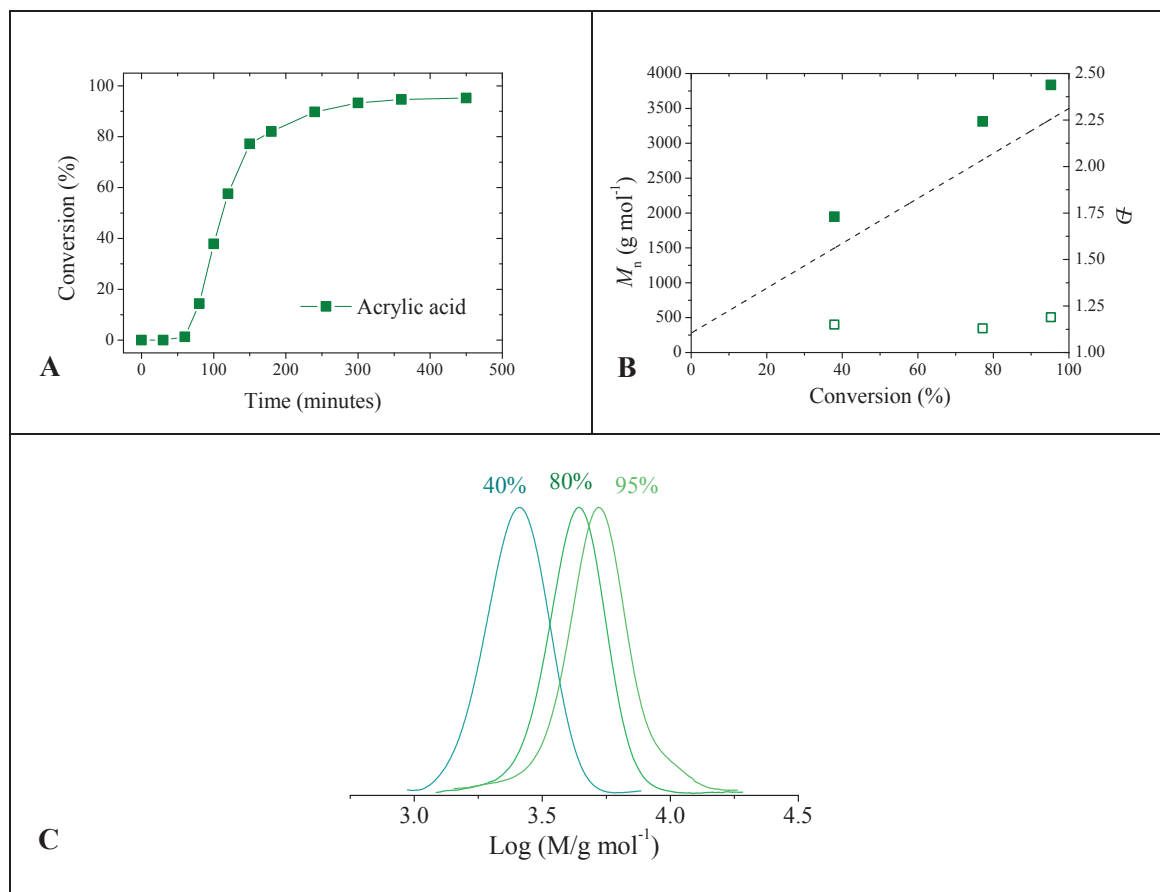


Figure 17. RAFT polymerization of AA in 1,4-dioxane. Evolution of (A) monomer conversion versus time, (B) M_n (■) and $D = M_w/M_n$ (□) versus conversion. The dashed line corresponds to theoretical evolution of M_n with conversion. (C) THF-SEC chromatogram evolution (log M) with conversion.

During the copolymerization of AA and BA, both monomers were converted at the same rate (Figure 18A), proving that no composition drift took place. Figure 18C also shows fairly symmetrical chromatograms that are shifted towards higher molar masses with conversion. Experimental molar masses corresponded very well to the theoretical values (Figure 18B). Low dispersity of around 1.1 was again obtained.

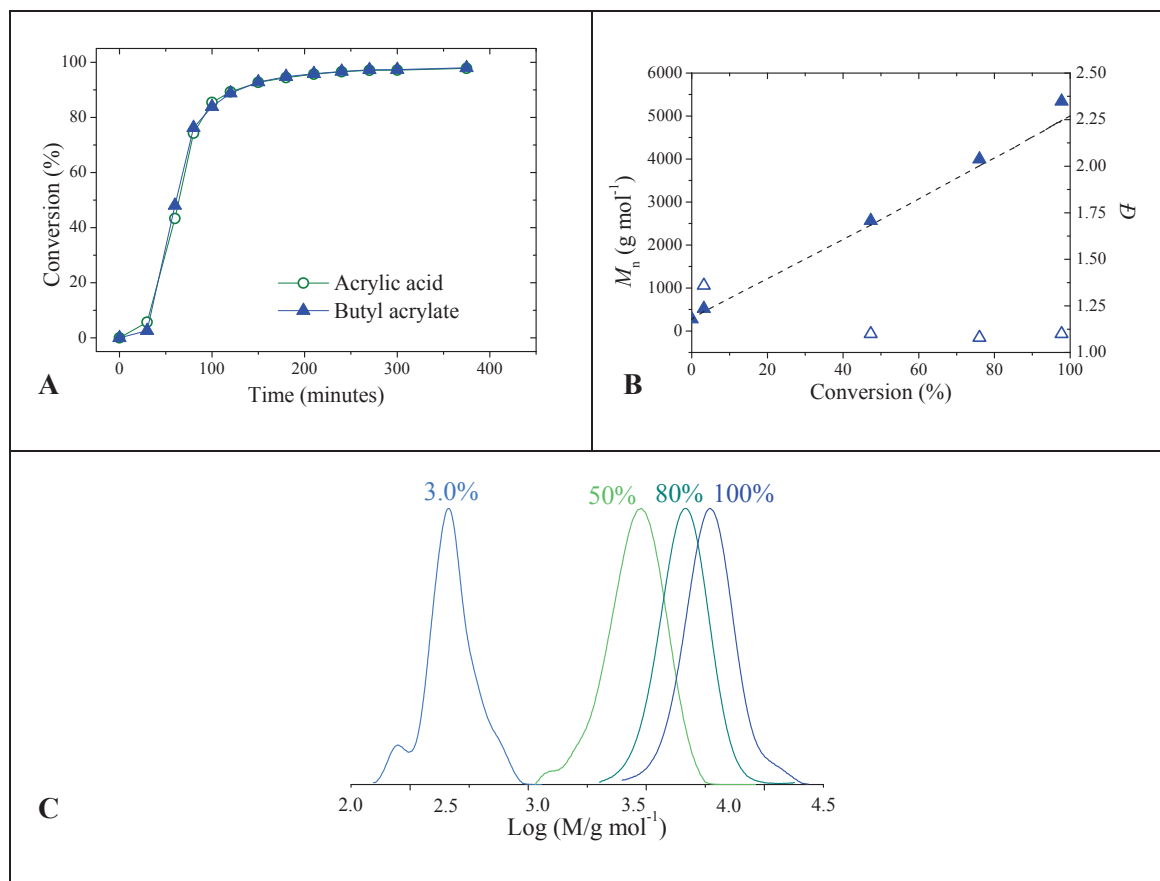


Figure 18. RAFT copolymerization of AA and BA in 1,4-dioxane. Evolution of (A) monomer conversion of AA (\circ) and BA (\blacktriangle) versus time, (B) M_n (\blacktriangle) and $D = M_w/M_n$ (\triangle) versus conversion. The dashed line corresponds to theoretical evolution of M_n with conversion. (C) THF-SEC chromatogram evolution (log M) with conversion.

The synthesis of methacrylic acid-based macroRAFT agents also generated well-defined (co)polymers. **Figure 19** presents a slightly lower polymerization rate for the polymerization of MAA than the one observed for acrylic acid-based copolymers, but 90% conversion was achieved and a linear increase of molar mass with conversion was obtained, accompanied by a nice shift of chromatograms towards high molar masses. However, final number-average molar masses were higher than the theoretical values. This trend is typical when the RAFT agent presents a poor chain transfer constant for the monomer being polymerized.

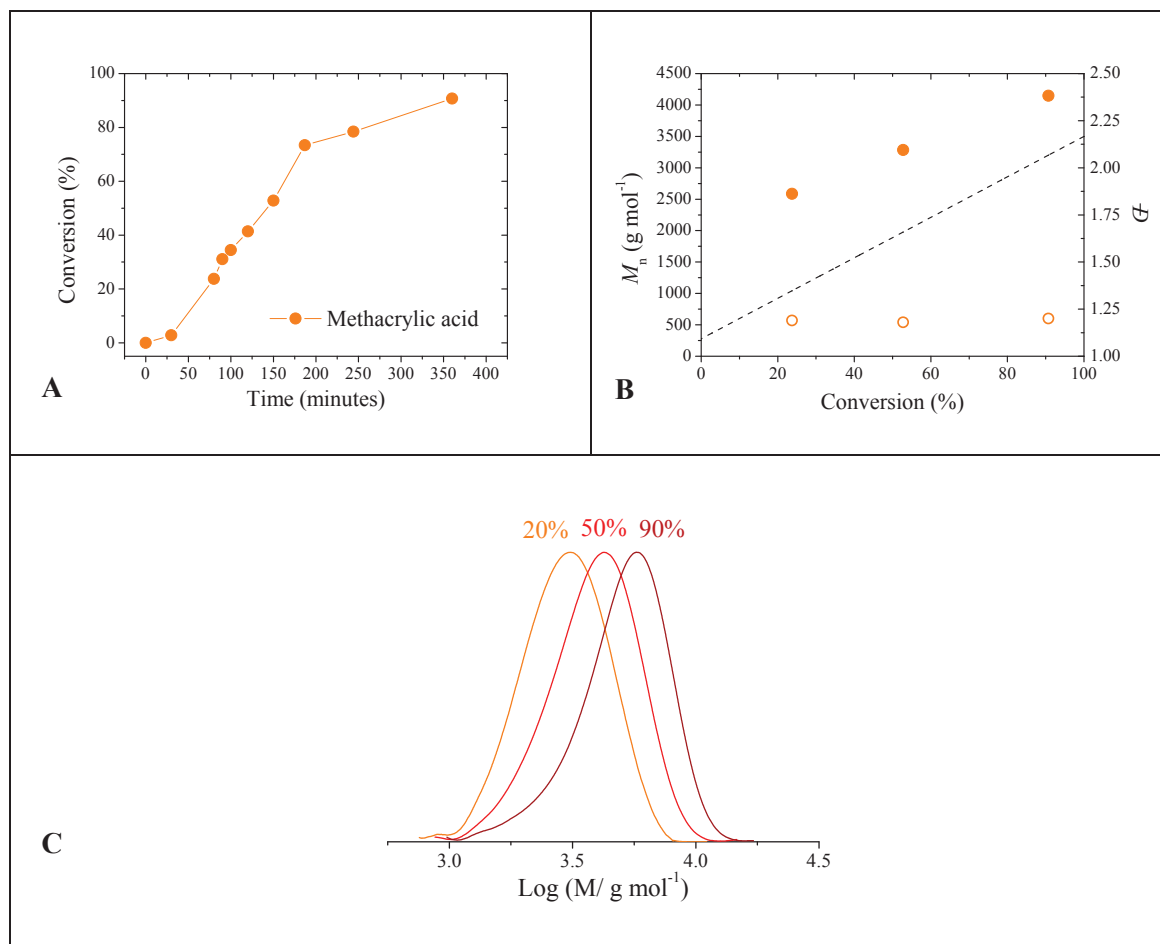


Figure 19. RAFT polymerization of MAA in 1,4-dioxane. Evolution of (A) monomer conversion versus time, (B) M_n (●) and $D = M_w/M_n$ (○) versus conversion. The dashed line corresponds to theoretical evolution of M_n with conversion. (C) THF-SEC chromatogram evolution ($\log M$) with conversion.

Methacrylic acid-based copolymer synthesis showed similar results. During the copolymerization of MAA and BMA both monomers were consumed at the same rate, confirming that no composition drift took place. **Figure 20** shows the linear evolution of molar mass with conversion and the complete shift of SEC traces towards high molar masses, again indicating a good control of the polymerization. Low molar mass dispersity of around 1.11 was obtained. Different from the homopolymerization of MAA, the copolymerization generated experimental molar masses close to the theoretical values. However, the careful observation of these results revealed the same behavior observed for PMAA: molar masses were higher than expected for low conversions, but this effect was less pronounced.

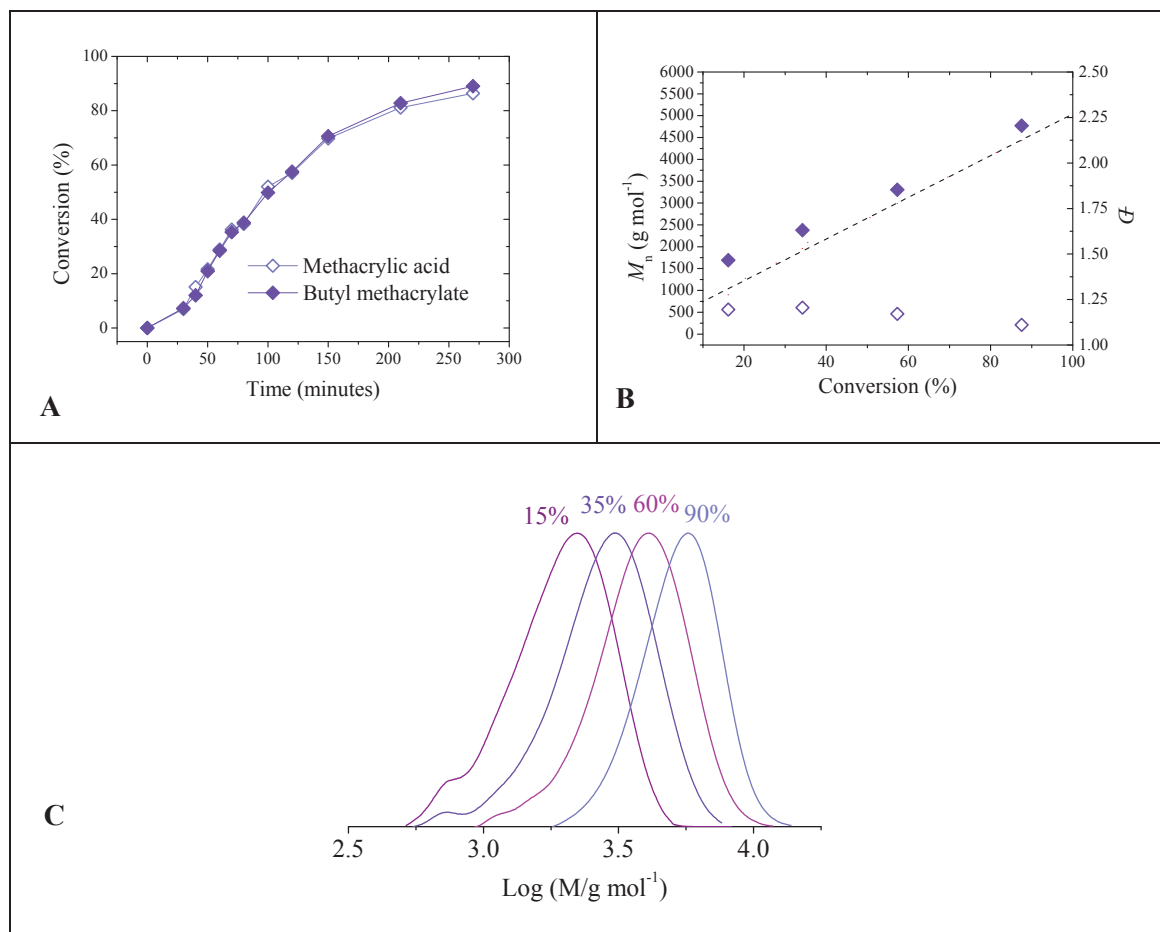


Figure 20. RAFT copolymerization of MAA and BMA in 1,4-dioxane. Evolution of (A) monomer conversion of MAA (\diamond) and BMA (\blacklozenge) versus time, (B) M_n (\blacklozenge) and $D = M_w/M_n$ (\diamond) versus conversion. The dashed line corresponds to theoretical evolution of M_n with conversion. (C) THF-SEC chromatogram evolution ($\log M$) with conversion.

Experimental molar masses were clearly closer to the theoretical values when copolymerizations were performed, which was observed for both acrylic acid- and methacrylic acid-based copolymers. Nevertheless, well-controlled statistical copolymers were formed in all cases.

II.3.3 Conclusions

Acrylic acid- and methacrylic acid-based macroRAFT agents were synthesized by RAFT polymerization in 1,4-dioxane solution using a trithiocarbonate RAFT agent. All syntheses were successfully controlled, since linear evolution of molar masses and narrow molar mass distributions were obtained.

Table 4 presents the macroRAFT agents further used to polymerize different monomers in emulsion. Some preliminary results will be presented in the next section.

Table 4. Results of the syntheses of the macroRAFT agents further employed to polymerize MMA/BA or Sty in emulsion polymerization.

macroRAFT	DP_n	M_n (g mol ⁻¹) ^a	\bar{D}
PAA-CTPPA	49	3 800	1.18
PMAA-CTPPA	41	3 800	1.19
P(AA-co-BA)-CTPPA	17/17	3 700	1.13
P(MAA-co-BMA)-CTPPA	11/11	2 700	1.15

^a M_n values have been recalculated to designate the non-methylated mass of the polymer

After synthesizing the different macroRAFTs, the next step was the study of the Imogolite nanotubes physicochemical properties. The next section will present the different Ge-Imogolite used and the most important characteristics of each batch.

II.4 Imogolite nanotubes

As reviewed in the bibliographic part, Imogolite nanotubes, aluminogermanate minerals of tubular crystalline structure, are positively charged on their outer surface and negatively charged on the inner surface. The outer surface charge depends on the pH, and it originates from the Al-OH-Al group protonation. The inner negative charge results from Ge-OH partial dissociation. The protonation and dissociation equilibriums can be expressed as follows:

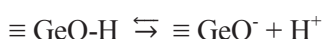
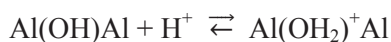


Figure 21 shows the schematic representation of single (SW) and double-walled (DW) Imogolite tubular structures with their typical dimensions.

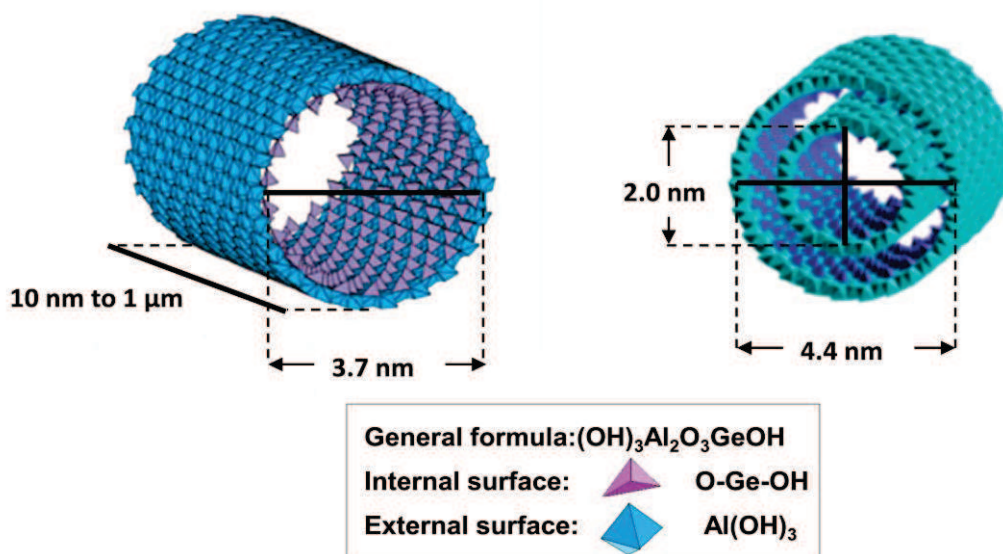


Figure 21. Schematic representation of structure, composition and dimensions of SW and DW Imogolite nanotubes.

Both SW and DW nanotubes were employed for the different studies carried out during this thesis.

Table 5 presents the dimensions (i.e. the external diameter (\varnothing_{ext}) and the average length (L)), concentrations, pH and type of the different batches of Ge-Imogolite provided by the group of

Dr. Antoine Thill (CEA, Saclay). These Imogolite nanotubes were synthesized as described elsewhere.⁵⁹

Table 5. General characteristics of Ge-Imogolite batches used in this thesis

Batch	\O_{ext}^a	Average length L (nm)	[Imogolite] (g L ⁻¹)	pH	Type
C1p55	3.7	75 ^a	23	6	SW
MA1p40	2	35 ^{b,c}	9.6	6.1	SW
C13p105	4.2	200 ^c	9.2	6.0	DW
EP1p37	4.4	500 ^c	6.5	5.9	DW

^a Average value measured by statistical counting from TEM images. ^b High concentration of proto-Imogolite. ^c Determined by SAXS.

It is noteworthy that the L values represent the average length calculated from the SAXS results. Actually, Imogolite nanotubes are highly polydisperse. The short tubes (C1p55 and MA1p40) may contain nanotubes between 10nm and 200 nm length, and the long tubes (C13p105 and EP1p37) may contain nanotubes between 20 nm and 1 μm length.

Figure 22 shows the scattering diagram of SW Ge-Imogolite nanotubes of average length 75 and 35 nm (batches C1p55 and MA1p40, respectively). The small distances corresponding to the tubes diameter are presented on the large scattering vector distances. The regular oscillations in this region, which are characteristic of SW tubes, can be observed for both batches between 0.1 and 1.0 \AA^{-1} .⁶¹ For an average length of 35 nm (MA1p40), the main peak in this region is smoother, indicating the presence of a high concentration of proto-Imogolite. At low scattering vectors, where long distances are represented, the inter-tube interaction can be evaluated. The presence of a slight signal in both curves at around 0.015 \AA^{-1} is attributed to tube-tube repulsions, resulting from the positive surface charges.

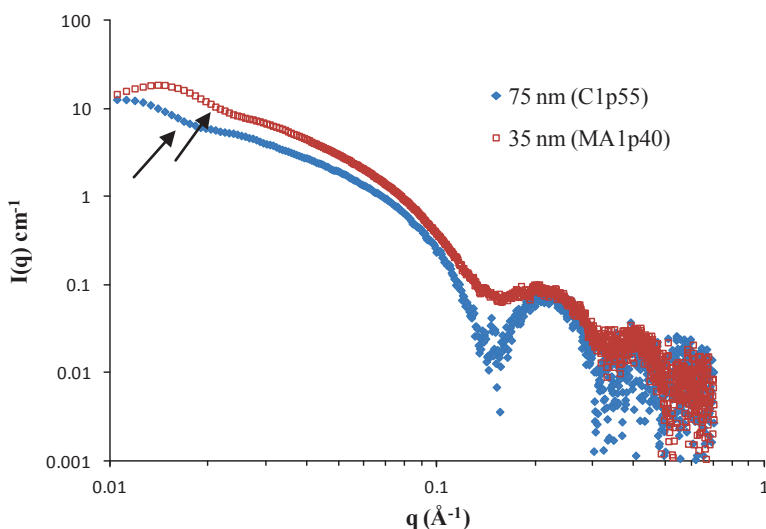


Figure 22. Scattering diagram of intensity $I(q) \text{ cm}^{-1}$ versus $q (\text{Å}^{-1})$ obtained through SAXS analysis of the SW Ge-Imogolite suspensions of batches C1p55 (\blacklozenge) ($L = 75 \text{ nm}$), and MA1p40 (\square) ($L = 35 \text{ nm}$) (see **Table 5** for details).

Figure 23 presents the SAXS scattering diagrams for the DW Ge-Imogolite batches of average lengths of 200 and 500 nm (batches C13p105 and EP1p37, respectively). In the region of large angle intensities, from 0.1 to 1.0 Å^{-1} , irregular oscillations characteristic of DW tubes can be observed. In the region of low scattering vectors, the signal corresponding to the tube-tube electrostatic repulsion is also visible.

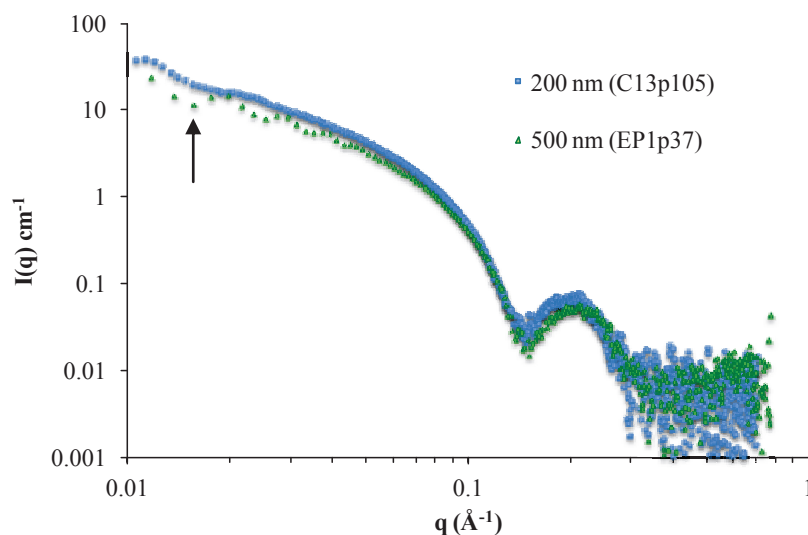


Figure 23. Scattering diagram of intensity $I(q) \text{ cm}^{-1}$ versus $q (\text{Å}^{-1})$ obtained through SAXS analysis of the DW Ge-Imogolite suspensions of batches C13p105 (\blacksquare) ($L = 200 \text{ nm}$), and EP1p37 (\blacktriangle) ($L = 500 \text{ nm}$) (see **Table 5** for details).

The isoelectric point (IEP) of the nanotubes was determined by zeta potential analyses (ZP), (**Figure 24**). This measurement was carried out on sample C1p55 (SW, L = 75 nm), and since all batches have the same surface chemistry, it was assumed that they would all have the same IEP. The inversion of surface charges was found at a pH of 9.0.

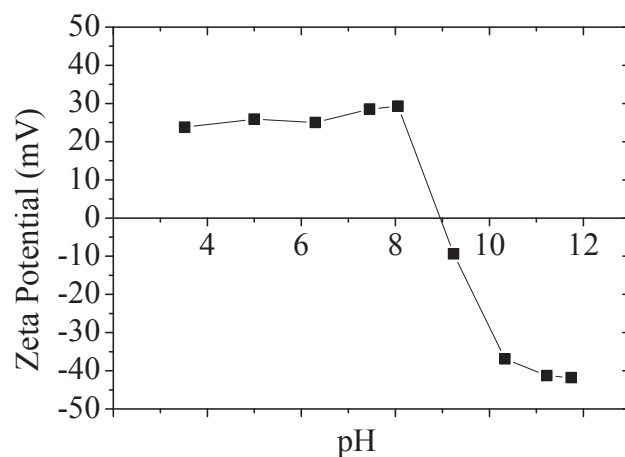


Figure 24. Zeta potential values versus pH of a diluted Imogolite suspension prepared using batch C1p55 (SW, L = 75 nm) of Imogolite.

For the preliminary studies, the Imogolite batch used was C1p55, corresponding to SW nanotubes of average length 75 nm. The next section presents the first encapsulation experiments carried out with the four macroRAFT agents previously synthesized. This study aimed to evaluate the efficiency of the four macroRAFTs and determine which one would be the most appropriate.

II.5 Preliminary Imogolite encapsulating experiments

The macroRAFT agents synthesized in section II.3 were employed in the macroRAFT-assisted encapsulating emulsion polymerization of Ge-Imogolite nanotubes (C1p55, $L = 75$ nm) in an attempt to evaluate their efficiency on encapsulating the tubes and stabilizing the system. These preliminary studies were carried out using a 80/20 (wt/wt) mixture of MMA and BA as hydrophobic monomers.

II.5.1 Experimental section

II.5.1.1 Materials

The macroRAFT agents: PAA₄₉-CTPPA, PMAA₄₁-CTPPA, P(AA₁₇-*co*-BuA₁₇)-CTPPA and P(MAA₁₁-*co*-BuMA₁₁)-CTPPA, were synthesized as described above (**Table 4**) and used after precipitation and drying under reduced pressure. 4,4'-azobis (cyanopentanoic acid) (ACPA, 99%, Sigma-Aldrich), methyl methacrylate (MMA, 99.5%, stabilized, Acros Organics) and *n*-butyl acrylate (BA, 99%, stabilized, Acros Organics) were used as received. The pH value of the macroRAFT solutions was adjusted using sodium hydroxide (NaOH, 1N, Sigma-Aldrich). Sodium hydrogen carbonate (NaHCO₃, 99%, Sigma-Aldrich) was used as received. Water was deionized before use (Purelab Classic UV, ElgaLab Water).

II.5.1.2 Methods

Emulsion polymerization reactions were conducted in semi-batch. In a typical run, the required amount of macroRAFT agent (2.6 or 3.7 mM) was put in 14 mL of deionized water. The calculated quantity of 1N NaOH solution (i.e. to achieve pH 8.0 or 6.0) was added, and the mixture was put in an ultrasound bath for a few minutes to help the dissolution of the polymer. The resulting solution was added to the Imogolite suspension and the mixture was left stirring for 60 minutes in a round-bottom glass flask. The system was purged with nitrogen flow for 30 minutes. The monomer mixture (MMA/BA, 80/20 wt/wt) was equally purged in a separate flask. Around 0.1 mL of monomer was introduced in the reaction before starting polymerization, and the rest of the monomer was fed at the rate of 0.03 g mL⁻¹ h⁻¹ during the reaction. The mixture was heated to 80 °C and the initiator solution previously degassed was introduced to start the polymerization. The monomer addition lasted 4 h. The polymerization was left reacting for 3 additional hours. Samples were taken at different times during the reaction to perform the kinetics studies.

II.5.1.3 Characterizations

The hydrodynamic average particle diameter (D_h) was determined by Dynamic Light Scattering (DLS) in a Nano Zetasizer Malvern instrument. The DLS technique is mainly adapted to spherical objects. Since our samples contained non-spherical particles, the results obtained were only considered as indicatives of particle size. Monomer conversion was determined by gravimetric analysis. For semi-batch, monomer conversion calculations took into account the amount of monomer added/taken at a time t . After drying and subsequent methylation of the COOH groups, M_n and \bar{D} were determined by size exclusion chromatography (SEC) analysis in THF solution, using the methodology described in section II.3.1.3. For SEC analysis, prior to methylation and injection, the polymer was extracted from the dried hybrid latex by soxhlet extraction in a cellulose cartridge using THF reflux at 90 °C for 5h. Particles morphology was determined by transmission electron microscopy (TEM). For TEM analysis, the diluted latex samples were dropped on a carbon/formvar-coated copper grid and dried under air. TEM images were examined at an accelerating voltage of 80 kV with a Philips CM120 transmission electron microscope (Centre Technologique des Microstructures (CT μ), platform of the Université Claude Bernard Lyon 1, Villeurbanne, France). Observations were made either at room temperature or under cryogenic conditions (cryo-TEM).

II.5.2 Results and Discussion

II.5.2.1 Effect of macroRAFT nature

In these preliminary studies, the influence of the macroRAFT nature on particles morphology and latex stability was investigated. The four macroRAFT agents evaluated had different solubilities in water. Their solubility can be rated in descending order as follows: PAA-CTPPA > PMAA-CTPPA > P(AA-co-BA)-CTPPA > P(MAA-co-BMA)-CTPPA.

For each macroRAFT, a reference polymerization in the absence of Imogolite was performed, to understand the behavior of these macromolecules in the aqueous phase during polymerization. Polymerization conditions and results for both series of experiments, with and without Imogolite, are shown in **Table 6**.

All polymerizations were conducted at pH = 8.0, which is alkaline enough to consider that near 100% of the acid units of all four macroRAFT agents were deprotonated and, consequently, negatively charged. Under these conditions we expect the NTs to remain individually dispersed in water and the macroRAFT to provide a good stability to the system.

The macroRAFT agents were not expected to form micelles, since the homopolymers were soluble in water and the copolymers were statistical. However, the copolymers could adopt a

coil conformation in the aqueous phase due to the presence of hydrophobic units of BA or BMA.

Table 6. Conditions and results of the emulsion polymerizations carried out with Imogolite suspensions modified with different macroRAFT agents

Entry	MacroRAFT	[macroRAFT] (mmol L ⁻¹)	X _{final} (%)	D _h /PDI	Stability
AC20m	PAA-CTPPA	2.6	40	205/0.02	√
AC20b	P(AA-co-BA)-CTPPA	2.5	95	58/0.03	√
AC20n	PMAA-CTPPA	2.9	76	41/0.07	√
AC20e	P(MAA-co-BMA)-CTPPA	2.5	91	67/0.165	√
AC212	PAA-CTPPA	1.2 ^a	12	123/0.012	√
AC21	P(AA-co-BA)-CTPPA	2.8	70	270/0.73	√
AC210	PMAA-CTPPA	2.7	40	-	X
AC22	P(MAA-co-BMA)-CTPPA	2.3	92	105/0.069	√

pH = 8.0. Pathway: MacroRAFT solution added dropwise to the Imogolite suspension. Monomers: 15 wt% of MMA/BA (80/20 wt/wt) based on water. [Imogolite] = 2.2 g L⁻¹. ^a [Imogolite] = 0.4 g L⁻¹.

Figure 25 presents kinetic results for the emulsion polymerization of MMA/BA using different macroRAFT agents in the presence or in the absence of Imogolite. In the absence of Imogolite (**Figure 25A**), it can be seen that an induction time was observed for all polymerizations, which was attributed to the time necessary for the amphiphilic block copolymers to self-assemble and form the first particles. Indeed, at the very beginning of the polymerization, the hydrophobic monomer present in the aqueous phase is inserted to the hydrophilic macroRAFT chains. After the addition of a certain number of monomer units, the block copolymer chains lose their solubility in water, and self-assemble to form self-stabilized particles. Polymerization continues inside these particles, and the polymerization rate undergoes a sudden increase. The induction time was shorter for the copolymer macroRAFT agents. Being more hydrophobic, due to the presence of BA or BMA units, the copolymer macroRAFT agents lose their solubility in water sooner, leading to a faster nucleation.

Slightly higher polymerization rates were obtained when the methacrylic acid-based macroRAFT was used. This can be explained by the addition of a radical to the macroRAFT and the fragmentation of the intermediate radical, whose efficiency depends on the chemical nature of the groups on each side of the radical. When an acrylic acid-based macroRAFT is used to polymerize the methacrylate-rich monomer mixture, the addition-fragmentation equilibrium is not favored, because fragmentation is preferential on the “methacrylate side”. This effect retards the establishment of the equilibrium. When using methacrylic acid-based macroRAFT, the equilibrium is rapidly and efficiently established. This effect was mostly overcome in the

case of the copolymer macroRAFTs. In these cases, the high local concentration of monomers, resulted from the early self-assembly of the block copolymer chains, accelerated the process, favoring the establishment of the equilibrium.

Regarding the control of polymerization, final molar masses of the latexes produced in the absence of Imogolite were measured by SEC. Experimental molar masses were higher than the theoretical values expected, and relatively broad molar mass distributions ($D \sim 2.0$) were obtained (see **Annex A.1**). From these results, the following polymerizations performed in the presence of Imogolite were not expected to present a good control. Nevertheless, as seen in chapter I, the control of polymerization is not crucial for the success of the encapsulation. The RAFT technique is used for its ability to reactivate the polymerization at the surface of the inorganic particles.

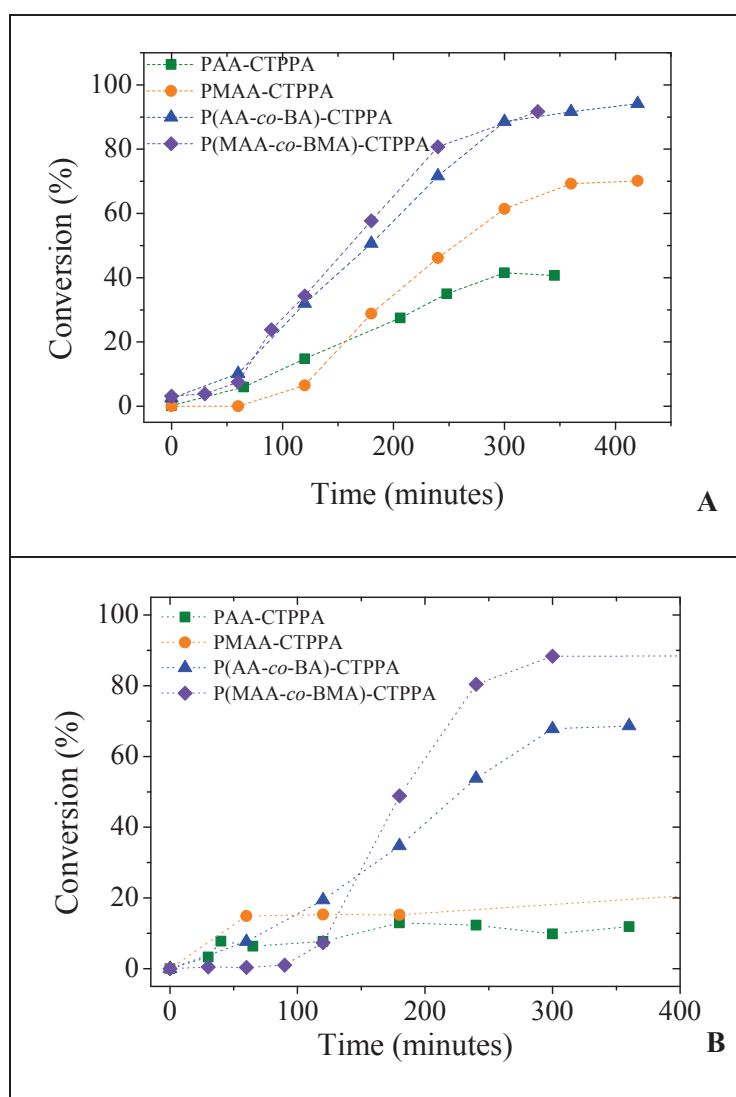


Figure 25. Evolution of MMA/BA (80/20 wt/wt) conversion versus time for RAFT emulsion polymerizations carried out at pH 8.0 (A) without Imogolite and (B) using 0.4 or 2.2 g L⁻¹ of Imogolite and different macroRAFT: PAA-CTPPA (■), PMAA-CTPPA (●), P(AA-co-BA)-CTPPA (▲) and P(MAA-co-BMA)-CTPPA (◆).

Figure 25B shows the evolution of monomer conversion with time for the polymerization of MMA/BA (80/20 wt/wt) at pH 8.0 in the presence of Imogolite modified with the same macroRAFT agents. As observed in the previous experiments, an induction time was observed for all polymerizations; higher conversion were obtained for the methacrylic acid-based macroRAFTs; and this effect was attenuated by the addition of hydrophobic monomers to the macroRAFT chain, which contributes to the increase of the local amount of monomer. These observations strongly suggested that the polymerization starts in the aqueous phase, following the polymerization-induced self-assembly (PISA) nucleation, as it was observed for the experiments performed in the absence of Imogolite. However, the presence of the tubes results in some differences in kinetics, probably resulting from the partitioning of the macroRAFT between the surface and the aqueous phase. A study of the interaction between the macroRAFT and the surface of Imogolite will be further presented.

Comparing the results from **Figure 25A** and B, it seems that the overall conversion was affected by the presence of Imogolite. The final conversion was highly limited when homopolymer macroRAFT agents were used, while the use of copolymers yielded conversions $> 70\%$. This could be an effect of radical trapping by the nanotubes, in which the primary radicals could migrate to the interior of the tubes by diffusion, if they were small enough to have access to these micropores.⁷² However, the inner diameter of SW Imogolite is between 1 and 2 nm, while the primary radical molecule is about 1.0 nm in length and 0.4 nm widthⁱ. Thus, it is very unlikely that these radicals enter the tubes cavity. Another explanation could lay on the radical flux during polymerization. Some experiments will be further presented in which the conversion limitation was specifically studied.

Particles morphology was investigated by TEM analyses. Hybrid latexes made using homopolymer macroRAFT agents were analyzed at room-temperature microscopy (**Figure 26 A** and B) and copolymer-based ones, under cryogenic conditions (**Figure 26C** and D). Stable latexes were obtained with the acrylic acid-based macroRAFTs, while the methacrylic acid-based ones led to the formation of instable latexes. Even though the polymer particles are not as well defined as under cryo-TEM, it can be seen on **Figure 26 (A)** and (B) that many isolated nanotubes are visible, suggesting poor affinity of the growing polymer chains for the Imogolite surface. The presence of latex particles can be ascribed to the presence of free macroRAFT in the aqueous phase. Indeed, these chains were probably reactivated during the copolymerization of MMA/BA to generate amphiphilic block copolymers able to self-assemble through a PISA mechanism, or more likely to stabilize nuclei formed by homogeneous nucleation. The

ⁱ The primary radical dimensions were calculated taking into account the atom-atom bond distances of C—C = 154 pm, C—N = 147 pm, C—O = 143 pm and O—H = 96 pm, and considering a linear conformation of the molecule.

proximity of some tubes to the particles surface may be due, to a certain extent, to the polymerization occurring on the surface of Imogolite, rendering the tubes hydrophobic enough to act as Pickering stabilizers. The polymerization started in the aqueous phase, but was not effectively transferred to the surface of nanotubes, due to a poor affinity of the monomer mixture for the PAA or PMAA-modified Imogolite. The presence of free NTs together with some stability issues led us to discard these homopolymer macroRAFTs.

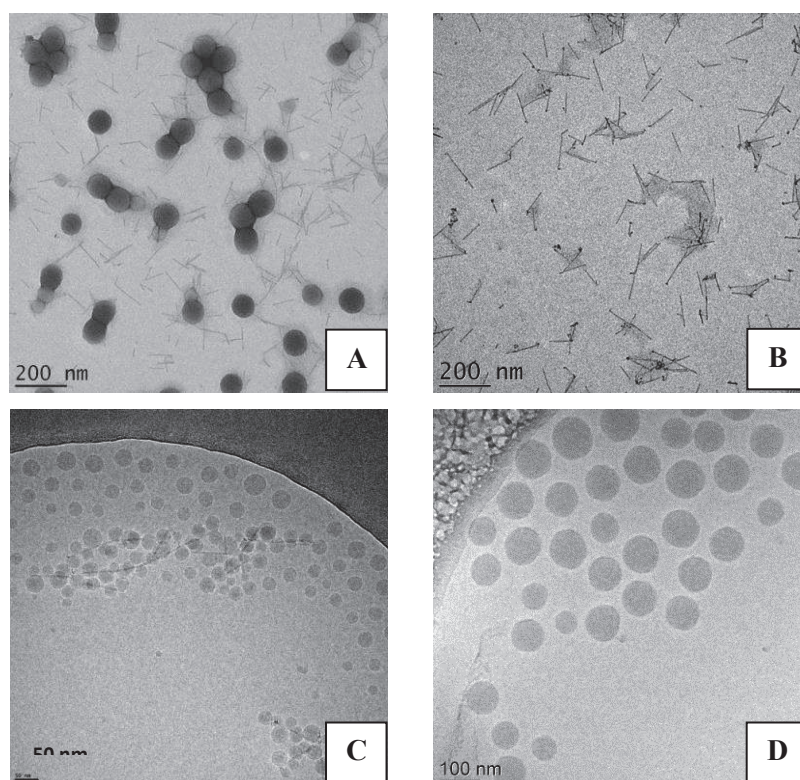


Figure 26. Conventional (A, B) and cryo (C, D) TEM images of hybrid latexes of Imogolite/P(MMA-co-BA) using (A) PAA-CTPPA; (B) PMAA-CTPPA; (C) P(AA-co-BA)-CTPPA and (D) P(MAA-co-BMA)-CTPPA.

In contrast, **Figure 26C** presents polymer-decorated Imogolite nanotubes and free polymer particles, but no free nanotubes. The polymer particles decorating the Imogolite seem to be “bound” to the surface. As those were characterized by cryo-TEM, drying artifacts can be discarded. Since, as it will be demonstrated later, the adsorption is much higher using copolymers, it was considered that all nanotubes have at least some portion of polymer on the surface initially, which contributes to the formation of polymer/Imogolite particles. Good colloidal stability was obtained for this latex synthesized with P(AA-co-BA)-CTPPA macroRAFT.

Figure 26D presents the morphology of the latex obtained with P(MAA-*co*-BMA)-CTPPA macroRAFT. When using this copolymer, some solids (around 8 wt%) could be observed after a few minutes of reaction in the bottom of the flask. Being the most hydrophobic of the four macroRAFT agents, this copolymer had a weaker stabilization ability, which could induce the aggregation and precipitation of the tubes. At the end of polymerization only polymer particles, originating from macroRAFT in solution would remain in suspension. Indeed, only free polymer particles are observed in **Figure 26D**.

Further studies were undertaken using P(AA-*co*-BA)-CTPPA macroRAFT agent to avoid stability problems and to provide a good interaction between macroRAFT and Imogolite.

To better understand the interaction between this macroRAFT and the surface, some adsorption studies were carried out, and the results are presented in the next section. The adsorption of the PAA-CTPPA macroRAFT was also investigated, in order to evaluate the effect of BA units in the macroRAFT chain.

II.6 Acrylic acid-based macroRAFT/Imogolite interactions

To achieve encapsulation, a link between the inorganic particles and the polymer must exist. As shown by Hawke *et al.*^{22, 24}, a clever way to establish this link is using macroRAFT agents as coupling agent and stabilizer. Thus, the interaction between the living chains and the nanoparticles has to be strong enough to provide this link.

Many works describe the adsorption of polymers, especially polyelectrolytes, on inorganic nanoparticles, notably silica^{106, 107}, clays^{108, 109} and metal oxides¹¹⁰⁻¹¹⁸. The main interaction described in these works is electrostatic interaction between opposite charges from the polymer and the inorganic particles. Hydrogen bonding is another type of interaction often described when working with PAA at low pH in particular¹¹⁰. In some cases, depending on the surface chemistry of the inorganic nanoparticles, metal-oxygen complexation may take place depending on the pH of the medium, forming strong organic-inorganic bonding.

This section will focus on the study of the interaction between the macroRAFT agents synthesized in section II.3 and the Imogolite nanotubes presented in section II.4. The interaction is expected to take place via the carboxylic acid groups of AA, which being deprotonated carry negative charges that can interact with positive charges from Imogolite surface through electrostatic attractive forces. The P(AA-*co*-BA)-CTPPA copolymer macroRAFT has its solubility limited to a pH > 6.0 – mainly due to the presence of very hydrophobic BA units – which made us work at neutral to basic pH. Because of that, we discarded hydrogen bonding in our case. We also expect that the presence of BA units contributes to the increase in adsorption through hydrophobic interactions (**Figure 27**).

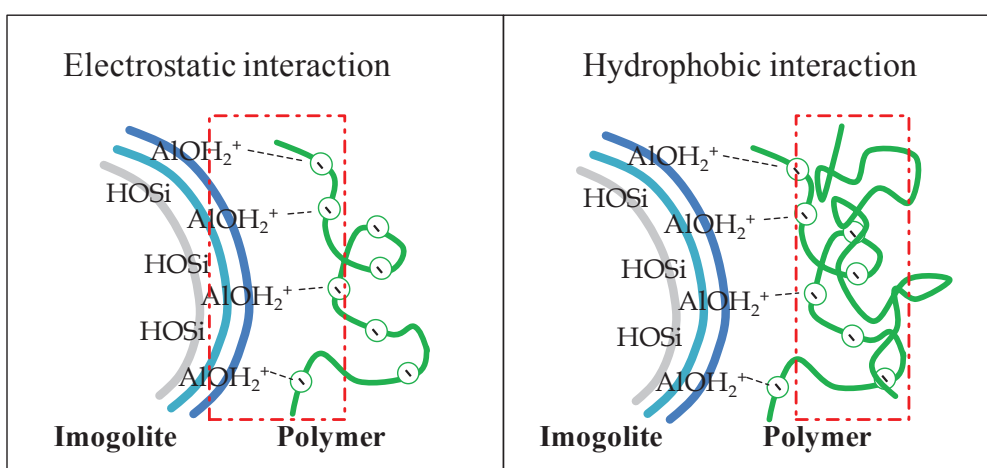


Figure 27. Illustration of the two main driving forces of interaction for the adsorption of macroRAFT copolymers to the Imogolite surface.

The interaction of PAA-CTPPA and P(AA-co-BA)-CTPPA macroRAFT agents with Imogolite nanotubes surface was studied and is presented in this section. The effect of different parameters was investigated, such as the chemical composition of the macroRAFT, the macroRAFT molar mass, the pH of the medium and the ionic strength.

II.6.1 Experimental section

II.6.1.1 Materials

The PAA-CTPPA and P(AA-co-BA)-CTPPA macroRAFT agents were synthesized as described above and used after precipitation and drying. Imogolite nanotubes were synthesized as described elsewhere⁵⁹ and dialyzed against pure water before use. The batch entry, the external diameter (\varnothing_{ext}), the average length (L), the concentration and the pH of the nanotubes used in this study are presented in **Table 7**. Sodium hydroxide (NaOH 1N, standard, Acros Organics) was used as received. Deionized water was used for all experiments.

Table 7. Main characteristics of the Imogolite nanotubes used in this study

Entry/Lot	\varnothing_{ext} (nm)	Average L ^a (nm)	[Imogolite] (g L ⁻¹)	pH	Structure
C1p55	3.7	75	23	6.0	SW

^a Average value measured by statistical counting from TEM images

II.6.1.2 Methods

In a typical run, the required amount of macroRAFT was introduced in water and the pH was adjusted using 1N NaOH solution. The mixture was submitted to an ultrasound bath for a few minutes, to facilitate macroRAFT dissolution. Once the macroRAFT was dissolved, the solution was added drop wise to the Imogolite suspension and the mixture was left under stirring for 120 minutes. Experimental conditions are detailed in **Table 8**. The mixture was then centrifuged at 50,000 rpm for 60 minutes. The supernatant was recovered and the amount of free macroRAFT was quantitatively measured by UV-visible analysis, in a Shimadzu UV-visible spectrometer. A calibration curve was previously built at $\lambda = 310$ nm to determine the free macroRAFT concentration. The adsorbed macroRAFT amount was calculated by subtraction of the free amount from the initial concentration.

Table 8. Summary of experimental conditions used for macroRAFT adsorption experiments

Entry	MacroRAFT	M_n (g mol ⁻¹)	[macroRAFT] (mmol L ⁻¹)	[Imogolite] (g L ⁻¹)	pH
1	PAA-CTPPA	3 500	6, 10, 15 and 20	2.0	8.0
2	P(AA _{16-co} -BA ₁₆)-CTPPA	3 500	4, 6, 10, 15 and 20	2.0	8.0
3	P(AA _{7-co} -BA ₇)-CTPPA	1 700	10, 15 and 20	2.0	8.0
4	P(AA _{16-co} -BA ₁₆)-CTPPA	3 500	2, 4, 6, 15 and 20	2.0	6.0

II.6.1.3 Characterizations

The hydrodynamic average particle diameter (D_h) was determined by DLS, as described in section II.5.1.3. For TEM analysis, sample preparation and imaging followed the procedure described in section II.5.1.3. Some images were obtained by high resolution cryo electron microscopy in a Tecnai G² Polara - 300kV FEG microscope under cryo conditions (-191 °C) (Institut de Biologie Structurale (IBS), Grenoble). SAXS measurements were carried out using a setup containing a rotating anode and a collimating optics providing a monochromatic beam of $\lambda = 0.1548$ nm of 2×2 mm² at the sample position. The total flux was 8×10^7 photon s⁻¹. The transmitted flux was continuously measured by a photodiode placed on the beam stop. The scattering vector q is defined as $q = k_d - k_i$, and has a modulus of $q = 4\pi/\lambda \sin(\theta)$, where λ is the incident wavelength and 2θ is the scattering angle. Samples were introduced in kapton cells. The supernatant was separated by centrifugation using a Beckman Coulter Optima – MAX TL Ultracentrifuge equipped with a TLA-110 rotor operating at 50 000 rpm.

II.6.2 Results and Discussion

The interaction between the P(AA-co-BA)-CTPPA macroRAFT agent and Imogolite surface was studied, and the results are presented in this section. The adsorption of this copolymer onto the surface of Imogolite was compared to that of PAA-CTPPA, to evaluate the effect of BA units. The effect of molar mass of the copolymer and of the pH of the medium was also investigated. To be sure that the RAFT functionality would resist the interaction conditions, especially the relatively high pH of 8.0, a stability study was first carried out. The macroRAFT P(AA-co-BA)-CTPPA was put in solution at pH 8.0 and left stirring for 7h at 80 °C. The UV-vis response of the triothiocarbonate function was followed during this time, and the results showed that no degradation took place (see **Annex A.2**).

II.6.2.1 Effect of macroRAFT nature

The effect of macroRAFT nature was investigated comparing the interaction of PAA-CTPPA and P(AA-co-BA)-CTPPA macroRAFT agents ($M_n = 3\,500\text{ g mol}^{-1}$ for both), with Imogolite. This study was carried out at pH 8.0, for which most of the AA units were deprotonated and negatively charged, while Imogolite was below its IEP and thus positively charged.

Figure 28 shows the results of adsorption of homopolymer and copolymer macroRAFT agents onto the surface of Imogolite. It is clearly seen that considerably higher adsorbed amounts are obtained for the macroRAFT copolymer. Two simultaneous events can explain this difference. One is related to the high charge density of PAA-CTPPA at the given pH (i.e. 8.0), which results in inter-chain repulsive forces that prevent further chains to adsorb. The copolymer chains have this repulsion minimized, since they contain less AA units.

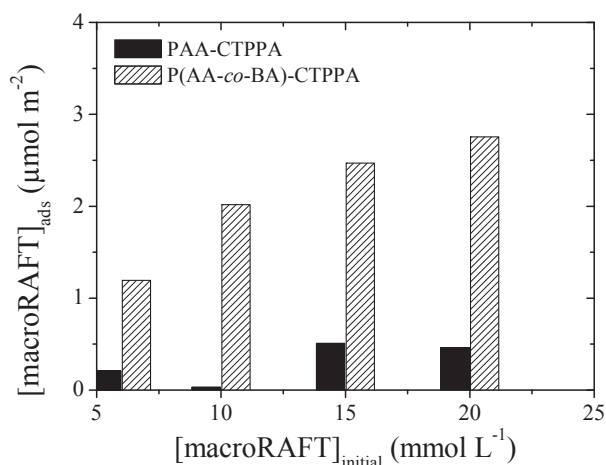


Figure 28. Adsorption of PAA-CTPPA and P(AA-co-BA)-CTPPA macroRAFT agents onto Imogolite surface at pH 8.0 for 2.0 g L^{-1} of nanotubes in water.

Chibowski *et al.*¹¹⁹ reported analogue observations when comparing the adsorption of a PAA onto the surface of Al_2O_3 at different pHs (i.e. different charge densities). The second event regards chains conformation in water. The copolymer chains, being more hydrophobic due to BA moieties, adopt a coil conformation that occupies a smaller volume, allowing the adsorption of further chains. Inter-chain hydrophobic interactions also contribute to further increase the adsorption of the macroRAFT onto the surface as schematically represented in **Figure 27**.

II.6.2.2 Effect of macroRAFT molar mass

It is known from literature that polyelectrolytes adsorption to inorganic surfaces is highly affected by the molar mass of the polymers^{110, 112, 113, 119}. Solubility in the dispersant medium, inter-chain electrostatic repulsion and polymer conformation are all parameters to be taken into account when adsorbing a polyelectrolyte to inorganic surfaces, and they can all vary with varying the molar mass of the polymer. Therefore, the effect of molar mass of the macroRAFT copolymer ($M_n = 1\,700\text{ g mol}^{-1}$ and $3\,500\text{ g mol}^{-1}$) was studied for a fixed pH of 8.0.

Figure 29 shows that the macroRAFT with a lower molar mass adsorbs less to the surface than the high molar mass copolymer. This behavior is in agreement with the literature¹¹³, where it has been shown that low molar mass polyelectrolytes present a coil conformation and adsorb in a train configuration to the surface, somehow blocking the availability of interaction sites. High molar mass polymers adsorb forming loops and tails still deployed in solution. These conformations occupy less space on the surface and contribute to polymer mobility, facilitating the adsorption of new chains. Moreover, they also contribute to particles stability by steric repulsions. It is important to note, however, that the works reported describing the effect of polymer molar mass on adsorption, used polymers with $M_n > 2\,000\text{ g mol}^{-1}$. In our case we work with low molar mass polymers. Nevertheless, the results seemed to be in agreement with what is described in the literature.

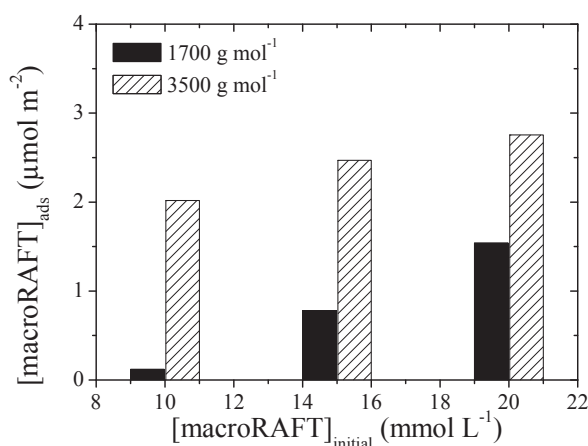


Figure 29. Adsorption of P(AA-co-BA)-CTPPA macroRAFT with $M_n = 1\,700\text{ g mol}^{-1}$ and $3\,500\text{ g mol}^{-1}$ onto Imogolite surface at pH 8.0 for 2.0 g L^{-1} of nanotubes in water.

II.6.2.3 Effect of pH

The effect of pH on the adsorption of the macroRAFT copolymer with $M_n = 3\,500\text{ g mol}^{-1}$ onto the Imogolite surface is presented in this section, working either at pH 8 or 6.

As mentioned above, two driving forces for polymer adsorption onto Imogolite surface can be considered: electrostatic attraction and hydrophobic interactions. Hydrophobic interactions are always present in our system, due to *n*-butyl acrylate moieties, but the electrostatic effects can be tuned by changing the pH. At low pH, which is a pH of 6.0 in our case, the carboxylic acid groups are partially deprotonated, and considerably less carboxylic acid groups are dissociated (-COO⁻). In consequence, the macroRAFT loses part of its ability to stabilize the colloidal objects, and some aggregates are formed. To obtain stable suspensions under these conditions the mixture was submitted to ultrasonic treatment prior to polymerization.

Figure 30 shows the adsorption isotherm of the P(AA-*co*-BA)-CTPPA macroRAFT agent onto the Imogolite surface at two pH values, 6.0 and 8.0. An increase of around 35% on the amount of macroRAFT adsorbed to the surface when decreasing the pH to 6.0 is observed. The difference between the adsorption at pH 6.0 and pH 8.0 is more evidenced at high macroRAFT concentrations, since chain-chain repulsion is more likely with the presence of a large number of chains in the medium.

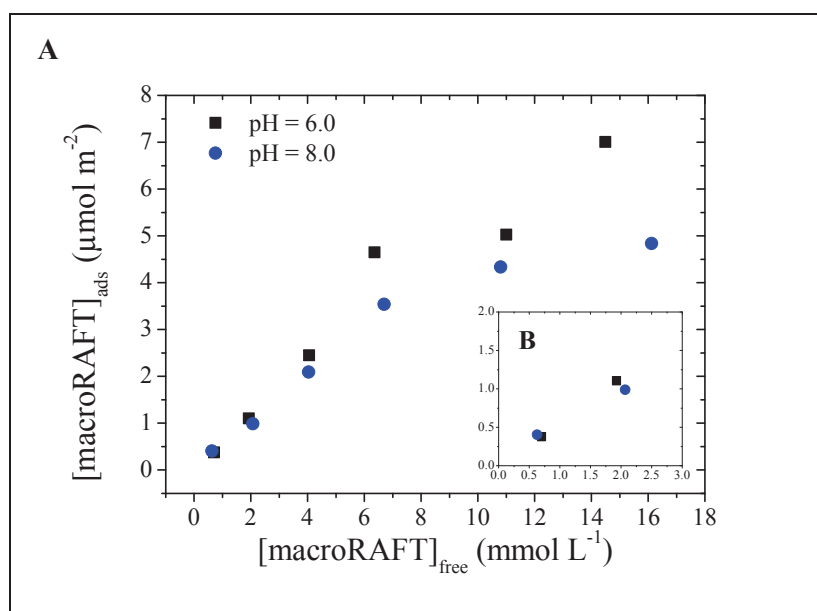


Figure 30. (A) Isotherm for macroRAFT adsorption onto the Imogolite surface at pH = 6.0 and 8.0. Nanotubes concentration = 2.0 g L^{-1} . MacroRAFT = P(AA-*co*-BA)-CTPPA, $M_n = 3\,500\text{ g mol}^{-1}$. (B) Zoom on the low copolymer concentration region.

The inversion of tendency for low macroRAFT concentrations, observed in **Figure 30B**, can be explained by the fact that at first, electrostatic interactions between negative charges from the

polymer and positive charges from the surface dominate. Since the macroRAFT concentration is very low, polymer inter-chain repulsion is irrelevant, and only the attraction forces play a role. However, this difference is minimal because decreasing the pH to 6.0, Imogolite nanotubes are more positively charged, favoring the adsorption through electrostatic interactions despite the lower negative charge of the polymer.

Figure 31 shows qualitative observations of the interaction of the copolymer macroRAFT with Imogolite at the two pHs studied. Clear differences could be visually observed regarding the stability of the hybrid suspensions. The left picture on Figure 31 suggests the formation of aggregates when the interaction is performed at pH 6.0, indicated by the opaque and milky aspect of the suspension. Since the copolymer is less charged at this pH, it has a lower capability of stabilizing the system, which results in aggregates formation. TEM images confirmed this observation, and small aggregates can be seen on the left image. At pH 8.0, the copolymer is mostly charged and consequently capable of providing stability to the system, avoiding the formation of aggregates.

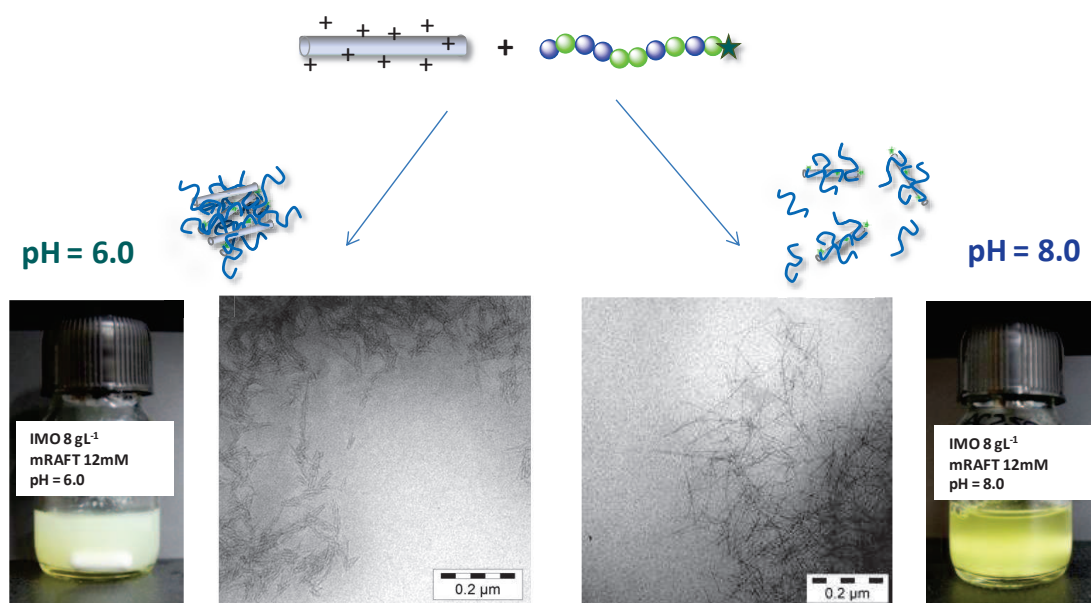


Figure 31. Qualitative illustration of the resulting interaction of the P(AA-co-BA)-CTPPA macroRAFT agent with Imogolite at pH 6.0 and 8.0.

The work of Liufu et al.¹¹² and Chibowski et al.¹¹³ reporting the adsorption of PAA (2000 g mol⁻¹) to TiO₂ and Fe₂O₃ surface, respectively, presented a maximum adsorption of around 0.3 μmol m⁻² at acid pH (3.0) and around 0.1 μmol m⁻² at basic pH (9.0). Taking these values as reference, we can consider that our macroRAFT, which adsorbs around 7.0 μmol m⁻² at pH = 6.0 and 5.0 μmol m⁻² at pH = 8.0, properly adsorbs onto Imogolite surface. It is noteworthy that in our case,

the amount of free macroRAFT in solution is always relatively high, suggesting a partitioning of the macroRAFT molecules between the aqueous phase and the surface.

The geometry of the inorganic nanoparticle also plays an important role on defining the adsorption of polymers to the surface. Cherstvy et al.¹²⁰ showed that considerable differences between the polyelectrolyte adsorption to a plane, a cylinder or a sphere are observed. In their work they have demonstrated that curved convex surfaces need much higher charge densities on the surface to trigger polyelectrolytes adsorption compared to a planar interface in the same solution. Furthermore, they have shown that the mechanism of adsorption is closer to the one for a planar interface when the curvature radius of the nanoparticle is increased.

Zeta Potential analyses were also performed to determine the surface charge of Imogolite for different macroRAFT concentrations (**Figure 32**). The results presented below show a clear charge inversion for the modification carried out at both pHs, 8.0 and 6.0.

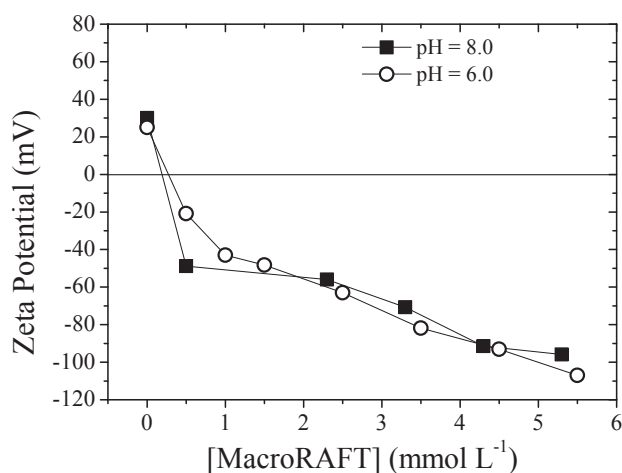


Figure 32. Zeta potential of Imogolite suspensions in the presence of different macroRAFT concentrations at pH 6.0 and 8.0.

The Imogolite nanotubes dispersed in water are positively charged, as presented in section II.4 and evidenced in **Figure 32**. Increasing macroRAFT concentration, the charges are first compensated and then inverted. This is another qualitative evidence of the macroRAFT adsorption to the surface of the Imogolite nanotubes. It is also interesting to observe that the series of data for both pHs are very close. At pH 8.0, the copolymer is more charged, but a lower amount of it is adsorbed ($5.0 \mu\text{mol m}^{-2}$). At pH 6.0, despite the higher amount of copolymer adsorbed ($7.0 \mu\text{mol m}^{-2}$), the overall charge density is lower, resulting in similar ZP values.

The dispersion state of modified nanotubes was measured through SAXS analyses. **Figure 33** presents SAXS scattering diagrams of pure Imogolite and Imogolite modified with macroRAFT at pH 8.0 and 6.0. At low scattering vectors, between 0.01 and 0.02 \AA^{-1} , for which big distances are represented, different intensities are obtained for each sample. Pure Imogolite and suspensions of macroRAFT/Imogolite at pH 8.0 present similar intensities, which are lower than that of the suspensions obtained at pH 6.0. This can be interpreted as a local increase in tubes concentration, which may be attributed to the formation of aggregates at pH 6.0. The black arrow at low $q = 0.15$ (\AA^{-1}) indicates the characteristic peak of Imogolite, corresponding to tube-tube electrostatic repulsion. This peak is not present for the other samples, indicating a modification of the surface charges after adsorption of the macroRAFT onto the surface. The effect of pH on the dispersion state of Imogolite/macroRAFT suspensions is illustrated by the appearance of a peak around 0.05 \AA^{-1} (dashed arrow) for the sample at pH 6.0, indicating the presence of an ordered structure, more likely aggregates. The effect of sonication was also studied, and the corresponding SAXS curve shows an even more defined peak around 0.05 \AA^{-1} . This observation suggests an increase in tubes organization inside the aggregates, probably resulting from the energy provided by sonication. A correlation distance of 7 nm could be calculated from this peak, which corresponds to the tubes center-to-center distance. It is known from literature that when Imogolite forms bundles the center-to-center distance is around 3.25 nm⁶⁶, ca. twice smaller than the distance determined in our case. This increase can be attributed to the presence of polymer chains on the tubes surface, increasing the tube-tube distance.

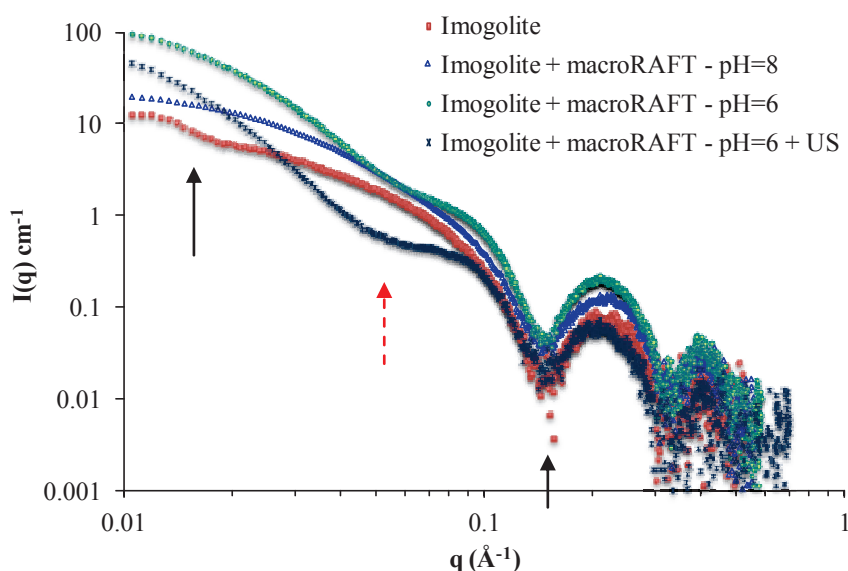


Figure 33. SAXS scattering diagram of pure Imogolite suspension (\square), Imogolite/macroRAFT suspension at pH 8.0 (Δ), Imogolite/macroRAFT suspension at pH 6.0 (\circ) and Imogolite/macroRAFT suspension at pH 6.0 after sonication (\times).

II.6.2.4 Effect of ionic strength

Another parameter that is known to influence polymer adsorption onto inorganic surface is the ionic strength (IS). Since mainly electrostatic interactions are responsible for the adsorption of polyelectrolytes to the surface, the state of the charges is very important, and is highly affected by the IS. Because of that, we briefly investigated the effect of this parameter on the adsorption of the macroRAFT to the Imogolite surface testing three conditions: in the absence of any salt, with 0.1 mol L^{-1} and with 1.0 mol L^{-1} of KCl salt (**Figure 34**).

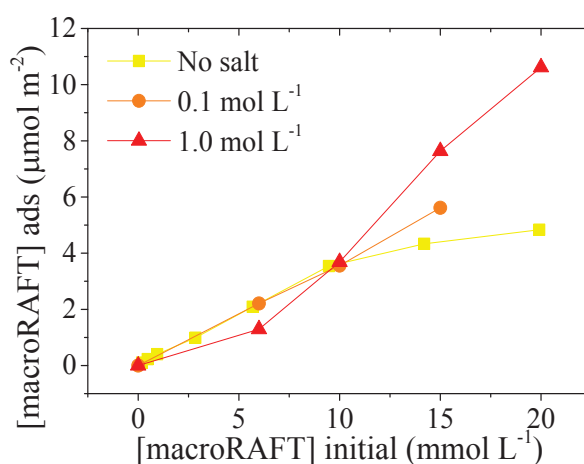


Figure 34. Adsorption isotherm of P(AA-co-BA)-CTPPA macroRAFT agent ($M_n = 3\,500 \text{ g mol}^{-1}$) onto the Imogolite surface for different ionic strengths. [Imogolite] = 2.0 g L^{-1} and pH = 8.0.

As expected, the adsorbed amounts increased with increasing the salt concentration, (i.e. with increasing ionic strength). The impact of ionic strength is not very important for low concentrations, for which the effect of inter-chain repulsion can be neglected. However, when increasing the macroRAFT concentration, the adsorbed significantly increased.

II.6.3 Conclusions

It was shown in this section that a weak adsorption of PAA-CTPPA compared to P(AA-co-BA)-CTPPA takes place when these macroRAFT agents are mixed with Imogolite in water. A strong partitioning of the macroRAFT between the surface and the aqueous phase was observed, and there is always a portion of free polymer in water. For P(AA-co-BA)-CTPPA, the adsorption can be increased by changing the pH of the system, making it slightly more acidic, or by increasing the ionic strength of the medium. Two mechanisms of adsorption were proposed:

through electrostatic interaction, which occurs at first; and via hydrophobic interaction mainly between polymer chains.

In the next series of polymerization experiments, the ionic strength was kept unchanged, since varying this parameter through salt addition can additionally increase the complexity of the system and disturb the initiator decomposition^{121, 122}.

The well characterized macroRAFT/Imogolite suspensions were then employed in the emulsion polymerization to encapsulate the nanotubes. The idea is to polymerize a hydrophobic monomer through the reactive RAFT function present on macroRAFT chain end and to surround the nanotubes by the hydrophobic polymer layer. Colloidal stability is provided by the hydrophilic macroRAFT block.

II.7 MacroRAFT-assisted encapsulating emulsion polymerization

This section will present the emulsion polymerizations performed with the purpose to encapsulate Imogolite using the modified nanotubes suspensions previously prepared. Different parameters such as macroRAFT molar mass and concentration, Imogolite concentration, pH and monomer composition were studied. The effect of each parameter on polymerization kinetics and latex stability and morphology were investigated.

II.7.1 Experimental section

II.7.1.1 Materials

The P(AA-*co*-BA)-CTPPA macroRAFT agent was synthesized as previously described and used after precipitating and drying at reduced pressure. The same batch of Imogolite nanotubes used for the previous section was used here, the C1p55 (L = 75nm, SW), which was dialyzed against pure water prior to use. The same reagents used in section II.5.1.1 were used here. Methyl acrylate (MA, 99%, stabilized, Acros Organics), potassium persulfate (KPS, 99%, Fischer Scientific) and 2,2'-Azobis[2-(2-imidazolin-2-yl)propane]dihydrochloride (ADIBA, 99%, Wako) were used as received.

II.7.1.2 Methods

Semi-batch emulsion polymerizations were carried out following the procedure described in section II.5.1.2. Typically, after mixing the macroRAFT solution at the specific pH (6.0 or 8.0) and the Imogolite suspension, the mixture was left stirring for 60 min. The system was purged under nitrogen for 30 minutes and a monomer shot of 0.15 mL previously degassed was made before starting polymerization. Samples were taken during the reaction for kinetic study.

To be sure that the 60 minutes of interaction were enough to achieve the adsorption equilibrium, one experiment was conducted in which the sample was interacted for a long period of time (36 days). The particles obtained after polymerization (see **Annex A.3**) presented the same morphology as that of the ones obtained after a 60 min interaction.

II.7.1.3 Characterizations

The final particle size, D_n , and the monomer conversion were determined as described in section II.5.1.3. Experimental M_n was determined as described in section II.3.1.3. For SEC analysis, prior to methylation and injection, the polymer was extracted from the dried hybrid latex by soxhlet extraction in a cellulose cartridge using THF reflux at 90 °C for 5h. TEM analyses were

also performed either at room temperature or under cryo conditions, using the devices and following the procedures described in sections II.5.1.3 and II.6.1.3 of this chapter.

II.7.2 Results and discussion

P(AA-*co*-BA)-CTPPA macroRAFT agents were used to encapsulate Imogolite nanotubes in a REEP process. The effect of various parameters on the final morphology and on the latex stability was investigated.

II.7.2.1 Effect of macroRAFT molar mass

The first studied parameter was the effect of the macroRAFT agent molar mass. The influence of this parameter for different macroRAFT concentrations was investigated on monomer conversion, particles average diameter, morphology and latex stability. **Table 9** summarizes the polymerization conditions and results.

Table 9. Polymerization conditions and results for the macroRAFT-assisted polymer-encapsulation of Imogolite nanotubes using P(AA-*co*-BA)-CTPPA macroRAFT agent of different molar masses and concentrations.

Entry	MacroRAFT (g mol ⁻¹)	[macroRAFT] (mmol L ⁻¹)	D_h (nm) / PDI	X_{final} (%)	Stability
AC28	1 100	3.5	123/0.29	42	X
AC27	1 100	7.2	70/0.09	48	√
AC215	3 500	3.7	25/0.15	40	√

MacroRAFT solution pH = 8.0; Imogolite pH = 6.0; Pathway: MacroRAFT solution added dropwise to the Imogolite suspension. Monomers: 15 wt% of MMA/BA (80/20 wt/wt) based on water

The three macroRAFT agents tested generated almost the same final conversion after polymerization (**Figure 35**). In the case of the macroRAFT of 1 100 g mol⁻¹, it is surprising that at both concentrations the same polymerization rates were obtained and final conversions were practically the same. When looking at the conversion profile of the polymerization in the presence of the longer macroRAFT (i.e. 3 500 g mol⁻¹), the polymerization rate was twice as high. This can be explained having in mind the mechanism that takes place in a PISA system, where the starting macroRAFT is hydrophilic and amphiphilic block copolymers are formed. In this context, it is known that the polymerization rate increases drastically after nucleation has taken place.¹²³ Correlating this information with our results, we can assume that the first particles are formed earlier when a longer macroRAFT is used. As discussed in the section II.5.2.2 of this chapter, the longer macroRAFT has a lower solubility in water, which means that it will become hydrophobic enough to self-assemble earlier than the low molar mass

macroRAFT. Another explanation could lie on the formation of aggregates, to some extent, of macroRAFT $3\,500\text{ g mol}^{-1}$ in water before polymerization. These aggregates would play the role of micelles, accelerating polymerization rate. Both explanations could explain the higher polymerization rate observed for the $3\,500\text{ g mol}^{-1}$ macroRAFT.

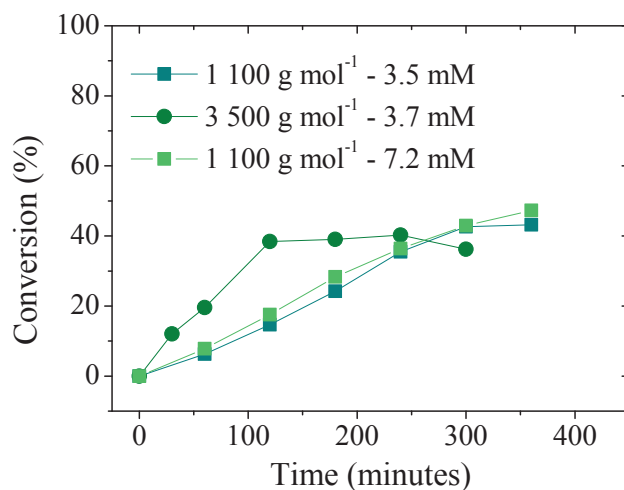


Figure 35. Monomer conversion versus time for the RAFT emulsion polymerization of MMA/BA (80/20 wt/wt) in the presence of 2.0 g L^{-1} of Imogolite nanotubes and 3.5 mmol L^{-1} (■) and 7.2 mmol L^{-1} (■) of P(AA-co-BA)-CTPPA macroRAFT of $1\,100\text{ g mol}^{-1}$ and 3.7 mmol L^{-1} of P(AA-co-BA)-CTPPA of $3\,500\text{ g mol}^{-1}$ (●).

In terms of morphology and latex stability, it can be seen in **Figure 36A** that when using a low concentration of the $1\,100\text{ g mol}^{-1}$ macroRAFT very inhomogeneous and non-spherical objects were formed, and Imogolite nanotubes were either free in water or on the particle surface. The heterogeneous morphology and size distribution can be related to the poor stability provided by the low molar mass macroRAFT. At the end of polymerization, the latex was relatively unstable and some aggregates could be observed with the naked eye.

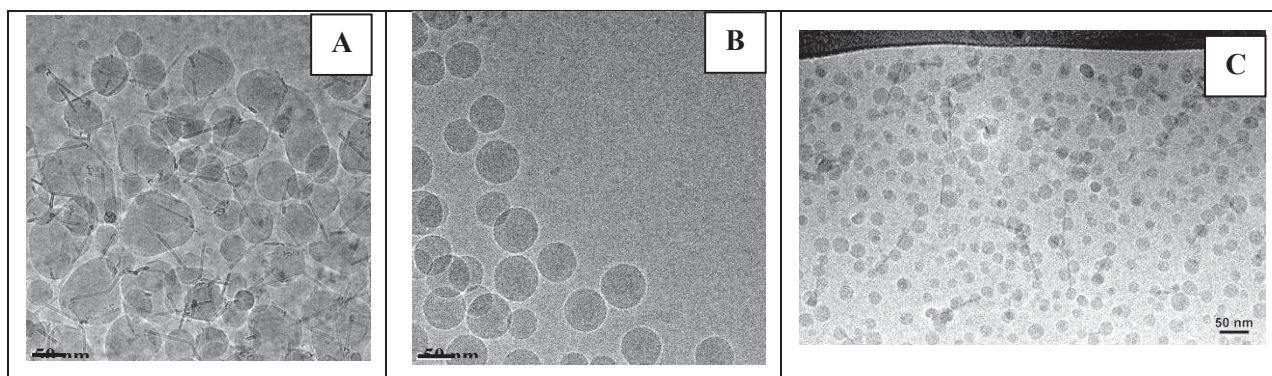


Figure 36. Cryo-TEM images of the hybrid latexes synthesized using (A) 3.7 mmol L^{-1} and (B) 7.2 mmol L^{-1} of a macroRAFT of $1\ 100 \text{ g mol}^{-1}$, and (C) 3.7 mmol L^{-1} of macroRAFT of $3\ 500 \text{ g mol}^{-1}$. Scale bars correspond to 50 nm.

When increasing the concentration of this macroRAFT, the particle diameter distribution seemed narrower (**Figure 36B**) and the final latex was stable, but Imogolite nanotubes were hardly seen. We attempted to perform microscopy of this sample in a more powerful microscope, but still no tubes could be observed. When we used the $3\ 500 \text{ g mol}^{-1}$ macroRAFT, however, the morphology obtained was quite different (**Figure 36C**). In this case the polymer particle's diameter was smaller and narrower in distribution, and the Imogolite tubes seem to be decorated with polymer particles. For this experiment, the adsorption of the macroRAFT to the surface was higher, as seen in section II.6.2.2, contributing to the wettability of the tubes and increasing the affinity of the hydrophobic monomers for the surface. Therefore, the polymerization could be, to some extent, transferred from the aqueous phase to the surface.

The polymer-decorated nanotubes obtained here could not be obtained via a simple physical mixture of preformed latex and Imogolite suspension. As recently reported by Kobayashi *et al.*¹⁰², the addition of Imogolite to preformed latexes causes its destabilization. The lack of stability is attributed to Imogolite-induced coagulation process, in which the tubes destabilize the latex by charge neutralization. Hence, the interest of using *in situ* RAFT polymerization is brought out when one aims at producing such hybrid colloids.

These observations also suggest that the high molar mass macroRAFT was successful in stabilizing the system, generating small and spherical polymer particles.

The next studies were thus performed with the $3\ 500 \text{ g mol}^{-1}$ acrylic acid-based copolymer macroRAFT, P(AA-*co*-BA)-CTPPA.

II.7.2.2 Effect of macroRAFT concentration

To optimize the system in which polymer-decorated nanotubes were obtained and additionally to control the hybrid morphology, we decided to investigate the effect of different parameters. In this section, the effect of macroRAFT concentration will be discussed.

Table 10. Polymerization conditions for the macroRAFT-assisted polymer-encapsulation of Imogolite using different concentrations of the $3\ 500\ \text{g mol}^{-1}$ P(AA-co-BA)-CTPPA.

Entry	[macroRAFT] (mmol L^{-1})	[Imogolite] (g L^{-1})
AC213	1.0	2.0
AC214	2.3	2.0
AC215	3.7	2.0
AC220	6.5	2.0
AC216	12.0	2.0

MacroRAFT solution pH = 8.0; Imogolite pH = 6.0; Pathway = macroRAFT solution added dropwise to the Imogolite suspension. Monomers: 15 wt% of MMA/BA (80/20 wt/wt) based on water

All polymerizations were performed in semi-batch, by contacting the macroRAFT with Imogolite for 1h, and using the same amount of Imogolite. The only change was the macroRAFT concentration.

The results presented in **Figure 37** show some significant differences with the increase of the macroRAFT amount. Higher polymerization rate and final conversion with increasing macroRAFT content were observed. To explain this difference, two lines of thought can be developed. The first one relates the concentration of macroRAFT with the number of particles (i.e. polymerization loci) formed. The higher the macroRAFT concentration, the higher the amount of free macroRAFT in water for a fixed Imogolite content, as shown in the adsorption studies, and the higher the number of particles formed by self-assembly. The increase in the number of particles, which corresponds to more active sites, results in a higher polymerization rate. For low macroRAFT concentration, not enough particles are formed to carry on with the reaction. Following this reasoning, the particles size should decrease with increasing macroRAFT concentration. However, since final conversion is not the same for all experiments, it is impossible to make such conclusions.

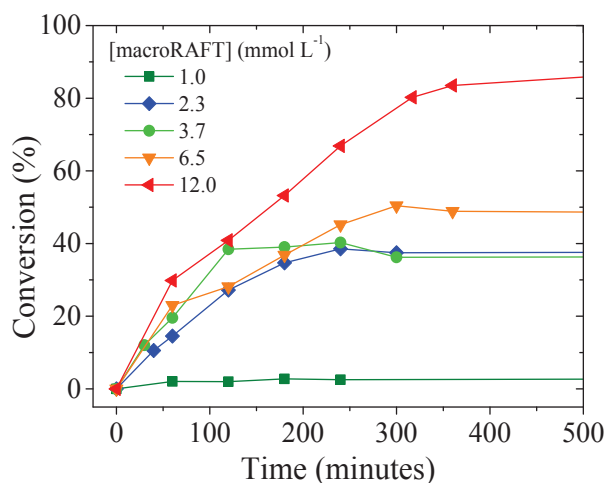


Figure 37. Monomer conversion versus time for the macroRAFT-assisted polymer-encapsulating emulsion polymerization of Imogolite in the presence of 1.0 mmol L⁻¹ (■), 2.3 mmol L⁻¹ (◆), 3.7 mmol L⁻¹ (●), 6.5 mmol L⁻¹ (▼) and 12 mmol L⁻¹ (▲) of macroRAFT.

In addition, as the ratio between macroRAFT and initiator is kept constant ($[\text{macroRAFT}]/[\text{ACPA}] = 3$), increasing macroRAFT amount simultaneously resulted in the increase of the initiator concentration, which also contributes to a higher polymerization rate. To verify the effect of the initiator flux directly, a study was carried out at different initiator concentrations and different initiator nature, and it will be presented further in this chapter.

Figure 38 shows TEM results of the latexes synthesized in this study. As expected, no significant difference between particles size was observed when increasing macroRAFT concentration, probably due to distinct conversion values. The only evident difference is for the lowest macroRAFT concentration, where no nucleation took place and thus no particles were formed. In terms of morphology (**Figure 38**), except for the lower macroRAFT concentration, the same hybrid morphology was obtained regardless of the macroRAFT concentration: polymer-decorated nanotubes. Since Imogolite amount was kept constant, a higher amount of free polymer particles was formed in the aqueous phase when increasing macroRAFT content.

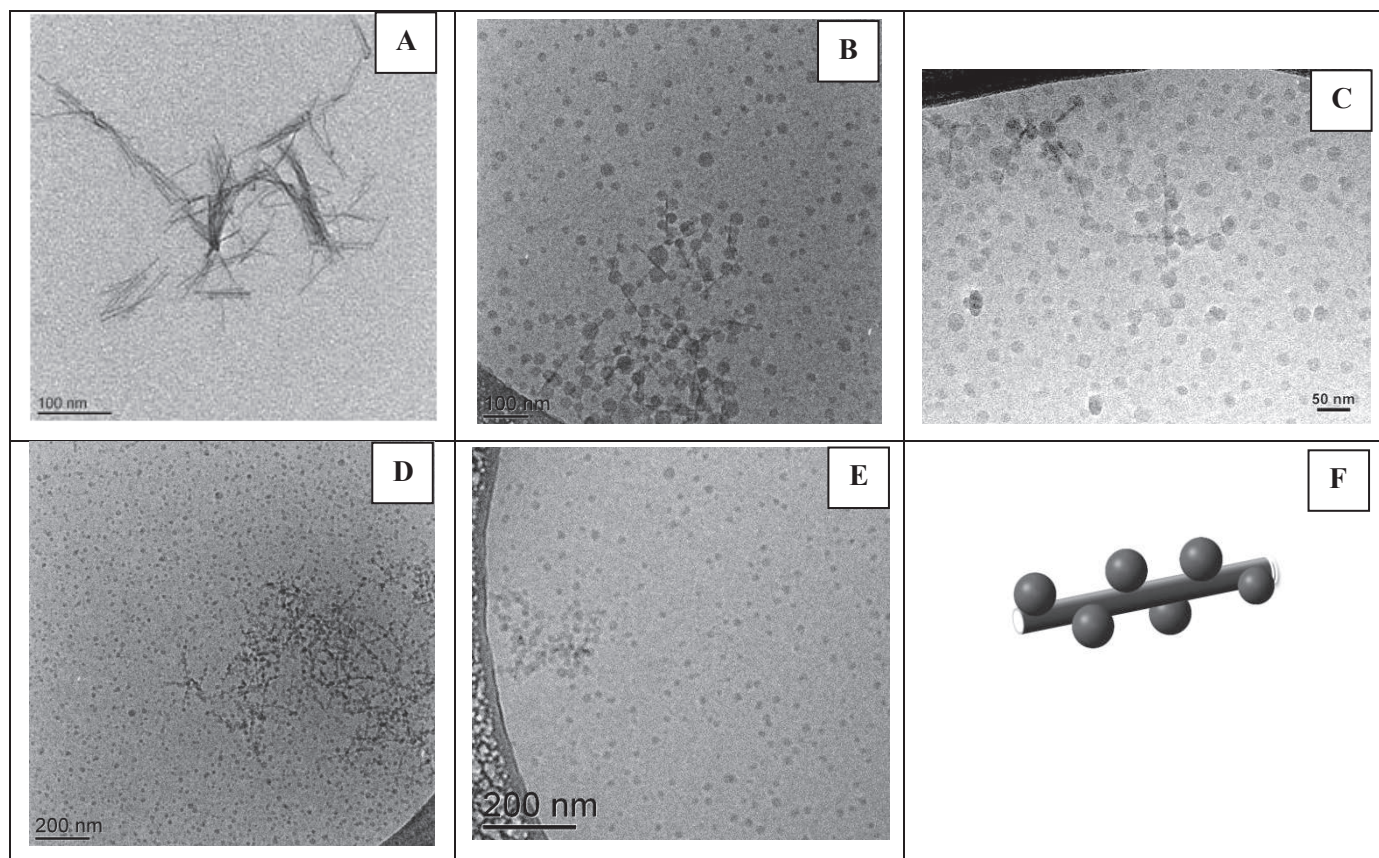


Figure 38. Cryo-TEM image of hybrid latexes synthesized via macroRAFT-assisted encapsulating emulsion polymerization of Imogolite in the presence of (A) 1.0 mmol L^{-1} , (B) 2.3 mmol L^{-1} , (C) 3.7 mmol L^{-1} , (D) 6.5 mmol L^{-1} and (E) 12 mmol L^{-1} of P(AA-co-BA)-CTPPA. (F) Schematic representation of the polymer-decorated Imogolite nanotubes.

This study showed that the amount of macroRAFT does not influence the final morphology. Even though a higher amount of macroRAFT was adsorbed onto the surface of Imogolite at high copolymer concentration, the hydrophilicity of the copolymer at $\text{pH} = 8.0$ did not favor the wettability of the tubes sufficiently to promote encapsulation, generating isolated nodules (particles) attached to the surface of Imogolite (**Figure 38F**).

II.7.2.3 Effect of the T_g of the encapsulating polymer

Van Herk *et al.*¹²⁴ showed that the T_g of the hydrophobic polymer highly influences the location of the inorganic particle in a hybrid colloid. Being soft (low T_g), the polymer favors the mobility of the inorganic particles, allowing it to migrate to the outside of the hybrid object when they are too hydrophilic. In this case, the final morphology is thermodynamically stable and the interfacial energy is minimized. By tuning the T_g of the polymer, increasing it, it is possible to obtain the morphology under a metastable state by a kinetic control, where the interfacial energy is not minimized but the hardness of the polymer freezes the inorganic particles inside. Having this reports as background we decided to increase the T_g of our hydrophobic polymer. Keeping

the same formulation as the entry AC215, in which we used 2.0 g L^{-1} and 3.7 mmol L^{-1} of P(AA-co-BA)-CTPPA, we studied the influence of the hydrophobic polymer T_g changing the monomer composition from MMA/BA – 80/20 wt/wt to MMA – 100% (**Table 11**).

Table 11. Conditions and results for the polymerization of MMA/BA (80/20 wt/wt) and MMA (100 wt/wt) using P(AA-co-BA)-CTPPA macroRAFT agent ($M_n = 3\,500 \text{ g mol}^{-1}$, $[\text{macroRAFT}] = 3.7 \text{ mmol L}^{-1}$).

Entry	Monomer	Composition (wt/wt)	D_h (nm) / PDI	X_{final} (%)	Stability
AC215	MMA/BA	80/20	25/0.15	40	√
AC219	MMA	100	36/0.20	82	√

MacroRAFT solution pH = 8.0; Imogolite pH = 6.0; Pathway = MacroRAFT solution added dropwise to the Imogolite suspension. 3.7 mmol L^{-1} of macroRAFT ($M_n = 3\,500 \text{ g mol}^{-1}$).

In terms of conversion it can be seen in **Figure 39** that the polymerization conducted in the presence of MMA alone achieved higher conversion values than the one using a portion of BA. One explanation could be linked to the blocking efficiency, discussed before. However, the opposite behavior would be expected, since BA should contribute to the addition to and the fragmentation of the intermediate radical. Plus, blocking efficiency should not interfere in semi-batch.

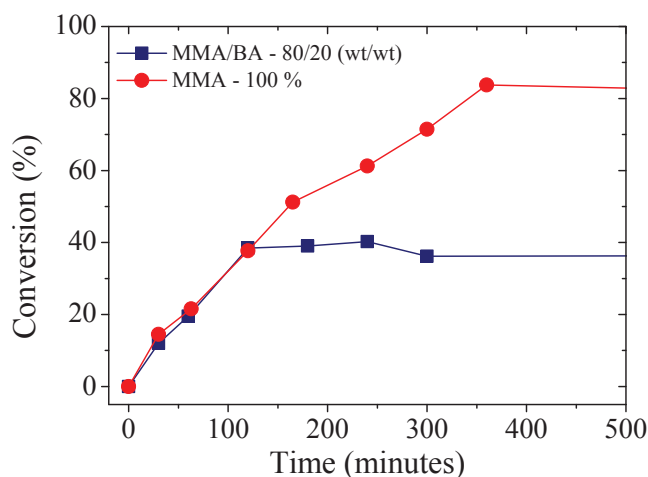


Figure 39. Monomer conversion versus time for the macroRAFT-assisted polymer-encapsulation of Imogolite using P(AA-co-BA)-CTPPA macroRAFT polymerizing MMA/BA (80/20 wt/wt) (■) and MMA (100%) (●).

When looking at polymerization rates at the first 2 hours of reaction, similar rates are observed. To better understand the effect of monomer composition on polymerization kinetics, experimental M_n and D should be compared. Since the separation of nanotubes from the final

latex and recover of the polymer was not straightforward, we did not perform SEC analyses for the present latexes. It is then quite difficult to take further conclusions concerning the polymerization kinetics.

Figure 40 shows TEM images of both low and high T_g latexes. As expected, when forming a higher T_g polymer (PMMA $T_g \sim 100$ °C), the final objects formed seemed to be better wetting the surface when compared to the lower T_g polymer (P(MMA-co-BA) 80/20 wt/wt $T_{g, \text{Fox}} \sim 48$ °C). For PMMA, non-spherical particles were formed even when they were not loaded with Imogolite. That indeed suggests a kinetic control and a metastable state. However, the tubes were not yet fully encapsulated as it could be expected.

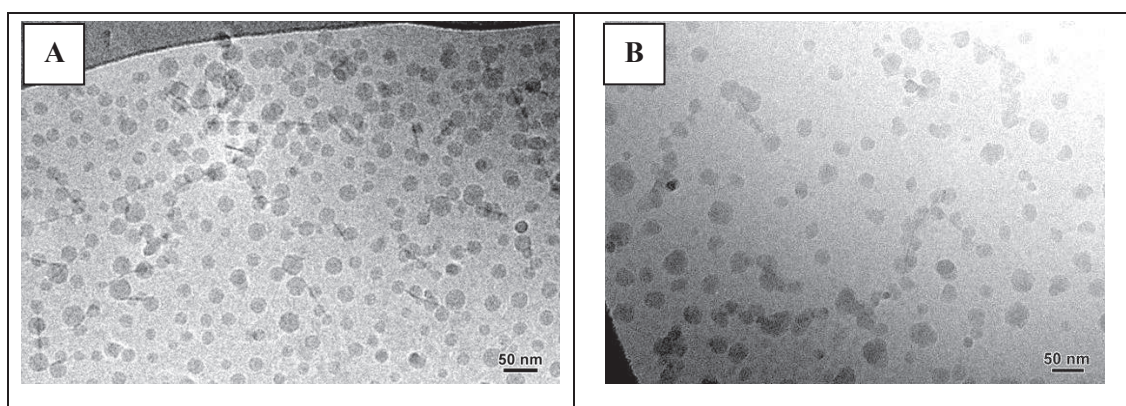


Figure 40. Cryo-TEM images of hybrid latexes obtained via the aqueous RAFT polymerization of (A) MMA/BA (80/20 wt/wt) and (B) MMA (100%) using 3.7 mmol L^{-1} of P(AA-co-BA)-CTPPA and 2.0 g L^{-1} of Imogolite.

II.7.2.4 How to increase monomer conversion while preserving particle morphology

Even though interesting and promising morphologies were being obtained, we still had a monomer conversion problem present in almost all polymerization conditions. In an attempt to increase the final monomer conversion of our polymerizations, some strategies were tested and are listed below.

II.7.2.4.1 Effect of initiator concentration

As it was found out in section II.7.2.2, the macroRAFT concentration influenced directly the final monomer conversion, which decreased with decreasing the amount of macroRAFT. This effect was attributed to initiator concentration, which also increases when increasing macroRAFT amount, since the [RAFT]/[ACPA] ratio was kept constant.

To verify the direct influence of the initiator concentration (i.e. the radical flux) on polymerization kinetics two experiments were done. The first one employed an initiator concentration of 3.9 mmol L^{-1} , three times higher than the previous experiments. The second one was conducted with 2.4 mmol L^{-1} of ACPA added in two shots. **Table 12** summarizes the polymerization conditions and results. The monomer conversion profiles of the different polymerizations are shown in **Figure 41**.

Table 12. Polymerization conditions and results for hybrid latexes synthesized using different initiator concentrations.

Entry	Initiator conc. (mmol L^{-1})	$D_h(\text{nm})/\text{PDI}$	$X_{\text{final}} (\%)$
AC215	1.2	25/0.3	40
AC240	2.4 in two shots	35/0.4	80
AC223	3.9	30/0.5	75

Imogolite concentration was 2.0 gL^{-1} ; MacroRAFT concentration was 3.7 mmol L^{-1} ; reactions were conducted at $\text{pH} = 8.0$. Temperature: $80 \text{ }^\circ\text{C}$.

In terms of kinetics, as expected, with increasing the initiator concentration a higher monomer conversion was achieved. However, surprisingly the polymerization rate slightly decreased with increasing initiator amount.

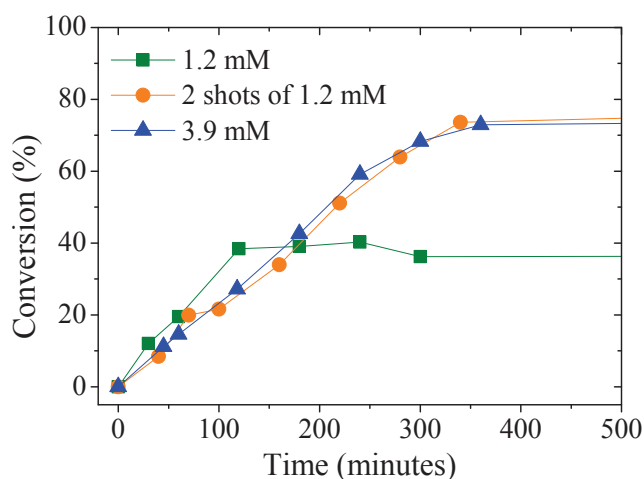


Figure 41. Monomer conversion versus time for the polymerization of MMA/BA (80/20 wt/wt) in the presence of 3.7 mmol L^{-1} of P(AA-co-BA)-CTPPA and with 2.0 g L^{-1} of Imogolite, using different initiator concentrations: 1.2 mmol L^{-1} (■), 2.4 mmol L^{-1} in two shots (●) and 3.9 mmol L^{-1} (▲).

Either when using high initiator concentration or when adding the initiator in two times, the same conversion profile is generated. This means that in one case we have enough initiator to provide the necessary radical flux to increase monomer consumption and in the other case two-

times addition guaranteed the presence of radicals for the whole polymerization time. These results suggest that the radical flux is directly related to the final conversion. When calculating the primary radical concentration at a given time $t = 120$ min, where conversion apparently stops for the experiment with low initiator amount, the following was found:

$$[A] = [A]_0 \times \exp^{-k_d t}$$

$$[A] = 1.2 \times 10^{-3} \times \exp^{-9.0 \cdot 10^{-5} \cdot 7200}$$

$$[A] = 0.628 \times 10^{-3} \text{ mol L}^{-1}$$

$[A]$ is the initiator concentration at the time t , $[A]_0$ is the initial concentration of initiator, k_d is the decomposition rate constant of ACPA in water at 80 °C ($k_d = 9.0 \cdot 10^{-5} \text{ s}^{-1}$)¹²⁵, and t is the given time (s). According to this calculation, the amount of initiator still present in the medium after 2 hours of reaction corresponds approximately to half of the initial concentration. In other words, this means that 120 min corresponds to the half-life of ACPA in water at 80 °C. Indeed, the calculated half-life time of ACPA at 80 °C in water is:

$$t_{1/2} = \frac{\ln(2)}{k_d} = 128 \text{ min}$$

Which is ca. 5 times lower than the half-life time of ACPA in water at 69 °C ($t_{1/2} = 10 \text{ h}$)¹²⁵. After 2h of reaction, the amount of initiator remaining in the medium is not sufficient to assure the continuity of polymerization.

According to the TEM results (**Figure 42**), the same hybrid morphology was obtained for both initiator concentrations. The free polymer particles also presented similar hydrodynamic particle diameter ($D_h \sim 30 \text{ nm}$), suggesting the same nucleation mechanism in both cases. Comparing these results with the ones obtained previously under the same conditions but with less initiator (entry AC215, **Figure 38C**), the same morphology of polymer-decorated nanotubes was observed. Particle size was also similar ($D_h \sim 25 \text{ nm}$), indicating the same nucleation mechanism.

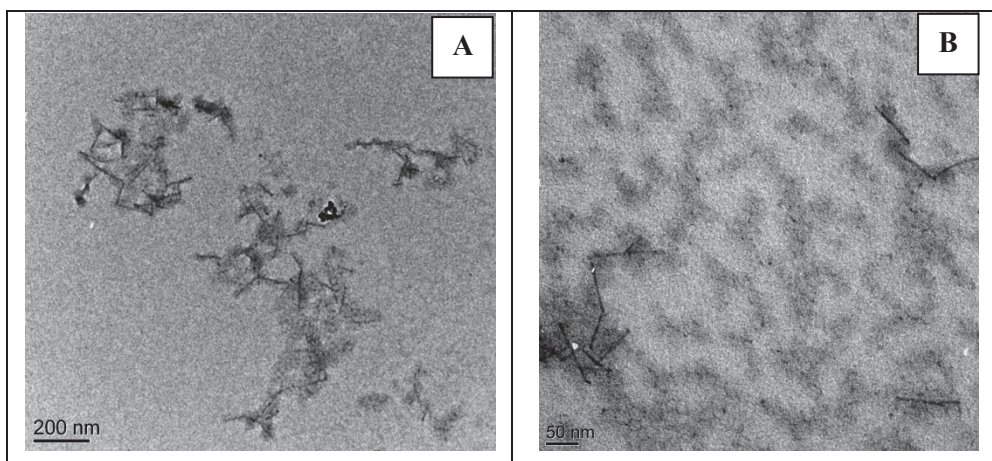


Figure 42. TEM images of hybrid latexes synthesized with 2.0 g L^{-1} of Imogolite, 3.7 mmol L^{-1} of macroRAFT and (A) 2.4 mmol L^{-1} and (B) 3.9 mmol L^{-1} of initiator.

II.7.2.6.2 Effect of polymerization temperature

Assuming that conversion limitation was coming from a radical flux problem, we also tried to play with the decomposition rate of the initiator, by decreasing polymerization temperature and observing the effect on monomer conversion.

As expected, by decreasing the decomposition rate of ACPA higher values of final conversion could be achieved (**Figure 43**). Decreasing the temperature by $10 \text{ }^{\circ}\text{C}$ results in a k_d value divided by two (at $70 \text{ }^{\circ}\text{C}$, $k_d = 4.6 \cdot 10^{-5} \text{ s}^{-1}$ in acetone)¹²⁵, leading to slower initiator decomposition and radical formation, making the radical flux last longer. As expected, the polymerization rate was nevertheless higher (at least before the conversion leveled off) at $80 \text{ }^{\circ}\text{C}$.

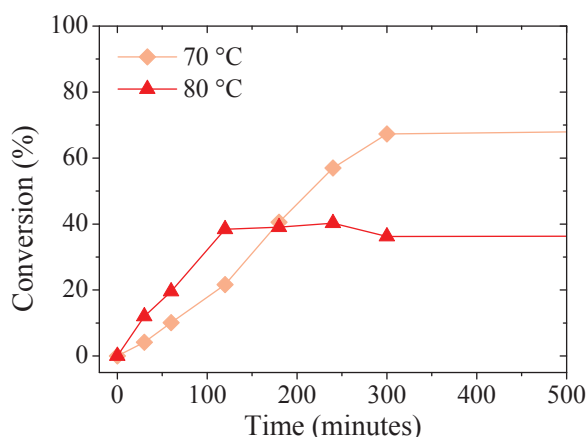


Figure 43. RAFT emulsion polymerization of MMA/BA (80/20 wt/wt) using 3.7 mmol L^{-1} of P(AA-co-BA)-CTPPA and 2.0 g L^{-1} of Imogolite. Monomer conversion versus time for the polymerization carried out at $70 \text{ }^{\circ}\text{C}$ (◆) and $80 \text{ }^{\circ}\text{C}$ (▲).

II.7.2.6.3 Effect of initiator nature

The last strategy tested to increase monomer conversion was the nature of the initiator. The ACPA initiator used so far was replaced by either a cationic azo initiator (ADIBA) or a persulfate-based initiator (KPS). Apart from their intrinsic features, the interaction of these initiators with the nanotubes could also affect the efficiency of the radicals to initiate polymerization. All polymerizations were performed at 80 °C (**Figure 44**).

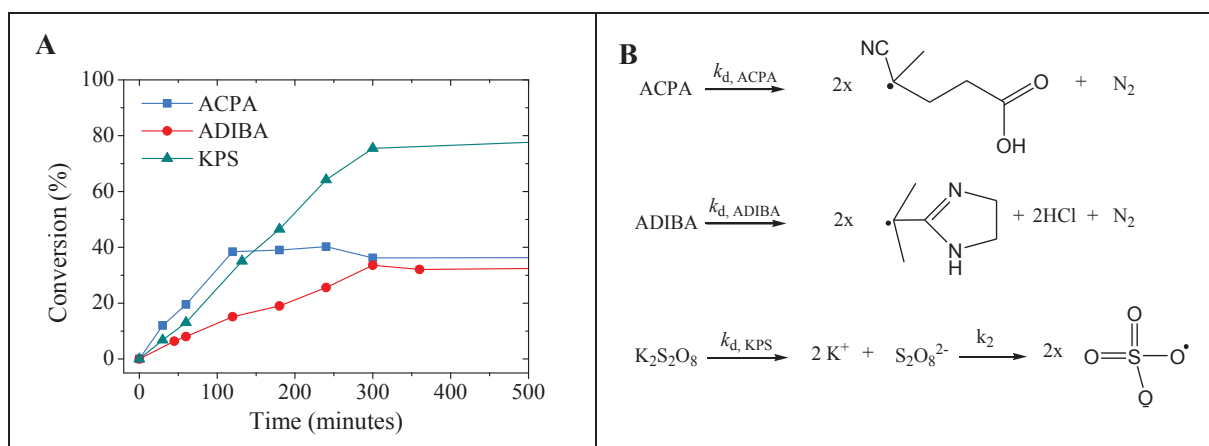


Figure 44. RAFT emulsion polymerization of MMA/BA (80/20 wt/wt) in the presence of 3.7 mmol L⁻¹ of P(AA-co-BA)-CTPPA and 2.0 g L⁻¹ of Imogolite at 80 °C using different initiators. (A) Monomer conversion versus time for the polymerization carried out with ACPA (■), ADIBA (●) and KPS (▲). (B) Decomposition reaction for the three initiators, with: k_d = decomposition rate constant and k_2 = S₂O₈²⁻ decomposition rate constant.

A clear difference between these three polymerizations is evidenced in **Figure 44A** in terms of kinetics. ACPA initiator seems to have led to the higher polymerization rates, which is in agreement with the data given in **Table 13**. After approximately 2 hours, however, polymerization stopped and monomer conversion reached a plateau, probably indicating a considerable reduction in the radical flux. As the calculations showed (section II.7.2.4), 2 hours corresponds to the half-life time of ACPA in the present conditions, explaining the plateau. On the other hand, ADIBA, which has the lower decomposition rate, led to lower polymerization rates. However, because of its low 10h half-life decomposition temperature, radicals were rapidly extinguished at 80 °C, and polymerization stopped. For KPS, the polymerization rate was intermediate to both previous experiments, in agreement with the intermediate k_d value. Final conversion was higher due to the higher 10 h half-life temperature of this initiator. It was concluded from this study that changing the initiator nature is also an efficient way to increase monomer conversion.

Table 13. 10h half-life and decomposition rate constants for the three initiators tested.

Initiator	10h half-life decomposition temperature in water (°C)	k_d (s ⁻¹) (at 80 °C in water) ¹²⁵
ACPA	69	$9.0 \cdot 10^{-5}$
ADIBA	44	$7.5 \cdot 10^{-6}$ ^a
KPS	70 ^b	$6.9 \cdot 10^{-5}$ ^b

^a In water at pH = 6.5. ^b In 0.1M NaOH.

In summary, this section presented the effect of different parameters on monomer conversion. It was shown that either increasing the initiator concentration, decreasing polymerization temperature or changing the initiator nature enabled the increase of final conversion. The effect of these three parameters on conversion is an indication that the origin of the limited conversion is related to the radical flux.

It was also shown that the radical flux did not affect particles morphology, and polymer-decorated nanotubes were obtained even at high initiator concentrations. Thus, further studies were carried out at 80 °C employing a higher initiator concentration to guarantee higher conversions.

II.7.2.7 Effect of Imogolite concentration

To better understand the influence of the free macroRAFT in water during polymerization and particles formation, and to optimize the morphology by minimizing the formation of isolated polymer particles, the effect of Imogolite concentration was investigated.

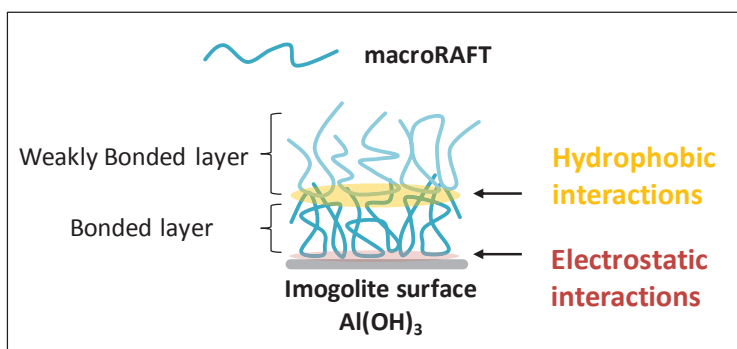
Since these free particles are formed from self-assembly of macroRAFT chains having grown in the aqueous phase, we had to decrease the amount of macroRAFT in water. The first idea was to perform a dialysis of the suspension of Imogolite modified with macroRAFT to extract the free macroRAFT and use the suspension of remaining macroRAFT-adsorbed nanotubes for the polymerization. The dialysis would also provide information about the strength and reversibility of the macroRAFT/Imogolite interaction. To avoid the formation of aggregates, the water pH was adjusted to 8.0. However, once we started the dialysis the suspension inside the dialyzing membrane became more and more unstable while free macroRAFT was being removed. The effect of aging on destabilization was discarded, since a previous study was made with an aged suspension and no stability problems were observed (see **Annex A.3**). After complete extraction of free macroRAFT, it was verified that the adsorption was irreversible, and the remaining tubes still had macroRAFT chains on the surface (i.e. 1.2 mmol L^{-1} of adsorbed chains determined by quantification of free macroRAFT by UV-vis, against 1.0 mmol L^{-1} determined in the adsorption studies). Additionally, the colloidal stability of the objects was proven to be also

dependent on the macroRAFT amount present in the aqueous phase. To explain this observation, we assumed a double-layer adsorption model (**Scheme 45**), in which the first adsorbed layer is unavailable for stabilization due to hydrophobicity. A second layer is then formed, through hydrophobic interactions, and this second layer is the one which provides stability. It is noteworthy that this second layer is weakly adsorbed, and can be removed by either dialysis or centrifugation. In consequence, it is not accounted in the adsorption studies, where separation was performed by centrifugation. **Table 14** compares the values obtained by dialysis and centrifugation of the adsorbed and free amount of macroRAFT. Indeed the amount of free macroRAFT measured by centrifugation is equivalent to the one removed by dialysis, supporting our hypothesis.

Table 14. MacroRAFT concentration in water and adsorbed to Imogolite surface as determined after separation by centrifugation and dialysis.

	[macroRAFT] _{free} (mmol L ⁻¹)	[macroRAFT] _{ads} (mmol L ⁻¹)
Centrifugation	2.7	1.0
Dialysis	2.4	1.2

Because of the lost in stability, the dialyzed suspension could not be polymerized, nor could be the centrifuged sample, since the precipitate could be hardly redispersed.



Scheme 45. Illustrative representation of the interaction mode of macroRAFT agent with Imogolite surface.

Another way to decrease the amount of free macroRAFT would be to decrease the initial amount of macroRAFT, but it was shown above (section II.7.2.2) that a strong decrease of the global amount of macroRAFT would result in a very low conversion. Because of that, in order to decrease the amount of free polymer chains in water, but keeping a reasonable total amount of macroRAFT in the medium, we increased the Imogolite content. By this means we increased the total surface area available for adsorption, which would necessarily diminish the amount of free macroRAFT in the aqueous phase. The macroRAFT concentration was thus fixed at 11.0

mmol L⁻¹, rather higher than the one used in the previous studies. **Table 15** presents the polymerization conditions used in this study.

Table 15. Polymerization conditions for the synthesis of hybrid latexes containing different amounts of Imogolite.

Entry	[macroRAFT] (mmol L ⁻¹)	[Imogolite] (g L ⁻¹)
AC216	11.0	2.0
AC221	11.0	6.4
AC239	10.0	8.0

MacroRAFT solution pH = 8.0; Imogolite pH = 6.0; Mixture pH = 7.8; Pathway: macroRAFT solution added dropwise to the Imogolite suspension. Monomers: 15 wt% of MMA/BA (80/20 wt/wt) based on water. Temperature: 80 °C. Initiator: ACPA.

As it can be seen in **Figure 46**, the final conversion was not affected by the Imogolite concentration. Practically the same polymerization rate and the same final conversion were obtained for whichever the Imogolite content.

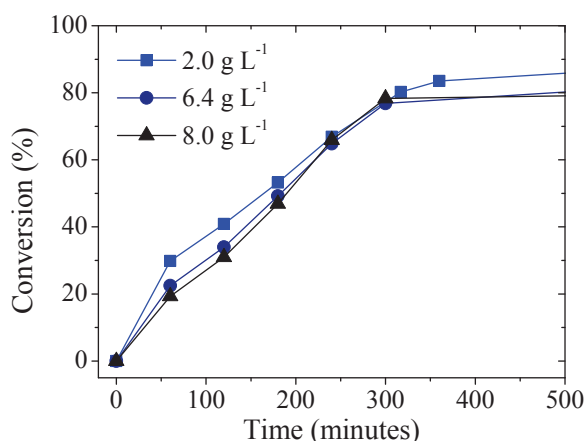


Figure 46. Monomer conversion versus time for the polymerization of MMA/BA (80/20 wt/wt) in the presence of 2.0 g L⁻¹ (■), 6.4 g L⁻¹ (●) and 8.0 g L⁻¹ (▲) of Imogolite and 10 mmol L⁻¹ of P(AA-co-BA)-CTPPA macroRAFT agent.

As **Figure 47** shows, the amount of secondary-nucleated polymer particles, originating from the polymerization of the free macroRAFT in the aqueous phase, could be minimized by increasing the Imogolite concentration. Polymer-decorated Imogolite nanotubes were obtained in all cases, suggesting that the adsorbed macroRAFT chains grow following a similar mechanism, whichever the macroRAFT concentration.

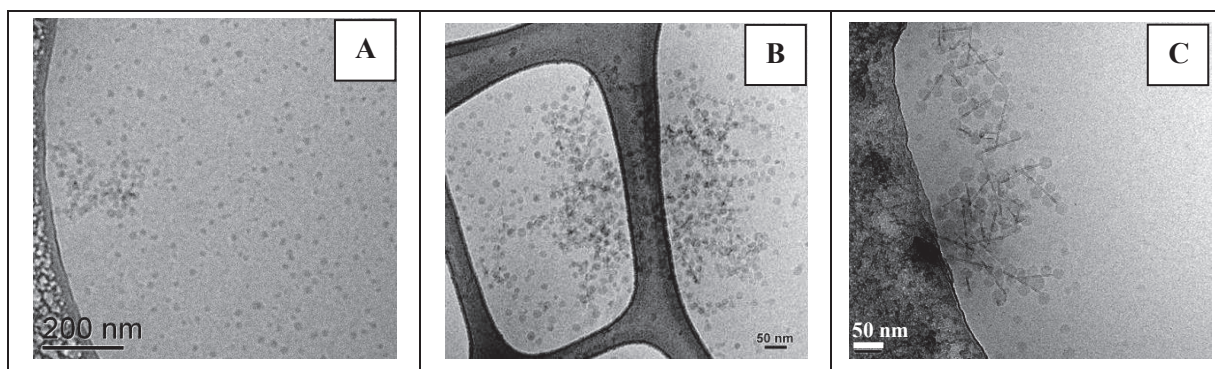


Figure 47. Cryo-TEM images of hybrid latexes obtained via RAFT emulsion polymerization of MMA/BA (80/20 wt/wt) at pH 8.0 in the presence of P(AA-*co*-BA)-CTPPA and containing (A) 2.0 g L^{-1} , (B) 6.4 g L^{-1} and (C) 8.0 g L^{-1} of Imogolite.

In summary, until now we have obtained polymer-decorated nanotubes, in which a relative good interaction between nanotubes and polymer was observed and polymerization appeared to be rapidly transferred from the aqueous phase to the surface of inorganic particles. For our final application this morphology is quite promising, since after film formation the polymer particles will coalesce on the surface of our nanotubes forming a shell and covering them. Furthermore, the presence of free particles contributes to the formation of the polymer matrix, and can be thus considered indifferent. Also, for certain applications where these free particles are not desired, the tubes concentration can be increased. Nevertheless, additional properties could arise from the encapsulation of the tubes. Thus, further studies focused on finding conditions in which Imogolite nanotubes would be encapsulated.

II.7.2.8 Effect of pH

The next parameter that was explored, having in mind the results obtained in the adsorption studies, was the pH of the suspension. It was seen in section II.6.2.3 that when the pH of the macroRAFT solution was 6.0, aggregates were formed. These aggregates could be further re-dispersed under ultrasound probe. MacroRAFT adsorption was increased of about 35% by decreasing the pH to 6.0, and the copolymer hydrophobicity also contributed to the tubes wettability. Since the success of the encapsulation is intimately related to the wettability of the inorganic surface²⁴, the suspensions prepared at pH 6.0 seem favorable to encapsulation.

This study was conducted using two formulations, one at low [Imogolite] (2.0 g L^{-1} of Imogolite; 3.7 mM of macroRAFT) and one at high [Imogolite] (8.0 g L^{-1} of Imogolite; 12 mM of macroRAFT). For each concentration the effect of pH was evaluated (6.0 or 8.0) (**Table 16**).

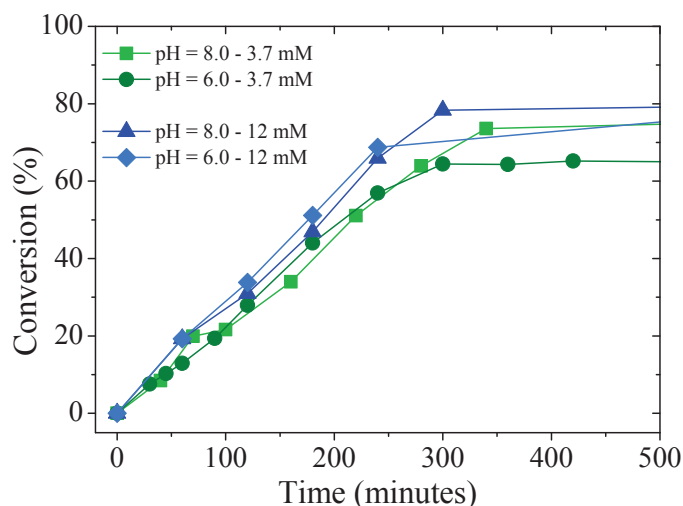
Table 16. Polymerization conditions for the synthesis of hybrid latexes synthesized at different pH values, [Imogolite] and [macroRAFT] concentrations.

Entry	[macroRAFT] (mol L ⁻¹)	[Imogolite] (g L ⁻¹)	pH macroRAFT	pH final
AC240	3.7	2.0	8.0	8.0
AC233	3.7	2.0	6.0	6.0
AC239	12.0	8.0	8.0	8.0
AC243	12.0	8.0	6.0	6.0

pH of Imogolite suspension = 6.0. Pathway = MacroRAFT solution added dropwise to the Imogolite suspension. Monomers: 15 wt% of MMA/BA (80/20 wt/wt) based on water. Temperature: 80 °C.

For polymerizations performed using 3.7 mmol L⁻¹ of macroRAFT, the [RAFT]/[ACPA] ratio was 1.5; while it was fixed at 3.0 for the polymerization carried out with 12 mmol L⁻¹ to guarantee a high conversion. Indeed, we showed previously that no change on morphology was observed when increasing the initiator concentration.

In terms of kinetics it can be seen that all four polymerizations have relatively similar rates and final conversion values (**Figure 48**). Logically, syntheses performed with higher amounts of macroRAFT employed more initiator, and consequently a slight increase in polymerization rate and final conversion was observed. However, all four kinetics are comparable and presented satisfactory consumption of monomers.

**Figure 48.** Monomer conversion versus time for the synthesis of hybrid latexes using 2.0 g L⁻¹ of Imogolite and 3.7 mmol L⁻¹ of macroRAFT at pH 8.0 (■) and 6.0 (●) and using 8.0 g L⁻¹ of Imogolite and 12 mmol L⁻¹ of macroRAFT at pH 8.0 (▲) and 6.0 (◆).

From TEM images (**Figure 49**) substantial differences can be seen for the final morphology of latexes synthesized at pH 8.0 and 6.0. At pH 8.0 (images A and C), as it was observed previously, polymer-decorated nanotubes were obtained. At pH 6.0 (images B and D),

aggregates of partially aligned tubes were obtained after the adsorption step, and the TEM photos show that these bundles of tubes were found encapsulated inside polymer particles after polymerization. The higher amount of macroRAFT adsorbed per particle indeed improved the wettability of the tubes and increased the number of RAFT functions per particle/aggregate. Consequently, the affinity of the hydrophobic monomers to the surface increased, helping the transfer of polymerization from the aqueous phase to the surface, favoring the encapsulation.

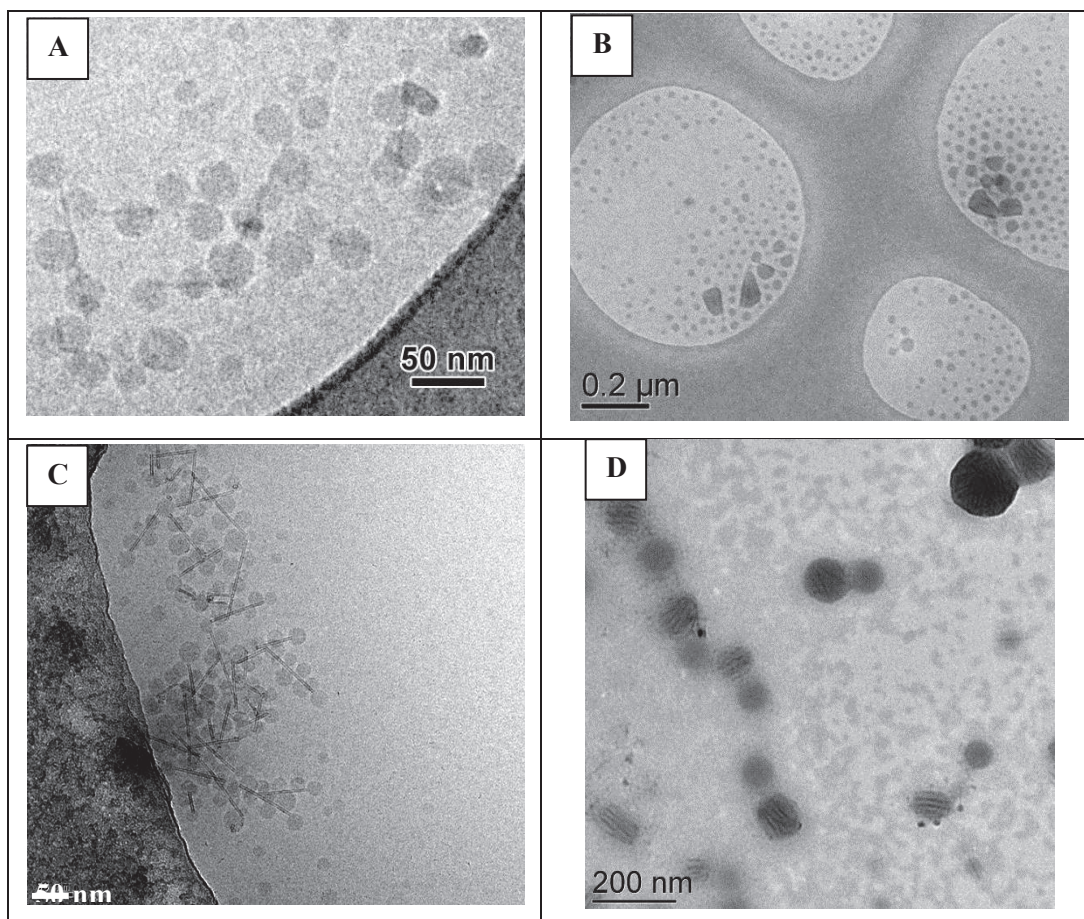


Figure 49. Cryo-TEM images (A, B and C) and low-temperature TEM (D) of hybrid latexes containing 2.0 g L^{-1} of Imogolite and 3.7 mmol L^{-1} of macroRAFT at (A) pH 8.0 and (B) 6.0, and containing 8.0 g L^{-1} of Imogolite and 12 mmol L^{-1} of macroRAFT at (C) pH 8.0 and (D) pH 6.0.

The results obtained in this study clearly evidence the importance of pH on the hybrid particles morphology. This parameter is actually a way to tune the macroRAFT hydrophobicity, which will consequently influence the adsorption of the polymer onto the inorganic surface and promote encapsulation. The formation of aggregates, already observed when performing the interaction between Imogolite and macroRAFT, is easily explained by the lower capacity of the polymer to stabilize the objects. The lower charge density of the polymer reduces its electrostatic interchain repulsions, which contributes to the higher adsorption. However, it also

reduces its capability of stabilizing individual nanotubes, resulting in tubes bundles encapsulation.

II.7.2.9 Effect of mixing and interaction pathway

As seen in the previous section, the only conditions in which encapsulation was achieved was when the tubes were aggregated (entry AC233 and AC243). Encapsulation under these conditions can be attributed to the hydrophobic character of the macroRAFT at pH 6.0, which provides the required affinity between the tubes and the monomer to enable successful encapsulation. However, this hydrophobic character also induces the formation of tube bundles (i.e. aggregates), due to the lower stabilization efficiency of the macroRAFT agents. To disperse these aggregates and obtain stable suspensions, the use of ultrasound was compulsory, adding another step to the process. In addition, the high energy provided by the US probe can break the tubes, decreasing their aspect ratio. Thus, this section was dedicated to study alternative pathways in which the aggregation would be controlled or avoided but still generating latexes with polymer-encapsulated nanotubes.

The aggregation can be potentially controlled or limited by playing with what is called the mixing or interaction pathway^{126, 127}. This technique consists in tuning the electrostatic complexation between oppositely charged building blocks (i.e. polyelectrolytes (PE) and inorganic nanoparticles (NP)). The *mixing pathway* is a strategy that takes into account the effect of the process (order and speed of addition) on the final morphology and size of the polymer/nanoparticle hybrids formed. Indeed, inhomogeneities in concentration during the formulation generate a gradient in the charge ratio Z between both charged components leading to very different structures and polydispersities. The NPs and PE concentration also affects the final clusters size, generating larger clusters at high building blocks concentrations¹²⁶. A post formulation concentration can overcome this limitation.

The *interaction pathway* consists in modulating the interactions of oppositely charged building blocks by screening/activating these electrostatic interactions. The screening of electrostatic interactions followed by the controlled activation of interactions was carried out by a desalting strategy. This strategy consists in mixing PE and NPs suspensions at very high salt concentrations (i.e. high ionic strengths), so that the charges are compensated by the counter ions and the interactions are completely screened. The mixture is then dialyzed to slowly remove the salt and smoothly activate the interaction, and at a certain ionic strength clustering starts to occur¹²⁷.

Recent works from Sekar et al.¹²⁸ and Yan et al.¹¹⁶ carried out with different nanoparticles (CeO₂, SiO₂, CNT and Fe₂O₃) covered with PAA_{2k} and different cationic PE

(poly(trimethylammonium ethylacrylate-*b*-poly(acrylamide) (PTEA_{11k}-*b*-PAM_{30k}), poly(diallyldimethylammonium chloride) (PDADMAC), poly(ethyleneimine) (PEI), poly(allylamine hydrochloride) (PAH) and poly(diallyldimethylammonium chloride) (PDDAC)), reported the use of waterborne desalting strategies. They have shown that the critical ionic strength in which clustering starts to occur is independent of building blocks concentration. However, the size of the aggregates was highly affected by this concentration. The group also showed that the cluster formation is kinetically controlled, and suspensions lost stability with time.

However, all the above mentioned works take into account that complete “electrostatic” screening of interactions between polyelectrolytes and nanoparticles is possible when no secondary forces such as H-bonding or hydrophobic interactions are present. In our case, hydrophobic interactions are always present due to BA moieties. Yet, we tried to apply this concept to our system anyway.

For the present study, since the aim was to verify the influence of the process on final morphology, no sampling was made during polymerization and only final conversion was determined by gravimetric analyses as well as morphology by TEM. In addition, the hydrophobic monomer mixture used for the encapsulating polymerizations was composed of methyl acrylate (MA)/BA at 80/20 wt/wt. This monomer mixture was chosen for its ability to form film-forming latexes. Further investigations of the effect of the hydrophobic monomer composition will be given in the next section (II.8).

Two Imogolite batches were used, one of an average SW tube length of 35 nm, but containing a significant amount of proto-Imogolite (MA1p40), and another one of average DW tubes length of 200 nm and without proto-Imogolite (C13p105). **Table 17** shows the experimental conditions and the different pathways used for each entry.

To explore the different mixing strategies we chose to work on the conditions in which aggregates are formed (pH = 6.0), trying to control the formation of these clusters to form finite-sized controlled morphologies. Imogolite concentration was fixed at 4.0 g L⁻¹, since the original Imogolite batches used were at 6.0 g L⁻¹. The corresponding macroRAFT concentration was then fixed at 6.0 mmol L⁻¹.

Table 17. Polymerization conditions, mixing pathway and results for the polymerization of MA/BA (80/20 wt/wt) using 4.0 g L⁻¹ of Imogolite and 6 mmol L⁻¹ of macroRAFT.

Entry	pH _{macroRAFT}	pH _{Imogolite}	pH _{final}	Pathway	D _h (nm)/PDI
AC251	5.7	6.0 ^a	5.9	1 ^c	129.6/0.37
AC253	5.6	6.0 ^a	7.4	2	357.7/0.89
AC264	5.8	6.0 ^a	7.4	2 ^c	3466/1.0
AC254	5.7	6.0 ^a	6.5	3 ^d	147.1/0.29
AC258	8.0	7.0 ^b	6.0	3 ^e	177.4/0.27
AC259	8.0	7.0 ^b	6.0	3 ^f	94.4/0.21

Monomers: 15 wt% of MA/BA (80/20 wt/wt). ^a Imogolite batch: SW, L = 35 nm (MA1p40).

^b Imogolite batch: DW, L = 200 nm (C13p105). ^c 5 minutes of sonication at 30% amplitude were applied. ^d pH adjusted by NaOH addition. ^e pH adjusted by the slow addition of hydrochloric acid. ^f pH adjusted by dialyzing the sample.

Pathways:
 1 - MacroRAFT sol. added dropwise to Imogolite suspension.
 2 - MacroRAFT sol. added dropwise to Imogolite suspension. pH adjusted with NaOH after interaction.
 3 - Imogolite susp. added by high speed injection to macroRAFT sol. pH adjusted with NaOH or HCl after interaction.

In a first study, the typical methodology at pH 6.0 (entry AC251), where the macroRAFT solution was added dropwise to the Imogolite suspension and the mixture was sonicated, was compared to a run in which the pH of the mixture was increased after interaction, to gain stability without sonication (entry AC253).

Some significant differences can be seen between both images (**Figure 50A** and **B**). The sample re-dispersed by sonication (AC251) presented encapsulated Imogolite aggregates after polymerization, indicated by the arrows in **Figure 50A**, as observed in the previous studies performed under the same conditions. The re-dispersion by increasing pH (AC253) seems to disaggregate part of the tubes, and they are found isolated after polymerization, as indicated by the red arrows in **Figure 50B**. The portion of tubes that remains aggregated is found encapsulated, and is indicated by the dashed arrows in the same image. The disaggregation can be attributed to the higher charge density of the macroRAFT at the higher pH, which result in interchain repulsion, breaking the weak aggregates formed. Even though the final latex presents some isolated tubes, there are still encapsulated aggregates in the sample, and the US step could be avoided.

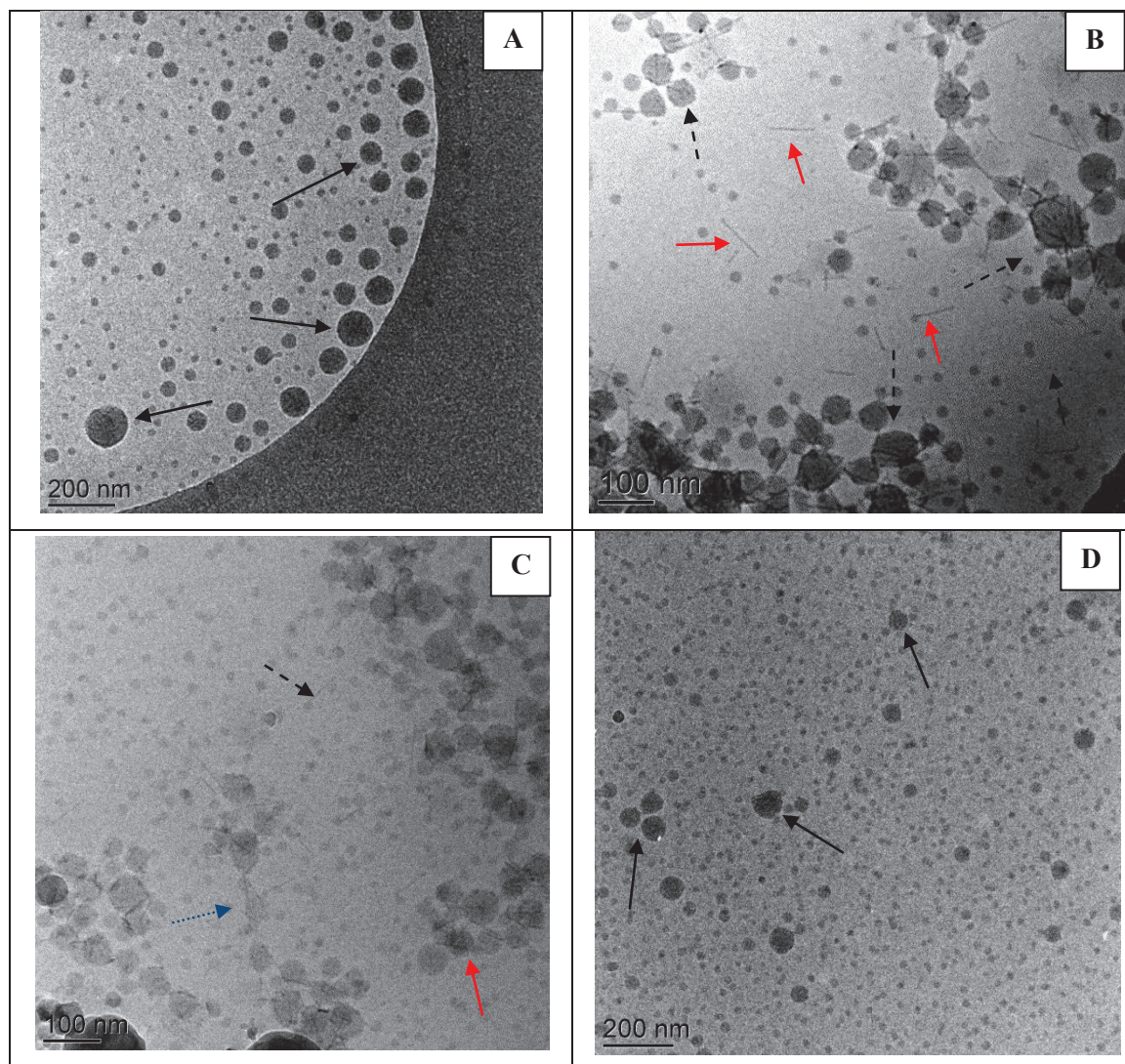


Figure 50. TEM images of hybrid latexes synthesized with 6.0 mmol L^{-1} of macroRAFT and 4.0 g L^{-1} of Imogolite MA1p40 polymerizing MA/BA at 80/20 wt/wt. (A, B and C) MacroRAFT solution at pH 6.0 was added dropwise to the Imogolite suspension. Sample was (A) submitted to US (AC251), (B) re-dispersed by increasing the pH (AC253), (C) re-dispersed by increasing the pH and submitted to US (AC264). (D) Imogolite suspension was added by high speed injection to the macroRAFT solution at pH 6.0 and the sample was re-dispersed by pH adjustment (AC254).

The effect of sonication on an already stable suspension of macroRAFT/Imogolite aggregates was investigated (Table 17, entry AC264). Figure 50C shows TEM results of the experiments in which macroRAFT was added dropwise to Imogolite suspension at pH 6.0, the pH was adjusted by NaOH addition to gain in stability and the sample was sonicated for 5 minutes to further improve the object dispersion. According to the image, inhomogeneous morphologies were obtained, isolated tubes, encapsulated bundles and partially encapsulated aggregates were formed (indicated by dashed, dotted and solid arrows, respectively). This variety of morphologies was attributed to the ultrasound energy, which most likely rearranged the tubes causing the break of some aggregates and the formation of new ones. Contrary to what is

observed at pH 6.0 (**Figure 50A**), the more hydrophilic macroRAFT is not able to maintain the bundle formation, and the tubes disaggregation is more susceptible to happen.

Figure 50B and **D** compare the experiments performed at pH = 6.0 and re-dispersed by pH adjustment, but following two different mixing pathways (**Table 17**, entries AC253 and AC254). **Figure 50B** presents the results for the mixture obtained by adding macroRAFT solution dropwise to the Imogolite suspension, as seen before (AC253). **Figure 50D** shows the results for the mixture obtained adding Imogolite suspension by high speed injection to macroRAFT solution (AC254). It can be seen that when Imogolite is added rapidly to macroRAFT solution the aggregates formed seem to have stronger interaction between Imogolite and macroRAFT, and are not undone by the pH increase. They are found encapsulated after polymerization, as indicated by the arrows. In addition, they seem to be smaller than the ones obtained after sonication.

Adding Imogolite to the macroRAFT solution prevents the tubes from crossing a charge neutralization point, since the macroRAFT concentration is always maximized. This could explain the formation of smaller aggregates when Imogolite is added to macroRAFT solution.

Next experiments were conducted to study the effect of the transition from the “low interaction state” to the “high interaction state”, analogously to the desalting strategy. These samples were prepared by the high speed injection of Imogolite suspension to the macroRAFT solution at pH = 8.0, followed by the decrease of pH by either HCl addition (AC258) or by dialysis (AC259). These entries were thus compared to AC254, in which the starting pH was 6.0 and it was increased to gain in stability.

Figure 51 shows the TEM results for the pH-shifting experiments. It can be seen that when starting from non-aggregated tubes (i.e. pH = 8.0) and slowly decreasing pH to 6.0 to induce aggregation, the formed clusters are less compact, and the tube-tube distance inside them seems higher (**Figure 51B** and **C**, dashed black arrows). However, this process apparently generated a mixture of different morphologies. Encapsulated tubes (dashed black arrows), polymer-decorated nanotubes (solid red arrows), Janus particles (solid green arrows) as well as the start of some fibers (dotted blue arrows) were observed.

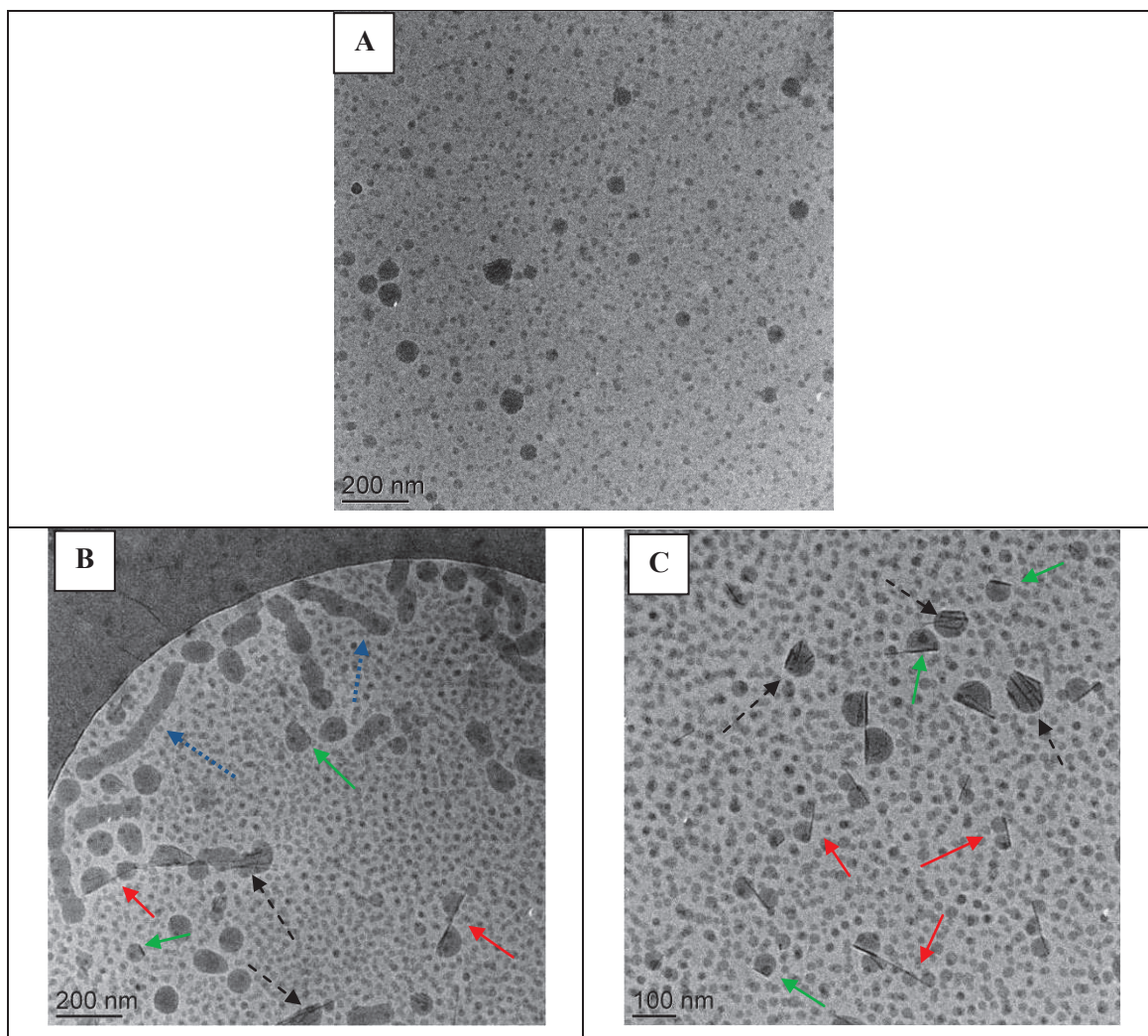


Figure 51. Cryo-TEM images of hybrid latexes synthesized with 6.0 mmol L^{-1} of macroRAFT and 4.0 g L^{-1} of Imogolite batch (A) MA1p40 and (B and C) C13p105. For all samples, Imogolite suspension was high-speed injected to macroRAFT solution. (A) Solution pH was 6.0 and suspension was re-dispersed by increasing pH (AC254). Initial pH was 8.0 and it was decreased to 6.0 by (B) acid addition (AC258) or (C) dialysis (AC259).

The high proportion of short fibers found for the acidified sample (**Figure 51B**) could be a result of the presence of additional ions (Cl^- originating from the hydrochloric acid addition) in the medium. The macroRAFT ability to stabilize the objects was thus affected both by the decrease in pH and by the increase of the ionic strength, which screened the macroRAFT charges supposed to provide electrostatic stability. This lack of stability likely favored fibers formation.¹²⁹ The dialyzed sample (**Figure 51C**) also presented a mixture of the morphologies described: some Janus particles, in which the polymer grows all along a specific side of the tube, encapsulated tube bundles and polymer-decorated nanotubes. However, the main difference between both samples was the absence of fibers in the dialyzed sample, probably due to the absence of additional acid.

Over viewing the results presented in this section it can be concluded that the mixing pathway (order of addition) indeed provides further control over the hybrid morphologies, despite the complex mechanism of aggregation, due to the presence of hydrophobic interactions additionally to electrostatic forces. Smaller aggregates were formed when inverting the mixing order and adding Imogolite rapidly to the macroRAFT solution. The pH-shifting strategy (i.e. interaction pathway) generated latexes with co-existing polymer-decorated tubes, encapsulated tube bundles, Janus particles and fiber-like morphologies. The addition of hydrochloric acid in the medium disturbed the stability of the particles, probably due to the increase of ionic strength, and led to the formation of fibers. When the slow desalting was carried out, through dialysis, no fibers were formed additionally to all the other kinds of hybrid particles. The formation of such a variety of morphologies by this pH-shifting strategy confirmed the complexity of this technique when applied to systems which undergo the action of so many external forces. Sonication step could be avoided by increasing the pH after interaction.

In conclusion, the mixing pathway considered as the most appropriate to form small and compact Imogolite aggregates preserving the system stability was the addition of the Imogolite suspension by high speed injection to the macroRAFT solution followed by pH adjustment via addition of NaOH.

II.7.3 Conclusions

MacroRAFT-assisted encapsulating emulsion polymerization (REEP) applied to Imogolite nanotubes was successfully performed using AA/BA-based macroRAFT agents of $M_n = 3\ 500\ \text{g mol}^{-1}$. Hybrid latexes of two main morphologies were obtained when the polymerization was performed at pH 8.0 and 6.0: polymer-decorated nanotubes and encapsulated nanotube bundles, respectively. The effect of macroRAFT nature and molar mass was evaluated. The chemical composition of the macroRAFT chains was shown to be an important parameter to produce stable and morphology-controlled hybrid latexes. A critical macroRAFT molar mass was found, below which latex stability was not achieved. Polymer-decorated nanotubes could be obtained and the presence of free polymer particles could be controlled by playing with macroRAFT or Imogolite concentrations. Encapsulated nanotube bundles were obtained when decreasing the pH of the medium from 8.0 to 6.0. The use of different mixing or interaction pathways to control the aggregates size and the final morphology proved to be quite complex, due to external interaction forces such as hydrophobic interactions present in our system. Notwithstanding this complexity, smaller aggregates could be obtained when changing the mixing pathway (adding Imogolite suspension to macroRAFT solution instead of the reverse). When playing with the interaction pathway by the pH-shifting strategy (starting at pH 8.0 and slowly decreasing the pH

to 6.0 by acid addition or dialysis), co-existing various morphologies were obtained (e.g. encapsulated tubes, polymer-decorated tubes and Janus particles).

Further studies focused on optimizing the monomer composition towards film-forming latexes and investigating the effect of this composition on final latex morphology. The next section is thus dedicated to producing polymer-decorated nanotube and encapsulated nanotube bundles with a low T_g polymer, able to form nanocomposite films by simple water evaporation.

II.8 Towards film-forming latexes

II.8.1 Latexes synthesis

In the present study we tried to reproduce the two morphologies obtained until now in a film-forming latex. The idea was to produce films by water evaporation to obtain hybrid materials whose mechanical properties could be analyzed. The monomer mixture of MMA/BA 80/20 wt/wt yields a copolymer with a theoretical T_g determined by the Fox equation close to 46 °C. A polymer with this T_g forms a fragile and breakable film at room temperature, and is not ideal for our film formation procedure. Thus, the effect of the monomer composition was investigated to obtain lower T_g copolymers and the targeted morphologies: polymer-decorated nanotubes and encapsulated nanotube bundles.

II.8.1.1 Experimental section

II.8.1.1.1 Materials

All reagents (i.e. the initiator, the monomers, NaOH and water) were the same as the ones reported in section II.7.1.1. P(AA-co-BA)-CTPPA ($M_n = 3\,500\text{ g mol}^{-1}$) was synthesized as described previously and used after precipitating and drying (section II.3.1.2). Four different Imogolite batches were used for this study: C1p55, MA1p40, C13p105 and EP1p37. Their main characteristics are shown in (Table 18). They were all dialyzed against pure water prior to use. Methyl acrylate (MA, 99.5%, stabilized, Acros Organics), styrene (STY, 99%, stabilized, Acros Organics) and sodium hydrogen carbonate (NaHCO_3) (99%, Sigma-Aldrich) were used as received.

Table 18. Characteristics of the Imogolite batches used in this section.

Entry/Lot	external	Average L (nm)	[Imogolite] (g L^{-1})	pH	Type
C1p55	3.7	75	23	5.99	SW
MA1p40	2	35*	9.6	6.1	SW
C13p105	4.2	200	9.2	6.0	DW
EP1p37	4.4	500	6.5	5.9	DW

*High concentration of protoimogolite

II.8.1.1.2 Methods

All reactions were carried out in semi-batch. The polymerization method was identical to the one described in section II.5.1.2. Different copolymers were synthesized in this section by varying the nature and the composition of the monomer mixture.

Table 19 shows the T_g s for pure PMMA, PS, PBA and PMA as well as those of the copolymers tested, as determined using the Fox equation.

Table 19. Fox Equation and T_g values for the different monomer mixtures tested.

<u>Fox equation</u>	<u>Monomer Mixture – wt/wt</u>	<u>$T_{g,1} / T_{g,2}$ (K)¹²⁵</u>	<u>T_g (K)/(°C)</u>
$\frac{1}{T_g} = \frac{w_1}{T_{g,1}} + \frac{w_2}{T_{g,2}}$	MMA/BA – 80/20	368 / 208	319 / 46
w_1 and w_2 = weight fraction	STY/BA – 70/30	368/208	299/26
monomer 1 and 2.	MMA/BA – 50/50	368 / 208	266 / -7
$T_{g,1}$ and $T_{g,2}$ = T_g of polymers 1 and 2	STY/BA – 50/50	368 / 208	266 / -7
in Kelvin	MA/BA – 80/20	281 / 208	263 / -10

Table 20 shows the water solubility of all monomers used for the synthesis of the copolymers.

Table 20. Solubility of the different monomers tested in water at 25 °C.

<u>Monomer</u>	<u>solubility (wt%) (water, 25 °C)^{130, 131}</u>
STY	0.02
BA	0.14
MMA	1.59
MA	6.0

II.8.1.1.3 Characterizations

The particle size (D_h), the monomer conversion, the number-average molar mass, M_n , molar mass dispersity \mathcal{D} , and particles morphology were determined by DLS, gravimetry, SEC and TEM measurements, respectively, as described in section II.7.1.3. Prior to SEC measurements, the polymer was extracted by soxhlet reflux in THF at 90 °C for 5h.

II.8.1.2 Results and Discussion

II.8.1.2.1 Effect of co-monomers composition

In this section, the effect of the monomer composition was studied under similar conditions as previously for MMA/BA (80/20 wt/wt). In a first series of experiments, MMA was replaced by styrene (STY) while the BA content was increased to 30%. This led to a T_g close to the ambient (i.e. 26 °C) (**Table 19**).

The polymerizations were performed at pH = 8.0 at low (2.0 g L^{-1}) and high (8.0 g L^{-1}) Imogolite concentrations while keeping a similar macroRAFT/Imogolite ratio. **Table 21** summarizes polymerization conditions for these experiments.

Table 21. Polymerization conditions for the synthesis of hybrid latexes using different monomer compositions.

Entry	Monomers	Monomer ratio (wt/wt)	[macroRAFT]	[Imogolite]	pH _{final}
AC215	MMA/BA	80/20	3.7	2.0	8.0
AC236	STY/BA	70/30	3.8	2.0	7.6
AC239	MMA/BA	80/20	12	8.0	8.0
AC245	STY/BA	70/30	12	8.0	7.8

Pathway = MacroRAFT solution added dropwise to the Imogolite suspension. Imogolite batch of L = 75 nm, SW (C1p55). Temperature: 80 °C.

Figure 52 shows the conversion versus time curves for this series of experiments. It can be seen that the four experiments have almost the same polymerization rate until 2h of reaction, but one set of experiments (i.e. low amount of macroRAFT and Imogolite) stops around 40% of monomer consumption and the other (i.e. high amount of macroRAFT and Imogolite) continues to reach conversion higher than 80%. This trend was observed for both monomer mixtures, suggesting that the composition of the hydrophobic monomer did not influence the polymerization rate. Again, the kinetics was only affected by the macroRAFT concentration, which means, by the initiator concentration.

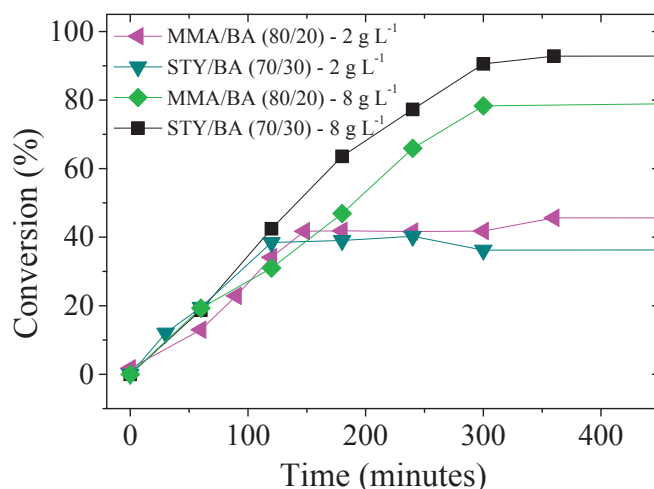


Figure 52. Monomer conversion versus time for the polymerization of MMA/BA (◀) and STY/BA (▼) at low concentrations ([Imogolite] = 2.0 g L^{-1} and [macroRAFT] = 3.7 mmol L^{-1}) and STY/BA (■) and MMA/BA (◇) at high concentrations ([Imogolite] = 8.0 g L^{-1} and [macroRAFT] = 12.0 mmol L^{-1}).

The TEM images shown in **Figure 53** reveal interesting changes in morphology according to the monomer composition. Observing the *in situ*-formed pure polymer particles, it can be seen that non-spherical particles were obtained when working with STY at both Imogolite concentrations. The formation of fibers and vesicles is visible in **Figure 53A** and **C**, as indicated by the solid arrows. The *in situ*-formed polymer particles are formed under a PISA mechanism, where the morphology is defined by the specific characteristics of each block of the amphiphilic block copolymers that compose the particles.¹²⁹ When we changed MMA for STY, we changed the chemical nature and increased the hydrophobicity of the second block. These changes favored the formation of thermodynamically stable non-spherical particles.

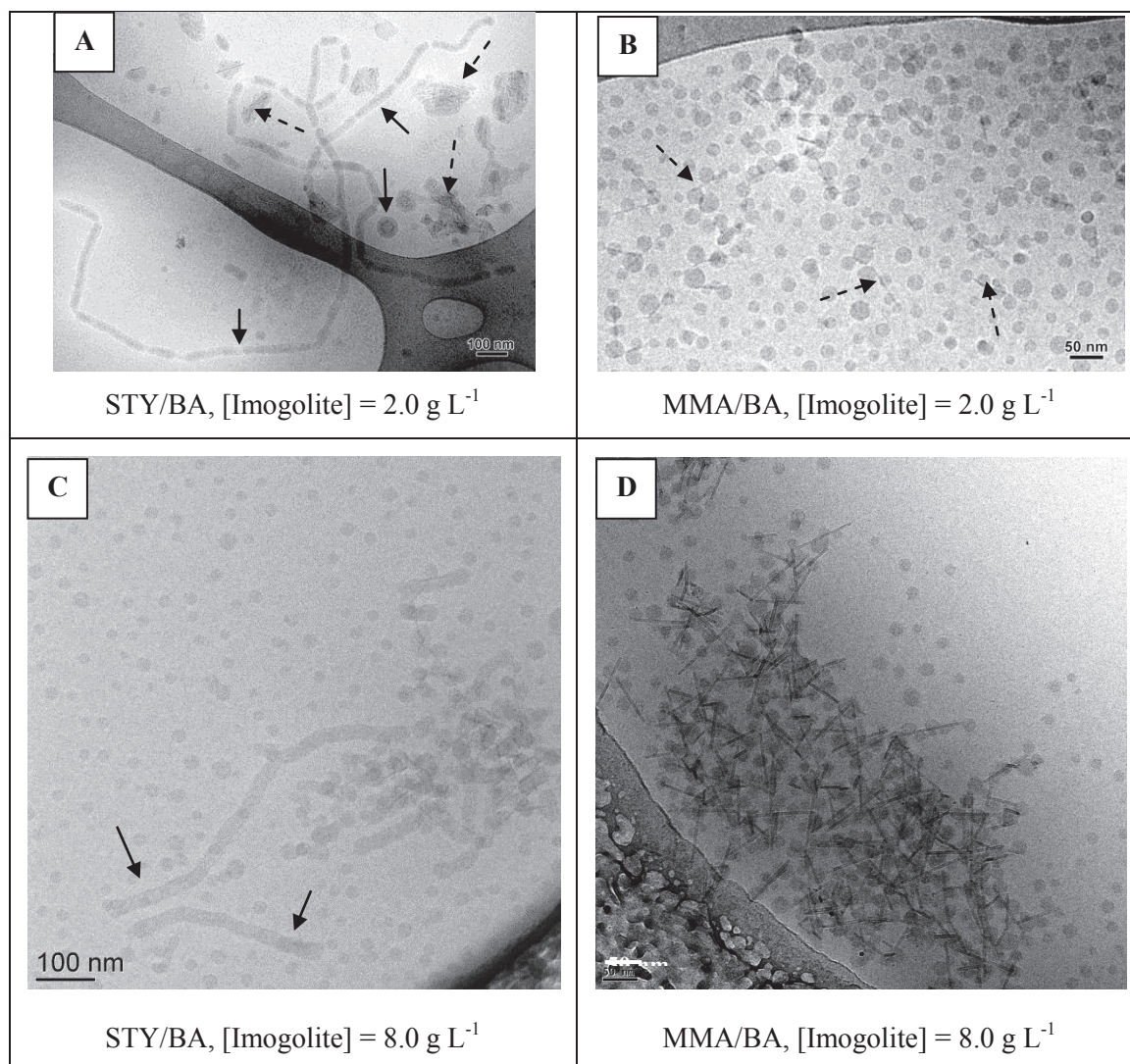


Figure 53. Cryo-TEM images of (A, C) poly(STY-*co*-BA) and (B, D) poly(MMA-*co*-BA) hybrid latexes for low (A, B) and high (C, D) Imogolite concentrations. (A, B) [macroRAFT] = 3.7 mmol L⁻¹) and (C, D) [macroRAFT] = 12.0 mmol L⁻¹). Polymerizations were performed at pH = 8.0.

Now looking at the morphologies for both compositions, some differences can also be observed. Especially at low concentrations, comparing **Figure 53A** and B, it can be seen that Imogolite is encapsulated when the polymer contains STY, while polymer-decorated tubes are obtained with MMA, as indicated by the dashed arrows. This also stands true for high macroRAFT and Imogolite concentrations (**Figure 53C** and D). The higher hydrophobicity of STY probably contributes to increase the affinity between the adsorbed macroRAFT and the monomer, which would enable the polymerization to preferentially take place on the tubes surface, generating encapsulated morphologies.

In conclusion, despite the formation of non-spherical objects like fibers and vesicles, the use of styrene as one of the co-monomers seems to favor tubes encapsulation. The addition of STY units to the growing chains would render the polymer more hydrophobic, which would have somehow the same effect as when decreasing the pH (section II.7.2.8).

In a following series of experiments, we increased the BA content for both MMA/BA and STY/BA mixtures, in order to further decrease Tg and generate film-forming latexes. The polymerizations were performed at high macroRAFT and Imogolite concentrations. The film-forming compositions were tested at both pHs, 8.0 and 6.0, with the objective to form polymer-decorated nanotubes and encapsulated nanotube bundles, respectively. **Table 22** summarizes the polymerization conditions of this new series of experiments.

Table 22. Polymerization conditions for the synthesis of hybrid latexes of MMA/BA and STY/BA of different compositions.

Entry	Monomers	Monomer ratio (wt/wt)	pH _{macroRAFT}	pH _{final}
AC245	STY/BA	70/30	8.0	8.0
AC248	STY/BA	50/50	8.0	8.0
AC246	MMA/BA	50/50	8.0	8.0
AC247	MMA/BA	50/50	6.0	6.0

[MacroRAFT] = 12.0 mM. [Imogolite] = 8.0 g L⁻¹. pH Imogolite = 6. Pathway = MacroRAFT solution added dropwise to the Imogolite suspension. Imogolite batch of L = 75 nm, SW (C1p55).

As indicated by the kinetics results shown in **Figure 54**, all polymerizations yielded satisfactory monomer consumption. With exception of the experiment made using MMA/BA at (50/50 wt/wt) and at pH 8.0, for which the final conversion was around 63%, all other experiments reached conversions around 80 to 90%. The viscosity of the latexes was observed to be higher compared to previous experiments, which usually indicates the presence of fibers.¹²⁹

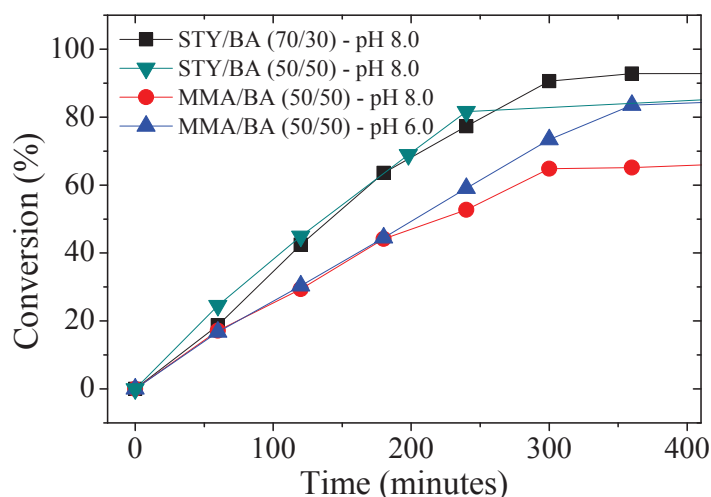


Figure 54. Monomer conversion versus time for the polymerization of STY/BA (70/30 wt/wt) at pH 8.0 (■), MMA/BA (50/50 wt/wt) at pH 8.0 (●), MMA/BA (50/50 wt/wt) at pH 6.0 (▲) and STY/BA (50/50 wt/wt) at pH 8.0 (▼) in the presence of 12.0 mmol L^{-1} of P(AA-co-BA)-CTPPA and 8.0 g L^{-1} of Imogolite.

Figure 55 shows the final morphology of the latexes, where the presence of fibers and vesicles was confirmed. The three latexes prepared at pH = 8.0 (i.e. STY/BA at 70/30 and 50/50 wt/wt, and MMA/BA at 50/50 wt/wt) formed co-existing encapsulated bundles, polymer-decorated nanotubes and partially encapsulated tubes, as indicated by the dashed arrows. Here, the change in morphology can be explained by the increase of the amount of BA, resulting in a higher hydrophobicity of the monomer mixture. This higher hydrophobicity induces the formation of partially encapsulated nanotubes, instead of the formation of exclusively polymer-decorated nanotubes, as expected at this pH. When decreasing the pH to 6.0, the hydrophobicity is increased even further, promoting the complete encapsulation of Imogolite bundles. The free chains in the aqueous phase self-assembled into spheres, fibers and vesicles. It is worth noting that the chemical nature of each monomer (i.e. molecular hindrance, radical stability, etc.) also plays an important role on defining the final morphology and driving the self-assembly of the amphiphilic block copolymers.

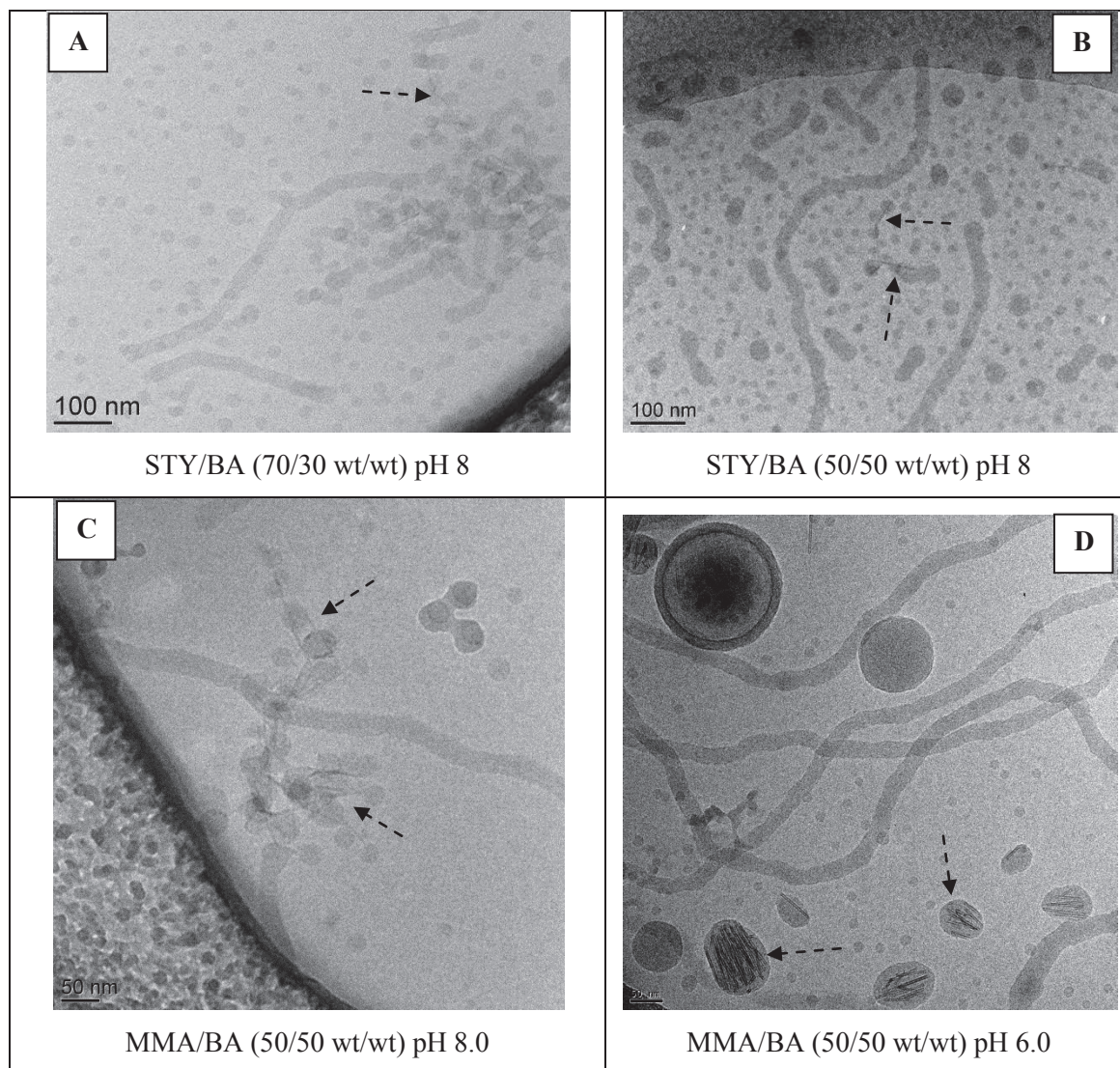


Figure 55. Cryo-TEM images of hybrid latexes of (A) STY/BA (70/30 wt/wt), (B) STY/BA (50/50 wt/wt), (C) MMA/BA (50/50 wt/wt) at pH 8.0 and (D) MMA/BA (50/50 wt/wt) at pH 6.0 synthesized with 8.0 g L^{-1} of Imogolite and 12.0 mmol L^{-1} of macroRAFT.

To better understand and further explain the formation of such morphologies (i.e. fibers and vesicles), it would be necessary to analyze the molar mass of the copolymers formed and determine if the polymerization followed or not a controlled mechanism. Unfortunately, the separation of Imogolite nanotubes from the latexes was a very time-consuming process, which was revealed to be more delicate than expected, and thus could not be performed for all the latexes.

In attempt to avoid the formation of non-spherical morphologies, we have decided to replace MMA by a monomer which would be able to conduct to the formation of a low T_g copolymer and at the same time would present a high solubility in water, since this parameter seemed to affect the particle morphology. We have then decided to work with methyl acrylate (MA). MA has a higher water solubility than STY (**Table 20**) and a homopolymer T_g of $8 \text{ }^\circ\text{C}$ (281K)¹²⁵

(Table 19). With this monomer, we kept the composition at MA/BA 80/20 wt/wt, and the copolymer T_g expected was around $-10\text{ }^\circ\text{C}$ (calculated using the Fox equation).

The experiments made using a monomer mixture of MA/BA at 80/20 wt/wt were prepared with the objective of forming encapsulated and polymer-decorated nanotubes at high Imogolite and macroRAFT concentrations. Table 23 summarizes these experimental conditions.

Table 23. Polymerization conditions and results for the synthesis of film-forming hybrid latexes of MA/BA (80/20 wt/wt).

Entry	pH _{final}	D_h (nm)/PDI	X_{final} (%)
AC249	6.0 ^a	90/0.3	72
AC250	8.0	20/0.2	100

[MacroRAFT] = 12.0 mM. [Imogolite] = 8.0 g L⁻¹. Pathway = MacroRAFT solution added dropwise to the Imogolite suspension. Imogolite batch of L = 75 nm, SW (C1p55). ^a Sample submitted to ultrasound for 5 minutes at 30% amplitude. Temperature: 80 °C.

Figure 56 shows the kinetic results for the polymerization of MA/BA (80/20 wt/wt) performed at different pHs. It can be seen that using MA the consumption of monomers is affected by the pH, and at pH 6.0, a lower final conversion was obtained.

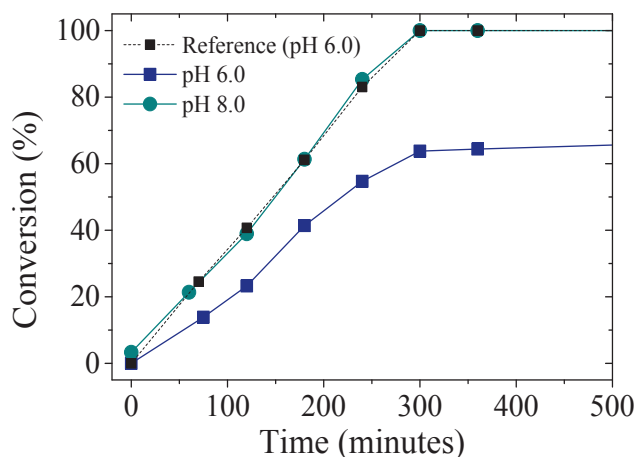


Figure 56. Monomer conversion versus time for the polymerization of MA/BA (80/20 wt/wt) without Imogolite (■, dotted line) and in the presence of Imogolite at pH 6.0 (■) and pH 8.0 (●).

For this particular hybrid latex, the Imogolite nanotubes were separated and the polymer molar mass was determined by SEC in THF (**Figure 57**). The molar mass of the reference latex with the same monomer composition (i.e. MA/BA 80/20 wt/wt) was also determined by SEC. Since this sample will be used to form films, for which mechanical properties will be measured, it was important to verify whether the molar mass obtained was in agreement with the theoretical value. This procedure was not carried out for all the latexes due to the difficulty of the Imogolite separation, as explained earlier.

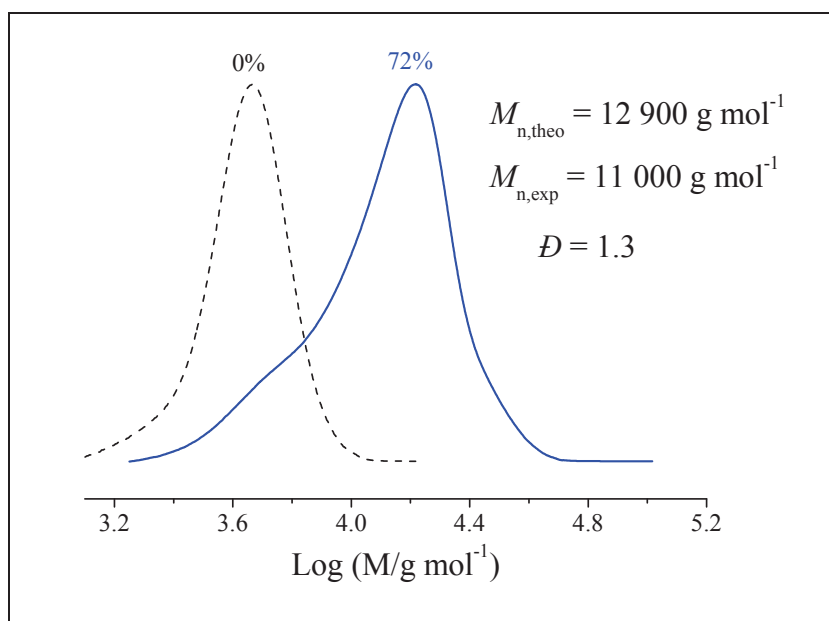


Figure 57. THF-SEC chromatogram evolution ($\log M$) with conversion of the pure polymer collected by soxhlet extraction from hybrid latex of polymer-encapsulated nanotube bundles synthesized with $[\text{Imogolite}] = 8.0 \text{ g L}^{-1}$ and $[\text{macroRAFT}] = 11.0 \text{ mmol L}^{-1}$ at $\text{pH} = 6.0$.

Figure 57 shows the THF-SEC result of the polymer extracted from the hybrid latex synthesized using MA/BA (80/20 wt/wt) at $\text{pH} 6.0$. The experimental M_n ($11\,000 \text{ g mol}^{-1}$) was close to the theoretical value ($12\,900 \text{ g mol}^{-1}$), and a narrow molar mass distribution was also obtained ($\bar{D} \sim 1.3$). This experiment revealed to be better controlled than the reference experiment (see **Annex A.4**).

Cryo-TEM analyses confirmed that in addition to the polymer-decorated nanotubes or encapsulated nanotubes bundles, only spherical polymer particles were formed (**Figure 58**). Even though the formation of fibers and vesicles could be avoided, changing MMA to MA led to another problem: the formation of a huge number of very small secondary nucleated polymer particles. This was attributed to the higher water solubility of MA compared with MMA, which favored secondary homogeneous nucleation. However, the formation of these free particles was

considered indifferent for our purpose of producing film-forming latexes with controlled morphologies.

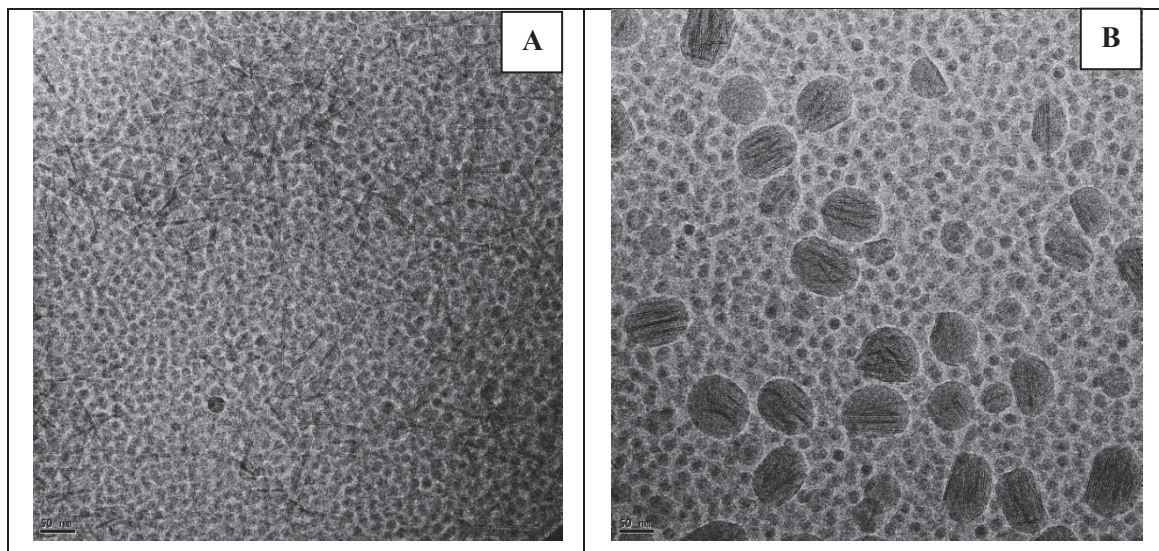


Figure 58. Cryo-TEM images of hybrid latexes of P(MA-*co*-BA)/Imogolite synthesized at (A) pH 8.0 and (B) pH 6.0 using P(AA-*co*-BA)-CTPPA macroRAFT agent.

II.8.1.2.2 Effect of tube length

To verify the applicability of our strategy to encapsulate tubes with different aspect ratios, we studied the influence of Imogolite nanotubes length (L) on morphology. In addition, micron-long Ge-Imogolite nanotubes have been shown to align themselves under external electrical field, which could generate materials with improved properties if the nanotubes present in our latexes could be aligned. In this section, the synthetic aspects as well as colloidal stability and final morphology of latexes synthesized in the presence of Imogolite nanotubes of different average L will be discussed.

Table 24 summarizes polymerization conditions and results. In this series of experiments, the tube length was varied for a fixed Imogolite content of around 2.1 % at both pH 6.0 and pH 8.0.

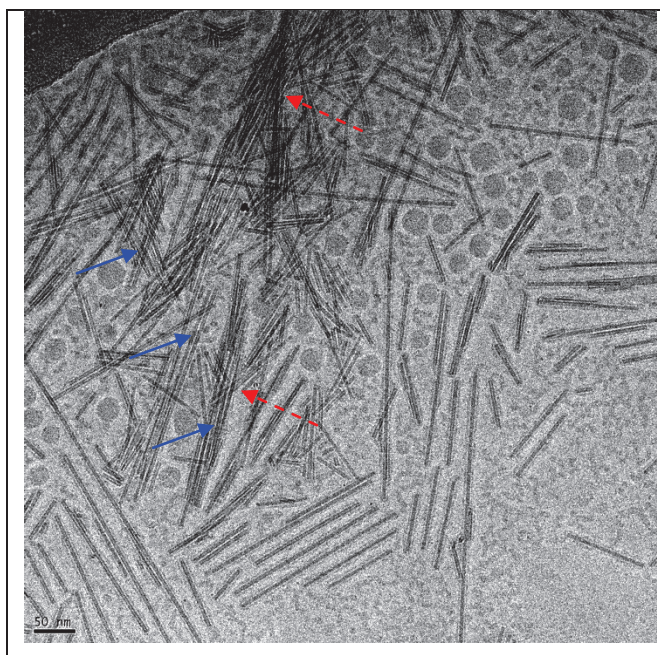
Table 24. Polymerization conditions and results for the synthesis of hybrid latexes of P(MA-co-BA) (80/20 wt/wt) containing Imogolite nanotubes of different lengths.

Entry	Imogolite / L (nm)	IMO wt% / Polymer	pH	X _{final} (%)	Morphology ^c
AC255	75	2.7	6.0	100	1
AC256	200	2.1	6.0	100	1
AC257	200	2.3	8.0	100	2
AC262	500	2.3	6.0	100	1
AC263	500	2.3	8.0	100	2

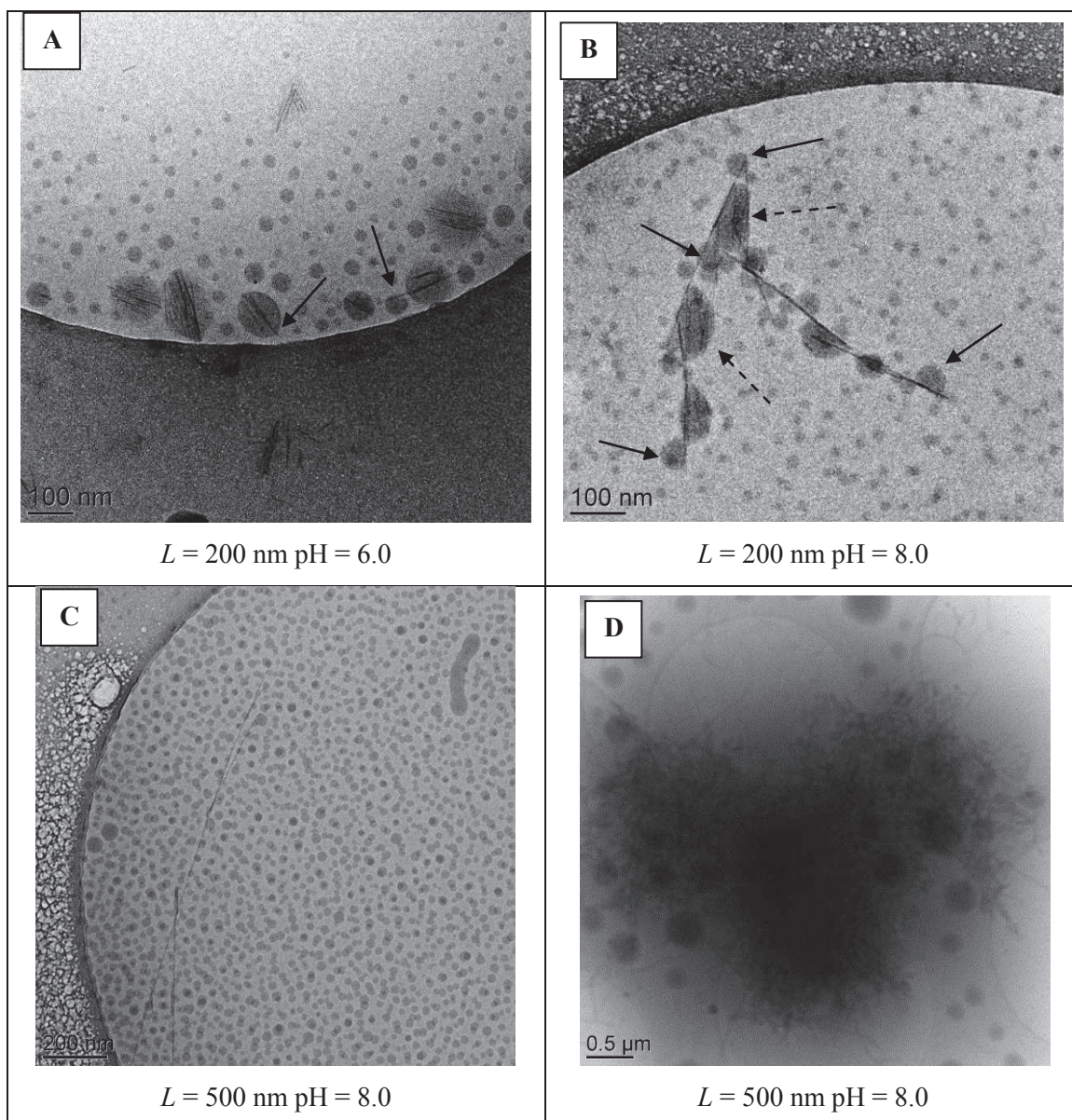
[MacroRAFT]: 6.0 mmol L⁻¹ and [Imogolite]: 4.0 g L⁻¹. ^c Morphologies 1 and 2 correspond to encapsulated bundles and polymer-decorated nanotubes, respectively. Temperature of polymerization: 80 °C.

All suspensions prepared at pH 8.0 were stable after macroRAFT addition, but the one with the longer tubes was the more viscous one. Suspensions prepared at pH 6.0 had to be submitted to ultrasound probe for 5 minutes to generate stable dispersions.

Prior to polymerization, the mixture of Imogolite with 500 nm average length and macroRAFT was analyzed by TEM to verify the dispersion state of such long tubes after treatment with our macroRAFT at pH = 6.0. **Figure 59** shows that aggregates were formed as expected, and they are quite well oriented inside the bundles (indicated by dashed arrows). Looking carefully it can be seen that the tubes do not touch one another (indicated by solid arrows), as it would be expected for pure Imogolite bundles. This suggests that the polymer is indeed around the tubes preventing them from close packing.

**Figure 59.** Cryo-TEM image of a suspension of macroRAFT-modified Imogolite tubes with average length of 500 nm at pH 6.0 after sonication for 5 minutes (30% amplitude).

The effect of the nanotubes length on morphology is shown in **Figure 60**. It appears that the aspect ratio indeed plays an important role on particles morphology. The morphologies obtained with the 200 nm length Imogolite nanotubes at pH 6.0 and 8.0 are similar to the results obtained with the shorter tubes (75 nm), except for some slight changes. For the encapsulated morphology, the extremity of the tube is seen uncovered in some particles when using these longer tubes (**Figure 60A**, arrows). In addition, when working at pH 8.0 the tubes were expected to be only decorated with polymer particles. Yet, a mixture of “empty” and loaded particles is found setting on the surface of Imogolite (**Figure 60B**, solid arrows = empty, dashed arrows = loaded). Both observations were related to the larger L which renders difficult the complete engulfment by the polymer and at the same time facilitates the formation of aggregates in the presence of macroRAFT, inducing some encapsulation at pH=8.0.



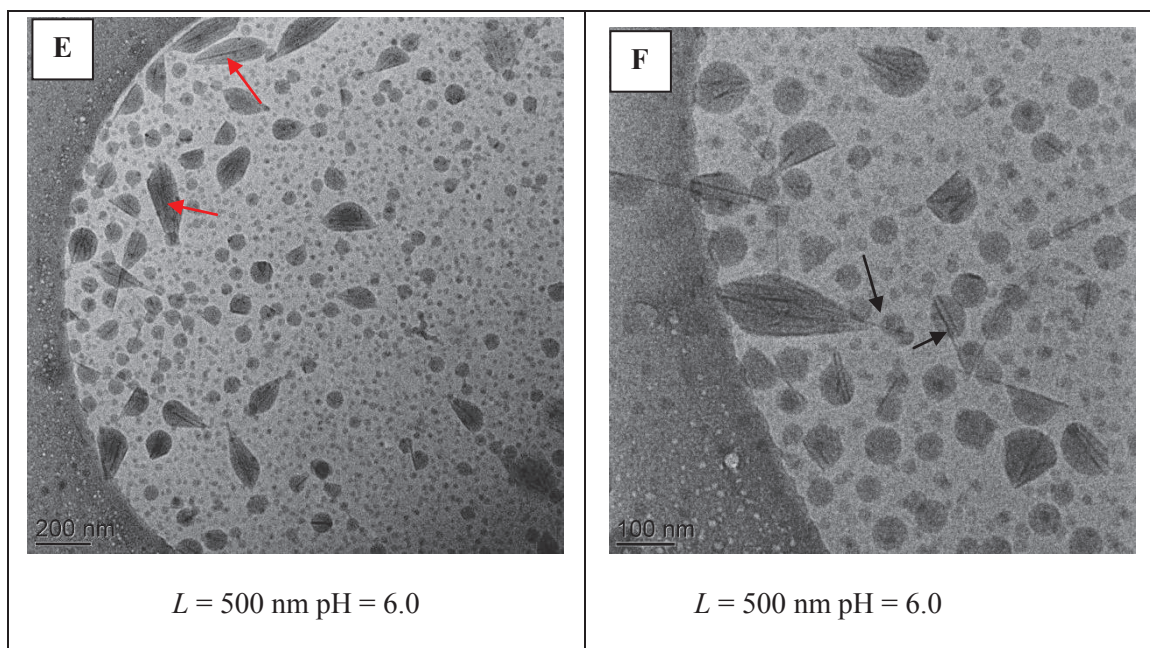


Figure 60. Cryo-TEM images of hybrid latexes of P(MA-co-BA) containing 4.0 g L^{-1} of Imogolite nanotubes of 200 nm length at (A) pH 6.0 and (B) pH 8.0; 500 nm average length at (C, D) pH 8.0, and (E, F) pH 6.0.

When working with longer tubes (500 nm) (**Figure 60 C-F**) more significant differences can be evidenced. The formation of polymer-decorated nanotubes does not seem to be affected by the length of the tubes, and very long tubes with spherical particles on the surface were obtained, as shown in the TEM image of the corresponding latex in **Figure 60C**. This latex, formed at pH 8.0 and containing extra-long tubes, presented a very high viscosity, probably due to tube-tube interaction forming some network-like aggregates, as seen in **Figure 60D**. Tube-tube interactions may be caused by electrostatic attraction between macroRAFT-modified negatively charged tubes with positively charged pristine tubes. These aggregates, which also contained some polymer particles linked to the Imogolite surface, were unstable with time, precipitating after a few hours. Phase separation was observed after a few days, where a clear solution was seen on top and a milky-white phase was seen on the bottom. At the end, only a few tubes remained in suspension. Fortunately, by vigorous stirring the latex became stable again, and stability lasted long enough for the films to be casted.

Concerning the experiment performed at pH = 6.0, **Figure 60F** shows that polymer is formed around the tubes but they tend to minimize the surface energy being as close to a sphere as possible, so the extremities of the tubes outstrip the polymer particles (indicated by the arrows in **Figure 60F**). When encapsulation is achieved, anisotropic elongated particles are formed with the entire tube inside, as indicated by the arrows in **Figure 60E**. The images suggest that the higher the aspect ratio, the more difficult the surrounding by the polymer is, making encapsulation a genuine challenge.

In summary, polymer-decorated nanotubes and encapsulated nanotube bundles could be obtained with Imogolite of different lengths. It was confirmed that the aspect ratio contributes to increase the challenge of encapsulating the inorganic nanotubes and controlling the morphology. However, satisfactory results were obtained and the latexes could be used to form films which mechanical properties were studied and will be presented in the next section of this chapter.

II.8.1.3 Conclusions

In this section the effect of the co-monomers composition was investigated in order to produce film-forming latexes. Different monomer mixtures (i.e. MMA/BA, STY/BA and MA/BA) at different compositions (80/20, 70/30 and 50/50 wt/wt) were investigated. It was shown that the hydrophobicity of the monomer mixture plays a crucial role on defining the morphology of particles formed. When a more hydrophobic monomer mixture was used, the Imogolite/polymer particles presented the tubes entirely or partially aggregated and encapsulated even at pH 8.0. This was attributed to the higher hydrophobicity together with the lower stability of the system, which generated results similar to the ones obtained before by decreasing the pH. Simultaneously, the block copolymers formed in the aqueous phase self-assembled into fibers and vesicles. The formation of non-spherical morphologies was attributed to the change in the hydrophilic/hydrophobic balance of the block copolymer. This morphology issues were overcome by replacing MMA or STY by MA, a more hydrophilic monomer which also presents lower polymer T_g . Using MA, film-forming hybrid latexes containing polymer-decorated tubes or encapsulated tube bundles could be obtained without the concurrent formation of fibers or vesicles.

The length of Imogolite nanotubes also had a strong influence on morphology. It was shown that the higher the aspect ratio of the tubes, the more difficult was the complete engulfment of the nanotubes, and elongated particles with protuberating tubes were obtained. On the other hand, the anisotropy of final particles was preserved, which was not achieved with low aspect ratio tubes. For the polymer-decorated long tubes, some stability issues were encountered, but the aspect ratio of the tubes did not affect the morphology formation.

The mechanical properties of hybrid films obtained from the latexes synthesized in this section were further investigated, in which the effect of the tubes length and the latex morphology was evaluated. The results are presented in the following section.

II.8.2 Film formation and properties

The successful incorporation of Imogolite tubes into film-forming latexes allowed us to produce hybrid films by water evaporation. As discussed in the bibliographic review, the incorporation of Imogolite nanotubes in the polymer matrix is expected to enhance the mechanical properties of the films. Mechanical properties of the pure polymer and composite films were studied for two different macroRAFT concentrations, which generated two different molar masses of the polymer constituting the matrix: $M_n = 15\ 000\ \text{g mol}^{-1}$ and $30\ 000\ \text{g mol}^{-1}$. The purpose of varying the molar mass was to evaluate the effect of the amount of AA-containing copolymer on mechanical properties. Indeed, it has been recently reported in the literature that the presence of acrylic acid units along the matrix allows inter-chain interactions, forming an ionic network that contributes to the increase of the film mechanical properties.¹³² For the high molar mass series of experiments, we also studied the effect of Imogolite length on mechanical properties. For each Imogolite length, two morphologies were evaluated: encapsulated bundles and polymer-decorated nanotubes.

II.8.2.1 Experimental section

II.8.2.1.1 Materials

Hybrid and pure polymer film-forming latexes were synthesized according to the methodology described in section II.7.1.1.2 and used without further purification. Silicon molds of 27 x 35 mm were used to cast the films. NaOH (1.0 N aqueous solution) was purchased from Sigma-Aldrich and used as received.

II.8.2.1.2 Methods

Polymer and polymer/Imogolite latexes were deposited in the silicon molds and films were cast by water evaporation at room temperature for 7 days. The resulting films were then dried under vacuum overnight prior to thermal and mechanical analyses. The films' thickness was designed to be between 0.3 and 0.4 mm.

II.8.2.1.3 Characterizations

Differential scanning calorimetry (DSC) measurements were carried out by heating 20 mg of sample from -30 to 300 °C or from -80 to 150 °C at a heating rate of 20 °C min⁻¹. This

temperature scan was repeated twice. The second set of scanning data was used to measure the glass transition temperature (T_g). DSC experiments were performed on a Mettler Toledo DSC.

The microstructure of the hybrid films was characterized by TEM analysis of a cross-section. The films were sliced using a Leica UC7 ultramicrotome under cryogenic conditions (realized by Christelle Boulé from CT μ of UCBL 1) and observed in a Philips CM120 microscope (Centre Technologique de Microstructures, CT μ , platform of University Claude Bernard Lyon 1, Villeurbanne, France) under the same conditions as described in section II.5.1.3.

The thermo-mechanical response of the material was evaluated through DMA analysis (realized by Dr. Cyril Vechambre and Dr. Laurent Chazeau from MATEIS laboratory). The measurements were performed in a homemade apparatus (MATEIS, INSA of Lyon) in torsion mode at 1 Hz and 10^{-3} rad angle from 150 K to 400 K with a heating rate of 1 K min^{-1} . Samples were typically 15 mm long (the distance between grips was then 10 mm), 3 mm wide and 0.3 mm thick. The analysis output was the variation of the complex shear modulus $G^* = G' + i.G''$ with temperature. The temperature at the maximum of loss modulus (G'') is defined as the mechanical main relaxation temperature.

SAXS and WAXS measurements were performed at the SWING beamline of the synchrotron SOLEIL (Orsay, France) as described elsewhere.¹³³ All measurements, performed by Dr. Erwan Paineau from CNRS and Dr. Antoine Thill from CEA, were carried out using a fixed energy of 9 keV and a sample to detector distance of 6.566 m for SAXS and 0.856 m for WAXS. The typical accessible range of scattering vector modulus q was $0.01 - 0.3 \text{ nm}^{-1}$ for SAXS and $0.3 - 6.0 \text{ nm}^{-1}$ for WAXS ($q = 4\pi(\sin\theta)/\lambda$, where 2θ is the scattering angle and $\lambda = 0.138 \text{ nm}$ is the wavelength). The transverse dimensions of the incident X-ray beam were approximately $300 \times 100 \text{ }\mu\text{m}^2$. 2D scattering patterns were collected in an AVIEX CCD camera formed by four detectors (with a pixel size of $167.2 \times 167.2 \text{ }\mu\text{m}^2$) and were corrected for water and glass scattering in the case of latexes. Films were analyzed without correction. Exposure times were of 100 ms. Samples of latexes were transferred into borosilicate cylindrical Lindemann capillary tubes (diameter of 1 mm, Mark-Rohrchen, Germany) and stored vertically after flame-sealing. A pair of external electrodes made of aluminum foil, in direct contact with the outer wall of the capillary, was used to apply the electric field on the sample. The electrodes are actually rings of foil, encircling completely the capillary, 2 mm apart along the capillary axis. A high frequency (500 kHz) field was applied to the electrodes, with amplitudes varying from 0 to 400 V. A detailed description of the electric-field setup is given in the literature.^{134, 135}

II.8.2.2 Results and Discussion

The microstructure and mechanical behavior of two series of latexes were investigated. The first series consisted on low molar mass copolymers ($M_n = 15\,000\text{ g mol}^{-1}$, $D = 1.3$) with Imogolite nanotubes of 75 nm of length and at 6.2 wt% related to polymer. For the second series, the latexes used contained copolymers with a higher molar mass ($M_n = 30\,000\text{ g mol}^{-1}$, $D = 1.5$) and Imogolite nanotubes of different lengths (i.e. 75 nm, 200 nm and 500 nm) at 2.3 wt% related to polymer. For each series, a reference film, without Imogolite, was also prepared to be compared with the nanocomposite films. The latexes used in this study are presented in **Table 25**.

Table 25. Characteristics of the reference and the hybrid latexes used to prepare the films.

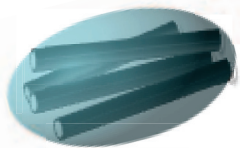
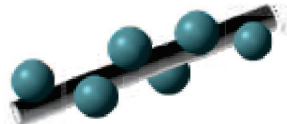

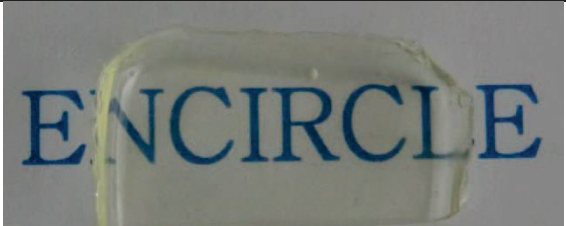


Entry	Imogolite / L (nm)	IMO wt% / Polymer	Morphology
AC20ab	-	Reference ^a	-
AC20ac	-	Reference ^b	-
AC249	75	6.2	1
AC250	75	6.2	2
AC251	75	2.3	1
AC252	75	2.3	2
AC256	200	2.3	1
AC257	200	2.3	2
AC262	500	2.3	1
AC263	500	2.3	2

^a Latex without Imogolite ($M_n = 15\,000\text{ g mol}^{-1}$, $D = 1.3$). ^b Latex without Imogolite ($M_n = 30\,000\text{ g mol}^{-1}$, $D = 1.5$). 1 = Encapsulated bundles. 2 = Polymer-decorated nanotubes.

Table 26 shows the visual aspect of the films formed with latexes of different morphologies containing Imogolite nanotubes of different lengths. The high transparency of the films would be a first indication of the uniform distribution of the tubes within the polymer matrix. However, the refractive indexes found for Imogolite and for the polymer ($1.47 - 1.51$ ¹³⁶ and 1.45 ,¹²⁵ respectively) are too close to conclude on the presence of aggregates.

To better understand the effect of the presence of Imogolite and the effect of the hybrid particles morphology on the final mechanical properties of the films, the microstructure of some of the films was investigated. The films containing the shorter tubes ($L = 75\text{ nm}$) and the ones containing the longer tubes ($L = 500\text{ nm}$) were cross-sectioned by cryo-ultramicrotomy, and the thin films were observed by TEM at room temperature.

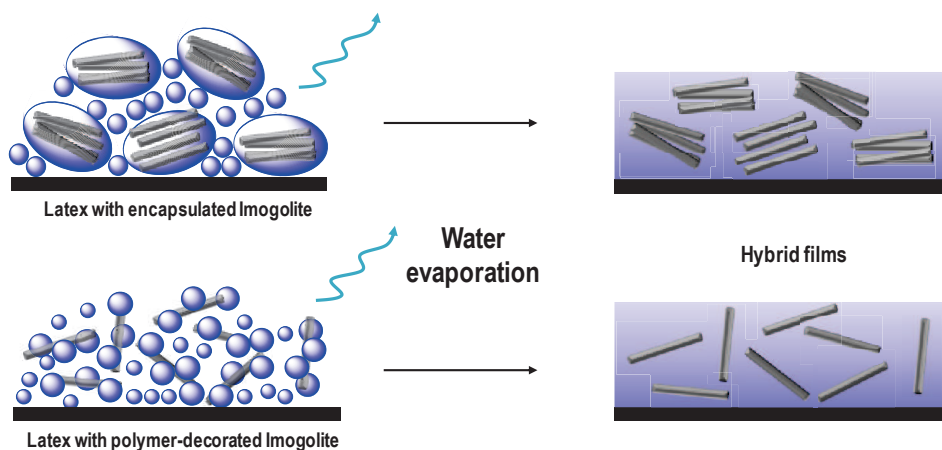
Table 26. Photographic images illustrating the films visual aspect according to particles morphology and Imogolite tubes length.

	
	
AC256 ($L = 200$ nm, encapsulated)	AC257 ($L = 200$ nm, decorated)
	
AC262 ($L = 500$ nm, encapsulated)	AC263 ($L = 500$ nm, decorated)

II.8.2.2.1 Films microstructure

The hybrid film microstructure can have an important influence on the overall behavior of the nanocomposite material. As seen in the bibliographic chapter, the inorganic fillers uniform distribution within a polymer matrix and the filler/matrix interface are key factors to improve mechanical strength, stiffness and resistance to break. The enhancement of mechanical properties originates from the fact that the polymer-filler interface acts as an extra rigid phase in the material, reducing the polymer mobility in these regions. In addition, the fillers can also form a percolating network, which further contributes to the enhancement of properties, facilitating the inter-nanoparticle energy transfer¹³⁷.

Without any external force applied, Imogolite nanotubes are expected to settle down in a certain manner, depending on the hybrid latex morphology. Especially for the short tubes, no preferential orientation was expected, although some differences between encapsulated bundles and polymer-decorated tubes regarding the tubes dispersion in the matrix could be anticipated (**Scheme 61**).



Scheme 61. Illustrative representation of the film formation of hybrid latexes with different morphologies and the predicted microstructures of the films.

As illustrated in **Scheme 61**, the encapsulated tubes are expected to remain in bundles with a relatively uniform spatial distribution of each aggregate. Moreover, the tubes inside each particle could probably keep their internal orientation, forming nano-domains of oriented tubes.

Indeed, **Figure 62A** shows the low magnification TEM images obtained for the hybrid films containing encapsulated short tubes. The light gray continuous phase corresponds to the polymer matrix, while the black objects correspond to Imogolite nanotubes. As evidenced in **Figure 62B**, the tubes maintained their relative orientation inside each aggregate, forming nano-domains of about 100 nm in which Imogolite was preferentially aligned in one direction. Even though such results are not prodigious, the possibility of duplicating such morphologies with longer tubes was quite encouraging.

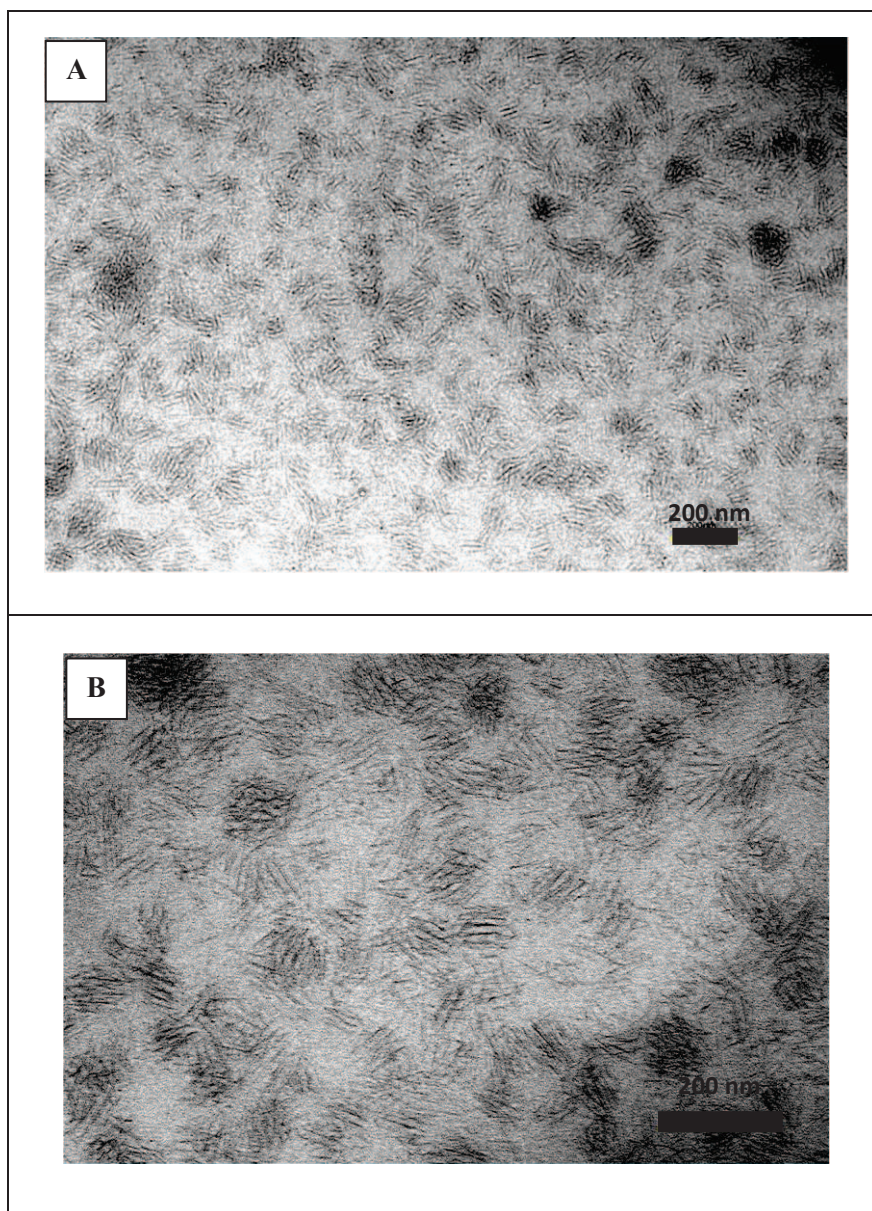


Figure 62. Low (A) and high (B) magnification TEM images of the cross-sectioned film containing encapsulated Imogolite of $L = 75$ nm and polymer $M_n \sim 15\,000$ g mol⁻¹.

Similar behavior was expected for the non-encapsulated morphology, except that in this case, the tubes should be isolated inside the polymer matrix, since no aggregates were formed (**Scheme 61**). TEM images showed equally fair distribution of the tubes compared to the previous sample, as shown in **Figure 63A** and B. As expected, no preferential alignment of the tubes was observed either.

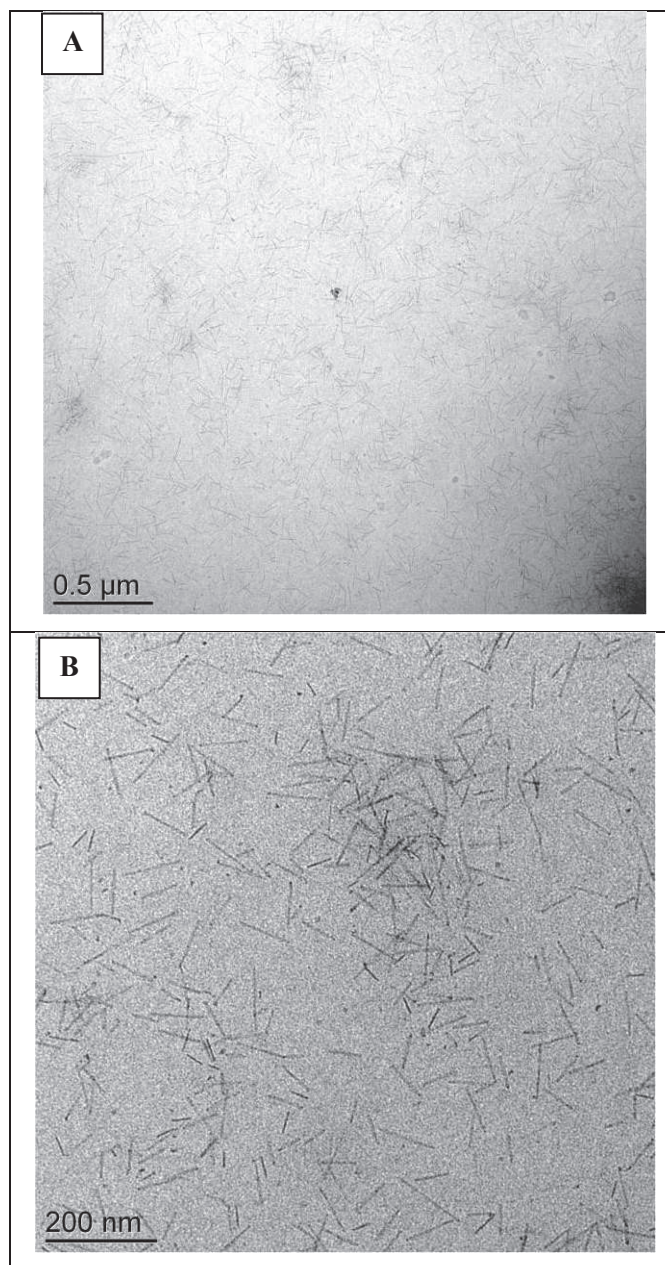


Figure 63. Low (A) and high (B) magnification TEM images of the cross-sectioned film containing polymer-decorated Imogolite of $L = 75$ nm and polymer $M_n \sim 15\,000$ g mol⁻¹.

Interestingly, when increasing Imogolite length to 500 nm, some trend on nanotubes orientation started to be drawn. As it can be seen in **Figure 64**, even for the sample in which Imogolite was encapsulated, some preferential alignment was observed. The high aspect ratio of the tubes has most likely driven the objects to settle down arranging their basal planes (i.e. tube longer axis) horizontally in the film. The high contrasted black short traces and dots, indicated by the circles, were attributed to nanotubes placed perpendicularly to the film plane. The polymer shell around these tubes and their short size (considering that they represent the portion of small tubes in the sample) facilitate their mobility, allowing them to adopt a vertical orientation. Observations of the high magnification TEM image (**Figure 64B**) revealed aggregates of tubes presenting some

orientation inside the particle domain, similarly to what had been seen for the tubes with $L = 75$ nm. It can also be attested that the aggregates are less homogeneous in terms of size, and tubes of various lengths are seen.

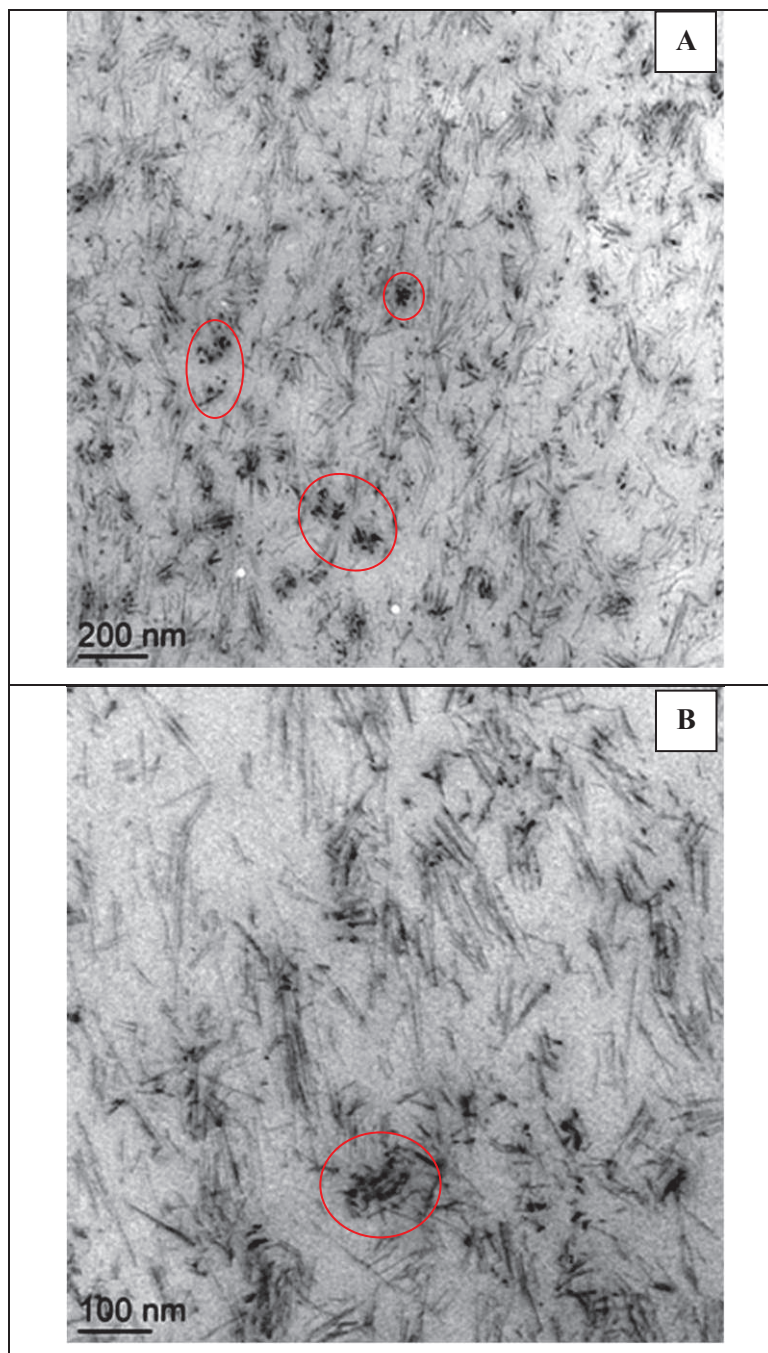


Figure 64. Low (A) and high (B) magnification TEM images of the cross-sectioned film containing encapsulated Imogolite of $L = 500$ nm and polymer $M_n \sim 30\,000$ g mol⁻¹.

The latexes containing the long tubes (i.e. $L = 500$ nm) non encapsulated, yielded films with an even higher self-organization of Imogolite in the matrix. As shown in **Figure 65A**, the preferential horizontal arrangement of the tubes is more pronounced than it was for the previous

sample (encapsulated long tubes). Being isolated in the matrix, their overall aspect ratio is kept quite high, which considerably reduces their mobility even further. With the mobility restraint, they naturally settle down horizontally during film formation, roughly following the orientation of the adjacent tubes.

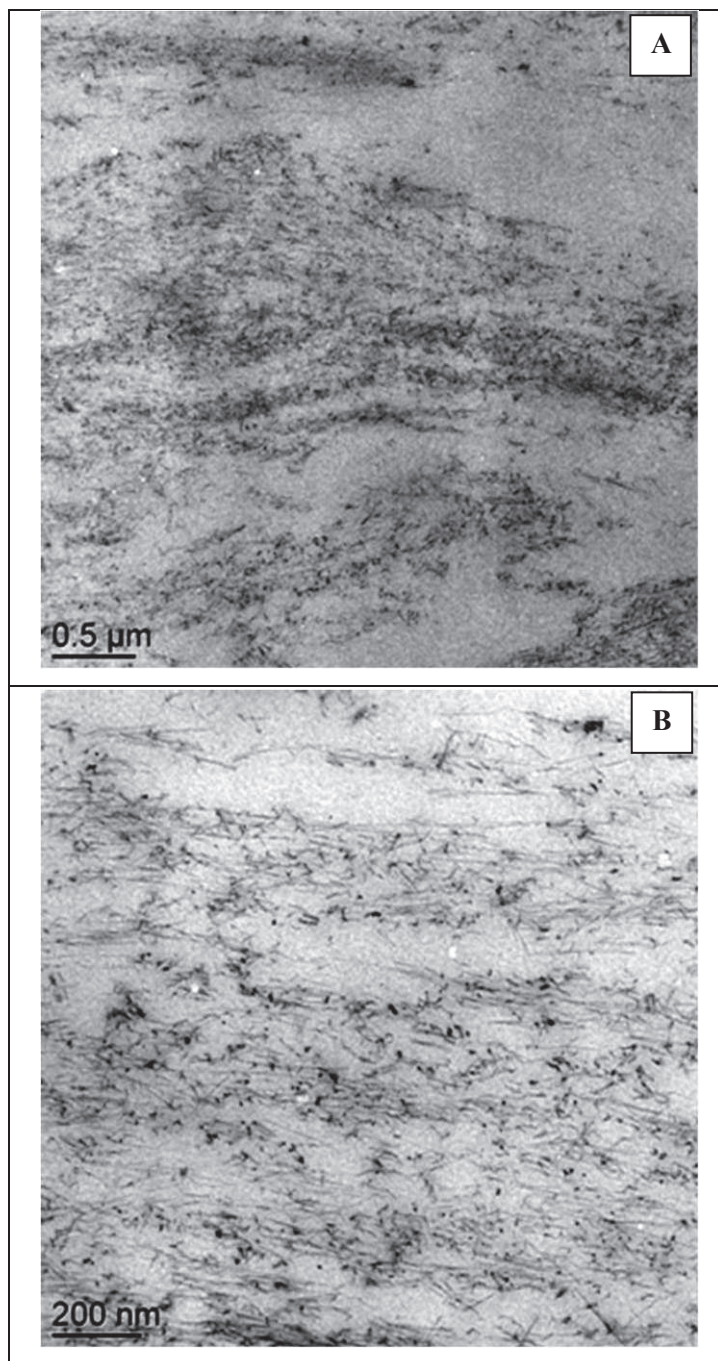


Figure 65. Low (A) and high (B) magnification TEM images of the cross-sectioned film containing polymer-decorated Imogolite of $L = 500$ nm and polymer $M_n \sim 30\,000$ g mol⁻¹.

Imogolite nanotubes provide a huge surface area for the development of the polymer-filler interface. Such high interface has probably an important effect on the film's properties. In addition, the partial alignment observed for the films containing long Imogolite nanotubes could also provide further increment in the film properties. In the next section, the mechanical tests performed for the films of pure polymer and for those containing Imogolite of different lengths will be presented.

II.8.2.2.2 Mechanical properties of the films

The thermo-mechanical response of pure polymer films and hybrid films containing Imogolite of different lengths and with different morphologies (i.e. different microstructures) was measured. Pure polymer films, composed of the same P(AA-co-BA)-*b*-P(MA-co-BA) block copolymer of two molar masses 15 000 and 30 000 g mol⁻¹ used in the hybrid series, were herein called "reference" samples. The results obtained for these polymer films were compared with the hybrid materials in order to determine if any reinforcement was provided by the nanotubes.

Thermo-mechanical response of films without Imogolite

Figure 66 shows the DMA results for both reference samples, at 15 000 and 30 000 g mol⁻¹. A relatively high mechanical strength was observed, initially not expected especially for the low T_g and low molar mass materials (i.e. 15 000 g mol⁻¹). The main events that can be extracted from the DMA results are: a glassy modulus of the order of the Giga-Pascal obtained for both samples; one main mechanical relaxation temperature (T_α) found in both cases, suggesting only one T_g for the final block copolymers; a viscoelastic behavior above the main mechanical relaxation, where the modulus is higher for the lower molar mass. The viscoelastic behavior above T_α is the sign of a non-purely elastic network, i.e. absence of cross-link points. This comportment is related to a weak network such as physical bonds or entanglements, and is common for uncross-linked polymers. However, the difference of the shear modulus in the rubbery state between the low and high molar masses is unexpected. In rubbery networks, it is expected that the shear modulus increases with the molar mass until it approaches the critical mass between entanglements (M_c).

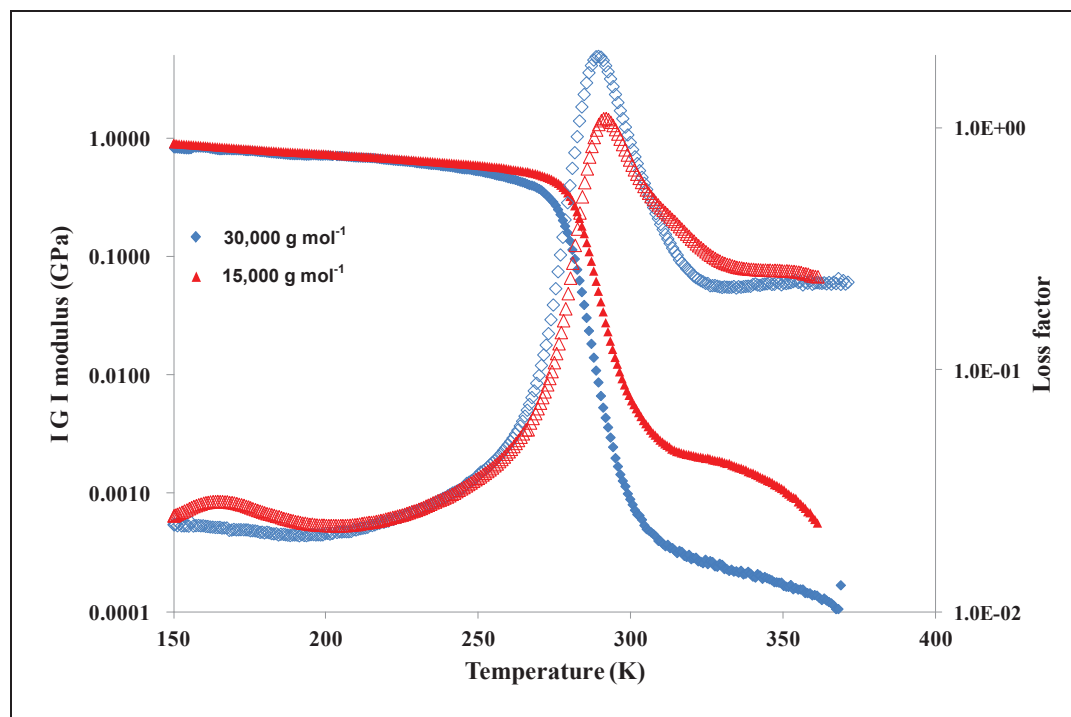
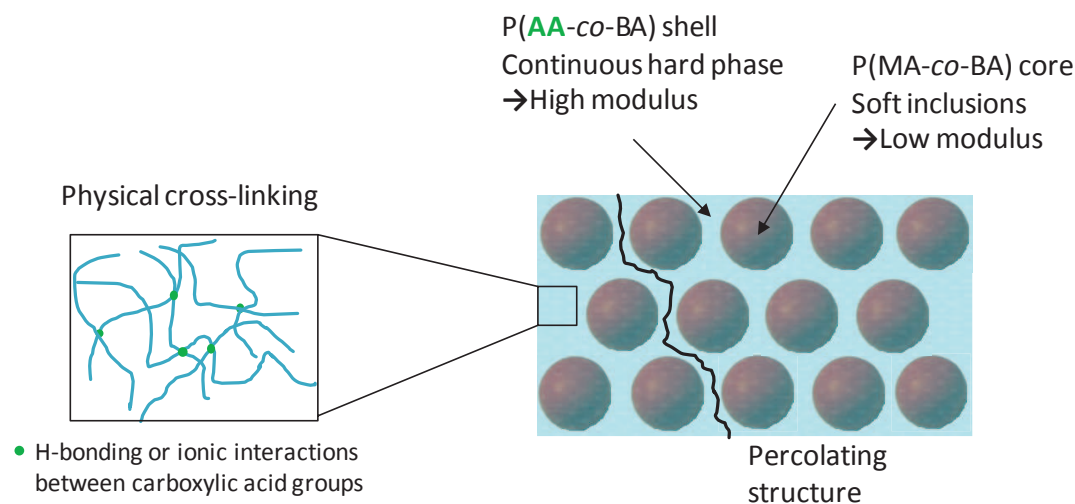


Figure 66. Storage modulus and loss factor as a function of temperature for polymer films of P(AA-co-BA)-*b*-P(MA-co-BA) of 15 000 g mol⁻¹ (▲) and 30 000 g mol⁻¹ (◆).

In regard of the latex composition, it is noticed that the lower mass showed a more pronounced shell content (i.e. 25%) than the higher mass (i.e. 13%). In a core/shell latex it is expected that during coalescence of particles a reminiscence of the core shell structure is maintained. The continuum phase in such structure is the shell (**Scheme 67**). Here the shell is composed of a statistic copolymer made of BA and AA of molar mass $M_n = 3\,500\text{ g mol}^{-1}$, for the two different molar masses (15 000 g mol⁻¹ and 30 000 g mol⁻¹), which is far below the critical entanglement masses ($M_c=3M_e$), where M_e is reported to be 26 500 g mol⁻¹ for BA and 1 000 g mol⁻¹ for AA¹³⁸. The shear modulus observed in the rubbery plateau must be viewed elsewhere than in the entangled regimes. For instance, PMAA is known for its tendency to form intermolecular H-bonding or dipole-dipole interactions of the acid groups, which could analogously happened with PAA.¹³⁹ A recent work from Chenal *et al.*¹³² is particularly relevant to show the influence of PAA when it is located at the outer surface of the latex particles prepared in emulsion polymerization. They showed that the PAA, although in a very low volume fraction (<5%) and below M_c , form a percolated phase which shows peculiar strength as well as a surprising resistance of the films for different organic solvents. This behavior was explained by the presence of a dense hydrogen bond network. Here, from the behavior observed for the two different compositions we conclude that the stiffness results from a percolated network of physical interactions (H-bond or ionic) (**Scheme 67**).

The results obtained from DMA allow proving that a reminiscence of the core-shell structure is maintained after particles coalescence as well as the presence of a physical network made of hydrogen bonds and/or electrostatic bonds.



Scheme 67. Illustrative representation of the film obtained from core/shell latex in which the core is a soft polymer and the shell is a hard polymer capable of physical cross-linking.

To investigate the stability of the core/shell structure, the films were submitted to a thermal treatment at 100 °C for 48h. After treatment the material was re-analyzed by DMA, and a superposition of results was found, confirming the stability of the core/shell structure.

In summary, the results obtained with the reference sample, in the absence of Imogolite, already presented some complex features, and the precise explanation of their thermal-mechanical response was less trivial than expected. Further investigation concerning the microstructure of the pure polymer films is certainly necessary to properly explain these results. However, some consistent conclusions could be drawn based on recent publications.

Effect of latex morphology

These results were then compared to the thermo-mechanical behavior of the hybrid films, to study the effect of Imogolite on the material's properties. In a first study, the effect of morphology was investigated for both low and high molar mass polymer matrixes.

Figure 68 shows the DMA results obtained for the films composed of low molar mass polymers ($15\,000\text{ g mol}^{-1}$) with encapsulated or polymer-decorated nanotubes. It is clearly seen that the

films containing the non-encapsulated tubes presented a higher modulus both below and above T_{α} (i.e. glass and rubbery modulus). This increase in stiffness results from a reinforcement of the continuum phase (shell) and where the interface between shell and Imogolite are high enough to induce such reinforcement of 1 decade. It can as well arise from percolation of Imogolite; however, **Figure 68** does not allow us to conclude on the presence of a percolation of Imogolite. Results obtained for the material containing encapsulated tubes also presented higher modulus when compared to the reference film. However, their rubbery modulus was lower than the one found for the films with non-encapsulated tubes. This increase in stiffness in the rubbery state for encapsulated tubes in comparison to the reference films was in a first attempt not expected. Reinforcing soft inclusions would lead to a very low increase of the stiffness. The possibility of a phase inversion was excluded as proven by **Figure 62**, confirming that the shell remains the continuum phase. We assume that this compartment arises from the dense packing of the tube in the core, creating a more pronounced reinforcement effect leading to materials made of soft matrix with hard inclusion, i.e. the shell must be view as softer than the core, with the interface between core and shell being considerably strong.

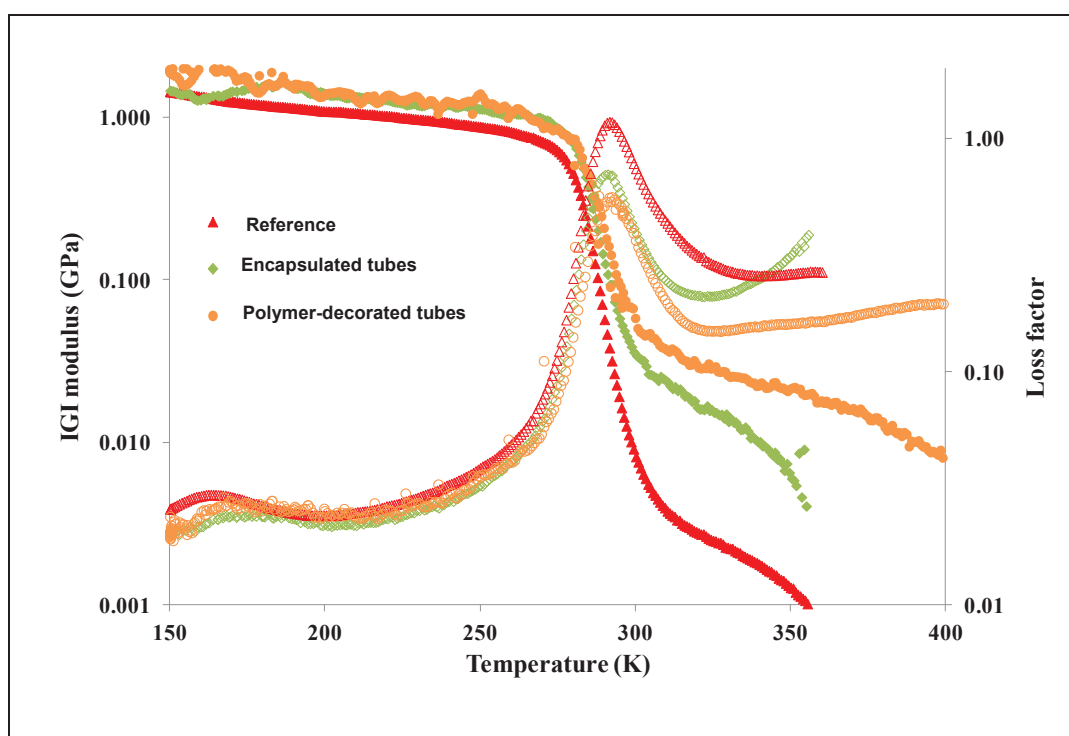


Figure 68. Storage modulus and loss factor as a function of temperature for polymer films of P(AA-co-BA)-*b*-P(MA-co-BA) of $15\ 000\ \text{g mol}^{-1}$ without Imogolite (\blacktriangle) and hybrid films of the same polymer with encapsulated Imogolite (\blacklozenge) and polymer-decorated Imogolite (\bullet).

Figure 69 shows the DMA results obtained for the films composed of high molar mass polymer ($30\ 000\ \text{g mol}^{-1}$) with encapsulated or polymer-decorated nanotubes. Again, the samples

containing non-encapsulated tubes presented the higher rubbery modulus. This was attributed to the presence of a strong interface between the tubes and the shell as well as the possibility of a percolating network of tubes, providing effective reinforcement to the material. Interestingly, for the sample containing encapsulated tubes, the behavior observed is analogous to the reference sample. This behavior is expected for a hard matrix containing soft inclusions, in absence of percolated networks. This difference of behavior in regard to the low molar mass sample containing encapsulated tubes (**Figure 68**) can be explained by a less dense packing of the tubes in the core, i.e. the tubes are able to move more freely. They are then considered as fillers in the soft inclusions, and do not contribute to the reinforcement of the continuous hard phase of the matrix.

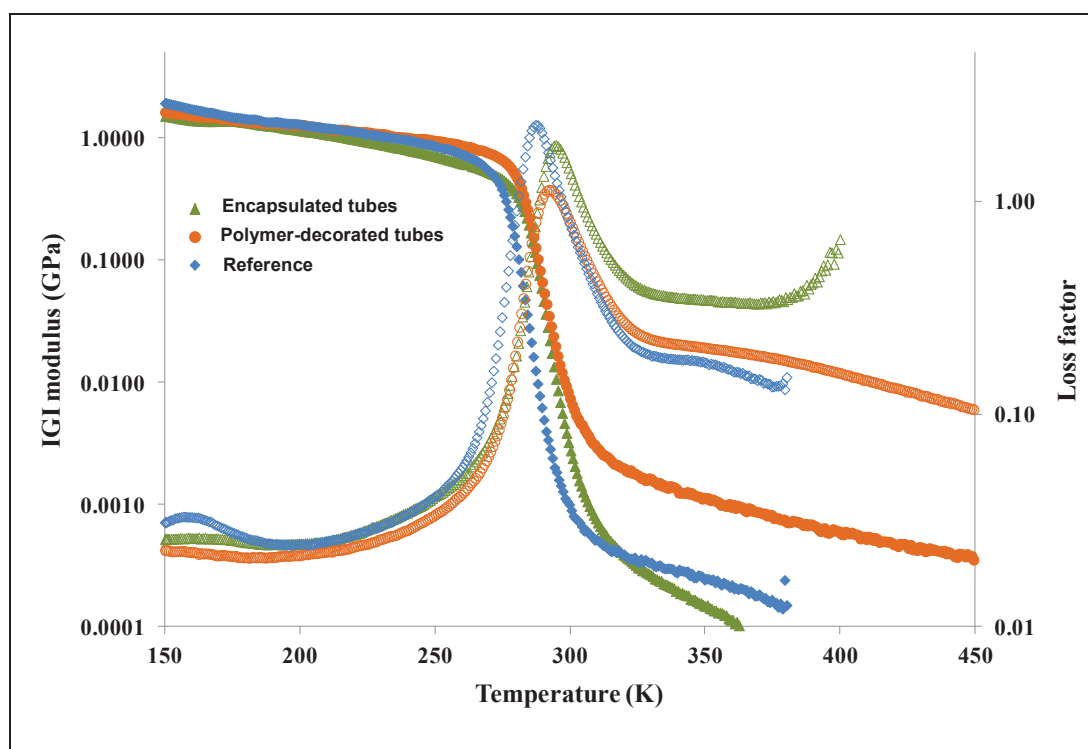


Figure 69. Storage modulus and loss factor as a function of temperature for polymer films of P(AA-co-BA)-*b*-P(MA-co-BA) of $30\,000\text{ g mol}^{-1}$ without Imogolite (\blacklozenge) and hybrid films of the same polymer with encapsulated Imogolite (\blacktriangle) and polymer-decorated Imogolite (\bullet).

Effect of Imogolite length (L)

The next series of results compared the nanotubes length between films of either polymer-decorated morphologies or encapsulated nanotubes. In this study, all films were composed of high molar mass copolymer ($30\,000\text{ g mol}^{-1}$).

As it can be seen in **Figure 70**, for the high molar mass copolymer films the encapsulation of the nanotubes inside the soft core impedes percolation and does not contribute to the effective

reinforcement of the material. For the sample containing the very long tubes, as it was seen in section II.8.1.2.2, some tubes are not completely covered by the polymer, surpassing the particle borders. It was also seen in section II.8.2.2.1 that after film formation, the tubes presented some level of organization, and their edges could be in contact with each other. It could then be assumed that the long tubes were more easily able to form a percolated network, thus contributing to the reinforcement of the material.

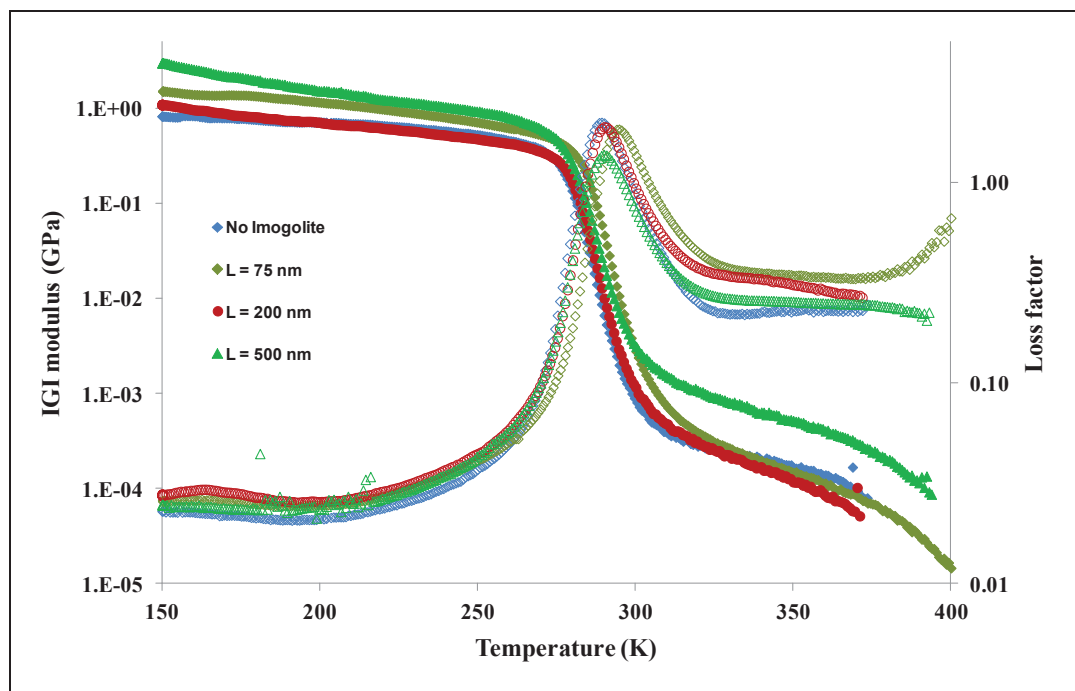


Figure 70. Storage modulus and loss factor as a function of temperature for polymer films of P(AA-co-BA)-*b*-P(MA-co-BA) of $30\,000\text{ g mol}^{-1}$ without Imogolite (♦) and hybrid films of the same copolymer with polymer-decorated Imogolite of 75 nm (◆), 200 nm (●) and 500 nm (▲).

Figure 71 shows the results obtained for the samples containing non-encapsulated tubes. For these samples, the presence of tubes resulted in the increase in the rubbery modulus compared to the reference sample. The stiffness in the rubbery plateau was found identical for samples containing Imogolite of 75 and 200 nm. This behavior may be explained by the absence of tube percolation and where the mechanical response arises from the interface between tubes and shell. When the tube length reached 500nm it is observed a huge increase of the stiffness in the rubbery plateau, which was of 2 orders of magnitude higher than the reference sample and 1 order of magnitude higher than the film containing shorter tubes. Such an increase must be viewed in the creation of a percolating network of tubes, i.e. physical contact between tubes, which was possible by the presence of non-decorated polymers area along all the tubes.

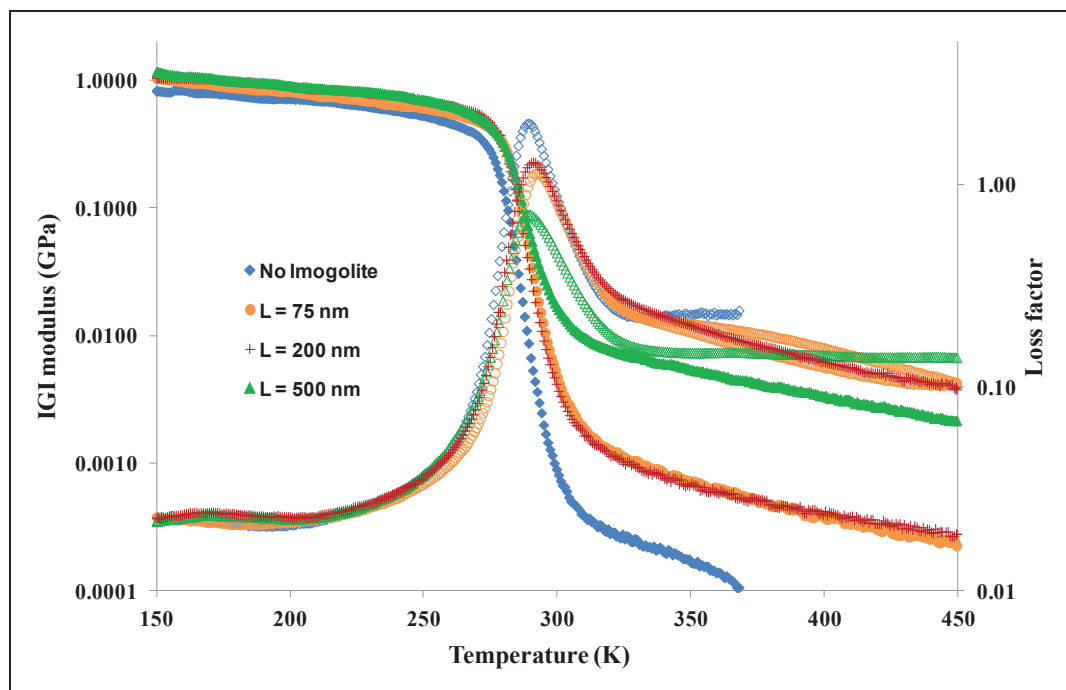


Figure 71. Storage modulus and loss factor as a function of temperature for polymer films of P(AA-co-BA)-*b*-P(MA-co-BA) of $30,000 \text{ g mol}^{-1}$ without Imogolite (\blacklozenge) and hybrid films of the same polymer with non-encapsulated Imogolite of 75 nm (\bullet), 200 nm ($+$) and 500 nm (\blacktriangle).

We were aware that the presence of hydrophilic moieties in the films increases its water adsorption. Thus, the relative humidity of the environment could also influence the results. Despite our efforts to vacuum dry the samples before analysis there was still the possibility that the films contained different water amounts.

The various parameters involved in the latexes synthesis (e.g. the AA ionization degree, the particles' morphology, the nanotubes length and orientation, etc.) should be taken into account to build a model and predict the film properties. All the data obtained in this work is being compiled and scrutinized in order to build a prediction model.

In conclusion, it was observed that the creation of a physical network in the pure polymer allows to obtain rubbery behavior, which was attributed to interactions (i.e. H-bonds and electrostatic) formed by the AA units in the hydrophilic block (macroRAFT). The incorporation of Imogolite into the matrix resulted in increased rubbery modulus when percolation was possible. The encapsulation of the short tubes (75 and 200 nm) impeded the inter connection between them, providing almost no reinforcement to the matrix when this latter was composed of high molar mass copolymers. Non-encapsulated tubes could effectively provide reinforcement to the material, and the reinforcement increased with increasing the tubes length. Further enhancement of the modulus was obtained when long tubes were used.

II.8.2.2.4 Nanotubes alignment under electric field

In a first step the latexes containing Imogolite tubes of 500 nm either encapsulated (AC262) or non-encapsulated (AC263) were analyzed by SAXS under electric field, to verify if an additional ordering resulting from the alignment of the tubes was seen.

The latexes were placed into borosilicate cylindrical capillary tubes and submitted to external electric field (e-field) at the same time as they were subjected to the X-ray beam. Different electric voltages were applied to observe the evolution of the structure under increasing electrical field intensity.

Figure 72 shows the X-ray diffraction patterns and the scattering diagrams obtained for the sample containing the long tubes encapsulated and submitted to increasing electrical field intensity. As the images show, no anisotropic organization was detected even under the application of the higher field (200 V/mm), indicated by the perfectly spherical patterns. Consistently with these results, the scattering diagrams showed only one structure peak corresponding to 32 nm, which stands for the Imogolite loaded particles, but no additional ordered structure was obtained. This behavior was attributed to both the high salinity of the sample, which increases the conductivity of the medium disturbing the effect of the e-field, and the presence of the polymer shell around the tubes, which could also hinder the Imogolite response to the e-field.

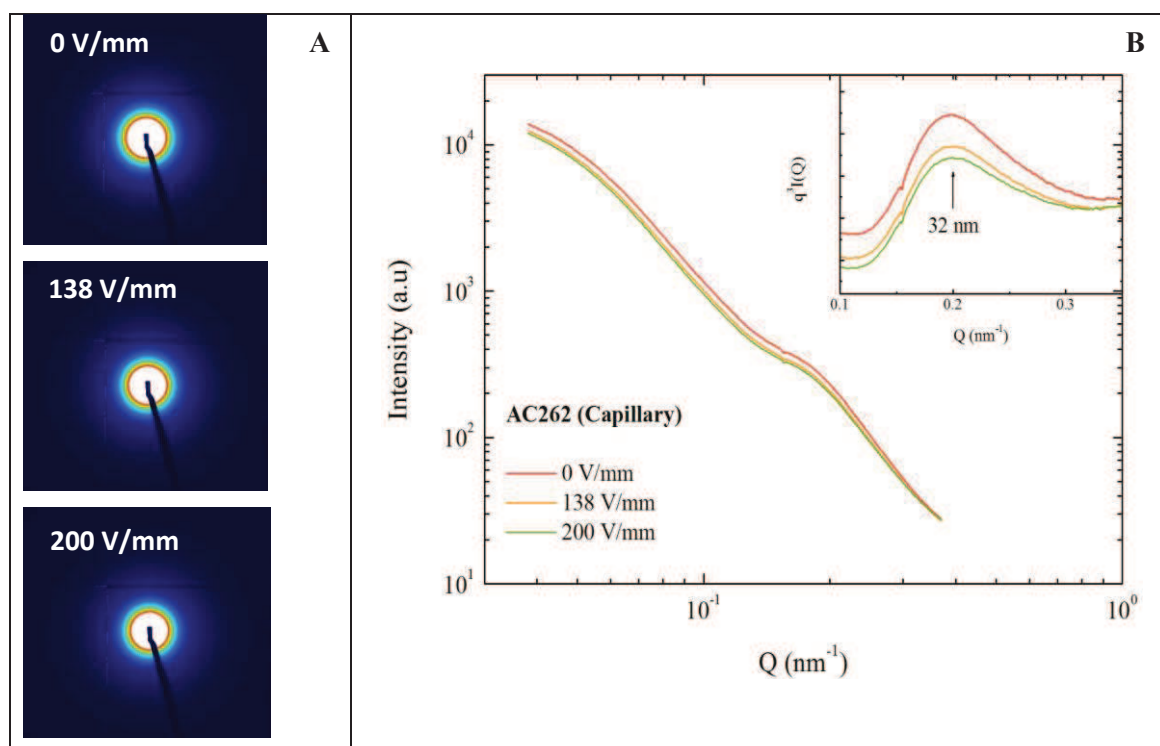


Figure 72. (A) X-ray diffraction patterns at increasing electric field intensities and (B) scattering diagram of intensity I (a.u.) versus Q (nm^{-1}) obtained through SAXS measurements of the latex containing Imogolite of 500 nm encapsulated.

The sample containing polymer-decorated tubes seemed more promising, since the tubes were still exposed and could probably respond better to the e-field. For this sample, the electric field intensity was constant, but four series of measurements were made at increasing times. The second and the fourth measurements are indicated as 2nd step and 4th step.

Figure 73 presents the results obtained for this sample. As it is seen, even for the non-encapsulated nanotubes the electrical field did not seem to have any effect on the Imogolite organization or orientation. According to the perfectly spherical X-ray scattering patterns, no ordering structure was formed, even after the four series of measurements. The scattering diagrams also accorded to these findings, and only one structure peak corresponding to 35 nm was observed, which suggests that no additional ordering took place. Actually, under the conditions in which the tubes are not encapsulated, the formation of aggregates is not expected. However, the very long tubes were more difficult to stabilize, and probably some bundles or swelled aggregates were formed, explaining the structure peak at around $1.5 \times 10^{-1} \text{ Q (nm}^{-1}\text{)}$.

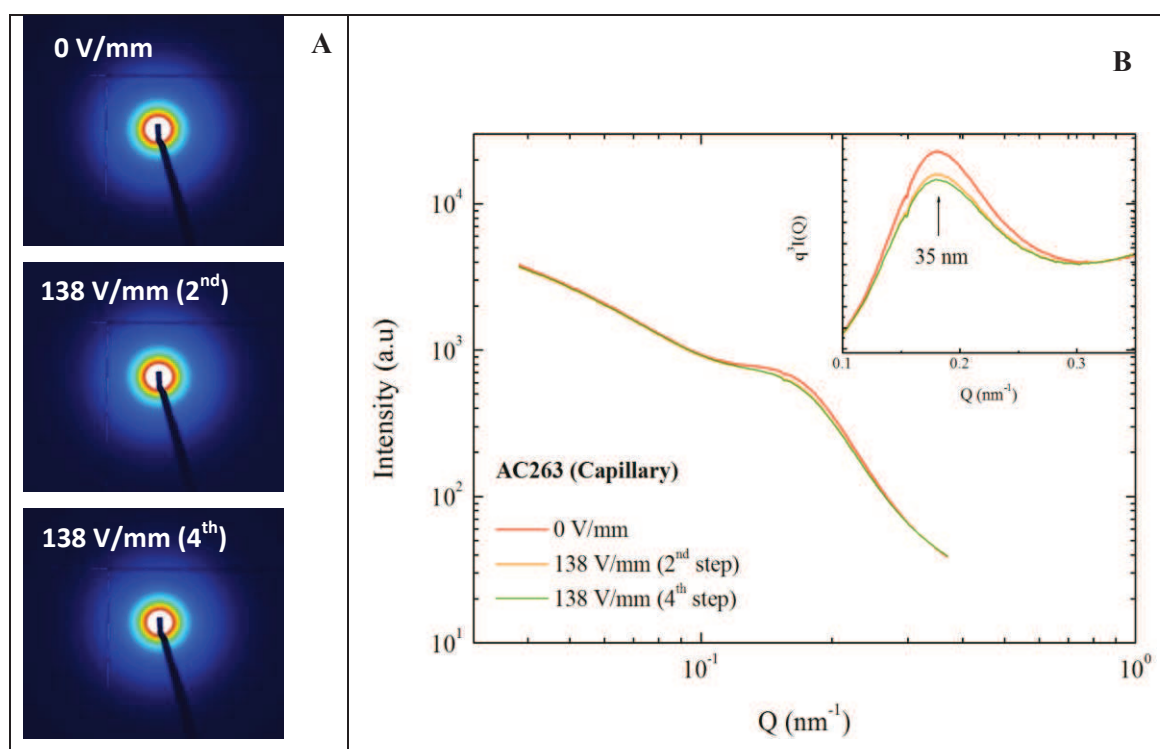
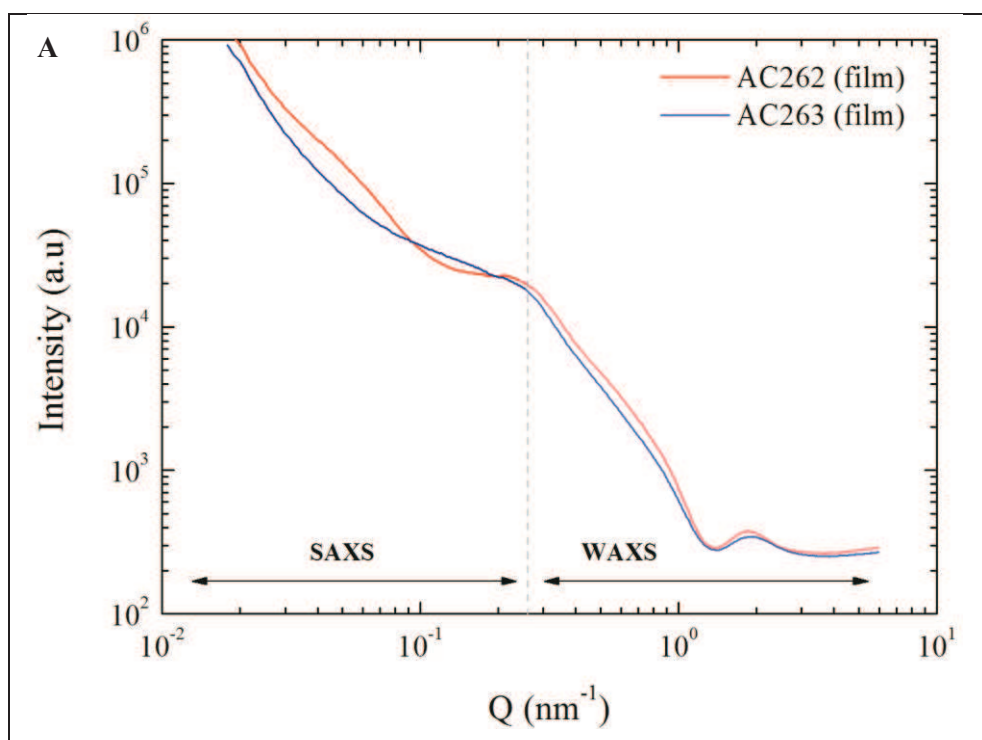


Figure 73. (A) X-ray diffraction patterns at increasing electric field intensities and (B) scattering diagram of intensity I (a.u.) versus Q (nm^{-1}) obtained through SAXS measurements of the latex containing Imogolite of 500 nm non-encapsulated.

The films obtained from these latexes (AC262 and AC263) when analyzed by TEM presented some orientation inside the matrix. To give further indication of such organization, both films containing encapsulated and non-encapsulated long Imogolite tubes were analyzed by combining SAXS and WAXS techniques in a SWING device. Because of the low thickness of

the films (0.3 mm), the measurements were made with the X-ray beam perpendicular to the film plane.

As **Figure 74** shows, again no proof of alignment could be extracted from these results. Perfectly spherical patterns were obtained for the two samples at both SAXS and WAXS modes, indicating an isotropic distribution of the tubes along the film plane. The scattering diagram of the whole range from small to wide angles also suggested an isotropic distribution of the tubes in the film plane. A change in the curve slope towards small angles was observed when comparing both samples. As it was observed for the suspensions of Imogolite after macroRAFT addition, when aggregates are formed (at pH 6.0), the slope changes, and an additional signal was present, attributed to the aggregate structures. The same profile is observed for the films containing encapsulated tubes, in which the signal corresponds to a structure on the order of hundreds of nanometers.



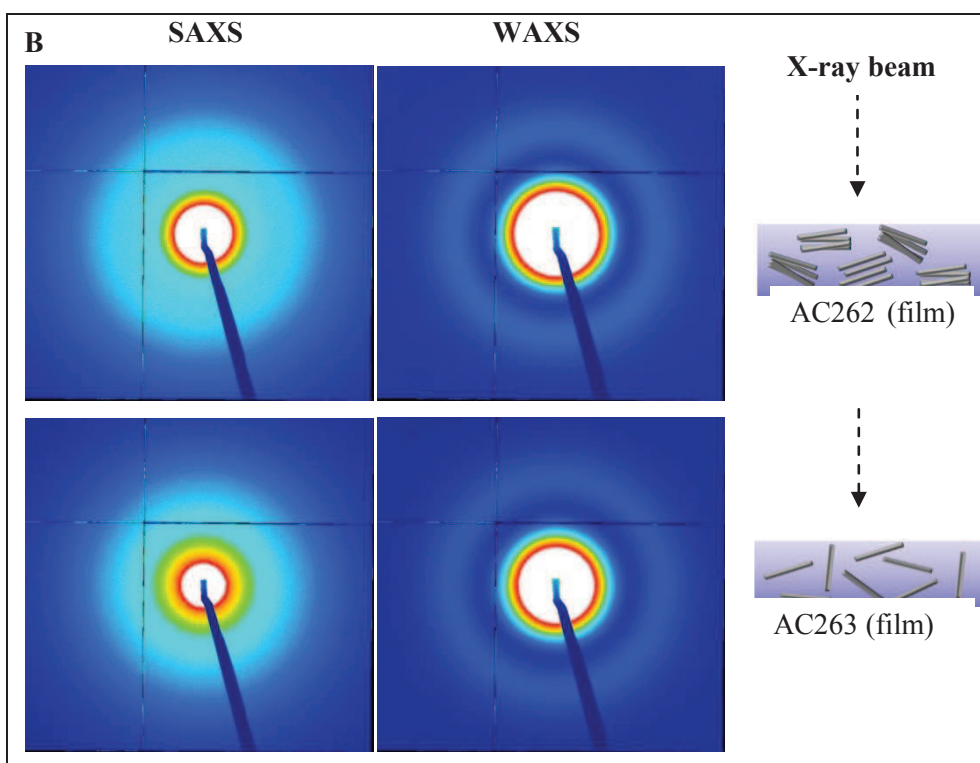


Figure 74. (A) Scattering diagram of intensity $I(\text{a.u.})$ versus $Q(\text{nm}^{-1})$ and (B) x-ray diffraction patterns obtained through SAXS and WAXS measurements of the films containing Imogolite of 500 nm encapsulated (top) and non-encapsulated (bottom). X-ray beam was perpendicular to the film plane.

Even though these results revealed an isotropic distribution of the tubes in the film plane, an anisotropic organization was expected parallel to the film plane, as observed by TEM of the cross-section. Thus, the films were analyzed by WAXS with the X-ray beam parallel to the film plane. **Figure 75** compares the results obtained at both X-ray beam directions. Indeed, some anisotropy was observed parallel to the film plane, indicated in the X-ray patterns (**Figure 75 B**) by the two darker spots above and below the central ring.

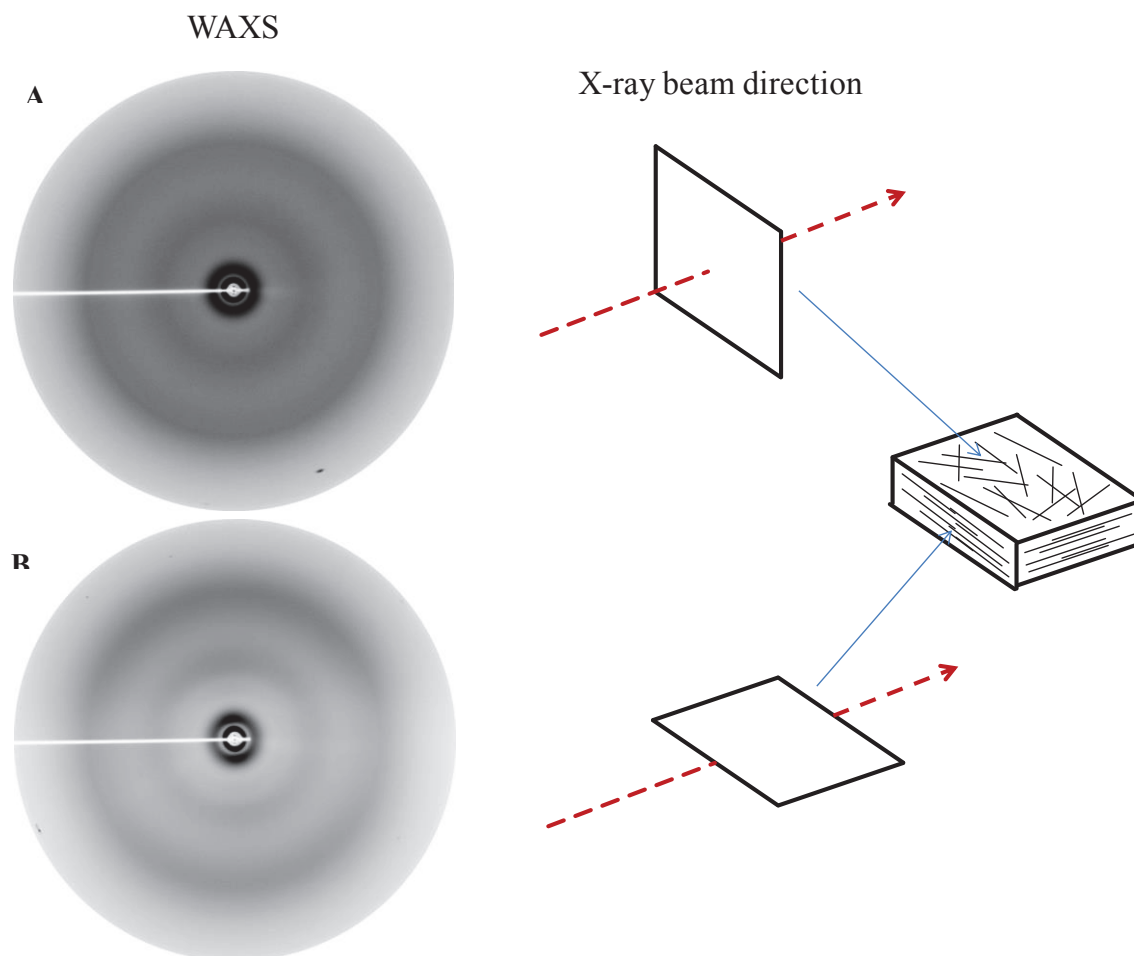


Figure 75. X-ray diffraction patterns obtained through WAXS measurements of the film containing Imogolite of 500 nm non-encapsulated where the x-ray beam was (A) perpendicular and (B) parallel to the film plane.

In conclusion, the alignment of the tubes in suspension in the latexes was unsuccessful due to the high conductivity of the medium, resulting from its high salinity. The latexes were dialyzed in an attempt to reduce the ion concentration and improve the tubes response to the electrical field. However, stability issues were encountered for the sample containing non-encapsulated tubes, which impeded the measurements. The sample with encapsulated tubes remained stable after dialysis, but due to technical problems with the SAXS device that operates under electric field, the analyses could not be performed.

The partial orientation observed by TEM when the microstructure of the films was investigated could not be confirmed by SAXS/WAXS when the measurements were made in a set up where the beam was perpendicular to the film plane. Further analyses adjusting the beam parallel to the film plane revealed certain anisotropic organization, with the tubes lying horizontally in the film.

II.8.2.3 Conclusions

In this section the microstructure and thermo-mechanical behavior of polymer/Imogolite films were analyzed by TEM of thin films and DMA, respectively. The effect of different parameters was investigated for films composed of low ($15\ 000\ \text{g mol}^{-1}$) and high ($30\ 000\ \text{g mol}^{-1}$) molar mass copolymers. The microstructure was shown to be dependent on the latex morphology, yielding uniformly distributed nanotube aggregates of around 100 nm when the tubes were encapsulated, and uniformly and individually distributed tubes when the Imogolite was not encapsulated. Imogolite nanotubes of 500 nm presented some partial alignment after film formation, which was attributed to the high aspect ratio of the tubes that naturally led them to arrange their long axis with the ones of the adjacent tubes.

Pure copolymer films presented unexpected high mechanical stiffness, which was attributed to the inter chain interactions (H-bond and ionic interactions) between the AA units present on the chains, providing some reinforcement to the overall soft copolymer. Hybrid films containing encapsulated tubes did not provide reinforcement to the matrix, due to the presence of the polymer layer around the tubes, which impeded their connection and thus the percolating network formation. Hybrid films containing non-encapsulated tubes presented higher rubbery modulus, indicating the efficient reinforcement provided by the tubes, which in this case can easily connect with each other and allow percolation. Increasing the nanotubes length led to the further increase of the material mechanical stiffness, attributed to the stronger percolation effect in this case. Additionally, the longest tubes provided a modulus improvement of 2 orders of magnitude, which can be correlated in particular to the high aspect ratio of these tubes.

Further attempts to align Imogolite nanotubes in the latexes under electric field failed due to the high conductivity of the as-prepared hybrid latexes. Neither encapsulated tubes nor non-encapsulated ones showed response to the electric field. The orientation of the tubes in the films was measured by a simultaneous SAXS/WAXS analysis, in a SWING device. When the X-ray beam was perpendicular to the film plane, no orientation was detected. Analyses made adjusting the beam parallel to the film plane revealed an anisotropic orientation of the nanotubes in the film.

II.9 General conclusions of chapter II

The objective of this chapter was to produce polymer-encapsulated Imogolite nanotubes using the macroRAFT-assisted encapsulating emulsion polymerization technique. In the first step, well-defined macroRAFT agents, based on acrylic acid or methacrylic acid monomers and containing or not *n*-butyl acrylate or butyl methacrylate units, were synthesized via RAFT polymerization. These macroRAFTs (i.e. PAA-CTPPA, PMAA-CTPPA, P(AA-*co*-BA)-CTPPA and P(MAA-*co*-BMA)-CTPPA) presented a linear increase of molar mass with conversion and narrow molar mass distributions, confirming the successful control of the polymerization.

Preliminary REEP experiments carried out with Imogolite and using these macroRAFTs showed a significant effect of the macroRAFT nature on final morphology. The PAA-CTPPA generated stable polymer particles, but Imogolite nanotubes were on the surface of polymer particles or isolated in the aqueous phase. It was concluded that this highly hydrophilic polymer could not efficiently transfer the polymerization from the aqueous phase to the surface of Imogolite, resulting in the formation of polymer particles isolated from the nanotubes. The PMAA-CTPPA formed smaller polymer particles than the previous macroRAFT, and these particles were apparently decorating the surface of Imogolite. However, both homopolymer macroRAFTs yielded very low monomer conversions. The P(AA-*co*-BA)-CTPPA generated stable latexes in which Imogolite was decorated with small polymer particles. The P(MAA-*co*-BMA)-CTPPA conducted to unstable latexes, in which polymer particles could be seen but no Imogolite nanotubes were found. These preliminary studies allowed us to discard the methacrylic acid-based macroRAFTs and the acrylic acid-based homopolymers.

The adsorption of the P(AA-*co*-BA)-CTPPA macroRAFT ($M_n = 3\,500\text{ g mol}^{-1}$) on the surface of Imogolite was then studied. The main driving force of adsorption was shown to be the electrostatic interactions between the positively charged Imogolite surface and the negatively charged carboxylic acid groups of the macroRAFT. It was shown that the presence of BA units in the chain contributed to a significant increase of the adsorption, attributed to additional interchain hydrophobic interactions. Adsorption could be further improved by decreasing the pH (from 8.0 to 6.0), which also contributed to increase the hydrophobicity of the copolymer. Nevertheless, at low pH, the macroRAFT stabilizing ability was decreased, inducing the formation of tube bundles. In these conditions, a sonication step was necessary to re-stabilize the suspension. The adsorption of a low molar mass macroRAFT (i.e. $M_n = 1\,100\text{ g mol}^{-1}$) was shown to be less important than that of the higher molar mass copolymer, which was attributed to the train conformation that this copolymer adopts, against the coil conformation adopted by the high molar mass macroRAFT and which occupies a smaller space.

The emulsion polymerizations were then carried out using the stable suspensions obtained after macroRAFT adsorption on the surface of Imogolite. Different parameters, like the macroRAFT molar mass and concentration, the Imogolite concentration, the pH and the hydrophobic monomer composition were investigated. The low molar mass macroRAFT, for which the experiments were conducted at pH = 8.0, could not provide sufficient stability to the system, and the latexes obtained were unstable. The high molar mass macroRAFT ($M_n = 3\,500\text{ g mol}^{-1}$), also used at pH = 8.0, led to the formation of polymer-decorated nanotubes, whichever the macroRAFT concentration. Increasing this concentration only led to the formation of a higher number of free polymer particles. Increasing the Imogolite concentration resulted in a lower amount of macroRAFT in the aqueous phase, which consequently conducted to a decrease in the number of free polymer particles, still forming polymer-decorated nanotubes.

All the previous polymerizations were conducted at pH = 8.0, and generated polymer-decorated nanotubes. The decrease in pH to 6.0 led to the formation of encapsulated Imogolite bundles after polymerization. The change in morphology was attributed to the higher hydrophobicity of the macroRAFT at this lower pH, which contributes to a better adsorption of the copolymer on the surface increasing the wettability of the nanotubes. Consequently, the objects/aggregates present a higher number of RAFT functionalities per particle/aggregate and a higher affinity with the hydrophobic monomers, both contributing to the encapsulation of the nanotube bundles.

In the attempt of controlling the aggregates size and going towards individual nanotube encapsulation, different mixing and interaction pathways were investigated. Stable and small Imogolite aggregates could be formed by inverting the order of mixing and adding the Imogolite suspension by high speed injection to the macroRAFT solution, followed by a slight increase of pH. Through this mixing pathway, stable suspensions could be obtained without sonication. The interaction pathway could not be controlled, due to the complexity of the interaction modes between the macroRAFT and the nanotubes, which involve more than electrostatic interactions (e.g. possible H-bonding and hydrophobic interactions).

To produce latexes with a T_g closer to the ambient temperature and facilitate latex's film-formation, the nature and composition of the hydrophobic monomers were varied. The use of a more hydrophobic monomer (e.g. STY) combined with BA, conducted to the encapsulation of Imogolite bundles, even at pH = 8.0. This result was attributed to the higher affinity of the monomer with the surface, which is a consequence of its lower solubility in water. In addition to the encapsulated bundles, polymer spheres, fibers and vesicles were also formed. The formation of these different morphologies was correlated to the higher hydrophobicity of the monomer mixture, which is known to affect the self-assembly of *in situ* formed amphiphilic block copolymers, favoring non-spherical morphologies. Increasing the BA amount in the monomer

mixture containing MMA also led to the formation of fibers and vesicles, additionally to encapsulated bundles and polymer-decorated nanotubes. Increasing the BA content also increased the hydrophobicity of the copolymer, promoting partial encapsulation of nanotubes and inducing the formation of non-spherical particles (i.e. fibers and vesicles). Since the water solubility of the hydrophobic monomers was shown to play an important role on defining particles morphology, we had to choose a monomer of high water solubility that would lead to the formation of a copolymer of low T_g . The monomer chosen was methyl acrylate (MA). Using this monomer, the BA amount could be minimized and the formation of fibers and vesicles was avoided, still producing film-forming latexes.

Pure polymer films and hybrid latex films containing polymer-decorated Imogolite or encapsulated Imogolite bundles were casted and analyzed by DMA. The mechanical stiffness of the pure matrix was attributed to the presence of an ionic network formed among the acrylic acid units along the material, which already confers some reinforcement to the matrix. Hybrid films formed from encapsulated Imogolite bundle latexes presented the same modulus as the pure matrix, which was a result of the Imogolite confinement inside polymer particles, preventing the formation of a percolating network. Hybrid films formed from polymer-decorated nanotube latexes presented increased modulus compared to the reference film, indicating the effective reinforcement of the material provided by the nanotubes once they can form a percolating structure. Increasing the tube length led to an increase of the modulus for the films formed from both encapsulated bundles and polymer-decorated nanotubes, attributed to the lower percolation threshold observed for these samples. In these cases, the tube-tube interaction was not hindered by the encapsulation, because some of the tubes protuberated out of the particles. Storage modulus of about 1 order of magnitude higher than the reference were obtained for the film containing the longer nanotubes and formed from polymer-decorated Imogolite latexes.

In this chapter, we have shown the efficiency of the macroRAFT-assisted encapsulating emulsion polymerization technique for the encapsulation of Imogolite nanotubes and the production of colloidal nanocomposites.

II.10 References

1. Hussain, F.; Hojjati, M.; Okamoto, M.; Gorga, R. E. *J. Comp. Mat.* **2006**, *40*, 1511-1575.
2. Alexandre, M.; Dubois, P. *Mat. Sci. & Eng. R-Rep.* **2000**, *28*, 1-63.
3. Miyamoto, N.; Shintate, M.; Ikeda, S.; Hoshida, Y.; Yamauchi, Y.; Motokawa, R.; Annaka, M. *Chem. Comm.* **2013**, *49*, 1082-1084.
4. Haraguchi, K.; Li, H.-J.; Song, L.; Murata, K. *Macromol.* **2007**, *40*, 6973-6980.
5. Koo, C. M.; Kim, S. O.; Chung, I. J. *Macromol.* **2003**, *36*, 2748-2757.
6. Dirix, Y.; Darribere, C.; Heffels, W.; Bastiaansen, C.; Caseri, W.; Smith, P. *Appl. Opt.* **1999**, *38*, 6581-6586.
7. Sun, L.; Boo, W. J.; Clearfield, A.; Sue, H. J.; Pham, H. Q. *J. Membr. Sci.* **2008**, *318*, 129-136.
8. Liang, Y.; Cao, W.; Li, Z.; Wang, Y.; Wu, Y.; Zhang, L. *Polym. Test.* **2008**, *27*, 270-276.
9. Herrera-Alonso, J. M.; Sedlakova, Z.; Marand, E. *J. Membr. Sci.* **2010**, *349*, 251-257.
10. Kim, S. W.; Cha, S.-H. *J. Appl. Polym. Sci.* **2014**.
11. Scherillo, G.; Lavorgna, M.; Buonocore, G.; Zhan, Y.; Xia, H.; Monsitieri, G.; Ambrosio, L. *ACS Appl. Mat. & Interf.* **2014**, Ahead of Print.
12. Viala, P.; Bourgeat-Lami, E.; Guyot, A.; Legrand, P.; Lefebvre, D. *Macromol. Symp.* **2002**, *187*, 651-661.
13. Bechthold, N.; Tiarks, F.; Willert, M.; Landfester, K.; Antonietti, M. *Macromol. Symp.* **2000**, *151*, 549-555.
14. Yang, Y.; Kong, X. Z.; Kan, C. Y.; Sun, C. G. *Polym. for Adv. Technol.* **1999**, *10*, 54-59.
15. Tiarks, F.; Landfester, K.; Antonietti, M. *Macromol. Chem. Phys.* **2001**, *202*, 51-60.
16. Negrete-Herrera, N.; Putaux, J.-L.; David, L.; De Haas, F.; Bourgeat-Lami, E. *Macromol. Rap. Comm.* **2007**, *28*, 1567-1573.
17. Cauvin, S.; Colver, P. J.; Bon, S. A. F. *Macromol.* **2005**, *38*, 7887-7889.
18. Putlitz, B. Z.; Landfester, K.; Fischer, H.; Antonietti, M. *Adv. Mater.* **2001**, *13*, 500-+.
19. Bourgeat-Lami, E. *J. Nanosci. and Nanotech.* **2002**, *2*, 1-24.
20. Bourgeat-Lami, E.; Guimaraes, T. R.; Pereira, A. M. C.; Alves, G. M.; Moreira, J. C.; Putaux, J.-L.; dos Santos, A. M. *Macromol. Rap. Comm.* **2010**, *31*, 1874-1880.
21. Sheibat-Othman, N.; Cenacchi-Pereira, A.-M.; Dos Santos, A. M.; Bourgeat-Lami, E. *J. Polym. Sci. Part A-Polym. Chem.* **2011**, *49*, 4771-4784.
22. Nguyen, D.; Zondanos, H. S.; Farrugia, J. M.; Serelis, A. K.; Such, C. H.; Hawkett, B. S. *Lang.* **2008**, *24*, 2140-2150.
23. Nguyen, D.; Such, C.; Hawkett, B. *J. Polym. Sci. Part A-Polym. Chem.* **2012**, *50*, 346-352.
24. Ali, S. I.; Heuts, J. P. A.; Hawkett, B. S.; van Herk, A. M. *Lang.* **2009**, *25*, 10523-10533.
25. Zgheib, N.; Putaux, J.-L.; Thill, A.; Bourgeat-Lami, E.; D'Agosto, F.; Lansalot, M. *Polym. Chem.* **2013**, *4*, 607-614.
26. Zhong, W.; Zeuna, J. N.; Claverie, J. P. *J. Polym. Sci. Part A-Polym. Chem.* **2012**, *50*, 4403-4407.

27. Nguyen, D.; Such, C. H.; Hawkett, B. S. *J. Polym. Sci. Part A-Polym. Chem.* **2013**, 51, 250-257.
28. Zhang, X.; Boisse, S.; Zhang, W.; Beaunier, P.; D'Agosto, F.; Rieger, J.; Charleux, B. *Macromol.* **2011**, 44, 4149-4158.
29. Zhang, W.; D'Agosto, F.; Boyron, O.; Rieger, J.; Charleux, B. *Macromol.* **2011**, 44, 7584-7593.
30. Yoshinaga, N.; Aomine, S. *Soil Sci. Plant Nutr.* **1962**, 8, 22-29.
31. Yamamoto, K.; Otsuka, H.; Takahara, A. *Polym. Jour.* **2007**, 39, 1-15.
32. Otsuka, H.; Takahara, A. *Inorg. Metall. Nanotub. Mat.: Recent Technol. Appl.* **2010**, 117, 169-190.
33. Ma, W.; Yah, W. O.; Otsuka, H.; Takahara, A. *Beilstein J. Nanotech.* **2012**, 3, 82-100.
34. Ma, W.; Yah, W. O.; Otsuka, H.; Takahara, A. *J. Mat. Chem.* **2012**, 22, 11887-11892.
35. Cradwick, P. D.; Wada, K.; Russell, J. D.; Yoshinag.N; Masson, C. R.; Farmer, V. C. *Nat.-Phys. Sci.* **1972**, 240, 187.
36. Parfitt, R. L. *Clay Miner.* **2009**, 44, 135-155.
37. Wada, K.; Yoshinag.N. *Amer. Mineralog.* **1969**, 54, 50.
38. Wada, K. *Amer. Mineralog.* **1967**, 52, 690.
39. Wada, K.; Matsubara, I., Differential formation of allophane, "Imogolite" and gibbsite in the Kitakami pumice bed. In *Trans. 9th International Congress Soil Science*, 1968; Vol. 3, pp 123-131.
40. Wada, K.; Yoshinaga, N.; Yotsumoto, H.; Ibe, K.; Aida, S. *Clay Miner.* **1970**, 8.
41. Levard, C. Nanoparticules naturelles : imogolites et allophanes. Structure, mécanismes de croissance et capacité de rétention des éléments traces métalliques. Université Paul Cezanne, Marseilles, 2008.
42. Abidin, Z.; Matsue, N.; Henmi, T. *J. Comp.-Aided Mat. Des.* **2007**, 14, 5-18.
43. Gustafsson, J. P.; Bhattacharya, P.; Karlton, E. *Appl. Geochem.* **1999**, 14, 707-718.
44. Tait, J. M.; Yoshinaga, N.; Mitchell, B. D. *Soil Sci. Plant Nutr.* **1978**, 24, 145-151.
45. Maitat, O.; Boudot, J. P.; Merlet, D.; Rouiller, J. *Wat. Air Soil Poll.* **2000**, 117, 217-243.
46. Arocena, J. M.; Sanborn, P. *Canad. J. Soil Sci.* **1999**, 79, 571-592.
47. Jongmans, A. G.; Vanoort, F.; Buurman, P.; Jaunet, A. M.; Vandoesburg, J. D. J. *Soil Science Society of America Journal* **1994**, 58, (2), 501-507.
48. Mendonca, T.; Melo, V. F.; Schaefer, C. E. G. R.; Simas, F. N. B.; Michel, R. F. M. *Soil Sci. Soc. Amer. J.* **2013**, 77, 1842-1851.
49. Sauer, D.; Sponagel, H.; Sommer, M.; Giani, L.; Jahn, R.; Stahr, K. *J. Plant Nutr. Soil Sci.* **2007**, 170, 581-597.
50. Miyauchi, N.; Aomine, S. *Soil Sci. Plant Nutr.* **1966**, 12.
51. Su, C.; Harsh, J. B. *Soil Sci. Soc. Amer. J.* **1996**, 60, 77-85.
52. Farmer, V. C.; Fraser, A. R.; Tait, J. M. *J. Chem. Soc.-Chem. Comm.* **1977**, 462-463.
53. Suzuki, M.; Inukai, K. *Inorg. Metall. Nanotub. Mater.: Recent Technol. Appl.* **2010**, 117, 159-167.
54. Farmer, V. C.; Adams, M. J.; Fraser, A. R.; Palmieri, F. *Clay Miner.* **1983**, 18, 459-472.
55. Nakanishi, R.; Wada, S.-I.; Suzuki, M.; Maeda, M. *Journal of the Faculty of Agriculture Kyushu University* **2007**, 52, 147-151.

56. Ohashi, F.; Wada, S. I.; Suzuki, M.; Maeda, M.; Tomura, S. *Clay Minerals* **2002**, 37, 451-456.
57. McBride, M. B.; Farmer, V. C.; Russell, J. D.; Tait, J. M.; Goodman, B. A. *Clay Minerals* **1984**, 19, 1-8.
58. Alvarez-Ramirez, F. *Journal of Computational and Theoretical Nanoscience* **2009**, 6, 1120-1124.
59. Levard, C.; Rose, J.; Masion, A.; Doelsch, E.; Borschneck, D.; Olivi, L.; Dominici, C.; Grauby, O.; Woicik, J. C.; Bottero, J.-Y. *Journal of the American Chemical Society* **2008**, 130, 5862.
60. Levard, C.; Masion, A.; Rose, J.; Doelsch, E.; Borschneck, D.; Dominici, C.; Ziarelli, F.; Bottero, J.-Y. *Journal of the American Chemical Society* **2009**, 131, 17080-+.
61. Maillet, P.; Levard, C.; Larquet, E.; Mariet, C.; Spalla, O.; Menguy, N.; Masion, A.; Doelsch, E.; Rose, J.; Thill, A. *Journal of the American Chemical Society* **2010**, 132, 1208.
62. Thill, A.; Maillet, P.; Guiose, B.; Spalla, O.; Belloni, L.; Chaurand, P.; Auffan, M.; Olivi, L.; Rose, J. *Journal of the American Chemical Society* **2012**, 134, 3780-3786.
63. Farmer, V. C.; Fraser, A. R.; Tait, J. M. *Geochimica Et Cosmochimica Acta* **1979**, 43, 1417-1420.
64. Horikawa, K. *Clay Science* **1975**, 4, 255-263.
65. Mackenzie, K. J. D.; Bowden, M. E.; Brown, I. W. M.; Meinhold, R. H. *Clays and Clay Minerals* **1989**, 37, 317-324.
66. Mukherjee, S.; Bartlow, V. A.; Nair, S. *Chemistry of Materials* **2005**, 17, 4900-4909.
67. Tsujimoto, Y.; Yoshida, A.; Kobayashi, M.; Adachi, Y. *Colloids and Surfaces A-Physicochemical and Engineering Aspects* **2013**, 435, 109-114.
68. Bragg, W. H.; Bragg, W. L. *Proceedings of the Royal Society of London Series A-Containing Papers of a Mathematical and Physical Character* **1913**, 88, 428-438.
69. Ackerman, W. C.; Smith, D. M.; Huling, J. C.; Kim, Y. W.; Bailey, J. K.; Brinker, C. J. *Langmuir* **1993**, 9, 1051-1057.
70. Tomura, S.; MAeda, M.; Inukai, K.; Ohashi, F.; Suzuki, M.; Shibasaki, Y.; Suzuki, S. *Clay Science* **1997**, 10, 195-203.
71. Suzuki, M.; Suzuki, S.; Maeda, M.; Tomura, S.; Mizota, T. *Journal of Ceramic Society of Japan* **2001**, 109, 874-881.
72. Lvov, Y.; Abdullayev, E. *Progress in Polymer Science* **2013**, 38, 1690-1719.
73. Yamamoto, K.; Otsuka, H.; Wada, S.-I.; Takahara, A. *Chemistry Letters* **2001**, 30, 1162-1163.
74. Yamamoto, K.; Otsuka, H.; Takahara, A.; Wada, S. I. *Journal of Adhesion* **2002**, 78, 591-602.
75. Ma, W.; Kim, J.; Otsuka, H.; Takahara, A. *Chemistry Letters* **2011**, 40, 159-161.
76. Yah, W. O.; Irie, A.; Jiravanichanun, N.; Otsuka, H.; Takahara, A. *Bulletin of the Chemical Society of Japan* **2011**, 84, 893-902.
77. Johnson, L. M.; Pinnavaia, T. J. *Langmuir* **1990**, 6, 307-311.
78. Choi, J. H.; Cho, Y. W.; Ha, W. S.; Lyoo, W. S.; Lee, C. J.; Ji, B. C.; Han, S. S.; Yoon, W. S. *Polymer International* **1998**, 47, 237-242.
79. Yang, H.; Chen, Y.; Su, Z. *Chemistry of Materials* **2007**, 19, 3087-3089.
80. Yah, W. O.; Irie, A.; Otsuka, H.; Sasaki, S.; Yagi, N.; Sato, M.; Koganezawa, T.; Takahara, A. In *Molecular Aggregation States of Imogolite/P3HT Nanofiber*

- Hybrid*, International Symposium on Future Trends in Soft Materials Research with Advanced Light Sources: Interdisciplinary of Bio- & Synthetic- Materials and Industrial Transferring, Hyogo, JAPAN, 2011Sep 01-03, 2010; Hyogo, JAPAN, 2010.
81. Yamamoto, K.; Otsuka, H.; Wada, S. I.; Sohn, D.; Takahara, A. *Soft Matter* **2005**, 1, 372-377.
 82. Yamamoto, K.; Otsuka, H.; Wada, S.-I.; Takahara, A. *Transactions of the Materials Research Society of Japan* **2004**, 29, 149-152.
 83. Wada, S.-I.; Eto, A.; Wada, K. *Journal of Soil Science* **1979**, 30, 347-355.
 84. Inoue, K.; Huang, P. M. *Soil Science Society of American Journal* **1986**, 50, 1623-1633.
 85. Shikinaka, K.; Koizumi, Y.; Osada, Y.; Shigehara, K. *Polymers for Advanced Technologies* **2011**, 22, 1212-1215.
 86. Henmi, T.; Wada, K. *Clay Minerals* **1974**, 10, 231-245.
 87. Harsh, J. B.; Traina, S. J.; Boyle, J.; Yang, Y. *Clays and Clay Minerals* **1992**, 40, 700-706.
 88. Imamura, S.; Hayashi, Y.; Kajiwara, K.; Hoshino, H.; Kaito, C. *Industrial & Engineering Chemistry Research* **1993**, 32, 600-603.
 89. Bonelli, B.; Bottero, I.; Ballarini, N.; Passeri, S.; Cavani, F.; Garrone, E. *Journal of Catalysis* **2009**, 264, 15-30.
 90. Shikinaka, K.; Koizumi, Y.; Kaneda, K.; Osada, Y.; Masunaga, H.; Shigehara, K. *Polymer* **2013**, 54, 2489-2492.
 91. Yamamoto, K.; Otsuka, H.; Wada, S. I.; Sohn, D.; Takahara, A. *Polymer* **2005**, 46, 12386-12392.
 92. Ma, W.; Otsuka, H.; Takahara, A. *Chemical Communications* **2011**, 47, 5813-5815.
 93. Ma, W.; Otsuka, H.; Takahara, A. *Polymer* **2011**, 52, 5543-5550.
 94. Lee, H.; Ryu, J.; Kim, D.; Joo, Y.; Lee, S. U.; Sohn, D. *Journal of Colloid and Interface Science* **2013**, 406, 165-171.
 95. Huang, T.; Xu, H.; Jiao, K.; Zhu, L.; Brown, H. R.; Wang, H. *Advanced Materials* **2007**, 19, 1622.
 96. Kim, J.; Koo, J.; Shirahase, T.; Takahara, A.; Sohn, D. *Chemistry Letters* **2009**, 38, 1112-1113.
 97. Inoue, N.; Otsuka, H.; Wada, S. I.; Takahara, A. *Chemistry Letters* **2006**, 35, 194-195.
 98. Jiravanichanun, N.; Yamamoto, K.; Kato, K.; Kim, J.; Horiuchi, S.; Yah, W.-O.; Otsuka, H.; Takahara, A. *Biomacromolecules* **2012**, 13, 276-281.
 99. Ishikawa, K.; Abe, S.; Yawaka, Y.; Suzuki, M.; Watari, F. *Journal of the Ceramic Society of Japan* **2010**, 118, 516-520.
 100. Yamazaki, S.; Maeda, H.; Obata, A.; Inukai, K.; Kato, K.; Kasuga, T. *Journal of Nanomaterials* **2012**.
 101. Maeda, H.; Kogo, Y.; Obata, A.; Inukai, K.; Kato, K.; Kasuga, T. *Journal of the Ceramic Society of Japan* **2013**, 121, 749-752.
 102. Kobayashi, M.; Nitani, M.; Satta, N.; Adachi, Y. *Colloids and Surfaces a-Physicochemical and Engineering Aspects* **2013**, 435, 139-146.
 103. Xu, X.; Smith, A. E.; Kirkland, S. E.; McCormick, C. L. *Macromolecules* **2008**, 41, 8429-8435.
 104. Boursier, T.; Chaduc, I.; Rieger, J.; D'Agosto, F.; Lansalot, M.; Charleux, B. *Polymer Chemistry* **2011**, 2, 355-362.

105. Hashimoto, N.; Aoyama, T.; Shioiri, T. *Chemical & Pharmaceutical Bulletin* **1981**, 29, 1475-1478.
106. Esumi, K.; Nakaie, Y.; Sakai, K.; Torigoe, K. *Colloids and Surfaces a-Physicochemical and Engineering Aspects* **2001**, 194, 7-12.
107. Schwarz, S.; Lunkwitz, K.; Kessler, B.; Spiegler, U.; Killmann, E.; Jaeger, W. *Colloids and Surfaces a-Physicochemical and Engineering Aspects* **2000**, 163, 17-27.
108. Alagha, L.; Wang, S.; Yan, L.; Xu, Z.; Masliyah, J. *Langmuir* **2013**, 29, 3989-3998.
109. Atmuri, A. K.; Bhatia, S. R. *Langmuir* **2013**, 29, 3179-3187.
110. Foissy, A.; Attar, A. E.; Lamarche, J. M. *Journal of Colloid and Interface Science* **1983**, 96, 275-287.
111. Pan, Z. H.; Campbell, A.; Somasundaran, P. *Colloids and Surfaces a-Physicochemical and Engineering Aspects* **2001**, 191, 71-78.
112. Liufu, S. C.; Mao, H. N.; Li, Y. P. *Journal of Colloid and Interface Science* **2005**, 281, 155-163.
113. Chibowski, S.; Wisniewska, M. *Colloids and Surfaces a-Physicochemical and Engineering Aspects* **2002**, 208, 131-145.
114. Fresnais, J.; Berret, J. F.; Frka-Petesic, B.; Sandre, O.; Perzynski, R. *Advanced Materials* **2008**, 20, 3877-+.
115. Yan, M.; Fresnais, J.; Berret, J. F. *Soft Matter* **2010**, 6, 1997-2005.
116. Yan, M.; Fresnais, J.; Sekar, S.; Chapel, J. P.; Berret, J. F. *Acs Applied Materials & Interfaces* **2011**, 3, 1049-1054.
117. Sehgal, A.; Lalatonne, Y.; Berret, J. F.; Morvan, M. *Langmuir* **2005**, 21, 9359-9364.
118. Warnant, J.; Garnier, J.; van Herk, A.; Dufils, P.-E.; Vinas, J.; Lacroix-Desmazes, P. *Polymer Chemistry* **2013**, 4, 5656-5663.
119. Chibowski, S.; Wisniewska, M.; Urban, T. *Adsorption-Journal of the International Adsorption Society* **2010**, 16, 321-332.
120. Cherstvy, A. G.; Winkler, R. G. *Physical Chemistry Chemical Physics* **2011**, 13, 11686-11693.
121. Ramos, J.; Forcada, J. *European Polymer Journal* **2007**, 43, 4647-4661.
122. Chaduc, I.; Lansalot, M.; D'Agosto, F.; Charleux, B. *Macromolecules* **2012**, 45, 1241-1247.
123. Chaduc, I.; Crepet, A.; Boyron, O.; Charleux, B.; D'Agosto, F.; Lansalot, M. *Macromolecules* **2013**, 46, 6013-6023.
124. Mballa, M. A. M.; Ali, S. I.; Heuts, J. P. A.; van Herk, A. M. *Polymer International* **2012**, 61, 861-865.
125. Brandrup, J.; Immergut, E. H.; Grulke, E. A., *Polymer Handbook*. 4th edition ed.; Wiley-Interscience: New York, 1999.
126. Qi, L.; Fresnais, J.; Berret, J.-F.; Castaing, J.-C.; Grillo, I.; Chapel, J.-P. *Journal of Physical Chemistry C* **2010**, 114, 12870-12877.
127. Qi, L.; Fresnais, J.; Berret, J.-F.; Castaing, J.-C.; Destremaut, F.; Salmon, J.-B.; Cousin, F.; Chapel, J.-P. *Journal of Physical Chemistry C* **2010**, 114, 16373-16381.
128. Sekar, S. Modulation de l'interaction électrostatique entre nanomatériaux en solutions et aux interfaces: Vers la génération de surfaces fonctionnelles hybrides. Université Bordeaux 1, Bordeaux, 2013.
129. Zhang, W.; D'Agosto, F.; Dugas, P.-Y.; Rieger, J.; Charleux, B. *Polymer* **2013**, 54, 2011-2019.

130. Green, D. W.; Perry, R. H., *Perry's Chemical Engineer's Handbook*. 8th ed.; McGraw-Hill Professional: 2008; p 2240.
131. Shaw, D. G.; Maczynski, A.; Goral, M.; Wisniewska-Gocłowska, B.; Skrzecz, A.; Owczarek, I.; Blazej, K.; Haulait-Pirson, M. C.; Hefter, G. T.; Maczynska, Z.; Szafranski, A. *Journal of Physical and Chemical Reference Data* **2005**, 34, 1489-1553.
132. Chenal, M.; Rieger, J.; Vechambre, C.; Chenal, J.-M.; Chazeau, L.; Creton, C.; Bouteiller, L. *Macromolecular Rapid Communications* **2013**, 34, 1524-1529.
133. Bihannic, I.; Baravian, C.; Duval, J. F. L.; Paineau, E.; Meneau, F.; Levitz, P.; de Silva, J. P.; Davidson, P.; Michot, L. J. *Journal of Physical Chemistry B* **2010**, 114, 16347-16355.
134. Dozov, I.; Paineau, E.; Davidson, P.; Antonova, K.; Baravian, C.; Bihannic, I.; Michot, L. J. *Journal of Physical Chemistry B* **2011**, 115, 7751-7765.
135. Paineau, E.; Dozov, I.; Philippe, A.-M.; Bihannic, I.; Meneau, F.; Baravian, C.; Michot, L. J.; Davidson, P. *Journal of Physical Chemistry B* **2012**, 116, 13516-13524.
136. Anthony, J. W.; Bideaux, R. A.; Bladh, K. W.; Nichols, M. C., *Handbook of Mineralogy*. Anthony, J. W.; Bideaux, R. A.; Bladh, K. W.; Nichols, M. C., Eds. Mineralogical Society of America: Chantilly, USA, 2003.
137. Tang, Z. Y.; Kotov, N. A. *Advanced Materials* **2005**, 17, 951-962.
138. Martin-Gomis, L.; Fernandez-Garcia, M.; de la Fuente, J. L.; Madruga, E. L.; Cerrada, M. L. *Macromolecular Chemistry and Physics* **2003**, 204, 2007-2016.
139. Koh, A. Y. C.; Mange, S.; Bothe, M.; Leyrer, R. J.; Gilbert, R. G. *Polymer* **2006**, 47, 1159-1165.

Chapter III – Polymer/LDH nanocomposite latexes

Table of contents

III.1. Introduction.....	193
III.2. Bibliographic study on Layered Double Hydroxide (LDH) materials.....	195
III.2.1 LDH structure.....	195
III.2.2 LDH synthesis.....	196
III.2.3 LDH modification and incorporation into polymer matrixes.....	203
III.2.4 Conclusions.....	222
III.3. Synthesis of colloidal suspensions of LDH platelets.....	223
III.3.1 Experimental section.....	223
III.3.2 Results and Discussion.....	227
III.3.3 Conclusions.....	232
III.4. LDH modification with RAFT and macroRAFT agents.....	234
III.4.1 Experimental section.....	234
III.4.2 Results and Discussion.....	237
III.4.3 Conclusions.....	249
III.5 <i>Grafting from</i> strategy.....	251
III.5.1 Experimental section.....	251
III.5.2 Results and Discussion.....	253
III.5.3 Conclusion.....	261
III.6. MacroRAFT-assisted encapsulating emulsion polymerization (REEP) of colloidal LDH.....	262
III.6.1 Experimental section.....	262
III.6.2 Results and Discussion.....	263
III.6.3 Conclusion.....	270
III.7. General conclusions of chapter III.....	272
III.8. References.....	274

III.1. Introduction

Layered double hydroxides (LDH) consist in a very interesting class of materials. They are composed of positively charged metal hydroxide layers, which are stacked together with compensating guest anions in the interlayer spaces. Unique physicochemical properties of LDHs can be designed by tailoring the metallic cations nature in the layers, the interlayer anion nature, and the crystallite size and structure. Depending on these parameters, LDH can present high surface area, high porosity, large aspect ratio, high and tunable charge density, increased surface reactivity, and biocompatibility. They can be used for applications such as catalysts¹, biotechnological devices², sorbents³, ion exchangers⁴, and fillers for polymeric nanocomposites⁵.

Polymer/LDH nanocomposites present several interesting features. The incorporation of LDH fillers into polymer matrixes confers advantageous properties to the material, such as high thermal stability, fire-retardant characteristic and increased mechanical strength (e.g. tensile, shear). It can also act as carrier of specific additives (e.g. anti-corrosion, anti-UV, dyes). As discussed previously, the mechanical reinforcement provided by the filler can be enhanced if the charge presents anisotropy (i.e. high aspect ratio). Thus, LDH, which contains thin layer thickness and large basal planes, are good candidates to produce nanocomposite materials with enhanced mechanical properties.⁵⁻⁷

To effectively disperse LDH platelets in polymer matrices, and thus obtain superior properties, one must achieve the complete exfoliation of the layers, so the polymer can diffuse to the LDH galleries. However, the strong interactions to which the sheets are subjected (i.e. electrostatic and H-bonding interactions) may render the exfoliation a difficult task. Therefore, a pre-treatment of the stacked hydrophilic LDH phase with organic compounds is usually necessary to compatibilize inorganic and organic parts. The intercalation of surfactants, monomers, initiators and polymers has been described in the literature for the synthesis of polymer/LDH nanocomposites.⁵ Different strategies can be used to produce these materials, including: (i) melt intercalation, (ii) exfoliation-adsorption, (iii) *in situ* intercalative polymerization (iv) and template synthesis. Processes (i) and (ii), in particular, rarely generate exfoliated structures, or require the use of organic solvents to achieve uniform dispersion of the platelets. On the other hand, the two other processes can be performed in various solvents (i.e. polar and non-polar) and systems (e.g. bulk, solution, dispersed media), and usually generates well-defined exfoliated structures. *In situ* polymerization is commonly described using surfactant-intercalated, monomer-intercalated or initiator-intercalated LDHs, in which the two former materials are employed in processes classified as *grafting through* and *grafting from* approaches, respectively.⁶

Reversible deactivation radical polymerization (RDRP) is a powerful tool to synthesize polymer/inorganic nanocomposites with well-defined morphologies/structures. Mainly atom-transfer radical polymerization (ATRP)^{8, 9} and reversible addition-fragmentation chain transfer (RAFT)^{10, 11} techniques have been described to synthesize polymer/LDH materials via *grafting from* in bulk and solution media. To the best of our knowledge, the use of RDRP for the synthesis of polymer/LDH nanocomposites in aqueous (dispersed) media via *grafting from* or other *in situ* polymerization has not been described to date.

In this chapter, we aim to improve the affinity of LDH with the polymer matrix by building a polymer corona or a polymer layer around the platelets. The polymer corona will be grown by a *grafting from* approach performed in aqueous solution under RAFT polymerization, starting from RAFT-intercalated LDH phases produced by template synthesis. To encapsulate the LDH platelets within a polymer layer, the macroRAFT-assisted encapsulating emulsion polymerization (REEP) technique will be employed, using the same approach as the one developed with Imogolite. First, a copolymer macroRAFT agent was adsorbed and/or intercalated into the LDH phase, without the need of any other chemical modification. This macroRAFT agent was then chain-extended in water to form composite particles, following the REEP technique.

In the first part, a bibliographic study on LDH was presented, including structural characteristics, synthesis pathways and utilization of these lamellar inorganic matrices for the production of polymer/LDH nanocomposites.

In the second part, the different steps towards the formation of a polymer corona or the encapsulation of LDHs were described. First, the synthesis of MgAl and ZnAl LDH pure phases was investigated through different routes (conventional and flash coprecipitation). In a second step, the modification of LDH layers with RAFT and macroRAFT agents was performed through anionic exchange or template synthesis. Starting from the LDH-RAFT materials, the growth of a polymer corona around the layers was explored through *grafting from* in aqueous solution. Finally, the encapsulation of LDH colloidal particles was performed using the REEP technique, and the effect of some parameters, like the nature of the LDH and the macroRAFT concentration, was investigated.

III.2. Bibliographic study on Layered Double Hydroxide (LDH) materials

LDH also called anionic clays or hydrotalcite compounds, are natural or synthetic materials constituted of positively charged layers and exchangeable compensating anions and water molecules in their interlamellar space. They were discovered in 1842 in Sweden, and were referred to as “a mineral that can be easily crushed into a white powder similar to talc”. They occur in nature in foliated and contorted plates and/or fibrous masses,¹² but their synthesis is also simple and efficient. The chemistry of LDHs is now widely studied, and their physicochemical properties make them interesting candidates for applications in catalysis, pharmaceutical, soil, nanocomposites, and materials science.¹³

Their structure, synthetic routes, modification conditions with organic compounds and applications will be briefly reviewed in this section.

III.2.1 LDH structure

The exact formula of hydrotalcites: $[\text{Mg}_6\text{Al}_2(\text{OH})_{16}\text{CO}_3 \cdot 4\text{H}_2\text{O}]$ was first elucidated by Prof. E. Manasse (Italy), in 1915,¹⁴ at the same time that the equivalent structure containing Mg and Fe and called pyroaurite was discovered. The general formula of LDHs is represented by $[\text{M}^{2+}_{(1-x)}\text{M}^{3+}_x(\text{OH})_2](\text{A}^{n-})_{x/n} \cdot z\text{H}_2\text{O}$, where M is a metal cation and A is an interlayer anion.

Their structure is derived from brucite, a mineral of minimal formula $\text{Mg}(\text{OH})_2$, in which the magnesium cations are localized in the center of the octahedron having hydroxyl anions in its vertices. These octahedra share their edges forming neutral planar layers, which are maintained together by hydrogen bonds. When the divalent cations of a brucite-type structure are isomorphically replaced by trivalent cations, the lamella presents a residual positive charge. To neutralize the system, compensating anions settle in the interlayer space. These anions together with water molecules promote the stacking of the double hydroxide sheet with a poorly ordered interlayer domain. In this case, the lamellae are maintained together not only by H-bonding, as it is the case for brucite, but also by electrostatic attraction between the positively charged layers and the interlayer anions.¹⁵ A schematic representation of the LDH structure is shown in **Figure 1**.

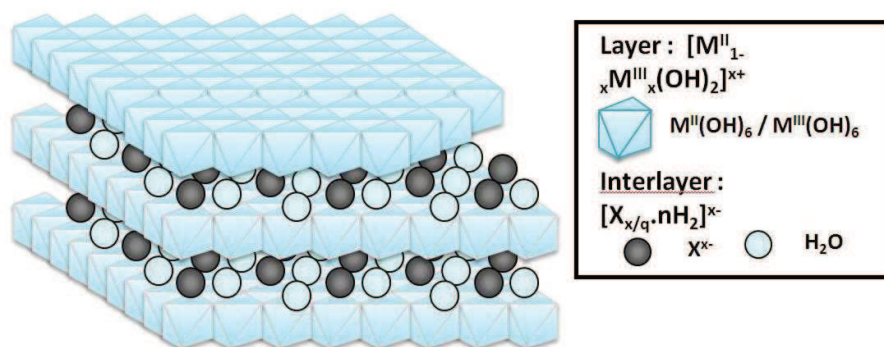


Figure 1. Schematic representation of layered double hydroxides (LDH) structure.

The inorganic layers of LDH can be stacked according to two different symmetries, resulting in 3R rhombohedral unit cells or 2H hexagonal unit cells. Most part of synthetic LDH presents rhombohedral symmetry.¹⁴

The first discovered phases had an Mg/Al-based composition. Natural minerals with the same structure but containing different divalent and trivalent metal cations (i.e. different from Mg^{2+} and from Al^{3+}) in the layers were later discovered. For synthetic LDHs, the M^{2+} is commonly Mg^{2+} , Zn^{2+} or Ni^{2+} , and the M^{3+} is commonly Al^{3+} , Ga^{3+} , Fe^{3+} or Mn^{3+} . LDHs may also contain M^+ and M^{4+} cations but these are limited to specific examples such as Li^+ and Ti^{4+} .^{16, 17}

Compared to cationic clays such as Montmorillonite and Laponite, which may be exfoliated in aqueous suspension, LDHs are more difficult to be delaminated. Their high charge density and anion content result in strong interlayer electrostatic interactions between the sheets and significant hydrophilic character.⁵

LDHs present a wide range of compositions varying according to the nature and the content of the metal cations, the type and the charge of the interlayer anions and the water content in the interlamellar domains. Further details about the different structures of LDHs can be found in review articles.^{18, 19}

III.2.2 LDH synthesis

Conventionally, LDHs are synthesized by the coprecipitation of metallic salts with a concentrated alkaline solution. Several alternative methods have been proposed, depending on the intended application. The sol-gel method,²⁰⁻²³ hydrothermal synthesis²⁴ and solvothermal synthesis²⁵ have also been described. The sol-gel method is usually employed when one aims to form LDH thin films. The control over the structural and textural properties of the final products

has been attempted by procedures such as microwave irradiation,²⁶⁻²⁸ ultrasonication²⁶ or the urea hydrolysis method.^{27, 28} Another interesting route proposed was the coprecipitation in alcoholic solution for the preparation of colloidal LDH.^{25, 29} In a conventional coprecipitation method, the morphology and particle size distribution depend on the supersaturation of the synthesis solutions.^{12, 30} The mixing method and the pH during the nucleation and precipitation process have been reported to be the most important synthesis variables, and can have a marked influence on particles size and texture of the resulting products.^{12, 31, 32}

The changes undergone by LDHs during calcination up to 500 °C are well-documented.^{33, 34} Typically, for a MgAl based LDH phase, below 200 °C, they only lose interlayer water; at 350 – 500 °C, however, they suffer dehydroxylation and decomposition of all carbonate into carbon dioxide and the corresponding metal oxide. The mixed oxides obtained exhibit peculiar properties, such as high specific surface areas with pore size in the mesoporous range.

Coprecipitation and sol–gel methods were compared by a few groups for the synthesis of Mg/M³⁺ (with M³⁺ being Al, Ga and In) and M²⁺/Al (with M²⁺ being Mg and Ni) LDH phases.^{35, 36} Armendia *et al.*³⁵ studied the effect of the trivalent metal nature and the synthetic route on final LDH crystallinity and composition. The authors observed that for all metals evaluated, LDHs with higher crystallinity were obtained by the coprecipitation method. On the other hand, the phases obtained by the sol–gel technique presented specific surface areas three times higher than the ones obtained by coprecipitation. After calcination, however, the difference in surface area was suppressed. In terms of the trivalent metal cation, it was observed that lower crystallinities and higher interlayer distances were obtained when the ion radius was increased, i.e. in the sequence Mg/Al > Mg/Ga > Mg/In, whichever the synthetic method used. Finally, the most basic Mg/Al phases showed no appreciable difference between both methods. In contrast, Prinetto *et al.*³⁶ reported a comparative study on the synthesis of Mg/Al and Ni/Al LDHs by coprecipitation and sol–gel methods. In this work, the authors observed that even after calcination the specific surface area provided by LDHs prepared via sol–gel was at least 10% higher than that of the ones obtained by coprecipitation. TEM analysis revealed different morphologic features of the sol–gel and coprecipitated materials, both as-prepared and after calcination. Thermo gravimetric - differential scanning calorimetry (TG-DSC) and IR spectroscopy evidenced the presence of organic species remaining as compensating anions in the interlayer space, inducing a rather different decomposition process for the sol – gel and coprecipitated samples. Regarding the N₂ adsorption-desorption isotherms, the coprecipitated samples presented isotherm shapes characteristic of clay minerals, while sol–gel materials presented profiles generally encountered in alkoxide gels.

A recent method was developed by Zhang *et al.*²⁴ to obtain highly crystalline and regular-shaped LDH phases, based on a mechano-hydrothermal synthesis. A two-step synthesis was conducted, that is, a mixture of MgO and Al₂O₃ was milled for 1h followed by hydrothermal treatment with NaNO₃ solution. In this method, the pre-milling process played a key role in LDH formation during subsequent hydrothermal treatment. Compared to conventional mechanochemical and hydrothermal methods, this method showed lower reaction temperatures and shorter time, yielding targeted products with better crystallinity, dispersion and regular shape.

Comparing both methodologies, the coprecipitation technique is simpler, as it consists only in the coprecipitation of metallic salts at constant or increasing pH under mild conditions. It leads to homogeneous chemical composition. In contrast, the sol–gel method requires long reflux periods and subsequent steps to obtain crystalline and pure structures. In the present thesis, we will utilize the coprecipitation method. However, to obtain colloidal LDH platelets through this method, it is generally necessary to employ a thermal treatment on the sample after coprecipitation, as it will be seen in the next section.

III.2.2.1 Synthesis of colloidal LDH

The synthesis of small and colloidal LDH phases has gained increasing attention in the past few years, due to the importance of low dimensional solids for the application in electronic, photonic, magnetic and mechanically resistant materials.⁵ In particular, the anisotropy of a two-dimensional (2D) nanosheet, with a thickness close to one nanometer and a lateral size ranging from a submicrometer to several tens of micrometers, allows them to serve either as an ideal 2D quantum system for the study of fundamental physics or as basic building blocks in the synthesis of functional solids.³⁷

Low dimensional LDH particles can be obtained by delamination of preformed phases, which generates positively charged thin platelets with a thickness of a few atomic layers, or by directly synthesizing small-sized LDH particles, generally forming colloidal LDH suspensions. The first process can be called “top down”, and the second “bottom up” (**Figure 2**).

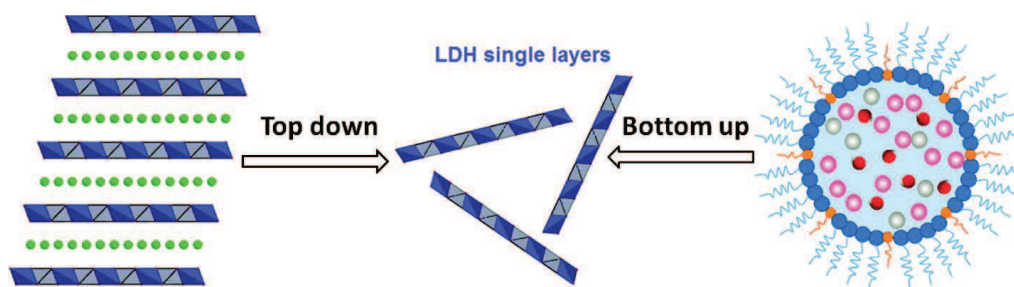


Figure 2. Synthesis schemes of top down and bottom up for LDH single layers production. Reproduced with permission from ref⁵. © 2012 American Chemical Society.

Various delamination (i.e. top down) techniques have been described to obtain single layer LDHs, and they are well-reviewed in the publication of Wang and O'Hare.⁵ Delaminations carried out in different solvents (e.g. butanol, toluene, formamide, water) and in some monomers (e.g. acrylates) are compiled in this extensive report. For the present work, we focused on the bottom up technique, where low dimensional and colloidal LDH phases are directly synthesized. In our specific work, the phases were not synthesized from inversed emulsions, as is it usually applied in bottom up synthesis. Instead, we tuned coprecipitation parameters to limit the growth of LDH layers and obtain low dimensional colloidal phases. The bottom up approach performed through coprecipitation method can be carried out in either solvent- or aqueous-based medium, and colloidal phases LDH phases can be obtained by both methods.

III.2.2.1.2 Water-based synthesis

Zhao *et al.*³⁸ reported the synthesis of low dimensional LDHs with uniform crystallite size using a new method based on separate nucleation and aging steps. The nucleation step was performed by the conventional coprecipitation method at constant pH or by rapid mixing of the metallic salt aqueous solutions in a colloid mill. Both nucleation steps were followed by hydrothermal treatment at 100 °C for 13h. Products obtained by the conventional and the new method were compared, and similar compositions, structures and properties were obtained in both cases. The main advantage of the method was that it afforded smaller particles with high aspect ratios, having a very narrow distribution of crystallite size. The authors have shown that the key features of this method were the very rapid mixing and nucleation process in a colloid mill followed by the separate aging step. Indeed, in a conventional coprecipitation process at constant pH, the mixing process takes considerable time such that the nuclei formed at the beginning of the process have much longer time to undergo crystal growth than those formed at

the end of the reaction leading to a large particle size distribution. In addition, they suggested that the extreme forces to which the nucleation mixture was subjected in the colloid mill prevented aggregation of the nuclei and resulted in uniform small sizes.

Xu *et al.*³⁹ reported a rather similar method for the production of Mg/Al LDHs, in which they performed fast coprecipitation of aqueous metal salt solution followed by controlled hydrothermal treatment under different conditions (time, temperature, and concentration). The relationship between the LDH particle size and the hydrothermal treatment conditions was investigated, and it was shown that LDH particle size can be precisely controlled between 40 and 300 nm by adjusting these conditions. After hydrothermal treatment, the LDH materials collected demonstrated a very good crystallinity, contrary to the freshly precipitated samples, as evidenced by XRD analyses. FTIR spectra were typical of LDH materials for the samples obtained before and after the hydrothermal treatment. However, it was observed that during treatment, the hydroxide layers afford a higher leaching of Mg²⁺ than Al³⁺, which slightly changed the Mg/Al ratio, leading to the formation of traces of gibbsite structure. Particle size measured presented narrower distributions after hydrothermal treatment. The authors studied the effect of treatment time, temperature and LDH concentration on final particle size. It was shown that the particle size and dispersion state were highly dependent on the hydrothermal treatment time. Very uniform suspensions with narrow particle size distributions were obtained after treatment at 100 °C for 4, 8, 16 or 48h. However, the 2h treatment was reported not to be enough to redisperse the aggregates formed during fast coprecipitation, while the long 144h treatment led to reaggregation of the bigger LDH crystallites (grown during treatment). Regardless of the aggregates, the primary particle size constantly increased with increasing hydrothermal treatment, and the relationship was almost linear, with a particle growth rate of roughly 1.5 nm h⁻¹. The temperature during hydrothermal treatment also influenced the final particle size. An increase in temperature by 10 °C led to an increase in the hydrodynamic diameter by 10 – 15 nm on average. This showed a quick growth of LDH crystallites at higher temperatures. Similarly to the effect of treatment time, too low or too high temperatures (80 °C or 150 °C, respectively) promoted LDH aggregation. The LDH particle size was influenced by its concentration to a much smaller extent. It was evidenced in this work that during the hydrothermal treatment, several events, such as disaggregation, particle growth, and reaggregation, occurred in series and/or in parallel, and thus the dispersion of LDH aggregates into individual LDH particles and the primary LDH particle size were strongly affected by hydrothermal treatment conditions.

Faour *et al.*⁴⁰ studied the effect of synthesis parameters on the NiAl-LDH particle size. In this work, the influence of coprecipitation parameters such as the nature of the precipitating agent and the application of a hydrothermal treatment on the microstructure, particle size and

morphology of carbonate containing NiAl-LDH was investigated for the first time. The authors compared the coprecipitation at constant pH, in strong alkaline solution and using urea decomposition, followed by hydrothermal treatment. The particle size of the samples was, as expected, very dependent on the synthetic route used for their preparation. It was observed a higher tendency to agglomerate as particle size decreased, and a net increase in particle size upon hydrothermal treatment. The “sand rose” aggregate (i.e. rigid spheroidal morphology of intergrown platelets) disruption observed for the samples recovered after hydrothermal treatment (HTT) compared to the freshly coprecipitated samples was ascribed to a dissolution/re-precipitation process occurring upon the hydrothermal treatment. Despite the aggregation disruption, the stacking fault of LDH platelets was not altered by hydrothermal treatment. In general, isolated hexagonal platelets of higher diameters were obtained after HT, whereas samples obtained just after stirring exhibited very small and ill-defined aggregated particles. The agreement between particle size and crystallite size was considered as an indication that the particles were probably small single crystals. The authors concluded that the hydrothermal treatment increased the crystallinity of the samples but did not alter the stacking arrangement nor eliminated stacking faults. The trend of increasing particles size after HT observed by the authors, oppositely to what had been observed by Xu *et al.*³⁹, can be to some extent attributed to the fact that samples were not washed before the hydrothermal treatment in the work of Faour *et al.*⁴⁰ The presence of remaining ions in the solution could promote a further growth of crystallites, causing the increase in particle size.

In conclusion, it was shown that fast coprecipitation provides a very equal chance for all possible precipitating species to form uniform nuclei, a prerequisite for the mono-dispersity, even though it is unnecessary to form a stable LDH suspension.^{38, 39} In addition, the subsequent heat-treatment not only improved the crystal lattice structure, helping to reduce the interconnection between the platelets, but also offered a strong Brownian motion, promoting the dispersion of the aggregates into individual LDH particles.³⁹ On the other hand, hydrothermal conditions favor the solubility of solids, also favoring a particle growth through Ostwald ripening phenomenon that consists of the dissolution of the small particles and recrystallization around the biggest ones. Thus, the synthesis parameters (e.g. coprecipitation mode, hydrothermal treatment conditions) must be judiciously tuned to control the particle size, dispersion state and morphology of LDH platelets.

III.2.2.1.1 Solvent-based synthesis

To obtain small sized and colloidally stable LDHs, different strategies have been described. The separation of conventionally co-precipitated samples by centrifugation was reported by Itaya *et*

*al.*⁴¹ In this work they recovered only the stable LDH remaining in the supernatant after centrifuging the co-precipitated samples in water. However, this strategy results in the loss of product, in addition to the extra step of platelets fractionation required. To overcome these drawbacks, Gardner *et al.*²⁵ developed a technique to directly synthesize colloidal LDHs. The work consisted in the coprecipitation of metallic salts with a base in alcoholic solution. The replacement of water by an alcohol afforded alkoxide anions in the reaction medium and the incorporation of these anions between the brucite-like sheets. Syntheses were made in methanol, ethanol, propanol and butanol, and alkoxide-intercalated LDHs were successfully obtained in all solvents. Dispersing the methoxide LDH in water at ambient temperature overnight led to complete hydrolysis of the methoxide ion and to the formation of a nearly transparent colloidal LDH suspension. Gursky *et al.*²⁹ further studied the formation of continuous thin films from hydrolyzed methoxide LDHs prepared by the same method. In this work it was shown that conventional co-precipitated LDHs aggregate, while uniform and continuous thin films could be obtained with the colloidal LDH suspensions.

A thermal treatment applied after the coprecipitation synthesis is also an efficient way of producing colloidal LDH phases. When the synthesis and the treatment are carried out in aqueous medium, the process is called hydrothermal treatment. Instead, when it is performed in a solvent-based medium, the process receives the name of solvothermal treatment.

To produce hollow nanospheres of LDH crystals using a templating approach, Gunawan *et al.*⁴² synthesized LDH colloidal particles by solvothermal synthesis and thermal treatment. In their work, MgAl-LDH nanocrystals were synthesized by coprecipitation of the magnesium and aluminum nitrate salts in pure methanol at ambient temperature. The following thermal treatment was performed in the same solvent (methanol) at 150 °C for 18h in an autoclave under autogeneous pressure. The product was recovered after consecutive washing and centrifuging cycles, and it was analyzed by XRD, FTIR and TEM. The XRD pattern of LDH nanocrystals indicated the formation of fairly crystalline LDH structures with a rhombohedral symmetry. The LDH thickness was estimated at 10 nm, based on the XRD (003) basal plane peak. FTIR results showed a strong absorption peak at 1384 cm⁻¹, attributed to the interlayer NO₃⁻ anions, and other peaks at 1054 and 2950 cm⁻¹, ascribed to the presence of methoxide ions originating from the solvent. Smaller particles (~30 nm) with narrow particle size distribution were obtained compared to the work of Xu *et al.* (50 – 300 nm),³⁹ based on dynamic light scattering (DLS) analysis, and stable translucent suspensions of LDH were generated (**Figure 3 A, B**). In Xu's work, the process was carried out in aqueous medium, by hydrothermal treatment. The authors of the present study justified the differences obtained in terms of particles size between both reports as a solvation effect of methanol and water as the synthesis medium. TEM images showed that the sample consisted of finely dispersed platelet-like nanocrystals (**Figure 3 C**).

The well-defined colloidal LDH nanocrystals formed were subsequently used to coat the surface of carbon nanospheres as templates, without the need of an exfoliation step, to produce hollow nanospheres for diverse application (e.g. catalysis, electrochemistry, drug-delivery systems).

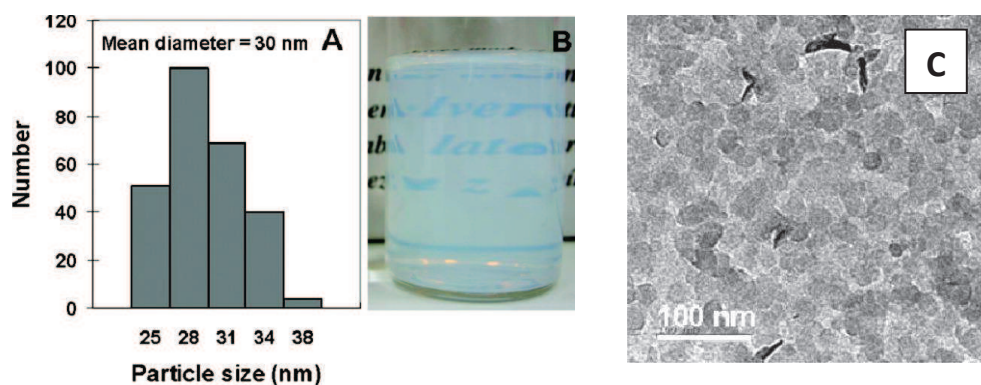


Figure 3. (A) Particle size distribution, (B) translucent and stable suspension and (C) TEM image of LDH phases. Reproduced with permission from ref⁴². © 2009 American Chemical Society.

III.2.3 LDH modification and incorporation into polymer matrixes

The versatile physicochemical properties adopted by LDH materials depending on their composition (i.e. nature of metal cations and interlayer anions), crystalline structure (i.e. surface area, aspect ratio, porosity, etc.), and charge density make them interesting materials for a vast range of applications. Their potential use in biotechnology (e.g. drug carriers)^{2, 15, 37, 43}, catalysis^{1, 22, 44}, wastewater treatment⁴⁵, as sorbents^{3, 46-49} and ionic exchangers^{4, 50, 51}, in electrochemical sensors⁵² and as fillers for advanced materials^{5-7, 53-56} (i.e. electronic, photonic, magnetic, mechanical, and composite materials) has been investigated.

Especially in the area of polymer nanocomposites, to achieve an effective enhancement of properties, the LDH materials are usually treated with organic or inorganic guest compounds. Their modification with a large variety of compounds has been reported in the past decades. For instance, surfactants,^{57, 58} organosilanes,⁵⁹⁻⁶¹ ethylene glycol,⁶² monomers,^{5, 63, 64} polymers^{5, 56, 65} and polyoxometalates (POMS)⁶⁶ intercalation has been investigated.

Three different routes can be distinguished to form organic compound-intercalated LDH sheets: (i) the intercalation (i.e. anionic exchange) of the organic species within preformed LDH,^{67, 68} (ii) the calcination/reconstruction of the LDH phases in the presence of organic species^{60, 69} (iii) and the in situ synthesis of the LDH phases in a solution containing the organic species.^{58, 70} A

fourth route will be further evocated, which is the in situ polymerization in presence of preformed LDH layers, but this strategy usually starts from precursor-intercalated LDHs, previously obtained by one of the former routes. An illustrative representation of the different pathways is given in **Figure 4**. For this thesis, strategies (A) and (B) of **Figure 4** were investigated.

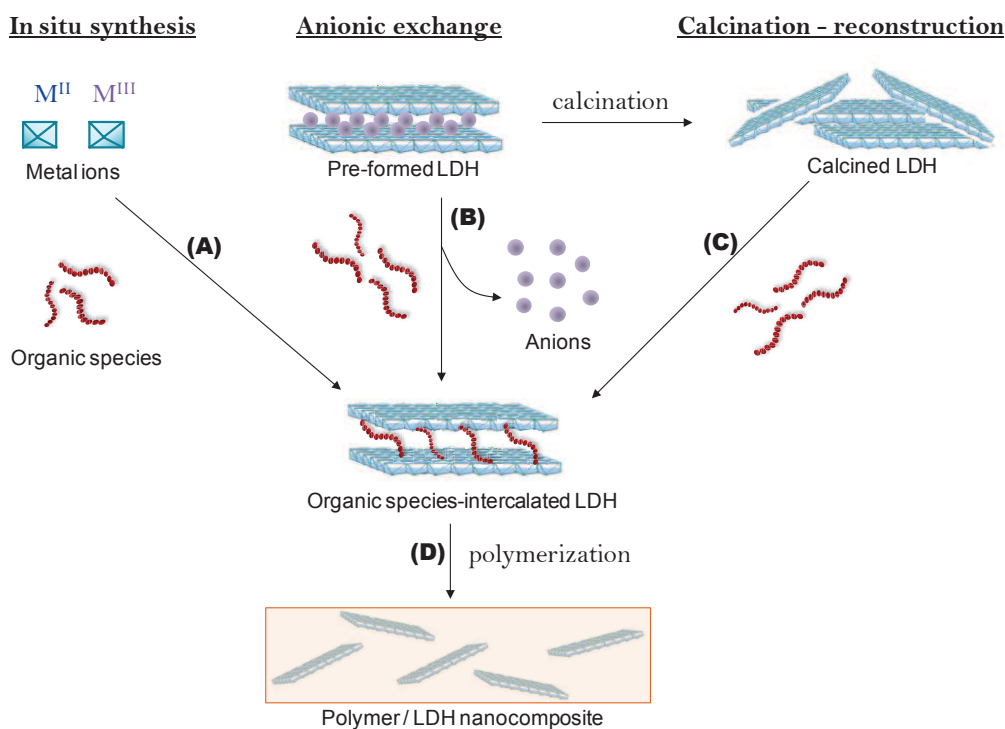


Figure 4. Pathway to LDH modification with organic compounds by (A) *in situ* synthesis of LDH in presence of the organic species, (B) anionic exchange, (C) calcination and reconstruction of the layered structure in presence of the organic species and (D) possible polymerization of the modified-LDH for the production of nanocomposites.

For the anionic exchange technique, the nature of the original interlayer anion and its affinity with the LDH layer is of great importance since it will define the efficiency of the intercalation. Chakraborty *et al.*⁷¹ have recently reported the influence of carbonate traces on the anionic exchange of nitrate ions. In this study it was found that the presence of CO_3^{2-} ions in the interlayer space of Mg/Al-LDH negatively affects its anion exchange capacity, which has direct relationship with the extent of drug-loading when used as a carrier for drug delivery, for instance, or for the intercalation of different organic compounds.

The modified-LDH materials can be used for different applications, as brought out earlier, and one of the most often described is the incorporation of LDH platelets into polymer matrixes, forming polymer/layered double hydroxide nanocomposites. Some reviews can be found related to this field of research.^{5-7, 56} In the present work, we will focus on the examples of polymer/LDH production by the use of *in situ* polymerization in presence of LDH layers and the *grafting from* technique, in aqueous and in dispersed media (i.e. aqueous solution, emulsion, miniemulsion or suspension polymerization).

III.2.3.1 Polymer/LDH nanocomposites by *in situ* polymerization

Various examples of the synthesis of polymer/LDH nanocomposites by *in situ* solution^{70, 72} or bulk^{63, 64, 73-78} polymerizations can be found in the literature. In contrast, only a few examples can be found regarding the production of LDH/nanocomposites by radical polymerization in aqueous and dispersed media. Indeed, it is a challenge to eliminate the strong electrostatic interactions between LDH layers in an aqueous system and successfully synthesize exfoliated polymer/LDH nanocomposites via *in situ* polymerization. Moreover, the sand rose morphology prevents both swelling and exfoliation of the sheets in water, wherein the swelling or exfoliation is one of the key factors for the preparation of exfoliated polymer/layered nanocomposites (PLNs)⁷⁹.

Vaysse *et al.*⁸⁰ reported the intercalation of acrylate monomers (acrylic acid and sodium acrylate) into the galleries of NiL-LDH phases, where L = Fe, Co and Mn. The intercalated acrylate monomers were further polymerized in aqueous solution using free radical polymerization initiated by potassium persulfate ($K_2S_2O_8$). The intercalation was carried out through an electron-transfer process (*chimie douce* method) consisting of successive oxidizing and reducing steps. The *in situ* radical polymerization was performed by introducing the monomer-intercalated LDH in a persulfate solution and heating to 60 °C for 24h. For the iron-based poly(acrylate)/LDH material, XRD analyses showed an interlayer distance of 12.6 Å, consistent with the polyacrylate anion intercalation. At the same time, some parasitic phases were detected, with interlayer distances of 10.3 Å. This second family of phases was ascribed to anionic exchanged phases containing persulfate or sulfate anions, originating from the potassium persulfate initiator. IR results confirmed the complete acrylate polymerization, evidenced by the disappearance of the $\nu(C=C)$ band. For cobalt and magnesium-based polymer/LDH samples, no parasitic phase was detected, which indicated that persulfate anion intercalation did not occur in these cases. Complete polymerization was indeed found, but a different mechanism was proposed alternatively to the persulfate initiation. It was proposed by the authors that acrylate radicals were formed from the oxidation of the acrylate species during

the synthesis process, leading to spontaneous polymerization. An experiment conducted in the absence of $K_2S_2O_8$ also generated polymeric species, confirming the hypothesis. Polymers recovered from the three experiments were analyzed by SEC. Results showed that the macromolecules were mainly made of oligomers (with molar masses from 300 to 900 $g\ mol^{-1}$), with small proportion of longer macromolecules (of molar masses between 900 and 2900 $g\ mol^{-1}$). The essential differences observed between Fe-based or Co- and Mn-based LDH-acrylate polymerization could not be explained by the authors. Even though polymerizations were performed in aqueous dispersions, no colloidal aspects were evoked by the authors.

Ding *et al.* reported the synthesis of polystyrene/Zn-Al nanocomposites via *in situ* emulsion⁸¹ and suspension⁷⁹ polymerization. Two surfactants were studied, *N*-lauroyl-glutamate (LG) and sodium dodecyl sulfate (SDS). A long chain spacer (*n*-hexadecane) was also employed to help with LDH exfoliation. First, the ZnAl-surfactant structure was synthesized by *in situ* LDH coprecipitation in a LG or SDS aqueous solution at pH range of 9.5 – 10 and containing *n*-hexadecane. To the freshly precipitated sample suspension, styrene and initiator ($K_2S_2O_8$ and Na_2SO_3 for emulsion and benzoyl peroxide (BPO) for suspension polymerizations) were added. The system was heated to 80 °C for 6h to allow polymerization to occur. The resulting nanocomposites were analyzed by FTIR, XRD and TEM. FTIR confirmed the presence of LG or SDS in the freshly precipitated LDH-surfactant samples as well as the presence of polystyrene in the PS/LDH nanocomposite obtained in both polymerization series (emulsion and suspension). XRD results showed that the layered framework of LDH was preserved in the PS matrix after nanocomposite synthesis. Low-angle XRD results showed no peak at $2\theta = 1.5 - 10^\circ$ for the samples prepared using LG. The absence of peaks was attributed to the exfoliation of LDH structure in the PS/LDH nanocomposite obtained using this surfactant. In contrast, the presence of two peaks around $2\theta = 3.2^\circ$ and 7.0° for the samples prepared using SDS indicated intercalated structures in the PS/LDH nanocomposite prepared using this surfactant. The authors claimed that TEM analyses were in good agreement with the XRD results, and well dispersed platelets were observed for the LG-containing samples (**Figure 5 B and C**). However, LDH platelets are hardly seen in the images. They also claimed that at low LDH loadings, individually exfoliated platelets were observed. When the LDH content was increased, stacks of platelets with interlayer space superior to 10 nm were found. Despite the stacking, the dispersion state was also considered by the authors as an exfoliated morphology. Comparing both methods, the authors claimed that the syntheses performed in emulsion polymerization generated exfoliated structures with LDH content up to 20 wt% when using LG surfactant (**Figure 5**). Exfoliated morphologies were obtained with a limited content of 10 wt% of LDH when the syntheses were carried out in suspension using the same surfactant. Again, even

though polymerizations were performed in suspension or emulsion system, no stability or colloidal aspects were discussed nor particle size measured.

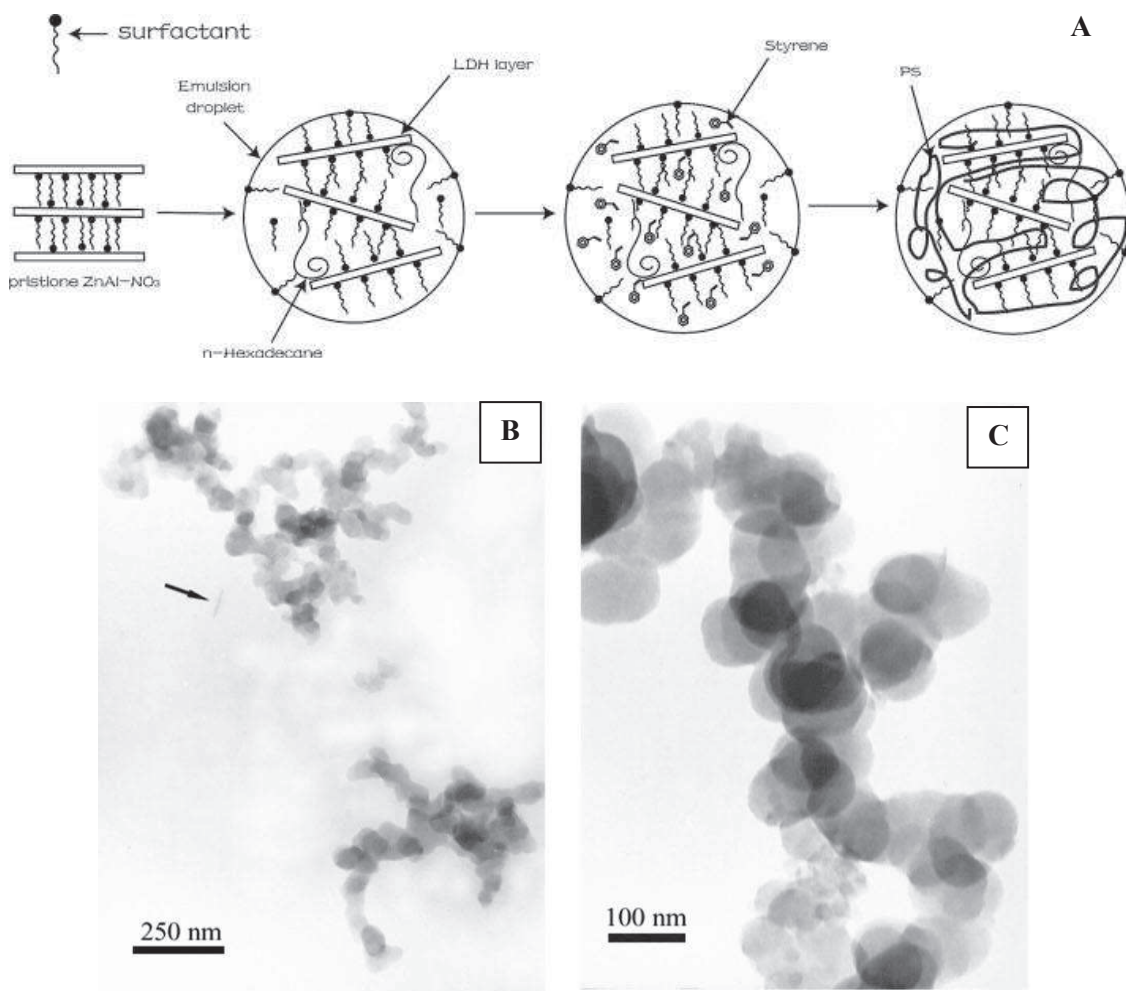


Figure 5. (A) Schematic diagram of the formation procedure of the exfoliated PS/LDH nanocomposites. (B) TEM and (C) HR-TEM images of the LG-containing sample prepared by emulsion polymerization. Reproduced with permission from ref⁸¹. © 2005 Elsevier.

Bao *et al.*⁸² studied the synthesis of poly(vinyl chloride)/layered double hydroxide (PVC/LDH) nanocomposite resins by *in situ* suspension polymerization of vinyl chloride monomer in the presence of LDHs intercalated with dodecyl sulfate anions (LDH-SDS). The surfactant-intercalated LDH phases were prepared by direct coprecipitation of Mg and Al nitrate solutions in presence of SDS at constant pH of 10.0. The resulting intercalated phase, after being washed and dried, was mixed to vinyl chloride monomer (VCM) and diethylhexyl peroxydicarbonate (EHP, initiator) under stirring in an autoclave for 1h. Water and suspending agents, poly(vinyl alcohol) (PVA) and hydroxypropylmethyl cellulose (HPMC), were then introduced and the

system was stirred for another hour. The medium was then heated to 57 °C to start polymerization. The pressure of the polymerization system was maintained at about 9.5 bar. The intercalation of SDS into LDH improved the compatibility of LDH with VCM and expended the layer spacing, which was a further benefit for the incorporation of LDH particles into the VCM droplets in suspension polymerization, and intercalation or exfoliation of LDH by PVC chains. The size of the pristine LDH-CO₃ and the modified LDH-SDS layers was in the range of 1 to 10 μm. The successful intercalation of SDS into LDH interlayer spaces was confirmed by XRD and FTIR. XRD results showed the maximum basal spacing of LDH-SDS to be 27.3 Å, while that of LDH-CO₃ was 7.8 Å. FTIR spectrum of the LDH-SDS contained strong absorption at 1197 and 1049 cm⁻¹, assigned to the stretching vibrations of RSO₄⁻. Characteristic peaks associated with vibrations of -CH₃ and -CH₂ groups also occurred at 2850 – 2950 cm⁻¹. These FTIR assignments further confirmed that the SDS anion was successfully intercalated into the LDH's gallery. Regarding the suspension polymerization step, it was shown that the mean particle sizes of the PVC/LDH-SDS composite were all smaller than that of pure PVC, and the particle size did not change as the weight fraction of LDH-SDS increased. Number average molar mass and molar mass distributions were not influenced by the presence or the weight fraction increase of LDH-SDS. TEM results evidenced that the size of dispersed LDH-SDS layers in the PVC matrix was greater (> 100 nm), and these layers were hardly intercalated or exfoliated in the PVC/LDH-SDS composite prepared by direct melt blending, comparing to the samples obtained via *in situ* polymerization. This was explained by the authors by the fact that the attraction force of LDH-SDS layers was still strong and it was difficult for PVC chains to intercalate in the melt blending process. Much smaller layers (from 10 to 50 nm) were observed in the samples prepared by *in situ* polymerization. After melt processing of the hybrid material, partially intercalated and partially exfoliated LDH-SDS/PVC nanocomposites were obtained. The resulting materials showed superior mechanical properties (storage modulus, tensile strength, Young's modulus and charpy notched impact strength) than the melt blended sample or than pure PVC.

Chen *et al.*⁸³ reported the production of a novel PMMA/MgAl LDH nanocomposite. The hybrid material was synthesized *in situ* by adding a sodium hydroxide aqueous solution to an emulsion consisting of an aqueous solution of metallic ions, SDS, MMA and BPO. The polymerization was then undertaken at 80 °C for 5h under N₂. For comparison, MgAl-SDS was prepared by anionic exchange and a conventional micro-composite was also prepared by mixing MgAl-SDS powder with PMMA in acetone solution. XRD of the nanocomposites synthesized by the new method together with the results of the calcined material gave a positive evidence of the intercalation of PMMA chains into the gallery of MgAl-LDH. TEM of the nanocomposite films showed the intercalated particles well dispersed in the PMMA matrix. Interestingly, although

the loading of MgAl-LDH was more than 30 wt%, good optical properties of PMMA/LDH films were obtained. The transparency was attributed to the very small size and uniform distribution of the intercalated particles. The final material also presented enhanced thermal properties resulting from the homogeneous distribution of the incorporated LDH particles to the matrix.

Qiu and Qu⁸⁴ synthesized PS/LDH nanocomposites via soap-free emulsion polymerization. Their method consisted on a two-step process, as shown in **Figure 6**. First, the MgAl-NO₃ phase was synthesized by conventional coprecipitation and followed by hydrothermal treatment. The LDH material was then dispersed in water and monomer and initiator were added. The medium was heated to 70 °C for 7 h to proceed with the free radical polymerization. XRD and TEM were used to monitor the changes of interlayer spacing and morphology during polymerization. Evolution of the interlayer distance suggested, at first, the intercalation of the initiator ions (S₂O₈²⁻), with an interlayer distance of 10.0 Å. As the polymerization time, *t*, increased to 60 minutes, only a broad diffraction peak was observed, corresponding to *d* = 11.3 Å. This distance was attributed to the intercalation of oligomers into the LDH gallery. For *t* > 120 minutes, the diffraction peaks of LDH component disappeared completely, which was attributed to the complete exfoliation of the MgAl-LDH in the polymer matrix. The morphological evolution of the nanocomposites, studied by TEM, led to similar conclusions. The increase in interlayer space with increasing polymerization time was confirmed by TEM. PS spheres were also observed, and no particular interaction was detected between the LDH layers and the latex spheres. The method was considered successful for the production of PS/LDH nanocomposites with uniform distribution of LDH layers in the matrix and with the merit of not using any low-molecular-weight surfactant. Even though latex particles were observed by TEM, no further discussion regarding particles size and emulsion/latex stability was given by the authors.

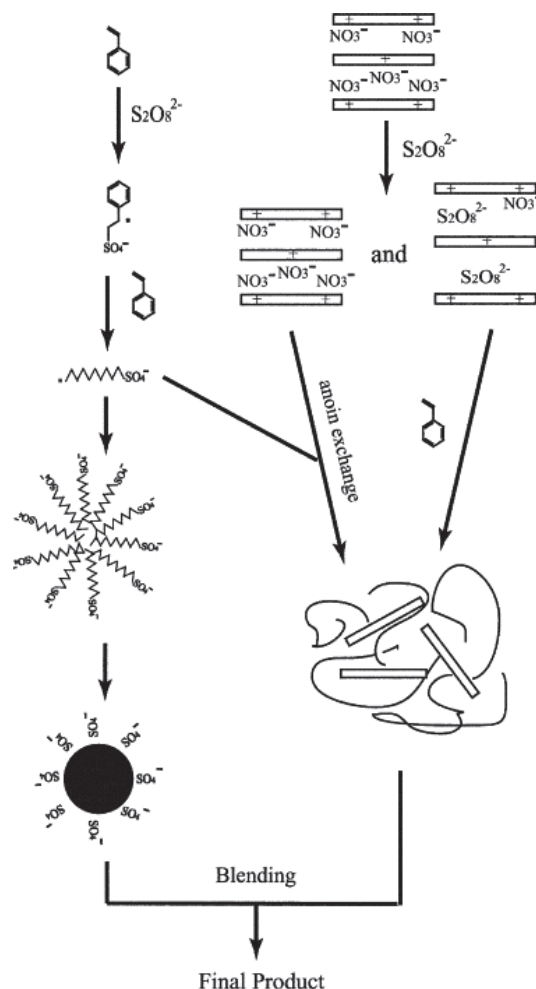


Figure 6. Schematic diagram of the formation procedure of an exfoliated PS/LDH nanocomposite via soap-free emulsion polymerization. Reproduced with permission from ref⁸⁴. © 2006 Elsevier.

III.2.3.2 Polymer/LDH nanocomposites by conventional and controlled “grafting from” polymerization

The infinite possibilities of intercalating organic compounds into the galleries of LDH phases open the way to explore different polymerization routes for the synthesis of polymer/LDH nanocomposites. The intercalation of surfactant molecules or molecular spacers into LDH is often performed prior to *in situ* polymerization, as reviewed in the previous section. The intercalation of monomers by covalent bonding or alternative strong attachment followed by its polymerization characterizes the “*grafting through*” approach, as shown in chapter I (section I.3.3.1), and has also been described in the literature.⁵⁶ Besides surfactant molecules and monomers, some polymerization initiators were also intercalated, to perform surface-initiated (i.e. “*grafting from*”) polymerization in LDH phases. This technique has been widely studied for other inorganic fillers as well, and some examples were presented in the bibliographic review of

this thesis (chapter I, section I.3.3.1). RDRP techniques derived from the “*grafting from*” approach are also possible through the intercalation of ATRP- or NMP-initiators, for instance. In the case of RAFT polymerization, the intercalated species is the chain transfer agent (i.e. RAFT agent). Various examples of *grafting from* using the RAFT technique and employing different fillers can be found in the literature and some of them were also presented in chapter I (section I.3.3.1.1). In this section, some examples of conventional and controlled “*grafting from*” approaches will be described for the synthesis of polymer/LDH nanocomposites.

III.2.3.2.1 Conventional grafting from polymerization

A novel approach to prepare exfoliated polymer/LDH nanocomposites was proposed by Yuan *et al.*⁸⁵ The method was based on the use of pre-exfoliated LDH layers containing a thiol-terminated monomer in the interlamellar space. First, the LDH was intercalated by SDS using the coprecipitation method for expanding the layer spacing. In a second step, a silane coupling agent, γ -(2,3-epoxypropoxy)propyl trimethoxysilane, was grafted into the interlayer of LDH to supply epoxy groups. Then, a trithiol terminal molecule, trimethylolpropane thioglycolic acetate (TMPT), was induced to the epoxidized LDH via the reaction of epoxy with thiol group. The obtained thiol-endcapped LDH (LDH-SH) hybrid presented a pre-exfoliated microstructure. This hybrid pre-exfoliated phase was then mixed to an acrylic resin and the system was UV-cured to obtain the hybrid nanocomposite. **Figure 7** shows the complete pathway used to obtain the exfoliated polymer/LDH nanocomposites. The kinetics of the UV-curable formulation was not greatly affected by the presence of the LDH-SH species. XRD and TEM analyses confirmed the formation of exfoliated microstructures in the final cured hybrid resin. Mechanical and thermal properties, as well as hardness were enhanced in different extents compared to the pure polymer. The authors claimed that the pre-exfoliated LDH-SH approach could be possibly extended to other polymerization systems.

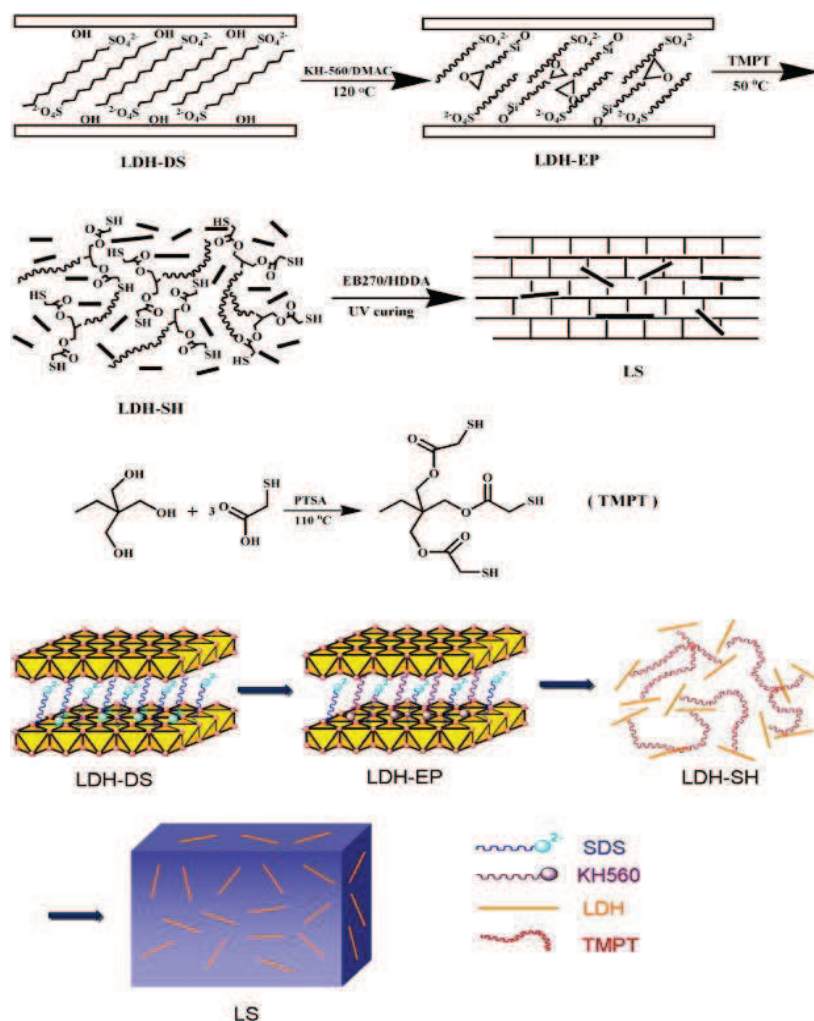


Figure 7. Diagram illustrating the preparation of exfoliated polymer/LDH nanocomposite by *in situ* polymerization. Reproduced from with permission from ref⁸⁵. © 2011 Elsevier.

Manzi-Nshuti *et al.*⁵⁵ described the surface-initiated polymerization of styrene with LDH layers in bulk polymerization. 4,4'-azobis (4-cyanopentanoic) acid (ACPA) initiator was first intercalated into the galleries of ZnAl and MgAl LDH phases. The ACPA-LDH hybrid phases were prepared by coprecipitation in aqueous solution at a constant pH of 10.0. The hybrid precipitate was aged at room temperature for 7 days. The intercalation was investigated by XRD and FTIR measurements. PS/LDH-ACPA nanocomposites were further prepared by mixing the LDH-ACPA phase with styrene, stirring for a day and heating the system to 100 °C. When the mixture became viscous, temperature was raised to 120 °C and it was left polymerizing for 8h. The resulting nanocomposites were analyzed by XRD and TEM. XRD results of the ZnAl-ACPA and MgAl-ACPA intercalated phases showed that both phases generated well intercalated structures (**Figure 8A**). ZnAl-ACPA LDH was however more crystalline, showing at least 5 reflections at equidistant 2θ values. It was also observed that 7 days of aging were

required for the complete intercalation of ACPA to take place, since shorter time (4 days) led to only partially initiator-intercalated structures. FTIR measurements also confirmed the intercalation of ACPA in both LDH phases; with the difference that the MgAl-ACPA sample was not fully exchanged and contained some nitrate anions in its interlayer.

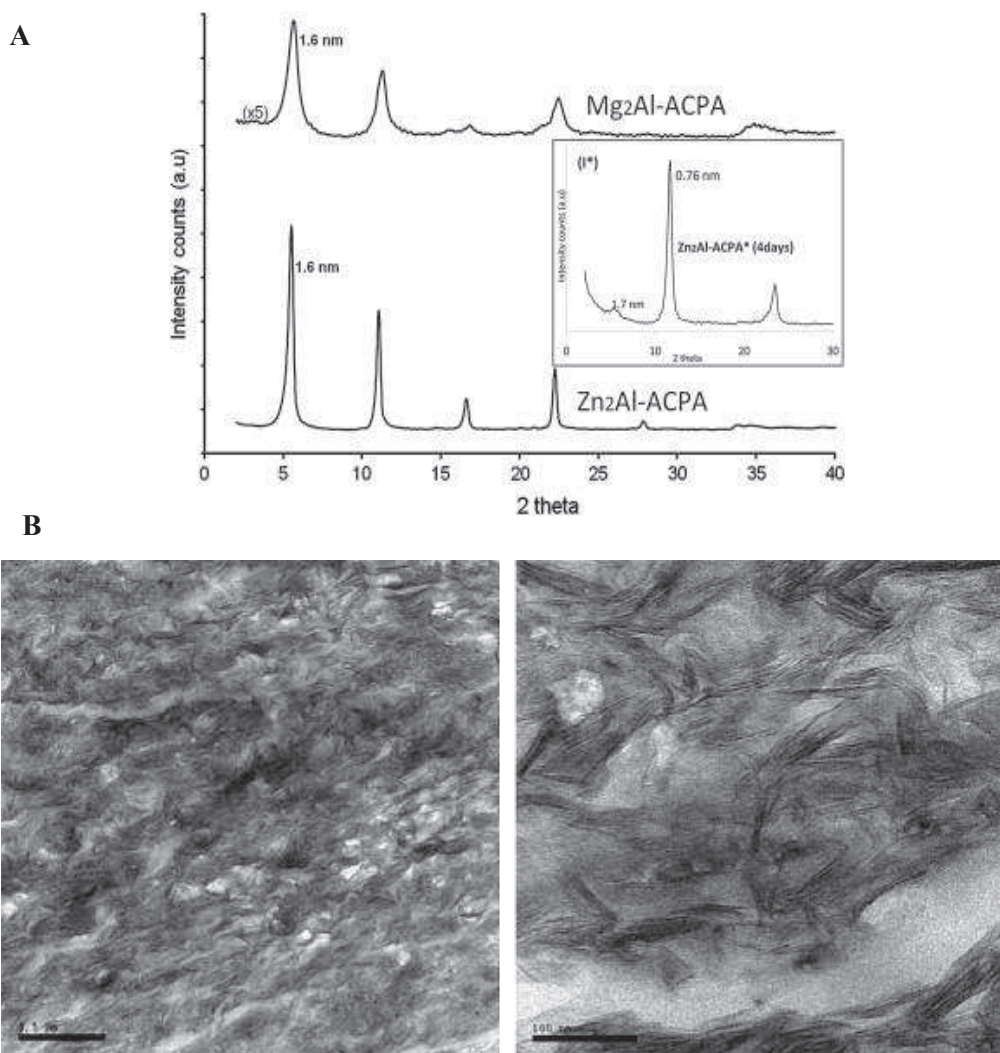


Figure 8. (A) Bright field TEM images of PS/3% ZnAl-ACPA at different magnifications. (B) XRD traces of ACPA-containing LDHs (aged for 7 days) of ZnAl and MgAl. The inset (I*) shows the XRD trace of a ZnAl-ACPA LDH that was aged for only 4 days. Reproduced with permission from ref⁵⁵. © 2009 Elsevier.

After polymerization, XRD and TEM results obtained for the nanocomposites showed the formation of mixed intercalated and exfoliated structures. The absence of diffraction peak observed in particular for the PS/3% ZnAl-ACPA sample was attributed to the effective

participation of the interlayer ACPA anions in polymerization initiation. TEM images of the nanocomposite produced with this ZnAl-LDH phase (**Figure 8 B**) showed good dispersion of the LDH layers in the polymer matrix, and mixed intercalated/exfoliated nanocomposite structures. It was concluded that when styrene was bulk polymerized in the presence of an initiator-containing LDH, an intercalated-exfoliated morphology was observed for nanocomposites of ZnAl-ACPA, while MgAl-ACPA led to microcomposite formation.

From these works it can be summarized that an effective intercalation of the precursor or initiator molecule in the interlayer space of LDH is crucial to control the final nanocomposite structure (aggregated, intercalated, and exfoliated). Completely exfoliated structures were obtained only when the organic molecule was fully intercalated in the LDH galleries.

III.2.3.2.2 Controlled grafting from polymerization

The grafting from polymerization of different monomers in presence of LDH layers has also been described using RDRP techniques, such as ATRP and RAFT. In the first case, an ATRP initiator is generally intercalated in the LDH interlayer prior to surface-initiated polymerization, while for RAFT-based processes, it is the chain transfer agent that is intercalated in the LDH interleaves.

For instance, Qiu *et al.*⁸⁶ used surface-initiated ATRP to produce polymer/LDH nanocomposites. In this study, they anchored an ATRP initiator inside the galleries of LDH hosts and further intercalated and polymerized styrene (**Figure 9 A**). The process generated directly dispersed PS/LDH nanocomposites. The ZnAl-LDH phases were first obtained by coprecipitation at constant pH (~ 8.0) from zinc and aluminium chloride salts. The nitrate anions of the LDH host were then exchanged by SDS generating the LDH-SDS phase. Exchange of SDS for α -bromobutyrate (BrB) was then carried out in ethanol/water mixture (5 % v/v) at 20 °C, yielding ZnAl-SDS-BrB. The ATRP initiator-containing LDH was then subjected to the bulk polymerization of styrene at 120 °C for 12h. The products of each step were analyzed by XRD to determine the interlayer space evolution with the intercalation of different organic species. XRD results of the ZnAl-SDS sample showed an interlayer distance of 2.64 nm, which was coherently attributed to the presence of dodecyl sulfate anions in the gallery. The partial substitution of SDS by the smaller BrB molecules was evidenced by the decrease on the layers distance from 2.64 nm to 2.42 nm. The XRD diffractogram obtained for the nanocomposite after 12h of reaction presented the absence of characteristic peaks, which was attributed to the complete exfoliation of the LDH nanolaminates. TEM results gave positive evidence of the good dispersion of exfoliated LDH layers in the PS matrix (**Figure 9 B**).

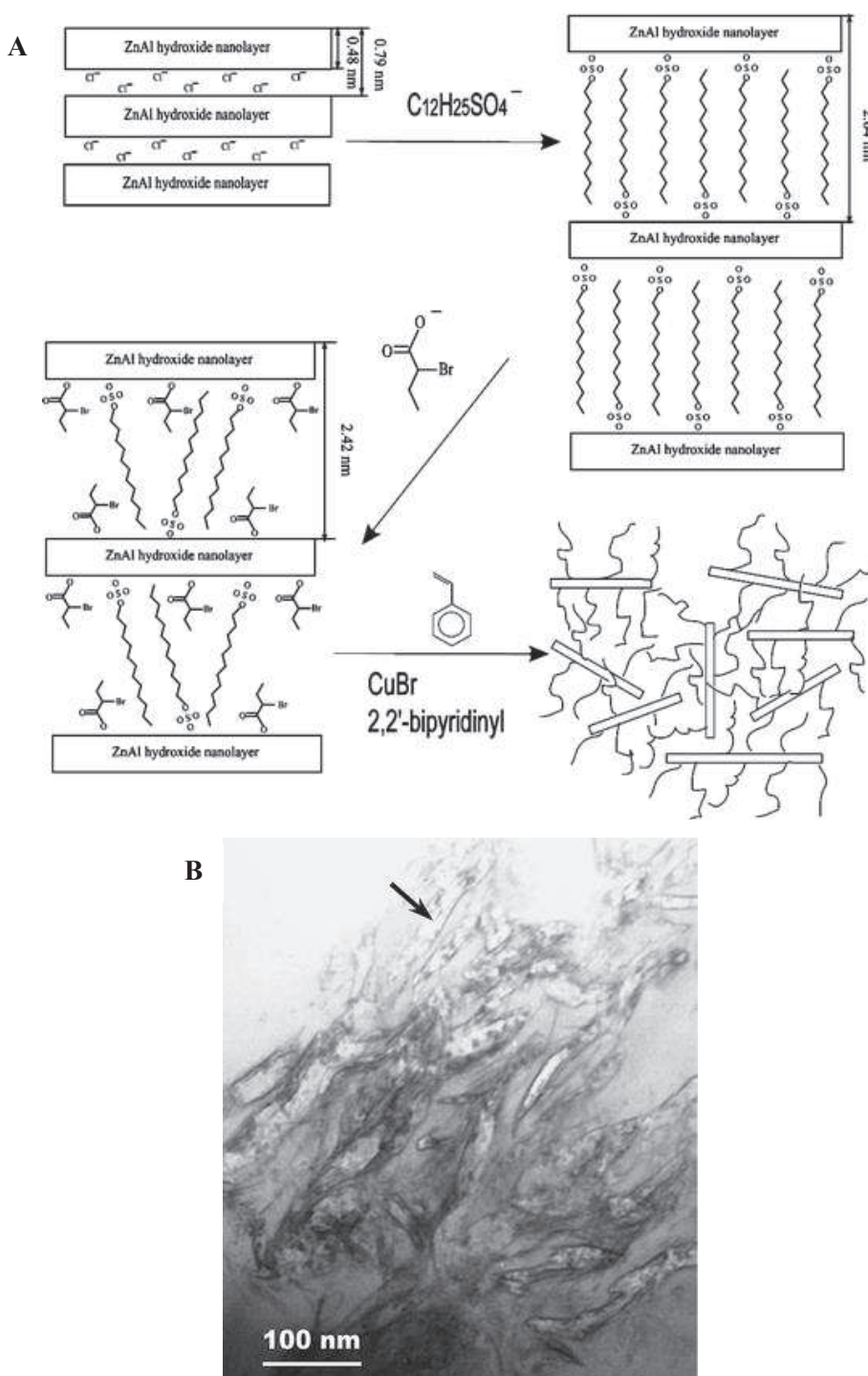


Figure 9. (A) Process of exfoliating LDH by *in situ* ATRP reactions. (B) TEM image of exfoliated PS/LDH nanocomposite. Reproduced with permission from ref⁸⁶. © 2005 Springer-Verlag.

Conventional *in situ* bulk polymerization was carried out to be compared with the experiment performed using controlled ATRP technique. The composites obtained by the conventional method only generated intercalated LDH structures in the matrix, confirming the efficiency of

the controlled technique to produce exfoliated nanocomposites. The thermal stability of the exfoliated nanocomposites, measured by TGA, also presented a marked improvement.⁸⁶

Hu *et al.*⁸ reported the preparation of well-defined hemocompatible layered double hydroxide-poly(sulfobetaine) nanohybrids for drug delivery by means of surface-initiated ATRP. The intercalation of the ATRP initiator into the conventionally coprecipitated LDH interlayer space was carried out in two steps: (i) modification of the LDH surface with 3-aminopropyl-triethoxysilane (APS) to produce the LDH surface with terminal $-NH_2$ groups, and (ii) reaction of the $-NH_2$ groups with α -bromoisobutyric acid (BIBA) in the presence of 1-ethyl-3-(3-dimethylaminopropyl) carbodiimide hydrochloride (EDAC) and *N*-hydroxysuccinimide (NHS) to produce the 2-bromoisobutyryl-immobilized nanoparticles (LDH-Br) (**Figure 10**). The LDH-Br phase was then employed in the surface-initiated polymerization of the 3-dimethyl (methacryloyloxyethyl) ammonium propane sulfonate (DMAPS) zwitterionic monomer in a methanol/water mixture and under typical conditions for ATRP (i.e. in presence of CuBr catalyst and 2,2'-bipyridinyl ligand). The successful intercalation of the ATRP initiator was evidenced by X-ray photoelectron spectroscopy (XPS) and TGA, and the surface density of ATRP initiator of LDH-Br was estimated to be about 2 initiators per nm^2 . Well-defined grafted PDMAPS chains were subsequently synthesized via ATRP of DMAPS from LDH-Br.

The morphologies of LDH-Br and LDH/PS (**Figure 10**) were compared, and larger particle size was found for the sample after polymerization, indicating the presence of polymer on the surface of LDH. Size exclusion chromatography was also performed to determine polymer's molar mass with increasing polymerization time. As expected, higher molar masses were obtained for longer ATRP times, and an average molar mass distribution of 1.56 was obtained. The blood compatibility of the well-functionalized LDH-g-PDMAPS particles was also investigated using a series of biological tests, and the PDMAPS grafting could substantially enhance the hemocompatibility of the LDH particles. The authors also claimed that the LDHPS hybrids could be used as biomaterials without causing any hemolysis.

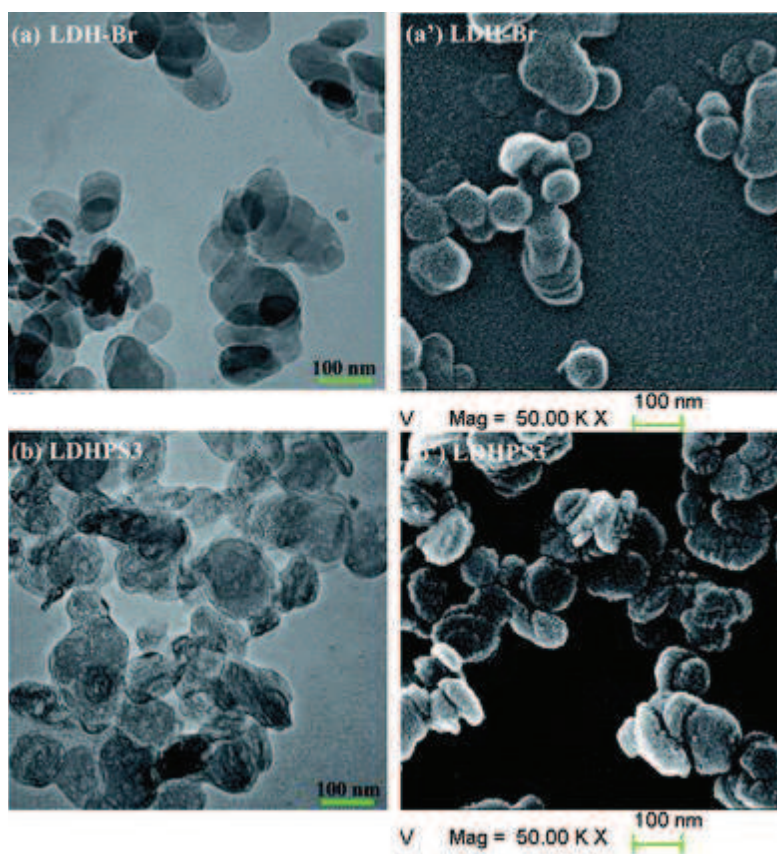
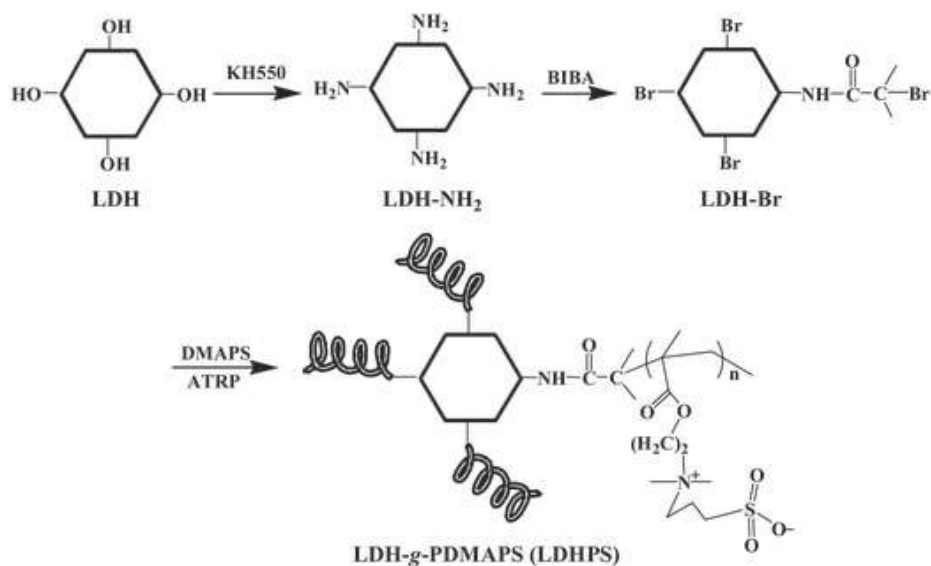


Figure 10. (1) Schematic diagram illustrating the immobilization of an ATRP initiator on MgAl LDH surface to produce LDH-Br surfaces, and surface-initiated ATRP of DMAPS to produce hemocompatible LDH/PS hybrids. (2) TEM (a, b) and SEM (a', b') images of LDH-Br and LDH/PS (after 24h). Reproduced with permission from ref.⁸. © 2012 The Royal Society of Chemistry.

Very recently, the same group reported a similar strategy to synthesize LDH-*grafted*-poly[2-(dimethylamino)ethyl methacrylate] (LDH-*g*-PDMAEMA) hybrids for biological applications via surface-initiated ATRP.⁹ In this work, the LDH layers, previously synthesized by conventional coprecipitation, were modified with 3-(glycidoxypropyl)triethoxysilane (GPTS) in a first step. The LDH terminal epoxy groups of the resulting material were then reacted with the amine groups of cystamine dihydrochloride, to attach the disulfide bonds onto LDH-NH₂. Finally, the amine groups of the LDH-NH₂ were reacted with BIBA in presence of EDAC and NHS, as previously described, to produce the LDH-Br nanoparticles. The LDH-Br hybrids were then subjected to the surface-initiated ATRP polymerization of DMAEMA in a methanol/water solution under similar conditions as those used in their previous work. **Figure 11** shows a diagram illustrating the preparation process. The resulting hybrid materials were characterized by XPS, TGA, SEM and TEM analyses. As evidenced before, the ATRP initiator could be successfully immobilized on the LDH surface, and the grafting from polymerization efficiently generated grafted PDMAEMA chains on the LDH surface. As observed for the LDH-*g*-PDMAEMA samples, the molar mass of the grafted PDMAEMA increased with increasing polymerization time, and an average molar mass distribution of 1.59 was obtained. The LDH-*g*-PDMAEMA hybrids (referred to as LDH-PD) were subsequently examined in terms of their ability to bind plasmid DNA (pDNA) through agarose gel electrophoresis, and the resulting LDH-PD/pDNA was tested in terms of biophysical properties, cell viability, gene transfection and cellular internalization. The LDH-PDs exhibited good ability to complex pDNA, suitable particle size and zeta potential for gene transfection. In comparison to the poor transfection efficiency of the pristine LDH particles, the LDH-PDs exhibited much higher levels to delivery genes in different cell lines. Moreover, the cationic PDMAEMA brushes could also significantly enhance the cellular uptake of LDH.

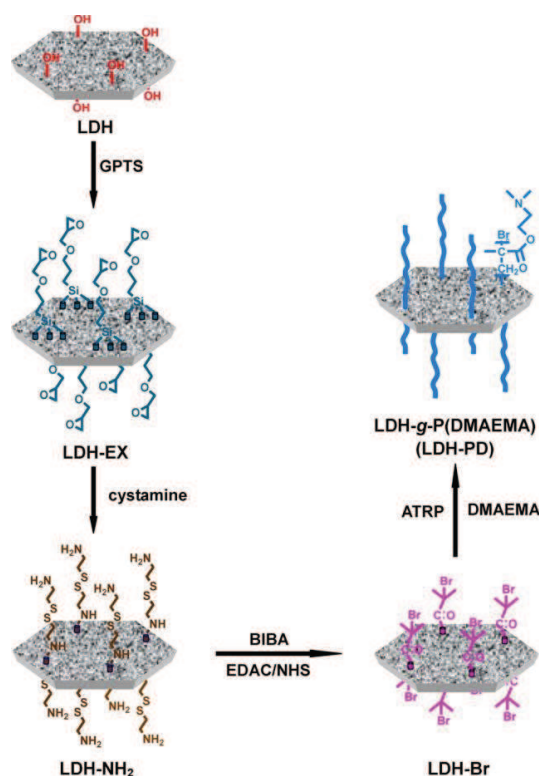


Figure 11. Schematic diagram illustrating the preparation of P(DMAEMA)-g-LDH hybrids via surface-initiated ATRP. Reproduced with permission from ref⁹. © 2013 American Chemical Society.

The intercalation of chain transfer agents into the interlayers of LDH has also been described in the literature. Ding *et al.*¹¹ reported the intercalation of a multifunctional agent, sodium 4-(benzodithioyl)-4-cyanopentanoic salt (SBC) (**Table 1**), to a ZnAl LDH, to synthesize polymer/LDH nanocomposites through a *grafting from* RAFT polymerization of styrene. Each SBC molecule was designed to have one relatively long alkyl chain, which significantly increased the basal spacing of the LDH, and two functional groups: one carboxylic acid, which could exchange the anions in the pristine LDH layers and helped SBC to be molecularly dissolved in water, thus facilitating its intercalation; and one dithiobenzoate group, which acted as a RAFT agent during the *in situ* RAFT polymerization. The ZnAl phase was prepared by conventional coprecipitation method and anionically exchanged with the SBC molecules in aqueous suspensions at pH 9.0. The ZnAl-SBC intercalated phase was mixed with styrene and *N,N'*-dimethylformamide (DMF). AIBN was used as initiator. After degassing the medium, the system was heated to 70 °C to promote the thermal decomposition of AIBN and start polymerization. After 24h, the hybrid nanocomposites were recovered by precipitation in methanol. The hybrid products were analyzed by FTIR, XRD and TEM to determine the morphology, and the pure polymer extracted was analyzed by SEC, to determine its molar mass and molar mass distribution. The successful intercalation of SBC into LDH layers was confirmed by FTIR, where the characteristic absorption bands of SBC ($\sim 3050\text{ cm}^{-1}$ for COO⁻,

2232 cm^{-1} for $-\text{CN}$ and 1048 cm^{-1} for $\text{C}=\text{S}$) appeared. Additionally, XRD results showed larger interlayer distances for the SBC-intercalated ZnAl compared to the pristine LDH: 2.49 nm and 0.78 nm, respectively. The occurrence of the polymerization after the second step was also confirmed by FTIR of the PS/LDH sample, where new characteristic overtone absorptions of the benzene ring in the range of 1700–2000 cm^{-1} were seen. XRD results obtained for the PS/LDH samples presented the (110) peak at wide angles, indicating the existence of LDH dispersed in the PS matrix. The low-angle XRD patterns obtained for the samples containing 1.2 and 5.1 wt% of LDH showed no peaks in the range of $2\theta = 1.5 - 10^\circ$, which was attributed to the complete exfoliation of the LDH layers in the matrix. However, samples containing higher loadings of LDH presented mixed intercalated-exfoliated structures. TEM images further evidenced the exfoliated character of the structures obtained with the lower LDH amount (1.2 wt%), but showed intercalated structures, with superposed layers, for the LDH amount of 5.2 wt% (Figure 12-2).

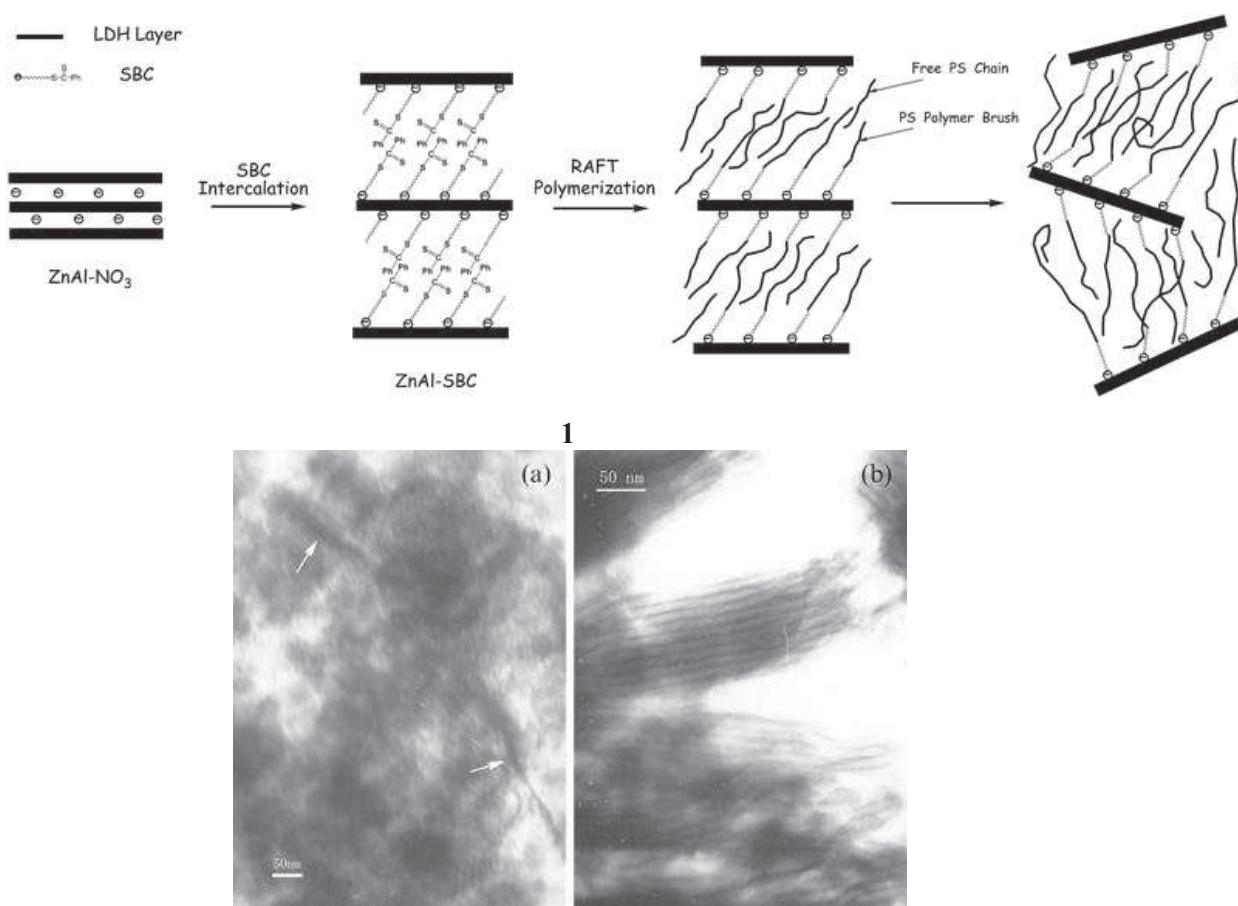
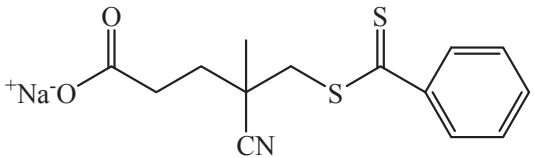
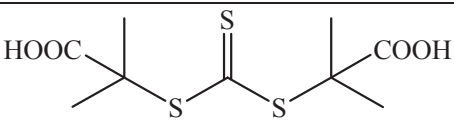


Figure 12. (1) Strategy for preparation of PS/LDH nanocomposites using the multifunctional agent SBC. (2) TEM images of nanocomposites containing (a) 1.2 wt% and (b) 5.1 wt% of ZnAl-SBC. Reproduced with permission from ref¹¹. © 2007 The Royal Society of Chemistry.

The authors discussed that based on the RAFT mechanism, the propagating radicals and the polymer chains having dithiobenzoate groups were on the interlayer surface or in the polymerization solution. Thus, the PS chains could be formed in two places, on the surface of interlayers and in the solution. They stated that the former were tethered on the LDH surface via electrostatic attractions between SBC and LDH cations, and the latter were free polymers. Both types of polymers were separated and analyzed by SEC, and equivalent molar mass and molar mass distributions were obtained. It was then concluded that both tethered and free polymer had the same possibility to propagate, and there was no difference in mechanism in their study and in bulk RAFT system. The narrow molar mass distributions obtained ($\mathcal{D} < 1.5$) were considered as an indication that the spatial confinement of the LDH layers neither restricted the diffusion of the chain radicals nor changed the mechanism of RAFT polymerization. Finally, compared to the conventionally obtained polymer/LDH nanocomposites, the materials prepared by the *in situ* RAFT polymerization method presented improved thermal stability, ascribed to the absence of small organic molecules and to the good dispersion of LDH layers.

Table 1. Chemical structure of the chain transfer agents used in the works reported by Ding *et al.*¹¹ and Jiang *et al.*¹⁰

 <p>Sodium 4-(benzodithioyl)-4-cyanopentanoic salt (SBC)</p>	Ding <i>et al.</i> , 2006
 <p>S,S'-bis(α,α'-dimethyl-α''-acetic acid) trithiocarbonate (CTA)</p>	Jiang <i>et al.</i> , 2013

Recently, Jiang *et al.*¹⁰ reported the RAFT *in situ* polymerization of a mixture of vinylidene chloride (VDC) and methyl acrylate (MA) in LDH interlayers. RAFT polymerization of VDC-MA was carried out in the presence of LDH intercalated with S,S'-bis(α,α' -dimethyl- α'' -acetic acid) trithiocarbonate (**Table 1**) (CTA-LDH). Intercalation was carried out by anionic exchange, and it was found that the layer spacing of LDH changed from 0.89 nm to 1.50 nm, indicating the entrance of CTA into the LDH interleaves. The *in situ* polymerizations were performed in dioxane solution. The average molar mass of P(VDC-*co*-MA) copolymers decreased with

increasing the amount of LDH-CTA, which was taken as a confirmation of the “living” nature of the P(VDC-*co*-MA) copolymers. LDH layers were shown to be gradually exfoliated in the process, and nanocomposites containing well-dispersed LDH nanolaminates were obtained. As expected, the thermal degradation temperature of the nanocomposite increased with increasing the LDH loading, and was higher than the one obtained for the pure copolymer.

II.2.4 Conclusions

It was seen in this bibliographic study that the physicochemical properties of LDH materials can be tuned by either changing the synthesis parameters or by modifying the layers with different compounds. This means that one can tune the LDH properties according to the targeted application.

For the present thesis, the synthesis of polymer/LDH nanocomposites was targeted, and to achieve that, MgAl and ZnAl LDH phases were synthesized. First, the coprecipitation and subsequent thermal treatment conditions were investigated, aiming at forming colloidal LDH suspensions. Once stable and well-defined suspensions of LDH phases were obtained, we studied the modification of such phases with RAFT and macroRAFT agents. Two routes for the modification of the LDHs were investigated: the adsorption/intercalation of RAFT and macroRAFT agents into preformed colloidal LDH phases and the *in situ* synthesis of LDH phases in RAFT or macroRAFT solutions. In a third step, the synthesis of core/corona particles by *grafting from* polymerization and the synthesis of core/shell particles by REEP technique were investigated.

III.3. Synthesis of colloidal suspensions of LDH platelets

As previously discussed, to achieve interesting properties for polymer/LDH nanocomposites, the inorganic layers must have high aspect ratios, which means considerably large plane sizes. On the other hand, colloidal stability is necessary to obtain stable latexes able to generate homogeneous films after water evaporation.

Conventional LDH synthesis, i.e. direct coprecipitation, yields large platelet like particles with high crystallinity. However the distribution of particle size is often very wide. Additionally, the large size of the sheets impairs their colloidal stability. As described above, different synthetic routes (e.g. hydrothermal, solvothermal) have been developed and reported in the literature to control the size of the layers, enabling the generation of colloidal LDH suspensions. Nevertheless, when colloidal stability is obtained, layers size is limited to a few hundreds of nanometers, decreasing the aspect ratio of the fillers.

To find optimal conditions for which colloidal stability would be achieved forming at the same time LDH phases with reasonable aspect ratios, we studied different synthetic routes. We first started from direct coprecipitation performed by continuous addition of metallic salt solutions or by rapid mixing (i.e. flash coprecipitation). The resulting suspensions obtained from the flash coprecipitations were then submitted to hydrothermal (HTT) or solvothermal (STT) treatments, according to the nature of the solvent to investigate the effect of each process on the final platelets properties.

For the syntheses performed by continuous direct coprecipitation (conventional method), two compositions were studied, in which aluminum was used as the trivalent metal and magnesium or zinc were employed as the divalent metal (Mg/Al and Zn/Al, respectively), and the interlayer anion was designed to be NO_3^- . For the series of syntheses carried out by flash coprecipitation, only Mg/Al was investigated. The counter-ions designated to occupy the interlayer space in this series were either nitrate, NO_3^- , chloride Cl^- or carbonate, CO_3^{2-} . The general formula of the LDH phases synthesized in both series was: $\text{Mg}_2\text{Al}(\text{OH})_6\text{NO}_3 \cdot 2\text{H}_2\text{O}$, $\text{Zn}_2\text{Al}(\text{OH})_6\text{NO}_3 \cdot 2\text{H}_2\text{O}$, $\text{Mg}_2\text{Al}(\text{OH})_6\text{CO}_3 \cdot 2\text{H}_2\text{O}$ or $\text{Mg}_2\text{Al}(\text{OH})_6\text{Cl} \cdot 2\text{H}_2\text{O}$.

III.3.1 Experimental section

III.3.1.1 Materials

The aluminum nitrate ($\text{Al}(\text{NO}_3)_3$, > 97%), aluminum chloride (AlCl_3 , > 97%), magnesium nitrate ($\text{Mg}(\text{NO}_3)_2$, > 97%), magnesium chloride (MgCl_2 , > 97%), zinc nitrate ($\text{Zn}(\text{NO}_3)_2$, >

99%), zinc chloride (ZnCl_2 , > 98%), potassium nitrate (KNO_3 , > 99%) and potassium chloride (KCl , > 98%) salts, and sodium hydroxide (NaOH , > 98%) were all purchased from Sigma-Aldrich and used without further purification.

III.3.1.2 Methods

III.3.1.2.1 Direct coprecipitation (conventional method)

LDH- NO_3 , i.e. $\text{Mg}_2\text{Al}(\text{OH})_6\text{NO}_3 \cdot 2\text{H}_2\text{O}$ and $\text{Zn}_2\text{Al}(\text{OH})_6\text{NO}_3 \cdot 2\text{H}_2\text{O}$, were synthesized by direct coprecipitation of $\text{Al}(\text{NO}_3)_3 \cdot 9\text{H}_2\text{O}$ and $\text{Mg}(\text{NO}_3)_2 \cdot 6\text{H}_2\text{O}$ or $\text{Zn}(\text{NO}_3)_2 \cdot 6\text{H}_2\text{O}$ salts, respectively, in the presence of NaOH 2.0 N and KNO_3 0.1 N. 120 mL of the KNO_3 solution were put in a Teflon flask equipped with a magnetic stirrer, and a nitrogen inlet and outlet. To this flask, 30 mL of the metal salt solution at 1.0 M and in a molar ratio of Mg/Al or $\text{Zn}/\text{Al} = 2$ was continuously added. The pH was adjusted at 10.5 by the simultaneous addition of a 2.0 M NaOH solution (approximately 30 mL were added in total). The system was kept under nitrogen flow and at room temperature during the whole synthesis. The salt addition last for approximately 2 hours, and the medium was left precipitating for an additional hour. **Figure 13** shows a picture of the system used for the synthesis. **Table 2** summarizes the synthesis conditions.

Table 2. Conditions used for the synthesis of LDH- NO_3 phases by direct coprecipitation

Entry	LDH phase	$\text{M}^{2+}/\text{M}^{3+}$ ratio	T °C _{co-ppt}	Solvent _{co-ppt}	Time (hours)
LDH-1	Mg/Al- NO_3	2	room	Water	3
LDH-2	Zn/Al- NO_3	2	room	Water	3



Figure 13. Typical system used to perform the direct coprecipitation of metallic salts for the synthesis of LDH phases.

The phases were recovered after three cycles of centrifugation and washing with water. The solids content was measured by gravimetric analyses, drying the product at 40 °C for 10 h, to determine the yield of the synthesis.

III.3.1.2.2 Flash coprecipitation followed by HTT or STT

For the flash coprecipitation, the metallic salt solution (M^{2+}/M^{3+} 2, 3 and 4) was rapidly added to the alkaline solution at 0 °C or at room temperature, depending on the series. After 30 minutes stirring, the resulting suspension was submitted to the hydrothermal (HTT) or solvothermal (STT) treatment. These treatments consisted in sealing the samples in solution in an autoclave under autogeneous pressure at a specific temperature and time. The washing cycles before thermal treatment were avoided to minimize carbonate contamination. Various conditions were tested to tune the particle size and obtain colloidal suspensions. Temperature and time of treatment were fixed according to the series. **Table 3** shows the LDH phases and corresponding syntheses conditions tested.

Table 3. Flash coprecipitation (co-ppt) and thermal treatment (TT) conditions for the synthesis of Mg/Al colloidal LDH phases

Entry	LDH phase	M ²⁺ /M ³⁺ ratio	T °C _{co-ppt}	Solvent _{TT}	T °C _{TT}	Time (hours) _{TT}
LDH-3	Mg/Al-NO ₃	2	room	Water	150	4
LDH-4	Mg/Al-NO ₃	4	room	Water	150	4
LDH-5	Mg/Al-Cl	2	room	Water	150	4
LDH-6	Mg/Al-Cl	4	room	Water	150	4
LDH-7	Mg/Al-NO ₃	2	0 °C	Water	100	2
LDH-8	Mg/Al-NO ₃	4	0 °C	Water	100	2
LDH-9	Mg/Al-NO ₃	2	room	Methanol	150	18
LDH-10	Mg/Al-NO ₃	2	0 °C	Methanol	100	5
LDH-11	Mg/Al-NO ₃	4	room	Methanol	150	18

III.3.1.3 Characterizations

The crystalline structure of the phases was determined by X-ray diffraction (XRD). XRD investigations were performed on a PANalytical X'Pert Pro diffractometer equipped with a X'Celerator Scientific detector and a Cu anticathode (K α_1 / K α_2). The instrument was used in the theta/theta reflection mode, fitted with a nickel filter, 0.04 radian Soller slits, 10 mm mask, 1/2 ° fixed divergence slit, and 1° fixed antiscatter slit. The diffracted beam was detected (detector active length = 2.122° (2 θ)) over a range of 5-70° (2 θ) with a step size of 0.0167° and a counting time of 350s/step. The chemical composition of the phases and the interlayer anions were determined by Fourier Transform Infrared Spectroscopy (FTIR). Attenuated Total Reflectance Fourier Transform Infrared (ATR-FTIR) spectra were measured in the range 400-4000 cm⁻¹ on a FTIR Nicolet 5700 spectrometer (Thermo Electron Corporation) equipped with a Smart Orbit accessory. The hydrodynamic average particles diameter (D_h) was determined by Dynamic Light Scattering (DLS) in a Nano Zetasizer Malvern instrument. Measurements, repeated three times for each sample, were made on as-made initial suspensions or on powder spread out in distilled water at a 5 g L⁻¹ concentration. Morphology was determined by transmission electron microscopy (TEM). For TEM analysis, the diluted samples were dropped on a carbon-coated copper grid and dried under air. TEM images were examined at an accelerating voltage of 80kV with a Philips transmission electron microscope (Centre Technologique des Microstructures (CT μ), platform of the Claude Bernard Lyon 1 University, Villeurbanne, France) and a Hitachi 7650 transmission electron microscope (Institut de Chimie de Clermont-Ferrand (ICCF), platform of the Blaise Pascal University, Clermont-Ferrand, France). Observations were made at room temperature.

III.3.2 Results and Discussion

III.3.2.1 Direct coprecipitation (conventional method)

A first series of experiments was conducted using the direct coprecipitation method. The resulting suspensions were visually unstable, leading to the precipitation of the LDH part on the bottom of the flask with an almost limpid solution on the top. From this observation, it was concluded that LDHs with very large particle size were formed (> 1000 nm), as it is expected for this conventional synthetic method. The size could not be measured by DLS, which generated very imprecise results. **Table 4** summarizes the synthesis conditions for both experiments.

Table 4. Conditions and final particle size for the synthesis of LDH layers by direct coprecipitation

Entry	LDH	pH	Dh (nm)
LDH-1	Mg/Al-NO ₃	10.5	> 1000 nm
LDH-2	Zn/Al-NO ₃	8.5	> 1000 nm

Method: continuous addition; Solvent: wter; M^{2+}/M^{3+} ratio = 2;
 T °C_{co-ppt} = room; Time: 24h.

The large size was explained by the fact that continuous and slow addition of salt solution allows the gradual growth of the crystalline LDH phase. At the early stages, once the addition starts, some nuclei are formed. With the progressive increment on salt concentration, these first crystals continue to grow, forming well-defined crystalline structures of larger sizes. Renucleation also occurs during the process, forming new particles. Nuclei formed at the beginning of the process have a much longer time to undergo crystal growth than those formed at the end of the process³⁸. Thus, the final product is expected to present a broad particle size distribution, with particle diameter up to 1000 nm.

The crystalline structure of the phases is shown in **Figure 14A**. Both phases present a typical diffractogram of a LDH structure. The reflections can be indexed with a hexagonal lattice of rhombohedral symmetry R-3m. The two intense peaks observed near 10 and 20° 2 θ correspond to the (003) and (006) plane reflections of the lamellar structure. The reticular distances obtained from the angular position of these two peaks by the application of the Bragg equation ($2 d_{hkl} \sin\theta = n\lambda$) correspond to $d_{003} = 8,85$ Å in the Mg/Al structure and $d_{003} = 8,80$ Å in the Zn/Al structure, respectively. They can be attributed to the presence of NO₃⁻ as the major compensating anion. However, it should be noted that for the Zn/Al structure, the characteristic peak of the (003) plane has a shoulder on the edge of the peak, with a value of 7.65 Å. This shouldering can be ascribed to the presence of a side phase, containing the CO₃²⁻ anions.

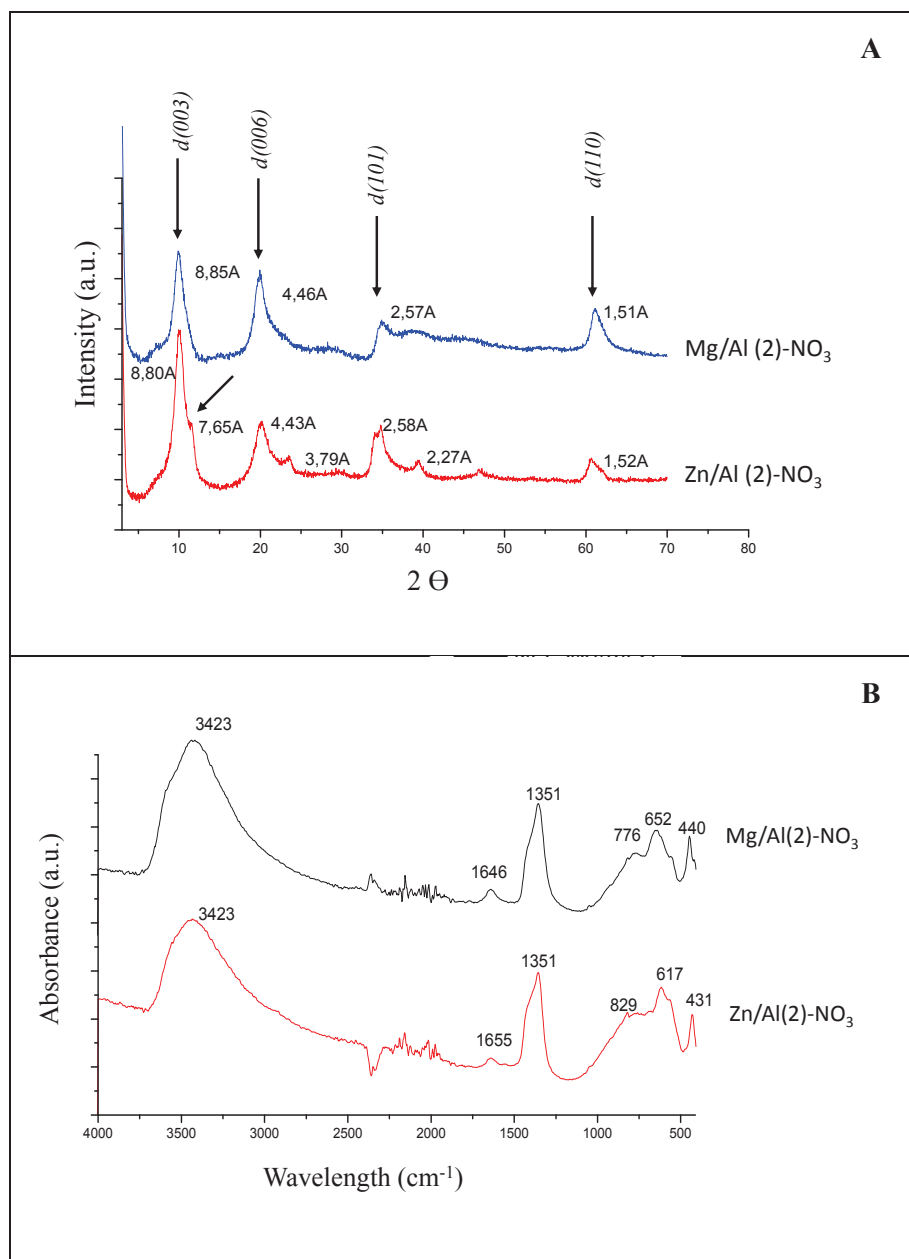


Figure 14. (A) X-ray diffractograms and (B) IR signature of Mg/Al-NO₃ (LDH-1) and Zn/Al-NO₃ (LDH-2) phases obtained by direct coprecipitation.

Figure 14B shows the FT-IR results obtained for the two phases. The characteristic bands of the LDH structure can be found for the two samples: OH⁻ groups at 3423 cm⁻¹, carbonate anions at 1351cm⁻¹, molecular deformation of water at 1646 cm⁻¹ and O-M-O network vibrations of the brucite layers below 829 cm⁻¹. It is important to remember that LDH phases have a strong affinity with carbonate ions, being easily contaminated.

As shown in **Figure 15**, the LDH phases obtained via direct coprecipitation present very large particles size distribution, with sheets diameter from 40 to 200 nm for Mg/Al and from 100 to

300 nm for Zn/Al. Higher particle sizes were expected, based on the visual observations regarding the lack of stability and DLS results. This can be explained by the fact that the very large particles precipitated and thus were not accounted when preparing the TEM grids. Because of that, they could not be observed by TEM, and only the portion of smaller particles could be imaged.

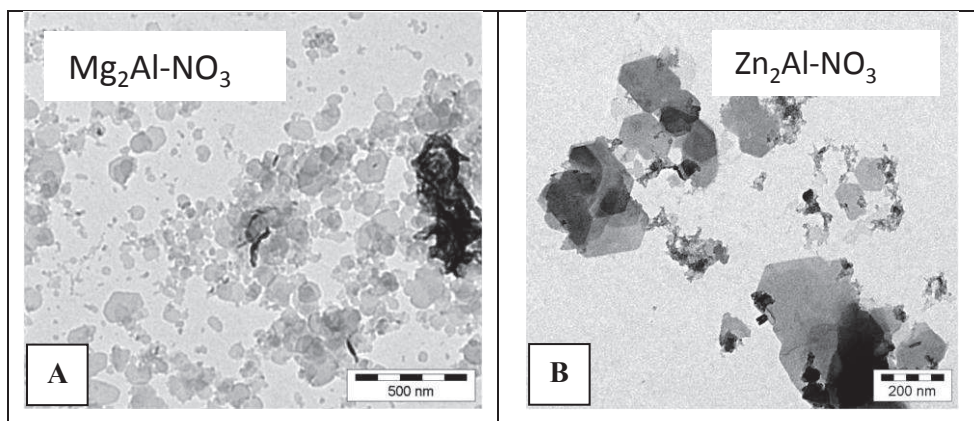


Figure 15. TEM images of (A) Mg/Al-NO₃ (LDH-1) and (B) Zn/Al-NO₃ (LDH-2) phases obtained by direct coprecipitation.

III.3.2.2 Effect of flash coprecipitation and HTT or STT processes

To obtain smaller LDH phases with narrower size distributions and colloidal stability, flash coprecipitation followed by HTT or STT was performed. This series of experiments was only performed for the Mg/Al LDHs. **Table 5** shows the synthesis conditions and final particle size of a series of LDH phases obtained after different flash coprecipitation in water or alcohol and followed by hydrothermal and solvothermal treatments, respectively. These experiments correspond to the ones shown in **Table 3**.

Table 5. LDH synthesis conditions and results for flash coprecipitations performed at different temperatures followed by thermal treatments.

Entry	LDH phase	T °C _{co-ppt}	Solv./T °C/Time (h)	D _h (nm)
LDH-3	Mg ₂ Al-NO ₃	room	Water / 150 / 4	91
LDH-4	Mg ₄ Al-CO ₃	room	Water / 150 / 4	77
LDH-5	Mg ₂ Al-Cl	room	Water / 150 / 4	77
LDH-6	Mg ₄ Al-Cl	room	Water / 150 / 4	> 1000
LDH-7	Mg ₂ Al-NO ₃	0 °C	Water / 100 / 2	92
LDH-8	Mg ₄ Al-NO ₃	0 °C	Water / 100 / 2	108
LDH-9	Mg ₂ Al-NO ₃	room	Methanol / 150 / 18	98
LDH-10	Mg ₂ Al-NO ₃	0 °C	Methanol / 100 / 5	130
LDH-11	Mg ₄ Al-NO ₃	room	Methanol / 150 / 18	91 / 610

As it can be seen, the phases obtained by flash coprecipitation and thermal treatment presented much lower particle size and particle size distribution than the ones obtained by direct coprecipitation. The smaller sizes can be the effect of the rapid addition combined with the lower temperature of coprecipitation. When the salt solution is added at once to the alkaline medium, a great number of crystalline nuclei are formed simultaneously. Their growth is limited to the amount of salt still available in the solution, and due to the formation of a great number of nuclei, only a small concentration of salt remains in solution. Consequently, narrow particle size distributions are obtained. The subsequent thermal treatment is employed to improve the crystallinity of the phases, and it can also affect their final size. As reported in the literature, different phenomena can occur during thermal treatment, like the Ostwald ripening effect (i.e. dissolution of smaller particles and recrystallization around the biggest ones) or the disaggregation and re-aggregation of preformed particles, affecting the final particle size.

The temperature is another important parameter to be taken into account. It can also be seen that the coprecipitations performed at 0 °C generated slightly larger phases. The crystallization rate was expected to decrease with decreasing temperature, thus forming smaller particles. However, the low temperature seems to have decreased the number of nuclei formed, also contributing to the increase of particle size. In addition, the following thermal treatment time was probably not sufficient to promote the disaggregation of the formed particles, and final size measured corresponded to aggregates of small particles. The same conclusion can be drawn concerning the use of alcohol as synthetic solvent.

Interestingly we observed that the nature of the interlayer anion strongly depends on the synthetic conditions, the coprecipitation at 0 °C and the use of organic solvent being in favor of nitrate intercalation instead of carbonate.

III.3.2.2.1 Characterization of colloidal LDH-NO₃ and LDH-CO₃

Here are detailed the results obtained for the synthesis of two colloidal phases: LDH-10 (Mg/Al-NO₃) and LDH-4 (Mg/Al-CO₃) (**Table 5**). These phases were synthesized using the optimized conditions determined in the previous studies.

Figure 16 and **Figure 17** present the results obtained for the phases produced by flash coprecipitation followed by HTT and STT, respectively. The phases obtained by flash coprecipitation in aqueous media and followed by hydrothermal treatment (LDH-4), the results of which are shown in **Figure 16 A**, presented sharp peaks corresponding to the characteristic reflections of the LDH planes, indicating the formation of highly crystalline phases. The FTIR

result presented in **Figure 16 B** showed the characteristic absorption band of carbonate ions, at 1345 cm^{-1} . The presence of the carbonate anions resulted from the spontaneous exchange of the NO_3^- anions against environmental/contaminating CO_3^{2-} anions during the washing of the suspension before hydrothermal treatment. DLS results and TEM images confirmed the formation of small particles (77 nm) with narrow particle size distributions, as shown in **Figure 16 C** and **D**.

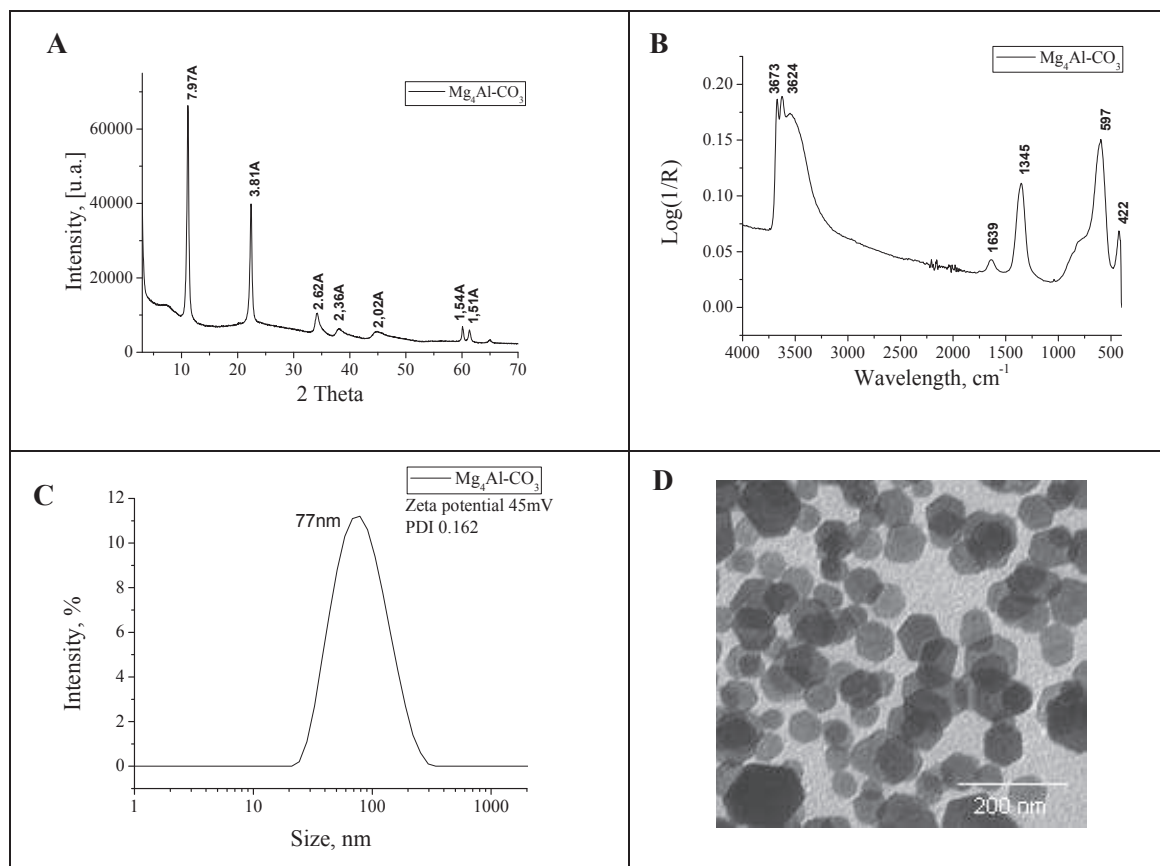


Figure 16. (A) X-ray diffractogram, (B) IR spectrum, (C) particles size and (D) TEM image of the $\text{Mg}_4\text{Al-CO}_3$ phase (LDH-4, **Table 5**) synthesized by flash coprecipitation at room temperature and followed by hydrothermal treatment at $150\text{ }^\circ\text{C}$ for 4h.

The sample prepared by flash coprecipitation in methanol at $0\text{ }^\circ\text{C}$ and followed by solvothermal treatment (LDH-10), the results of which are shown in **Figure 17 A**, presented all the peaks corresponding to the characteristic reflections of the LDH planes, indicating the successful formation of LDH phases. However, broader peaks were obtained for this synthesis, compared to both previous experiments, indicating a lower crystallinity. FTIR results presented in **Figure 17 B** showed the characteristic absorption band of nitrate anions, at 1355 cm^{-1} . Small particle sizes (130 nm) were obtained, but less narrow particle size distribution was observed on the

TEM image (**Figure 17 C and D**). The differences observed between samples prepared by hydrothermal and solvothermal treatment in terms of composition, crystallinity and particles size can be attributed to solvation effects of methanol and water during the treatment.

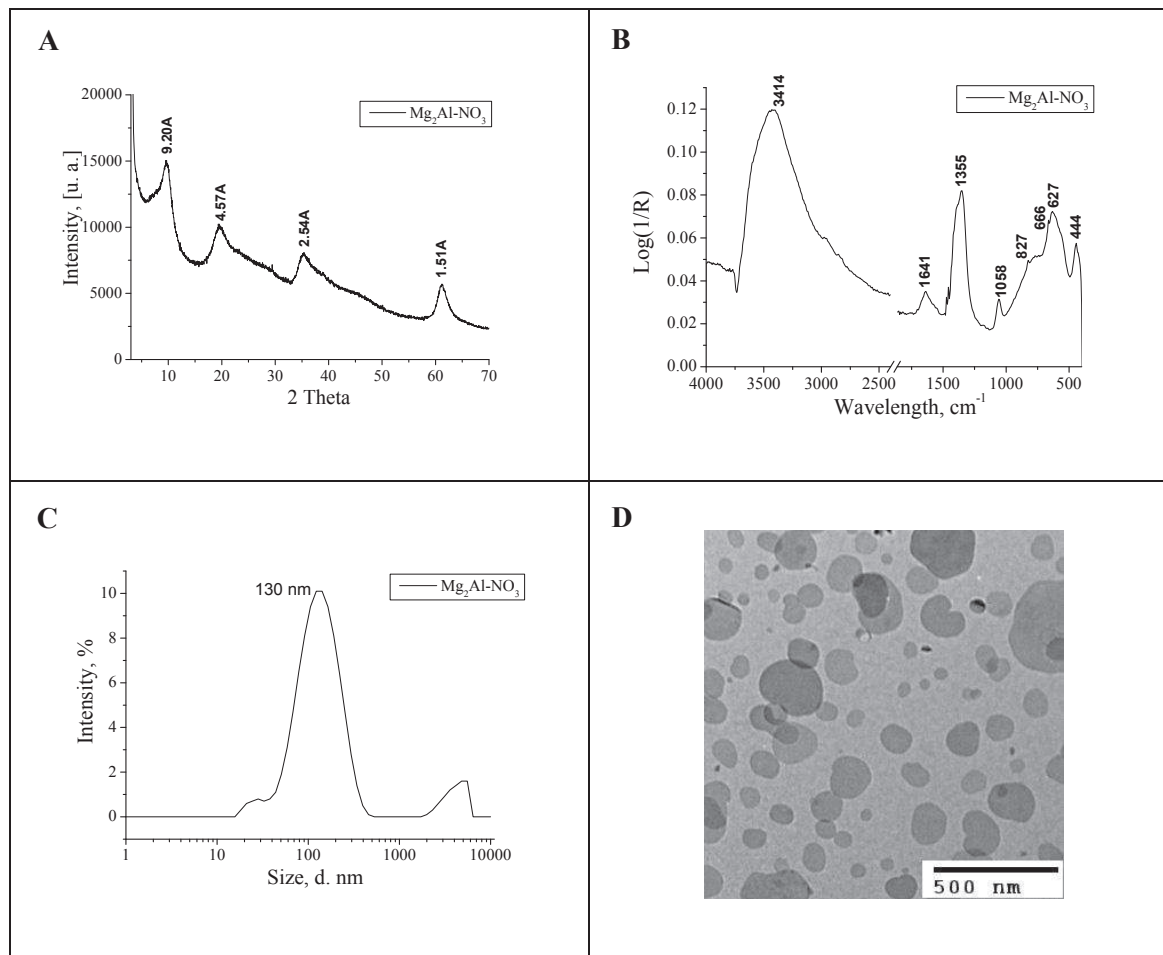


Figure 17. (A) X-ray diffractogram, (B) IR spectrum, (C) particles size and (D) TEM image of the $\text{Mg}_2\text{Al-NO}_3$ phase (LDH-10, **Table 5**) synthesized by flash coprecipitation at 0 °C and followed by solvothermal treatment at 100 °C for 5h.

These well-defined Mg/Al-CO_3^{2-} and Mg/Al-NO_3^- phases were used for the adsorption/intercalation studies and were further employed for the encapsulation by REEP.

III.3.3 Conclusions

Different parameters affect the precipitation of the LDH precursors, influencing the final particle size, crystallinity and composition. This section presented mainly the effect of the process (i.e. addition mode), the temperature, the time and the thermal treatment conditions on

the final characteristics of the LDH phase. The process had a great influence over the size of the LDH particles. The continuous addition of the metallic salt solution yielded large particles with wide size distributions, while the rapid addition generated smaller LDH particles. The temperature also presented an effect on the final particles size, and particles were considerably larger when the temperature was decreased from ambient to 0 °C. Sharper peaks were found for the sample synthesized at room temperature, suggesting a higher crystalline order. When the solvent was changed from water to methanol, small particles of nitrate intercalated LDH were obtained with slightly higher particle size distributions, but broader XRD traces were obtained, suggesting less ordered crystalline structures. The LDH particle size is a very important parameter, but to assure a good modification of the phases with guest compounds, the composition and, in particular, the nature of the interlayer anion are equally very important factors.

For the next study, the conventionally precipitated LDH phases were used to perform anionic exchange investigations, while the colloidal phases obtained by flash coprecipitation and hydrothermal or solvothermal treatment were used for the adsorption studies. **Table 6** presents the main properties of the LDH phases used in this thesis.

Table 6. Main properties of the LDH phases used in this work

LDH phase	D_h (nm)	Suspension state
Mg/Al-NO ₃ ⁻	> 1000	precipitated
Zn/Al-NO ₃ ⁻	> 1000	precipitated
Mg/Al-NO ₃ ⁻	130	colloidal
Mg/Al-CO ₃ ²⁻	77	colloidal

III.4. LDH modification with RAFT and macroRAFT agents

In order to attach a functional molecule to the surface, and allow the *grafting from* polymerization of a hydrosoluble monomer, or to improve the affinity and compatibility of the hydrophilic LDH phases with the hydrophobic monomers, which will be polymerized by RAFT in emulsion, the RAFT and macroRAFT agents were used to modify the LDHs. Various modification approaches were tested: the intercalation of the organic RAFT or macroRAFT by anionic exchange; the study of the adsorption of the macroRAFT agents onto the surface and/or the interlayer space of LDH phases; and the direct coprecipitation, in which the LDH phases were synthesized in presence of RAFT or macroRAFT agent solutions. The first two approaches (i.e. intercalation and adsorption) rely on the same process, but different concentrations and different protocols were employed for each study.

The phases modified with the RAFT agent would be used for the *grafting from* and production of core/corona particles, while the ones modified with the macroRAFT agent would be used for the encapsulation by REEP and production of core/shell particles.

The LDH modification was conducted using different phases. On one side, the large-sized Mg/Al and Zn/Al phases obtained by conventional coprecipitation method, as presented in section III.3.2.1, were used to study the anionic exchange of RAFT and macroRAFT agents. On the other side, colloidal phases of Mg/Al, containing either NO_3^- or CO_3^{2-} anions, were used to study the macroRAFT adsorption/intercalation into the interlayer spaces. The colloidal Mg/Al- CO_3^{2-} phase was obtained by flash coprecipitation followed by HTT whereas the colloidal Mg/Al- NO_3^- phase was obtained by flash coprecipitation followed by STT, as presented in section III.3.2.3.

III.4.1 Experimental section

III.4.1.1 Materials

Mg/Al- NO_3 , Zn/Al- NO_3 and Mg/Al- CO_3 phases were synthesized as described in section III.3.1.2, either by direct coprecipitation or by flash coprecipitation followed by hydrothermal or solvothermal treatment (see **Table 6**). 4-cyano-4-thiothiopropylsulfanyl pentanoic acid (CTPPA) RAFT agent was synthesized as described elsewhere.^{87, 88} P(AA-co-BA)-CTPPA macroRAFT agent ($M_n = 3\ 200$ or $4\ 200\ \text{g mol}^{-1}$) was synthesized as described in section II.5 of chapter II. For the synthesis of LDH in presence of RAFT and macroRAFT, the same reagents as those reported in section III.3.1.1 were employed.

III.4.1.2 Methods

III.4.1.2.2 RAFT and macroRAFT intercalation

Intercalation of RAFT and macroRAFT molecules into the interlayer space of LDH phases was carried out via anionic exchange. Typically, the LDH precursors (100 mg) were dispersed in 50 mL of water and 25 mL of a solution containing the calculated amount of the organic molecules were added to have an excess of 2 carboxylic acid units per aluminum from LDH, calculated based on its general formula ($\text{Mg}_2\text{Al}(\text{OH})_6\text{NO}_3 \cdot 2\text{H}_2\text{O}$ or $\text{Zn}_2\text{Al}(\text{OH})_6\text{NO}_3 \cdot 2\text{H}_2\text{O}$) and its molar mass (275.58 and 357.76 g mol^{-1} , respectively). **Table 7** details the amount added for each experiment. The mixtures were stirred for 24h at 400 rpm under nitrogen atmosphere, to avoid carbonate contamination (**Figure 18**).

Table 7. Molar amount of RAFT and macroRAFT agents used for the anionic exchanges and pH of the final suspensions.

LDH	Molecule	Amount (mmol L^{-1})	pH
Mg/Al-NO_3^{a*}	CTPPA 277 g mol^{-1}	9.7	9.8
	macroRAFT 3 200 g mol^{-1}	0.7	10
	macroRAFT 4 200 g mol^{-1}	0.4	10.1
Zn/Al-NO_3^{b**}	CTPPA 277 g mol^{-1}	7.5	9.2
	macroRAFT 3 200 g mol^{-1}	0.5	9.2
	macroRAFT 4 200 g mol^{-1}	0.4	9.3

^a $[\text{Mg/Al}] = 4.8 \text{ mmol L}^{-1}$. ^b $[\text{Zn/Al}] = 3.7 \text{ mmol L}^{-1}$. * pH 8.5. ** pH 6.5.
MacroRAFT : P(AA-co-BA)-CTPPA



Figure 18. Set up used to perform the anionic exchange experiments.

The pH of the mixtures was adjusted in order to obtain alkaline medium, in which the structure and crystallinity of the LDH phases would be preserved. At the same time, it would enable the solubilization of the RAFT and macroRAFT molecules, which require $\text{pH} > 7.0$. **Table 7** shows the pH of each mixture.

After 24h of exchange, the intercalated LDH phases were recovered after three cycles of centrifugation and washing with deionized water. Part of the suspension was dried to perform the XRD and FTIR analyses.

The hydrothermal treatment, when performed, was carried out following the same procedure described in section II.3.1.2, where the temperature was adjusted to $80\text{ }^{\circ}\text{C}$ and the sample was left stirring for 24h.

III.4.1.2.3 MacroRAFT adsorption

For this study, the colloidal LDH- NO_3 , $\text{Mg}_2\text{Al}(\text{OH})_6\text{NO}_3 \cdot 2\text{H}_2\text{O}$, of 130 nm average particle size, the colloidal LDH- CO_3 , $\text{Mg}_2\text{Al}(\text{OH})_6\text{CO}_3 \cdot 2\text{H}_2\text{O}$, of 77 nm average particles size, and the $3\text{ }200\text{ g mol}^{-1}$ P(AA-co-BA)-CTPPA macroRAFT agent were used. LDH concentration was fixed at $10\text{mg}/5\text{mL}$ (corresponding to 2.0 g L^{-1}) and macroRAFT concentration was increased from 0.04 mmol L^{-1} to 20 mmol L^{-1} . The adsorptions were carried out as follows: 10 mg of LDH phase were introduced to 13 individual vials, and 3.7 mL of deionized water were introduced to each one of the vials. 1.3 mL of macroRAFT solution at different concentrations and at $\text{pH} = 8.0$ were introduced to the vials to complete 5 mL. The vials were closed and left stirring at 700 rpm for 6 hours in a thermostatically controlled water bath. **Table 8** shows the concentrations of macroRAFT agent tested.

Table 8. MacroRAFT concentrations put in contact with LDH- NO_3 and LDH- CO_3 phases.

Vial	1	2	3	4	5	6	7	8	9	10	11	12	13
[macroRAFT] (mmol L^{-1})	0.04	0.2	0.5	1.0	2.0	3.0	4.0	6.0	8.0	10.0	12.0	15.0	20.0

After interaction, the suspensions were centrifuged for 30 minutes at 10 000 rpm to separately recover the supernatant and the water-swelled powder. The supernatant was analyzed by UV-visible analyses to determine the amount of free macroRAFT in the aqueous phase. The solid was analyzed by XRD and FTIR to determine the interlayer distance and the presence or not of macroRAFT in the structure.

A calibration curve correlating the macroRAFT concentration with its UV absorbance at 310 nm was previously built to determine the macroRAFT concentration in the supernatant. All UV analyses were performed in a Shimadzu UV-visible spectrometer. The adsorbed macroRAFT amount was calculated by subtracting the free amount from the initial concentration.

III.4.1.2.4 LDH synthesis in presence of RAFT or macroRAFT agents

The direct coprecipitation in presence of CTPPA or P(AA-co-BA)-CTPPA (either 3 200 or 4 200 g mol⁻¹) macroRAFT agents were carried out following the same procedure as that described in section III.3.1.2. An initial solution of the organic molecules, containing an equivalent excess of 2 carboxylic acid units per aluminum, was prepared and poured to the Teflon reactor. The metallic salt solution was added continuously to this first solution. The NaOH solution was also gradually added to control the pH. The addition was done during 1 hour. The solution was left under stirring at room temperature overnight. The product was recovered after two cycles of centrifuging and washing with water, and the solids content was measured to determine the yield of the synthesis, as described in section III.3.1.2. The crystalline structure and the composition were determined by XRD and FTIR analyses of the dried phases. The set up employed for the syntheses was similar to the one showed in **Figure 13**.

III.4.1.3 Characterizations

All hybrid phases were submitted to the same characterizations as for the pure LDH phases, described in section II.3.1.3, except for TEM analyses, which were not performed for these studies.

III.4.2 Results and Discussion

III.4.2.1 RAFT and macroRAFT intercalation

RAFT and macroRAFT agents (of 3200 and 4200 g mol⁻¹) were intercalated by anionic exchange into Mg/Al or Zn/Al precursors previously synthesized by direct coprecipitation. The aim of the intercalation of the RAFT agent was to produce LDH phases containing a reactive species on their inner layers and outer surface, enabling the *in situ* polymerization by *grafting from*. Thereby, these phases would allow the formation of core/corona or core/shell particles, with a soluble polymer brush or an insoluble polymer layer around the LDH platelets,

respectively. In contrast, the objective of intercalating macroRAFT agents into the LDH interlayer space was to tether this reactive hydrosoluble copolymer capable of chain-extending forming an amphiphilic block copolymer on the surface of LDH, promoting the encapsulation of the platelets with an insoluble polymer layer. Both processes should be carried out in aqueous medium.

The results obtained after the anionic exchange of RAFT and macroRAFT species are shown in **Figure 19**.

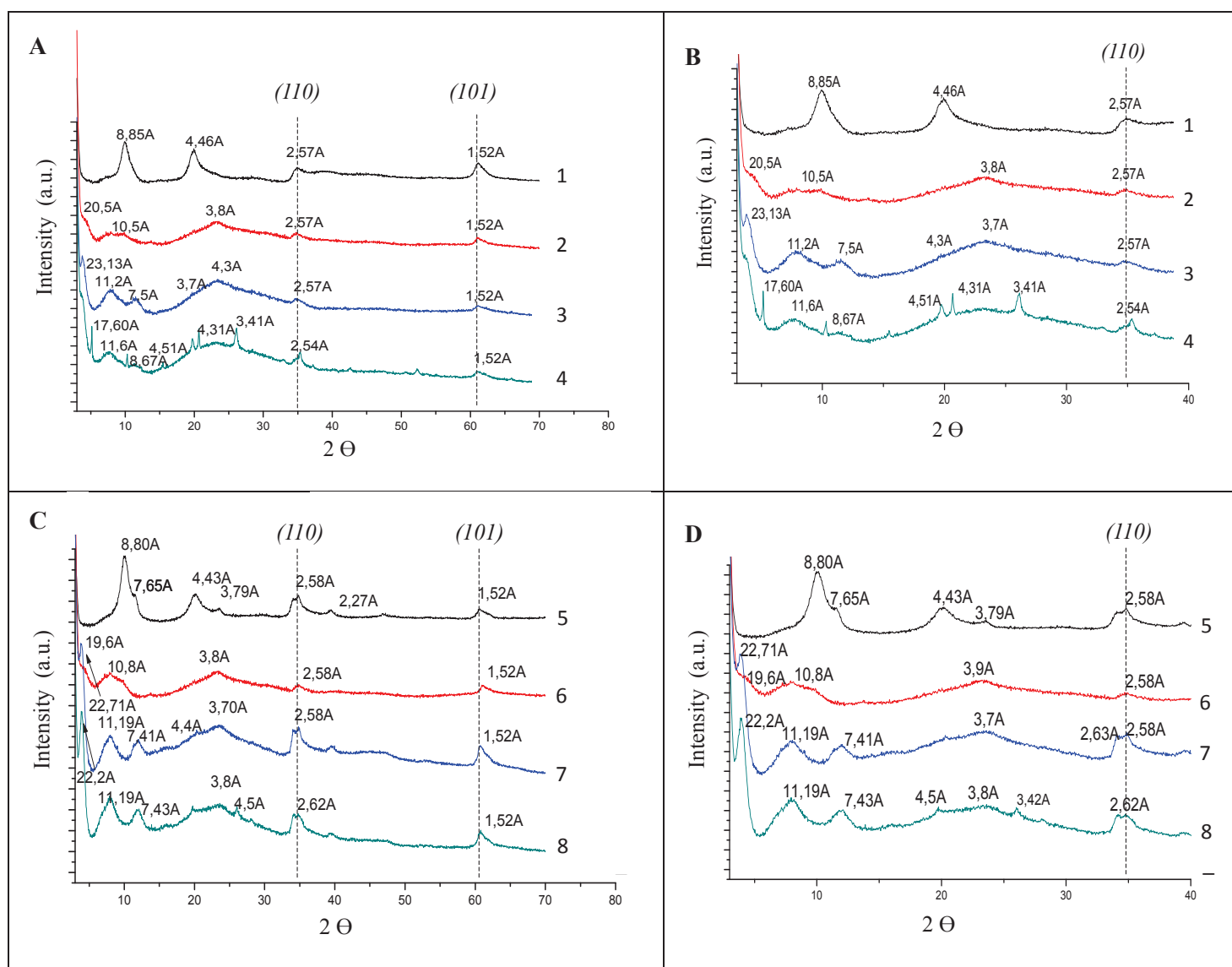


Figure 19. X-ray diffractograms of hybrid (A, B) Mg/Al and (C, D) Zn/Al phases obtained by anionic exchange. X-ray diffractograms in the range from 0 to 40 2θ for (B) Mg/Al and (D) Zn/Al phases. **1:** Mg/Al-NO₃, **2:** Mg/Al-CTPPA, **3:** Mg/Al-macroRAFT 3 200 g mol⁻¹, **4:** Mg/Al-macroRAFT 4 200 g mol⁻¹, **5:** Zn/Al-NO₃, **6:** Zn/Al-CTPPA, **7:** Zn/Al-macroRAFT 3 200 g mol⁻¹ and **8:** Zn/Al-macroRAFT 4 200 g mol⁻¹.

After anionic exchange, the characteristic diffraction lines of LDH sheets are present (rays (101) at ~ 2.6 Å and (110) at ~ 1.52 Å), thus confirming the maintenance of the LDH structure. The 2θ values corresponding to the reticular distance of d_{003} shift to lower angles for all the hybrid samples compared to the LDH pure phase. This shifting indicates an increase in the interlayer space and suggests the intercalation of the RAFT and macroRAFT agents, which are more voluminous than the nitrate anions. In addition, the harmonic rays of (003), (006) and (009) are very large, suggesting a certain disorder in the interlayer domain. In the case of the RAFT agent in particular, series of 001 harmonic lines characteristic of the interlayer domain is not observed.

Attempting to improve the ordering of the interlayer space of the hybrid phases obtained after intercalation, the LDH phases were submitted to a hydrothermal treatment at 80 °C for 24 h. The resulting diffractogram of the Mg/Al-RAFT sample is shown in **Figure 20** as an example. The treatment only resulted in a slight improvement of the crystallinity. Indeed, the 001 lines are slightly more defined (pointed out in **Figure 20**), but no significant change occurred during treatment.

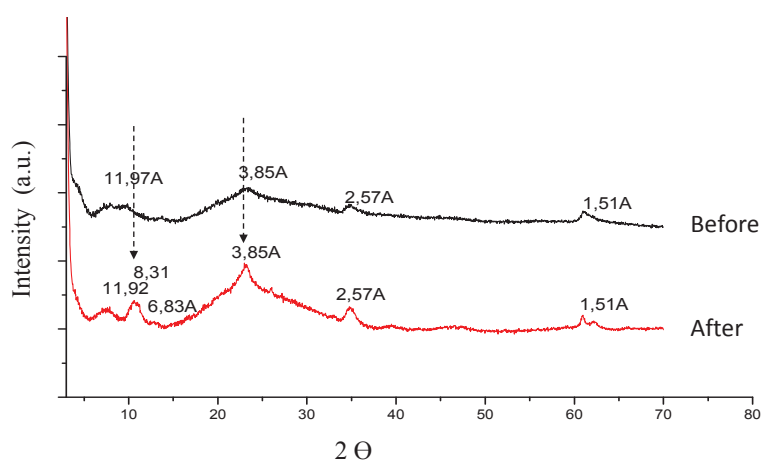


Figure 20. X-ray diffractograms of Mg/Al-CTPPA hybrid phase obtained after anionic exchange and followed by the hydrothermal treatment.

Infrared spectra of the hybrid structures obtained by the ion exchange method using Mg_2Al-NO_3 and Zn_2Al-NO_3 as host phases are compared in **Figure 21**. Comparing the results for the pure LDH phases, the same characteristic bands of LDH structure presented in section III.3.2 are present here, confirming that the LDH structure was preserved during the exchange. The spectra of the hybrid phases, in addition to the characteristic bands of LDH, present supplementary

bands in the region from 3000 to 950 cm^{-1} . These bands were ascribed to the CH_3 , CH_2 , CH , $\text{C}=\text{S}$, COO^- and $\text{C}=\text{O}$ groups of the RAFT and macroRAFT agents.

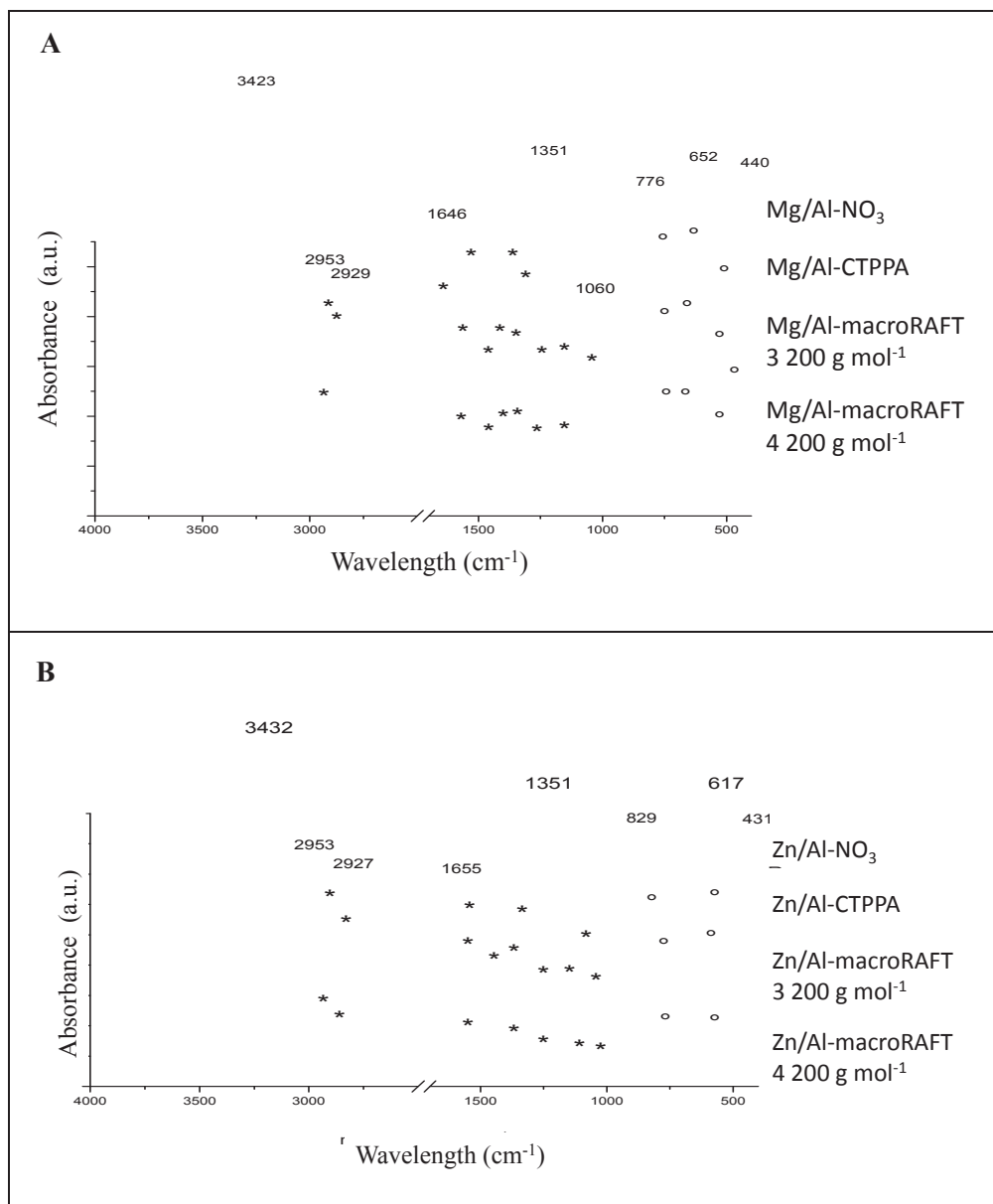


Figure 21. Infrared spectra of the hybrid phases obtained after anionic exchange with RAFT and macroRAFT agents using (a) Mg/Al and (b) Zn/Al LDH, obtained by direct coprecipitation, as the host structure. (*) Characteristic peaks of the organic species, (°) characteristic peaks of the metal structure.

These results confirm the intercalation of RAFT and macroRAFT agents into the interlayer spaces of both LDH phases tested. XRD and FTIR measurements evidenced the preservation of the LDH structure even after exchange and indicated the presence of a guest component, attributed to the organic RAFT or macroRAFT agents. The final hybrid particles could be

dispersed in water, but presented limited colloidal stability. Since the LDH precursor phases employed were quite large in size and presented broad particle size distributions, their stability was not favored. Especially in the case of the intercalation with the macroRAFT agent, it was expected that the presence of this relatively hydrophilic copolymer would help the stabilization of the LDH particles. However, the amount of copolymer intercalated was not sufficient to provide stability to such large sheets.

Despite the successful intercalation of the RAFT agent inside LDH galleries, the phases could not be used to perform the *grafting from* polymerization and produce core/corona particles, because of the low colloidal stability of the particles. Likewise, the macroRAFT-intercalated LDH phases obtained in this study could not be used for the production of core/shell particles by REEP, due to the instability of the suspensions.

Because of that, alternative modification strategies were studied. First, LDH-macroRAFT phases were aimed by macroRAFT adsorption into preformed colloidal LDH precursor. Then, LDH-RAFT or LDH-macroRAFT phases were targeted by direct LDH synthesis in presence of RAFT or macroRAFT solution. The results obtained for these two strategies are presented in the next sections.

III.4.2.2 MacroRAFT adsorption onto colloidal LDHs

This study was carried out using colloidal LDH nanoparticles as precursor, to obtain hybrid phases which could be more easily dispersed in water. To favor the adsorption and the stabilization of the hybrids, the macroRAFT agent of 3200 g mol^{-1} was employed to perform this study. Different samples were prepared, each one with a different macroRAFT concentration.

As **Figure 22** shows, the macroRAFT can effectively adsorb onto the LDH surface. However, a partitioning of the copolymer between the aqueous phase and the surface is observed for almost the whole range of concentrations tested. This adsorption behavior is similar to what was observed for macroRAFT adsorption on Imogolite (section II.6.2.3 in chapter II).

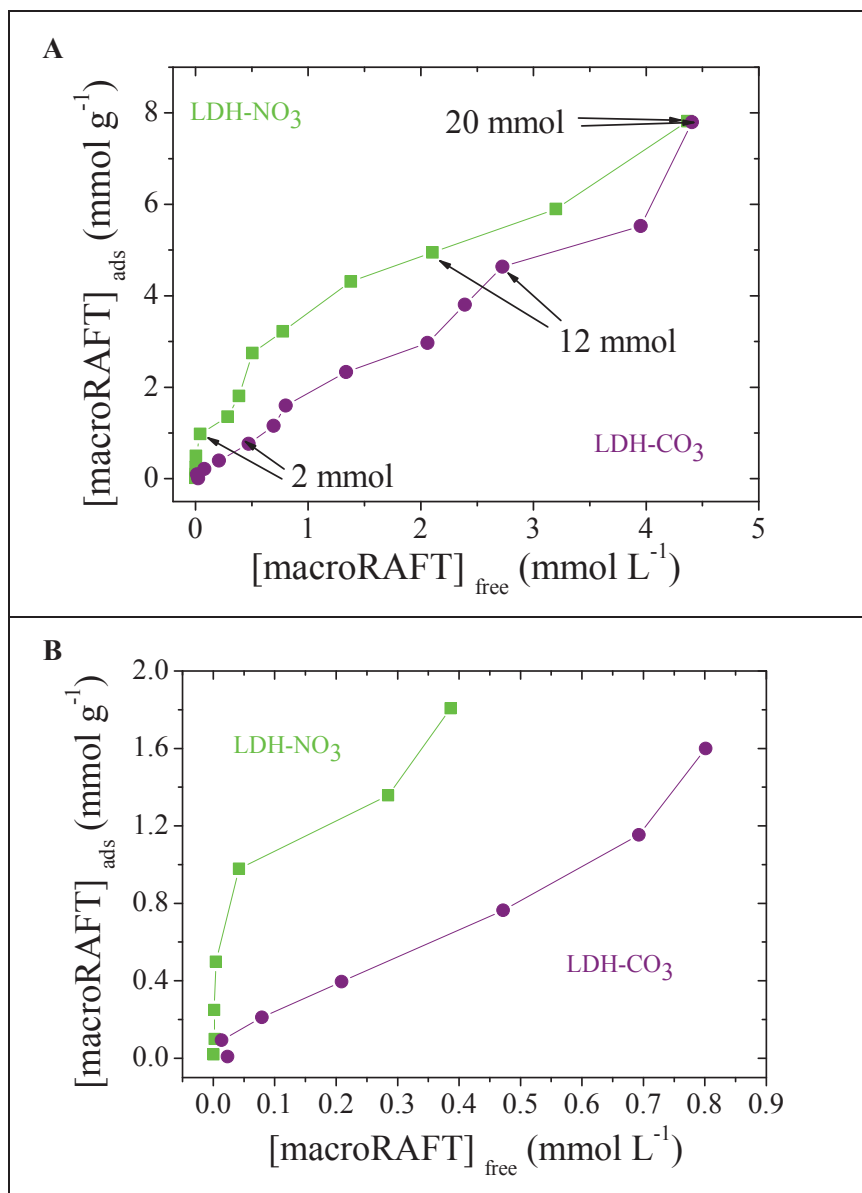


Figure 22. MacroRAFT 3 200 g mol^{-1} adsorption to Mg/Al- CO_3 (■) and Mg/Al- NO_3 (●) phase. Adsorbed versus free amount of macroRAFT in a range from (A) 0.04 to 20 mmol L^{-1} and (B) from 0 to 0.8 mmol L^{-1} of free macroRAFT.

Comparing the two LDH phases, it can be seen that the NO_3^- -containing phase presented higher adsorption values than the CO_3^{2-} one. This can be explained by the fact that NO_3^- ions are more easily exchanged, allowing the intercalation of the macroRAFT agent into the galleries of LDH in addition to its adsorption to the surface. On the contrary, CO_3^{2-} ions do not exchange under mild conditions, preventing the intercalation of the copolymer. In this case, the macroRAFT is exclusively adsorbed to the surface, which results in a lower adsorption amount (as seen in **Figure 22 B**). The schematic representation of both cases is illustrated in **Figure 23**.

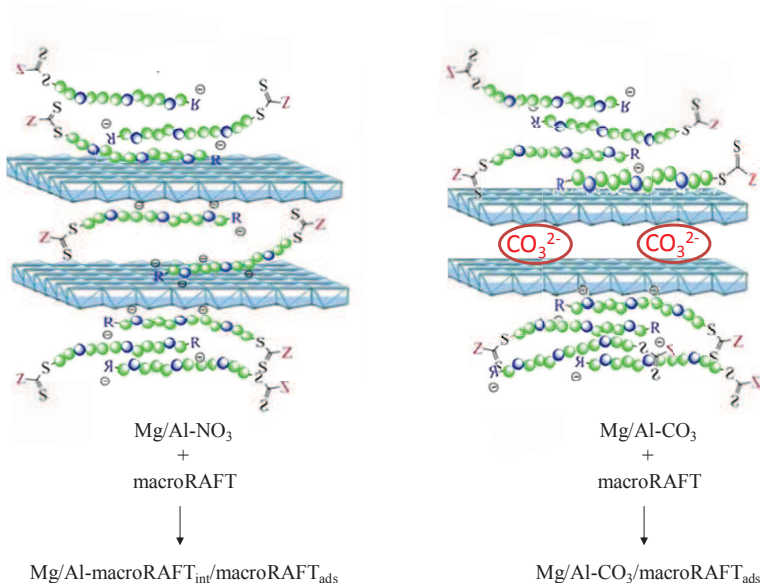


Figure 23. Illustrative representation of the macroRAFT adsorption and intercalation into the galleries of LDH-NO₃ and adsorption to the surface of LDH-CO₃.

From the studies performed using Imogolite, it was found that decreasing the pH could lead to an increase in adsorption of around 35%, which was attributed to the increased hydrophobicity of the macroRAFT at these conditions, favoring adsorption. However, in the present case, the driving force of adsorption seems to rely on the interaction between the macroRAFT and the positive sites (i.e. hydroxyl groups) on the surface of LDH. Thus, to increase the adsorption, one must increase the charge density (i.e. the number of interacting sites). However, the charge density of LDHs is not a function of pH, and cannot be tuned by acidification. A low pH would, nevertheless, decrease the competition with CO₃²⁻ exchange, minimizing the contaminations by this anion. However, since the amount of macroRAFT adsorbed to the surface of LDH was more than two times higher than the amount adsorbed to the surface of Imogolite at this alkaline pH (i.e. 1.35 g macroRAFT/g of Imogolite against 3.69 g of macroRAFT/g of LDH for an initial concentration of 10.5 g L⁻¹ of macroRAFT), an optimization of the adsorption by the decrease of pH was not attempted. The following studies thus continued at pH = 8.0.

It is important to note that the colloidal stability of the LDH-NO₃ hybrid suspensions was affected by the macroRAFT presence at certain concentrations. The particles were not stable until the macroRAFT concentration achieved 2 mmol L⁻¹, while for LDH-CO₃, no destabilization was observed, whatever the macroRAFT concentration. It can be seen in **Figure 22 A** that 2 mmol L⁻¹ corresponds to the condition in which no free macroRAFT is present. It can be thus considered that all LDH charges are compensated by the negative charges of the macroRAFT, and there are no additional charges to stabilize the system. Charge neutralization

did not occur for the LDH- CO_3 . This is because only external surface charges are available in this case, and the minimum amount of macroRAFT used was sufficient to provide extra charges which stabilized the particles.

Figure 24 shows the XRD and FTIR results for the hybrids obtained after adsorption of different concentrations of macroRAFT to the NO_3^- and CO_3^{2-} -containing LDH phases. It can be seen that the LDH structure remained intact (i.e. same interlayer distance) after interaction of macroRAFT with the carbonated sample (**Figure 24** A bottom), suggesting that only a physisorption occurred, with no intercalation of macroRAFT.

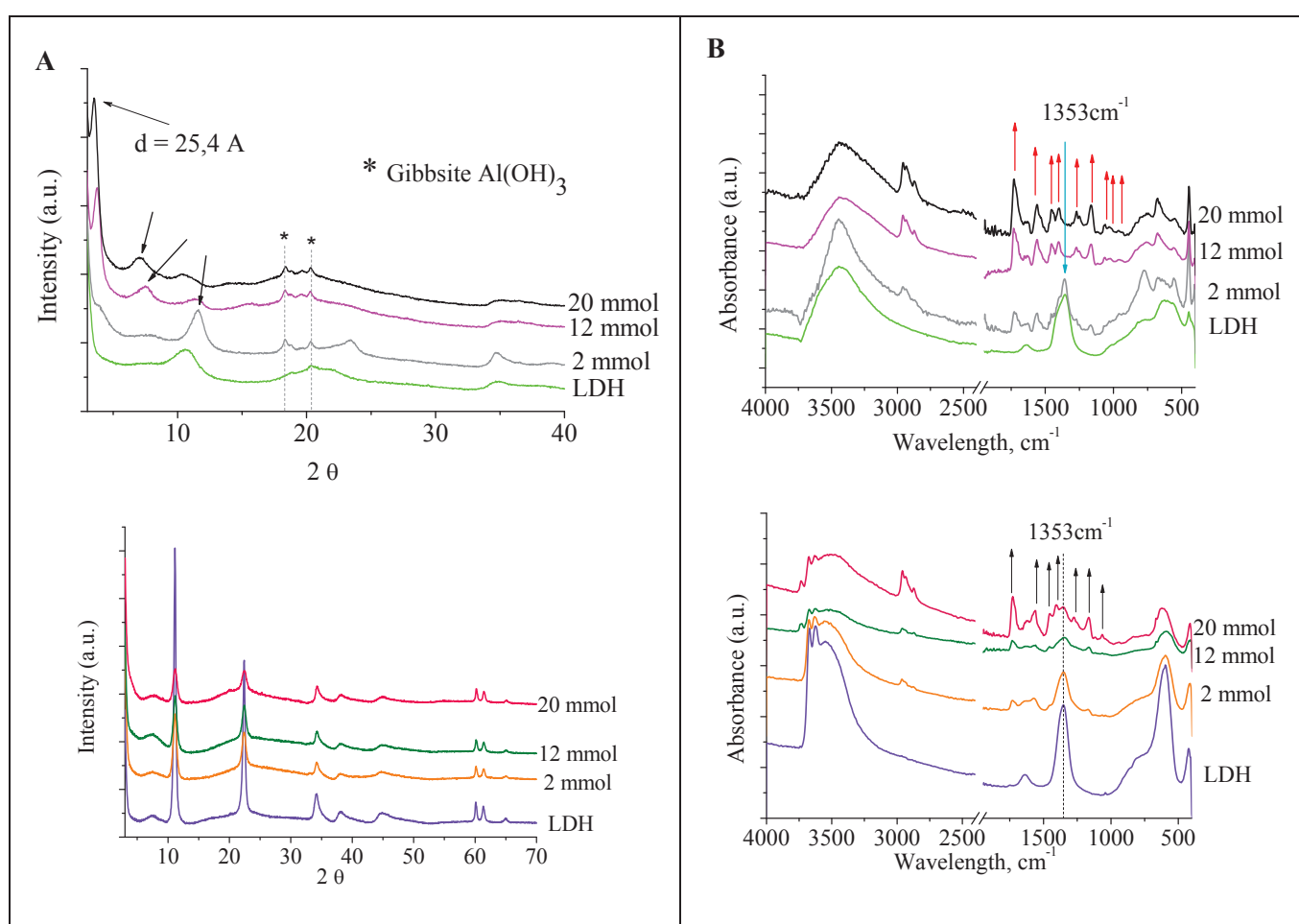


Figure 24. (A) X-ray diffractograms and (B) IR spectra of LDH/macroRAFT hybrids obtained after adsorption of increasing amounts of P(AA-co-BA)-CTPPA ($M_n = 3200 \text{ g mol}^{-1}$). Top: LDH = Mg/Al- NO_3^- ; and bottom: LDH = Mg/Al- CO_3^{2-} .

For the NO_3^- -containing sample (**Figure 24** A top) with 2 mmol L^{-1} of macroRAFT, a clear shift of the d_{003} plane towards higher angles can be seen. This shift indicates a modification of the interlayer distance, and it was ascribed to the exchange of NO_3^- ions by CO_3^{2-} ones. For the

sample containing a higher concentration of macroRAFT, the shifting goes towards smaller angles, which is attributed to an increase on the interlayer space caused by the intercalation of the macroRAFT macromolecules. Diffraction lines of a side phase corresponding to $\text{Al}(\text{OH})_3$ also appears on the diagram during the adsorption phenomenon.

The XRD results were corroborated by FTIR analyses (**Figure 24 B** bottom) that show a peak at 1353 cm^{-1} , corresponding to carbonate ions, present in all samples prepared with the LDH-CO_3 phase. Additional bands indicated the presence of the macroRAFT in the samples containing higher copolymer concentrations (indicated by the arrows), but the interlayer anions nature was not affected. As expected, **Figure 24 B** top shows the appearance of the CO_3^{2-} band (1353 cm^{-1}) for the sample LDH-NO_3 containing 2 mmol L^{-1} of macroRAFT. The spectra of the samples containing higher macroRAFT concentrations indicate the disappearance of the NO_3^- peak and the characteristic bands of the organic macromolecule (indicated by the arrows), confirming the intercalation.

Through the strategy described in this section, Mg/Al colloidal LDHs containing macroRAFT ($M_n = 3\ 200\text{ g mol}^{-1}$) intercalated in the interlayer space and adsorbed to the surface were produced. These phases were further used in the REEP experiments carried out to encapsulate the LDH layers within a polymer shell.

III.4.2.3 LDH synthesis in presence of RAFT or macroRAFT agents

The direct coprecipitation of Mg/Al and Zn/Al phases was performed in a solution of RAFT or macroRAFT (3200 or 4200 g mol^{-1}) agents. This strategy was employed in the attempt to form colloiddally stable LDH phases containing RAFT or macroRAFT species in the interlayer space.

Figure 25 presents XRD and FTIR results of the Mg/Al LDH phases synthesized in a RAFT or macroRAFT solution.

As can be seen in **Figure 25 A**, the phases obtained in presence of the organic molecules present a very poor crystallinity. The peaks of the (012) and the (110) planes (indicated by the arrows), characteristic of an LDH structure, are absent for the samples prepared using the macroRAFT agents (**Figure 25 A**, diagrams 3 and 4). The absence of such peaks suggests that the LDH layered structure was not formed. For the samples containing the RAFT agent (**Figure 25 A**, diagram 2), even though the (012) and (110) plane peaks are present, very broad and undefined peaks were obtained, indicating a highly disordered structure in the interlayer space.

The FTIR results (**Figure 25 B**) are in agreement with the results discussed before. The samples containing the macroRAFT agents (**Figure 25 B**, spectra 3 and 4) do not present the oxygen-

metal-oxygen network vibrations of the brucite layer below 829 cm^{-1} , suggesting the absence of the lamellar structures. Despite the lower definition, the hybrid phase containing the RAFT agent (**Figure 25 B**, spectrum 2) presents these O-M-O vibrations, indicating the formation of the LDH phase.

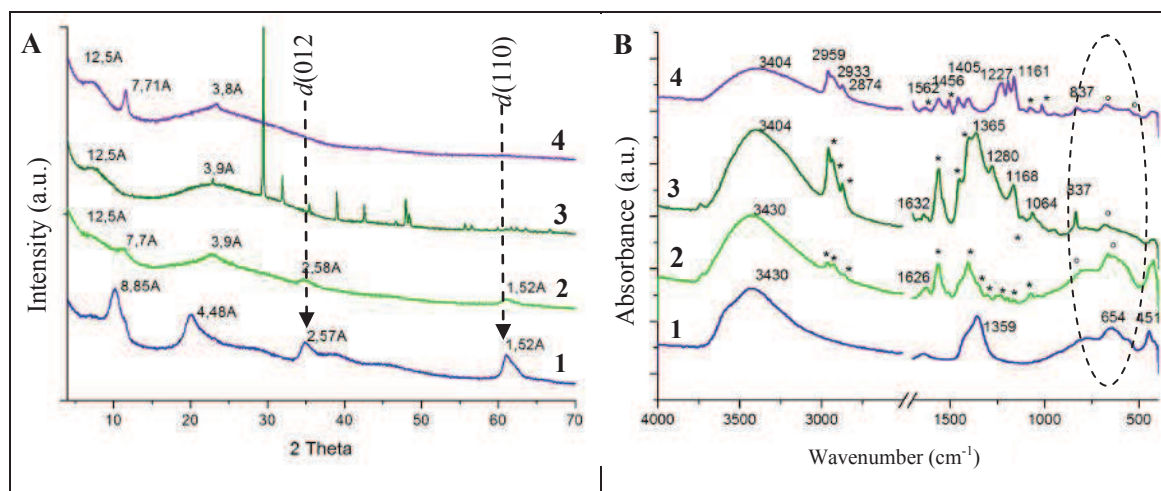


Figure 25. (A) X-ray diffractograms and (B) infrared spectra of Mg/Al-RAFT and Mg/Al-macroRAFT phases obtained via direct coprecipitation. **1** = Mg/Al-NO₃ reference; **2** = Mg/Al-RAFT; **3** = Mg/Al-macroRAFT 3200 g mol⁻¹ and **4** = Mg/Al-macroRAFT 4200 g mol⁻¹.

Similar results were obtained for the direct coprecipitations carried out using Zn/Al metallic salts (**Figure 26**). In presence of the macroRAFT agents (**Figure 26 A and B**, diagrams and spectra 3 and 4), the characteristic lines or bands of a LDH structure usually obtained in XRD and FTIR, respectively, are not observed in this case. In contrast, the sample formed in presence of the RAFT agent (**Figure 26 A and B**, diagram and spectrum 2), not only presented the characteristic signature of the LDH structure but also indicated a much more ordered crystalline phase. Sharp peaks presenting multiple plane harmonics were found (**Figure 26 A**, diagram 2), suggesting both an ordered crystalline phase and an ordered organization of the RAFT agent in the interlayer spaces.

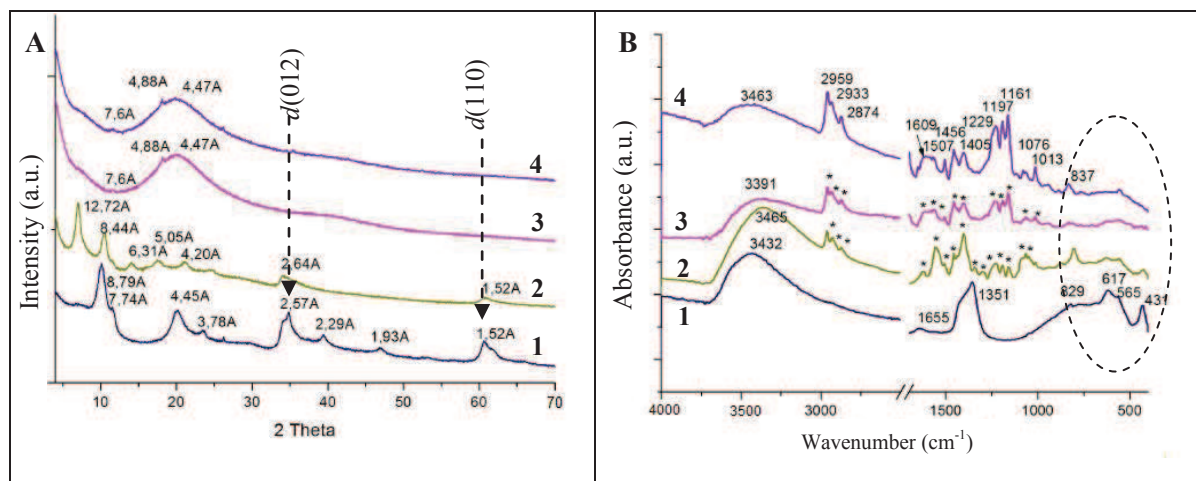


Figure 26. (A) X-ray diffractograms and (B) infrared spectra of Zn/Al-RAFT and Zn/Al-macroRAFT phases obtained via hybrid coprecipitation. **1** = Zn/Al-NO₃ reference; **2** = Zn/Al-RAFT; **3** = Zn/Al-macroRAFT 3200 g mol⁻¹; and **4** = Zn/Al-macroRAFT 4200 g mol⁻¹.

The XRD pattern of the Zn/Al-RAFT sample (previously shown in **Figure 26 A**, diagram 2) was put in evidence in **Figure 27**. In this figure, the subsequent harmonic peaks are clearly seen and the corresponding layer distances are also indicated. Planes and distances corresponded to: $d(003) = 24.96 \text{ \AA}$; $d(006) = 12.52 \text{ \AA}$; $d(009) = 8.23 \text{ \AA}$; $d(012) = 6.13 \text{ \AA}$; $d(015) = 4.91 \text{ \AA}$; $d(018) = 4.07 \text{ \AA}$ and $d(021) = 3.59 \text{ \AA}$.

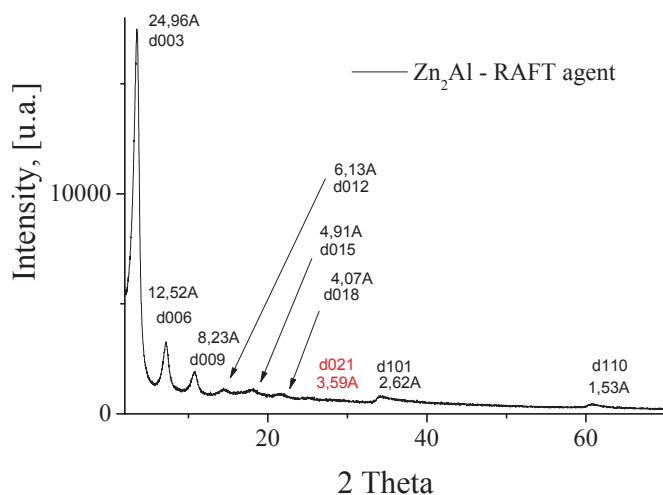


Figure 27. X-ray diffractogram of the hybrid Zn₂Al-RAFT phase obtained by hybrid coprecipitation.

To get better insight into the RAFT molecules conformation inside the interlayer space 1D electronic density profile obtained from the 001 harmonic reflections of the sample was drawn (**Figure 28**).

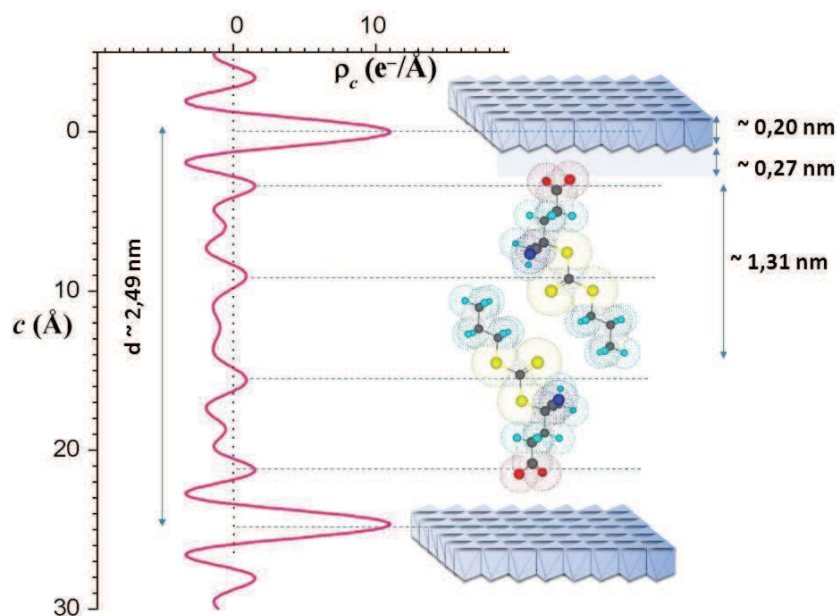


Figure 28. 1D Electronic density profile obtained from the 001 harmonics of the Zn_2Al -RAFT hybrid phase.

According to **Figure 28**, the RAFT molecules clearly adopt a bilayer and interpenetrated configuration between the LDH layers, where the RAFT molecule is anchored through the carboxylic acid group. The presence of the RAFT agent inside the host structure resulted in the formation of a hydrophobic interlayer domain.

The Zn/Al -RAFT hybrid phase was also analyzed by TGA after two washing cycles. The amount of RAFT agent present in the phase could be determined by comparing the weight loss of the pure LDH phase, the pure RAFT agent and the hybrid LDH-RAFT phase. From **Figure 29**, the amount of RAFT agent in the structure was calculated to be of 44 wt%. The theoretical value expected was of 48 wt%, calculated considering that for each aluminum atom one RAFT agent molecule would be present. The experimental value is thus in good agreement with the theoretical amount of macroRAFT expected.

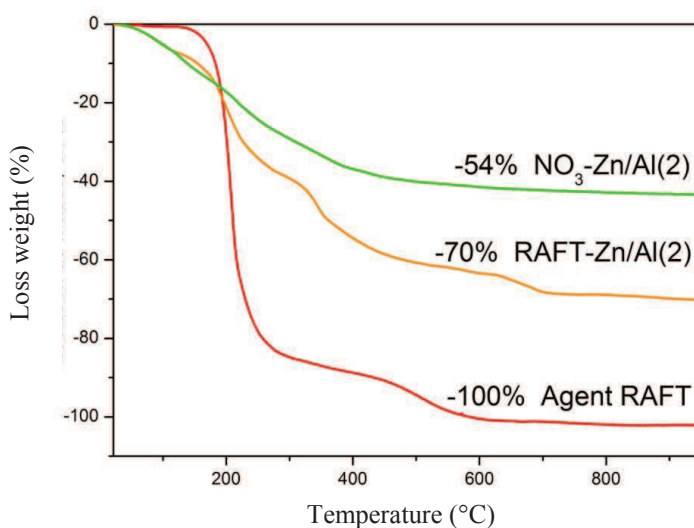


Figure 29. Weight loss versus temperature for the pure Zn/Al-NO₃ sample, the hybrid Zn/Al-RAFT sample and the pure RAFT agent.

In conclusion, the hybrid coprecipitations were found to be more challenging than the ionic exchanges. When long charged molecules were used such as macroRAFT agents, the coprecipitation and formation of the LDH crystalline structure was hampered, either by complexation with the metal ions or by steric effects.

When the RAFT agent was used, highly crystalline structures were obtained for a ZnAl LDH composition, presenting the characteristic XRD and FTIR signature of an intercalated LDH material. According to the RAFT agent molecule size and the value of the interlamellar gallery, the RAFT agent conformation in the interlayer space was proposed as an interpenetrated bilayer configuration, and 1D electronic profile strongly supported this assumption. The amount of RAFT agent incorporated into the inorganic structure was 44 wt%, as determined by TGA.

III.4.3 Conclusions

Different approaches were investigated to modify the LDH phase with the organic RAFT or macroRAFT agents and to access to colloidal hybrid LDH phases. The anionic exchanges starting with LDH phases synthesized by direct coprecipitation were successful for all three molecules tested: RAFT, macroRAFT 3200 g mol⁻¹ and macroRAFT 4200 g mol⁻¹. Successful intercalation of the organic compounds was confirmed by XRD and FTIR measurements, where the increase of the interlayer space and the replacement of the interlayer anions were observed, respectively. However, since the initial phases were not colloidally stable, the final hybrid

phases were not stable either, rendering the encapsulation via emulsion polymerization impossible.

The phases obtained by the adsorption of the macroRAFT 3200 g mol^{-1} to the LDH surface presented either intercalated or physisorbed structures, depending on the interlayer anion initially present in the host structure. Nitrate anions could be easily exchanged, generating macroRAFT rich hybrids. Carbonate anions were not exchanged, generating hybrids with only physisorbed copolymer chains on the surface. A limiting macroRAFT concentration was necessary to stabilize the LDH-NO₃ host. These stable hybrid phases were selected to be further engaged in emulsion polymerization reactions, since they contained considerable amounts of macroRAFT and were quite stable in aqueous suspensions.

Hybrid coprecipitations revealed to be less trivial than expected when working with preformed copolymers. The long macroRAFT chains prevented the formation of the LDH structure, resulting in amorphous heterogeneous phases. It was concluded that this approach was not adapted to intercalate long polymeric chains.

The synthesis performed using the RAFT agent, however, generated highly crystalline materials with the organic molecules well organized in the interlayer space. These phases could be dispersed in water generating relatively well stabilized suspensions. The dispersion of the highly hydrophobic RAFT agent in an aqueous suspension inspired us to perform a grafting polymerization of a hydrosoluble monomer from the surface of these RAFT-modified layers, to produce core/corona particles. These studies are presented in the next section.

III.5 Grafting from strategy

Taking advantage of the stability of the hybrid phases containing intercalated RAFT agent in water, the *grafting from* polymerization of *N*-acryloylmorpholine (NAM) was performed in aqueous solution. The idea was to verify if a polymer could grow from the surface and the interior of the LDH phases, forming a polymer corona around the LDH phases and preserving their stability in aqueous suspensions. Stabilization was expected to be provided by the water-soluble polymer, PNAM. **Figure 30** shows the schematic representation of the strategy presented in this section.

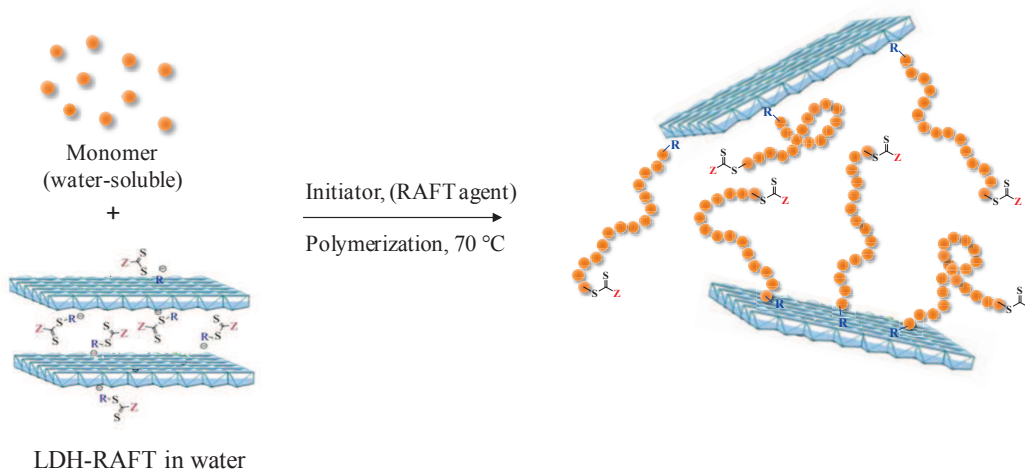


Figure 30. Illustrative representation of the *grafting from* polymerization route with RAFT-modified LDH phases.

III.5.1 Experimental section

III.5.1.1 Materials

Zn/Al-RAFT hybrid phases prepared as described in section III.4.1.2.4 and shown in section III.4.2.3 were used in two series of experiments: one without washing the Zn/Al-RAFT phase after synthesis, and another one after washing. The monomer: *N*-acryloylmorpholine (NAM) (97%), the initiator: 2,2'-azobis(2-methylpropionamide)dihydrochloride (AIBA) (99%), and 1,3,5-trioxane (>99%) were all purchased from Sigma-Aldrich and used as received. Water was deionized before use (Purelab Classic UV, ElgaLab Water).

III.5.1.2 Methods

Polymerizations were carried out as follows: typically, the initial hybrid suspension of Zn/Al-RAFT phase (3.2 g L⁻¹) was poured to a glass flask and the monomer (1.0 mol L⁻¹), the initiator

(3.0 mmol L⁻¹) and 1,3,5-trioxane (0.1 mol L⁻¹) were added. For the washed suspensions, an additional amount of free RAFT agent was added. The system was purged with nitrogen for 30 minutes under stirring. The flask was then sealed and immersed in an oil bath at 80 °C to start polymerization. Samples were periodically taken to follow the polymerization kinetics.

One reference polymerization, in the absence of LDH, was performed for each hybrid polymerization under the same conditions, for comparison purpose. **Table 9** shows the polymerization conditions of each entry. The amount of RAFT agent present in the washed sample was calculated based on TGA results. For the non-washed samples, the amount of RAFT was considered to be the total amount initially added, comprising the part which was most likely in the LDH interlayer and the remaining part that was in the aqueous phase.

Table 9. Polymerization conditions for the *grafting from* of NAM from the surface of RAFT modified Zn/Al LDH phases.

Entry	LDH-RAFT phase	free RAFT added	Stability at t ₀	[RAFT] (mmol L ⁻¹)	[RAFT]/[AIBA]	[LDH] (g L ⁻¹)
AC31	Washed	Yes	poor	14.5	3.3	2.3
AC33	Non-washed	No	satisfactory	19.7	6	3.2
AC34	Non-washed	No	satisfactory	5.2	1.5	9.9
AC301	0	Yes	-	14.2	4.5	0
AC303	0	Yes	-	14.3	4.5	0
AC304	0	Yes	-	14.4	3.8	0

Temperature = 70 °C. pH = 6.5, imposed by the LDH suspension.

III.5.1.3 Characterization

All samples taken during polymerization were characterized by ¹H liquid NMR spectroscopy by diluting the crude reaction medium in DMSO-d₆. Monomer conversion was determined by the relative integration of the protons of 1,3,5-trioxane and the vinylic protons of the monomers. To do so, 1,3,5-trioxane was added in a ratio of 1/12 related to monomer.

The molar mass of the polymer was determined by SEC analyses, as described in section II.5.1.3, after recovering the free polymer by centrifugation and methylating it. Average particle size, crystalline structure and composition were determined by DLS, XRD and FTIR measurements, respectively, as described in section III.3.1.3. For TEM analysis, the diluted samples were dropped on a carbon-coated copper grid and frozen in liquid ethane. TEM images were examined at an accelerating voltage of 80kV with a Philips CM120 transmission electron microscope (Centre Technologique des Microstructures (CTμ), platform of the Claude Bernard Lyon 1 University, Villeurbanne, France) under cryogenic conditions.

III.5.2 Results and Discussion

The molar mass of the final polymer and the particle size of the resulting hybrids synthesized by *grafting from* polymerization of NAM in presence of Zn/Al-CTPPA hybrid phase are presented in **Table 10**.

Table 10. Results of the reference polymerizations and the *grafting from* polymerizations of NAM in presence of Zn/Al-CTPPA hybrid phases.

Entry	D_h (nm)/PDI	$M_{n, \text{theo}}$ (g mol ⁻¹)	$M_{n, \text{exp}}$ (g mol ⁻¹)	\mathcal{D}
AC301	-	19 100	11 400	1.1
AC303	-	10 000	5 100	1.1
AC304	-	10 100	6 300	1.09
AC31	> 900/1.0 ^b	29 000	18700	1.09
AC33	> 1000/1.0 ^c	7 800	11500	1.08
AC34	500-800/1.0 ^c	27 800	7500	1.08

^a Values calculated based on the ratio of $M_{n, \text{exp}}/M_{n, \text{theo}}$ for the reference experiment. ^b Washed and dried initial phase. ^c Non-washed and non-dried initial phase.

As it is known from the literature, the presence of free control agent contributes to a better control of the polymerization, decreasing the probability of termination by recombination.⁸⁹ Because of that, additional free RAFT (CTPPA) agent was added in this experiment. Polymerization was performed using a washed Zn/Al-CTPPA phase, with no free RAFT present in the suspension. Besides, a blank experiment without LDH was also performed.

Figure 31 A shows a slightly shorter induction time for the reaction performed in presence of the hybrid phases (AC31). However, very similar profiles are found, revealing very fast polymerization rates. **Figure 31** B shows the SEC chromatograms of the polymer recovered from the reference polymerization (dashed lines) and the final polymer separated from the hybrid particles (solid lines). A narrow peak was obtained, suggesting the formation of only one family of polymers with quite narrow molar mass distributions ($\mathcal{D} = 1.09$) in both experiments. In both cases, the $M_{n, \text{exp}}$ presented considerably lower value than the $M_{n, \text{theo}}$ expected (**Table 10**). These results can be explained by the use of PS standard, which is not adapted to accurately measure PNAM molar mass, as described in the literature.⁹⁰ The final LDH/PNAM particle size was measured by DLS, and results are presented in **Figure 31** C. The lack of stability, observed visually as some of the particles precipitated to the bottom of the flask, was confirmed by DLS, where very large particle size and PDI were obtained. It is noteworthy that at t_0 some destabilization had already been observed. However, it was hoped that with the progress of polymerization the polymer chains formed could provide enough stability to disperse the objects

previously unstable. It was observed, however, that the polymer chains formed could not provide the necessary stability to the system. This was attributed to the fact that the LDH-CTPPA phase was initially dried, favoring the stacking of the sheets and forming large aggregates, which were difficult to disperse. Because of that, the following experiments were conducted with non-washed and non-dried hybrid phases.

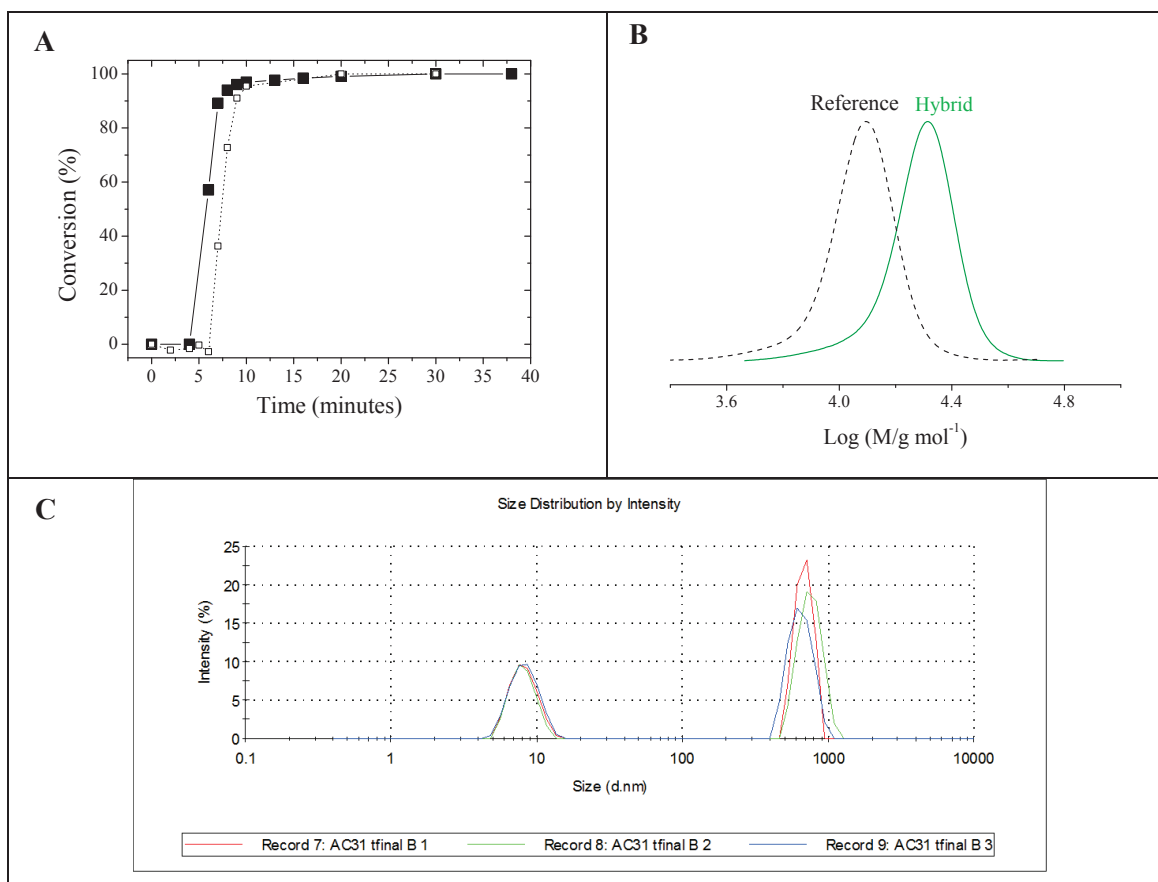


Figure 31. Reference (AC301) and *grafting from* (AC31) RAFT polymerization of NAM in water in presence of washed LDH-RAFT phase and free RAFT agent in the medium. Evolution of (A) monomer conversion versus time for the reference (AC301) (□) and the hybrid (AC31) (■) experiments, (B) THF-SEC chromatogram (log M) of the polymer recovered after the reference and the hybrid polymerization and (C) Average particle size distribution by intensity of the final hybrid particles suspended in water. (C) The figure shows three measurement runs.

The next experiment was thus performed with the crude Zn/Al-CTPPA hybrid phase, without washing or drying step. Since the amount of free RAFT agent was not removed before the polymerization, no additional RAFT agent was added.

As observed for the previous polymerization, the induction time was shorter for the experiment containing LDH (**Figure 32 A**) (AC33). In this case, the polymerization rate was also slightly higher, achieving 100% conversion after 35 minutes, against 50 minutes for the reference experiment (AC303). In terms of polymerization control, **Figure 32 B** shows quite narrow chromatogram peaks shifting towards higher molar masses with conversion. Narrow molar mass distributions ($D = 1.08$) were also obtained, indicating a good control of the polymerization. A small shoulder was however present on the high molar mass side of the chromatograms likely indicating the occurrence of irreversible termination by coupling. Again, the reference experiment (AC303) presented molar masses quite lower than the theoretical value expected (**Table 10**), attributed to the mismatch with PS standards. However, the hybrid sample (AC33) presented higher molar masses than the theoretical ones (**Table 10**), and this result cannot be attributed to the PS standard. In this case, it seems to be an indication that part of the RAFT agent did not participate in the polymerization. Samples were visually more stable than in the experiment performed with washed LDH-RAFT, but very large average particles size and high PDI were found by DLS (**Figure 32 C**). Again, the polymer chains formed could not provide enough stability to the system, and particles precipitated after a few hours. To better investigate the hybrid phases obtained, XRD and FTIR analyses of the samples taken during the polymerization were undertaken.

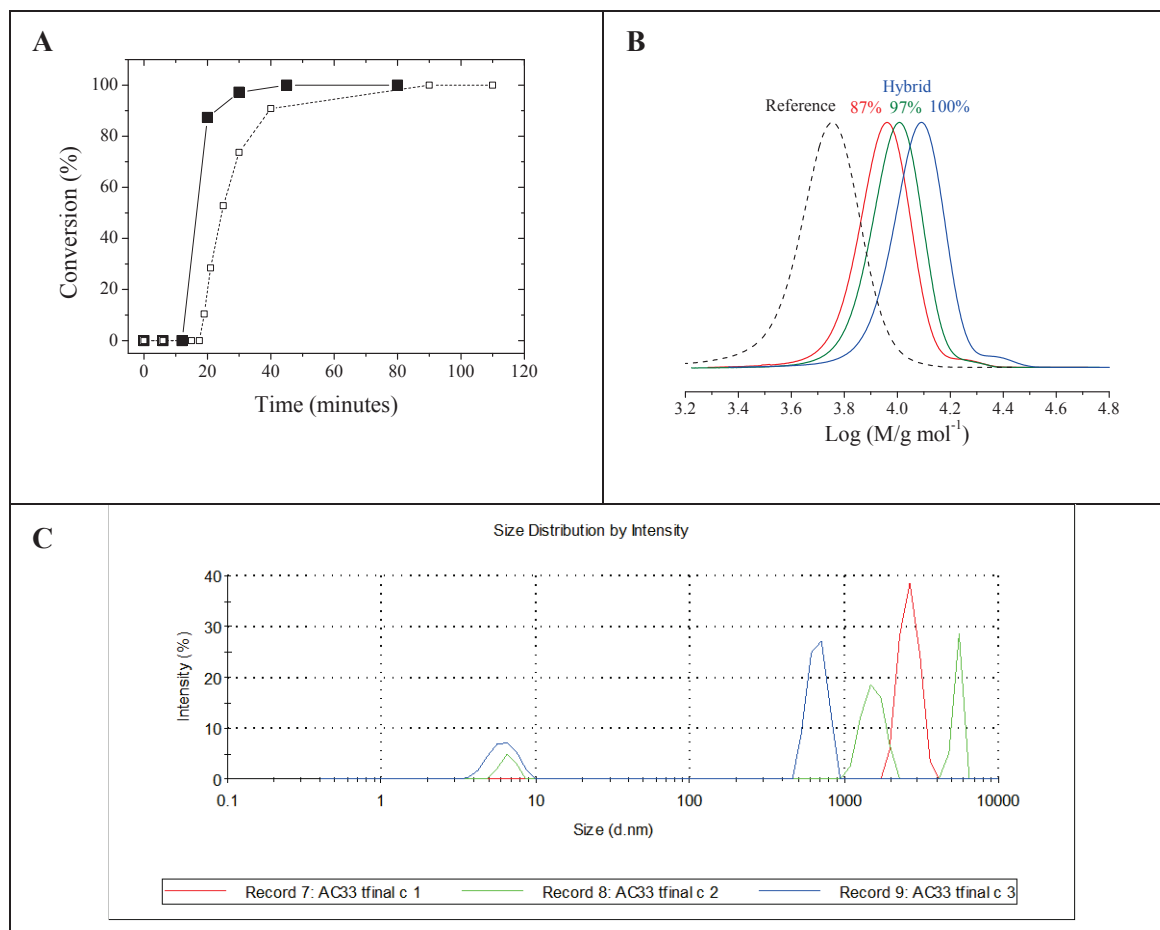


Figure 32. Reference (AC303) and *grafting from* (AC33) RAFT polymerization of NAM in water in presence of non-washed LDH-RAFT. Evolution of (A) monomer conversion versus time for the reference (AC303) (\square) and the hybrid (AC33) (\blacksquare) experiments, (B) THF-SEC chromatogram ($\log M$) of the polymer recovered after the reference and the hybrid polymerization and (C) average particle size distribution by intensity of the final hybrid particles suspended in water. (C) The figure shows three measurement runs.

As can be seen in **Figure 33**, at the beginning of the polymerization, the interlayer space seems to suffer a slight increase, evidenced in **Figure 33 B** (AC33-0%). This sample corresponds to $t = 10$ minutes (i.e. t_{10}), in which the system was still in an induction period. This enlargement could be thus ascribed to some monomer swelling effect. However, once polymerization is triggered, the interlayer space decreases considerably, suggesting the exchange of the oligomer/polymer chains by much smaller ions. Considering the small $d(003)$ distance of 0.76 nm, carbonate ions are most likely occupying the inter-lamellar domains. It was hypothesized that the exchange takes place because the polymer becomes too hydrophilic and tends to migrate to the aqueous phase. At the same time, the carboxylic acid anchoring groups on the oligomer/polymer chains extremity cannot compete with the carbonate ions, also contributing to the migration of the organic species to the aqueous phase. Another hypothesis could be the non-

participation of the adsorbed-RAFT agent to the polymerization. As reported by Illaik *et al.*,⁷⁶ where 4[12-(methacryloylamino)dodecanoylamino] benzene sulfonate acid (MADABS) was intercalated, the strong interdigitation of the organic molecules in the interlayer spaces abated the *in situ* polymerization. This could also explain the higher molar masses obtained compared to the theoretical values.

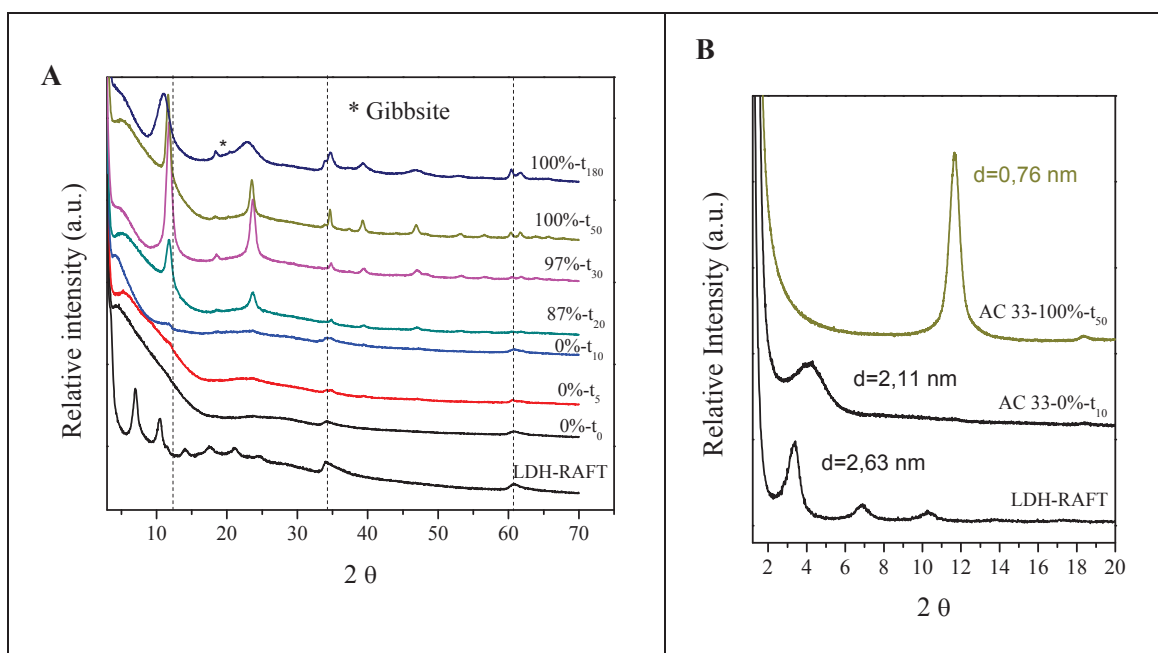


Figure 33. X-ray diffractograms in the range of (A) 0 – 70° 2 θ and (B) 0 – 20° 2 θ of the hybrid phases (AC33) recovered at different times of polymerization (0, 5, 10, 20, 30, 50 and 180 minutes).

Figure 34 presents the infrared spectra of the hybrid samples, which confirms the presence of carbonate anions in the interlayer space at the end of polymerization. It is noteworthy that the very intense band at $\sim 1350\text{ cm}^{-1}$ present for sample t_0 corresponds to the nitrate anions. As the sample was not washed before polymerization, to avoid stability issues, a high concentration of remaining nitrate ions was still present.

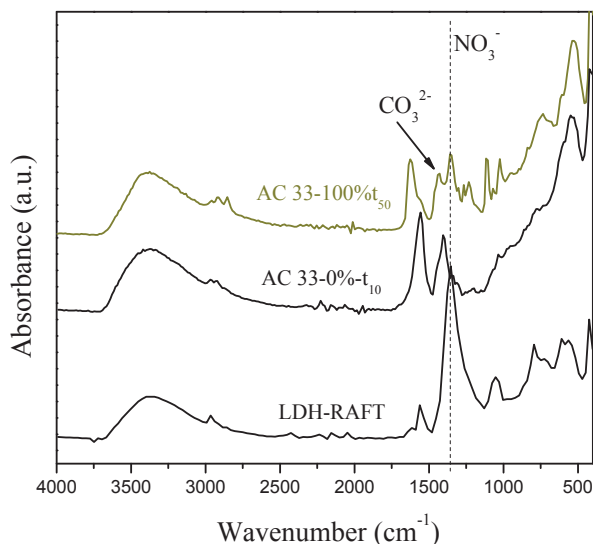


Figure 34. Infrared spectra of the hybrid phases (AC33) recovered at 0, 10 and 50 minutes of reaction.

A second attempt of *grafting from* NAM polymerization starting with Zn/Al-RAFT phase non-washed was done decreasing the total amount of RAFT agent in the medium (from 19.7 mmol L⁻¹ to 5.2 mmol L⁻¹) and increasing the amount of LDH (from 3.2 g L⁻¹ to 9.9 g L⁻¹) (AC34). This way, the amount of free RAFT agent should be reduced.

The starting hybrid phase was relatively stable in water, being easily dispersed under stirring. Some deposition was however observed when the sample was left without stirring for a few hours.

Figure 35 A shows that as observed before, similar conversion profiles were obtained for both polymerizations, i.e. the reference (AC304) and the LDH-containing experiment (AC34). 100% conversion was achieved after 35 minutes. Regarding the molar mass evolution (**Figure 35 B**), narrow peaks were obtained, presenting a complete shifting towards higher molar masses with conversion. Narrow molar mass distributions were also obtained ($D = 1.08$), despite the lower [RAFT]/[AIBA] ratio compared to the previous experiments. In terms of particles size (**Figure 35 C**), however, very high D_h and large PDI values were measured, indicating the lack of stability of the final material.

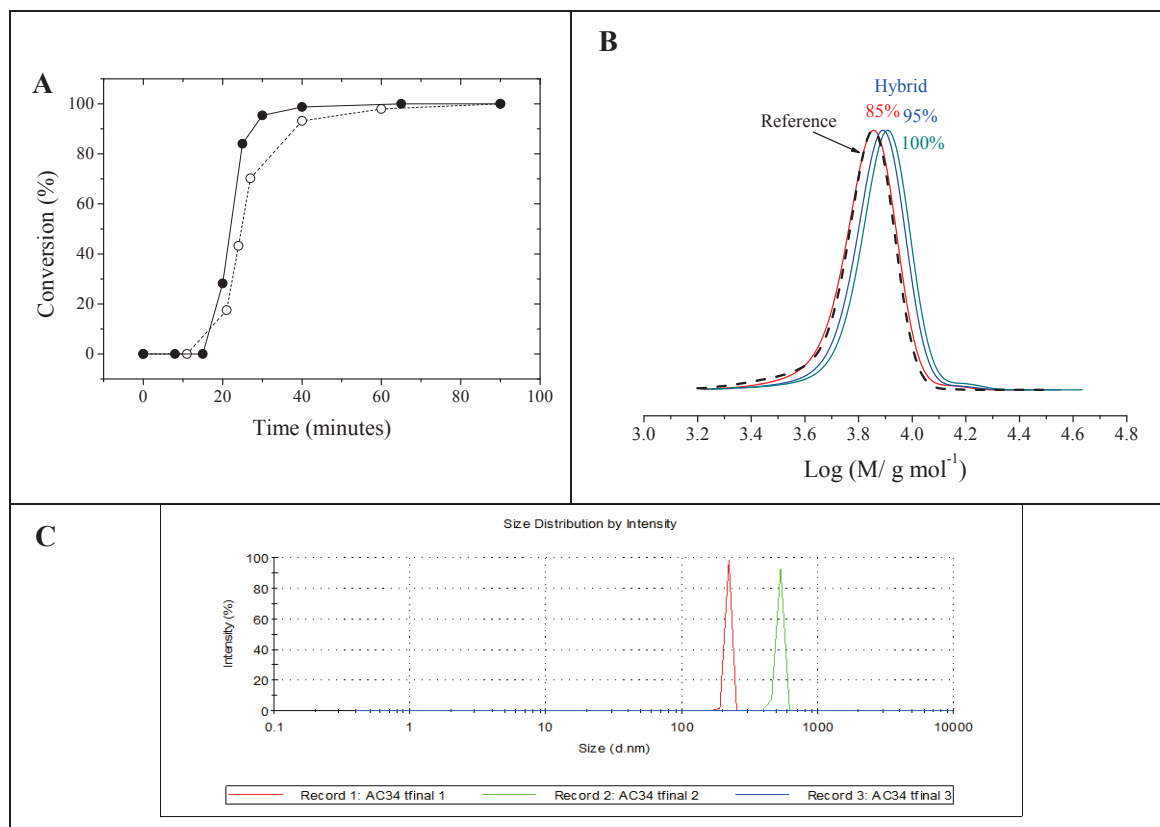


Figure 35. Reference (AC304) and *grafting from* (AC34) RAFT polymerization of NAM in water in presence of LDH-RAFT. Evolution of (A) monomer conversion versus time for the reference (AC304) (○) and the hybrid (AC34) (●) experiments, (B) THF-SEC chromatogram ($\log M$) of the final polymer recovered after the reference and the hybrid polymerization and (C) average particle size distribution by intensity of the final hybrid particles suspended in water. (C) The figure shows three measurement runs.

Analyzing the X-ray diffractograms (**Figure 36**) of the samples obtained during the reaction containing 5.2 mmol L^{-1} of RAFT and 9.9 g L^{-1} of LDH, conclusions similar to the ones of the previous polymerization (with 19.7 mmol L^{-1} of RAFT agent and 3.2 g L^{-1} of LDH) could be drawn. In this case, the first sample taken after t_0 (i.e. at t_{20}) already presented lower $d(003)$ distances compared to the sample at t_0 , that is, before polymerization started. Since the first sample was taken after 20 minutes of reaction, which corresponds to 10 minutes later compared to the previous experiment, the oligomer chains had already been exchanged by carbonate ions. **Figure 36 B** shows in detail the interlayer distance at t_0 , corresponding to 2.63 nm and attributed to the presence of RAFT in the LDH galleries, and the small distances at t_{20} and t_{90} , corresponding to 0.76 nm and ascribed to the presence of carbonate ions.

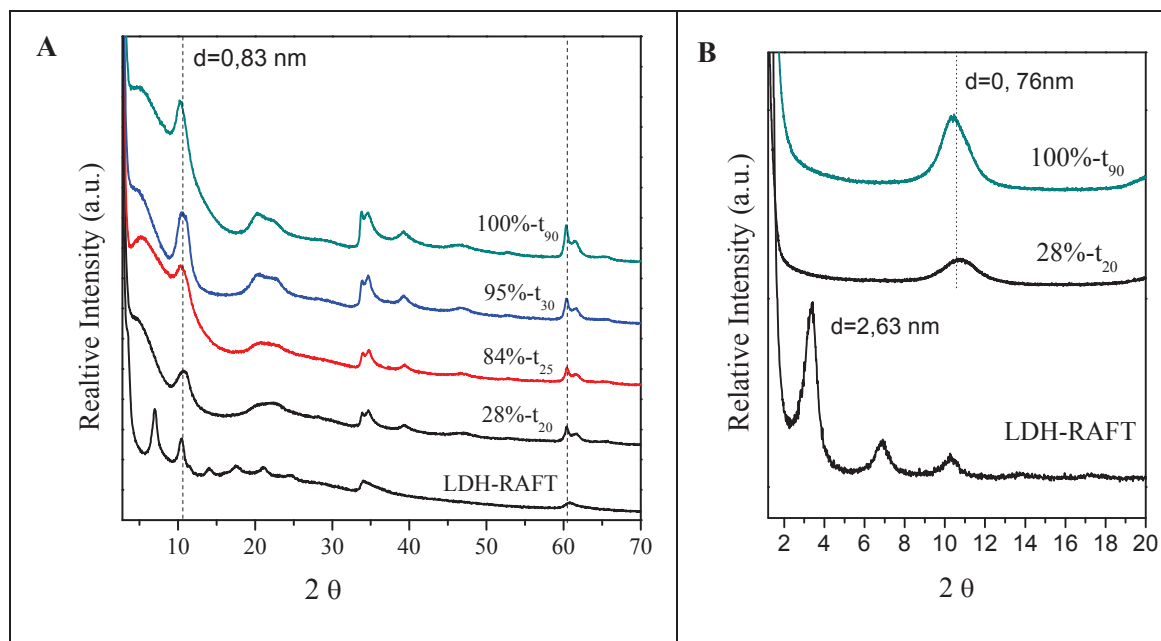


Figure 36. X-ray diffractograms in the range of (A) 0 – 70° 2θ and (B) 0 – 20° 2θ of the hybrid phases (AC34) recovered at different times of polymerization (20, 25, 30 and 90 minutes).

Infrared spectra presented in **Figure 37** again confirm the presence of CO_3^{2-} ions in the interlayer spaces after polymerization was triggered.

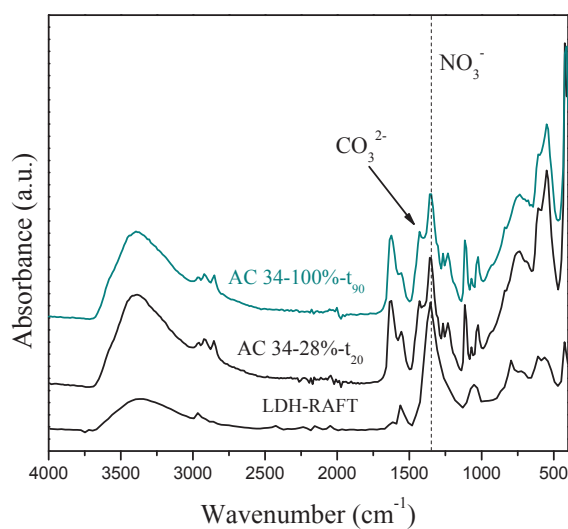


Figure 37. Infrared spectra of the hybrid phases recovered at 0, 20 and 90 minutes of reaction.

TEM analysis of the final suspension did not provide further proof of the formation of polymer brushes on the LDH surface, neither of the exfoliation of the LDH sheets.

III.5.3 Conclusion

In conclusion of the works presented in this section, it was observed that the *grafting from* of NAM from the surface of RAFT-containing LDH phases was unsuccessful. Even though there is a possibility that polymerization starts on the surface, the polymer is soon transferred to the aqueous phase. The migration is attributed to hydrophilicity of PNAM together with the competition between the carboxylic groups and the carbonate ions to interact with the LDH surface. The lack of stability of the final suspension is a consequence of the detachment of polymer chains from the surface.

III.6. MacroRAFT-assisted encapsulating emulsion polymerization (REEP) of colloidal LDH

In section III.4.2.2 the successful adsorption/intercalation of macroRAFT agent to the surface of preformed colloiddally stable Mg/Al LDH phases was presented. Two types of LDH, containing NO_3^- or CO_3^{2-} interlayer anions, were studied. Both led to stable dispersions of Mg/Al-macroRAFT particles, with the copolymer being adsorbed and intercalated in the case of LDH- NO_3 , or only adsorbed in the case of LDH- CO_3 .

Starting from these stable colloidal dispersions of LDH/macroRAFT, the strategy developed by Nguyen *et al.*⁹¹ and described in chapter II for the synthesis of polymer-encapsulated Imogolite nanotubes (REEP strategy) was used here to encapsulate the LDH platelets. **Figure 38** shows the schematic illustration of the encapsulation process.

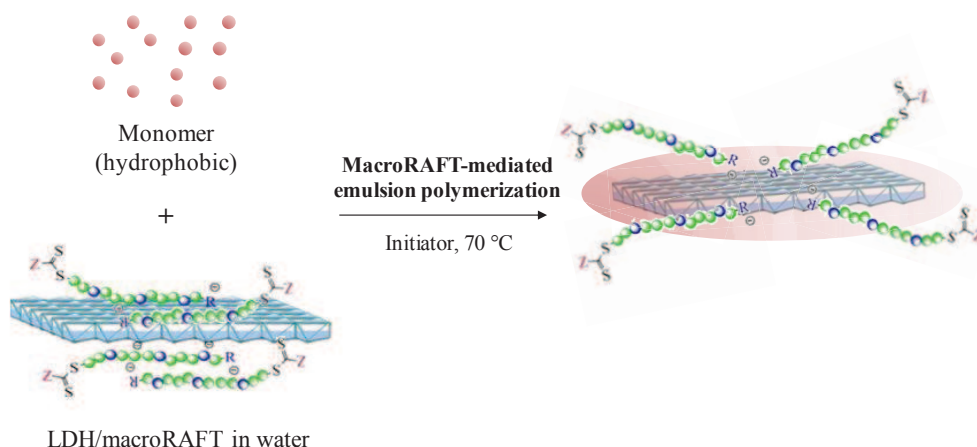


Figure 38. Illustrative representation of the macro-RAFT assisted LDH encapsulation by a polymer layer through surfactant-free emulsion polymerization.

III.6.1 Experimental section

III.6.1.1 Materials

The LDH phases, Mg/Al- NO_3 and Mg/Al- CO_3 , were synthesized by flash coprecipitation as described in section III.3.2.2. To obtain Mg/Al- CO_3 colloidal phases, the hydrothermal treatment was performed at 150 °C for 5h. To obtain Mg/Al- NO_3 colloidal phases, the solvothermal synthesis was applied, under the same treatment conditions. The macroRAFT agent, P(AA-co-BA)-CTPPA ($M_n = 3500 \text{ g mol}^{-1}$), was synthesized as described in section II.5 and purified prior to use. The monomers: methyl acrylate (MA, 99%, stabilized, Acros Organics) and butyl acrylate (BA, 99%, stabilized, Acros Organics), the initiators: 2,2'-

azobis(2-methylpropionamide)dihydrochloride (AIBA, 99%, Sigma-Aldrich) and 2,2'-azobis(*N,N'*-dimethyleneisobutyramidine) dihydrochloride (ADIBA, 99%, Wako), sodium hydrogen carbonate (NaHCO₃, 99%, Sigma-Aldrich) and NaOH solution (1N, standard, Acros Organics) were used as received. Water was deionized before use (Purelab Classic UV, ElgaLab Water).

III.6.1.2 Methods

LDH modification with macroRAFT agent was carried out in water. Typically, the LDH suspension was added by high speed injection to the macroRAFT solution at pH = 8.0. The mixture was left stirring during the night. When LDH-NO₃ was used, the system was left under nitrogen atmosphere, to avoid carbonate contamination. The LDH/macroRAFT suspensions were then polymerized in emulsion. Semi-batch emulsion polymerizations were performed as described in section II.9.1.2 and carried out for 7h. Instead of the anionic ACPA, the initiator used for these polymerizations was either AIBA or ADIBA. These cationic initiators were chosen to avoid competition between the macroRAFT and the initiator exchange with the nitrate anions. We focused on studying the final morphology of the particles formed, thus no sampling was made during polymerization to follow monomer conversion. The final particles size, monomer conversion and morphology were measured at the end of polymerization.

III.6.1.3 Characterization

The final latexes were characterized as described in section II.6.1.3. TEM analyses were performed using the same devices as described in section II.6.1.3, but were carried out under cryogenic conditions.

III.6.2 Results and Discussion

The macroRAFT-assisted encapsulating emulsion polymerization of LDH was performed using colloidal phases containing two types of interlayer anions: nitrates or carbonates. Nitrates can be easily exchanged, allowing the intercalation of the guest species in addition to its adsorption to the external surface. For carbonate anions, the exchange requires rough conditions (i.e. acidic pH and elevated temperatures) to take place. In this former case, only the physisorption of the macroRAFT agent on the external surface was considered, due to the mild conditions employed. The effect of LDH type (carbonate- or nitrate-based LDH) and macroRAFT concentration on the final morphology and monomer conversion was investigated.

III.6.2.1 Effect of macroRAFT concentration and LDH interlayer anion

Two series of experiments, one with LDH-NO₃ and the other with LDH-CO₃, were performed to investigate the effect of macroRAFT concentration. For each series, two macroRAFT concentrations were tested: 3.0 mmol L⁻¹ and 10.0 mmol L⁻¹. For the LDH-NO₃, the lower concentration corresponded to the minimum concentration necessary to obtain stable macroRAFT/LDH suspensions, and it also corresponded to a concentration in which very few macroRAFT was present in the aqueous phase. For the LDH-CO₃, no limiting macroRAFT concentration was observed, but changing the amount of macroRAFT would certainly affect the amount of free copolymer in water.

Table 11. Conditions and results of the semi-batch emulsion polymerization of MA/BA (80/20 wt/wt) in presence of LDH-CO₃ and LDH-NO₃ colloidal phases.

LDH type	[macroRAFT] (mmol L ⁻¹)	D_{h, t_0} (nm)/PDI	D_h (nm)/PDI	X_{final} (%)
Mg/Al-NO ₃	3.0	221 / 0.4	181 / 0.2	2.0
Mg/Al-NO ₃ ^a	3.0	123 / 0.1	136 / 0.2	3.0
Mg/Al-NO ₃	10.0	203 / 0.3	176 / 0.3	47.0
Mg/Al-CO ₃	3.0	141 / 0.2	114 / 0.2	8.5
Mg/Al-CO ₃	10.0	130 / 0.2	109 / 0.3	88.0

[LDH]: 2.0 g L⁻¹; MacroRAFT: P(AA-co-BA)-CTPPA of 3500 g mol⁻¹; pH = 8.5; initiator = AIBA; [macroRAFT]/[AIBA]: 1.5; Temperature: 70 °C; $D_{h, LDH-NO_3}$ = 122 nm; $D_{h, LDH-CO_3}$ = 170 nm. ^a 5 minutes of sonication were applied prior to polymerization.

All polymerizations yielded stable latexes. The particles size was measured at t_0 and at the end of polymerization (**Table 11**). All experiments seemed to follow a general trend, in which the initial particles size was higher and decreased after polymerization. This decrease could result from the reorganization of the particles, probably caused by exfoliation of the sheets due to the polymer growth in the interlayer spaces. Another hypothesis would be the presence of additional small polymer particles, originated from secondary nucleation, that are also taken into account in the D_h measurements. For LDH-CO₃ samples, the second hypothesis was most likely valid, since no intercalation of macroRAFT happened for these phases. A third consideration could also take into account that at t_0 the objects are anisotropic, for which DLS measurements are less adequate. At the end of the polymerization, some of the objects became spherical, probably resulting in more accurate DLS measurements. This last consideration is particularly true for the samples in which the anisotropy was not preserved.

According to **Table 11**, very low or limited monomer conversions were obtained in both series of experiments. Polymerizations using LDH-NO₃ phases stopped at very low conversions, and a maximum of 50% conversion could be achieved when the higher macroRAFT concentration was used. Reasonable monomer conversion could only be achieved with the LDH-CO₃ phase when adding 10.0 mmol L⁻¹ of macroRAFT, where almost 90% of conversion was reached. This general conversion limitation was attributed to the hydrolysis of the initiator, which will be discussed further below.

Figure 39 shows the TEM images of the particles obtained by emulsion polymerization in the series of experiments employing LDH-NO₃ phase. It can be seen that the LDH layers were successfully encapsulated in the polymer particles. However, each particle contained several LDH layers, i.e. the sheets were not individually encapsulated. The aggregation of the LDH layers and the further encapsulation of these aggregates generated spherical-like isotropic particles. In addition, some stacking of layers can also be seen in some particles (pointed by the arrows), suggesting the unsuccessful exfoliation of the sheets.

Comparing both macroRAFT concentrations, 3 mmol L⁻¹ (**Figure 39 A**) and 10 mmol L⁻¹ (**Figure 39 B**), it is clearly seen that numerous free polymer particles are formed in the second case. This could be the result of secondary nucleation, originating from the large amount of free macroRAFT in the aqueous phase.

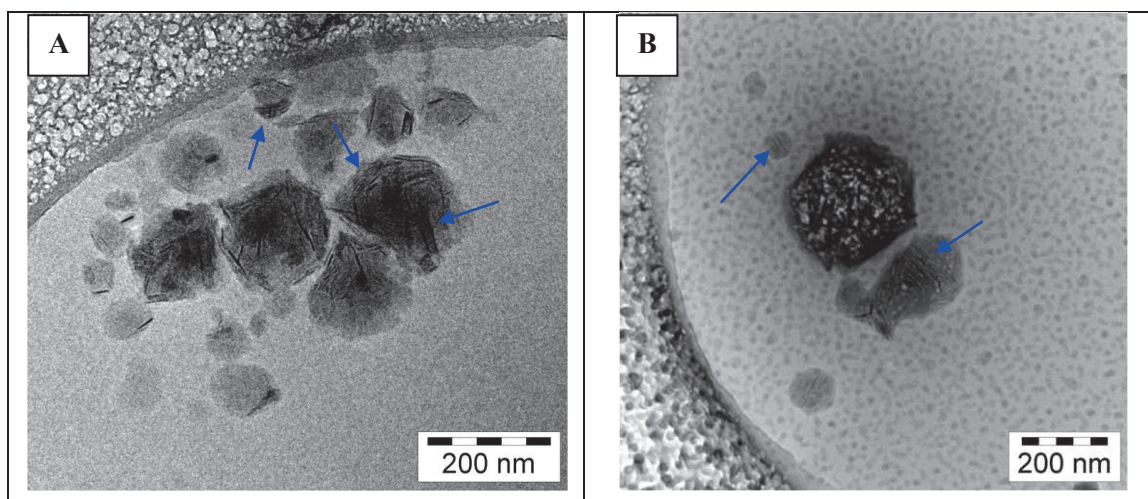


Figure 39. TEM images of the final particles obtained by macroRAFT-assisted LDH-NO₃ encapsulation by emulsion polymerization of MA/BA (80/20 wt/wt) using (A) 3.0 mmol L⁻¹ or (B) 10.0 mmol L⁻¹ of P(AA-*co*-BA)-CTPPA macroRAFT of 3500 g mol⁻¹ at pH 8.0.

Despite these optimization-needing points, it is noteworthy that the successful encapsulation of LDH particles was achieved under the same conditions in which Imogolite nanotubes could not be encapsulated, as shown in section II.9. This crucial difference between the two systems is likely related to the affinity of the macroRAFT for the inorganic surface, which defines its adsorption to the fillers. The strong interaction between the carboxylic acid units of the macroRAFT and the positively charged LDH layer favored the adsorption of the copolymers to the filler, even at pH 8.0, increasing its wettability. Consequently, the hydrophobic monomers had a higher affinity with the surface, contributing to the chain extension of the adsorbed macroRAFT, thus promoting encapsulation.

In the attempt to improve the dispersion of the macroRAFT/LDH suspensions and favor the monoencapsulation of the platelets, the sample containing LDH-NO₃ and 3.0 mmol L⁻¹ of macroRAFT was repeated with an additional step of sonication before the polymerization. It was expected that improving their initial dispersion, the layers could be individually encapsulated. **Figure 40** shows the TEM images of the final latex obtained. Despite the presence of some contaminations in the TEM grid (glass and ethane crystals), a few hybrid particles could be found (arrows). It appears that the LDH layers are indeed more individualized, and aggregates are rarely seen. In addition, the individual layers are coated with polymer, forming elongated core-shell particles with the inorganic phase in the core (**Figure 40 B**).

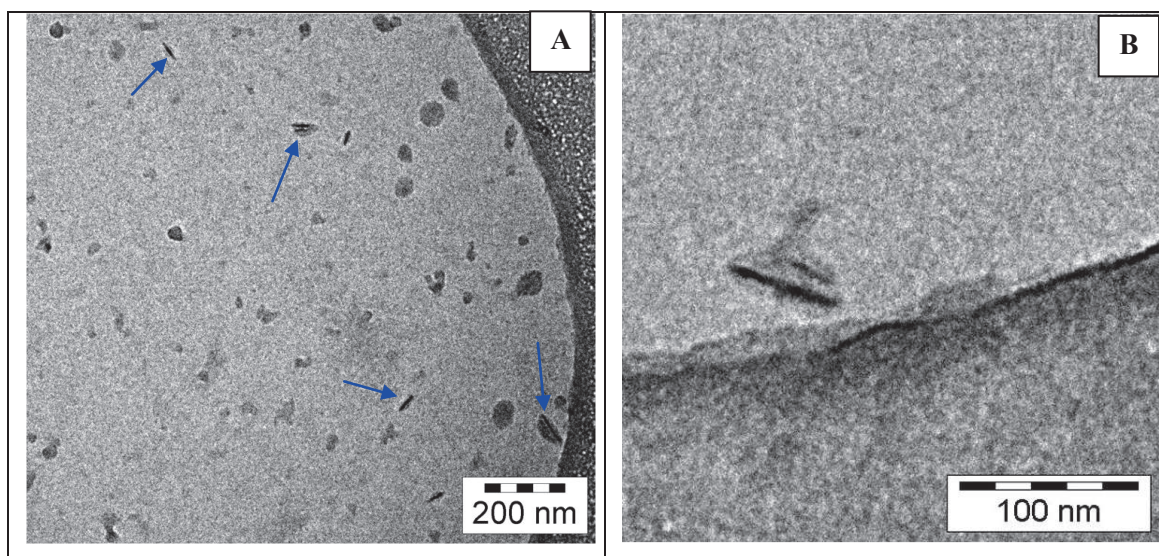


Figure 40. (A) Low and (B) high magnified TEM images of the final particles obtained by macroRAFT-assisted LDH-NO₃ encapsulation by emulsion polymerization of MA/BA (80/20 wt/wt) using 3.0 mmol L⁻¹ of P(AA-*co*-BA)-CTPPA macroRAFT ($M_n = 3\,500\text{ g mol}^{-1}$) at pH 8.0, after 5 min. of sonication of the macroRAFT/LDH suspension.

An alternative strategy was employed in an attempt to provide more stability to each LDH sheet, leading to the individual encapsulation of the platelets without the need for sonication. The strategy consisted in using a more hydrophilic macroRAFT agent, containing a molar ratio of 75% of AA and 25% of BA. The higher number of AA units would increase the charge density of the copolymer, which was expected to enhance its stabilizing capability. This new macroRAFT had the same molar mass as the previous one (i.e. $M_n = 3\,500\text{ g mol}^{-1}$), and was used to modify the LDH phase under exactly the same conditions as described previously. To achieve higher conversion, the amount of macroRAFT was fixed at 10 mmol L^{-1} . The final latex presented monomer conversion of 80% after 7 hours of reaction, and the final particles size D_h and PDI were: 196 nm and 0.2, respectively.

Figure 41 shows the TEM images of the particles obtained using the AA rich macroRAFT. A huge number of secondary-nucleated polymer particles were formed, probably resulting from the high hydrophilicity of the macroRAFT, which drives it to the aqueous phase in detriment to its adsorption to the surface. Hybrid morphologies obtained presented mostly individual LDH platelets, but encapsulation did not seem complete. The edges of the layers were apparently uncoated, and dumbbell-like particles (indicated by the arrows) were formed. The formation of what seemed like multiple dumbbell particles was also found (arrows on **Figure 41 B**). The higher hydrophilicity of the copolymer prevented aggregate formation, and the LDH layers remained individually dispersed. However, the adsorption of the copolymer to the surface of LDH was, to some extent, limited by the increase on AA moieties. This increase corresponds to a higher number of “interacting groups” in the macroRAFT chain. As a result, each chain will occupy a larger number of positive sites in the surface, preventing other chains to adsorb.

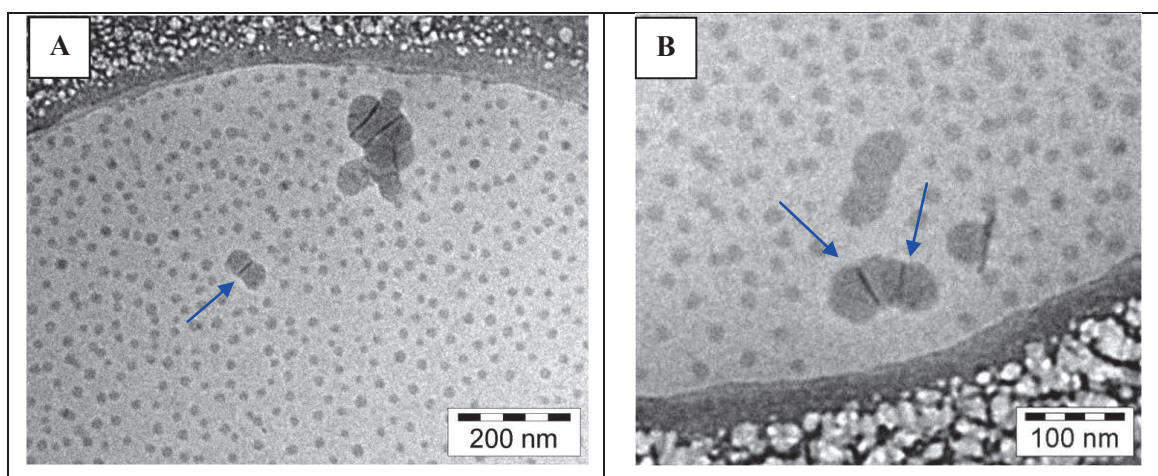


Figure 41. (A) Low and (B) high magnified TEM images of the final particles obtained by macroRAFT-assisted LDH-NO₃ encapsulation by emulsion polymerization of MA/BA (80/20 wt/wt) using 10.0 mmol L^{-1} of P(AA_{75%}-co-BA_{25%})-CTPPA macroRAFT ($M_n = 3\,500\text{ g mol}^{-1}$) at pH 8.0.

As a result, the lower amount of macroRAFT on the surface decreases the affinity of the hydrophobic monomer with the particles, creating an environment less favorable to encapsulation. These results are similar to what has been shown with Imogolite nanotubes when increasing the pH, although the nature of the interactions is different for LDHs.

Figure 42 shows the TEM results of the particles obtained for the series of experiments performed using the LDH-CO₃ phase. The LDH platelets were successfully encapsulated, and contrary to the previous series of polymerizations, they seem to be much more individualized. Indeed, individual sheets could be seen surrounded by polymer, and they were found parallel (dashed arrows) or perpendicular (solid arrows) to the grid. In these cases, the anisotropy of the final object was preserved, and elongated particles were formed (**Figure 42 A**).

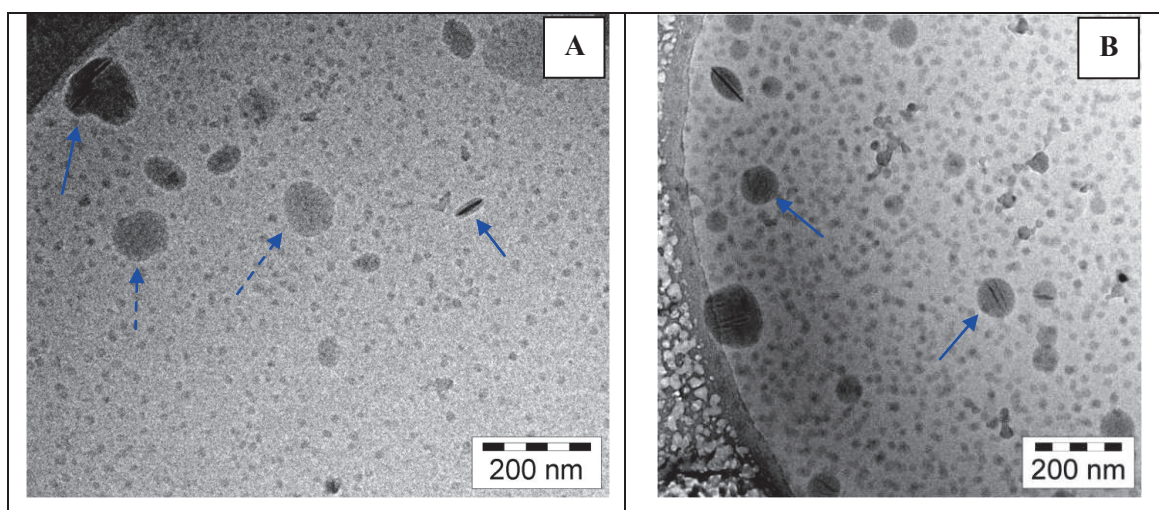


Figure 42. TEM images of the final particles obtained by macroRAFT-assisted LDH-CO₃ encapsulation by emulsion polymerization of MA/BA (80/20 wt/wt) using (A) 3.0 mmol L⁻¹ or (B) 10.0 mmol L⁻¹ of P(AA-co-BA)-CTPPA macroRAFT ($M_n = 3\,500\text{ g mol}^{-1}$) at pH 8.0.

As observed for the LDH-NO₃ series, increasing the macroRAFT concentration again resulted in the formation of a higher number of free polymer particles (**Figure 42 B**). At the same time, LDH platelets were found encapsulated inside spherical particles. Since monomer conversion for this experiment reached a higher value (~90%), the polymer shell formed around LDH was thicker, and it adopted a spherical conformation, minimizing the surface area.

Interestingly, even at the lower macroRAFT concentration a lot of free particles were formed. Since this LDH phase does not allow intercalation of the copolymer, the lowest amount of macroRAFT used was more than enough to cover the particles, leaving the excess in the

aqueous phase. This portion of free macroRAFT agent most likely undergoes secondary nucleation, forming a new crop of free particles.

In order to optimize the monomer conversion for low macroRAFT concentrations, two experiments were performed using the LDH-CO₃ phase. The first one was carried out doubling the initiator concentration, to investigate the effect of the radical flux. The second experiment was carried out in batch. Even though batch systems were unsuccessful for the Imogolite encapsulation, the robustness of the LDH system was expected to overcome the monomer accumulation and droplets formation, and eventually originate encapsulated LDH. **Table 12** presents the conditions and results of these polymerizations.

Table 12. Conditions and final conversion for the emulsion polymerization of MA/BA (80/20 wt/wt) in presence of LDH-CO₃ and macroRAFT agent.

Entry	[macroRAFT]/[AIBA]	Monomer feed	X _{final} (%)
AC68	0.8	Semi-batch	2.0
AC69	1.5	Batch	2.0

[LDH]: 2.0 g L⁻¹; macroRAFT: P(AA-co-BA)-CTPPA of 3 500 g mol⁻¹;
 [macroRAFT]: 3.0 mmol L⁻¹ pH = 8.5; initiator: AIBA; Temperature: 70 °C; D_{h, LDH-CO₃} = 170 nm.

As shown in **Table 12**, both experiments were unsuccessful in increasing the monomer conversion. Even when the initiator concentration was increased to two times the usual concentration, the same final conversion was obtained (~ 2.0 %). The addition of the monomer in a single step (batch) did not influence the monomer consumption either.

The low conversions obtained for all experiments were then correlated to the initiator efficiency. Indeed, AIBA is known for undergoing hydrolysis at basic pH,⁹² which reduces the formation of radicals effectively participating to the initiation process.

An analogous water-soluble azo initiator which is less sensitive to hydrolysis is 2,2'-azobis(*N,N'*-dimethyleneisobutyramidine) dihydrochloride (ADIBA) was thus tested (**Figure 43**). We performed an experiment under the same conditions as AC65 (see **Table 11**), but using ADIBA instead of AIBA.

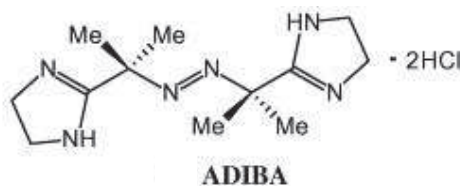


Figure 43. Chemical structure of 2,2'-azobis(*N,N'*-dimethyleneisobutyramidine) dihydrochloride (ADIBA) initiator.

In a first step, the polymerization was carried out at the same temperature (70 °C), even though ADIBA has a higher decomposition rate constant and consequently a lower 10h half-life decomposition temperature (44 °C). This experiment yielded a stable latex with 30 % of conversion, which was encouraging, considering the low amount of macroRAFT agent (3.0 mmol L⁻¹) and the relatively high temperature (70 °C) used. In a second step, another experiment was made at 60 °C under the same conditions (i.e. same LDH, macroRAFT and initiator concentrations), and a stable latex with 90% of conversion was obtained. The high conversion obtained was attributed to the higher radical flux provided by ADIBA initiator.

Figure 44 shows the TEM images of the latex synthesized using ADIBA at 60 °C. As it can be seen, the LDH platelets were successfully encapsulated. The platelets were found parallel to the grid plane (indicated by dashed arrows) or perpendicular to the grid plane (indicated by solid arrows), but in both cases they are completely encapsulated by the polymer shell. The high conversion also contributed to the formation of spherical particles, as discussed previously.

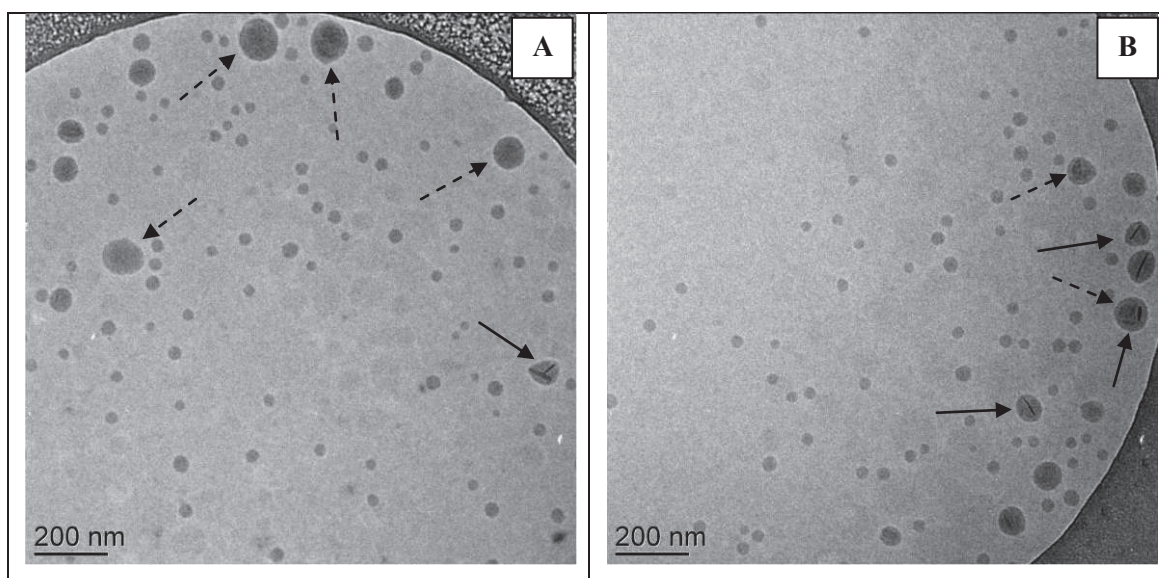


Figure 44. (A) and (B) TEM images of the final particles obtained by macroRAFT-assisted LDH-CO₃ encapsulation by emulsion polymerization of MA/BA (80/20 wt/wt) using 3.0 mmol L⁻¹ of P(AA-co-BA)-CTPPA macroRAFT ($M_n = 3\,500\text{ g mol}^{-1}$) at pH = 8.0, 60 °C and ADIBA as initiator.

III.6.3 Conclusion

In this section the encapsulation of LDH colloidal particles was achieved through the REEP technique. The same macroRAFT agent previously employed for the encapsulation of Imogolite was used here: P(AA-co-BA)-CTPPA ($M_n = 3\,500\text{ g mol}^{-1}$). This macroRAFT was shown to

have good affinity with the LDH surface and interlayer space, as shown in section III.4.2.2. The polymer-encapsulated morphology was obtained using hydrotalcite-like phases containing two types of interlayer anion, NO_3^- and CO_3^{2-} . Comparing the morphology obtained for both phases, some substantial differences were observed. Nitrated LDH formed aggregates of exfoliated layers encapsulated inside polymer particles. Carbonated phases generated mostly isolated and anisotropic stacks of layers encapsulated by a thin polymer shell. These anisotropic particles tended to become spherical with increasing macroRAFT amount and, consequently, monomer conversion. In other words, the polymer amount in the particle was increased, favoring the spherical morphology. More individualized LDH- NO_3 platelets could be obtained when submitting the sample to sonication leading to elongated core-shell nanocomposite particles. For the carbonate-containing LDH, in which no macroRAFT was present in the interlayer space, a higher amount of free polymer particles was formed during polymerization, due to the higher concentration of macroRAFT initially present in the aqueous phase. Monomer conversion issues could be resolved by changing the AIBA initiator, which was believed to hydrolyze during the process, for ADIBA, more resistant against hydrolysis under the same conditions.

In conclusion, the REEP technique was proven to be also efficient for the encapsulation of LDH layers. Compared to the experiments carried out with Imogolite, the encapsulation of LDH phases seemed to be more straightforward, leading to isolated object encapsulation even at high pH (i.e. pH = 8.0), which illustrates the impact of the inorganic particle's surface chemistry and the nature of the interactions between the surface and the macroRAFT on final morphology.

III.7. General conclusions of chapter III

The objective of this chapter was to encapsulate LDH phases with either a soluble polymer corona through the *grafting from* method or an insoluble polymer shell through macroRAFT-assisted encapsulating emulsion polymerization. In a first step, the effect of the parameters involved in the synthesis of colloidal LDH phases was studied for the synthesis of Mg/Al LDHs. The coprecipitation process, the temperature and the solvent used had a great influence over the final particle size, composition and crystallinity of the phases. Flash coprecipitation yielded smaller particles ($D_h \sim 100$ nm) compared to continuous coprecipitation ($D_h > 1000$ nm). The synthesis performed at room temperature generated phases with a higher crystallinity compared to that obtained for the samples synthesized at 0 °C. The coprecipitation performed in methanol and followed by solvothermal treatment formed phases containing NO_3^- anions in the interlayer space, minimizing the carbonate contamination, while the phases coprecipitated in water and followed by hydrothermal treatment had mainly CO_3^{2-} anions in the interlayer galleries.

The second step involved the modification of the conventional and colloidal LDH precursors with RAFT and macroRAFT agents. This modification was investigated through three main approaches: i) anionic exchange of the interlayer anions by RAFT or macroRAFT species, performed using conventional LDHs, ii) intercalation and/or adsorption of macroRAFT agents to colloidal LDHs, and iii) direct coprecipitation of LDH precursors in a RAFT or macroRAFT solution. The RAFT and macroRAFT agents could be well-intercalated into the galleries of LDH by the first approach, but the hybrid phases obtained presented a very low crystallinity and a very large particle size. Highly stable LDH/macroRAFT hybrid phases could be obtained in the second strategy, allowing the utilization of these materials in the REEP process. Well-defined LDH-RAFT phases were formed following the third strategy. The RAFT agent molecules could be successfully incorporated to the structure adopting a bilayer configuration between the sheets, whereas the macroRAFT macromolecules were too long to enable the coprecipitation and the crystalline growth. The LDH-RAFT hybrid phases were further used in the *grafting from* polymerization of a hydrosoluble monomer in the attempt to produce core/corona particles.

The tentative experiments carried out by *grafting from* aqueous polymerization of NAM on the surface of LDH have generated well defined polymer chains, with narrow molar mass distributions. However, by monitoring the evolution of the reaction by XRD analysis it was observed that the chains were detached from the surface as soon as the polymerization was triggered. The system became instable and LDH particles precipitated at the end of polymerization. These results were attributed to a combination of two factors: the high

hydrosolubility of the polymer, which promotes its migration to the solution, and the few numbers of anchoring sites, which are not sufficient to compete with the carbonate exchange.

The LDH/macroRAFT colloidal phases obtained by the adsorption studies were employed in the REEP process to encapsulate the LDH with a polymer shell. Two LDH precursors were studied, one containing NO_3^- anions, and thus allowing both adsorption and intercalation of the macroRAFT agent, and one containing CO_3^{2-} anions, being non-exchangeable and thus allowing only the adsorption of the macroRAFT agent to the outer surface. For each LDH, two series of experiments were performed, one with 3 mmol L^{-1} and the other with 10 mmol L^{-1} of macroRAFT. The polymerizations were carried out at pH 8.0, and they all generated polymer-encapsulated LDHs. When the LDH- NO_3 precursor was employed, aggregates of platelets were encapsulated forming stable latexes. The aggregation was attributed to the lower amount of macroRAFT available for stabilization, which is a consequence of the high amount of interacting sites in the inner and outer parts of the LDH. The formation of aggregates was avoided by applying a sonication step. Elongated core/shell particles of isolated LDHs were obtained when using the LDH- CO_3 precursors. In this case, the macroRAFT could only interact with the outer surface, leaving the extra charges of the chains available for stabilization. The macroRAFT concentration had a main effect on the final conversion, which was also correlated to the amount of initiator for a $[\text{macroRAFT}]/[\text{initiator}]$ constant ratio. Higher amounts of macroRAFT led to higher conversions. In addition, a huge amount of secondary-nucleated “empty” polymer particles was formed using the higher macroRAFT concentration, originating from the portion of free macroRAFT present in the aqueous phase. This high number of polymerization loci could also affect the monomer consumption, increasing final conversion. Generally, the polymerizations performed with low macroRAFT content and with LDH- NO_3 precursors led to the lower conversions ($\sim 2 \%$), and the polymerizations carried out with high macroRAFT content and with LDH- CO_3 achieved the higher conversion values ($\sim 88 \%$). For the same macroRAFT concentration (i.e. the same initiator concentration), LDH- CO_3 precursors yielded higher conversions than LDH- NO_3 ones, which indicates the influence of the number of polymerization loci on final conversion. The replacement of AIBA by ADIBA allowed us to overcome the conversion limitation, and a stable latex of polymer-encapsulated LDH with 90% conversion could be obtained.

Finally, this chapter showed the efficiency of the REEP technique for the encapsulation of LDH platelets. Comparing the results obtained for the platelets with those obtained for Imogolite nanotubes, it can be concluded that is not only the nature of the macroRAFT agents that defines the success of encapsulation, but the surface chemistry of the inorganic particles and the nature of the interaction between the macroRAFT and the surface are also key factors in the morphology control.

III.8. References

1. Xu, X.; Lu, R.; Zhao, X.; Xu, S.; Lei, X.; Zhang, F.; Evans, D. G. *Applied Catalysis B-Environmental* **2011**, 102, 147-156.
2. Alcantara, A. C. S.; Aranda, P.; Darder, M.; Ruiz-Hitzky, E. *Journal of Materials Chemistry* **2010**, 20, 9495-9504.
3. Wang, Q.; Luo, J.; Zhong, Z.; Borgna, A. *Energy & Environmental Science* **2011**, 4, 42-55.
4. Millange, F.; Walton, R. I.; Lei, L. X.; O'Hare, D. *Chemistry of Materials* **2000**, 12, 1990-1994.
5. Wang, Q.; O'Hare, D. *Chemical Reviews* **2012**, 112, 4124-4155.
6. Costa, F. R.; Saphiannikova, M.; Wagenknecht, U.; Heinrich, G.; Springer-Verlag, B. *Wax Crystal Control: Nanocomposites, Stimuli-Responsive Polymers* **2008**, 210, 101-168.
7. Utracki, L. A.; Sepehr, M.; Boccaleri, E. *Polymers for Advanced Technologies* **2007**, 18, 1-37.
8. Hu, H.; Wang, X. B.; Xu, S. L.; Yang, W. T.; Xu, F. J.; Shen, J.; Mao, C. *Journal of Materials Chemistry* **2012**, 22, 15362-15369.
9. Hu, H.; Xiu, K. M.; Xu, S. L.; Yang, W. T.; Xu, F. J. *Bioconjugate Chemistry* **2013**, 24, 968-978.
10. Jiang, F.-y.; Yang, J.; Bao, Y.-z. *Acta Polymerica Sinica* **2013**, 1131-1136.
11. Ding, P.; Zhang, M.; Gai, J.; Qu, B. *Journal of Materials Chemistry* **2007**, 17, 1117-1122.
12. Cavani, F.; Trifiro, F.; Vaccari, A. *Catalysis Today* **1991**, 11, 173-301.
13. Forano, C.; Costantino, U.; Prevot, V.; Taviot-Gueho, C., Layered Double Hydroxides (LDH). In *Handbook of Clay Science*, 2nd ed.; Bergaya, F.; Lagaly, G., Eds. Elsevier: 2013; Vol. 5, pp 745-782.
14. Manasse, E. *Atti Soc. Toscana Sc. Nat., Proc. Verb.* **1915**, 24, 92-105.
15. Cunha, V. R. R.; Ferreira, A. M. d. C.; Constantino, V. R. L.; Tronto, J.; Valim, J. B. *Quimica Nova* **2010**, 33, 159-171.
16. O'Hare, D.; Evans, J. S. O.; Fogg, A.; O'Brien, S. *Polyhedron* **2000**, 19, 297-305.
17. Shao, M.; Han, J.; Wei, M.; Evans, D. G.; Duan, X. *Chemical Engineering Journal* **2011**, 168, 519-524.
18. Bookin, A. S.; Drits, V. A. *Clays and Clay Minerals* **1993**, 41, 551-557.
19. Drits, V. A.; Bookin, A. S., Crystal structure and X-ray identification of layered double hydroxides. In *Layered Double Hydroxides: Present and Future*, Rives, V., Ed. Nova Science Publisher: New York, 2001; pp 39-92.
20. Lopez, T.; Bosch, P.; Ramos, E.; Gomez, R.; Novaro, O.; Acosta, D.; Figueras, F. *Langmuir* **1996**, 12, 189-192.
21. Tichit, D.; Lorret, O.; Coq, B.; Prinetto, F.; Ghiotti, G. *Microporous and Mesoporous Materials* **2005**, 80, 213-220.
22. Prince, J.; Montoya, A.; Ferrat, G.; Valente, J. S. *Chemistry of Materials* **2009**, 21, 5826-5835.
23. Valente, J. S.; Lima, E.; Toledo-Antonio, J. A.; Cortes-Jacome, M. A.; Lartundo-Rojas, L.; Montiel, R.; Prince, J. *Journal of Physical Chemistry C* **2010**, 114, 2089-2099.
24. Zhang, F.; Du, N.; Song, S.; Liu, J.; Hou, W. *Journal of Solid State Chemistry* **2013**, 206, 45-50.
25. Gardner, E.; Huntoon, K. M.; Pinnavaia, T. J. *Advanced Materials* **2001**, 13, 1263-1266.
26. Climent, M. J.; Corma, A.; Iborra, S.; Epping, K.; Velty, A. *Journal of Catalysis* **2004**, 225, 316-326.
27. Benito, P.; Labajos, F. M.; Rives, V. *Crystal Growth & Design* **2006**, 6, 1961-1966.
28. Benito, P.; Herrero, M.; Barriga, C.; Labajos, F. M.; Rives, V. *Inorganic Chemistry* **2008**, 47, 5453-5463.
29. Gursky, J. A.; Blough, S. D.; Luna, C.; Gomez, C.; Luevano, A. N.; Gardner, E. A. *Journal of the American Chemical Society* **2006**, 128, 8376-8377.

30. Reichle, W. T. *Journal of Catalysis* **1985**, 94, 547-557.
31. Courthy, P.; Marcilly, C., In *Preparation of Catalysts III*, Poncelet, G.; Grange, P.; Jacobs, P. A., Eds. Elsevier: Amsterdam, 1983; p 485.
32. Chang, Z.; Evans, D. G.; Duan, X.; Vial, C.; Ghanbaja, J.; Prevot, V.; de Roy, M.; Forano, C. *Journal of Solid State Chemistry* **2005**, 178, 2766-2777.
33. Reichle, W. T.; Kang, S. Y.; Everhardt, D. S. *Journal of Catalysis* **1986**, 101, 352-359.
34. Miyata, S. *Clays and Clay Minerals* **1975**, 23, 369-&.
35. Aramendia, M. A.; Borau, V.; Jimenez, U.; Marinas, J. M.; Ruiz, J. R.; Urbano, F. J. *Journal of Solid State Chemistry* **2002**, 168, 156-161.
36. Prinetto, F.; Ghiotti, G.; Graffin, P.; Tichit, D. *Microporous and Mesoporous Materials* **2000**, 39, 229-247.
37. Ma, R.; Sasaki, T. *Advanced Materials* **2010**, 22, 5082-5104.
38. Zhao, Y.; Li, F.; Zhang, R.; Evans, D. G.; Duan, X. *Chemistry of Materials* **2002**, 14, 4286-4291.
39. Xu, Z. P.; Stevenson, G.; Lu, C.-Q.; Lu, G. Q. *Journal of Physical Chemistry B* **2006**, 110, 16923-16929.
40. Faour, A.; Prevot, V.; Taviot-Gueho, C. *Journal of Physics and Chemistry of Solids* **2010**, 71, 487-490.
41. Itaya, K.; Chang, H. C.; Uchida, I. *Inorganic Chemistry* **1987**, 26, 624-626.
42. Gunawan, P.; Xu, R. *Chemistry of Materials* **2009**, 21, (5), 781-+.
43. Prevot, V.; Szczepaniak, C.; Jaber, M. *Journal of Colloid and Interface Science* **2011**, 356, 566-572.
44. Zhao, Y.; Wei, M.; Lu, J.; Wang, Z. L.; Duan, X. *Acs Nano* **2009**, 3, 4009-4016.
45. Ogawa, M.; Kaneko, S. *Langmuir* **2013**, 29, 14469-14472.
46. Touati, S.; Mansouri, H.; Bengueddach, A.; de Roy, A.; Forano, C.; Prevot, V. *Chemical Communications* **2012**, 48, 7197-7199.
47. Wang, Q.; Tay, H. H.; Guo, Z.; Chen, L.; Liu, Y.; Chang, J.; Zhong, Z.; Luo, J.; Borgna, A. *Applied Clay Science* **2012**, 55, 18-26.
48. Wang, Q.; Wu, Z.; Tay, H. H.; Chen, L.; Liu, Y.; Chang, J.; Zhong, Z.; Luo, J.; Borgna, A. *Catalysis Today* **2011**, 164, 198-203.
49. Chubar, N.; Gerda, V.; Megantari, O.; Micusik, M.; Omastova, M.; Heister, K.; Man, P.; Fraissard, J. *Chemical Engineering Journal* **2013**, 234, 284-299.
50. Chisem, I. C.; Jones, W. *Journal of Materials Chemistry* **1994**, 4, 1737-1744.
51. Fogg, A. M.; Dunn, J. S.; Shyu, S. G.; Cary, D. R.; O'Hare, D. *Chemistry of Materials* **1998**, 10, 351-355.
52. Mousty, C.; Prevot, V. *Analytical and Bioanalytical Chemistry* **2013**, 405, 3513-3523.
53. Nyambo, C.; Songtipya, P.; Manias, E.; Jimenez-Gasco, M. M.; Wilkie, C. A. *Journal of Materials Chemistry* **2008**, 18, 4827-4838.
54. Plank, J.; Zhimin, D.; Keller, H.; Von Hoessle, F.; Seidl, W. *Cement and Concrete Research* **2010**, 40, 45-57.
55. Manzi-Nshuti, C.; Chen, D.; Su, S.; Wilkie, C. A. *Polymer Degradation and Stability* **2009**, 94, 1290-1297.
56. Leroux, F.; Besse, J. P. *Chemistry of Materials* **2001**, 13, 3507-3515.
57. You, Y. W.; Zhao, H. T.; Vance, G. F. *Colloids and Surfaces a-Physicochemical and Engineering Aspects* **2002**, 205, 161-172.
58. Zhu, J.; Yuan, P.; He, H.; Frost, R.; Tao, Q.; Shen, W.; Bostrom, T. *Journal of Colloid and Interface Science* **2008**, 319, 498-504.
59. Park, A. Y.; Kwon, H.; Woo, A. J.; Kim, S. J. *Advanced Materials* **2005**, 17, 106-+.
60. Tao, Q.; Zhu, J.; Frost, R. L.; Bostrom, T. E.; Wellard, R. M.; Wei, J.; Yuan, P.; He, H. *Langmuir* **2010**, 26, 2769-2773.
61. Wypych, F.; Bail, A.; Halma, M.; Nakagaki, S. *Journal of Catalysis* **2005**, 234, 431-437.
62. Guimaraes, J. L.; Marangoni, R.; Ramos, L. P.; Wypych, F. *Journal of Colloid and Interface Science* **2000**, 227, 445-451.
63. O'Leary, S.; O'Hare, D.; Seeley, G. *Chemical Communications* **2002**, 1506-1507.

64. Leroux, F.; Meddar, L.; Mailhot, B.; Morlat-Therias, S.; Gardette, J. L. *Polymer* **2005**, 46, 3571-3578.
65. Mangiacapra, P.; Raimondo, M.; Tammara, L.; Vittoria, V.; Malinconico, M.; Laurienzo, P. *Biomacromolecules* **2007**, 8, 773-779.
66. Omwoma, S.; Chen, W.; Tsunashima, R.; Song, Y.-F. *Coordination Chemistry Reviews* **2014**, 258, 58-71.
67. Qiu, L. Z.; Chen, W.; Qu, B. J. *Polymer Degradation and Stability* **2005**, 87, 433-440.
68. Li, B. G.; Hu, Y.; Zhang, R.; Chen, Z. Y.; Fan, W. C. *Materials Research Bulletin* **2003**, 38, 1567-1572.
69. Leroux, F.; Adachi-Pagano, M.; Intissar, M.; Chauviere, S.; Forano, C.; Besse, J. P. *Journal of Materials Chemistry* **2001**, 11, 105-112.
70. Kotal, M.; Srivastava, S. K.; Manu, S. K.; Saxena, A. K.; Pandey, K. N. *Polymer International* **2013**, 62, 728-735.
71. Chakraborty, J.; Sengupta, S.; Dasgupta, S.; Chakraborty, M.; Ghosh, S.; Mallik, S.; Das, K. L.; Basu, D. *Journal of Industrial and Engineering Chemistry* **2012**, 18, 2211-2216.
72. Hsueh, H. B.; Chen, C. Y. *Polymer* **2003**, 44, 1151-1161.
73. Nogueira, T.; Botan, R.; Wypych, F.; Lona, L. *Journal of Applied Polymer Science* **2012**, 124, 1764-1770.
74. Nogueira, T.; Botan, R.; Macedo Neto, J. C.; Wypych, F.; Lona, L. *Advances in Polymer Technology* **2013**, 32, E660-E674.
75. Herrero, M.; Martinez-Gallegos, S.; Labajos, F. M.; Rives, V. *Journal of Solid State Chemistry* **2011**, 184, 2862-2869.
76. Illaik, A.; Taviot-Gueho, C.; Lavis, J.; Cornmereuc, S.; Verney, V.; Leroux, F. *Chemistry of Materials* **2008**, 20, 4854-4860.
77. Marangoni, R.; Taviot-Gueho, C.; Illaik, A.; Wypych, F.; Leroux, F. *Journal of Colloid and Interface Science* **2008**, 326, 366-373.
78. Roland-Swanson, C.; Besse, J. P.; Leroux, F. *Chemistry of Materials* **2004**, 16, 5512-5517.
79. Ding, P.; Qu, B. *Journal of Applied Polymer Science* **2006**, 101, 3758-3766.
80. Vaysse, C.; Guerlou-Demourgues, L.; Delmas, C.; Duguet, E. *Macromolecules* **2004**, 37, 45-51.
81. Ding, P.; Qu, B. J. *Journal of Colloid and Interface Science* **2005**, 291, 13-18.
82. Bao, Y.-Z.; Huang, Z.-M.; Weng, Z.-X. *Journal of Applied Polymer Science* **2006**, 102, 1471-1477.
83. Chen, W.; Feng, L.; Qu, B. J. *Solid State Communications* **2004**, 130, 259-263.
84. Qiu, L.; Qu, B. *Journal of Colloid and Interface Science* **2006**, 301, 347-351.
85. Yuan, Y.; Zhang, Y.; Shi, W. *Applied Clay Science* **2011**, 53, 608-614.
86. Qiu, L. Z.; Chen, W.; Qu, B. J. *Colloid and Polymer Science* **2005**, 283, 1241-1245.
87. Xu, X.; Smith, A. E.; Kirkland, S. E.; McCormick, C. L. *Macromolecules* **2008**, 41, 8429-8435.
88. Boursier, T.; Chaduc, I.; Rieger, J.; D'Agosto, F.; Lansalot, M.; Charleux, B. *Polymer Chemistry* **2011**, 2, 355-362.
89. Tsujii, Y.; Ejaz, M.; Sato, K.; Goto, A.; Fukuda, T. *Macromolecules* **2001**, 34, 8872-8878.
90. D'Agosto, F.; Hughes, R.; Charreyre, M. T.; Pichot, C.; Gilbert, R. G. *Macromolecules* **2003**, 36, 621-629.
91. Nguyen, D.; Zondanos, H. S.; Farrugia, J. M.; Serelis, A. K.; Such, C. H.; Hawket, B. S. *Langmuir* **2008**, 24, 2140-2150.
92. Ramos, J.; Forcada, J. *European Polymer Journal* **2007**, 43, 4647-4661.

General Conclusions

In this thesis, we aimed to synthesize hybrid latexes of polymer/Imogolite nanotubes and polymer/layered double hydroxides (LDH) capable of forming nanocomposite films with controlled microstructure and nanoparticle distribution in the matrix. To synthesize film-forming stable hybrid latexes, we have chosen to work with the macroRAFT-assisted encapsulating emulsion polymerization (REEP) technique.

In the first chapter, the advantages of using anisotropic inorganic nanoparticles as fillers for polymer nanocomposites was reviewed, as well as the various possible routes to obtain polymer/inorganic materials. Special attention was given to the processes performed in aqueous dispersed media and applying reversible deactivation radical polymerization techniques (NMP, ATRP or RAFT).

The second chapter described the elaboration of polymer/Imogolite nanotubes hybrid latexes using REEP. First, a bibliographic study of Imogolite structure, synthesis and physicochemical characteristics was undertaken, to understand their surface properties. Imogolite nanotubes are aluminosilicate materials of a few nanometers of diameter (from 2 to 5 nm) and up to several hundreds of nanometers long. They are composed of an external positively charged gibbsite-like aluminium hydroxide layer and of an internal negatively charged silicon hydroxide layer. They can be naturally found or synthetically produced. Well-defined synthetic analogues in which the silicon atoms are replaced by germanium (Ge-Imogolite), and of general formula $(\text{OH})_3\text{Al}_2\text{O}_3\text{GeOH}$, could be recently produced in large amounts, enabling the use and development of such fillers in materials science. Ge-Imogolite was used in this work. The use of Imogolite nanotubes to produce polymer nanocomposites is of great interest due to their high aspect ratio, surface area and rigidity. Reported works usually employed Si-Imogolite, and only a few works were done using polymers other than PVA, PMMA or PAAm. No examples of the use of RDRP in aqueous dispersed media for the production of polymer/Imogolite nanocomposites have been reported until now.

After the bibliographic study, the experimental part was presented. First, well-defined random macroRAFT agents containing (meth)acrylic acid and *n*-butyl (meth)acrylate units were synthesized by RAFT solution polymerization, and presented controlled molar masses and narrow molar mass distributions. The results obtained in preliminary experiments on Imogolite encapsulation discarded the methacrylic acid-based macroRAFTs due to stability issues. The adsorption of the acrylic acid-based copolymers onto the surface of the nanotubes was then studied. The presence of BA units in the chains, the macroRAFT molar mass and the pH of the

medium highly influenced copolymer adsorption. Copolymers containing BA units tended to better adsorb, and the amount of adsorbed macroRAFT increased even further with decreasing pH. However, at low pH (i.e. 6.0), less carboxylic acid units in the macroRAFT chains were deprotonated, decreasing their ability to stabilize the objects and causing the aggregation of Imogolite nanotubes into bundles. An additional sonication step was required to stabilize the suspension.

The stable aqueous suspensions of Imogolite/macroRAFT were then engaged in the macroRAFT-assisted encapsulating emulsion polymerization of a hydrophobic monomer mixture of MMA/BA (80/20 wt/wt) continuously added to the medium. The effect of different parameters, like the nature, the molar mass and the concentration of macroRAFT, the Imogolite concentration, the pH of the medium and the hydrophobic monomer composition on final latex morphology was evaluated. The key factor for successful encapsulation was found to be the adsorption of the macroRAFT onto the surface of Imogolite, which is what defines the wettability of the inorganic particles and their subsequent affinity for the hydrophobic monomers. This parameter could be tuned by introducing BA units in the macroRAFT chain and by regulating the pH of the medium. Tentative experiments were carried out to control the mixing and the interaction pathways of the process to avoid the formation of aggregates, but the complexity of the interactions involved in the adsorption of the macroRAFT onto the surface of Imogolite rendered the process hard to control. Smaller bundles were formed, but the formation of aggregates could not be avoided.

The composition of the hydrophobic monomer mixture was varied in an attempt to produce film-forming nanocomposite latexes containing either polymer-decorated Imogolite nanotubes or encapsulated Imogolite bundles. Thus, the initially fixed composition of MMA/BA (80/20 wt/wt) was changed to (50/50 wt/wt) and the experiments carried out at both pH 6.0 and 8.0. A new monomer mixture (STY/BA) was also polymerized at two compositions: 70/30 and 50/50 wt/wt at pH 8.0. The monomer nature was shown to have a significant influence on the final morphology. Experiments carried out using styrene-containing mixtures led to the formation of irregular Imogolite aggregates, which were encapsulated for both compositions. Additionally to the encapsulated Imogolite aggregates, polymer fibers and vesicles were also formed; these last ones originating from the self-assembly process that took place in the aqueous phase concomitantly to the polymerization occurring on the surface of the nanotubes. When the MMA/BA mixture (50/50 wt/wt) was polymerized at pH 8.0, polymer-decorated nanotubes were formed together with fibers and vesicles. The same mixture at pH 6.0 generated encapsulated Imogolite bundles plus fibers and vesicles. The self-assembly of the amphiphilic block copolymers formed during polymerization, especially in the aqueous phase, was affected

by the changes in the hydrophilic/hydrophobic balance of the block copolymers, caused by the change in the hydrophobic monomer nature. These changes led to the formation of these unexpected morphologies (i.e. fibers and vesicles). The formation of fibers and vesicles could be avoided by replacing MMA by MA, which is a monomer of similar water-solubility but leading to a homopolymer with a lower T_g (~ 8 °C). With this monomer, the mixture composition could be kept at MA/BA (80/20 wt/wt), with no fibers formation, yielding film-forming hybrid latexes of polymer-decorated nanotubes or encapsulated Imogolite bundles.

Films were casted with the stable latexes containing either polymer-decorated Imogolite tubes or encapsulated Imogolite bundles. The nanotubes length was of 75 nm in both cases. TEM results of the thin films revealed an even distribution of the tubes within the polymer matrix. Polymer-decorated tubes resulted in individually and uniformly dispersed tubes in the matrix, which were able to contribute to the formation of a percolating structure, while encapsulated bundles resulted in uniformly dispersed Imogolite bundles, which did not contribute to a significant reinforcement. Films produced from latexes containing longer nanotubes (average length 500 nm) presented partially oriented tubes inside the matrix. The alignment was attributed to the effect of the gravitational force onto the tubes with high aspect ratio, which tended to arrange their longer axis with the one of the adjacent tubes, resulting in the partial orientation parallel to the film plane. Mechanical strength of the films was higher for the samples in which a percolating structure was formed. The thick polymer layer around the encapsulated Imogolite bundles hindered the percolation effect, and storage modulus was lower for these samples.

The encapsulation of layered double hydroxide materials within a polymer particle was carried out following two different approaches: the *grafting from* approach, in which a soluble polymer was grown from the surface of the platelets forming core/corona particles; and the REEP approach, in which a non soluble polymer was formed around the platelets forming core/shell particles. In the first step, well-defined colloidal LDH platelets containing either NO₃⁻ or CO₃²⁻ interlayer anions were synthesized. These phases were then modified with RAFT or macroRAFT agents following two routes: *in situ* hybrid co-precipitation and anionic exchange. Well-defined RAFT-intercalated LDHs could be produced following the first route, and these phases were employed in the *grafting from* approach. The macroRAFT agent could be adsorbed and intercalated by the second route, and the LDH/macroRAFT phase was employed in the REEP experiments. The *grafting from* approach could not lead to core/corona particles. XRD results from the samples taken during reaction revealed that the polymerization probably started from the surface of LDH, but the growing chains were rapidly detached from the surface and replaced by CO₃²⁻ anions, resulting in the LDH loss of stability. For the REEP experiments, both

LDH-NO₃⁻ and LDH-CO₃²⁻ were modified with macroRAFT by anionic exchange. LDH-NO₃⁻ generated adsorbed and intercalated-macroRAFT platelets, while LDH-CO₃²⁻ only enabled the macroRAFT adsorption to the surface, since CO₃²⁻ anions could be hardly exchanged under mild conditions. The stable suspensions of LDH/macroRAFT were engaged in the polymerization of a hydrophobic monomer mixture of MA/BA (80/20 wt/wt), as optimized in the previous chapter, and carried out at pH 8.0. Both adsorbed and adsorbed/intercalated phases generated encapsulated LDH platelets, but the particles containing macroRAFT in the interlayer space yielded encapsulated LDH aggregates, while the ones containing macroRAFT only on the surface generated individually encapsulated LDH platelets.

Interestingly, the REEP technique applied to two different inorganic particles using the same macroRAFT and under the same conditions generated latexes with different morphologies. It can be concluded that the key factor governing the successful encapsulation of the inorganic particles by this technique does not rely only on the macroRAFT nature and composition. Its interaction with the surface and the surface chemistry of the inorganic particles itself also plays an important role. During the different studies performed in this thesis, the parameters highlighted as the most important ones are: the presence of BA units in the macroRAFT chain and the pH of the medium, both contributing to the higher adsorption of the macroRAFT onto the surface of the inorganic particles; and the nature of the interactions between the inorganic surface and the macroRAFT, defined by the macroRAFT nature and the surface chemistry of the filler. All these parameters converge to one single parameter: the number of RAFT functions per object. Indeed, the amount of macroRAFT adsorbed onto the surface of LDH-CO₃²⁻ at pH = 8.0 is at least two times higher than the one adsorbed to the surface of Imogolite under the same conditions, which results in a considerably greater number of RAFT functions per particle. Contrary to what is said in the literature, the use of a low molar mass macroRAFT is not sufficient to provide the necessary amount of RAFT functions per particle. Depending on the nature of the inorganic particle, the adsorption of such short copolymers can be very low, and encapsulation may not be achieved.

Finally, it was shown in this thesis that macroRAFT-assisted encapsulating emulsion polymerization is a powerful technique to encapsulate various inorganic particles, exemplified here with Imogolite nanotubes and LDH layers, and produce nanocomposite materials. This technique is very versatile allowing for a vast range of monomers to be polymerized leading to the formation of a polymer shell around the inorganic particles as long as one designs appropriate macroRAFT agents with high affinity for the inorganic surface and sufficient hydrophobicity to move the locus of the polymerization from the aqueous phase to the particles surface.

Annexes

Table of contents

A.1 SEC results of the polymerizations performed in the absence of Imogolite using acrylic acid- and methacrylic acid-based macroRAFT agents.....	283
A.2 Stability of the RAFT functionality of the acrylic acid-based macroRAFT copolymer with time at 80 °C and pH = 8.0.....	285
A.3 Effect of the interaction time on final hybrid latex morphology	286
A.4 SEC results of the polymerization of MA/BA (80/20 wt/wt) using P(AA-co-BA)-CTPPA macroRAFT at pH = 6.0.....	288

A.1 SEC results of the polymerizations performed in the absence of Imogolite using acrylic acid- and methacrylic acid-based macroRAFT agents

The SEC results obtained for the latexes synthesized by emulsion polymerization using the four different macroRAFTs: PAA-CTPPA ($M_n = 3\,800\text{ g mol}^{-1}$), PMAA-CTPPA ($M_n = 3\,800\text{ g mol}^{-1}$), P(AA-*co*-BA)-CTPPA ($M_n = 3\,700\text{ g mol}^{-1}$) and P(MAA-*co*-BMA)-CTPPA ($M_n = 2\,700\text{ g mol}^{-1}$), in the absence of Imogolite are shown in **Figure 1**.

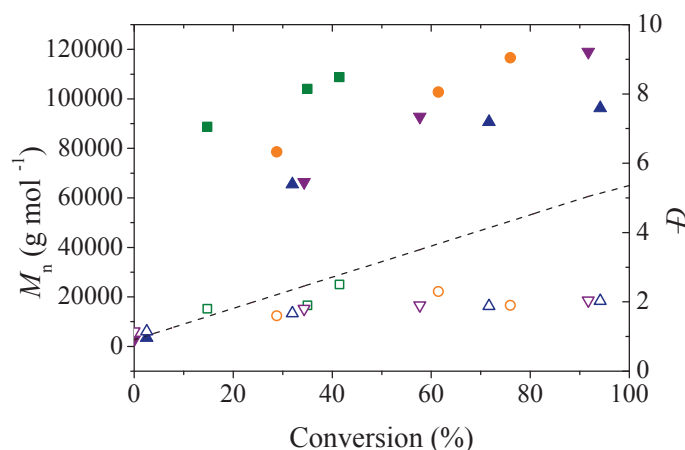


Figure 1. Number-average molar mass M_n (filled symbols) and $D = M_w/M_n$ (empty symbols) versus conversion for the MMA/BA (80/20 wt/wt) emulsion polymerization in presence of PAA-CTPPA ($M_n = 3\,800\text{ g mol}^{-1}$) (■), PMAA-CTPPA ($M_n = 3\,800\text{ g mol}^{-1}$) (●), P(AA-*co*-BA)-CTPPA ($M_n = 3\,700\text{ g mol}^{-1}$) (▲) and P(MAA-*co*-BMA)-CTPPA ($M_n = 2\,700\text{ g mol}^{-1}$) (▼).

Considerably high M_n values were obtained for all polymerizations, indicating a poor control in every case. Molar mass dispersities (D) were all near 2.0. THF-SEC results, presented in **Figure 2**, also support these observations. An incomplete shifting of chromatogram peaks toward high molar mass values was observed, and a signal ascribed to unreacted macroRAFT chains was still observed after the end of all the reactions.

As seen in the bibliographic review, the control of polymerization is not crucial for the sake of the REEP process and the success of encapsulation. Thus, the works continued under these conditions.

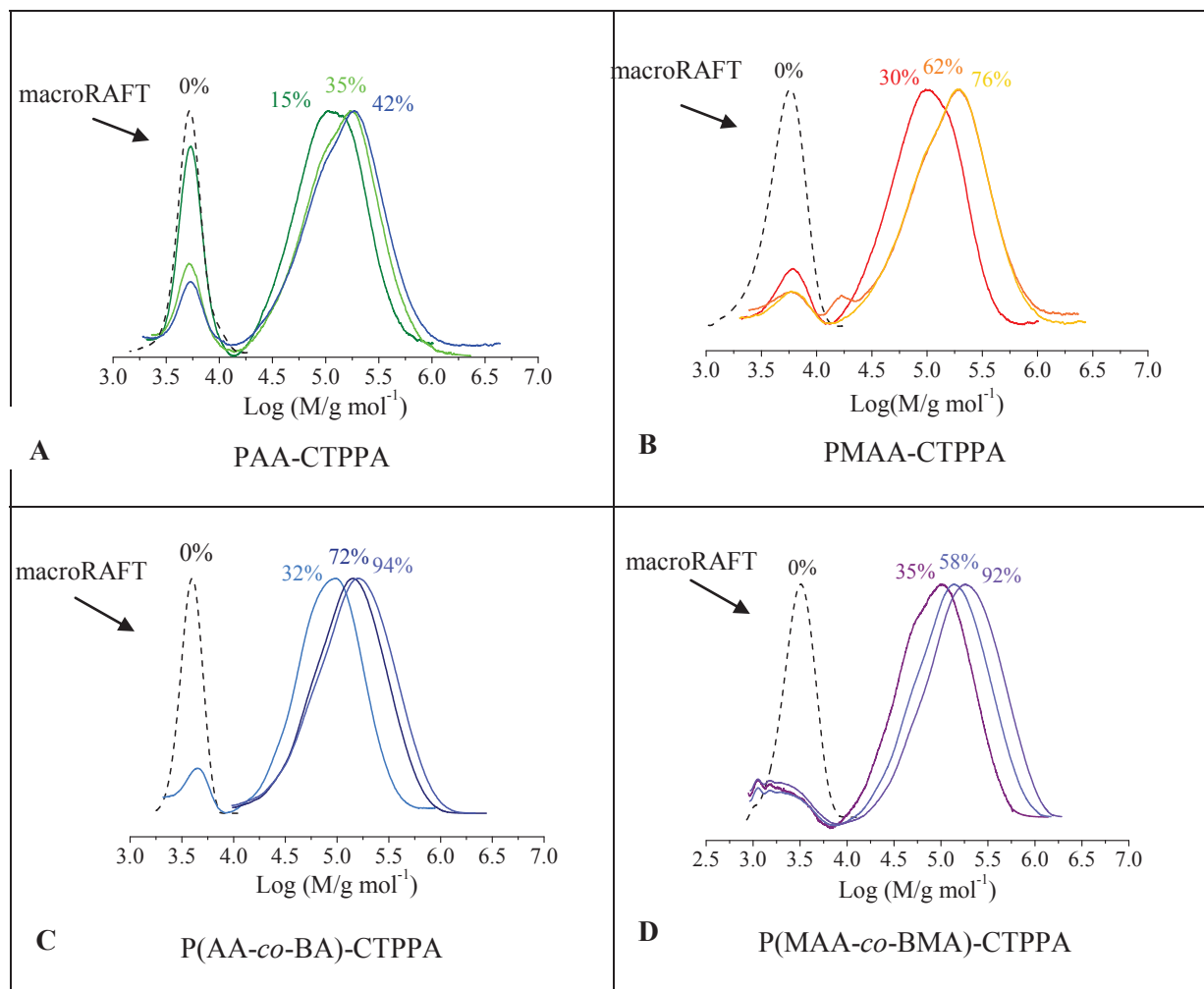


Figure 2. THF-SEC chromatogram evolution ($\log M$) versus conversion for the latexes obtained by the emulsion polymerization of MMA/BA (80/20 wt/wt) in presence of (A) PAA-CTPPA ($M_n = 3\,800\text{ g mol}^{-1}$), (B) PMAA-CTPPA ($M_n = 3\,800\text{ g mol}^{-1}$), (C) P(AA-co-BA)-CTPPA ($M_n = 3\,700\text{ g mol}^{-1}$) and (D) P(MAA-co-BMA)-CTPPA ($M_n = 2\,700\text{ g mol}^{-1}$).

A.2 Stability of the RAFT functionality of the acrylic acid-based macroRAFT copolymer with time at 80 °C and pH = 8.0

To be sure that the RAFT function would not suffer hydrolysis at the conditions employed during the interaction step and the polymerization (i.e. pH = 8.0 and 80 °C), the stability of the RAFT group from P(AA-*co*-BA)-CTPPA macroRAFT was determined. As **Figure 3** shows, no degradation was observed after several hours under these conditions.

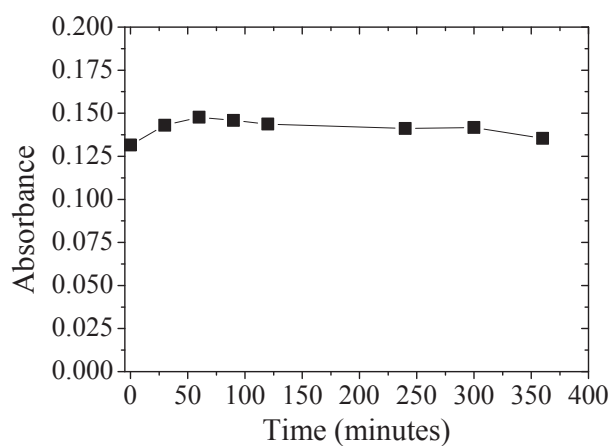


Figure 3. P(AA-*co*-BA)-CTPPA RAFT UV-vis absorbance with time in aqueous solution at pH 8.0 and 80 °C.

A.3 Effect of the interaction time on final hybrid latex morphology

To study the effect of time on the adsorption of macroRAFT onto the surface of Imogolite and consequently the effect on latex morphology, a suspension prepared under the same conditions as previously (2.0 g L^{-1} of Imogolite, 3.7 mmol L^{-1} of macroRAFT and $\text{pH} = 8.0$) was left aging for 36 days. After this period, the suspension was partially unstable. Before performing the polymerization, it was sonicated for 5 minutes at 30% amplitude, to better disperse the objects. **Table 1** summarizes polymerization conditions and results comparing this experiment with a conventionally prepared one.

Table 1. Polymerization conditions and results for the macroRAFT-assisted polymer-encapsulation of Imogolite under different interaction times (1 hour and 36 days).

Entry	Interaction time	D_h (nm) / PDI	X_{final} (%)	Stability
AC215	1 hour	25/0.15	40	√
AC241	36 days	70/0.09	40	√

MacroRAFT $M_n = 3\,500 \text{ g mol}^{-1}$; [MacroRAFT] = 3.7 mmol L^{-1} ; MacroRAFT solution $\text{pH} = 8.0$; [Imogolite] = 2.0 g L^{-1} ; Imogolite $\text{pH} = 6.0$; Pathway = MacroRAFT solution added dropwise to the Imogolite suspension. Monomers: 15wt% of MMA/BA (80/20 wt/wt) based on water.

Figure 4 compares the monomer conversion as a function of time for both experiments: the one submitted to 1 h of interaction and the one to 36 days of interaction. Both polymerizations achieved the same final conversion. However, the aged suspension when polymerized presented a lower polymerization rate then the fresh one.

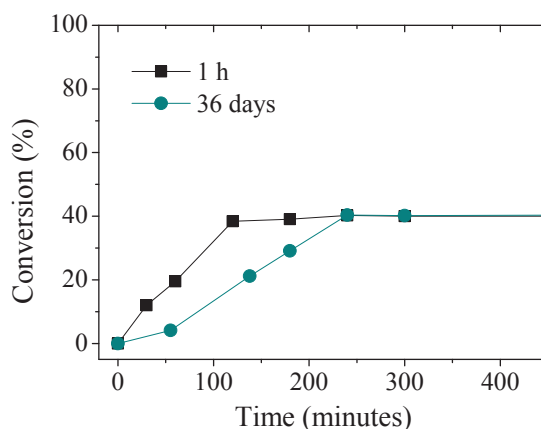


Figure 4. Monomer conversion versus time for the macroRAFT-assisted polymer-encapsulation of Imogolite in presence of 3.7 mmol L^{-1} of P(AA-co-BA)-CTPPA after 1h (■) and 36 days (●) of interaction.

In terms of morphology (**Figure 5**), both latexes presented polymer-decorated nanotubes. Free polymer particles were also present in both latexes.

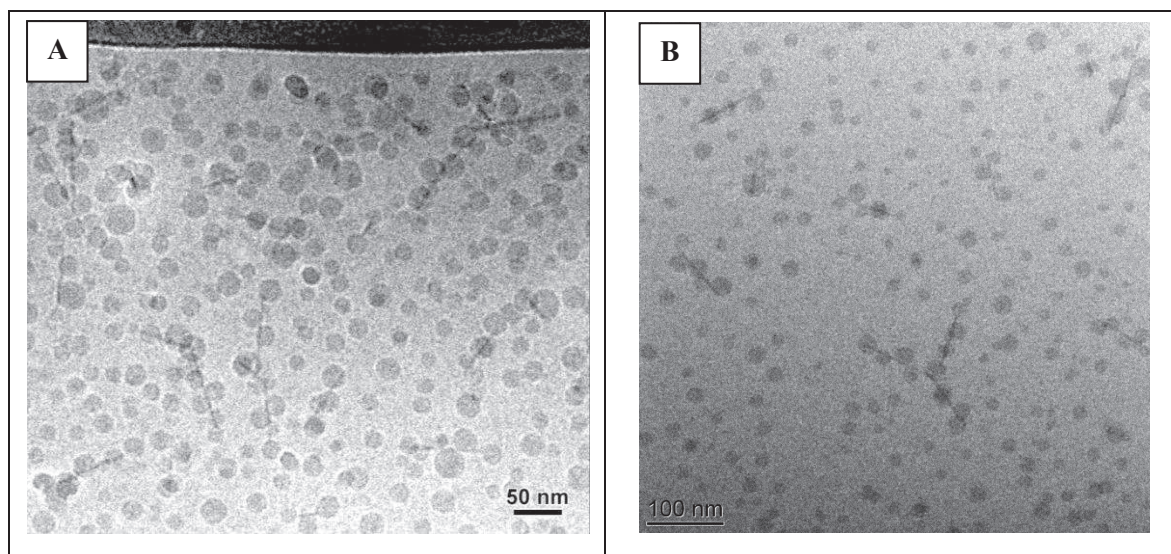


Figure 5. Cryo-TEM images of hybrid latexes synthesized via macroRAFT-assisted encapsulating emulsion polymerization using Imogolite nanotubes and 3.7 mmol L^{-1} of P(AA-co-BA)-CTPPA ($3\,500 \text{ g mol}^{-1}$) after (A) 1h and (B) 36 days of interaction time.

In conclusion, it was proven that the interaction time between macroRAFT and Imogolite does not influence the final morphology obtained.

A.4 SEC results of the polymerization of MA/BA (80/20 wt/wt) using P(AA-co-BA)-CTPPA macroRAFT at pH = 6.0

To verify the performance of our acrylic acid-based macroRAFT copolymer on controlling the polymerization of MA/BA mixture (80/20 wt/wt) in emulsion, a reference experiment was done in absence of nanotubes. The kinetics and SEC results are shown in **Figure 6**.

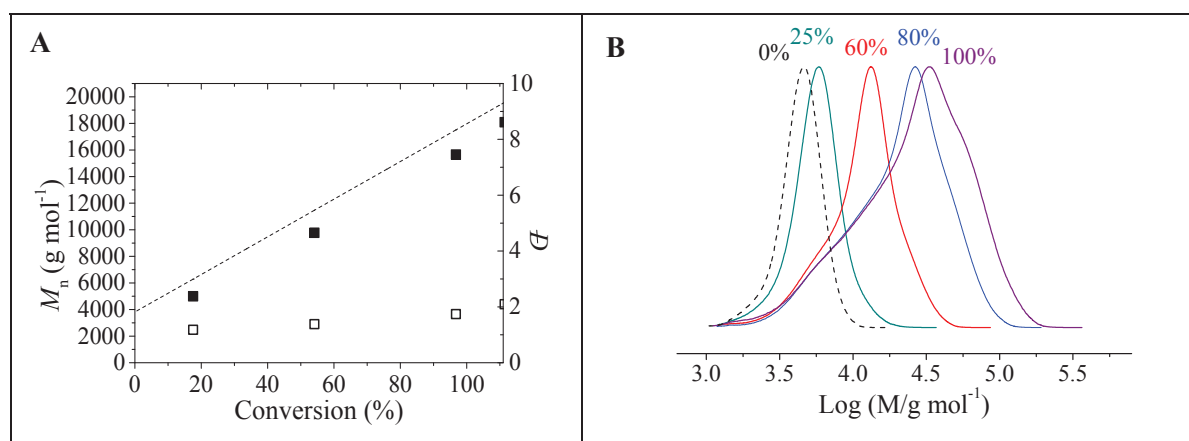


Figure 6. (A) Molar mass ($M_{n, \text{exp}}$) evolution and molar mass dispersity ($D = M_w/M_n$) versus conversion and (C) THF-SEC chromatograms.

It can be seen that as shown previously, our macroRAFT is not able to completely control the polymerization. Despite the linear increase of molar mass with conversion (**Figure 6 A**), a final number-average molar mass of $18,000 \text{ g mol}^{-1}$ and a dispersity of 2.1 were obtained, the second one being a quite wide molar mass distribution. In addition, asymmetric SEC chromatogram profiles can be observed in **Figure 6 B**, indicating the uneven growth of the polymer chains. The macroRAFT signal, also present in the peak corresponding to 100% of conversion, suggests that some of the macroRAFT agent chains did not participate entirely in the polymerization, resulting in a low molar mass polymer family. These low molar mass chains probably contributed to decrease the total number-average molar mass value, which explains the $M_{n, \text{exp}}$ being lower than the $M_{n, \text{theo}}$.

Résumé en français

Introduction générale.....	291
Chapitre I – Revue bibliographique	294
Chapitre II – Synthèse de latex hybrides polymère/nanotubes d’Imogolite.....	295
Chapitre III – Synthèse de latex hybrides polymère/nanofeuillets d’HDL	302
Conclusions générales et perspectives	306
References:	311

Introduction générale

Indubitablement, l'incorporation de particules inorganiques à des matrices polymères confère des propriétés très intéressantes aux matériaux. L'association de ces matériaux physiquement distincts permet la combinaison entre les meilleurs attributs de la partie inorganique, comme la rigidité, la résistance mécanique, inertie chimique, résistance thermal et propriétés optiques (transparence et opacité), avec les avantages de mise en œuvre et facilité de processabilité de la partie organique. Ce type de matériaux présentent un grand intérêt pour des diverses applications, comme dans les industries alimentaire, d'encre, de peintures, d'adhésives, de revêtement pour papier, de textiles, pharmaceutique et cosmétique.¹ Des développements récents ont aussi possibilité l'utilisation de ce type de matériaux dans des nouvelles technologies électroniques et photoniques.²

Les propriétés physiques des nanocomposites peuvent être d'avantage améliorées par l'orientation contrôlée des charges dans la matrice polymère.² L'assemblage unidimensionnel (1D) des particules inorganiques au sein de la matrice polymère est récemment devenu un sujet d'intense recherche, parallèlement au développement des nouvelles stratégies de synthèse de nanocomposites contenant des particules anisotropes polymère/inorganique.

Diverses stratégies de synthèse des nanocomposites colloïdes ont été reportées, y compris l'heterocoagulation, la technique d'assemblage layer-by-layer, et la polymérisation *in situ*.^{3,4} Entre les diverses méthodes existant, la polymérisation en émulsion suscite un grand intérêt grâce à sa vaste application industriel pour la production de divers produits (ex. peintures, adhésives, modificateurs d'impact), et a été particulièrement bien étudiée.¹

Une de plus grandes contributions des chimistes de synthèse pour le domaine de la chimie de polymères a été le développement de la polymérisation radicalaire contrôlée/vivante (c.à.d. CRP). Cette technique permet la préparation de polymères fonctionnels bien définis.⁵ L'application de la CRP en milieux aqueux dispersé, particulièrement en émulsion, a ouvert des nouvelles possibilités pour l'utilisation de cette technique pour l'élaboration de matériaux colloïdes fonctionnels.⁵⁻⁷

La polymérisation par transfert réversible de chaînes par addition-fragmentation (RAFT) est considéré un des méthodes de CRP le plus versatiles. Il a l'avantage de d'être capable de polymériser une vaste gamme de monomères à température douce en milieu aqueux dispersé. Le procédé RAFT permet également la préparation de polymères contenant une distribution étroite de masses molaires et des architectures contrôlée/avancées. Un autre avantage de cette technique est la possibilité de formation des architectures qui peuvent être facilement désassemblé par l'enlèvement du groupe dithioester labile.⁷ Ces caractéristiques font de la polymérisation RAFT un outil très intéressant pour l'élaboration de nanocomposites colloïdaux fonctionnels de polymère/inorganique.⁸

Récemment, une nouvelle stratégie basée sur la technique RAFT en émulsion a été développée pour produire des nanocomposites colloïdaux. Le procédé consiste à utiliser des copolymères hydrophiles vivants obtenus par RAFT (nommés macroRAFT) comme agents de couplage et stabilisants pendant la polymérisation des monomères hydrophobes en présence de particules inorganiques. La croissance ordonnée des chaînes de polymère résulte dans la formation d'une couche uniforme de polymère autour des particules inorganiques en les encapsulant. Ce procédé permet ainsi l'obtention de latex hybrides sans addition de petites molécules stabilisantes, conventionnellement additionnées (tensioactif). L'encapsulation de pigments^{9, 10}, de plaquettes de Gibbsite¹¹, de l'oxyde de cérium¹² et de nanotubes de carbone^{13, 14} ont été reportés.

Dans ce travail nous allons explorer l'utilisation de cette technique, définie comme « macroRAFT-assisted encapsulating emulsion polymerization » (REEP), pour produire des hybrides colloïdaux de polymère/nanotube d'aluminogermanate (Ge-Imogolite) et de polymère/hydroxides double lamellaire (HDL). Le procédé utilisé dans ce travail utilise des agents macroRAFT hydrosoluble contenant des unités acide acrylique (AA). Ces agents RAFT ont été conçus de manière à être capables d'interagir avec les charges positives provenant des groupes hydroxyles à la surface des Imogolites et les nombreux groupes hydroxyles présents à la fois à la surface et aux domaines interlamellaires des HDL. En faisant varier la solubilité de l'agent macroRAFT dans l'eau, des suspensions de macroRAFT/particules inorganiques de différentes morphologies ont été obtenues. Ces suspensions ont ensuite participé à la polymérisation d'un mélange de monomères hydrophobes en émulsion, générant des latex hybrides de morphologie anisotrope contrôlée.

Ce manuscrit est divisé en trois chapitres.

Le **chapitre I** présente une révision bibliographique sur les différentes stratégies utilisées pour aligner les charges inorganiques au sein de matrices polymères ainsi que les diverses techniques d'incorporation de particules anisotropes dans des nanocomposites. L'application de techniques basées sur la polymérisation radicalaire contrôlée pour produire des nanoparticules hybrides polymère/nanoparticules inorganiques anisotropes est aussi révisée.

Le **chapitre II** est focalisé sur la synthèse de latex hybrides polymère/Imogolite. L'étude de l'influence de divers paramètres sur la morphologie finale et les propriétés des films est aussi présentée. Tout d'abord, une partie bibliographique portant sur les caractéristiques de nanotubes d'Imogolite et leurs applications pour la production de matériaux polymère/Imogolite est donnée. La partie expérimentale présente ensuite l'effet des différents paramètres, comme la nature, la masse molaire et la concentration du macroRAFT, la concentration en Imogolite et la longueur de tubes, le pH du milieu, et les voies de mélange et d'interaction, sur la morphologie finale de latex. Enfin, l'effet

de la composition du monomère hydrophobe a été étudié visant la production de latex filmifiants, dont les microstructures et les propriétés mécaniques ont été évaluées par la suite.

Le chapitre III présente la synthèse des hybrides polymère/HDL en milieu aqueux. Premièrement, la synthèse des HDL colloïdaux a été optimisée. Ensuite, la modification de ces phases HDL avec des agents RAFT et macroRAFT a été étudiée par deux voies : échange anionique et coprécipitation hybride *in situ*. Dans un premier temps, la stratégie de *grafting from* d'un monomère hydrosoluble (4-acryloylmorpholine, NAM) a été tentée à partir de phases HDL/RAFT bien définies ; le but étant de former une couche de polymère soluble (couronne) autour des HDL. Enfin, à partir des phases HDL bien définies contenant de l'agent macroRAFT adsorbé/intercalé, la technique REEP a été employée. Cette voie a généré des nanofeuillets d'HDL bien dispersés et individuellement encapsulés.

Enfin, les conclusions générales ainsi que quelques perspectives de futurs travaux sont présentées à la fin du manuscrit.

Chapitre I – Revue bibliographique

Il a été montré dans la revue bibliographique que l'alignement de particules inorganiques au sein d'une matrice polymère peut apporter des propriétés mécaniques, optiques et électroniques intéressantes pour les matériaux.

Les différentes techniques utilisées pour aligner les charges inorganiques dans la matrice ont été décrites. Une attention particulière a été donnée aux exemples d'incorporation de particules inorganiques anisotropes, surtout ceux qui utilisaient des procédés de polymérisation radicalaire contrôlée en milieu aqueux.

Des exemples de production de particules hybrides du type cœur/couronne par les techniques de *grafting from* et *grafting to* ont été décrits. La production de particules hybrides du type cœur/écorce a été illustrée par les techniques de co-assemblage de copolymères à blocs amphiphiles en présence de particules inorganiques et par « macroRAFT-assisted encapsulating emulsion polymerization » (REEP).

Chapitre II – Synthèse de latex hybrides polymère/nanotubes d’Imogolite

Nanotubes d’Imogolite utilisés dans cette thèse

Les études d’encapsulation de nanotubes ont été conduites avec des Imogolites du type aluminogermanate. Quatre lots d’Imogolite ont été utilisés, avec des tubes de différentes longueurs (75 nm, 200 nm et 500 nm) et des parois de différents types (simple-paroi, SW, ou double-paroi, DW). Le Tableau 1 présente les principales caractéristiques de chaque lot.

Tableau 1. Caractéristiques générales des différents lots de Ge-Imogolite utilisés dans cette thèse.

Lot	Ø_{ext}^a	L^a Moyenne (nm)	[Imogolite] (g L ⁻¹)	pH	Type
C1p55	3.7	75	23	6	SW
MA1p40	2	35 ^b	9.6	6.1	SW
C13p105	4.2	200	9.2	6.0	DW
EP1p37	4.4	500	6.5	5.9	DW

^a Calculé à partir de la modélisation du résultat SAXS. ^b Lot avec grande concentration de proto-Imogolite.

Synthèse des agents macroRAFT

Quatre différents macroRAFT ont été synthétisés afin d’être utilisés pour la synthèse de latex hybrides polymère/Imogolite et polymère/HDL. Deux familles de polymère ont été choisies, une à base de monomères méthacryliques, et l’autre à base de monomères acryliques. Les macroRAFT suivants ont été synthétisés : PAA-CTPPA, PMAA-CTPPA, P(AA-co-BA)-CTPPA et P(MAA-co-BMA)-CTPPA. Les polymérisations ont été menées en solution dans le 1,4-dioxane à 80 °C. Un bon contrôle de la polymérisation a été obtenu pour chacune des expériences les synthèses, donnant des polymères avec des masses molaires contrôlées et une distribution étroite de masses molaires dans tous les cas.

Résultats préliminaire d’encapsulation de nanotubes d’Imogolite

Les quatre macroRAFT synthétisés ont été évalués par rapport à leurs efficacités d’encapsulation en suivant la technique REEP. Parallèlement aux études d’encapsulation, les macroRAFT ont aussi été utilisés pour la polymérisation du même mélange de monomères hydrophobes en absence de nanotubes. Des résultats cinétiques similaires ont été trouvés pour les polymérisations menées en absence ou en présence de nanotubes. Ce comportement cinétique très proche a été attribué à un même mécanisme de nucléation. Vraisemblablement, la polymérisation commence dans la phase aqueuse, avec les chaînes de macroRAFT qui sont présentes dans l’eau. Ces chaînes additionnent progressivement des unités de monomère hydrophobe, jusqu’à devenir insoluble dans l’eau. Ces chaînes de copolymère à blocs amphiphiles, qui à ce point ne sont plus solubles dans l’eau, s’auto-assemblent pour former les premières particules, où la polymérisation aura dorénavant lieu. En

présence d'Imogolite, les copolymères à blocs amphiphiles qui se forment ont deux options : soit s'auto-assembler dans l'eau pour former une nouvelle particule, soit s'assembler aux chaînes en croissance à la surface, pour continuer la polymérisation à la surface des nanotubes. Les deux événements ont lieu simultanément. En comparant les résultats obtenus avec les quatre différents macroRAFT, il semble avoir eu un meilleur contrôle lorsque les macroRAFT méthacryliques ont été utilisés. Cependant, l'emploi de l'homopolymère méthacrylique n'a pas conduit à la consommation complète des monomères, et le copolymère méthacrylique n'a pas pu stabiliser le système, conduisant à la coagulation du latex. La Figure 1 montre les résultats de TEM obtenus pour les latex hybrides synthétisés en présence des quatre différents macroRAFTs. En raison de ces résultats, les études suivantes ont été menées avec la famille de macroRAFTs acryliques.

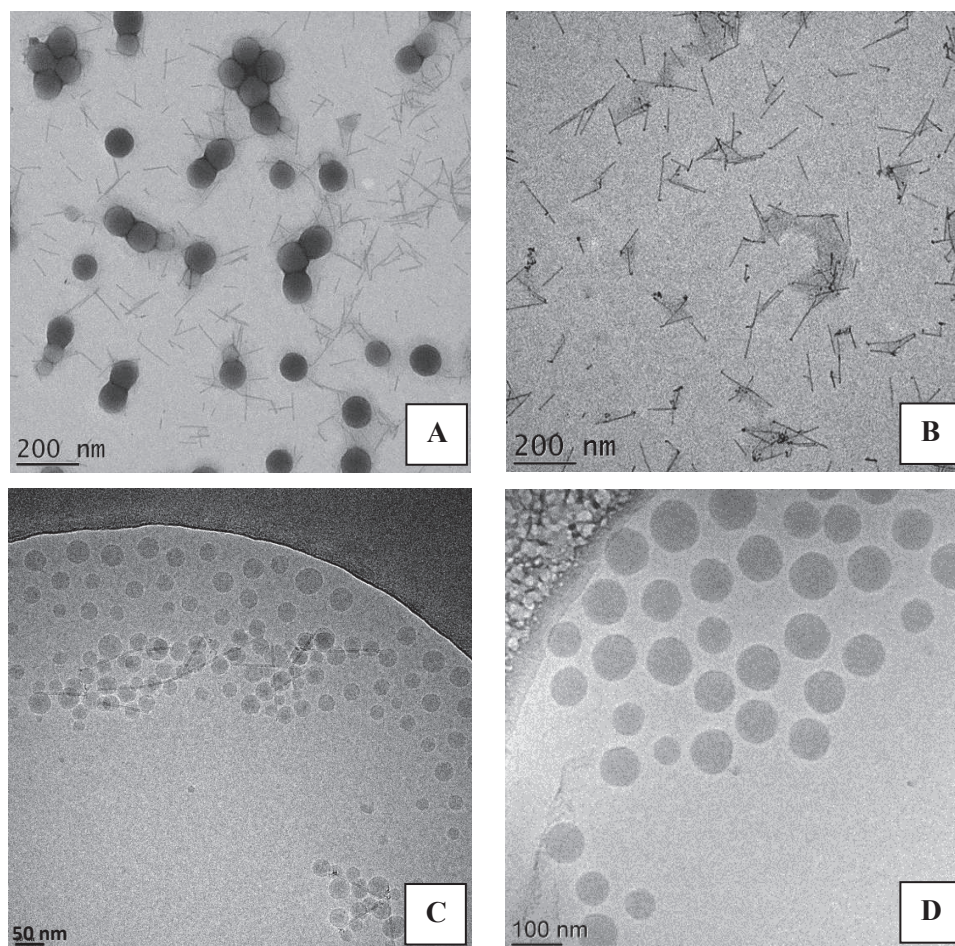


Figure 1. Images TEM (a, b) et cryo TEM (c, d) de latex hybrides Imogolite/P(MMA-co-BA) synthétisés par REEP en utilisant (a) PAA-CTPPA; (b) PMAA-CTPPA; (c) P(AA-co-BA)-CTPPA et (d) P(MAA-co-BMA)-CTPPA.

Adsorption de macroRAFTs acryliques à la surface de l'Imogolite

L'adsorption de deux macroRAFT de la famille des acryliques à la surface de nanotubes d'Imogolite a été étudiée. Le macroRAFT PAA-CTPPA de 3500 g mol^{-1} et le macroRAFT P(AA-co-BA)-CTPPA de 3500 g mol^{-1} et 1100 g mol^{-1} ont été évalués.

L'adsorption de l'homopolymère a été comparée à celle du copolymère sous les mêmes conditions (même masse molaire (3500 g mol^{-1}) et même pH (8.0)). Le copolymère a présenté une adsorption significativement supérieure à celle de l'homopolymère, ce qui a été attribué à la présence des unités BA dans la chaîne. Ces unités confèrent au copolymère un caractère plus hydrophobe, diminuant son affinité avec l'eau et favorisant son adsorption à la surface inorganique. En comparant les résultats obtenus avec les copolymères de masses molaires différentes, il a été montré que celui avec la plus grande masse molaire s'adsorbait plus fortement à la surface. Ces résultats sont en accord avec ce qui est trouvé dans la littérature sur l'adsorption de polymères du type polyélectrolytes à des surfaces inorganiques. Ensuite, le copolymère de 3500 g mol^{-1} a été adsorbé sous deux pH différents, 8,0 et 6,0. Il a été trouvé qu'en diminuant le pH, l'adsorption augmentait. Cet effet a été attribué à la fois au caractère plus hydrophobe du copolymère à pH acide, ce qui diminue sa solubilité dans l'eau, et à la diminution de l'effet de répulsion entre les chaînes. Ces deux facteurs contribuent à une plus forte adsorption. La Figure 2 représente schématiquement l'adsorption du macroRAFT à la surface de nanotubes d'Imogolites sous les différentes conditions étudiées.

Cependant, les conditions qui ont mené à une adsorption plus importante étaient également les conditions dans lesquelles le macroRAFT était moins chargé. C'est pourquoi dans ces conditions des agrégats d'Imogolite ont été formés. Un passage aux ultrasons de 5 minutes a été nécessaire pour rendre la suspension stable.

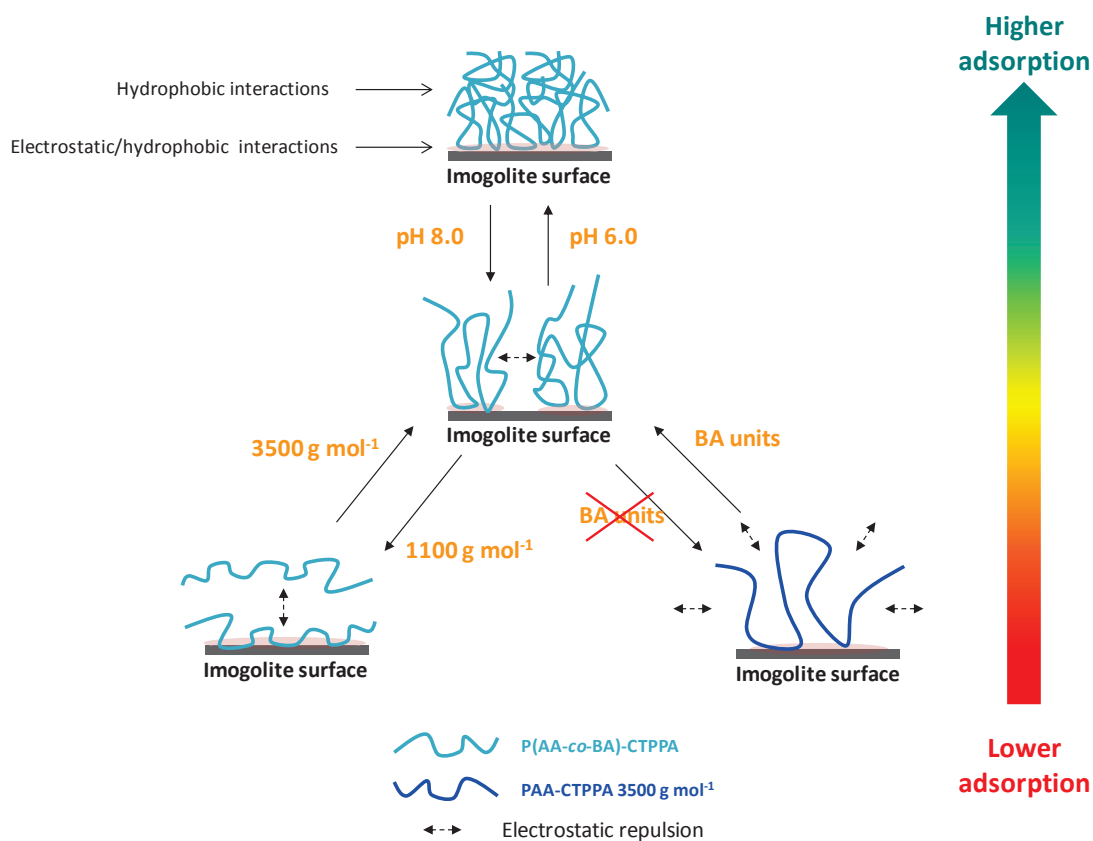


Figure 2. Illustration de l'adsorption du macroRAFT à la surface de nanotubes selon les différentes conditions.

Encapsulation de nanotubes d'Imogolite par REEP

Les études d'encapsulation ont été menées avec le macroRAFT copolymère de la famille des acryliques, en raison des résultats préliminaires et des résultats d'adsorption obtenus précédemment. Différents paramètres ont été étudiés, comme la masse molaire et la concentration en agent macroRAFT, la concentration en Imogolite, et le pH du milieu. Le macroRAFT de faible masse molaire n'a pas pu assurer une stabilité suffisante au système, et des latex instables ont été formés. Pour les polymérisations réalisées à pH 8,0, des nanotubes d'Imogolite décorés avec des particules de polymères ont été obtenus quelque soit la concentration d'agent macroRAFT 3500 g mol⁻¹ et d'Imogolite utilisés. L'effet de ces deux paramètres s'est montré être surtout lié au nombre et à la taille de particules de latex libres. L'augmentation de la concentration en macroRAFT résulte surtout dans la formation d'un plus grand nombre de particules de latex libres. En augmentant la concentration en Imogolite, le nombre de particules libres a pu être diminué, grâce à la diminution de la concentration de macroRAFT libre dans la phase aqueuse.

En diminuant le pH du milieu, des agrégats d'Imogolite/macroRAFT ont été formés, comme démontré par les études d'adsorption. Par contre, après polymérisation du monomère hydrophobe, ces agrégats ont été trouvés encapsulés au sein de particules de polymère. Le succès de l'encapsulation peut être

expliqué par l'association de plusieurs facteurs. La quantité de macroRAFT adsorbé étant supérieur, un plus grand nombre de fonctionnalité RAFT par particule est obtenu, ce qui contribue à la croissance d'une couche de polymère plus uniforme autour des tubes. De plus, la mouillabilité des tubes est améliorée grâce à la présence d'un plus grand nombre de chaînes de copolymère à la surface. Ainsi, l'affinité des objets avec le monomère hydrophobe est également promue, ce qui favorise la coalescence des nodules formés à la surface et par conséquent, l'encapsulation.

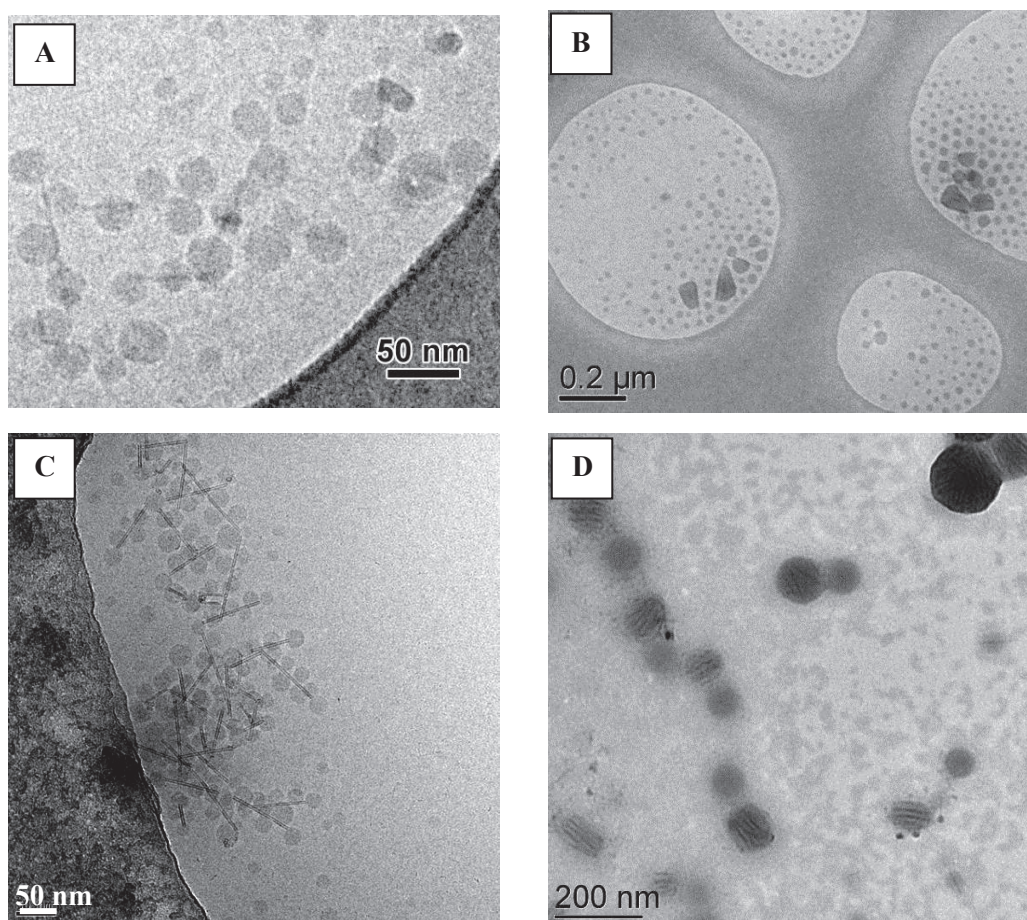


Figure 3. Images cryo-TEM (a, b and c) et TEM conventionnelle à basse température (d) des latex hybrides contenant 2.0 g L^{-1} d'Imogolite et 3.7 mmol L^{-1} de macroRAFT à (a) pH 8.0 et (b) 6.0, et contenant 8.0 g L^{-1} d'Imogolite et 12 mmol L^{-1} de macroRAFT à (c) pH 8.0 et (d) pH 6.0.

La Figure 3 montre les morphologies obtenues à pH 8,0 et 6,0 pour deux concentrations en Imogolite et macroRAFT. La figure montre que la morphologie hybride polymère/Imogolite est la même pour les deux concentrations testées, seulement le nombre de particules libres diminue.

Visant à diminuer la taille des agrégats formés à pH 6,0, et dans la tentative de réussir la mono-encapsulation (i.e. l'encapsulation de tubes individuels), nous avons joué sur le procédé de mélange et d'interaction du macroRAFT avec l'Imogolite. Similairement à ce qui a été fait et reporté dans la littérature concernant l'adsorption de polyélectrolytes sur des surfaces inorganiques, nous avons étudié différentes voies de mélange et d'interaction.

Les différentes voies de mélange peuvent varier en termes de vitesse d'ajout, d'ordre d'ajout et utilisation de l'ultrason ou non. Les premières expériences ont été réalisées en ajoutant la solution de macroRAFT goutte à goutte à la suspension d'Imogolite sous agitation. Suivant ce procédé, lorsque le macroRAFT est ajouté, sa concentration augmente peu à peu jusqu'à atteindre la concentration désirée. Cependant, pendant cette augmentation graduelle, le système traverse la zone de neutralisation de charges, quand la concentration en fonction carboxylique est égale à la concentration en fonction OH_2^+ de la surface. Dans cette zone, des agrégats peuvent être formés. En augmentant davantage la concentration en macroRAFT, ces agrégats peuvent être défaits par l'excès de charges quand le macroRAFT est suffisamment chargé (i.e. à pH 8.0). Par contre, si le macroRAFT n'est pas assez chargé, comme à pH 6.0, ces agrégats ne sont pas défaits. En inversant l'ordre d'ajout, la concentration est diminuée petit à petit au lieu d'être augmentée. De cette manière, le système ne traverse pas le point de neutralisation de charges, évitant ainsi la formation d'agrégats. En inversant l'ordre d'ajout, des agrégats de taille inférieure ont pu être obtenus. Par contre, la formation d'agrégats n'a pas pu être complètement inhibée, probablement à cause de la faible densité de charges du macroRAFT à pH 6,0, qui le rend plus hydrophobe.

Les différentes voies d'interaction reposent sur « l'activation/désactivation » des interactions entre le macroRAFT et la surface. Dans le cas des polyélectrolytes, les interactions sont électrostatiques. Par conséquent, elles peuvent être « désactivées » par exemple par ajout de sel. Les deux éléments, PE et NPs, sont ensuite mélangés, mais aucune interaction ne se produit. Par la suite, une désalinisation lente a lieu, ce qui active les interactions de manière contrôlée. Cette méthode est très efficace pour contrôler la taille des agrégats formés à partir de nanoparticules et PE. Cependant, dans le présent travail, les interactions entre le macroRAFT et les nanotubes d'Imogolite ne sont pas seulement de nature électrostatique, mais ils comprennent aussi des interactions hydrophobes. Une méthode analogue à la désalinisation a été envisagée. La suspension d'Imogolite a été mélangée avec une solution de macroRAFT à pH 8,0, dans des conditions où les agrégats ne sont pas formés. Ensuite, le pH du milieu a été baissé pour induire une formation d'agrégats de manière contrôlée, soit par l'addition d'acide, soit par dialyse du système. Ces deux stratégies ont effectivement évité la formation de gros agrégats. Cependant, les tubes individuels n'étaient pas encapsulés après la polymérisation. Des nanotubes décorés de particules de latex, des particules janus, quelques agrégats encapsulés et quelques fibres de polymère ont été formés. La diversité des morphologies a été attribuée à l'état transitoire du système après l'ajout de sel ou la dialyse. Il semblerait que les conditions utilisées n'étaient pas suffisantes pour « désactiver » complètement les interactions, et pour promouvoir l'encapsulation.

Synthèse de latex hybrides polymère/Imogolite filmifiables

Afin de former des latex hybrides capables de former des films, la composition du mélange de monomères hydrophobes a été variée. Quatre nouvelles compositions ont été testées : STY/BA (70/30 wt%) et (50/50 wt%) ; MMA/BA (50/50 wt%) et MA/BA (80/20 wt%). Ces compositions ont été polymérisées à deux pH (8,0 et 6,0), afin de former des nanotubes décorés avec des particules de latex et des agrégats d'Imogolite encapsulés.

Les latex synthétisés avec les mélanges contenant du styrène ont tous présentés des agrégats d'Imogolite encapsulés, quel que soit le pH -. Ces observations ont appuyé le fait que la nature et l'affinité du monomère hydrophobe par la surface jouent également un rôle important dans la morphologie final. Ces latex contenant du styrène ont aussi présenté des fibres et des vésicules coexistant avec les particules polymère/Imogolite.

Les latex synthétisés avec le mélange MMA/BA à 50/50 wt% ont aussi présenté des fibres et des vésicules en plus des morphologies attendues : nanotubes décorés et agrégats encapsulés, à pH 8,0 et 6,0, respectivement. La formation de ces morphologies du type fibres et vésicules a été attribué aux changements subis par le copolymère à blocs amphiphile formé pendant la polymérisation. En changeant la composition du bloc hydrophobe, la nature chimique du copolymère, la fraction chimique de chacun de ses composants et son hydrophilie ont été modifiés, ce qui a conduit à la formation de fibres et vésicules.

Pour éviter la formation de fibres et vésicules tout en conservant une composition filmifiable, le monomère MMA a été remplacé par de l'acrylate de méthyle (MA). Ces deux monomères possèdent une solubilité similaire, mais le second présente une T_g inférieure. Enfin, les latex synthétisés avec un mélange MA/BA (80/20 wt%) ont pu générer des nanotubes décorés de particules de latex à pH 8,0 et des agrégats de nanotubes encapsulés à pH 6,0, en formant seulement des sphères en phase aqueuse. La T_g finale du copolymère formé, calculé par la loi de Fox, était de $-10\text{ }^\circ\text{C}$, et des films ont pu facilement être formés par simple évaporation de l'eau (Figure 4).

Des latex contenant des nanotubes de différentes longueurs ont été synthétisés afin d'évaluer l'effet de ce paramètre dans la microstructure et dans les propriétés mécaniques des films. Concernant la microstructure, il a été montré que les tubes de longueur moyenne 500 nm ont présenté une orientation ordonnée partielle dans la matrice, parallèle au plan du film. Cet alignement spontané résulte du facteur de forme important des tubes, qui favorise leur organisation parallèle entre un tube et l'autre.

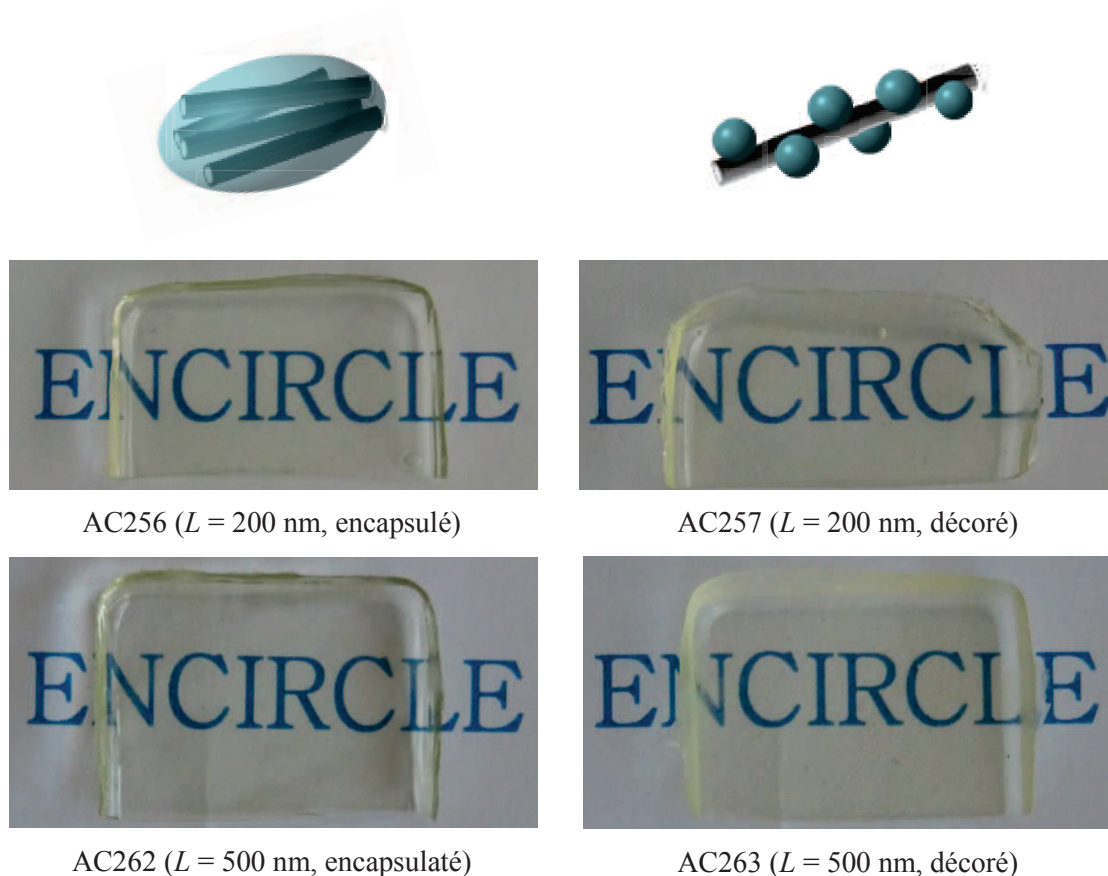


Figure 4. Films hybrides formés à partir de latex de différentes morphologies polymère/Imogolite et avec des nanotubes de différentes longueurs.

Les propriétés mécaniques des films hybrides ont montré un renforcement mécanique de la matrice polymère quand la formation d'un réseau percolant était favorisée. Les échantillons contenant des agrégats d'Imogolite encapsulés ont présenté le même comportement thermomécanique que la matrice. La couche de polymère autour des agrégats a vraisemblablement empêché le contact entre les tubes, inhibant la percolation et le transfert d'énergie entre les tubes.

Chapitre III – Synthèse de latex hybrides polymère/nanofeuillets d'HDL

Synthèse de plaquettes d'HDL colloïdales

Différentes conditions de synthèse ont été évaluées pour la formation de plaquettes colloïdales d'HDL. Les conditions de coprécipitation, comme l'ajout continu ou l'ajout rapide des solutions de sel métallique, à température ambiante ou à 0 °C, avec un procédé hydrothermal ou solvothermal ont été étudié. Les meilleurs résultats en termes de taille, cristallinité et stabilité de la suspension ont été obtenus avec un ajout rapide de solution de sel, à température ambiante soit par les deux procédés de traitement thermal. Pour avoir des ions CO_3^{2-} dans le domaine interlamellaire, le procédé hydrothermal s'est montré plus efficace. Pour avoir des ions NO_3^- , le traitement solvothermal était plus adapté.

Modification des HDL avec de l'agent RAFT ou macroRAFT

Les agents RAFT ou macroRAFT ont été intercalés dans les espaces interlamellaires des HDL afin d'utiliser les phases hybrides résultantes soit dans une polymérisation *grafting from*, soit par REEP. L'objectif dans un cas était de produire des particules cœur/couronne, en polymérisant un monomère hydrosoluble à partir de la surface par *grafting from*. Et dans l'autre cas, la méthode REEP nous permet d'encapsuler les particules inorganiques en polymérisant un monomère hydrophobe à partir du macroRAFT, formant ainsi des particules cœur/écorce.

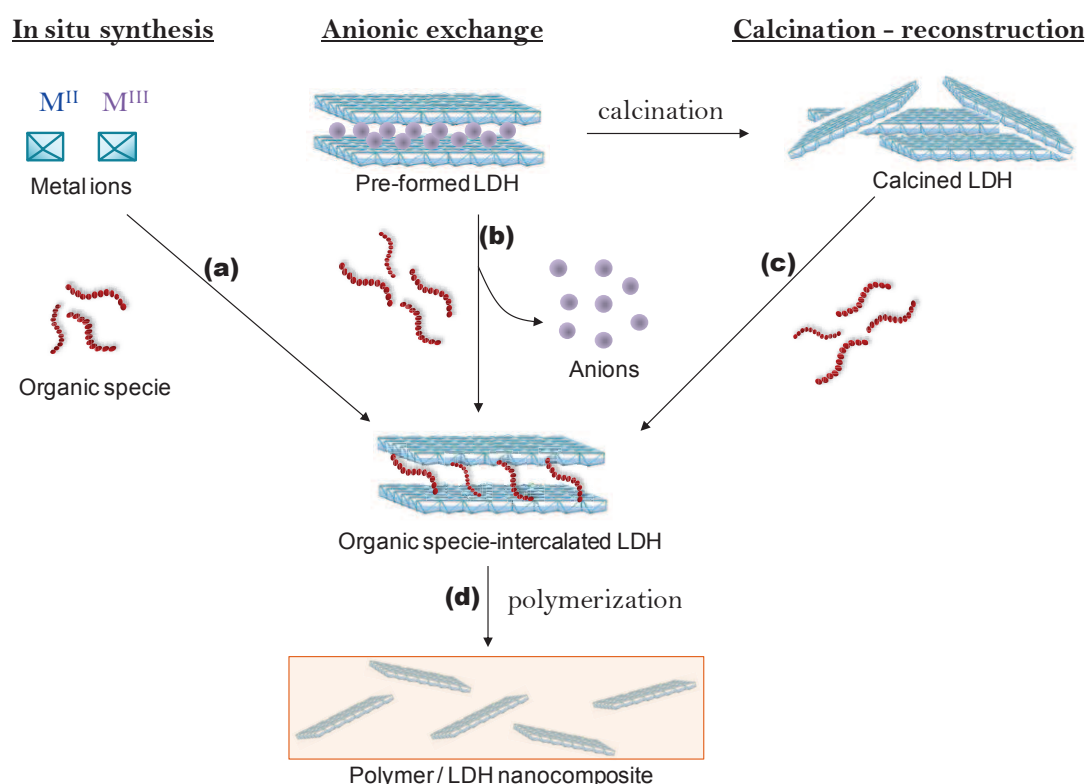


Figure 5. Différentes voies de modification d'HDL avec des composés organiques. (a) synthèse in situ des HDL en présence des espèces organiques, (b) échange anionique, (c) calcination et reconstruction des structures lamellaires en présence des espèces organiques et (d) production de nanocomposites à partir de la polymérisation en présence des phases HDL modifiés.

Deux stratégies de modification ont été étudiées (voies (a) et (b), Figure 5). La première méthode consistait dans un procédé d'échange anionique, réalisé avec des phases HDL conventionnelles ou colloïdales. Les HDL conventionnels ont été intercalé avec de l'agent RAFT et de l'agent macroRAFT. Ces phases, synthétisées par coprécipitation, présentaient une taille de particules élevées, et par conséquent, une stabilité réduite dans l'eau. Malgré le succès de l'échange anionique, ces phases non pas pu être utilisées en raison de leur faible stabilité. Ensuite, l'agent macroRAFT a été intercalé dans les phases colloïdales. Deux types de phases HDL colloïdales ont été utilisés, une contenant des ions NO_3^- et l'autre contenant des ions CO_3^{2-} dans les domaines interlamellaires. Les HDL- NO_3^- ont formé des phases HDL/macroRAFT contenant le macroRAFT adsorbé et intercalé, et les anions NO_3^-

ont pu être effectivement échangés par des molécules de macroRAFT. Cependant, les HDL-CO₃²⁻ ont formés des phases contenant le macroRAFT exclusivement adsorbé, ce qui a été attribué à l'échange limité des anions CO₃²⁻. Ces phases ont conservé leur aspect colloïdal même après échange, présentant une bonne stabilité dans l'eau.

La deuxième méthode était la synthèse *in situ* des HDL par coprecipitation hybride en présence des agents RAFT et macroRAFT. Par cette méthode, des HDL-RAFT cristallins, contenant les molécules d'agent RAFT bien ordonnées dans l'interfeuillet ont été obtenus. Il a été aussi montré que l'agent RAFT s'est intercalé en double couche entre les feuillets. Le taux d'agent RAFT, déterminé par ATG, a été de 44 % en masse. Ces phases étaient stables dans l'eau pour une courte durée de temps, étant cependant redispersable sous agitation. En présence des agents macroRAFT, les HDL n'ont pas pu être bien formés. Des phases amorphes, et en très faible quantité ont été formées. Cela a été attribué au grand nombre de groupes acide carboxylique présent dans les longues chaînes de macroRAFT, qui peuvent se complexer avec les ions métalliques et défavoriser la formation des structures cristallines bien définies.

Des phases HDL-RAFT et HDL/macroRAFT stables dans l'eau et bien définies ont été obtenues par coprecipitation hybride *in situ* et par échange anionique à partir des phases colloïdales, respectivement. Les HDL-RAFT ont été par la suite employés dans le procédé *grafting from*, tandis que les phases HDL/macroRAFT ont été encapsulées par REEP.

***Grafting from* d'un polymère soluble à la surface des HDL**

A partir des fonctions RAFT présentes dans les domaines interlamellaires des HDL, le monomère hydrosoluble *N*-acryloylmorpholine (NAM) a été polymérisé en solution dans l'eau. Pour éviter l'échange entre les molécules d'agent RAFT et l'amorceur anionique ACPA, un amorceur cationique a été utilisé (AIBA). En raison de l'instabilité des phases hybrides avec le temps, les plaquettes d'HDL ont été retrouvées précipitées à la fin de la polymérisation. Malgré la faible distribution de masses molaires, ce qui suggère un bon contrôle de la polymérisation, les masses molaires expérimentales étaient assez éloignées des valeurs théoriques attendues. De ce fait, il a été conclu que la quantité d'agent RAFT participant à la polymérisation n'était pas égale à la quantité d'agent RAFT présent dans l'échantillon. De plus, les analyses DRX et IR ont révélé une augmentation de l'espace interlamellaire, après ajout du monomère et avant le début de la polymérisation, suivi par une diminution irréversible de la distance interfeuillets. Ces deux changements ont été attribués au gonflement des phases par le monomère, et à l'échange entre les oligomères et des anions CO₃²⁻ en début de polymérisation. Vraisemblablement, la fonction acide carboxylique présente dans l'extrémité de chaîne n'a pas été suffisante pour maintenir le polymère accroché aux feuillets, ce qui a conduit à la

migration du polymère vers la solution. De ce fait, en fin de polymérisation les phases HDL-CO₃²⁻ ont précipités laissant le polymère en solution.

Encapsulation de plaquettes d'HDL par REEP

Les plaquettes HDL contenant le macroRAFT intercalé et/ou adsorbé (i.e. HDL-NO₃⁻ ou HDL-CO₃²⁻) ont été utilisés dans la polymérisation d'un mélange de monomères hydrophobes composé de MA/BA (80/20 % en masse) par REEP. Les polymérisations ont été menées à 70 °C, à pH 8,0 en utilisant l'AIBA comme amorceur. L'effet de différentes concentrations en macroRAFT sur la morphologie finale de latex hybrides a été étudié pour les deux types d'HDL : CO₃²⁻ et NO₃⁻. Il a été démontré que quel que soit la concentration en macroRAFT, les plaquettes d'HDL ont été trouvées encapsulées en fin de polymérisation. Cependant, des conversions limitées ont été obtenues, surtout pour les synthèses réalisées à une faible concentration en macroRAFT.

Les deux types d'HDL ont été encapsulés par cette méthode, mais les phases contenant du macroRAFT intercalé ont montré une tendance à former des agrégats. L'interaction des fonctions acide carboxylique avec les groupes hydroxyles des espaces interlamellaires réduit le nombre de charges négatives disponibles à la stabilisation du système, ce qui conduit à la formation des agrégats. L'introduction d'une étape de sonication avant polymérisation a pu éviter la formation des agrégats, et des plaquettes individuellement encapsulés ont été retrouvées. La conversion finale de monomère a pu être améliorée en remplaçant l'amorceur AIBA, sensible à l'hydrolyse à des pH élevés, par de l'ADIBA, également cationique mais résistant à l'hydrolyse.

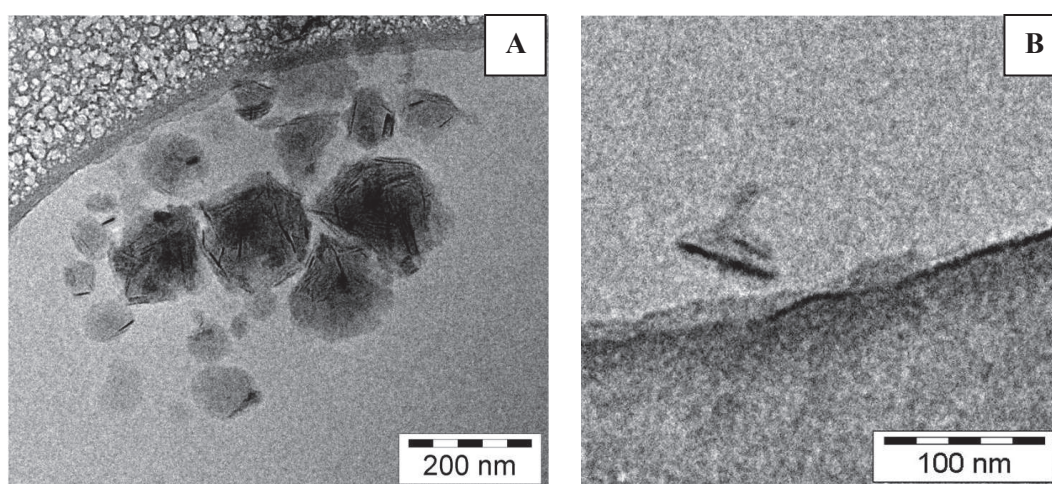


Figure 6. Images TEM de latex obtenus après la polymérisation d'un mélange MA/BA (80/20 % en masse) par REEP avec des HDL-NO₃ et avec 3.0 mmol L⁻¹ de P(AA-co-BA)-CTPPA ($M_n = 3500$ g mol⁻¹) à pH = 8,0 (a) sans et (b) avec une étape de sonication.

En comparant les résultats obtenus avec les plaquettes d'HDL avec ceux obtenus avec les nanotubes d'Imogolite, il est possible de conclure que les interactions entre le macroRAFT et la surface, ainsi que

la nature chimique de la surface inorganique, jouent un rôle fondamental dans l'encapsulation. En utilisant les mêmes conditions de synthèse (i.e. même macroRAFT, même pH, même composition de monomères hydrophobes), des morphologies différentes ont été obtenues avec les HDL ou les Imogolites. Des nanotubes d'Imogolite décorés de particules de polymère ont été obtenus à ce pH, ce qui a été attribué à la faible quantité de macroRAFT adsorbé et la faible mouillabilité de la surface. Au même pH, deux fois plus de macroRAFT a été adsorbé à la surface des HDL, ce qui a conduit à une meilleure mouillabilité des plaquettes et à une meilleure affinité entre la surface et le monomère hydrophobe, ces deux facteurs contribuant à l'encapsulation des plaquettes.

Conclusions générales et perspectives

Cette thèse avait pour objectif la synthèse de latex hybrides de polymère/nanotubes d'Imogolite et de polymère/hydroxydes double lamellaire (HDL) capables de former des films présentant une distribution homogène des charges dans la matrice polymère et une microstructure contrôlée. Pour synthétiser des latex hybrides filmifiables sans tensioactif, nous avons choisi de travailler avec la technique d'encapsulation par « macroRAFT-assisted encapsulating emulsion polymerization » (REEP).

Dans le premier chapitre, les avantages résultants de l'utilisation de particules anisotropes comme charge dans des matrices polymère a été étudié. Les différentes voies d'obtention de matériaux hybrides polymère/inorganique ont été également revues. L'étude s'est focalisée sur les exemples de procédé réalisé en milieux aqueux dispersé, dans lesquels les techniques de polymérisation radicalaire contrôlée (NMP, ATRP ou RAFT) ont été utilisées.

Le chapitre II décrit l'élaboration de latex hybrides polymère/nanotubes d'Imogolite par utilisation de la technique REEP. Tout d'abord, une étude bibliographique sur la structure, la synthèse et les caractéristiques physicochimiques des nanotubes d'Imogolite a été présentée, pour comprendre les propriétés de surface de ces objets. Ces nanotubes d'Imogolite sont composés d'une structure tubulaire d'aluminogermanate avec quelques nanomètre de diamètre (~2 – 5 nm). La longueur des tubes est très variable, pouvant aller d'une dizaine de nanomètres à plusieurs centaines de nanomètres. Ils sont composé d'une couche externe d'hydroxyde d'aluminium type Gibbsite ($\text{Al}(\text{OH})_3$) chargée positivement, et d'une couche interne d'hydroxyde de silicium chargée négativement. Ces tubes sont trouvés naturellement en faible quantité dans les sols volcaniques, mais ils peuvent être aussi synthétisés en laboratoire. Des analogues synthétiques de ces tubes, où les atomes de silicium sont remplacés par des atomes de germanium, ont pu être synthétisés récemment en grande quantité. Ces analogues, ci référencé Ge-Imogolite, possèdent la formule générale suivante : $(\text{OH})_3\text{Al}_2\text{O}_3\text{GeOH}$. Le succès de cette synthèse a ouvert des nouvelles possibilités pour l'utilisation et le développement de ce

type de particule inorganique dans la science de matériaux. Des nanotubes de Ge-Imogolite ont été utilisés dans le présent travail. L'utilisation de nanotubes d'Imogolite pour la production de nanocomposites polymérique présente un grand intérêt grâce à son aspect de forme, sa surface spécifique développée et sa rigidité. La grande majorité des travaux reportés auparavant concernant la production de nanocomposites polymère/Imogolite a utilisé des Si-Imogolite avec des polymères du type PVA, PMAA or PAAm quasi exclusivement. Des exemples de production de nanocomposite polymère/Imogolite en milieux aqueux dispersé utilisant la polymérisation radicalaire contrôlée n'ont pas été trouvés.

Après cette première partie bibliographique, la partie expérimentale a été présentée. Dans un premier temps, les agents macroRAFT contenant des unités d'acide (meth)acrylique et de *n*-(meth)acrylate de butyle ont été synthétisés par polymérisation RAFT en solution. Ces copolymères ont présenté des masses molaires contrôlées et une distribution de masses molaires étroite. Les copolymères à base de monomères méthacryliques ont été écartés après une étude préliminaire d'encapsulation des nanotubes, à cause de problèmes de stabilité. Ensuite, l'adsorption des macroRAFTs acryliques à la surface des Imogolites a été étudiée. Les paramètres qui ont plus fortement influencé l'adsorption du copolymère à la surface des tubes ont été la présence d'unités BA dans la chaîne du copolymère, la masse molaire du macroRAFT et le pH du milieu. Les chaînes contenant des unités BA ont montré une tendance à s'adsorber en plus grande quantité à la surface, comparées aux chaînes composées de pur AA, surtout à des faibles pH. Cependant, à faible pH (i.e. 6.0), les unités carboxyliques du macroRAFT sont moins chargées, ce qui diminue le pouvoir stabilisant des copolymères. De ce fait, des agrégats de nanotubes d'Imogolite sont formés. Pour rendre la suspension stable, une étape de sonification a été nécessaire.

Ces suspensions d'Imogolite/polymère ont ensuite participé à la polymérisation d'un mélange de monomères hydrophobes : méthacrylate de méthyle/acrylate de *n*-butyle (MMA/BA), à 80/20 wt%, en semi-batch suivant la technique REEP. L'effet de différents paramètres, comme la nature, la masse molaire et la concentration du macroRAFT, la concentration en Imogolite, le pH du milieu et la composition du mélange de monomères hydrophobes sur la morphologie finale des latex a été évalué. Un des facteurs clé pour obtenir l'encapsulation des tubes s'est avéré être l'adsorption du macroRAFT à la surface des nanotubes. Ce facteur affecte directement la mouillabilité des particules inorganiques, ce qui contrôle aussi son affinité avec les monomères hydrophobes. Ce paramètre a pu être réglé en jouant avec la présence des unités BA dans la chaîne du macroRAFT et en changeant le pH du milieu. Pour contrôler la taille des agrégats d'Imogolite formé à faible pH, des expériences ont été faites où le procédé de mélange (ordre d'ajout) et l'interaction entre le macroRAFT et les nanotubes d'Imogolite ont été manipulés. Cependant, la complexité du système, c.à.d. la présence d'interaction hydrophobe et

la limite de solubilité du macroRAFT, a rendu le procédé très difficile à contrôler. En variant l'ordre d'ajout, la taille des agrégats a pu être diminuée, mais leur formation n'a pas pu être supprimée.

Afin d'obtenir des latex hybrides filmifiants, contenant soit des nanotubes d'Imogolite décorés de particules de polymère, soit des agrégats d'Imogolite encapsulés, la composition du mélange de monomères hydrophobes a été varié. La composition initialement fixée à MMA/BA (80/20 wt%) a été remplacée par un mélange MMA/BA (50/50 wt%), et polymérisé à pH 8,0 et 6,0. Nous avons aussi testé un nouveau mélange de monomères : STY/BA, à deux compositions différentes : 70/30 wt% et 50/50 wt%. Le mélange STY/BA a été polymérisé à pH 8,0, quel que soit la composition. La nature du monomère eut une influence importante sur la morphologie finale obtenue. Les expériences réalisées avec du styrène ont formé des agrégats irréguliers d'Imogolite, et ces agrégats ont été trouvés encapsulés à la fin de la polymérisation, quel que soit la composition utilisée. En plus des agrégats encapsulés, des fibres et des vésicules ont été aussi formées. Ces dernières sont originaires du procédé d'auto-assemblage qui a lieu dans la phase aqueuse, parallèlement à la polymérisation qui a lieu à la surface des particules. Quand le mélange MMA/BA a été utilisé à 50/50 wt% à pH 8,0, des nanotubes d'Imogolite décorés de particules de polymère ont été formés, ainsi que des fibres et des vésicules. Le même mélange de monomères, à la même composition, quand polymérisé à pH 6,0, a généré des agrégats d'Imogolite encapsulés plus des fibres et des vésicules. Le procédé d'auto-assemblage des copolymères à bloc amphiphiles qui sont formés pendant la polymérisation, particulièrement dans la phase aqueuse, a été affecté par les changements dans la fraction volumique de chaque bloque. Cette dernière varie avec la nature du monomère. Ces changements ont mené à la formation de morphologies inattendues (i.e. fibres et vésicules). La formation de ce type de morphologie a pu être évitée en remplaçant le MMA par de l'acrylate de méthyle (MA). Il s'agit d'un monomère avec une solubilité dans l'eau similaire à celle du MMA, mais avec une T_g du homopolymère correspondant assez inférieure (~ 8 °C). Avec ce monomère, la composition a pu être conservée à 80/20 wt%, dans laquelle des fibres et des vésicules n'étaient pas formées, formant un latex hybride filmifiant contenant soit des nanotubes décorés de particules de polymère, soit des agrégats d'Imogolite encapsulés.

A partir de latex hybrides contenant une des deux morphologies, des films ont été formés par simple évaporation de l'eau. Les résultats TEM de la coupe mince des films ont révélé une distribution uniforme des tubes tout le long de la matrice polymère. Les latex contenant des nanotubes décorés ont formés des films avec les tubes individuellement distribués, tandis que les latex contenant des agrégats encapsulés ont formés des films avec une distribution homogène des agrégats tout au long de la matrice. Les films produits à partir de latex contenant des nanotubes très longs (longueur moyenne = 500 nm) ont montré une orientation partielle de tubes parallèlement au plan du film. Cet alignement a été attribué à l'effet de la force gravitationnelle sur les tubes. Possédant un facteur de forme important,

ces tubes ont tendance à arranger son plus grand axe avec celui du tube voisin, ce qui résulte dans l'alignement partiel des Imogolite dans la matrice.

Les modules de résistance mécanique plus élevés ont été retrouvés dans les films permettant la formation d'un réseau percolant. La couche épaisse de polymère autour des agrégats encapsulés a empêché l'effet de la percolation, conduisant à des modules inférieurs pour ces échantillons.

Pour l'encapsulation des HDL, présenté dans le chapitre III, deux voies ont été testées : le *grafting from*, dans lequel un polymère soluble dans le milieu a été généré à partir de la surface formant une structure cœur/couronne; et la technique REEP, dans laquelle un polymère non soluble dans le milieu a été formé autour des particules formant une structure cœur/écorce. Tout d'abord, des particules colloïdales d'HDL contenant des ions NO_3^- ou CO_3^{2-} dans les domaines interlamellaires ont été synthétisées. Ces particules (phases) ont été ensuite modifiées avec des agents RAFT ou macroRAFT par deux voies : coprécipitation hybride in situ ou échange anionique. Des phases HDL-RAFT bien définies ont été produites par la première voie, et ces phases ont été utilisées pour les études de *grafting from*. L'agent macroRAFT a pu être adsorbé ou intercalé par la seconde voie, et les phases HDL/macroRAFT obtenues ont été employées dans les polymérisations suivant la REEP.

Les particules hybrides cœur/couronne avec un cœur HDL et une couronne de poly(4-acryloylmorpholine) (PNAM) n'ont pas pu être obtenues par *grafting from*. Les résultats DRX ont montré que la polymérisation a vraisemblablement commencé à la surface des particules, mais les chaînes ont été rapidement échangées par des ions CO_3^{2-} et transférées à la phase aqueuse. Par conséquent, les particules ont perdu leur stabilité.

Pour la voie REEP, deux phases LDH- NO_3^- et LDH- CO_3^{2-} ont été modifiées avec de l'agent macroRAFT par échange anionique. Les phases LDH- NO_3^- ont généré des particules hybrides avec du macroRAFT adsorbé et intercalé, tandis que les phases LDH- CO_3^{2-} ont formé des phases hybrides avec le macroRAFT seulement adsorbé à la surface. Cette différence provient du fait que les ions CO_3^{2-} sont difficilement échangés dans des conditions douces. Les suspensions stables de HDL/macroRAFT ont participé à la polymérisation du mélange de monomères MA/BA, 80/20 wt%, comme précédemment optimisé, et la polymérisation a été réalisée à pH 8.0. Toutes les deux phases, avec le macroRAFT adsorbé et adsorbé/intercalé, ont formé des latex avec des plaquettes encapsulées. Les phases contenant de l'agent macroRAFT dans les domaines interlamellaires ont formé des agrégats, qui ont été trouvés encapsulés à la fin de la polymérisation. Les phases contenant le macroRAFT adsorbé exclusivement à la surface ont généré des latex avec des plaquettes individuellement encapsulées.

C'est intéressant de constater que la technique REEP appliquée à deux charges inorganiques différentes, malgré l'utilisation du même macroRAFT et des mêmes conditions de polymérisation, a

généralisé des morphologies substantiellement différentes. Ceci mène à la conclusion que le succès de l'encapsulation ne dépend pas seulement de la nature et de la composition de l'agent macroRAFT, mais aussi de son interaction avec la surface ainsi que des caractéristiques chimiques des particules inorganiques. Au long de tous les études réalisées pendant cette thèse, les paramètres mis en évidence comme étant les plus influents sur l'encapsulation ont été : la présence d'unités BA dans la chaîne du macroRAFT et le pH du milieu, les deux contribuant à l'augmentation de l'adsorption du macroRAFT à la surface ; ainsi que la nature des interactions entre la surface inorganique et le macroRAFT, celle-ci étant définie par la nature du macroRAFT et la chimie de surface des charges inorganiques. Tous ces paramètres peuvent être corrélés ensemble dans un seul paramètre : le nombre de fonctionnalités RAFT par particule. En effet, en comparant les résultats obtenus avec les nanotubes d'Imogolite et les plaquettes d'HDL, la quantité de macroRAFT adsorbé à la surface des HDL est au moins deux fois plus élevée que celle adsorbé à la surface des Imogolites sous les mêmes conditions. Ceci signifie qu'une concentration considérablement plus élevée de fonctionnalités RAFT est présente par particule d'HDL. Toutefois, contrairement à ce qui est attesté dans la littérature, l'utilisation d'un macroRAFT de faible masse molaire n'est pas suffisante pour garantir un grand nombre d'unités RAFT par particule, et ainsi l'encapsulation des charges. Selon la nature de la charge inorganique, l'adsorption de polymères de faible masse molaire peut être très faible, ce qui ne favorise pas l'encapsulation.

Enfin, il a été montré dans cette thèse que la technique de « macroRAFT-assisted encapsulating emulsion polymerization » est un outil qui permet l'encapsulation de diverses charges inorganiques, produisant des matériaux nanocomposites aux microstructures contrôlées. Elle peut également être considérée comme une technique universelle, à condition que l'agent macroRAFT adapté pour chaque charge inorganique soit conçu.

References:

1. Bourgeat-Lami, E.; Lansalot, M. *Hybrid Latex Particles: Preparation with (Mini) Emulsion Polymerization* **2010**, 233, 53-123.
2. Tang, Z. Y.; Kotov, N. A. *Advanced Materials* **2005**, 17, (8), 951-962.
3. Bourgeat-Lami, E. *Journal of Nanoscience and Nanotechnology* **2002**, 2, (1), 1-24.
4. Bourgeat-Lami, E.; Duguet, E., Polymer Encapsulation of Inorganic Particles. In *Functional Coatings*, Ghosh, S. K., Ed. Wiley-VCH Verlag GmbH & Co. KGaA: 2006; pp 85-152.
5. Qiu, J.; Charleux, B.; Matyjaszewski, K. *Progress in Polymer Science* **2001**, 26, (10), 2083-2134.
6. Cunningham, M. F. *Progress in Polymer Science* **2008**, 33, (4), 365-398.
7. McLeary, J. B.; Klumperman, B. *Soft Matter* **2006**, 2, (1), 45-53.
8. Charleux, B.; D'Agosto, F.; Delaittre, G. *Hybrid Latex Particles: Preparation with (Mini) Emulsion Polymerization* **2010**, 233, 125-183.
9. Nguyen, D.; Zondanos, H. S.; Farrugia, J. M.; Serelis, A. K.; Such, C. H.; Hawket, B. S. *Langmuir* **2008**, 24, (5), 2140-2150.
10. Nguyen, D.; Such, C.; Hawket, B. *Journal of Polymer Science Part a-Polymer Chemistry* **2012**, 50, (2), 346-352.
11. Ali, S. I.; Heuts, J. P. A.; Hawket, B. S.; van Herk, A. M. *Langmuir* **2009**, 25, (18), 10523-10533.
12. Zgheib, N.; Putaux, J.-L.; Thill, A.; Bourgeat-Lami, E.; D'Agosto, F.; Lansalot, M. *Polymer Chemistry* **2013**, 4, (3), 607-614.
13. Zhong, W.; Zeuna, J. N.; Claverie, J. P. *Journal of Polymer Science Part a-Polymer Chemistry* **2012**, 50, (21), 4403-4407.
14. Nguyen, D.; Such, C. H.; Hawket, B. S. *Journal of Polymer Science Part a-Polymer Chemistry* **2013**, 51, (2), 250-257.